

Formation and Composition of Planets around Stars of Different Masses

Inaugural dissertation
of the Faculty of Science

University of Bern

handed in by

Remo Burn

from Trub BE

2020

Supervisors of the doctoral thesis

Prof. Dr. Yann Alibert and Prof. Dr. Willy Benz

Physics Institute of the University of Bern

Formation and Composition of Planets around Stars of Different Masses

Inaugural dissertation
of the Faculty of Science

University of Bern

handed in by

Remo Burn

from Trub BE

2020

Supervisors of the doctoral thesis

Prof. Dr. Yann Alibert and Prof. Dr. Willy Benz

Physics Institute of the University of Bern

Accepted by the Faculty of Science.

Bern, June 12, 2020

The Dean

Prof. Dr. Zoltan Balogh

Contents

Acknowledgments	v
1. Introduction	1
1.1. Thesis overview	1
1.2. Exoplanetary observations	2
1.2.1. Radial velocity	2
1.2.2. Transit	4
1.2.3. Microlensing	6
1.2.4. Direct imaging	7
1.2.5. Other methods	9
1.3. Exoplanet demographics	12
1.4. The cradle of planets: Protoplanetary disks	15
1.4.1. Disk formation	15
1.4.2. Types of disks	16
1.4.3. Minimum mass Solar nebula	17
1.4.4. Disk lifetimes	20
1.4.5. Stellar accretion rates	21
1.4.6. Dust observations in the ALMA era	21
1.4.7. Scattered light	24
2. Models of disk processes	27
2.1. Vertical structure	27
2.2. Azimuthal velocities	29
2.2.1. Gas angular velocity	30
2.2.2. Dust angular velocity	31
2.3. Disk evolution	31
2.3.1. The viscous accretion rate	32
2.3.2. Viscosity	32
2.4. Thermal physics	34
2.4.1. Irradiated razor-thin disk	34
2.4.2. Viscous heating	35
2.5. Composition of disks	38
2.6. Photo-evaporation of disks	41
2.6.1. X-ray luminosity	44
2.6.2. Numerical X-Ray photo-evaporation models	44
2.6.3. Photo-evaporation outlook	49
2.7. The disk modeling challenge	50

2.8.	Radial drift	55
2.9.	Distribution of planetesimals in protoplanetary disks	58
2.9.1.	Size distribution	58
2.9.2.	Eccentricity and inclination distribution	60
2.9.3.	Eccentricity and inclination damping and stirring	61
2.10.	Frequency of collisions and accretion rates	67
2.10.1.	Particle in a Box	67
2.10.2.	Gravitational focusing	68
2.10.3.	Orbiting particles	70
2.11.	Letter I: The formation of Jupiter by hybrid pebble-planetesimal accretion	75
3.	Ablation of drifting bodies	93
3.1.	Evidence on the structure of cometary nuclei	93
3.2.	Cometary nucleus models	94
3.2.1.	Energy conservation	95
3.2.2.	Mass conservation	96
3.2.3.	Heat conduction	96
3.3.	Paper I: Radial drift and concurrent ablation of boulder-sized objects	98
4.	Planet formation	117
4.1.	Growth stages	117
4.2.	Envelope structure	118
4.2.1.	Governing equations	119
4.2.2.	Boundary conditions	120
4.2.3.	Maximum gas accretion	121
4.2.4.	Attached phase	122
4.2.5.	Detached phase	122
4.3.	Orbital migration	123
4.3.1.	Type I	124
4.3.2.	Type II	126
4.4.	N-body interactions	127
4.4.1.	Close encounters	127
4.4.2.	Mean motion resonances	128
5.	Planetary population synthesis	131
5.1.	Principle	131
5.2.	Randomized initial conditions	132
5.3.	Fixed parameters	133
5.4.	Paper II: Pebbles versus planetesimals: the outcomes of population synthesis models	138
5.4.1.	Pebble accretion	139
5.4.2.	Project specific changes to the Bern model of planet formation	139

5.5. Letter II: A water budget dichotomy of rocky protoplanets from ^{26}Al -heating	159
5.6. Paper III: NGPPS IV. Planetary systems around low-mass stars	168
6. Conclusion and outlook	189
A. Derivations and concepts	211
A.1. Disk gas angular velocity as a function of z	211
A.2. Derivation of the disk evolution equation	212
A.3. Numerical scheme for disk evolution modeling	214
A.4. Elliptic integrals	215
A.5. Analytical accretion rate approximations	216
A.6. Disk Mass – Sigma Relation	217
B. Declaration of consent and curriculum vitae	219

Acknowledgments

First of all, I would like to thank Prof. Willy Benz for his decision to trust me with a position and his continuous support during all the years. Willy serves as a prime example of how to be a group manager, researcher, and advisor but also a colleague to all of us. I feel honored to be part of the last group of students he will supervise before gaining more liberty as an emeritus.

To Prof. Yann Alibert, I am deeply thankful for his everyday advice and guidance on how to successfully complete research projects. He let me enjoy a lot of freedom to satisfy my curiosity while still leading me towards successfully finishing tasks. With a healthy portion of humor but even more scientific insight it was a fun, enjoyable, and enlightening experience to be part of his group.

I would like to thank Prof. Shigeru Ida, who kindly accepted to referee this thesis. It is a privilege to receive feedback from an external referee as distinguished in our field.

Many thanks to Dr. Ulysse Marboeuf who shared his expertise and tools with me when I was very new to the whole field.

Another set of thanks go to Prof. Christoph Mordasini and Dr. Alexandre Emshuber for guiding me towards becoming a proper user and developer of the *Bern model*, dubbed the *Beast* for a reason. They tamed the beast for me and I learned more about planet formation than I ever thought would be there to learn. I am also thankful to Christoph for giving me the opportunity to collaborate and get in contact with groups all around the world.

Being part of a group of three students that started their PhD at the same time, I would like to thank Jonas Haldemann and Natacha Brügger for countless interesting discussions and collaborations.

Furthermore, I would like to thank the whole TAPS group at the University of Bern. They bore with me chairing our weekly meeting and it was a pleasure to come to work everyday to meet everybody. I treasure the whole group as researchers and friends.

I acknowledge the financial support from the Swiss Society for Astrophysics and Astronomy and the NCCR PlanetS to travel to interesting meetings in Switzerland and abroad.

I would also like to thank the Swiss National Science foundation who financially supported this project and decided to provide the opportunity to continue to do research at the Max-Planck institute in Heidelberg and I'm looking forward to joining my collaborators that already became friends there.

Ich danke meiner Familie für ihre Unterstützung und Geduld während der langen Dauer dieser Arbeit und meines gesamten Lebens. Ausserdem danke ich meinen

ehemaligen Mitbewohnern Demian Halter und Stephanie Vögeli für ihre Geduld im Alltag und ihre Freundschaft. Euch allen ein grosses Mersi!

Zu guter Letzt möchte ich meiner Partnerin Simona Busco für ihre Liebe und unglaublich ausdauernde, ununterbrochene Unterstützung danken. Grazie!

Thank you very much.

1. Introduction

For centuries, people wondered if the Earth is a unique planet and what life could look like on other worlds. Would it be similar to our life? Could life be submerged in liquids other than water? The greek philosopher Epicurus of Samos wrote approximately 300 BC that there must be multiple "worlds" and that "in all worlds there are living creatures and plants and other things we see in this world; for indeed no one could prove that in a world of one kind there might or might not have been the kinds of seeds from which living things and plants and all the rest of things we see are composed, and that in a world of another kind they could not have been" (Oates, 1940, p. 12-13). Nowadays, these questions move from the realm of philosophy to natural sciences. In physics, we can at least address the question of how likely the formation of planets similar to the Earth is and what they consist of.

For these reasons, this thesis is dedicated to the question of how and with what compositions planets form around different stars. Research like this is mainly motivated by the outstanding discoveries of numerous *exoplanets* in recent years. According to the definition of the International Astronomical Union (IAU), "a *planet* is a celestial body that (a) is in orbit around the Sun, (b) has sufficient mass for its self-gravity to overcome rigid body forces so that it assumes a hydrostatic equilibrium (nearly round) shape, and (c) has cleared the neighborhood around its orbit."¹ Extending this definition to different stars than our Sun analogously defines an *exoplanet*. However, for exoplanets, the current working definition includes an upper-mass limit of $\sim 13 M_{\text{Jup}}$, the boundary at which deuterium starts to fuse in the interior of the object and it would be considered a *brown dwarf*.²

The first exoplanet around a Sun-like star – the bright star 51 Pegasi – was observed by Swiss astronomers Michel Mayor and his PhD-student Didier Queloz in 1995 (Mayor & Queloz, 1995) and is called 51 Pegasi b (51 Peg b). For this groundbreaking discovery, they were awarded the Nobel Prize in Physics in 2019, which highlights the recognition that the field of exoplanetary sciences has gained since.

1.1. Thesis overview

In the remainder of this introduction, we review exoplanet and protoplanetary disk observations. Both, the techniques and the gained overall picture will be discussed. Having established the current knowledge of the ground truth, we will move to how

¹Definition from the IAU General Assembly in 2006 (iau.org/news/pressreleases/detail/iau0603/)

²Definition by the Working Group on Extrasolar Planets of the IAU (see their position statement astro.berkeley.edu/~basri/defineplanet/IAU-WGExSP.htm)

protoplanetary disks can be modeled in Chapter 2. There, we focus on one dimensional models, which can be used to provide input to planet formation studies. This chapter also includes processes that occur in protoplanetary disks such as collisions and drift of solid bodies. In Chapter 3, we focus on the sublimation of ice on a solid body in the framework of a cometary nucleus model. Chapter 4 is dedicated to summarizing the relevant processes of the used planet formation model. Afterwards, we introduce the concept of planetary population synthesis in Chapter 5 where we also summarize pebble accretion, ^{26}Al heating of planetesimals and changes due to the stellar mass. The focus remains on the impact of these parameters on the resulting synthetic planetary population. Finally, we conclude and give an outlook on future works in Chapter 6.

1.2. Exoplanetary observations

There exist several ways to determine the presence of a planet in orbit around a different star. Here, we will briefly describe the major exoplanet detection techniques. All of the methods do have their inherent advantages as well as disadvantages and measure different quantities. In addition, we will also quickly review future prospects and major upcoming missions.

1.2.1. Radial velocity

The first exoplanet around a Sun-like star was discovered using the *radial-velocity* (RV) method (Mayor & Queloz, 1995). This approach relies on the precise measurement of the wavelengths of multiple spectral lines in the spectrum of a star. The findings can then be used to determine the velocity of the star respective to the line-of-sight of the observer. This is possible because the wavelength of all the spectral lines is minutely shifted as the star moves due to the Doppler shift. If there are periodic variations over day- or year-timescales, the derived radial velocity component can be attributed to an object gravitationally pulling on the observable star. Mayor & Queloz (1995) measured the velocity of 51 Pegasi to be on the order of a few tens of ms^{-1} (see the original data in Fig. 1.1). They could only reach this level of precision thanks to their new high-resolution spectrograph ELODIE at the observatory of Haute-Provence in France. Having a higher spectral resolution helps to determine minute changes of spectral-line positions in addition to resolving more lines.

Nowadays, the best facilities reach radial-velocity precisions of 10 cm s^{-1} (Pepe et al., 2014). Therefore, the radial-velocity method allows for detection of considerably less massive planets than 51 Pegasi b. Especially for close-in planets, the radial-velocity method can discover planets with masses as low as the mass of the Earth. The lowest-mass planet discovered by RV orbits the star YZ Ceti (Astudillo-Defru et al., 2017) and has a minimum mass below one Earth mass ($0.7 M_{\oplus}$). This star is itself very small with a mass of $(0.14 \pm 0.01) M_{\odot}$ (Schweitzer et al., 2019, M_{\odot} : Solar mass). As a lighter star is affected more by the gravity of a planet with a given

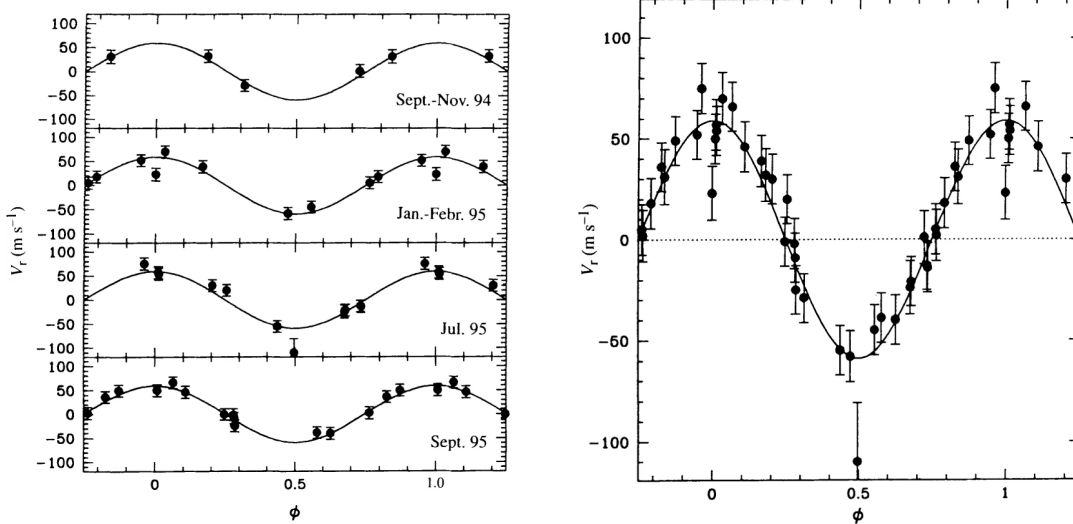


Figure 1.1.: Original data for the radial velocity of 51 Peg as a function of a fitted planetary orbital period of 4.229 days by [Mayor & Queloz \(1995\)](#). The left panel shows the radial velocity measured at four different times, whereas the right panel shows the same data but phase folded and corrected for a long-term trend.

mass than a heavier star, this shows that the smallest planets can be discovered by RV around the lightest stars. Therefore, this motivates the study of planet formation around low-mass stars.

Due to the nature of the RV technique, information can be gained on the mass of the planet multiplied by the sine of the inclination of the planet's orbit with respect to the line-of-sight ($M \sin i$). Therefore, this value is a lower limit to the true mass of the exoplanet and would only be exact if the orbit of the planet was exactly aligned with our line-of-sight ($\sin i = 1$). This limitation can rarely be overcome if the inclination of the orbit can be measured. For multi-planetary systems, N -body modeling of the gravitational interactions between the planets can help to constrain the true masses. Sometimes repeated astrometry measurements of the star, that is measuring the position of the star in the sky to a very high precision, can reveal the motion of the star in the plane normal to the line-of-sight. Thus, this is in principle ideal to resolve the issue. However, most often, neither of the two are possible due to too faint signals compared to the precision of the instruments involved. Therefore, $M \sin i$ values have to be used for population-wide comparisons of theory and observations.

Another downside to the radial velocity exoplanet dataset is that no well characterized surveys were conducted. Instead, the limits to detections are different for each star. This is mainly due to time and weather constraints on the ground-based observational facilities that have to be used. Therefore, inferring clear statistical occurrence rates of exoplanets at lower masses becomes almost impossible. The best available census of exoplanets with RV was conducted by [Mayor et al. \(2011\)](#) and has not been updated since.

1.2.2. Transit

The approach with which most exoplanet candidates were found so far, is not RV but the *transit* method. There, the light of the star is continuously measured to a very high precision. If a planet passes in front of the star with respect to the observer, the measured flux decreases. This event is called a transit. As soon as the exoplanet leaves the stellar disk again, the flux increases to the previous value (see Fig. 1.2). Therefore, such a transit event leaves a unique signature in the *lightcurve*, which is the measured flux as a function of time. This kind of measurement is sensitive to the ratio of the radius of the planet to the radius of the star. This is because the transit depth, which is the decrease in the lightcurve during the transit, is directly proportional to the relative area that is covered by the planet. Therefore, good knowledge on the stellar properties are required to calculate planetary radii. In fact, before the *Gaia* mission, knowledge on the stellar radius was the limiting factor that inhibited finding more precise planetary radii (Noteworthy is the California Kepler Survey that adressed this issue, see [Petigura et al., 2017](#); [Fulton et al., 2017](#)).

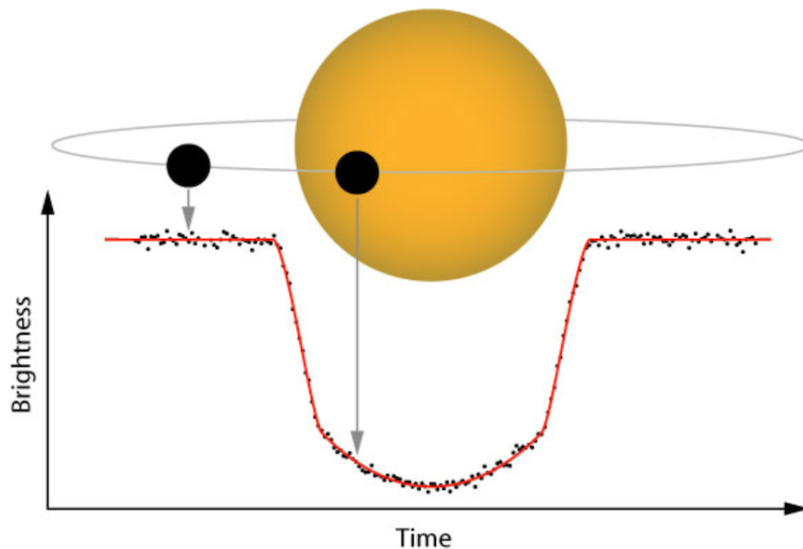


Figure 1.2.: Schematic representation of a transiting planet and the corresponding observed brightness as a function of time (lightcurve). Image credit: NASA

The first successful transit measurement of the previously known exoplanet HD 209458 b was conducted by [Charbonneau et al. \(1999\)](#). Transit signals of exoplanets as large and close-in as HD 209458 b are very significant. A 9.9 cm aperture telescope was large enough to clearly detect the transit from the ground. A key data-analysis step is to remove noise introduced by the Earth's atmosphere by comparing the flux of the target star to multiple other background stars which show similar variations.

Even though transit measurements can be done using telescopes on the ground, they are most successfully performed with space-based telescopes. In space, the obtained lightcurves are free of atmospheric noise, which leads to a higher precision.

The main driver of discoveries using the transit method in the past few years was the *Kepler* space telescope (Borucki et al., 2010) which provided over 4000 exoplanetary candidates (Thompson et al., 2016, 2018).

Even though transit surveys were very successful, the major downside of the transit method is that it requires the planet to move in front of the stellar disk. Due to the orbital geometry, this happens quite frequently for close-in planets but becomes very unlikely to be observable for planets more distant to their host star. Therefore, transit surveys provide very detailed information only on the particular subset of close-in exoplanets.

Furthermore, to confirm an exoplanet discovery in a regime where the signal becomes comparable to the noise-level of the instrument, multiple transit events have to be measured and the data has to be stacked. In particular, this is required to find the smallest exoplanets. However, this necessitates an observation time that is multiple times the orbital period of the planet. *Kepler* was observing the same stars for almost four years. Therefore, it yields data for small planets with orbital periods below approximately one year. Moreover, *Kepler* was unique in this regard as current transit missions (like *TESS*, Ricker et al., 2014) observe the same stars for a shorter duration. Overall, the sensitivity of the transit method drops much faster with separation from the star compared to RV but it is nevertheless the most likely method to get information on the physical size of exoplanets. In Figs. 1.4 and 1.5 these trends are clearly visible.

A major advantage of the transit technique are the constraints on the atmospheric composition that can be gained. Measuring the spectrum of a star during and out of a planetary transit allows for taking the difference between the two observations. Therefore, the light passing through the planetary atmosphere – if present – can be analyzed. Spectral lines can then be attributed to molecules in the exoplanetary atmosphere. This analysis called *transmission spectroscopy* was done successfully in low-resolution for a number of large, transiting planets using the *Hubble* and *Spitzer* space telescopes (Sing et al., 2016). A recent outstanding discovery was the detection of water vapor on K2-18 b, a $8M_{\oplus}$ mass planet receiving similar stellar flux as the Earth (Benneke et al., 2019; Tsiaras et al., 2019). K2-18 b most likely also contains a lot of hydrogen and helium and orbits a star with a mass of only 0.36 times the stellar mass. Therefore, it is a world quite different to our Earth. Nevertheless, this discovery highlights the power of transit transmission spectroscopy – especially for lower stellar masses.

Even more challenging, but also noteworthy, are observations of secondary transits. A secondary transit occurs when the planet moves behind the star with respect to the observers' line-of-sight. Then, the light that is reflected or emitted by the planet is subtracted from the total measured flux of the star and its planets. For close-in giant planets, this signal is observable and further constrains the planetary composition (Charbonneau et al., 2005, for a recent review see Alonso, 2018).

1.2.3. Microlensing

The third of the major exoplanet detection methods makes use of the *microlensing* effect. Different from the two other methods, not the light of the exoplanet host star is observed but the light of a star in the background of the exoplanetary system. This background star is termed the *source*. The light of the source is then bent due to the gravity of the exoplanetary system, which acts as gravitational *lens*. This process was already described in terms of Newtonian gravity by [von Soldner \(1804\)](#) and within the framework of special relativity by [Einstein \(1911\)](#). With the addition of corrections due to general relativity, the theoretical description was completed later on ([Einstein, 1936](#)). However, at these times, the authors concluded that the effect should not be observable for stars other than the Sun. Only much later, two images of the same quasar were found by [Walsh et al. \(1979\)](#).

In the case of exoplanetary sciences, a normal star and its orbiting planets are not massive enough to lead to a resolvable mirror object. Instead, what can be observed is a magnification of the combined light of the lens and the source. If resolved over time, the magnification might show signatures that are inconsistent with the lens being a single point mass. Instead, if smaller magnitude brightening events are observed, these short, tiny variations can be attributed to exoplanets in the lens system. Therefore, information about the mass-ratio of the planet mass to the host star mass can be derived ([Wambsganss, 2006](#)). Additionally, the timing of the event gives information about the current projected separation of the planet perpendicular to the line-of-sight of the observer. However, if the distance of the lens and the source systems to the observer are not known, this separation cannot be precisely determined.

The first definite observation of a microlensing event caused by an exoplanet was conducted by [Bond et al. \(2004\)](#) in 2003 (see also [Bennett et al., 2006](#); [Bond, 2012](#)). Currently, planets discovered by microlensing are however still quite rare (see [Fig. 1.4](#)) and follow-up with updated observational facilities is not possible because the events are not recurring. After a short period spanning over a few days, where the source and the lens are aligned, they move apart forever and most often the planets cannot be observed with other techniques. Mainly, this is because the majority of the sources are located towards the center of the galaxy and the strongest lenses correspondingly at half the distance to the galactic center (~ 4 kpc). This is much further away than the other known exoplanetary systems, which are mostly located in the Solar neighborhood (~ 30 pc). Even the stars observed by *Kepler*, which are further away, are considerably closer with distances of ~ 1 kpc.

The main reason why microlensing can be considered a major exoplanet-detection method is because in the future, the numbers of detections are thought to increase substantially. The next NASA flagship space telescope, WFIRST, will spend a lot of its time looking for microlensing events. WFIRST aims to reach a resolution similar to the *Hubble* space telescope, but with a much larger field of view. The search for exoplanets using the microlensing technique is scheduled to take place for six 72-day periods ([Spergel et al., 2015](#)). These observations will yield ~ 1400 exoplanet

discoveries (Penny et al., 2019).

For statistical studies, the WFIRST yield will prove to be very beneficial. This is mainly because the sensitivity of the microlensing technique is highest at planetary separations close to the Einstein radius $R_E = D_L \sqrt{\frac{4GM_L}{c^2} \left(\frac{1}{D_L} - \frac{1}{D_S} \right)}$, where D is the distance to the star, and the subscripts L and S stand for the lens and the source respectively. Typically, $R_E \approx 3.5 \text{ au} \sqrt{M_L/M_\odot}$. Therefore, microlensing is not most sensitive to the regions closest to the star like the RV and transit methods. Instead, it provides information about planets located further away from the star at distances comparable to the water iceline. As gravitational lensing events are not repeatable, it provides purely statistical properties of the exoplanet population and can rarely be used to characterize individual exoplanets.

1.2.4. Direct imaging

Maybe the most straightforward method to detect an exoplanet is to look for the light originating from the exoplanetary surface. This can be reflected starlight in optical or emitted radiation in infrared wavelengths. The main challenge to detect signals from exoplanets is not the sensitivity of the instruments but to resolve the light of the exoplanet in contrast to the light of the host star. One of the most promising ways to overcome this challenge is by using *coronagraphs*, which are covers put in front of a telescope to block the light of the target star. Detections are therefore more easily possible at large separations of the exoplanets to the host star.

In addition, the planets have to be bright enough to be discovered. This is currently only the case if they are hot and therefore emit light themselves. As we will see in Chapter 4, the accretional energy during planetary assembly is large enough to heat planets to thousands of kelvin, before they gradually cool. Therefore, planets that can be most easily discovered by direct imaging are young, massive objects at large separations. The contrast issue is more easily resolved for cooler stars that emit less light. For a recent review on direct imaging we refer to Bowler (2016).

To have any chance to reach the low-mass exoplanetary regime with direct imaging, the largest ground-based telescopes or the *Hubble* space telescope were used. On the ground, they are mainly ESO's very large telescopes (VLT, 8.2 m aperture) in Paranal in Chile or the *Keck* (10 m) and *Gemini* (8.1 m) telescopes at Mauna Kea in Hawai'i. An adaptive optics (AO) system is installed on all of these facilities and is used to remove most of the atmospheric noise. This highlights the technological challenge of direct imaging searches compared to transit measurements which can be done with amateur equipment to discover similarly massive exoplanets.

A fundamental challenge concerning directly imaged exoplanets is to determine the mass of the objects. As the measurement is sensitive to the luminosity, the masses are inferred based on age-luminosity relationships from models of planetary cooling over time (Baraffe et al., 2003; Linder et al., 2019).

The first exoplanet discovered using direct imaging orbits the nearby (25 ly) star Fomalhaut (Kalas et al., 2008). However, the most famous directly imaged system

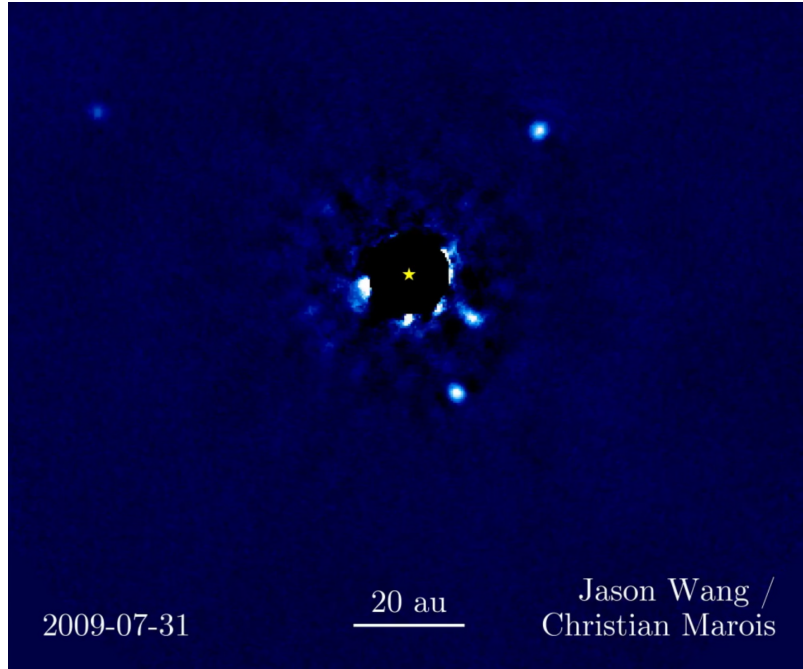


Figure 1.3.: Observational image of the HR 8799 system taken from eso.org/public/videos/eso1905b. The central part is blocked by a coronagraph and the position of the star is indicated by the yellow symbol. The latest discovered planet, HR 8799 e, is the innermost planet (to the right of the star). Other bright spots are *speckles*, noise introduced by the combination of a coronagraph with adaptive optics. A video showing the time evolution of the system is available at the ESO webpage and facilitates distinguishing the random noise from the moving planets.

of planets orbits HR 8799 (shown in Fig. 1.3). It was found using the large *Keck* and *Gemini* telescopes (Marois et al., 2008). The system features four known planets (Marois et al., 2010) with semi-major axes ranging from 14 au to 68 au and masses around $4 M_{\text{Jup}}$ to $9 M_{\text{Jup}}$ (Bowler, 2016).

Despite the techniques' fundamental challenges, the major benefit of direct imaging lies in the wealth of information that can be provided. Since light of the planet itself is observed, its spectrum will give information about the planet itself (Kalas et al., 2008; Janson et al., 2010). If absorption of light can be seen, it provides information about the presence of an atmosphere and its composition. This is an important step to determine if an exoplanet could host life. Compared to transmission spectroscopy, getting spectra of *any* exoplanet would be possible in principle and not only of the transiting ones.

In the future, many projects aim to directly observe exoplanets: Soon, most likely in 2021, the James Webb Space Telescope (JWST) will launch and its near- and mid-infrared instruments (NIRCam and MIRI) are equipped with coronagraphs to

conduct direct imaging measurements of giant exoplanets with much better spectral resolution than what is currently possible from space. Additionally, the next generation of extremely large telescopes is under construction and is expected to improve the angular resolution and sensitivity so much that observations of cold gas giants will be possible. Additionally, ESO's Extremely Large Telescope (under construction, first light expected in 2025) could even directly image rocky planets around one of the nearest stars (Quanz et al., 2015). Furthermore, two (LUVOIR, The LUVOIR Team, 2019 and HabEx, Gaudi et al., 2020) out of the four space based large mission concepts handed in for the 2020 NASA Decadal Survey include direct imaging of exoplanets as one of their core goals and aim to push the detection limits to Earth-analogue planets.

1.2.5. Other methods

As mentioned previously, signatures of gravitational interactions between multiple planets in a system can be used to determine the planetary masses. In addition to providing masses to previously known exoplanets, it can also be used to indirectly infer the presence of additional planets in the system. In practice, the instant of the transit can be determined to a very high precision. If the repeated transit timing is slightly non-periodic, these *transit timing variations* (TTV) are fitted with models of the gravitational interaction of the bodies (N-body models) in the system varying the masses or postulating additional planets. The most significant solution is not always trivial to find, since N-body dynamics can get chaotic or very complicated patterns can emerge for more bodies.

Another technique that will become more important in the future is *astrometry*. This is a very old subject of astronomy where the position of stars are determined. The reason why astrometry can potentially be used for exoplanet detections is the very high precision that the satellite *Gaia* offers. With *Gaia*, it will be possible to determine the position and the velocities of many stars accurate enough to resolve the motion of host stars caused by their exoplanets' gravitational pull. This is similar to what is measured by the RV method, but more sensitive to the direction perpendicular to the line-of-sight. So far, the positions, velocities, and magnitudes of more than 1.3×10^9 stars and other sources are published (*Gaia* Data Release 2, Gaia Collaboration et al., 2018). However, this data does not yet contain information about the variability of these quantities, which would be required to detect exoplanets. The variability will be included in the *Gaia* Data Release 3, scheduled before the end of 2021.³ By then, thousands of giant planets at distances of a few au should be detected by this method (Lunine, 2010; Lattanzi & Sozzetti, 2010). For the closest stars, also less massive planets are in principle detectable. The all-sky coverage and the same statistics for all sources of *Gaia* will make this dataset very valuable for comparison to theory.

To conclude this section, we note that the first exoplanets were discovered around

³According to [Gaia News Webpage](#) accessed on the 7.4.2020

pulsars – rapidly rotating neutron stars – by measuring the timing of their radio-frequency pulses (Wolszczan & Frail, 1992). Furthermore, observations of protoplanetary disks can be used to infer the presence of planets (*disk kinematics* in Fig. 1.4, see also Sect. 1.4) at large orbital separations. Moreover, the light from the planetary surface added to the light from the star might show detectable variations over the course of an orbit, this *orbital brightness modulation* is only rarely recovered for the exoplanets closest to their host star. The first few of such planets were discovered by Charpinet et al. (2011). Similarly, brightness modulations caused by relativistic effects due to the planet-induced doppler shift of the star were discovered by Faigler et al. (2013).

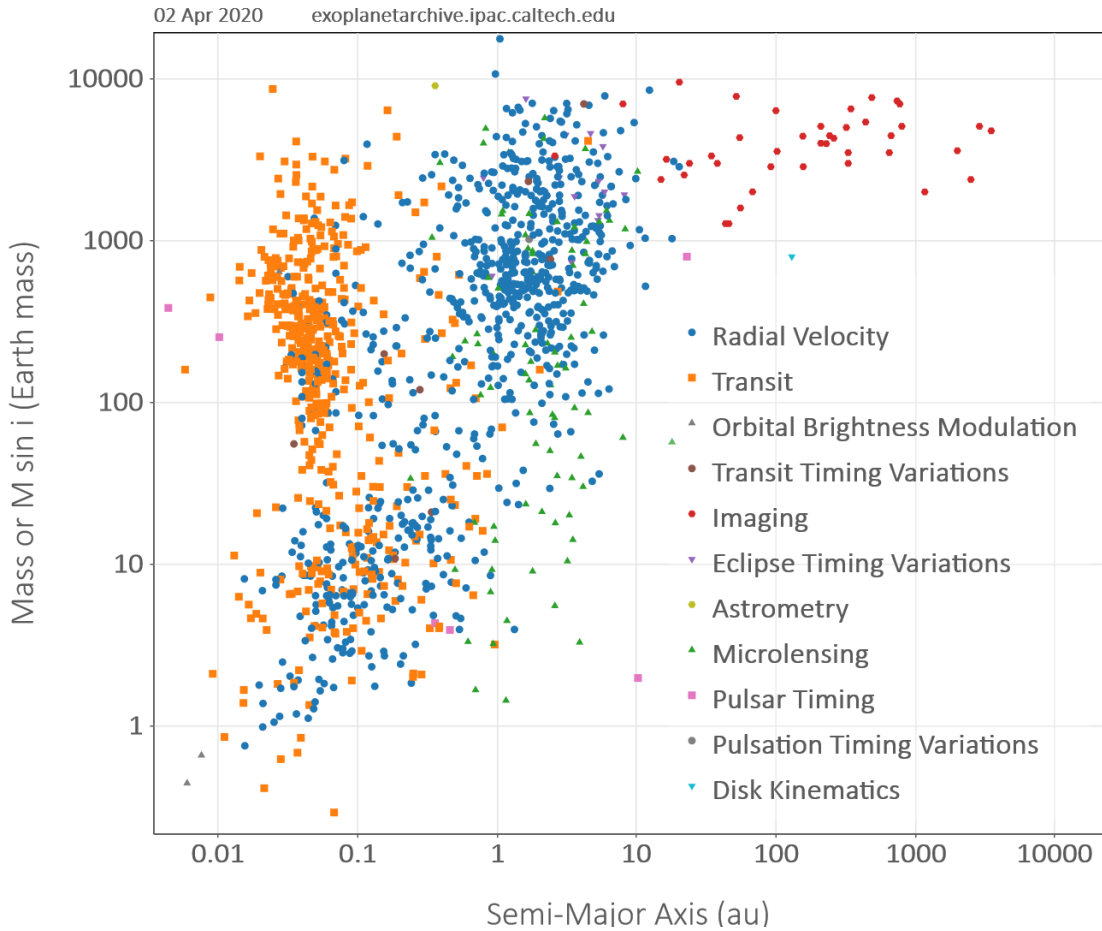


Figure 1.4.: Semi-major axis versus mass diagram of observed exoplanets.⁴ The different detection methods are indicated and exoplanets without mass constraints are omitted. Frequently, a planet was discovered by transit surveys and its mass was later-on determined by follow-up radial velocity observations or transit-timing variations.

⁴Diagram created using Filtergraph, an online data visualization tool developed at Vanderbilt University (Burger et al., 2013).

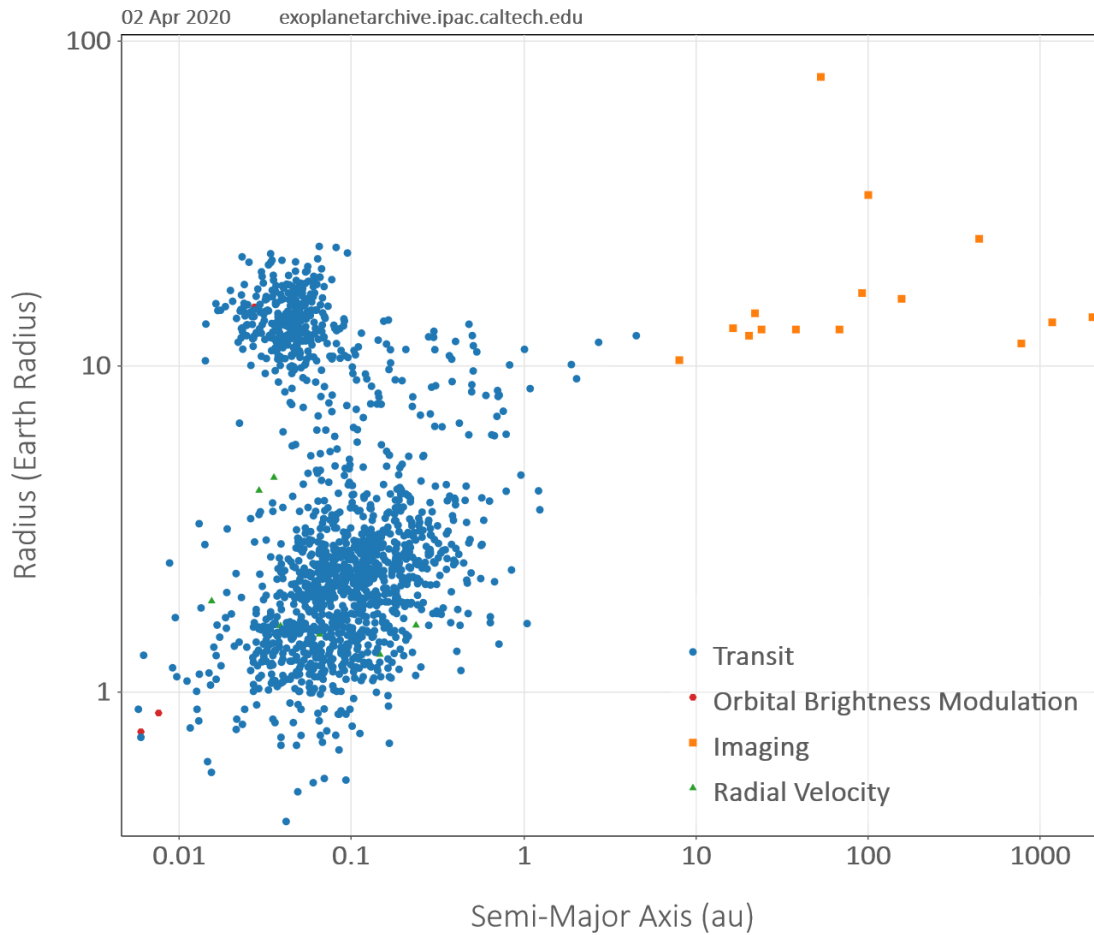


Figure 1.5.: Semi-major axis versus radius diagram of observed exoplanets.⁴ The different detection methods are indicated and exoplanets without a determined radius are omitted. Therefore, the diagram is mainly populated by planets that transit their host star with respect to our line-of-sight. Rarely, a planet was discovered by RV and follow-up observations revealed a matching transit to determine the radius.

1.3. Exoplanet demographics

Given the inherent biases to all the exoplanet observation techniques, a bias correction is required to infer the true exoplanet population. Typically, the distribution of exoplanets is explored in the orbital period or semi-major axis versus mass or radius plane. Additional dimensions like the stellar mass or luminosity are less commonly explored because the data is still relatively sparse.

Nowadays, the oldest work which is still relevant was published by [Mayor et al. \(2011\)](#) and relies on large radial velocity surveys. In this work, the radial velocity measurements with the CORALIE and the HARPS spectrographs are combined. In total, 822 non-active stars with 155 detected planets are included. For both instruments and two versions of CORALIE the detection limits are estimated to statistically infer the underlying population of exoplanets as a function of their mass and period. In this work, only Solar-type stars are considered. [Mayor et al. \(2011\)](#) find a clear dominating population of low-mass planets making giants relatively rare after correcting for detection biases. In [Fig. 1.4](#), this is not immediately clear and highlights the importance of knowing and correcting for detection biases. Additionally, they find that very few planets exist with periods below 6 days and above ~ 100 days. This decrease of the frequency of planets for large orbital periods is noteworthy because it is in contrast to the Solar System. However, when only looking at planets with $M \sin i > 50 M_{\oplus}$, [Mayor et al. \(2011\)](#) find that the number of giant planets increases with the orbital period. Therefore, the close-in population of planets is dominated by lower-mass planets. Recently, a similar analysis of the orbital periods of giant planets was done by [Fernandes et al. \(2019\)](#). Their observational data is based on the same dataset and they compare the RV data to theoretical models and results from *Kepler*. They highlight a decrease of the occurrence rate of giant planets at orbital periods larger than 1000 days and an overall good qualitative fit to both *Kepler* and results from population synthesis (see [5](#)).

Another important general trend known by radial velocity surveys is the correlation of giant planet frequency with metallicity. Metallicity is measuring the amount of elements heavier than hydrogen and helium in stars. As a proxy, the fraction of iron to hydrogen Fe/H is used. By convention, the logarithmic quantity

$$[\text{Fe}/\text{H}] = \log_{10} \left[\frac{\text{Fe}/\text{H}}{(\text{Fe}/\text{H})_{\odot}} \right], \quad (1.1)$$

where $(\text{Fe}/\text{H})_{\odot} = 0.0149$ is the iron to hydrogen mass ratio in the Sun ([Lodders, 2003](#)). Such a correlation was found and confirmed already by earlier works ([Gonzalez, 1997](#); [Santos et al., 2001, 2003](#)) and [Mayor et al. \(2011\)](#) find the same for the massive planets in their sample. For lower-mass planets ($M \sin i < 30 M_{\oplus}$) no correlation with host star metallicity is found. This trend is explainable by core accretion theory if the stellar metallicity is indicative of the amount of solids that were available for accretion ([Ida & Lin, 2004b](#); [Alibert et al., 2011](#); [Mordasini et al., 2012a](#)). It also rules out gravitational instability as the main giant planet formation pathway for Jupiter-mass planets at orbital periods within a few years.

A very valuable dataset is provided by *Kepler*. The latest data release of the nominal 3.5 yr mission was presented in [Thompson et al. \(2016\)](#) and the completeness and reliability were estimated by [Thompson et al. \(2018\)](#). This dataset and estimates were used by multiple groups to calculate occurrence rates of exoplanets ([Mulders et al., 2018](#); [Hsu et al., 2019](#); [Bryson et al., 2019](#)). Those works provide the currently best estimates based on transit missions. However, they cannot be considered to be the *final* estimates of *Kepler* occurrence rates because the stellar properties are still being revised ([Berger et al., 2020](#)) and the statistical methods influence the results ([Bryson et al., 2019](#)). Newer datasets provided by the K2 (using the *Kepler* spacecraft but frequently changing the field of view) and TESS missions will only improve the statistics where the parameter space is already well sampled – at short orbital periods.

The lessons learned from *Kepler* are manifold, here we highlight only a fraction:

- The main finding is that small exoplanets are very abundant. [Mulders et al. \(2018\)](#) estimate that 40% to 84% of stars host planets larger than half an Earth radius. Furthermore, quite commonly there are multiple planets per star confirming the radial velocity estimates of many low-mass planets ([Mayor et al., 2011](#)).
- A major contribution by the exoplanet statistics provided by *Kepler* was to resolve a gap in the radius distribution at $\sim 2 R_{\oplus}$ ([Fulton et al., 2017](#)). Such a gap was predicted to exist due to photo-evaporative loss of primordial hydrogen-helium envelopes ([Owen & Wu, 2013](#); [Lopez & Fortney, 2013](#); [Jin et al., 2014](#)). If photo-evaporation causes the two populations to split, the location of the gap indicates that the majority of planets with radii below the gap are rocky ([Jin & Mordasini, 2018](#)).
- In contrast to radial velocity, transit measurements provide some constraints on the inclination of the transiting planets. Modeling mutual inclination distributions between the planets in discovered systems showed that single-transit systems are under-produced if the planets' inclinations are sampled from a single distribution ([Lissauer et al., 2011](#)). This feature, later dubbed the *Kepler Dichotomy*, hints at two different pathways to assemble planetary systems: in almost a single plane with consistently low mutual inclinations or in a more chaotic fashion ending up with very large mutual inclinations. The latter pathway would commonly lead to individually observable transits. For the latter distribution, stellar rotation rates misaligned with the protoplanetary disk have been proposed to lead to instabilities thus pumping mutual inclinations ([Spalding & Batygin, 2016](#)). However, doubts are also raised that the dichotomy is not physical but a remnant of not accounting for multiplicity when calculating how complete the *Kepler* measurement was ([Zink et al., 2019](#)).
- Combined with mass measurements by RV or TTV, the *Kepler* sample facilitates the study of planetary densities and thus compositions of some exoplanets

down to Earth size. Because of the distant stars that were observed with *Kepler*, this is not possible for many exoplanets. Instead, dedicated transit measurements by K2, TESS, CHEOPS, Spitzer or Hubble are often more valuable.

- Converting the radii of the *Kepler* planets to masses, [Pascucci et al. \(2018\)](#) find a peak occurrence rate at planetary to stellar mass ratios of 2.8×10^{-5} . It lies at the same location for Sun-like stars as well as less massive stars.

Owing to the different sensitivities, microlensing searches give complementary results to radial velocity and transit surveys. [Suzuki et al. \(2016\)](#) derived planet-to-star mass ratios for the large MOA-II microlensing survey running for five years. They determined a peak frequency at mass ratios of 1×10^{-4} , which would be at masses similar to Neptune. Due to the insensitivity of microlensing surveys to close-in planets, these results are only applicable to planets outside the snowline. [Suzuki et al. \(2018\)](#) then used the same dataset to compare the observational data to population-synthesis studies. They concluded that the models significantly underproduce the number of Neptune-mass planets due to runaway gas accretion. Therefore, the microlensing dataset indicates that runaway gas accretion should be significantly slowed down. However, the population-synthesis studies used for comparison were assuming a Solar-type star. With a lower stellar mass and a reduced viscous α value, a better fit to the microlensing data was achieved (see Sect. 4.2.3 for the dependency of the gas accretion rate on α). In the future, a comparison should sample over the observed stellar masses also for this better fitting theoretical calculation and more data would be desirable for the observational data. In [Suzuki et al. \(2016\)](#) only 23 planetary signals are included. With future surveys, the drawn conclusions will be more clear. However, already now, there is enough evidence to warrant a fundamental revision of the exact gas accretion process, which is currently led by works performing three dimensional radiation-hydrodynamic simulations of the accretion process ([Szulágyi et al., 2016](#); [Cimerman et al., 2017](#)).

Currently, direct imaging surveys start to provide valuable insights into the demographics of exoplanets at wide separations around young stars. [Nielsen et al. \(2019\)](#) find a clear giant planet occurrence rate dependency on stellar mass for their survey of 300 stars conducted with the Gemini South telescope. More giants are in wider orbits around stars with $M_\star > 1.5 M_\odot$. Furthermore, giants tend to orbit closer to 10 au rather than 100 au and the inferred distributions should be dominated by low-mass close-in planets. In contrast, [Nielsen et al. \(2019\)](#) find an opposite trend for brown dwarfs with masses larger than $13 M_{\text{Jup}}$ – wide-orbit large-mass. This is indicative of a core-accretion formation pathway for giant planets and a gravitational instability formation pathway for more massive objects. This conclusion is in agreement to the recent analysis of [Wagner et al. \(2019\)](#) who used archival direct imaging data. The findings of [Nielsen et al. \(2019\)](#) are more specific than the previous study of [Galicher et al. \(2016\)](#) which relied on lower-precision measurements and less systems with giant planets. More direct imaging surveys are currently being conducted or analyzed, we mention here the two surveys with most targets apart from the continuation of the Gemini Survey ([Nielsen et al., 2019](#)): SHINE, including 400 to 600 stars using the

SPHERE instrument at the VLT (Chauvin et al., 2017) and ISPY-NACO, observing 200 stars using the NACO instrument also at the VLT (Launhardt et al., 2020).

In the future, a major work-package for planetary scientists will be to combine datasets originating from different techniques and surveys. This is required to get a full census of exoplanets. For a potential roadmap to the future of exoplanet demographics, we refer to the recent white paper by Bennett et al. (2019).

1.4. The cradle of planets: Protoplanetary disks

1.4.1. Disk formation

Planet formation cannot be discussed without basic knowledge about the environment in which planets form: the protoplanetary disks. Therefore, the discussion starts with the formation of stars or young stellar objects (YSO) and their disks. In the picture drawn by Shu (1977), a gravitationally bound, isothermal sphere with an initial rotation rate starts to contract. Early-on, this contraction is still sub-sonic and thus it can be considered to be in hydrostatic equilibrium. Once gravitationally unstable, the most central region quickly collapses to form a denser core distinguishable from the envelope.

To model this subsequent stage, collapse models need to include super-sonic flows, turbulence, varying temperatures, magnetic fields and external conditions from the giant molecular cloud within which the individual star is forming (McKee & Ostriker, 2007). Independent from the exact involved physics, the formation of a thinner disk of gas and dust follows from basic principles: Since a collapsing cloud of gas must initially have a slight rotation in a random direction, its total angular momentum is not zero and has to be conserved. Therefore, during the collapse, large angular momentum material falls onto a disk oriented normal to the total angular momentum vector instead of onto the star. Since the mass is now much closer to the rotational center, the rotational velocities have to increase to conserve angular momentum.

For the Solar System, this resulted in most of the mass ending up in the Sun but most of the angular momentum staying in the disk. This is known because at the present day, the giant planets still carry much more angular momentum than the Sun and there is no realistic source of angular momentum other than the protoplanetary disk out of which the planets formed.

The timeframe for planet formation is given by the eventual dispersal of the disk. It is usually longer-lived than the infalling spherical envelope. Nevertheless, it is still removed over million year timescales (Haisch, Jr. et al., 2001, see also Sect. 1.4.4) by accretion processes (Sect. 2.3), magnetohydrodynamic winds (Bai et al., 2016) and photo-evaporation due to X-ray and EUV-radiation (Sect. 2.6).

1.4.2. Types of disks

There are some constraints from observation as to how protoplanetary disks are structured. Meeus et al. (2001) classified them into Group I and II, where the disk emission belonging to Group I can be modeled by a black body and a power law part, whereas to model Group II disks, a power law is sufficient.

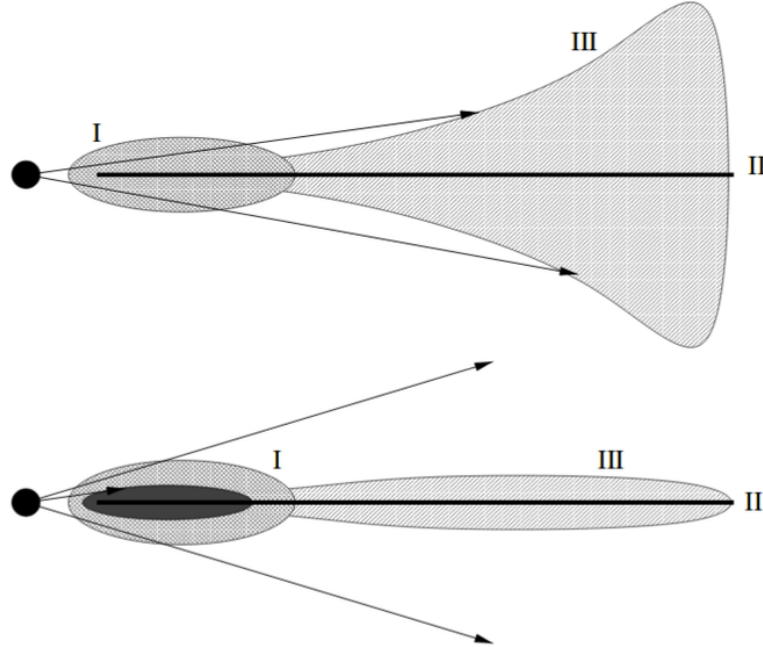


Figure 1.6.: Schematic view of protoplanetary disks by Meeus et al. (2001). The disk is split into three parts: an inner part (I), the midplane (II) and a flaring part (III). The upper panel shows Group I type disks, where the star illuminates the disk and causes the flaring. The lower panel shows a Group II type disk, where the outer part is shielded from radiation and thus much less puffed-up.

They put forward an explanation for the different emission types. The disk should have either a flared structure, where the direct radiation of the central star reaches the outer part, or a pin-like structure, where the outer part of the disk is shielded by a "puffed up" (Meeus et al., 2001) inner part. The former corresponds to Group I with the additional power law emission from the flared part and the latter corresponds to Group II. This idea is shown in Figure 1.6.

Another more general categorization for YSO is done using the different slopes of the spectral energy distribution

$$\alpha_\lambda = \frac{d \log(\lambda F_\lambda)}{d \log(\lambda)}, \quad (1.2)$$

where λ is the wavelength and F_λ is the flux of light at a given wavelength λ . For the categorization, the values of α_λ in the infrared regime for λ ranging from $2 \mu\text{m}$

to $25\ \mu\text{m}$ ($\alpha_{2-25\ \mu\text{m}}$) are used (Lada & Wilking, 1984; Lada, 1987; Greene et al., 1994; Williams & Cieza, 2011; Williams et al., 2019). Four categories are then defined:

- Class 0 (Andre et al., 1993): $F_{2-25\ \mu\text{m}} \simeq 0$, therefore no $\alpha_{2-25\ \mu\text{m}}$ can be defined. However, these objects are clear sources of millimeter wavelength light.
- Class I: $\alpha_{2-25\ \mu\text{m}} > 0$. This corresponds to a rising spectrum. Lada (1987) additionally puts an upper limit of $\alpha_{2-25\ \mu\text{m}} < 3$.
- Class II: $-1.6 < \alpha_{2-25\ \mu\text{m}} < 0$, so a falling infrared spectrum.
- Class III: none or only weak infrared excess with $\alpha_{2-25\ \mu\text{m}} < -1.6$ (Greene et al., 1994). Again, Lada (1987) also constrain $\alpha_{2-25\ \mu\text{m}} > -3$.

Some authors (Greene et al., 1994) additionally discriminate the *Flat Spectrum* cases with $-0.3 < \alpha_{2-25\ \mu\text{m}} < 0.3$ as a separate class.

These categories can be attributed to different stages in the temporal evolution of young stellar objects. Class 0 objects are the youngest distinct sources of light. They describe a protostar with a denser central object surrounded by an envelope of gas and dust, which is still very dense and contains most of the mass. They were first found as a distinct class by Andre et al. (1993). The next stage – and first stage of the more classical categorization – is called Class I, where less mass is in the envelope and more on the central object ($M_{\star} > M_{\text{env}}$, Williams & Cieza, 2011). This leads to less optically thick envelopes. During those stages of collapse, a protoplanetary (or proto-stellar) disk is formed due to conservation of angular momentum. Later on, Class II objects have completely accreted their envelopes but not yet their disks from which the infrared excess originates. Lastly, Class III objects do not show this infrared excess, thus the disk should have mostly dissipated (Lada & Wilking, 1984; Lada, 1987).

To avoid confusion, note that the objects belonging to Group I and II usually are Class II objects and there seems to be no evidence for a trend of evolution from Group I to Group II or vice-versa (Garufi et al., 2017), whereas the Classes track the time evolution.

As we discuss in this chapter, there are many more details to be known about the protoplanetary disk structure than these categorization schemes. Furthermore, the observational data has drastically increased in recent years. Therefore, this simple picture is quite outdated but the nomenclature is still present in the literature. Most often, the Group I disks in Figure 1.6 are considered to be more common and the models reviewed in Section 2 usually describe such a flared disk.

1.4.3. Minimum mass Solar nebula

Instead of trying to get information from other protoplanetary disks, what was done in the past was to use the Solar System as a benchmark. A minimum mass Solar nebula can be constructed by taking into account the known solid and gas masses

of the Solar System planets (Kusaka et al., 1970, updated by Hayashi, 1981). They assume that all the mass in the region from $\sqrt{r_{n-1}r_n}$ to $\sqrt{r_n r_{n+1}}$, where r_n is the distance to the star of the n -th Solar System planet, accreted on the n -th planet.

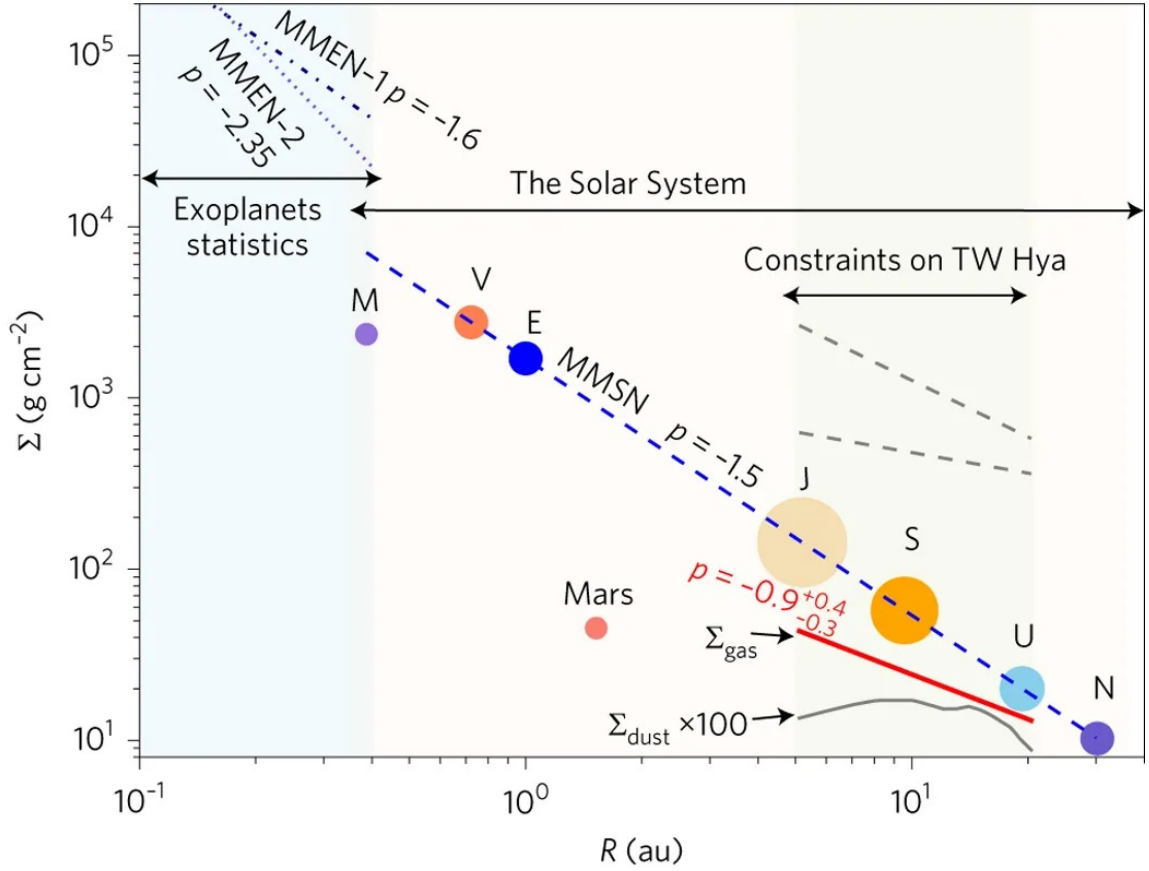


Figure 1.7.: Surface density profiles as a function of separation taken from Zhang et al. (2017). In addition to their gas surface density profile derived for the protoplanetary disk TW Hydra (red solid line), they include the Minimum mass Solar nebula gas profile (MMSN, blue dashed line) by Hayashi (1981) and constraints on the gas part of the Minimum mass extrasolar nebula from Chiang & Laughlin (2013) (MMEN-1) and Schlichting (2014) (MMEN-2, steeper slope).

Under this assumption, they construct the minimum mass that the Solar nebula needed to have. It is interesting, that a single radial surface density slope of -1.5 roughly matches all the data for each planet if a jump at the water-iceline is taken into account.

Fig. 1.7 highlights the discrepancy in derived surface density slopes based on extrasolar planets, the Solar System, and disk observations. The steeper slopes derived from planetary data compared to data from disks can be interpreted as indicators of radially inwards migration of planets (Lin et al., 1996) or drift of solids (Weidenschilling, 1977) or both.

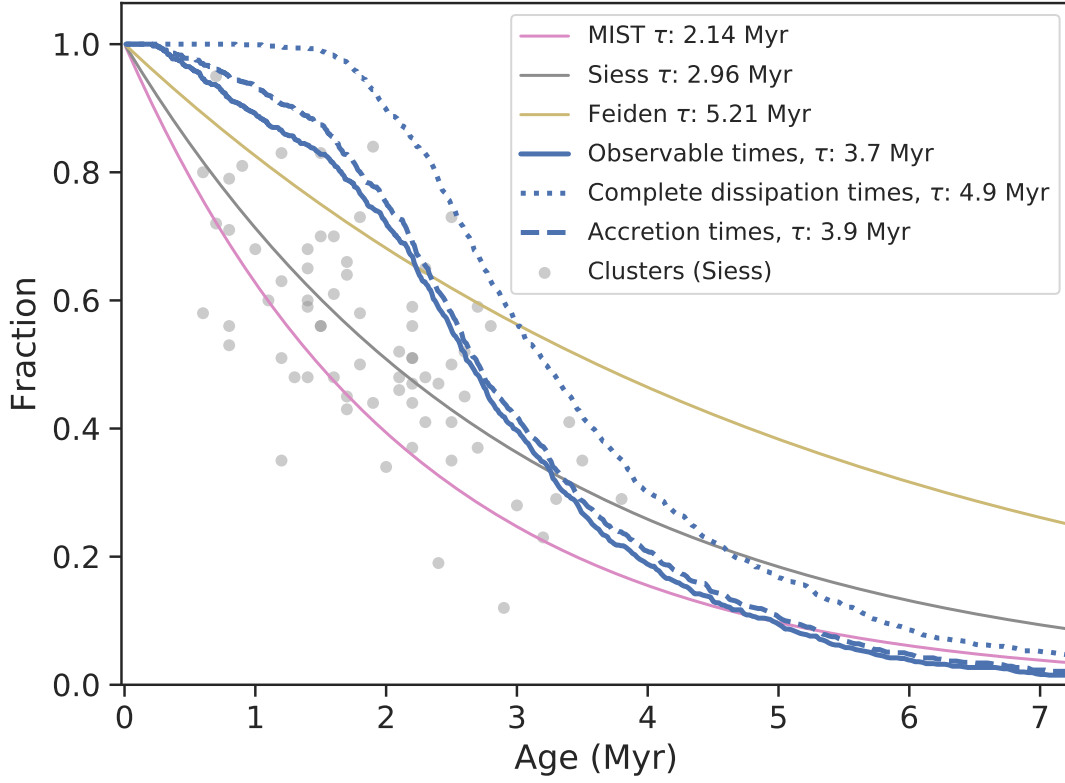


Figure 1.8.: Fraction of stars with disks as a function of time. The observational cluster data compiled by [Richert et al. \(2018\)](#) is marked as gray dots using the pre-main sequence (PMS) evolution model of [Siess et al. \(2000\)](#). Exponential fits to the observational data for the PMS evolution models of [Choi et al. \(2016\)](#) (MIST), [Siess et al. \(2000\)](#) and [Feiden \(2016\)](#) are added to highlight its influence. The latter is a simplified PMS model compared to the former two but includes magnetic fields. The model data for a synthetic planetary population (NGPPS identifier: NG76) with 100 embryos embedded in each disk around Solar-mass stars is shown with thicker blue lines for different dissipation criteria: complete dissipation to the minimum surface density (dotted line), to the criterion by [Kimura et al. \(2016\)](#) (solid line), and to a mass accretion rate lower than $10^{-11} M_{\odot} \text{ yr}^{-1}$ similar to [Fedele et al. \(2010\)](#) (dashed). In contrast to [Fedele et al. \(2010\)](#), we do not find shorter lifetimes using the accretion criterion.

1.4.4. Disk lifetimes

A very important constraint on planet formation is the limiting timescale by the dispersal of the disk. If disks were very long-lived, the accretion of gas would have to be less efficient to still allow for the formation of gas giants. However, observations show that the disk is relatively short-lived (~ 3 Myr) compared to the overall lifetime of stars. Already [Pollack et al. \(1996\)](#) discuss in-depth the constraints put on planet formation by the disk lifetimes and do not manage to achieve the fast assembly times for their nominal models. This also gave rise to include planetary migration which helps to accelerate giant planet growth ([Alibert et al., 2004a,b](#)).

The observational data for disk lifetimes is based on sets of stellar clusters. Assuming that the stars in one cluster are approximately of the same age, the fraction of stars that show an excess of infrared light (i.e. the fraction of Class I or II objects, see [Sect 1.4.2](#)) or the presence of accretional signatures ([Mamajek et al., 2009](#)) is directly linked to how many disks have dissipated. This is only true if all stars did have disks at their formation and if the observational signatures are not misinterpreted.

For multiple clusters, this fraction of stars with disks can be plotted as a function of time ([Strom et al., 1989](#); [Haisch, Jr. et al., 2001](#); [Mamajek et al., 2009](#)). Usually, the observational data is best fitted with an exponential decay with a half-life on the order of a few Myr. We note that the notions of half-life and characteristic times are both commonly used and should not be confused.

[Fedele et al. \(2010\)](#) found systematically lower lifetimes if they use stellar accretion compared to infrared excess. They suggest that this discrepancy could be linked to planets in the inner few au halting accretion onto the star. In [Fig. 1.8](#), we show fractions of modeled stars with disks from a recent population synthesis. We do not reproduce the findings of [Fedele et al. \(2010\)](#) if we use a criterion for model infrared excess and accretion rates (thick line, respectively dashed line). Instead, the two criteria give very similar results.

Another potentially major issue related to disk lifetime estimates was raised by [Richert et al. \(2018\)](#) who compare different pre-main sequence stellar-evolution models to infer the age of the clusters. They found very different lifetimes due to this systematic shift of the time-axis. We briefly touch on this topic in [Paper III](#), where we use the data to constrain a free model parameter that regulates the dispersal time of the disk and fits using the different stellar models are shown in [Fig. 1.8](#).

When comparing modeled disks to disk lifetimes, it has to be defined when a disk is considered as dispersed. For models, an arbitrary low-mass disk can still be tracked. However, the infrared excess might no longer be observable. Therefore, we adopted a simple prescription from [Kimura et al. \(2016\)](#) to define which disks are observable and which are dispersed (see [Paper III](#)). Compared to the numerical limit of a very low surface density everywhere in the disk, the observability condition yields shorter lifetimes by a few 100 kyr.

1.4.5. Stellar accretion rates

Corresponding to a thinning out of the disk and the envelopes of YSO, gas has to fall onto the central object. The velocities that can be reached due to the gravitational potential of the star are on the order of 300 km s^{-1} , thus the matter is highly super-sonic when it reaches close to the stellar photosphere (see [Hartmann et al., 2016](#), for a recent review). The resulting shock leads to the energy being released and gas temperatures of $1 \times 10^6 \text{ K}$ in a narrow region. The corresponding emission should be at X-ray wavelengths, but is usually not directly observable. Instead, it is absorbed and a continuum emission in the ultraviolet regime corresponding to lower temperatures can be measured (e.g. [Bertout et al., 1988](#); [Gullbring et al., 1998](#); [Alcalá et al., 2017](#)). Additionally, some high frequency spectral lines can be used to measure stellar accretion processes (e.g. [Natta et al., 2006](#); [Fang et al., 2013](#); [Manara et al., 2015](#)).

Both methodologies consistently find stellar accretion rates on the orders of $10^{-10} M_{\odot} \text{ yr}^{-1}$ to $10^{-7} M_{\odot} \text{ yr}^{-1}$. Together with the disk lifetime, this puts clear constraints on the disk evolution which need to be considered in models. [Manara et al. \(2019\)](#) compared measured accretion rates to a population synthesis and found that giant planet formation can explain some high-mass disks with low stellar-accretion rates. However, they are produced too frequently in the theoretical population synthesis.

For the project of looking at the influence of the stellar mass ([Paper III](#)), we use the dataset of [Alcalá et al. \(2017\)](#) for comparison. This work determines many stellar accretion rates by measuring the ultraviolet continuum excess with the Very Large Telescope. They took spectra of more than 90% of the young stellar objects in the four main stellar Lupus clouds. These regions are known to be very young with estimated ages ranging from 1 Myr to 3 Myr. Therefore, it is ideal to compare to planetary population syntheses, since especially giant planet formation has to be a rapid process.

1.4.6. Dust observations in the ALMA era

The Atacama Large Millimeter/Submillimeter Array (ALMA) got first light in 2011 and has subsequently led to a revolution in the field of protoplanetary disk observations. As the name suggests, ALMA is sensitive to radio-wavelength signals. Thanks to its elevated and dry location at 5000 m altitude in the Atacama desert in Chile, the incoming astrophysical signal is less absorbed by atmospheric water vapor. ALMA consists of 50 12-meter antennas – the "main-array" – and an additional "compact array" of four 12-meter and twelve 7-meter dishes. The data of all the dishes contained in an array is combined to act as a single telescope.

If light is integrated over a range of wavelengths, the instrument is most sensitive to the continuum flux in millimeter or submillimeter wavelengths emitted by an astrophysical source. For protoplanetary disks, this mainly probes cold dust ($T \simeq 10 \text{ K}$) which thermally emits light. This emission is proportional to the dust opacity for radio-frequency light, which is closely linked to the physical size of the dust.

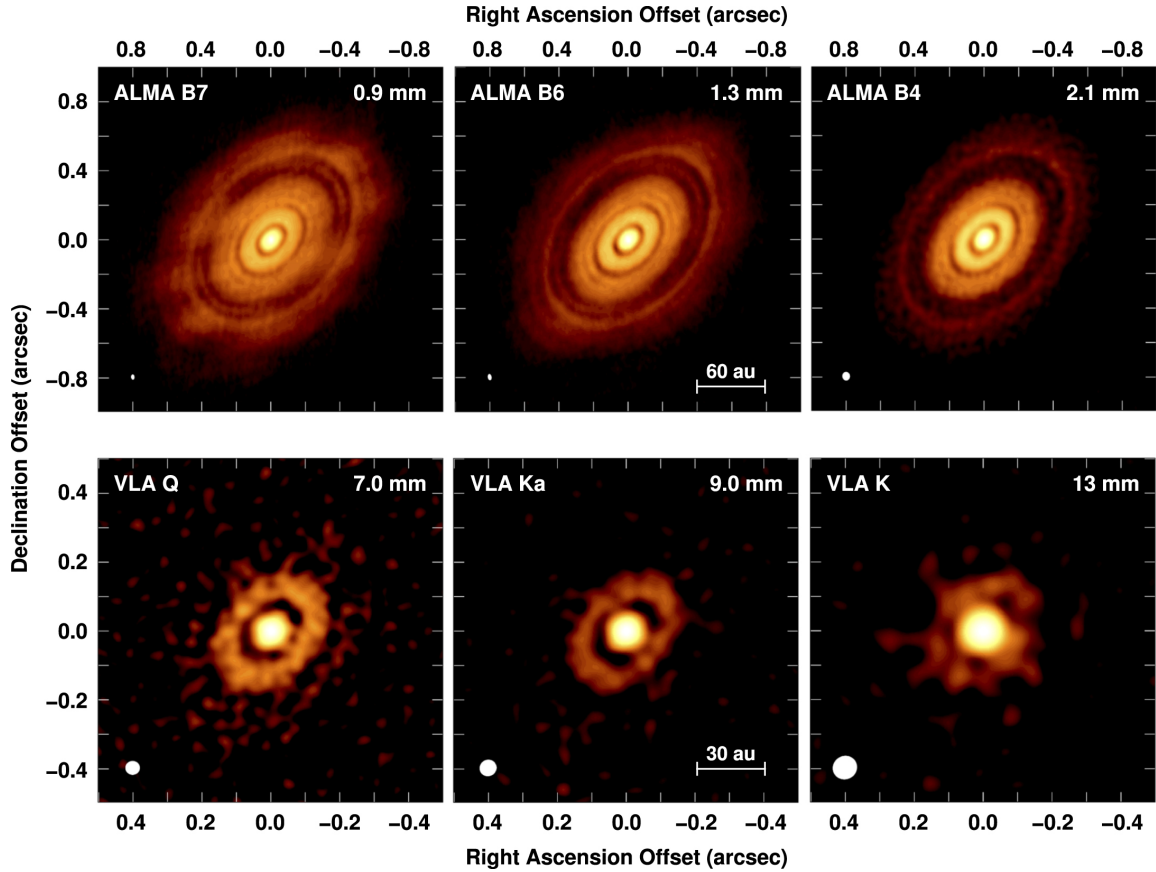


Figure 1.9.: ALMA and VLA images of the HL Tau disk from [Carrasco-González et al. \(2019\)](#). The ALMA bandwidths (top right of each panel) are shorter than those of the VLA and the disks can be better resolved with ALMA.

Particles much larger or smaller than the observed wavelength do not contribute significantly.

In addition to thermal emission, some molecules produce lines in the spectrum due to rotational transitions. This can be used to constrain the chemistry or the gas content (e.g. [Ansdell et al., 2016](#)) in a disk if the wavelength range is chosen accordingly.

The first observations focused on the brightest known disks and led to the discovery of a wealth of substructures ([ALMA-Partnership et al., 2015](#); [Isella et al., 2016](#); [Andrews et al., 2018a](#)). Figure 1.9 shows a few of those well-resolved targets and also highlights the difference of the ALMA resolution compared to the older Very Large Array (VLA). Especially the DSHARP survey ([Andrews et al., 2018a](#)) completes the picture that large, bright disks commonly have axis-symmetric rings and gaps, quite a fraction shows global spirals and some have axis-asymmetric features.

However, the DSHARP project should not be mistaken for a complete census of all kinds of disks. It only focuses on the disks with most flux detected. Other works use

lower-resolution but observe all disks of a given cluster to constrain the distribution of all kinds of disks (Ansdell et al., 2016; Barenfeld et al., 2016; Pascucci et al., 2016; Ansdell et al., 2018; Williams et al., 2019). The findings of these works do not reveal common substructures because many disks are compact and structures would be smaller than what can be resolved by ALMA. However, these works are very valuable to infer realistic total dust masses and radii of disks.

Two main findings are very noteworthy (a short discussion can also be found in Paper III). First, Ansdell et al. (2017) report larger gas disk radii compared to dust disk radii in the overall sample of disks. Gas disk radii are larger by a factor of 1.94 ± 0.04 . This finding was possible thanks to combining continuum measurements sensitive to the dust content with observations of the same disks but sensitive to multiple spectral lines due to rotational transition of the CO-molecule. The factor of roughly two was found independent of the exact definition of the disk radius. Two disk radius definitions were tested: one where 68% of the total measured flux emerges from regions starwards of the disk radius and one where 90% of the flux lies within. These larger gas radii can be interpreted as indicators of radial drift of dust. If micrometer-sized dust particles coagulate and grow in the outer regions of the disk, they will spiral towards the star (see Sect. 2.8) and thus, the outer regions will gradually deplete of dust but not of gas.

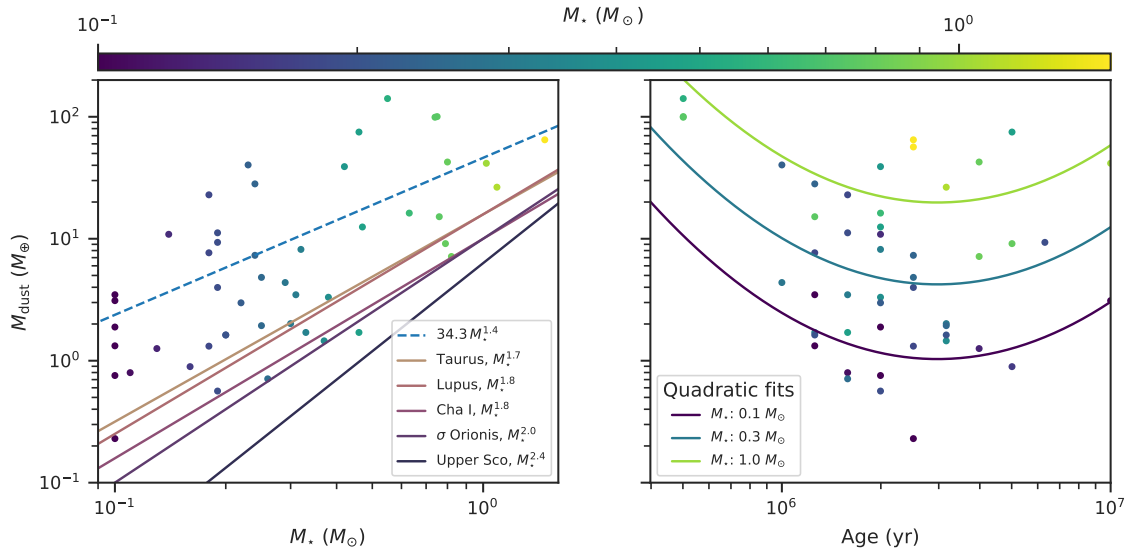


Figure 1.10.: Dust mass measured with ALMA in the Lupus star forming region by Ansdell et al. (2016) as a function of stellar mass (left) and age (right). Errorbars and upper limits were omitted. The dashed line in the left panel shows a linear fit on the shown data, whereas the colored straight lines show fits obtained by Ansdell et al. (2017) using a Bayesian framework to include non-detections as upper limits and errorbars for multiple star forming regions. The order and color of the lines correspond to an increasing estimated age of the different regions.

The second finding is about the relation of total dust disk mass to stellar mass. [Pascucci et al. \(2016\)](#) and [Ansdell et al. \(2017\)](#) find that it is not a linear relationship. In [Fig. 1.10](#), we show that more massive stars do have a higher dust to stellar mass fraction than low-mass stars. However, by linearly fitting this slope of logarithms of disk mass as a function of stellar mass leads to different results depending on the stellar cluster. In fact, there is a tendency of steeper slopes with higher ages. Extrapolating those observed slopes to time zero gives a result that is consistent with a constant disk to stellar mass ratio for all stellar masses. Therefore, these trends could be purely due to evolutionary processes. Currently, dust evolution models are still fine-tuned to Solar masses, and the relationship should be explored by theorists in the future.

Additionally, [Fig. 1.10](#) shows the dependence of the dust disk mass on the age of the source. Ages of individual sources are estimated by [Andrews et al. \(2018b\)](#) using X-shooter spectra collected at the VLT by [Alcalá et al. \(2014, 2017\)](#) and a stellar evolution model ([Choi et al., 2016](#)). However, this comes with a large uncertainty of ~ 0.5 dex, which is why we omitted the error bars for better visibility. The data is best fit with a model linear in log stellar mass but quadratic in log age using linear regression and ignoring errorbars and upper limits of undetected sources. This means that there are indicators that the dust mass drops – as expected – with age, but then starts to increase again. This could originate from a second generation of dust that is produced in collisions. Although this trend is far from being statistically significant using only the shown data from the Lupus cluster, [Williams et al. \(2019\)](#) also report a potential increase of dust masses between 1 Myr and 3 Myr because the disks in the very young Ophiuchus star forming region are measured to be smaller than those in Lupus. This gives some more credibility to this quick analysis.

To conclude the discussion about ALMA, we would like to highlight the newly found constraints on the distribution of disk masses. Especially noteworthy is that for the first time studies were published focusing separately on the early Class 0 and Class I stages ([Tychoniec et al., 2018](#); [Williams et al., 2019](#); [Tobin et al., 2020](#)). Although they are not able to precisely determine the gas masses and instead assume a dust to gas ratio, these works are nevertheless well suited as initial conditions for planet formation models. This is natural because the already evolved Class II disks should not be used as an *initial* state. Indeed, the found disk masses are much larger than what was reported for Class II objects [Ansdell et al. \(2016\)](#); [Barenfeld et al. \(2016\)](#). This is still true despite a reduction of a factor on the order of two in [Williams et al. \(2019\)](#) compared to [Tychoniec et al. \(2018\)](#).

1.4.7. Scattered light

In contrast to the observations done by ALMA, which are sensitive to millimeter-sized particles, observations at shorter wavelengths in the visible or near infrared range track dust particles of micrometer size. These tiny grains do not settle to the midplane as easily as mm-sized particles and are therefore good tracers of the gas. Hence, observations of scattered light are very valuable to get constraints on the

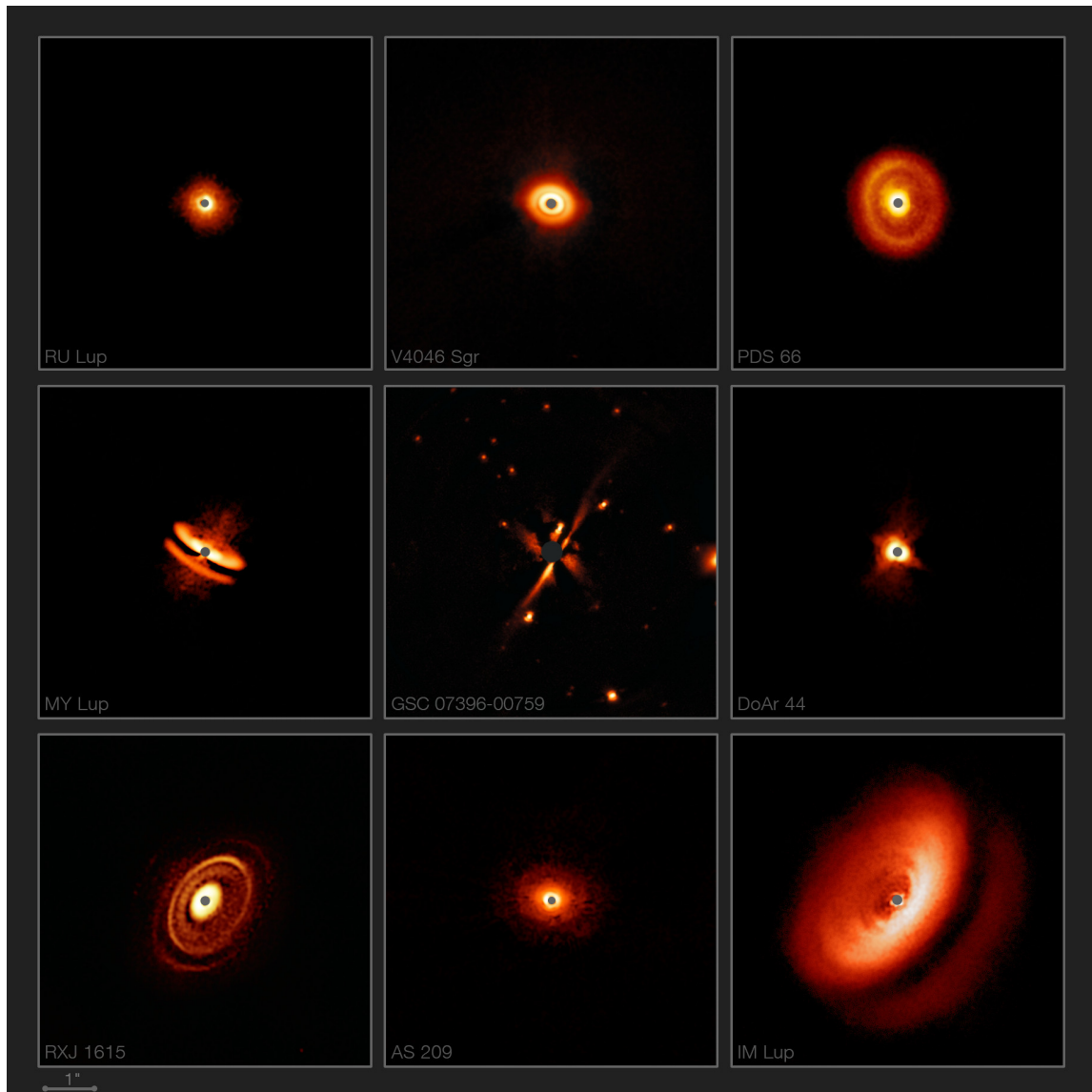


Figure 1.11.: VLT/SPHERE images of protoplanetary disks. SPHERE observations track the micrometer sized dust in protoplanetary disks and are not sensitive to the light of the star thanks to observing only polarized light. Unpolarized light from the star becomes partially polarized when it is scattered on the dust particles. Image credit: ESO; [Avenhaus et al. \(2018\)](#); [Sissa et al. \(2018\)](#); DARTT-S and SHINE collaborations

gaseous part of protoplanetary disks. For example, the aspect ratio h/r of the disk can be measured (see Sect. 2.1). Doing this, [Avenhaus et al. \(2018\)](#) find a relation of $h/r \propto r^{(1.219 \pm 0.026) - 1}$. However, they note that measurements are sensitive to the scattering surface of the disk and do not necessarily track the scale height.

In principle, scattered light observations meet the same challenges as the direct imaging searches for exoplanets (see Sect. 1.2.4) which is the extreme brightness of the star in contrast to the desired signal. For scattered light observations, this can be overcome using polarimetric differential imaging. This is an observational technique that splits the light into two beams and uses different angles of a linear polarization filter before recombining the gathered data to only show the contribution of linearly polarized light ([Kuhn et al., 2001](#); [Hinkley et al., 2009](#); [Quanz et al., 2011](#); [Avenhaus et al., 2014](#)). Therefore, the unpolarized light of the star is filtered out and only polarized light, stemming from reflection and scattering from the grains, remains.

The major disadvantage is that considerably less light remains after these steps. Therefore, the largest ground based telescopes have to be used to image protoplanetary disks in this fashion. Nevertheless, especially the images (see Fig. 1.11) collected using the SPHERE ([Beuzit et al., 2019](#)) instrument commissioned in 2014 at the VLT are contributing a lot to the understanding of the physics in protoplanetary disks.

The recent project Disks Around T Tauri Stars with SPHERE (DARTTS) aims at obtaining a census of disks in polarized light instead of focusing on individual sources ([Avenhaus et al., 2018](#); [Garufi et al., 2020](#)). For now, this survey still targets the brightest disks to be able to gather data (similar to the DSHARP survey using ALMA) and is not a complete survey of all disks. However, the statistics for Solar-type stars is drastically increasing. We highlight two of the findings of [Garufi et al. \(2020\)](#): In the presence of a nearby companion star, they did rarely detect a disk and for their younger targets, disk sub-structures like rings are only present in the ALMA observations and not in the scattered light. The latter finding would fit well to the picture of a planet first trapping dust in the midplane before it influences the global vertical structure of the disk. Especially such comparisons of ALMA and SPHERE data should be very fruitful for a better understanding of disk processes.

2. Models of disk processes

The structure and dynamics of the protoplanetary disk is essential for all the studied processes here. Therefore, we discuss in more detail the governing equations to model such a disk. Overall, the aim is to have a simple, mostly analytic model, where only the radial direction is resolved numerically (1D disk). This can then be used to obtain realistic conditions for the dynamics and thermodynamics of bodies embedded in the central, denser parts of the disk. The derivation loosely follows [Armitage \(2019\)](#) and the used variables are defined in [Table 2.1](#).

Symbol	Unit (cgs)	Description
r	cm	Distance to the central star projected onto the disk plane
z	cm	Elevation above the disk midplane
φ	rad	Azimuthal angle
θ	rad	Polar angle measured from the disk midplane
Ω	rad s ⁻¹	Angular velocity
λ	m	Wavelength
F_λ	erg cm ⁻² s ⁻¹	Flux at wavelength λ
P	barye	Pressure
n	cm ⁻³	Number density
T	K	Temperature
ρ	g cm ⁻³	Gas density
Σ	g cm ⁻²	Gas surface density
μ		Mean molecular mass of the gas
ℓ	cm	Mean free path
ν	cm ² s ⁻¹	kinematic viscosity of the gas
M_\star	g	Stellar mass
h	cm	Vertical scale height of the gas disk

Table 2.1.: Variables used for the disk part.

2.1. Vertical structure

For many cases, the protoplanetary disk can be approximated to be thin and has negligible mass compared to the star. In the vertical direction, it is supported by gas pressure and is thus in hydrostatic equilibrium forced by gravity and the pressure gradient.

We approximate the interior of the disk to be isothermal in the vertical direction. For now, we assume the temperature T as given. The gas can be assumed to be ideal for almost all regions of the disk, thus

$$P = nk_B T = \frac{\rho k_B T}{\mu m_H}, \quad (2.1)$$

where m_H is the hydrogen mass and k_B the Boltzmann constant.

Using a spherical or cylindrical coordinate system is very natural for a radially symmetric disk. The condition for vertical hydrostatic equilibrium is expressed as

$$\frac{1}{\rho} \frac{dP}{dz} = -g_z = -\frac{GM_\star}{r^2 + z^2} \sin \theta, \quad (2.2)$$

where $\sin \theta = z/\sqrt{r^2 + z^2}$. Here, we used the aforementioned assumption $M_{\text{Disk}} \ll M_\star$. Replacing the sine yields

$$\frac{1}{\rho} \frac{\partial P}{\partial z} = -\frac{GM_\star z}{(r^2 + z^2)^{3/2}} \approx -\Omega_{\text{K,mid}}^2 z, \quad (2.3)$$

where the last expression can be used because the disk is assumed to be flat $z \ll r$. We introduced the *Keplerian orbital velocity* at the midplane

$$\Omega_{\text{K,mid}} \equiv v_{\text{K,mid}}/r \equiv \sqrt{GM_\star/r^3}. \quad (2.4)$$

Expressed in terms of the density, using the ideal gas law (2.1) and the isothermal assumption, we get

$$\frac{1}{\rho} \frac{\partial \rho}{\partial z} = -\frac{\Omega_{\text{K,mid}}^2 \mu m_H z}{k_B T}, \quad (2.5)$$

which can be integrated to result in

$$\rho(z) = \rho_0 \exp(-z^2/2h^2) \quad (2.6)$$

with the integration constant $\rho_0 \equiv \rho(0)$ being the density at the midplane and

$$h \equiv \sqrt{\frac{k_B T}{\Omega_{\text{K,mid}}^2 \mu m_H}} \quad (2.7)$$

is the *vertical scale height*, which is commonly written as $h = c_{sT}/\Omega_K$, where $c_{sT} = \sqrt{\frac{k_B T}{\mu m_H}}$ is the isothermal sound speed. This is the sound speed assuming no heat release during compression, or – in different terms – the one with an adiabatic index $\gamma = 1$. Finally, integrating ρ over z defines the *surface density*

$$\Sigma \equiv \int_{-\infty}^{\infty} \rho(z) dz = \rho_0 h \sqrt{2\pi}. \quad (2.8)$$

Now, we briefly explore the case of the disk being thick, that is without the simplification of $z \ll r$ we used in equation (2.3). Note that we keep the strong assumption of an isothermal structure. Then, we get the differential equation

$$\frac{1}{\rho} \frac{\partial \rho}{\partial z} = - \frac{GM_* \mu m_H z}{k_B T (r^2 + z^2)^{3/2}}, \quad (2.9)$$

which is separated as well and performing the integration yields

$$\ln(\rho) = \underbrace{\frac{GM_* \mu m_H}{k_B T}}_{r^3/h^2} \frac{1}{\sqrt{r^2 + z^2}} + C \quad (2.10)$$

$$\Rightarrow \rho(z) = C \exp \left[\frac{r^2}{h^2} \left(1 + \frac{z^2}{r^2} \right)^{-\frac{1}{2}} \right], \quad (2.11)$$

where C is an integration constant that can be expressed using the previously defined ρ_0 by requiring

$$\rho(0) \stackrel{!}{=} \rho_0. \quad (2.12)$$

Hence $C = \rho_0 e^{-\frac{r^2}{h^2}}$ and the resulting density profile in z direction is

$$\rho(z) = \rho_0 \exp \left[\frac{r^2}{h^2} \left(\left(1 + \frac{z^2}{r^2} \right)^{-\frac{1}{2}} - 1 \right) \right]. \quad (2.13)$$

A Taylor expansion of the term in brackets around $z^2/r^2 = 0$ reveals that equation (2.6) is equivalent to the first order expansion. In principle, refined approximations could be used, but it is revealed quickly that assuming a constant temperature also has a large influence. Therefore, only two-dimensional models that resolve the vertical structure usually correct for the height over the midplane. However, we note that it is essential to keep in mind the simplifications, especially when considering young disks with aspect ratios h/r on the order of 0.1

2.2. Azimuthal velocities

The radial structure of the disk is governed by the momentum equation (Euler equation, i.e. Navier-Stokes without viscosity)

$$\frac{\partial \vec{v}}{\partial t} + (\vec{v} \cdot \nabla) \vec{v} = - \frac{1}{\rho} \nabla P - F, \quad (2.14)$$

where F are the acting forces. In the most simple case only gravity of the central star is acting. The radial dependence of the density is an observational question or can be modeled in time dependent models, but not in the static case. However, we can address the azimuthal velocity in that case.

We apply the gradient operator in cylindrical coordinates on the vector \vec{v} for a static disk $v_r = v_z = 0$. Then, the radial component of equation (2.14) reduces to

$$\frac{v_\phi^2}{r} = g_r + \frac{1}{\rho} \frac{\partial P}{\partial r}, \quad (2.15)$$

where P is the pressure, $g_r = \frac{GM_\star r}{(r^2+z^2)^{3/2}}$ the radial component of the gravitational acceleration and the lefthand side of (2.15) is the appearing centrifugal force term.

2.2.1. Gas angular velocity

Studying the case of non-zero pressure in equation (2.15) will give results for the disk gas. In contrast, we will later focus on $P = 0$ to obtain the angular velocity of the dust.

Introducing the gas angular velocity $\Omega_g(r, z) = \frac{v_\phi}{r}$ in equation (2.15) yields

$$r\Omega_g^2 = \frac{GM_\star r}{(r^2+z^2)^{3/2}} + \frac{1}{\rho} \frac{\partial P}{\partial r}. \quad (2.16)$$

We can specify the disk by power-law profiles of the surface density and the temperature as was done in [Takeuchi & Lin \(2002\)](#)

$$\rho(r, z) = \rho_0 r^p e^{-\frac{z^2}{2h(r)^2}} \quad (2.17)$$

$$c_s(r)^2 = c_0^2 r^q. \quad (2.18)$$

Then,

$$h(r) = \frac{c_s(r)}{\Omega_{\text{K,mid}}(r)} = h_0 r^{(q+3)/2}, \quad (2.19)$$

where h_0 , c_0 and ρ_0 denote the scale height, sound speed and density at a fixed distance of 1 AU and the radius power law scales in units of 1 AU.

Because the derivation is quite long, we show in [Appendix A.1](#) that

$$\Omega_g(r, z) \approx \Omega_{\text{K,mid}} \left(1 + \frac{1}{2} \frac{h^2}{r^2} \left[q + p + \frac{z^2 q}{2h^2} \right] \right), \quad (2.20)$$

which reduces to

$$\Omega_g(r, z) \approx \Omega_{\text{K,mid}} \left(1 - \frac{h^2}{2r^2} \left[\frac{11}{4} + \frac{9z^2}{8h^2} \right] \right) \quad (2.21)$$

for the typical values $p = -9/4$ and $q = -1/2$.

By means of this expression, it becomes apparent that the vertical differences of the gas angular velocity is not straightforward even assuming an isothermal disk. For realistic disk flows, the vertical direction needs to be resolved. However, if the relevant part of the disk is concentrated around the midplane, the simple picture is still useful.

2.2.2. Dust angular velocity

The angular velocity of dust particles is given by

$$r\Omega_K(r, z)^2 = \frac{GM_\star r}{(r^2 + z^2)^{3/2}}, \quad (2.22)$$

which is the same equation as (2.16), but without the pressure gradient dependent term. Large particles do not feel the gradient in pressure, hence they move with the Keplerian angular velocity $\Omega_K(r, z)$. Note that here we explicitly neglect gas drag, which will be discussed in Sect. 2.8.

The Taylor expansion around $z = 0$ yields

$$\Omega_K(r, z) \approx \Omega_{K, \text{mid}} \sqrt{1 - \frac{3z^2}{2r^2}} \quad (2.23)$$

and with a Taylor expanded root the Keplerian orbital velocity is

$$\Omega_K(r, z) = \Omega_{K, \text{mid}} \left(1 - \frac{3z^2}{4r^2} \right). \quad (2.24)$$

We conclude for now that the orbital angular velocity of solid particles differs from the gas angular velocity and that this difference is a function of z .

2.3. Disk evolution

Disks are observed to evolve. To explain this, the classical approach is to treat the disk as an axis-symmetric, vertically thin sheet consisting of a viscous fluid. This viscosity cannot be the molecular viscosity of the gas, but could be induced as the outcome of turbulences (Shakura & Sunyaev, 1973).

We assume the disk to have a viscosity ν , which will be justified in Sect. 2.3.2. Thus, angular momentum is transported in the orthogonal direction to a shear between two annuli of gas. Overall, one can expect differences in angular momentum to diffuse in the disk.

The equations governing this process were derived in the work of Lynden-Bell & Pringle (1974) (see also Pringle, 1981), by using the continuity and angular momentum conservation equation. Noteworthy in this context is the earlier analytical work by von Weizsäcker (1948), who first derived the equations of motion for rotating masses of gas. In Appendix A.2, we follow these works and derive the disk evolution equation

$$\frac{d\Sigma}{dt} = \frac{3}{r} \frac{d}{dr} \left(r^{1/2} \frac{d}{dr} (r^{1/2} \nu \Sigma) \right). \quad (2.25)$$

The key assumption to reduce the continuity and the angular momentum conservation equation to a single equation is to approximate the angular velocity of the gas in the midplane as time independent and Keplerian ($\Omega \approx \Omega_K = \sqrt{GM_\star/r^3}$). Without

Keplerian rotation, for example due to the self-gravity of the disk, equation (A.22) can be used for a time-independent Ω .

Equation (2.25) is a nonlinear diffusion equation for Σ . Analytical solutions can be found (Armitage, 2015; Pringle, 1981; Lynden-Bell & Pringle, 1974) if the viscosity is independent of Σ and the equation thus is linear. Most of the mass moves inward in these solutions, and only the tail of the distribution moves outward. Hence, this process drives the accretion of gas by the central star.

A further driver of the disk's dispersal is photo-evaporation (see also Sect. 2.6). Photo-evaporative terms can be added to the right-hand side of equation (2.25) and will be discussed in Sect. 2.6.

2.3.1. The viscous accretion rate

Of particular interest is the rate of accretion onto the star \dot{M} given by viscous evolution governed by equation (2.25) to compare it to observed stellar accretion rates (Sect. 1.4.5). Furthermore, the flow of gas past a growing planet is an important quantity to constrain its accretion and migration (Sects. 4.2.3 and 4.3). In an intermediate step of the derivation in Appendix A.2 (equation A.21) the expression

$$rv_r\Sigma = \frac{1}{(r^2\Omega)'} \frac{\partial}{\partial r} (r^3\nu\Sigma\Omega') \quad (2.26)$$

was found, where the prime ' denotes the derivative with respect to r .

Evaluating all the derivatives with respect to r for the combined term $\nu\Sigma$ being constant in r yields $v_r = -\frac{3\nu}{2r}$. Using this radial velocity of the gas, the total accretion rate onto the star (i.e. taken from the disk, resulting in a sign change) is

$$\dot{M} = -2\pi r v_r \Sigma = 3\pi \Sigma \nu. \quad (2.27)$$

This admittedly quite circular argument shows that if $\nu\Sigma$ is constant in r , the flow towards the star will also be constant over the disk and can be expressed using equation (2.27) and is directly proportional to $\nu\Sigma$. Therefore, this is called the *steady state* solution.

2.3.2. Viscosity

Above, it was assumed that the disk has a kinematic viscosity ν . However, the viscosity is used to mimic the behavior of different physical processes and does not represent a known molecular viscosity due to micro-physics. This is because the viscosity of a gas is on the order of $\nu \sim v_{\text{th}}\ell$, where v_{th} is the thermal speed of the molecules of the gas and ℓ its mean free path. It is given by

$$\ell \sim \frac{1}{n\sigma}, \quad (2.28)$$

where n is the number density and σ is the collision cross-section of the molecules. Since the disk mainly consists of hydrogen molecules with a radius of $r \sim 10^{-8}$ cm,

$\sigma \sim \pi(10^{-8} \text{ cm})^2$ and at around 1 AU, $n \sim 10^{15} \text{ cm}^{-3}$ and $v_{\text{th}} \sim 10^5 \text{ cm s}^{-1}$. With this we can estimate the mean free path

$$\ell \sim 3 \text{ cm} \quad (2.29)$$

and the viscosity

$$\nu \sim 3 \times 10^5 \text{ cm}^2 \text{ s}^{-1}. \quad (2.30)$$

The diffusion time scale for an equation of the form of equation (2.25) is $\tau_\nu \sim (\Delta r)^2/\nu$ [Armitage \(2015\)](#), i.e. for a disk with a characteristic size R , the surface density will evolve on time scales of the order of

$$\tau_\nu \approx \frac{R^2}{\nu}, \quad (2.31)$$

which would be 10^{13} yr. This is by far longer than what is observed to be the lifetime of protoplanetary disks.

To still be able to explain the evolution according to (2.25), the viscosity has to have an other origin. Shakura & Sunyaev proposed in their paper about black hole accretion disks ([Shakura & Sunyaev, 1973](#)) that small scale turbulences cause a transport of angular momentum which replaces the molecular viscosity in a way nowadays called the Shakura-Sunyaev α -prescription. They estimate that if the maximal size of a turbulent cell is l and its velocity is v_t , then

$$\nu = \alpha v_t l. \quad (2.32)$$

As a standard approach one can replace v_t and l by characteristic velocities, such as the isothermal sound speed c_{sT} , and the scale height h of the disk to obtain

$$\nu = \alpha c_{sT} h. \quad (2.33)$$

This is justified because if a turbulent cell had a size larger than h , it would span into regions where there is very little gas present. [Shakura & Sunyaev \(1973\)](#) already restrict α to be smaller than unity, since $\alpha > 1$ would mean that there are supersonic turbulences, which would heat the gas and slow itself down.

In section 2.1 we saw that $h \approx c_{sT}/\Omega_K$, thus the viscosity can be approximated by $\nu = \alpha c_{sT}^2/\Omega_K$ or using the scale height instead of the sound speed by

$$\nu = \alpha h^2 \Omega_K. \quad (2.34)$$

α is in general a function of the radius and not constant but is often assumed to be constant (usually set to values between 0.1 and 10^{-5}) to allow a theory of the disk structure that depends on one single free parameter α . Note that the α given by the molecular viscosity would be smaller than 10^{-11} . In reality, there is likely a more complicated behavior of the viscosity that depends on the exact physical process driving accretion.

Nowadays, there are still multiple potential drivers of accretion discussed. The main competitors are disk winds induced by magnetic fields ([Konigl, 1989](#); [Gressel](#)

et al., 2015; Bai et al., 2016) or turbulence due to hydrodynamic instabilities (see Fromang & Lesur, 2019, for a review). If the driver of accretion are winds induced by magnetic fields, the assumption of a single constant α everywhere in the disk would be wrong and instead a prescription like the one presented in Bai (2016) could be used. However, magnetic field strengths cannot be directly measured and the rate of ionization of the gas disk is not known. Both are important parameters in the magnetic wind-driven scenario (Hartmann & Bae, 2018).

Alternatively, if the disk is turbulent, the α prescription can be used as an approximation. Potentially, a dependence of α on r or the time might be warranted once the exact drivers are known. For a long time, the magnetorotational instability (MRI) was a good candidate to drive turbulence (Gammie, 1996). However, recent models showed that the instability is suppressed if more detailed non-ideal magnetohydrodynamic effects are considered (e.g. Bai & Stone, 2013). Instead, purely hydrodynamic instabilities could be responsible for turbulence in most regions of the protoplanetary disk. Two instabilities that are good candidates to drive moderate amounts of turbulence (up to $\alpha \sim 10^{-4}$) are the vertical shearing instability (Nelson et al., 2013; Stoll & Kley, 2014; Cui & Bai, 2020) or convective overstability (Klahr & Hubbard, 2014).

2.4. Thermal physics

For the derivations above, a temperature T at the disk midplane was assumed. Here, we show how to analytically estimate the midplane temperature.

2.4.1. Irradiated razor-thin disk

A first estimation of the disk temperature can be made by approximating the disk as a thin layer around the star, which absorbs all the flux from the star passing through it and having the emission of a black body.

The radius R_\star and temperature T_\star of the star are usually given by observation of the star.

Our variables are the radial distance of the star r and the angle θ which is measured at a surface element from the line connecting it to the center of the star.

The total flux of one surface element of the flat disk at a distance r is then

$$F = \int I_\star \sin \theta \cos \phi \underbrace{d\Omega}_{\sin \theta d\theta d\phi}, \quad (2.35)$$

where $I_\star = \frac{1}{\pi} \sigma T_\star^4$ is the brightness of the star described using Stefan's constant σ .

Performing the intergral with limits $-\pi/2 < \phi < \pi/2$ and $0 < \theta < \sin^{-1} \left(\frac{R_\star}{r} \right)$ yields

$$F = \frac{\sigma T_\star^4}{\pi} \left[\sin^{-1} \left(\frac{R_\star}{r} \right) - \left(\frac{R_\star}{r} \right) \sqrt{1 - \left(\frac{R_\star}{r} \right)^2} \right]. \quad (2.36)$$

Note that this represents the flux coming only from one side of the disk and should be doubled for the full flux being absorbed by the disk at a given distance. We can now equate this flux to the emission σT_{surf}^4 to obtain

$$\left(\frac{T_{\text{surf}}}{T_{\star}}\right)^4 = \frac{1}{\pi} \left[\sin^{-1} \left(\frac{R_{\star}}{r} \right) - \left(\frac{R_{\star}}{r} \right) \sqrt{1 - \left(\frac{R_{\star}}{r} \right)^2} \right]. \quad (2.37)$$

The Taylor expansion to first order in $(R_{\star}/r) \ll 1$ yields

$$T_{\text{surf}} = \left(\frac{2}{3\pi} \right)^{1/4} \left(\frac{R_{\star}}{r} \right)^{3/4} T_{\star} + \mathcal{O} \left(\frac{R_{\star}}{r} \right)^{5/4} \quad (2.38)$$

for a thin, flat, passive disk. This leads to the conclusion that $h/r \propto r^{1/8}$, meaning that the disk grows thicker with distance. This effect is called *flaring*.

Considering that the disk does have an increasing h/r , would modify the received flux from the star (equation 2.35). Therefore, the precise treatment considering the flaring is slightly more involved and can be found in [Kenyon & Hartmann \(1987\)](#). A useful simple expression was found by [Ruden & Pollack \(1991\)](#) under the assumption that the disk is still thin and that the location is distant enough from the star

$$T_{\text{surf}} \approx T_{\star} \left[\frac{2}{3\pi} \left(\frac{R_{\star}}{r} \right)^3 + \frac{1}{2} \left(\frac{R_{\star}}{r} \right)^2 \frac{H}{r} \left(\frac{d \ln H}{d \ln r} - 1 \right) \right]^{1/4}, \quad (2.39)$$

where the first term is the same as in equation (2.38) and the second term in brackets originates from the fact that $dH/dr > 0$.

2.4.2. Viscous heating

In Sect. 2.4.1, we considered the temperature due to stellar irradiation. Therefore, the temperature T_{surf} describes the temperature at a layer of the disk that corresponds to how deep the stellar irradiation can penetrate. This surface is located at the transition from the optically thick to optically thin layer. However, aside from stellar irradiation, dissipation of gravitational potential energy due to accretion also needs to be included to calculate midplane temperatures. For the denser parts of the disk, it often poses the dominant energy source. Let us first assume that there is no stellar irradiation and the disk to be optically thick in the radial direction. Then, we can derive the temperature profile in the z direction due to viscous heating, i.e. energy released due to shear effects in a viscous fluid.

As long as the isothermal region is large, the density approximately follows the derived $\rho(z)$ from equation (2.6), which we assume here to be the true profile.

To approximate $T(z)$ for the viscously heated disk we follow quite closely the lecture notes of [Dullemond \(2013\)](#) and assume that the energy dissipation due to viscosity is strongly concentrated around the midplane.

Since the optically thick region is treated here, we use the so called *radiative diffusion theory* which is applicable if the mean free path of the photons is short compared to the typical length scales. In this case, the energy flux follows a diffusion equation

$$F = -D \nabla U, \quad (2.40)$$

where D is a diffusion coefficient and U is the energy density of radiation. In a three dimensional space, D is in general

$$D = \frac{1}{3} v l_p, \quad (2.41)$$

where v is the average velocity of the particles and l_p is the mean free path. For photons $v = c$, i.e. the speed of light, and $l_p = \frac{1}{\kappa_R \rho}$, where κ_R is the Rosseland mean opacity.

The energy density of radiation can be found from statistical quantum mechanics and integrating over all wavelength, yielding

$$U(T) = \frac{8\pi^5 k_B^4}{15c^3 h_P^3} T^4 = \frac{4\sigma}{c} T^4, \quad (2.42)$$

where h_P is Planck's and σ is Stefan's constant.

Then, equation (2.40) can be written considering only the upward z component of energy flux as

$$F_z^+(z) = -\frac{c}{3\kappa_R \rho(z)} \frac{4\sigma}{c} \frac{dT^4}{dz}, \quad (2.43)$$

yielding

$$F_z^+(z) = -\frac{16\sigma T^3}{3\kappa_R \rho(z)} \frac{dT}{dz}. \quad (2.44)$$

This describes the transport of energy in the radial direction. The dissipation is in the viscously dominated part of the disk due to viscous shear. The energy dissipation rate is

$$\dot{E}_{\text{visc}} = \Sigma \nu \left(r \frac{d\Omega}{dr} \right)^2, \quad (2.45)$$

which is for Keplerian angular velocity $\Omega = \Omega_K$

$$\dot{E}_{\text{visc}} = \Sigma \nu r^2 \left((-3/2) \sqrt{GM_\star} r^{-5/2} \right)^2 = \frac{9}{4} \Sigma \nu \Omega_K^2. \quad (2.46)$$

In the mean, half of this energy is transported upwards, i.e. $\frac{1}{2} \dot{E}_{\text{visc}} = F_z^+$, leading to

$$\frac{1}{2} \dot{E}_{\text{visc}} = -\frac{16\sigma T^3}{3\kappa_R \rho(z)} \frac{dT}{dz} \quad (2.47)$$

$$\Rightarrow \dot{E}_{\text{visc}} \int_0^{z_{ph}} \rho(z) dz = -\frac{32\sigma}{3\kappa_R} \int_{T_{\text{mid}}}^{T_{ph}} T^3 dT \quad (2.48)$$

$$\Rightarrow \dot{E}_{\text{visc}} \frac{1}{2} \Sigma = -\frac{8\sigma}{3\kappa_R} (T_{ph}^4 - T_{\text{mid}}^4), \quad (2.49)$$

where T_{ph} and z_{ph} are the temperature and height of the photosphere, i.e. the location where the radiation is radiated away due to the gas becoming optically thin. We assumed $z_{ph} \gg h$ to replace $\int_0^{z_{ph}} \rho dz \approx \int_0^\infty \rho dz = \frac{1}{2}\Sigma$. Rearranging the terms, leads to an expression for the difference between the surface (or photosphere) temperature T_{ph} and the central temperature T_{mid} of the disk

$$T_{mid}^4 - T_{ph}^4 = \frac{3\kappa_R \Sigma \dot{E}_{visc}}{16\sigma} = \frac{3\tau_R \dot{E}_{visc}}{8\sigma} = \frac{27\kappa_R \Sigma^2 \nu \Omega_K^2}{64\sigma}, \quad (2.50)$$

where $\tau_R = \frac{1}{2}\kappa_R \Sigma$.¹

Of interest would now be to get an expression for T_{mid} . For this we can use the energy balance at the photosphere

$$\sigma T_{ph}^4 = \sigma T_{cloud}^4 + \frac{1}{2} \dot{E}_{visc}, \quad (2.51)$$

where the right hand terms include heating from the environment and heating propagated from the disk midplane (i.e. we assume thermodynamical equilibrium). The left hand term is the black body cooling rate and

$$T_{cloud} \approx (\sigma(10\text{ K})^4 + \sigma T_{surf}^4)^{1/4} \ll T_{mid} \quad (2.52)$$

is some ambient temperature, which should have a floor value of the order of 10 K from the galactic neighborhood and can include contributions from stellar irradiation such as equation (2.39) derived in the previous Section. Using the result in equation (2.50) to replace T_{ph} yields

$$T_{mid}^4 - \frac{3\kappa_R \Sigma \dot{E}_{visc}}{16\sigma} = T_{cloud}^4 + \frac{1}{2\sigma} \dot{E}_{visc} \quad (2.53)$$

$$\Rightarrow T_{mid}^4 = T_{cloud}^4 + \frac{1}{2\sigma} \left(1 + \frac{3\kappa_R \Sigma}{8}\right) \dot{E}_{visc}. \quad (2.54)$$

As mentioned before, we assumed that the disk is optically thick, i.e. $\kappa_R \Sigma \gg 1$, thus, we can simplify the expression to obtain

$$T_{mid}^4 = T_{cloud}^4 + \frac{3\kappa_R \Sigma \dot{E}_{visc}}{16\sigma}. \quad (2.55)$$

If we are in the optically thin regime, Nakamoto & Nakagawa (1994) derived a surface temperature, which is equal to the midplane temperature, of

$$T_{ph}^4 = T_{mid}^4 = \frac{\dot{E}_{visc}}{4\sigma\kappa_P\Sigma} + T_{cloud}^4, \quad (2.56)$$

¹Note that this definition of τ_R differs from the one used in Nakamoto & Nakagawa (1994), where they use $\tau_R = \kappa_R \Sigma$.

where κ_P is the Planck opacity. An approximative equation that works for both regimes is then

$$T_{\text{mid}}^4 = \frac{1}{4\sigma} \left(\frac{3\kappa_R\Sigma}{4} + \frac{1}{\kappa_P\Sigma} \right) \dot{E}_{\text{visc}} + T_{\text{cloud}}^4, \quad (2.57)$$

which is close to equation 3.10 by Nakamoto & Nakagawa (1994), only missing a shock heating term from an ongoing infall of gas onto the disk.

Equation (2.57) is a useful analytic approximation to the midplane temperature. We would like to stress again that many assumptions were made to get this result. Nevertheless it is of great importance to have a temperature on the right order of magnitude to use for planetary growth which scales correctly using different physical assumptions. Especially for the composition of forming planets, the temperature structure of the disk is very important.

2.5. Composition of disks

Having a model for the temperature and pressure in the disk allows us to calculate which chemical species can be present in solid form as a function of the location. The point at which the conditions in the disk reach the condensation point for a certain molecule is called an *iceline* or *snowline*. The latter is more commonly used for the H₂O iceline.

It is important to notice that not only the temperature, but also the gas pressure are important to determine the condensation point. Furthermore, it is not strictly correct to talk about a single point but a smooth transition should be considered using a sublimation rate following the Hertz-Knudsen-Langmuir prescription (Hertz, 1882; Delsemme & Miller, 1971). Therefore, one has to specify a timescale for comparison to determine the icelines (Marboeuf et al., 2014b). For many practical applications, it is however sufficient to use a single point because the sublimation rate is a steep function of the temperature.

Furthermore, there is a dependence of the temperature and pressure on the vertical direction of the disk. Therefore, the icelines are in fact ice-surfaces that are typically closest to the star in the disk midplane and extend further out at higher elevations above the midplane. This is important for observational studies of the disk.

Another aspect of the icelines will be explored in Paper I, where we will study the effect of the motion of a particle in the disk. Commonly used definitions of the iceline rely on the temperature and pressure of the disk but do not consider that particles also drift towards the star in the disk (Sect. 2.8). We will follow a body undergoing radial drift and calculate its ablation in the disk to find a better estimate of the location in the disk where no water exist anymore. The water iceline induces the largest jump in the surface density of solids because H₂O is the most common ice in protoplanetary disks. Therefore, its significance for planet formation is largest.

In addition to sublimation, chemistry acts depending on the temperature and pressure as well as the abundance of elements. For infinite time and fixed thermal conditions, chemical reactions push a system towards an equilibrium that minimizes

the Gibbs free energy (Gibbs, 1873). This approach was used by Thiabaud et al. (2014) to calculate the abundance of 32 common molecules (Bond et al., 2010) in the disk’s gas and solid phases. The model takes as input the disk temperature and pressure as well as the abundance of 16 elements as measured in stars (e.g. Lodders, 2003, for the Sun) and outputs elemental abundances of solid grains as a function of the distance to the star. The top panel of 2.1 shows the resulting relative abundances for a disk with a gas disk mass of $0.034 M_{\odot}$, a solid to gas mass ratio of 0.0159 and a viscous α of 2×10^{-3} (equivalent as for the disk shown in Sect. 2.7). The major drop at ~ 3 au is due to the H_2O iceline, where a jump in the total amount of solids occurs. Marboeuf et al. (2014b) consider condensation and trapping in ices of volatile molecules (i.e. molecules which are likely to sublime in typical disk conditions) to enlarge the total amount of solids. Such a kind of trapping of molecules in the lattice structure of a different ice can occur in a protoplanetary disk and the structure is described as a *clathrate*.

For the results shown in Fig. 2.1, we follow the works of Thiabaud et al. (2014) and Marboeuf et al. (2014b) for solar elemental abundances (Lodders, 2003) but use the newer disk model, where the disk midplane temperature is calculated following the analytic works of Nakamoto & Nakagawa (1994); Hueso & Guillot (2005). Apart from this major relevant difference, the initial surface density profile is chosen differently. Additionally, the analysis of refractory sulfur, calcium and aluminium is enabled thanks to tracking them individually as opposed to summing them up with the remaining untracked species (Ti, P, Cr, Na, H and He). It is important to notice that H and He are not commonly present in solids despite being the most abundant elements in protoplanetary disks. The dominant refractory elements are iron, oxygen, silicon and magnesium and water ice is the dominant icy species followed by carbon-dioxide (CO_2), methanol (CH_3OH) and carbon-monoxide (CO).

A planet accreting these molecules incorporated in solid planetesimals at the different location incorporates them and the chemistry on the planet becomes much more complex. However, the elemental ratios of the overall planet cannot be changed unless the elements get lost back to space, which is only common for hydrogen and helium. The abundance of all heavier elements on the planet stays the same and determines the planetary composition. The compositions of planets using this model are discussed in Thiabaud et al. (2014, 2015); Marboeuf et al. (2014a) and an updated analysis in the framework of the NGPPS papers (see Chapter 5) is planned.

As mentioned, the major assumption that enters this model is that the Gibbs energy minimum is reached (for the refractory part of the model), which requires chemical reactions to proceed faster than the typical timescale of planet formation of $\sim Myr$. This is most likely not true in the outer regions of the disk where the pressure is low and the chance for two molecules to encounter each other and react is low. For higher pressures within a few astronomical units, the assumption is more justified for the most common molecules (Henning & Semenov, 2013; Thiabaud et al., 2014; Eistrup et al., 2016, 2018).

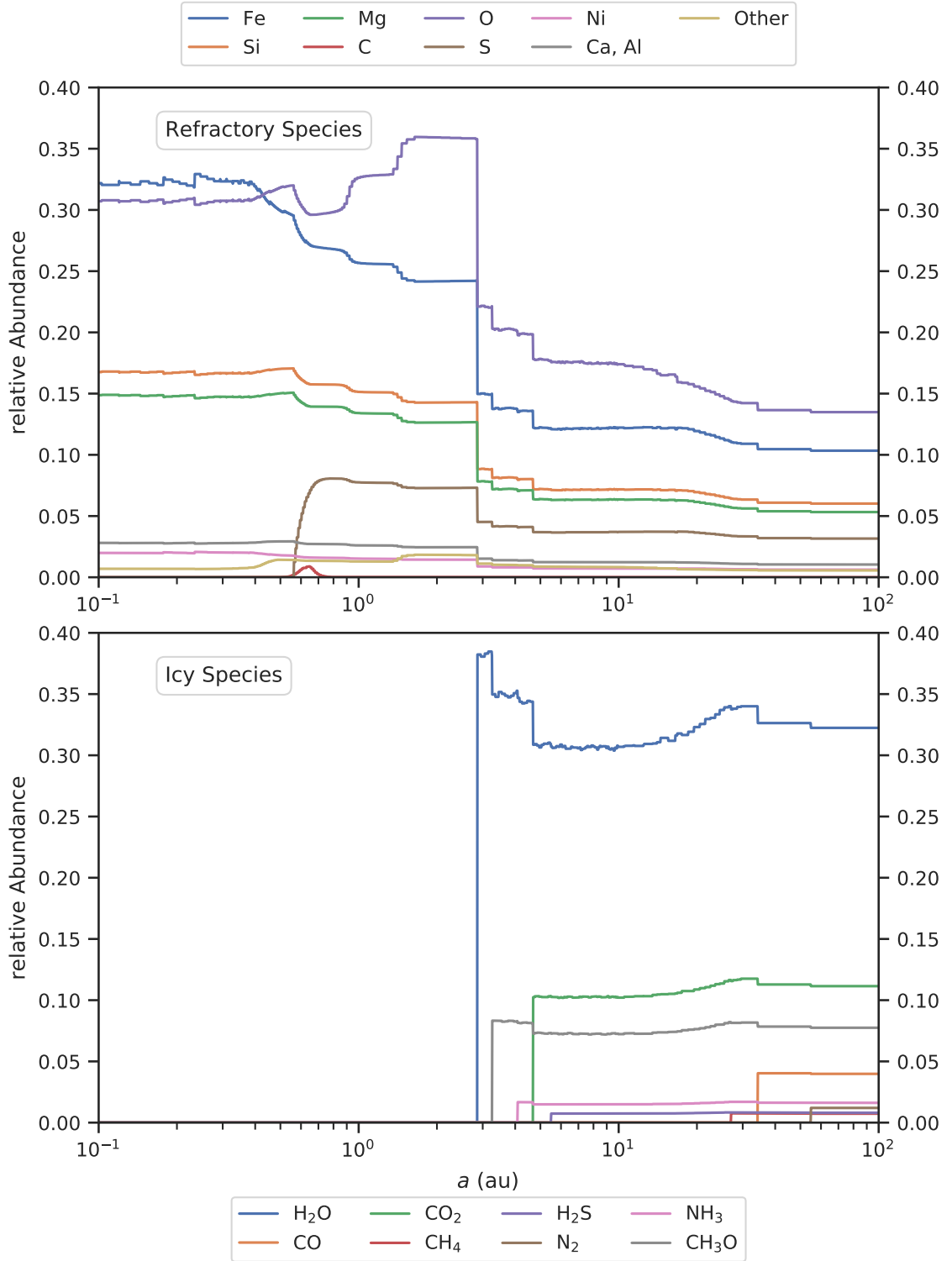


Figure 2.1.: Abundance of elements in refractory species and ices compared to the total amount of solids in the disk. The top panel and the corresponding legend above it correspond to elements in refractory species (Thiabaud et al., 2014). Ca and Al and Ti, P, Cr, Na, H and He (*Other*) are grouped together. The elements contained in the icy species (Marboeuf et al., 2014b, bottom panel) are not included in the abundances of the top panel.

2.6. Photo-evaporation of disks

The process of photo-evaporation occurs if high-energy radiation ionizes and excites a neutral gas. In that case, the excited gas particle can disperse if the energy received is large enough to escape the gravitational potential in which the gas is placed. This process can occur for planetary atmospheres as well as for protoplanetary disks. Here, we will focus on the evaporation of disks. This problem was first addressed in-depth by [Hollenbach et al. \(1994\)](#) and belongs now to the standard processes in the disk (see [Alexander et al., 2014](#), for a recent review). It is considered important in the later stages of the disk evolution, where a pure viscous disk would gradually thin out. However, observations indicate that the dispersal of the disk is rapid ([Armitage, 2019](#)). This rapid stage can be attributed to photo-evaporation.

Two categories of photo-evaporation can be distinguished depending on the origin of the radiation: *Internal* photo-evaporation due to the central star and *external* photo-evaporation driven by nearby massive stars. Furthermore, a range of radiation energies from very high X-ray ([Ercolano & Rosotti, 2015](#)) ($\lambda \sim 0.01$ nm to 10 nm) over the extreme ultraviolet (λ up to ~ 30 nm) to the far ultraviolet (λ up to 200 nm) has been considered. Independent of the origin of the radiation, the concept of a *gravitational radius* r_g is useful. It describes the location in the disk where the ionized gas can escape the disk. This can be derived by equating the orbital velocity with the sound speed reached after excitation

$$\sqrt{\frac{GM_\star}{r_g}} = \sqrt{\frac{k_B T_i}{\mu m_H}}, \quad (2.58)$$

where T_i is the temperature of the gas after ionization. If we solve for the characteristic gravitational radius we get

$$r_g = \frac{\mu m_H GM_\star}{k_B T_i}. \quad (2.59)$$

Note that this description is equivalent to equating the thermal energy $k_B T_i$ to the gravitational binding energy of an individual gas particle $\frac{GM_\star \mu m_H}{r_g}$, which helps to understand why the sound speed is chosen and not the thermal velocity or some other characteristic speed of a gas.

This estimate of the gravitational radius is quite simple. A more detailed analysis of when particles can be launched as a ionized wind leads to a Bernoulli equation ([Liffman, 2003](#))

$$\frac{1}{2}v_K^2 + \frac{\gamma}{\gamma - 1} \frac{k_B T_i}{\mu m_H} - \frac{GM_\star}{r} = E, \quad (2.60)$$

where γ is the adiabatic index, a purely Keplerian motion for the gas was assumed and the heat capacity at constant pressure was used. The particle can escape if $E > 0$, thus a critical radius results:

$$r_c = \frac{(\gamma - 1)GM_\star \mu m_H}{2\gamma k_B T_i}. \quad (2.61)$$

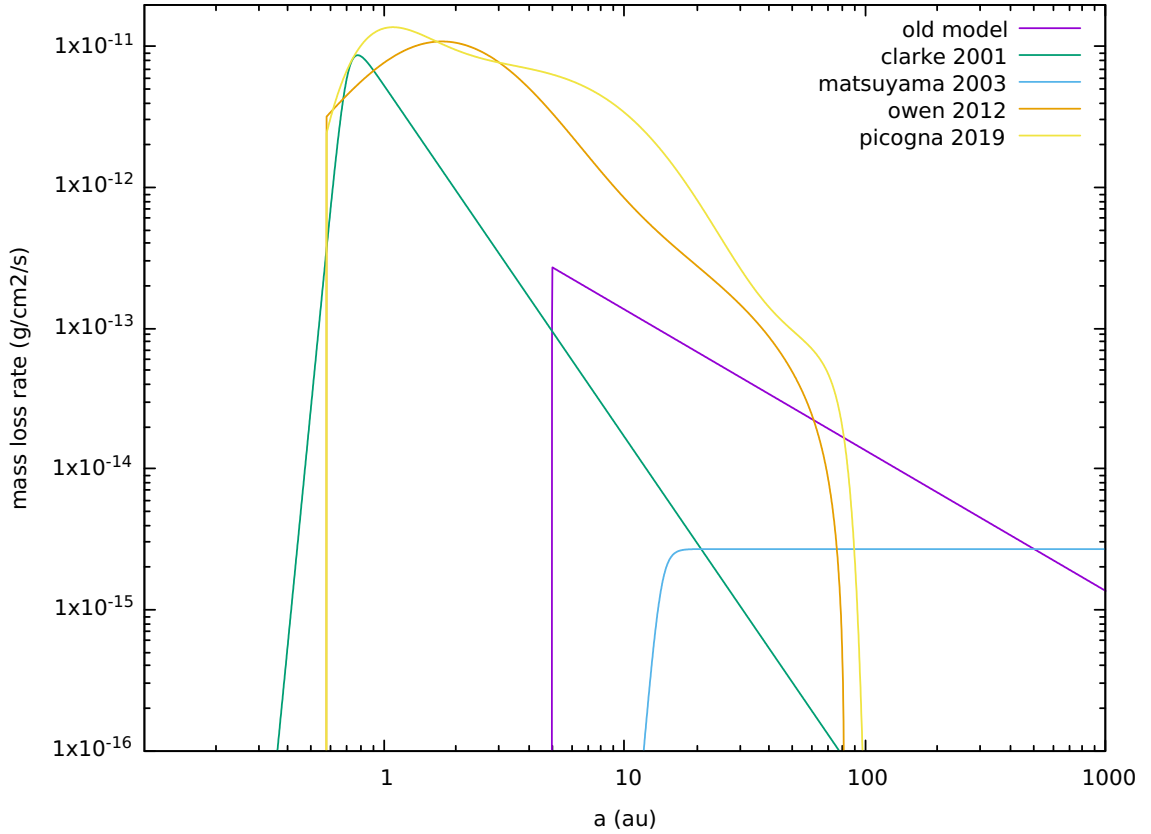


Figure 2.2.: Comparison of mass loss profiles for different photo-evaporation models. For reference, we also show the *old model*, which follows a simple dependency of $\dot{\Sigma}_w \propto r^{-1}$ used in Veras & Armitage (2004); Mordasini et al. (2009a), as well as in Paper I to mimic external photo-evaporation. The profile following the external photo-evaporation case in Matsuyama et al. (2003) was scaled arbitrarily for this plot and is used in the newer works of the Bern group (Mordasini et al., 2012b). The profiles from Owen et al. (2012) and Picogna et al. (2019) are fits to results from a similar numerical model taking into account X-ray and EUV radiation from the star. Similarly, the profile from Clarke et al. (2001) also models internal photo-evaporation based on the analytical model by Hollenbach et al. (1994).

If the gas is monatomic $\gamma = 5/3$, then $r_c = 0.2r_g$. In the literature, different values for the critical radius r_c are found ranging from 0.1 to 0.2 r_g (Alexander et al., 2014).

For extreme-ultra-violet radiation, the temperature of the ions is on the order of 10^4 K (Hollenbach et al., 1994; Clarke et al., 2001) whereas lower-energy radiation in the far-ultra violet the temperatures are close to 10^3 K. Interestingly, the higher X-ray energy does not lead to higher temperatures but also to $T \sim 10^3$ K because the radiation is not absorbed by a single particle. This is because only extreme-ultra-violet radiation spans the energy region for hydrogen ionization (13.6 eV). Therefore, the corresponding gravitational and critical radii differ by a factor of 10. For EUV, the critical radius is $r_{c,\text{EUV}} \approx 1.45$ au.

This generally leads to the conclusion that EUV acts very close to the star, whereas FUV and X-Ray radiation might be dominant for the outer regions of the disk. Since there is much more mass to evaporate at distant regions, FUV or X-Ray radiation should dominate the overall effect on the disk dispersal (Gorti & Hollenbach, 2008; Ercolano & Rosotti, 2015). In principle, both the overall spectrum of ionizing and hydrogen-dissociating radiation should be taken into account and the combined mass loss should be studied. For X-Ray and EUV, this is already completed by the works of Owen et al. (2012); Picogna et al. (2019).

Despite the fact that EUV radiation does not contribute a lot to the total mass loss of the disk, it is nevertheless very important in shaping the disk profile. As gas accretes onto the star, the surface density decreases and at some point in time, the viscous flow becomes insufficient to replenish the photo-evaporative mass loss per area $\dot{\Sigma}_w$ (Clarke et al., 2001). As the gas drifts with a viscous radial speed of $v_r = -\frac{3\nu}{2r}$ (see Sect. 2.3.1), we can derive a critical Σ_{crit} for which the mass in the annulus decreases. This leads to the opening of a hole.

$$\frac{3\nu\rho_{\text{crit}}}{2r} = \dot{\Sigma}_w \quad (2.62)$$

$$\Rightarrow \Sigma_{\text{crit}} = \frac{2\sqrt{2\pi}rh}{3\nu}\dot{\Sigma}_w = \frac{2\sqrt{2\pi}}{3\alpha} \frac{r}{h} \frac{\dot{\Sigma}_w}{\Omega_K}, \quad (2.63)$$

where we used the α description of the viscosity (equation 2.34) to obtain the last equality. Therefore, where Σ falls below Σ_{crit} , a hole in the disk forms and the gas in the region starwards of the hole will quickly accrete onto the star. This is because the inflow of gas from outer regions is missing. Such inner cavities tend to open where the $\dot{\Sigma}_w$ profile peaks, that is, close to the critical radius (equation 2.61). This is made clear in Fig. 2.3, where we see that using the steady-state flow for Σ_{crit} gives a good first approximation to gauge if holes will open. The surface density in the outer regions is also below Σ_{crit} because of external photo-evaporation being used.

Nowadays, detailed numerical calculations provide realistic mass loss rates due to photo-evaporation. In the first analytical work, Hollenbach et al. (1994) found that the time to recombine dissociated hydrogen limits the amount of loss. In that case a mass loss rate $\dot{M}_w \propto \frac{\Phi_i r_g}{\alpha_2} \mu m_H c_s$ results, where Φ_i is the photon luminosity in photons per second of the star and α_2 is the recombination coefficient. Hollenbach et al. (1994) estimated the radial profile to drop with $r^{5/2}$. Clarke et al. (2001)

adapted the results to the case of Sun-like stars and the resulting mass loss rate as a function of the semi-major axis for a Sun-like star can be seen in Fig. 2.2.

Over the course of this thesis, the newer photo-evaporation descriptions from Owen et al. (2012) and from Picogna et al. (2019) were implemented in the disk module of the Bern model of global planet formation and evolution (Bern model). Therefore, we restate in the remainder of this chapter their analytical fits to the numerical modeling results and describe in some detail the numerical implementation. For comparison to the older works, these newer profiles are shown in Fig. 2.2.

2.6.1. X-ray luminosity

Before describing the detailed evaporation results, we briefly discuss the most important parameter for X-ray driven photo-evaporation: The luminosity of the star in the X-ray wavelength regime L_X . The X-ray luminosity of young stars is most likely created by accretion shocks as supersonic gas falling onto the stellar surface decelerates. Therefore, the X-ray luminosity should in principle scale with the accretion rate, but only low accretion rates are required to reproduce the observations $\sim 10^{-10} M_\odot \text{ yr}^{-1}$ and how much radiation is absorbed in the shock region is not well known.

From analytical theory, accretion-induced X-ray luminosity should amount to $L_X \sim L_{\text{acc}} \approx 0.8 \frac{GM_{\text{acc}} M_\star}{R_\star}$ (Calvet & Gullbring, 1998; Güdel & Nazé, 2009; Hartmann, 2009; Hartmann et al., 2016). Observationally, the samples of young accreting protostars (Class II) in Lupus and Orion are consistent with $L_X \propto M_\star^{3/2}$ (Preibisch et al., 2005; Güdel et al., 2007). Similar measurements can be used to derive accretion rate dependencies on stellar mass ranging from 1.8 (Alcalá et al., 2014) to 2.1 (Hartmann et al., 2016) with a potential steeper slope for stellar masses below $0.2 M_\odot$ (Alcalá et al., 2017, see also Paper III). The distribution of L_X as found by Güdel et al. (2007) but for all targets scaled to a star of mass $0.7 M_\odot$ can be seen in Fig. 2.4.

Theory would predict an accretion-induced L_X independent of the rotation rate of the star. However, for X-rays produced in older stars and the Sun, it is clear that the X-ray radiation is produced by magnetic phenomena in the stellar photosphere. For this process, L_X depends on the strength of the stellar magnetic field which is produced by a magnetic dynamo. Thus, L_X induced by magnetic activity scales with the rotation rate Ω_\star of the star as $L_X \propto \Omega_\star^2$ (Pizzolato et al., 2003). Accretion-induced L_X seems to dominate for young stars but the magnetically induced luminosity should not be neglected.

2.6.2. Numerical X-Ray photo-evaporation models

Photo-evaporation can be considered if a term $\dot{\Sigma}_w$ is added to the right hand side of equation (2.25). Numerically, this is then considered as the disk evolution is solved. Owen et al. (2012) and Picogna et al. (2019) do provide overall mass loss rates \dot{M}_w and profiles for $\dot{\Sigma}_w(r)$ that then have to be scaled by a normalization factor n_X to fulfill $\dot{M}_w = n_X \int_0^\infty 2\pi r \dot{\Sigma}_w(r) dr$.

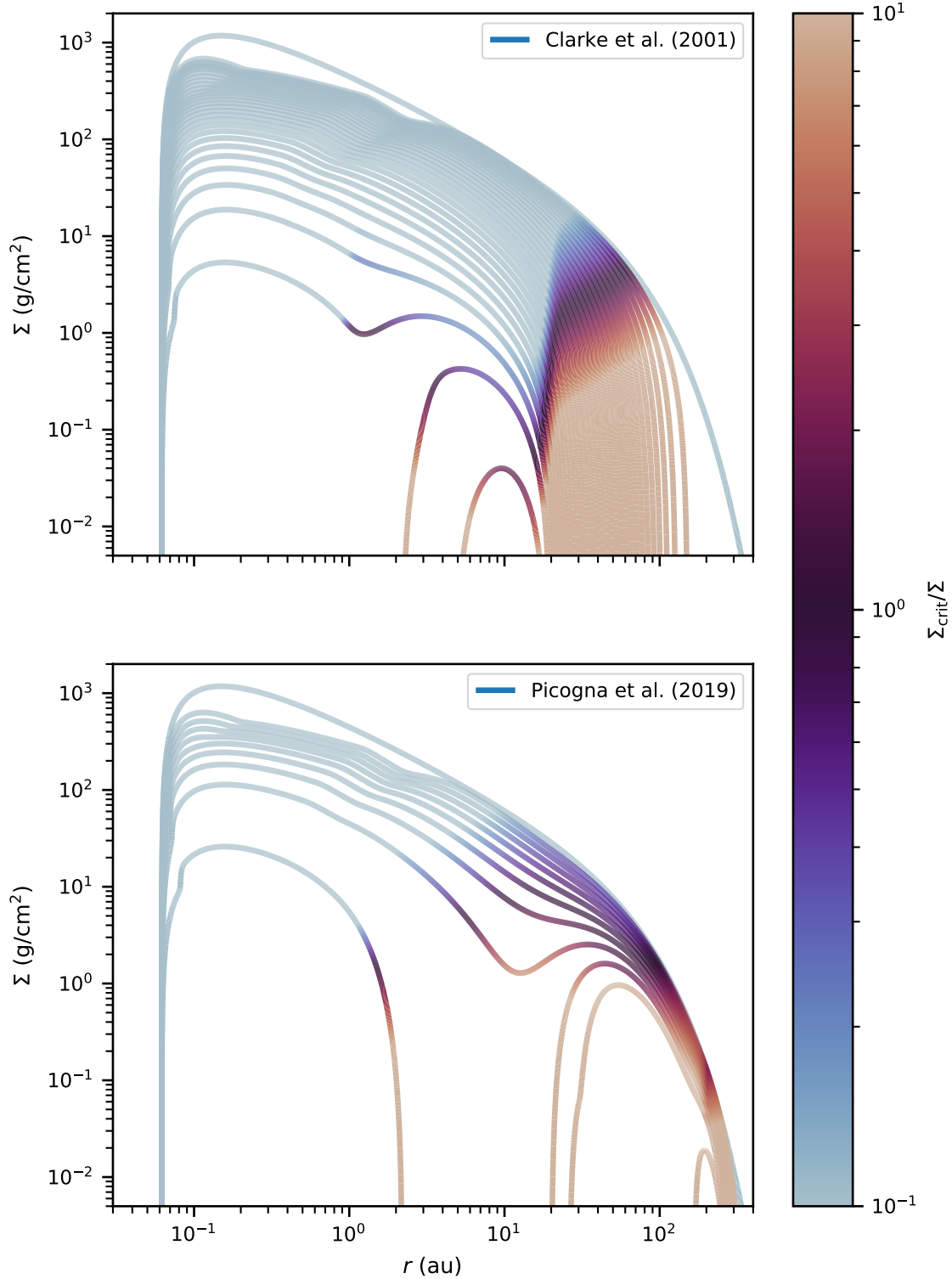


Figure 2.3.: Surface density profiles for a disk with nominal photo-evaporation (Clarke et al., 2001, top panel) and one with internal photo-evaporation based on Picogna et al. (2019) (bottom). The time between two drawn profiles is set to $\sim 1 \times 10^5$ yr and the fraction $\Sigma_{\text{crit}}/\Sigma$ is indicated by the line-color. Dark and red regions would not have enough gas flow towards them to sustain the photo-evaporative loss.

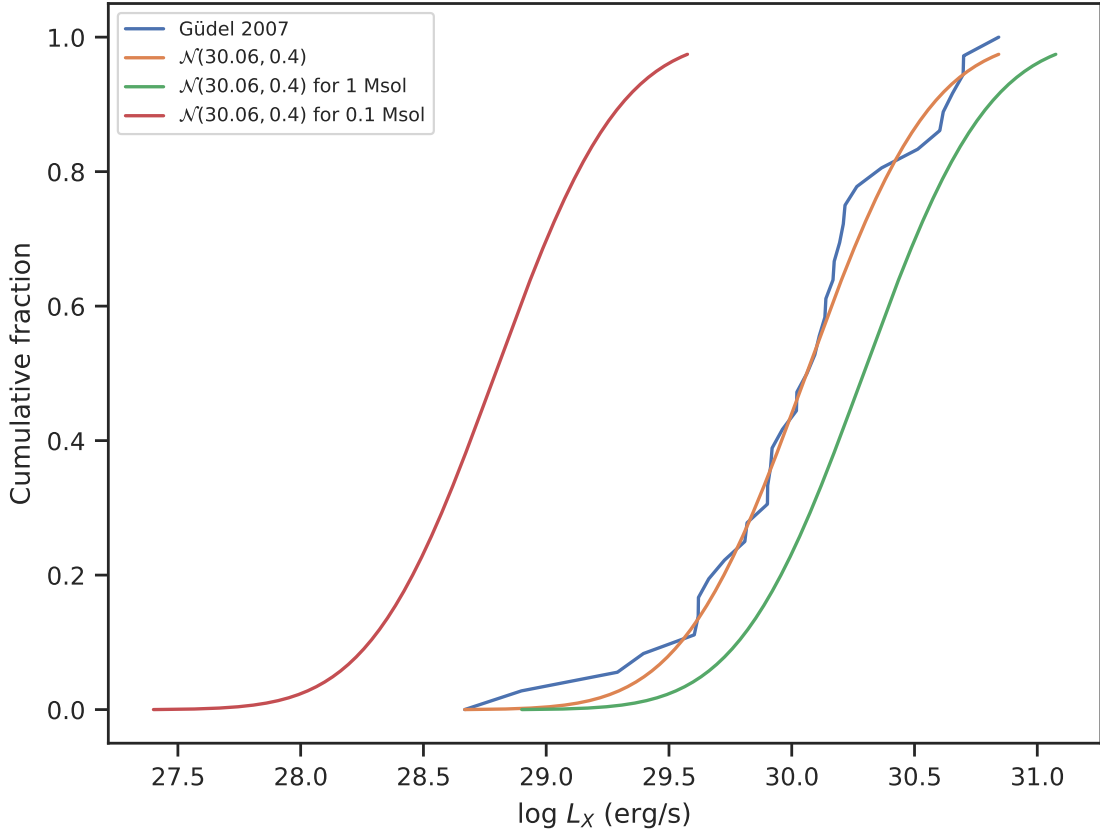


Figure 2.4.: Cumulative fraction of observed X-ray luminosities (Güdel et al., 2007) and corresponding numerical fits. The observed luminosities were scaled to represent a $0.7 M_{\odot}$ star using the relation $L_X \propto M_{\star}^{1.5}$. A Gaussian distribution with mean value of $\mu = 30.06$ and standard deviation $\sigma = 0.4$ does well match the observed distribution in $\log_{10} L_X$ space. For reference, the scaled distributions for $0.1 M_{\odot}$ and $1.0 M_{\odot}$ are shown.

However, this is not straightforward because if there are regions where the surface density drops to zero, $\dot{\Sigma}_w$ also amounts to zero. Therefore, it is not possible to fix $\dot{\Sigma}_w$ in time for the case of disk cavities.

Because the numerical simulations are snapshots in terms of the disk evolution, they generally consider either an extended disk or the case of a disk with a considerable inner cavity. Therefore, it is not directly applicable to disks that have gaps carved by planets or small cavities. To overcome this issue, we decided to not keep \dot{M}_w constant over all the disk's lifetime. Instead, we determine the normalization for the extended case at the beginning of the simulation, when the disk structure is free of any kind of gaps. Afterwards, this n_X is kept for the remainder of the first phase of photo-evaporation, which means that $\dot{\Sigma}_w(r)$ is constant in time as long as $\Sigma(r) > 0$.

This is done until the criterion of a considerable hole being opened is met. The hole criterion is inspired from [Owen et al. \(2011, 2012\)](#) and is fulfilled if the radius of the inner hole reaches the region of relevant photo-evaporation $x_{\text{hole}} > 2$ (see definitions below). The hole radius r_{hole} is defined as the location where the integrated radial column number density through the midplane reaches the maximum X-ray penetration depth of 10^{22} cm^{-2} . This is then translated to the dimensionless units $x_{\text{hole}} = 0.85 \left(\frac{r_{\text{hole}}}{\text{au}}\right) \left(\frac{M_{\star}}{M_{\odot}}\right)^{-1}$ by [Owen et al. \(2012\)](#). This hole opening criterion is used in our implementation for both photo-evaporation models.

Once a hole has opened, the profile and overall mass loss rates change and we determine the normalization constant at the time of hole-opening. Afterwards, as the disk disperses, the normalization is kept constant. This leads to a time dependent $\dot{M}_{w,\text{hole}}$ during the hole phase. This treatment is chosen despite the results in [Picogna et al. \(2019\)](#) showing no dependency of $\dot{M}_{w,\text{hole}}$ on the hole radius. The reason is numerical stability at the latest stages when the disk becomes a very narrow ring. Then, the normalization would locally lead to almost infinite $\dot{\Sigma}_{w,\text{hole}}$. Thanks to the profile $\dot{\Sigma}_{w,\text{hole}}$ depending on the hole radius, $\dot{M}_{w,\text{hole}}$ does not change by factors larger than 10 during the dispersal of the disks modeled here.

[Owen et al. \(2012\)](#) XEUV evaporation

[Owen et al. \(2012\)](#) fit their numerical results and find for the total mass-loss rate of an the extended disk

$$\dot{M}_{w,\text{Owen}} = 6.25 \times 10^{-9} \left(\frac{M_{\star}}{M_{\odot}}\right)^{-0.068} \left(\frac{L_X}{10^{30} \text{ erg s}^{-1}}\right)^{1.14} M_{\odot} \text{ yr}^{-1}. \quad (2.64)$$

For the profile, they introduce the variable $x \equiv 0.85 \left(\frac{r}{\text{au}}\right) \left(\frac{M_{\star}}{M_{\odot}}\right)^{-1}$. If x is below 0.7, no evaporation occurs, which corresponds to the concept of gravitationally bound gas despite the heating. For $x > 0.7$

$$\begin{aligned} \dot{\Sigma}_{w,\text{Owen}}(x) \propto & 10^{[a_1 \log_{10}(x)^6 + b_1 \log_{10}(x)^5 + c_1 \log_{10}(x)^4 + d_1 \log_{10}^3 + e_1 \log_{10}^2 + f_1 \log_{10} + g_1]} \\ & \times \frac{1}{x^2} \left[\frac{6a_1 \ln(x)^5}{\ln(10)^7} + \frac{5b_1 \ln(x)^4}{\ln(10)^6} + \frac{4c_1 \ln(x)^3}{\ln(10)^5} \right. \\ & \left. + \frac{3d_1 \ln(x)^2}{\ln(10)^4} + \frac{2e_1 \ln(x)}{\ln(10)^3} + \frac{f_1}{\ln(10)^2} \right] \exp \left[- \left(\frac{x}{100}\right)^{10} \right], \end{aligned} \quad (2.65)$$

where we would like to point out that both the natural logarithm \ln and the logarithm to basis 10 \log_{10} are used. The constants are $a_1 = 0.15138$, $b_1 = -1.2182$, $c_1 = 3.4046$, $d_1 = -3.5717$, $e_1 = -0.32762$, $f_1 = 3.6064$ and $g_1 = -2.4918$.

During the hole stage, [Owen et al. \(2012\)](#) found

$$\dot{M}_{w,\text{hole,Owen}} = 4.8 \times 10^{-9} \left(\frac{M_{\star}}{M_{\odot}}\right)^{-0.148} \left(\frac{L_X}{10^{30} \text{ erg s}^{-1}}\right)^{1.14} M_{\odot} \text{ yr}^{-1} \quad (2.66)$$

and a new radial coordinate is introduced

$$y = 0.95(r - r_{\text{hole}}) \left(\frac{M_{\star}}{1 M_{\odot}} \right)^{-1}. \quad (2.67)$$

Then, the profile at $y > 0$ is described by

$$\dot{\Sigma}_{w,\text{hole,Owen}}(y) = \left[\frac{a_2 b_2 \exp(b_2 y)}{r} + \frac{c_2 d_2 \exp(d_2 y)}{r} + \frac{e_2 f_2 \exp(f_2 y)}{r} \right] \exp \left[- \left(\frac{y}{57} \right)^{10} \right] \quad (2.68)$$

and the constants are given by $a_2 = -0.438226$, $b_2 = -0.10658387$, $c_2 = 0.5699464$, $d_2 = 0.010732277$, $e_2 = -0.131809597$ and $f_2 = -1.32285709$. Within the hole radius, that is for $y < 0$, no evaporation takes place.

Picogna et al. (2019) XEUV evaporation

Similar to Owen et al. (2012), Picogna et al. (2019) introduce a new radial variable

$$r_1 = 0.7 \left(\frac{r}{1 \text{ au}} \right) \left(\frac{M_{\star}}{1 M_{\odot}} \right)^{-1} \quad (2.69)$$

and $r_e = \ln(r_1)$, $r_{10} = \log_{10}(r_1)$. Then, for $r_1 > 0.7$, the evaporation profile for a $0.7 M_{\odot}$ star is given by (Picogna et al., 2019, equations 2,3, and 4)

$$\begin{aligned} \dot{\Sigma}_{w,\text{Picogna}}(r_1) \propto 10^{[a_X r_{10}^6 + b_X r_{10}^5 + c_X r_{10}^4 + d_X r_{10}^3 + e_X r_{10}^2 + f_X r_{10} + g_X]} \\ \times \left(\frac{6a_X r_e^5}{r_1^2 \ln(10)^7} + \frac{5b_X r_e^4}{r_1^2 \ln(10)^6} + \frac{4c_X r_e^3}{r_1^2 \ln(10)^5} \right. \\ \left. + \frac{3d_X r_e^2}{r_1^2 \ln(10)^4} + \frac{2e_X r_e}{r_1^2 \ln(10)^3} + \frac{f_X}{r_1^2 \ln(10)^2} \right), \end{aligned} \quad (2.70)$$

where $a_X = -0.5885$, $b_X = 4.3130$, $c_X = -12.1214$, $d_X = 16.3587$, $e_X = -11.4721$, $f_X = 5.7248$ and $g_X = -2.8562$. The total mass loss rate used for the normalization is given by

$$\log_{10} \left(\frac{\dot{M}_{w,\text{Picogna}}}{1 M_{\odot}/\text{yr}} \right) = a_L \exp \left(\frac{(\ln(\log_{10}(L_X)) - b_L)^2}{c_L} \right) + d_L, \quad (2.71)$$

where $a_L = -2.7326$, $b_L = 3.3307$, $c_L = -2.9868 \times 10^{-3}$, $d_L = -7.2580$. $\dot{M}_{w,\text{Picogna}}$ is scaled $\propto M_{\star}^{-0.068}$ following Owen et al. (2012) because the calculations were done at fixed stellar mass in Picogna et al. (2019).

After an inner hole in the disk has opened, an additional transition disk evaporation is employed, yielding higher total mass loss rates $\dot{M}_{w,\text{hole}}$ during this stage. The total transitional mass loss rate is given by

$$\log_{10} \left(\frac{\dot{M}_{w,\text{hole,Picogna}}}{1 M_{\odot}/\text{yr}} \right) = 0.965 \times \log_{10} \left(\frac{\dot{M}_{w,\text{Picogna}}}{1 M_{\odot}/\text{yr}} \right) - 9.592 \times 10^{-3} \times \frac{r_{\text{hole}}}{(1 \text{ au})} \quad (2.72)$$

and the profile is given by (Picogna et al., 2019)²

$$\dot{\Sigma}_{w,\text{hole,Picogna}} \propto \frac{b_t - a_t c_t}{\left(b_t + c_t \left(\frac{r}{1 \text{ au}} - \frac{r_{\text{hole}}}{1 \text{ au}}\right)\right)^2}, \quad (2.73)$$

where $a_t = 0.9058$, $b_t = 12.876$, $c_t = 0.9056$. To prevent unphysical evaporation, we restrict r_{hole} to be smaller than $120 \text{ au} \times \left(\frac{M_\star}{0.7 M_\odot}\right)$.

Using the internal X-ray and EUV evaporation rates alone yields *relic disks*, i.e. rings of gas outside of $\sim 100 \text{ au}$ that are not efficiently removed (Owen et al., 2011, 2012). These remnants are not observed and are efficiently removed by FUV evaporation according to Gorti & Hollenbach (2008). We can thus employ a FUV evaporation rate of $3 \times 10^{-8} M_\odot/\text{yr}$ (Gorti & Hollenbach, 2008) with a flat profile and a cut-off (Matsuyama et al., 2003; Mordasini et al., 2012b) shown in Fig. 2.2. A full X-ray, EUV and FUV model that is based on realistic hydrodynamic simulations would be preferable to this solution but is not available as of yet (Ercolano & Pascucci, 2017).

We show a comparison of disk profiles with the nominal Clarke-Matsuyama-Mordasini (Clarke et al., 2001; Matsuyama et al., 2003; Mordasini et al., 2012b) photo-evaporation to the new Picogna-Gorti (Picogna et al., 2019; Matsuyama et al., 2003; Gorti & Hollenbach, 2008) evaporation in Fig. 2.3. For the initial X-ray luminosity the mean of the distribution for Solar-mass stars discussed in Sect. 2.6.1 was chosen.

A striking difference is the location of the opening hole. However, the early evolution is very similar between the models. The Owen et al. (2012) prescription leads to similar profiles as the Picogna prescription, with a hole that opens in-between the holes caused by the Clarke- and the Picogna-model. This can be understood from the photo-evaporation profiles shown in Fig. 2.2.

2.6.3. Photo-evaporation outlook

Technically, there were a few challenges to overcome originating from the normalization and the complicated form of the fits to the numerical results. It would be desirable to have a clearer picture of the photo-evaporation formulas during the transition from a disk without a hole to the disk with a hole. Currently, this is an abrupt jump at a physically motivated but quite arbitrary time.

In the future, more physics could be added. For example one should consider the implementation of profiles following the work by Wölfer et al. (2019) for the case of carbon-depleted disks. Having the different photo-evaporation models implemented in the same planet formation code now allows for comparison of the resulting populations of planets. Currently, this has not yet been done with the Bern model but is addressed by Monsch et al. (in prep) using a different numerical code. Before this can be tackled with the Bern model and the new descriptions, the disk modeling challenge formulated in the next section should be fulfilled.

²This profile has a simpler functional form than the one reported in Picogna et al. (2019) but is a fit to the same data.

2.7. The disk modeling challenge

Having reviewed the observational constraints on protoplanetary disks (Sect. 1.4) and how to model it as an α -disk with photo-evaporation, we can formulate a challenge that all protoplanetary disk models have to fulfill: Protoplanetary disks have to be modeled fulfilling all observational constraints. In detail, this means that (1) a protoplanetary disk has to exist for approximately 3 Myr and (2) the accretion onto the star has to be on the order of $10^{-10} M_{\odot} \text{ yr}^{-1}$ to $10^{-7} M_{\odot} \text{ yr}^{-1}$ given (3) an initial mass based on observations (e.g. [Tychoniec et al., 2018](#); [Williams et al., 2019](#)), (4) a realistic viscous α on the order of 10^{-4} ([Stoll & Kley, 2014](#)), and (5) a photo-evaporation rate in agreement with the most recent models ([Picogna et al., 2019](#)). The free parameters, which can be tuned, are few, but the main handle is the initial profile of the surface density Σ . In the case of using a profile following [Andrews et al. \(2009\)](#)

$$\Sigma(r) = \Sigma_0 \left(\frac{r}{5.2 \text{ au}} \right)^{-\beta} \exp \left[- \left(\frac{r}{r_{\text{out}}} \right)^{(2-\beta)} \right], \quad (2.74)$$

this narrows down the choices of parameters to only the characteristic radius R_{out} , the slope β and the overall normalization Σ_0 .

[Hartmann & Bae \(2018\)](#) recently solved this challenge in the case without photo-evaporation but including a prescription for the magnetic winds, residual infall from the stellar envelope (Class I stage, see Sect. 1.4.2), and FU orionis outbursts ([Bell & Lin, 1994](#); [Hartmann & Kenyon, 1996](#)). They find, that the models can be brought into agreement with observations for reasonably large surface densities at the inner regions. By bringing more mass close to the star, the measured accretion rates can be reproduced, which is not the case if more shallow profiles are chosen.

In Figs. 2.5 and 2.6, we show a first approach to overcome the disk modeling challenge. A typical initial disk mass from [Tychoniec et al. \(2018\)](#) is fixed for all simulations, but we modify the initial profile and the α -viscosity to see which choice can match the observational constraints. As mentioned above, the goal would be to match observed accretion rates with α set to 2×10^{-4} . However, this does not work with the parameters that are shown.

The main constraint that is not met are the high observed accretion rates. In the top right panels of Figs. 2.5 and 2.6, a fit from [Hartmann et al. \(2016\)](#) to numerous accretion rate measurements is shown. They calculate a time-dependency of the accretion rate with a slope of -1.07 . Observational data uses the total age of the object as time variable, which naturally includes the protostellar phase (see Sect. 1.4.1). However, in our models, we do not model the infall of matter on the protoplanetary disk, nor the formation of the stellar core. Therefore, time $t = 0$ in our simulations is set later than in observations. To account for this, [Hartmann & Bae \(2018\)](#) shift their initial time by 0.4 Myr, which lies between previous estimates of 0.1 Myr to 0.2 Myr by [Kenyon & Hartmann \(1995\)](#) and the more recent estimate of 0.54 Myr of combined Class I and II lifetime by [Evans et al. \(2009\)](#). We subtract 0.5 Myr in close agreement to the latter work. This leads to a distortion of the

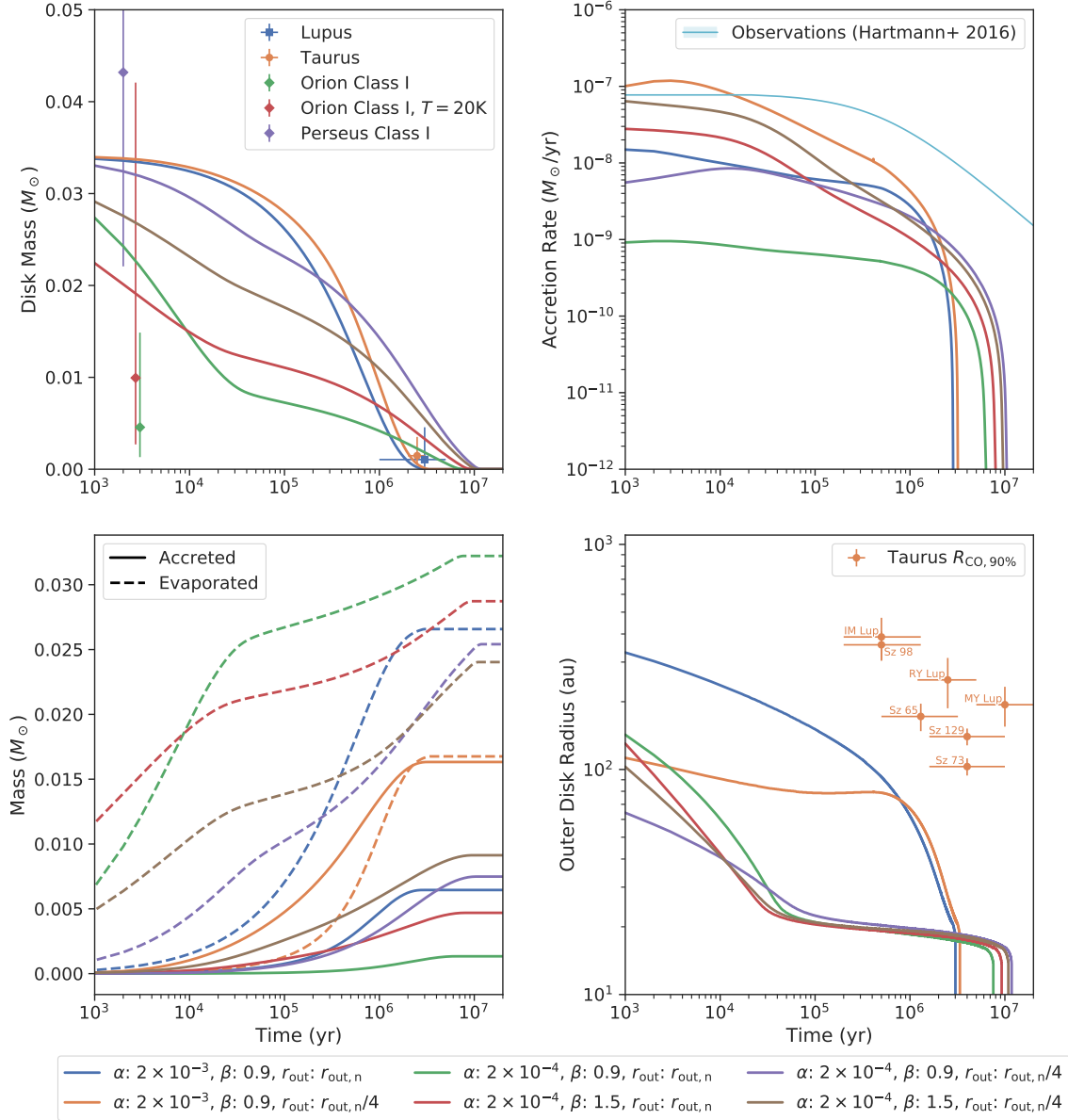


Figure 2.5.: Comparison of the evolution of disks with different α and initial profiles. Observational median ALMA dust disk masses (Tobin et al., 2020) times an assumed factor 100 are shown with their interquartile range. The Class I disk masses are shown at arbitrary times and would roughly correspond to time $t = 0$ in our simulation. In the top right panel, the fit to stellar accretion rates of Hartmann et al. (2016) is shown shifted to earlier times by an assumed protostellar lifetime of 0.5 Myr (Hartmann & Bae, 2018). Disk photo-evaporation follows the nominal model (Mordasini et al., 2012b) and $\dot{M}_{\text{wind}} \propto \alpha^{-2}$ to get disk lifetimes of a similar order of magnitude. The initial mass of all disks is set to $0.034 M_{\odot}$ following the NGPPS series (see Paper III) and nominal $r_{\text{out},n} = 61.776 \text{ au}$ obtained using the relation $r_{\text{out}} \propto M_{\text{disk}}^{1.6}$ (Andrews et al., 2009, 2018b).

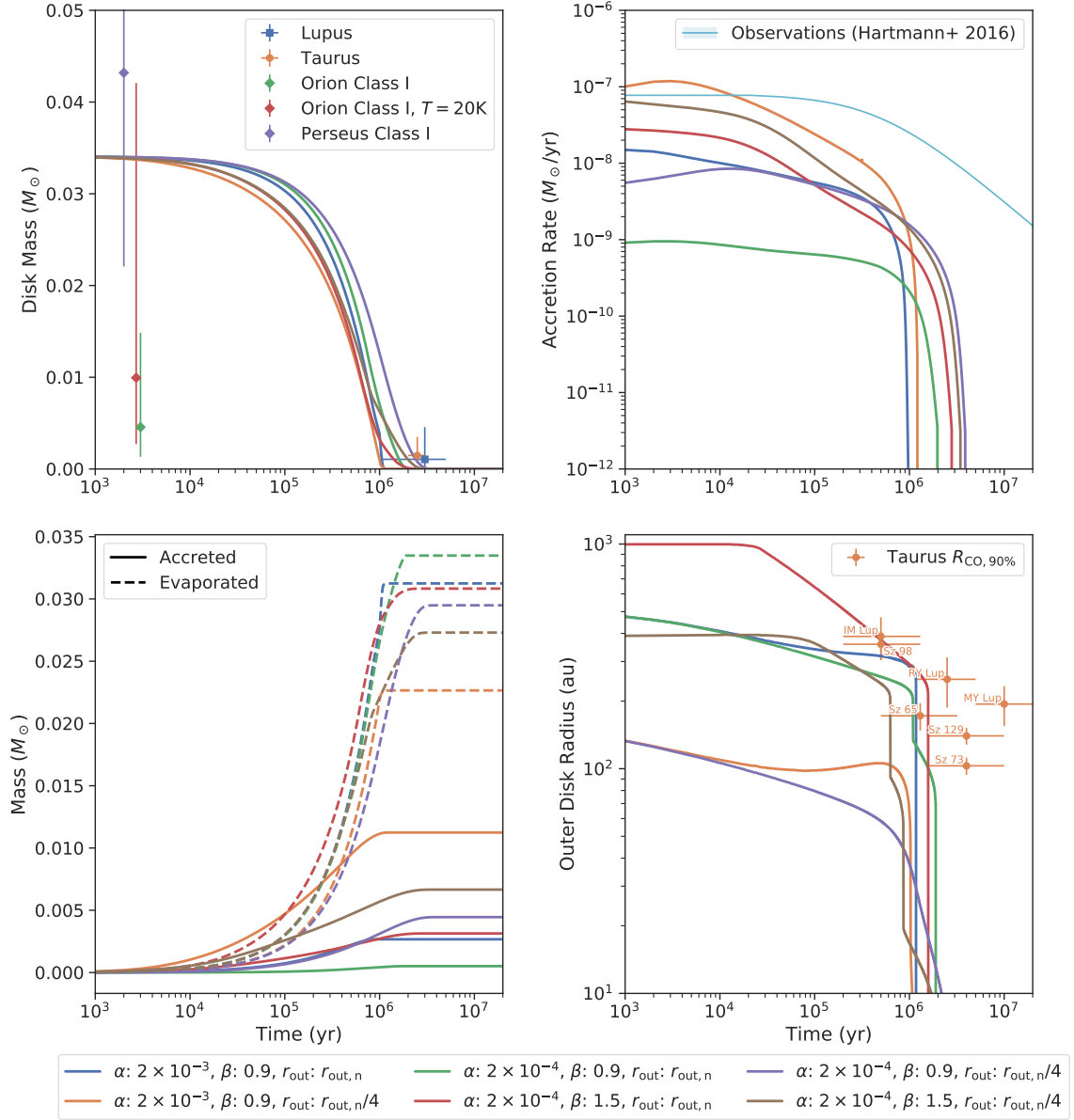


Figure 2.6.: As Fig. 2.5 but with internal disk photo-evaporation following Picogna et al. (2019). The X-ray luminosity is set to $1.96 \times 10^{39} \text{ erg s}^{-1}$; the mean of the scaled Gaussian distribution shown in Fig. 2.4 for $1 M_{\odot}$ (green line). In contrast to Fig. 2.5, we do not modify the external photo-evaporation rate for the different α cases. Instead, a fixed external evaporation with $\dot{M}_{\text{wind}} = 3 \times 10^{-8} M_{\odot} \text{ yr}^{-1}$ is chosen (Gorti & Hollenbach, 2008).

power-law in the log-log plot towards early times.

Despite accounting for previous protostellar phases, no close match to observed accretion rates is found for any parameter of evaporation model. Instead we miss an order of magnitude of accretion at the important later times. Initially, the mass seems to be chosen large enough to sustain accretion rates on the order of $10^{-7} M_{\odot} \text{ yr}^{-1}$ for high α or compact disks $r_{\text{out}} = r_{\text{out,n}}/4$, where $r_{\text{out,n}} = 61.776$ au is the nominal radius for the chosen disk mass following the relation of disk size to disk mass found by radio-astronomers for evolved disks [Andrews et al. \(2009, 2018b\)](#). This nominal disk radius does not necessarily have to be an initial condition since the observations were done for Class II disks. It is therefore valid to treat this parameter as free. [Hartmann & Bae \(2018\)](#) calculate that the mass available for accretion onto a $1.0 M_{\odot}$ star after the Class I stage amounts to $0.073 M_{\odot}$, which is a factor 2 more than our chosen initial mass. This means that, in order to stay at least in proximity to measured accretion rates, most of the disk gas would have to be accreted onto the star and should not be lost by photo-evaporation. In the bottom left panels of Figs. 2.5 and 2.6, we see that this is not the case for our simulations. At most, $\sim 50\%$ of the gas mass can be accreted onto the star and this is only possible for high α . This naturally explains a factor 4 difference to observations.

The problem might not be as severe as the accretion rate panel might suggest, because the region of uncertainty around the [Hartmann et al. \(2016\)](#) fit only accounts for the intrinsic scatter of the disk population. It does not take into account the uncertainty of the age determination, which could differ by a factor of two or three. However, it is unreasonable to think that all objects are much younger than derived using standard pre-main sequence evolution models ([Siess et al., 2000](#); [Choi et al., 2016](#)). Instead, taking into account magnetic fields in the pre-main sequence evolution generally seems to lead to estimating the objects to be older ([Feiden, 2016](#)).

[Hartmann & Bae \(2018\)](#) locate the reason for the disagreement in the measured disk masses relying on assumptions on the temperature and the opacity of the disk. Furthermore, as soon as the disk becomes optically thick in the mm wavelengths, only a lower limit to the local mass can be derived. Therefore, it is a valid way to solve the disparity, by pumping a lot of mass into the optically thick region of the disk close to the star.

This would imply that the masses derived for the gas disks from ALMA for Class I objects are lower-limits that lie an order of magnitude (for Orion and Oph [Williams et al., 2019](#); [Tobin et al., 2020](#)) or at least a factor 4 (for Perseus [Tychoniec et al., 2018](#)) below the real disk masses. Indeed, the observations with ALMA show a large dependency on the assumed temperature profile. In the top left panels of Figs. 2.5 and 2.6, we show the derived median masses of Class I objects with interquartile ranges in Orion from [Tobin et al. \(2020\)](#), once with their temperature profile depending on the stellar flux that the disk receives and once with a constant temperature of 20 K everywhere. The resulting distribution of disk masses is very sensitive to this choice. [Tobin et al. \(2020\)](#) use their methodology to re-analyze the Perseus data from [Tychoniec et al. \(2018\)](#) and derive slightly larger masses, also shown in the top left panels. Additionally, we show the mass distribution of evolved Class II objects

in Lupus (Ansdell et al., 2016) and Taurus (Tripathi et al., 2017) as listed by Tobin et al. (2020). For Class II objects, the optically thick region should be considerably smaller compared to Class 0 and Class I objects and the derived disk masses should be closer to reality.

An additional point to take into account is the assumed dust to gas ratio of 1% that is used here to convert dust masses to gas masses. This roughly corresponds to stellar metallicities (Lodders, 2003; Santos et al., 2003) and the interstellar matter (Bohlin et al., 1978). However, it might be different in disks where the dust is being processed and was found to lead to a slight over-estimation for Class II gas disk masses (Ansdell et al., 2016). A serious disk challenger would have to model dust growth and transport in disks and compare modeled (sub)mm-fluxes to observational data from Class 0 to Class II stages for a distribution of disk parameters instead of a fixed disk mass. Therefore, the model would need to further include infall of matter onto the planetary disk. Additionally, the disk gravity should be taken into account since we reach disk masses that are on the order of tens of percent of the stellar mass. Certainly, the disk gravity starts to play a role in this mass range.

The latest development based on ALMA data is to use the observed disk radii. Ansdell et al. (2018) and Barenfeld et al. (2017) measure disk sizes using CO isotopologues. The disks in the Taurus region were additionally observed in X-rays (Alcalá et al., 2017), which allows for estimating an age for each disk based on pre-main sequence models (Trapman et al., 2020). Sources with estimated masses ranging from $0.7 M_{\odot}$ to $1.5 M_{\odot}$ are shown and labeled in the bottom right panels of Figs. 2.5 and 2.6. Those disk radii are in principle not directly comparable to the numerical outer disk radii. Instead we should follow Trapman et al. (2020) in modeling chemistry including photo-dissociation and neither use a numerical limit nor the characteristic radius to compare the results to the observed 90% CO radii. However, the shown data can be considered lower limits to the measure we chose here.

Finally, we would like to touch on the subject of different photo-evaporation models. In the context of observational constraints, a similarly good match for both models was possible. Compared to the measured 90% CO radii, the newer photo-evaporation model reproduces the results better. This is mainly because external photo-evaporation – which removes mass in the outermost regions – is reduced in those model runs. Therefore, the disks in Fig. 2.6 do are not truncated as much as those in Fig. 2.5.

Photo-evaporation does not influence the early stages due to having constant loss rates in time, which are much smaller than accretion rates in the beginning. Therefore, modeled accretion onto the star is much more dependent on α and the initial disk profile that is chosen. However, for similar parameters, the evaporation model by Picogna et al. (2019) led to a maximum of about a third of the initial mass being accreted onto the star. Therefore, in the spirit of Hartmann & Bae (2018), disk masses would have to be increased by a factor six compared to the Tychoniec et al. (2018) masses. Nevertheless, the new photo-evaporation model making use of physical input for photo-evaporation in the form of observed L_X is very valuable to narrow the parameter space of possible disk configurations.

2.8. Radial drift

The results of Sect. 2.2 lead to the conclusion that dust particles at the midplane orbit at different azimuthal velocities (Ω_K) compared to the gas (Ω_g). Therefore, the particles will feel a headwind and thus drag. Since they lose angular momentum, this will lead to a spiraling motion of all particles towards the central star. This was already noted by Whipple (1972) and explored in more depth by Weidenschilling (1977). They found that for typical disk conditions, the fastest drifting bodies are meter-sized. For larger and smaller particles, the drift speed quickly decreases and is negligible for micrometer-sized particles and kilometer-sized planetesimals.

The results of Paper I heavily rely on the radial drift speed. Therefore, we show in the appendix of Paper I a comparison of the commonly used approximative formula compared to the results solving the differential equations of motion. The discussion of drift processes in Paper I is quite in-depth, but the derivation of the approximative radial drift formula is too long to be suited for repetition in the published paper. Therefore, we derive the approximative equations here that can be used to calculate the radial drift of particles in a disk. The derivation follows the traditional work of Whipple (1972) and the newer conclusive derivation by Takeuchi & Lin (2002). Noteworthy are also the works of Adachi et al. (1976) who derived the equations of motion not only for particles on circular orbits but more generally for arbitrary eccentricities and inclinations of the particle. In addition, the work by Nakagawa et al. (1986) is also insightful and the first to consider the feedback of drifting dust onto the motion of the gas particles.

In the following, we focus on particles at the disk midplane. Therefore, the Keplerian (orbital) velocity $v_{K,\text{mid}}$ ($\Omega_{K,\text{mid}}$) is shortened to v_K (Ω_K) for better readability. We note that in general, all formulas depend on the elevation above the midplane z .

We will begin by following equation (2.16), leading to the azimuthal velocity of the gas

$$v_{g,\varphi} = v_K \sqrt{1 + 2 \underbrace{\frac{r}{2v_K^2 \rho} \frac{\partial P}{\partial r}}_{\equiv -\eta}}, \quad (2.75)$$

where we defined the useful quantity

$$\eta \equiv -\frac{r}{2v_K^2 \rho} \frac{dP}{dr} \quad (2.76)$$

to measure the non-Keplerianity of the gas flow. This implies

$$v_K = \frac{v_{g,\varphi}}{\sqrt{1 - 2\eta}}. \quad (2.77)$$

The equation of motion restricted to the r - φ plane for a dust particle at the midplane in a co-rotating frame of reference is

$$\frac{dv_{p,r}}{dt} = \underbrace{\frac{v_{p,\varphi}^2}{r}}_{F_{\text{cent}}} - \underbrace{\frac{GM_\star}{r^2}}_{F_G} - F_{D,r}/m_p \quad (2.78)$$

$$\frac{dv_{p,\varphi}}{dt} = -F_{D,\varphi}/m_p \quad (2.79)$$

where the drag force F_D and the particle mass m_p were introduced. The drag force depends on the relative velocity Δv between the gas and the dust particles which is in the azimuthal direction

$$(\Delta v)_\varphi \approx -\eta v_K. \quad (2.80)$$

First-order approximation

For the case of no radial velocity and exactly Keplerian orbits ($v_{p,\varphi} = v_K$) of the dust particles (as in [Whipple, 1972](#)), equation (2.79) simplifies to

$$\frac{dv_K}{dt} = \frac{d}{dt} \left(\sqrt{\frac{GM_\star}{r}} \right) = -\frac{1}{2} \underbrace{\sqrt{\frac{GM_\star}{r^3}}}_{\Omega_K} \frac{dr}{dt} = -F_{D,\varphi}/m_p \quad (2.81)$$

and naturally yields a radial drift speed

$$dr/dt = v_{p,r,\text{Whipple}} = \frac{2F_{D,\varphi}}{m_p \Omega_K}. \quad (2.82)$$

Using the definition by [Whipple \(1972\)](#) for the stopping time $t_s = m_p \Delta v / F_D$, this then reads as

$$v_{p,r,\text{Whipple}} = \frac{2\Delta v}{t_s \Omega_K} \approx -\frac{2r\eta}{t_s}. \quad (2.83)$$

Higher-order approximation

However, from equations (2.78) and (2.79) it is apparent that the above assumptions are not consistent with the force balance. Therefore, [Takeuchi & Lin \(2002\)](#) take more terms into account. In the following, we loosely follow their derivation.

First, equation (2.78) can be simplified. We begin by modifying the term

$$\frac{v_{p,\varphi}^2}{r} - \frac{GM_\star}{r^2} = \frac{v_{p,\varphi}^2}{r} - \frac{v_K^2}{r} \quad (2.84)$$

$$= \frac{v_{p,\varphi}^2}{r} - \frac{v_{g,\varphi}^2}{r(1-2\eta)} \quad (2.85)$$

$$= \frac{v_{p,\varphi}^2 - 2\eta v_{p,\varphi}^2 - v_{g,\varphi}^2}{r(1-2\eta)}. \quad (2.86)$$

This can be approximated as

$$\frac{v_{p,\varphi}^2}{r} - \frac{GM_\star}{r^2} \approx \frac{v_{p,\varphi}^2 - 2\eta v_{p,\varphi}^2 - v_{g,\varphi}^2}{r} \quad (2.87)$$

$$\approx \frac{-2\eta v_{p,\varphi}^2}{r} + \frac{v_{p,\varphi}^2 - v_{g,\varphi}^2}{r} \quad (2.88)$$

$$\approx \frac{-2\eta v_{p,\varphi}^2}{r} + \frac{(v_{p,\varphi} + v_{g,\varphi})(v_{p,\varphi} - v_{g,\varphi})}{r} \quad (2.89)$$

$$\approx \frac{-2\eta v_K^2}{r} + \frac{2v_K(v_{p,\varphi} - v_{g,\varphi})}{r}, \quad (2.90)$$

where we used the Keplerian velocity for the particle velocity in the small term proportional to η and we approximated the sum of the two velocities as twice Keplerian. These simplifications introduce errors proportional to η^2 .

Combined with introducing the stopping time in the final term, equation (2.78) then reads as

$$\frac{dv_{p,r}}{dt} = -2\eta \frac{v_K^2}{r} + 2\frac{v_K}{r}(v_{p,\varphi} - v_{g,\varphi}) - \frac{1}{t_s}(v_{p,r} - v_{g,r}). \quad (2.91)$$

Now, we use the derived equation (2.83) giving an expression for $\Delta v = (v_{g,\varphi} - v_{p,\varphi})$ to replace the middle term. This leads to

$$\frac{dv_{p,r}}{dt} = -2\eta \frac{v_K^2}{r} - \frac{2v_K}{r} \frac{v_{p,r} t_s \Omega_K}{2} - \frac{1}{t_s}(v_{p,r} - v_{g,r}). \quad (2.92)$$

Solving for $v_{p,r}$ in steady-state, that is setting the time derivative to zero, leads to

$$\left(\frac{1}{t_s} + \frac{\Omega_K t_s v_K}{r} \right) v_{p,r} = -2\eta \frac{v_K^2}{r} + \frac{v_{g,r}}{t_s} \quad (2.93)$$

$$\Rightarrow \left(\frac{1}{\Omega_K t_s} + t_s \Omega_K \right) v_{p,r} = -2\eta v_K + \frac{v_{g,r}}{\Omega_K t_s} \quad (2.94)$$

which gives a more appropriate formula for the drift speed

$$v_{p,r} = \frac{-2\eta v_K + \frac{v_{g,r}}{\Omega_K t_s}}{\frac{1}{t_s \Omega_K} + t_s \Omega_K}. \quad (2.95)$$

Defining the dimensionless stopping time or *Stokes number* as $s = t_s \Omega_K$ further simplifies the equation

$$v_{p,r} = \frac{-2\eta v_K + s^{-1} v_{g,r}}{s^{-1} + s}. \quad (2.96)$$

Equations (2.83) or (2.96) can easily be implemented and depend on the drag regime. For a discussion of the drag regimes, we refer to [Paper I](#). Here, we would like to mention that for large bodies, the quadratic drag regime applies and Stokes numbers are large $s \gg 1$. Therefore, expression (2.96) reduces to (2.83), which is what is used in [Paper I](#) for the quadratic regime. Additionally, a comparison of the analytic expression to numerically solving the equations of motion can be found in the appendix of [Paper I](#).

2.9. Distribution of planetesimals in protoplanetary disks

Before we can address how frequent collisions between bodies embedded in a protoplanetary disk are, we have to establish how the bodies are distributed in terms of their size and the eccentricity and inclination of their orbits. The eccentricity e and inclination i of a body determines its velocity relative to a second body on a circular orbit (Sect. 2.9.2); therefore, the expressions of velocity of a body or its e and i are used in the literature to describe the same quantity. A body is said to be *excited* if it has large velocities or e and i . As will be described in detail, a large velocity might lead to a larger flux of bodies through the intersecting cross-section of a target body. However, this is countered by a smaller cross-section and a lower number density of particles due to a larger spread in space.

A note on the notation: We will now switch to describing bodies using the semi-major axis a , eccentricities e and inclinations i to describe the location. a will also be used for bodies on circular orbits instead of the equivalent distance to the star r used above. This allows us to use r for the radius of the body; although we will put subscripts t or p for target and projectile radii (see Table 2.2).

Symbol	Unit (cgs)	Description
a	cm	Semi-major axis of a body on a Keplerian orbit
e		Eccentricity of a body on a Keplerian orbit
e^*		Dispersion of an eccentricity distribution
i	rad	Inclination of the orbital plane of a body
i^*	rad	Dispersion of an inclination distribution
r_m, r_t, r_p	cm	Radii of a generic body with mass m , the target and the projectile
ρ	g cm^{-3}	Gas density
ρ_m	g cm^{-3}	Bulk density of a solid body with mass m
ρ_{solids}	g cm^{-3}	Volume density of solids distributed in space
Σ_{solids}	g cm^{-2}	Surface density of solids measured as solid mass per area
v	cm s^{-1}	Relative velocity between the target and the projectile
n	cm^{-3}	Volume number density of particles
Γ	s^{-1}	Collision rate

Table 2.2.: Variables used to describe collisions and planetesimal populations

2.9.1. Size distribution

Not all bodies in a disk have the same size. Instead, a distribution of sizes or masses is found. Usually, the distributions are approximated as power laws. Therefore, slopes can be introduced in multiple different ways:

- The number of particles of *mass* m is given by $N(m)$ such that $N(m)dm$ is the

number of bodies in the interval $[m, m + dm]$. A slope α is introduced, such that $N(m) \propto m^{-\alpha}$, which implies $d \log n / d \log m = -\alpha$.

- Similarly, the number of particles can be described by introducing a slope depending on the *cumulative mass* as $\int_0^m N(m') dm' \propto m^{-s}$. Therefore, $N(m) \propto -sm^{-s-1}$, which implies $\alpha = s + 1$.
- Instead of using the mass as a variable, the population of sizes can also be described using the *radius* r_b . The differential distribution is then described as $N(r_m) \propto m^{-q}$ and assuming a constant bulk density leads to $N(m)dm = N(m(r_m))dr_m dm / dr_m$ which in turn is equal to $4\pi r_m^2 \rho_m N(m(r))dr_m \propto r_m^2 r_m^{-3\alpha}$, therefore $\alpha = (q + 2)/3$. Note that some authors introduce the exponents without the minus signs and again, the cumulative size distribution can be expressed using the radius as a variable.

This short excursion into basic analysis was required to be able to interpret the different notations that are used in the literature.

From theory, [Dohnanyi \(1969\)](#) estimated which slope would result if the collisions led to catastrophic break-up or erosion of the bodies. [Dohnanyi \(1969\)](#) found that the result is (to first order) independent on the size distribution of fragments that is produced by catastrophic break-up for the steady-state (or self-similar) solution which results in $\alpha = 11/6$ (see also [Tanaka et al., 1996](#); [Makino et al., 1998](#)). Modern works consider the size-dependent velocity distribution ([Pan & Schlichting, 2012](#)) or updated results from SPH simulations ([Benz & Asphaug, 1999](#)) taking the internal structure of the target body into account ([Jutzi et al., 2010](#)).

Observations more readily give size distributions because the flux emitted by asteroids or comets depends on the visible area. Therefore, a conversion to mass distributions is only possible assuming or knowing the densities of the bodies. For small enough objects, a fixed density can be used. Another issue with observations is that they give constraints on the present-day distribution. The debate is still ongoing if the larger asteroid-belt objects are primordial and would represent the distribution as it was during the formation of planets ([Morbidelli et al., 2009](#)) or they were also collisionally processed over the Gyrs to the present-day ([Weidenschilling, 2011](#)).

Observational data exist for many regions in the Solar System and all kinds of small Solar System bodies. In [Paper I](#), we focus on a process related to the water iceline and small bodies with sizes smaller than ~ 1 km. The location of the water iceline depends on the disk model and assumptions but is consistently found to lie in the range from ~ 1 au to Jupiter's orbit at 5.2 au. Therefore, small asteroids ([Ryan et al., 2015](#)) and Jupiter-family comets ([Fernández et al., 1999](#); [Tancredi et al., 2006](#); [Fernández et al., 2013](#)) are most relevant for the the discussion in [Appendix B of Paper I](#). It is important to be aware of the size regime of interest because there is a break in the observed power-law of Kuiper Belt Object sizes at ~ 10 km ([Bernstein et al., 2004](#); [Fraser & Kavelaars, 2009](#)).

For planet formation, the dominant size in mass in the protoplanetary disk are relevant. Therefore, slopes steeper than $\alpha = 2$ would be dominated by low-mass

objects. This will be discussed further in Sect. 5.3, where we justify the choice of small planetesimal sizes. However, the proximity of measured slopes to the value of $\alpha = 2$ indicates that a distribution of planetesimal sizes should in principle be modeled. This would allow for studying fragmentation and dynamical friction (see below and [Ida & Makino, 1992b](#)) in the proximity of a planet and their feedback onto planetary growth (see also [Letter I](#)).

2.9.2. Eccentricity and inclination distribution

[Ida & Makino \(1992a\)](#) found that the squares of the eccentricity and inclination of a population of planetesimals in the protoplanetary disk can be described as a Gaussian distribution

$$f_e d\tilde{e}^2 = \frac{1}{(\tilde{e}^*)^2} \exp\left\{-\frac{\tilde{e}^2}{(\tilde{e}^*)^2}\right\} d\tilde{e}^2 \quad (2.97)$$

$$f_i d\tilde{i}^2 = \frac{1}{(\tilde{i}^*)^2} \exp\left\{-\frac{\tilde{i}^2}{(\tilde{i}^*)^2}\right\} d\tilde{i}^2, \quad (2.98)$$

where the notation for the reduced eccentricity $\tilde{e} = e/h_{12}$, respectively the reduced inclination $\tilde{i} = i/h_{12}$, with³ $h_{12} = ((m_1 + m_2)/(3M_\star))^{1/3}$ is introduced. The dispersions i^* and e^* respectively are used to characterize the spread of the distribution and depend on a variety of physical effects. The reduced dispersions $\tilde{e}^* = e^*/h_{12}$ and \tilde{i}^*/h_{12} are defined analogously to the reduced values of the eccentricity and inclination.

Here, we have to discuss that the effect of a protoplanet on the eccentricity and inclination distribution is not included in [Ida & Makino \(1992a\)](#). The same authors continue to investigate the influence of the planet on the distribution in their following papers ([Ida & Makino, 1992b, 1993](#)), coming to the conclusion that scattering of planetesimals by the larger planet leads to a "heating" of the population of planetesimals, i.e. their eccentricities and inclinations increase. Based on this effect, we will see that the growth rate of the protoplanet decreases because gravitational focusing becomes less efficient (i.e. the second term in equation (2.146) decreases). This regime of growth of a large body is called the *oligarchic regime*.

If there is no planet present, the assumption of a Gaussian distribution of eccentricities and inclinations is justified by N -body simulations ([Ida & Makino, 1992a; Inaba et al., 2001](#)). In the vicinity of a planet, the distribution can change. We do not consider this effect here, because it should be treated in N -body simulations. Instead, we assume that the form of the distribution stays the same even if there is a planet; thus equations (2.97) and (2.98) are employed universally.

Since the literature uses different notations, we transform equations (2.97) and

³ m_1 and m_2 being the masses of two particles that interact (in the following often the protoplanet and a planetesimal or two planetesimals). See also section 2.10.3.

(2.98) by evaluating the differential $d\tilde{e}^2 = 2\tilde{e}d\tilde{e}$, respectively $d\tilde{i}^2 = 2\tilde{i}d\tilde{i}$ to obtain

$$f_{Re} d\tilde{e} \equiv 2f_e \tilde{e} d\tilde{e} = \frac{2\tilde{e}}{(\tilde{e}^*)^2} \exp\left\{\left(-\frac{\tilde{e}^2}{(\tilde{e}^*)^2}\right)\right\} d\tilde{e} \quad (2.99)$$

$$f_{Ri} d\tilde{i} \equiv 2f_i \tilde{i} d\tilde{i} = \frac{2\tilde{i}}{(\tilde{i}^*)^2} \exp\left\{\left(-\frac{\tilde{i}^2}{(\tilde{i}^*)^2}\right)\right\} d\tilde{i} \quad (2.100)$$

or combined

$$f_R d\tilde{e} d\tilde{i} \equiv \frac{4\tilde{e}\tilde{i}}{(\tilde{e}^*)^2(\tilde{i}^*)^2} \exp\left\{\left(-\frac{\tilde{e}^2}{(\tilde{e}^*)^2} - \frac{\tilde{i}^2}{(\tilde{i}^*)^2}\right)\right\} d\tilde{e} d\tilde{i}, \quad (2.101)$$

which are Rayleigh distributions. Thus, the distribution in terms of the squared values is a Gaussian, but the eccentricities and inclinations are in fact distributed according to a Rayleigh distribution and the different notions are equivalent.

For completeness, we also mention that the velocity of a planetesimal relative to the mean circular orbit in the disk midplane with the same semi-major axis a is

$$v \approx \sqrt{e^2 + i^2} v_k \quad (2.102)$$

for small e and i . More precisely, the velocity of one planetesimal relative to the local mean circular orbit averaged over an epicycle is

$$v_{lc} = \sqrt{\frac{5e^2}{8} + \frac{i^2}{2}} v_k, \quad (2.103)$$

as given in [Lissauer & Stewart \(1993\)](#). The former is used in e.g. [Nakazawa et al. \(1989a\)](#) for the two-body approximation in their appendix B, whereas the latter is used in [Fortier et al. \(2013\)](#) and our works.

2.9.3. Eccentricity and inclination damping and stirring

The eccentricities and inclinations of a population of planetesimals are distributed according to equation (2.101), but the dispersions e^* and i^* are subject to physical processes due to interactions with the gas, the planetesimals, and the planets in the disk.

We consider a population consisting of planetesimals with a given fixed mass m , which is influenced by two different processes: gravitational perturbation and gas drag. For different masses, direct collisions and dynamical friction would influence the eccentricity and inclination of the populations for the different mass bins. However, for a population consisting of bodies of a single mass there is no such effect. A treatment for the case of populations with multiple masses can be found in [Inaba et al. \(2001\)](#) and would be out of the scope of this chapter.

The overall eccentricity and inclination dispersion evolution of a population of planetesimals with a single mass m can thus be written as

$$\frac{de^{*2}}{dt} = \left. \frac{de^{*2}}{dt} \right|_{\text{drag}} + \left. \frac{de^{*2}}{dt} \right|_{\text{VS},M} + \left. \frac{de^{*2}}{dt} \right|_{\text{VS},m} \quad (2.104)$$

$$\frac{di^{*2}}{dt} = \left. \frac{di^{*2}}{dt} \right|_{\text{drag}} + \left. \frac{di^{*2}}{dt} \right|_{\text{VS},M} + \left. \frac{di^{*2}}{dt} \right|_{\text{VS},m}, \quad (2.105)$$

where VS is used to abbreviate viscous stirring, i.e. gravitational interactions with a planet (VS, M) or the population of planetesimals (VS, m). Note that here the non reduced eccentricity and inclination dispersions e^* and i^* are used.

Gas drag damping

The eccentricity and inclination damping by gas drag averaged over one period and applicable for small e , i , and η is derived in Adachi et al. (1976) and the radial component as well as the physical background is discussed in section 2.8. They depend on the drag regime the bodies are in. Here, we first state the result for the quadratic regime by Inaba et al. (2001) who improved the equations by Adachi et al. (1976) to match numerical results for comparable e, i and η and averaged over the distribution function. They found,

$$\frac{\tau}{e^{*2}} \left. \frac{de^{*2}}{dt} \right|_{\text{drag}, Re \gtrsim 20} = -2 \left(\frac{9}{4\pi} E[3/4]^2 e^{*2} + \frac{1}{\pi} i^{*2} + \frac{9}{4} \eta^2 \right) \quad (2.106)$$

$$\frac{\tau}{i^{*2}} \left. \frac{di^{*2}}{dt} \right|_{\text{drag}, Re \gtrsim 20} = - \left(\frac{1}{\pi} E[3/4]^2 e^{*2} + \frac{4}{\pi} i^{*2} + \eta^2 \right), \quad (2.107)$$

where $E[k]$ is the elliptic integral of the second kind (see section A.4),

$$\tau = \frac{2m}{C_D \pi r_m^2 \rho a \Omega_K} = \frac{8r_m \rho_m}{3C_D \rho v_k} \quad (2.108)$$

and

$$\eta = - \frac{1}{2\Omega_K^2 a \rho} \frac{dP}{da} \quad (2.109)$$

is defined in the same way as in section 2.8, but we call the radial variable a instead of r , as the orbits are now not necessarily circular.

For the Epstein and Stokes regime of the drag, the formula simplifies and the result without averaging over the distribution function is

$$\frac{1}{e^2} \left. \frac{de^2}{dt} \right|_{\text{drag}, r_m < \lambda} = \frac{2}{i^2} \left. \frac{di^2}{dt} \right|_{\text{drag}, r_m < \lambda} = - \frac{c_s \rho}{\rho_m r_m}, \quad (2.110)$$

respectively

$$\frac{1}{e^2} \left. \frac{de^2}{dt} \right|_{\text{drag}, Re < 20} = \frac{2}{i} \left. \frac{di^2}{dt} \right|_{\text{drag}, Re < 20} = - \frac{3}{2} \frac{\lambda c_s \rho}{\rho_m r_m^2}. \quad (2.111)$$

Note that these last two equations are valid for eccentricities and inclinations and not their dispersions. However up to factors of order unity it can be used for their evolution as well, as in Fortier et al. (2013).

Gravitational stirring

The planetesimal eccentricities and inclinations are excited by gravitational interaction among themselves (VS, m) and possibly with a forming planet (VS, M). The expressions are based on the results in Ohtsuki et al. (2002). The first application is the viscous stirring of a body with a large mass M , thus we neglect the terms which are small in m (Ohtsuki et al., 2002, equation 6, respectively 7) and spread the planetesimal mass out over a region of b Hills radii (called the feeding zone ($b \approx 10$)) (Chambers, 2014) to get a number density $n_M = 1/(2\pi a^2 b h_{mM})$, where $h_{mM} = \left(\frac{m+M}{3M_\star}\right)^{1/3} \approx (M/(3M_\star))^{1/3}$,

$$\left.\frac{de^{*2}}{dt}\right|_{\text{VS},M} = f(\Delta) \frac{M\Omega_K}{3bM_\star 2\pi} P_{\text{VS}} \quad (2.112)$$

$$\left.\frac{di^{*2}}{dt}\right|_{\text{VS},M} = f(\Delta) \frac{M\Omega_K}{3bM_\star 2\pi} Q_{\text{VS}}, \quad (2.113)$$

where

$$f(\Delta) = \left[1 + \left(\frac{\Delta}{nah_{mM}}\right)^5\right]^{-1} \quad (2.114)$$

is a factor to ensure that the perturbation of the planet is confined to its neighborhood within $n \simeq b$ Hill radii (Guilera et al., 2010) and

$$P_{\text{VS}} = \left(\frac{73(\tilde{e}^*)^2}{10\Lambda^2}\right) \ln(1 + 10\Lambda^2/(\tilde{e}^*)^2) + \left(\frac{72I_{\text{PVS}}(\beta)}{\pi\tilde{e}^*\tilde{i}^*}\right) \ln(1 + \Lambda^2) \quad (2.115)$$

$$Q_{\text{VS}} = \left(\frac{4(\tilde{i}^*)^2 + 0.2\tilde{i}^*(\tilde{e}^*)^3}{10\Lambda^2\tilde{e}^*}\right) \ln(1 + 10\Lambda^2 * \tilde{e}^*) + \left(\frac{72I_{\text{QVS}}(\beta)}{\pi\tilde{e}^*\tilde{i}^*}\right) \ln(1 + \Lambda^2), \quad (2.116)$$

with $\Lambda = \tilde{i}((\tilde{e}^*)^2 + (\tilde{i}^*)^2)/12$. Here, the integrals

$$I_{\text{PVS}} = \int_0^1 \frac{5K(\theta) - 12(1 - \lambda^2)E(\theta)/(1 + 3\lambda^2)}{\beta + (\beta^{-1} - \beta)\lambda^2} d\lambda \quad (2.117)$$

$$I_{\text{QVS}} = \int_0^1 \frac{K(\theta) - 12\lambda^2 E(\theta)/(1 + 3\lambda^2)}{\beta + (\beta^{-1} - \beta)\lambda^2} d\lambda, \quad (2.118)$$

with $\beta = \tilde{i}/\tilde{e}$ and $\theta = \sqrt{(3 - 3\lambda^2)}/2$, appear. K and E are the elliptic integrals A.4. I_{PVS} and I_{QVS} can, according to Chambers (2006), be approximated for $0 \leq \beta \leq 1$ to within 3% by

$$I_{\text{PVS}}(\beta) \cong \frac{\beta - 0.36251}{0.061547 + 0.16112\beta + 0.054473\beta^2} \quad (2.119)$$

$$I_{\text{QVS}}(\beta) \cong \frac{0.71946 - \beta}{0.21239 + 0.49764\beta + 0.14369\beta^2}. \quad (2.120)$$

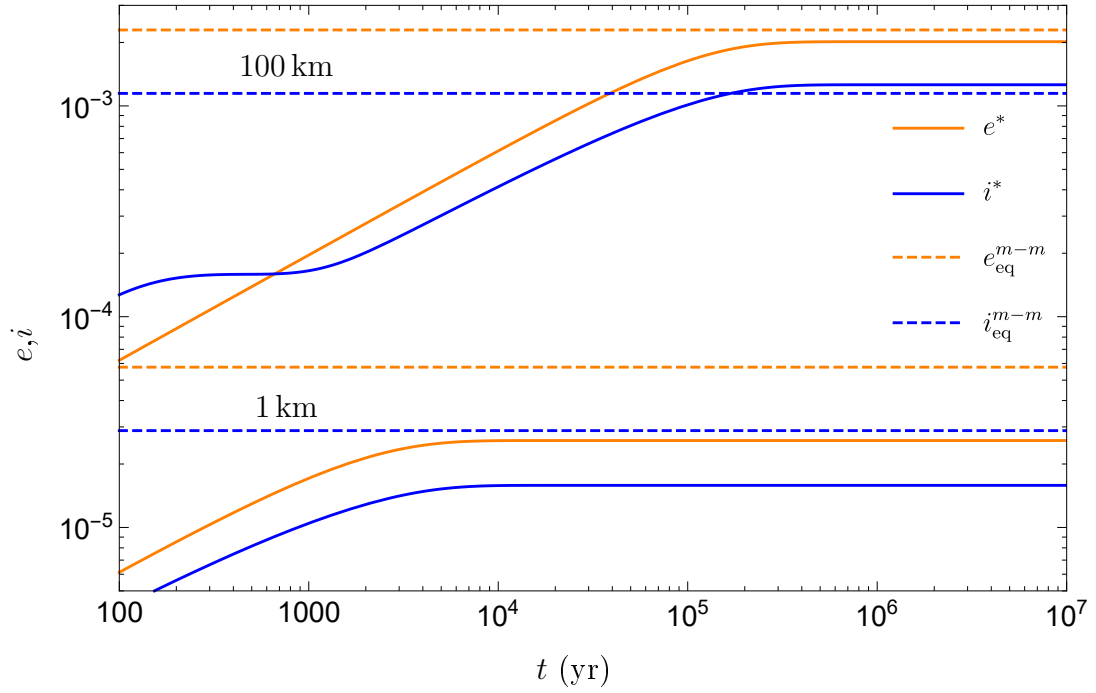


Figure 2.7.: Eccentricity and inclination of a population of planetesimals at 1 au from self-stirring. The upper lines correspond to planetesimals with a radius of 100 km, while the lower values are for radii of 1 km. Equation (2.104) and (2.105) were solved without the term for stirring due to a planet. For comparison, the equilibrium values from Fortier et al. (2013) for e_{eq}^{m-m} respectively i_{eq}^{m-m} are indicated (dashed lines).

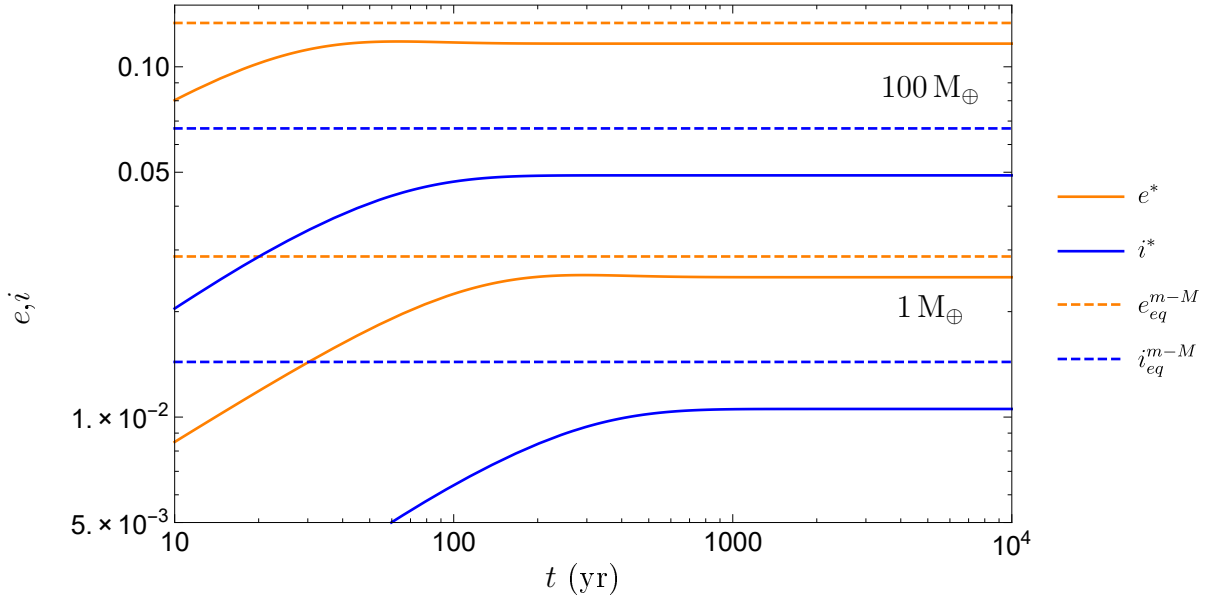


Figure 2.8.: Eccentricity and inclination of a population of km-sized planetesimals from self- and embryo-induced-stirring at 1 au. Equation (2.104) and (2.105) are solved including gravitational stirring due to a $1 M_{\oplus}$ (lower lines) or a $100 M_{\oplus}$ (upper lines) mass planet and the population of planetesimals itself. For comparison the equilibrium values as in Fortier et al. (2013) for e_{eq}^{m-M} respectively i_{eq}^{m-M} are indicated (dashed lines).

Again, the reduced eccentricity and inclination dispersions are used which we restate for better readability

$$\tilde{e}^* \equiv e^*/h_{mM}, \quad \tilde{i}^* \equiv i^*/h_{mM}. \quad (2.121)$$

For the viscous stirring amongst planetesimals, we use $\tilde{e}^* = e^*/h_{mm}$ and $\tilde{i}^* = e^*/h_{mm}$ with $h_{mm} = (2m/(3M_*))^{1/3}$. Then the eccentricity and inclination evolve as

$$\left. \frac{de^{*2}}{dt} \right|_{\text{VS},m} = \frac{1}{6} \sqrt{\frac{Ga}{M_*}} \Sigma_{\text{solids}} h_{mm} P_{\text{VS}} \quad (2.122)$$

$$\left. \frac{di^{*2}}{dt} \right|_{\text{VS},m} = \frac{1}{6} \sqrt{\frac{Ga}{M_*}} \Sigma_{\text{solids}} h_{mm} Q_{\text{VS}}, \quad (2.123)$$

where P_{VS} and Q_{VS} are given as above, but need to be evaluated with the adjusted reduced eccentricity and inclination.

To approximate the equilibrium value between gas drag and either viscous stirring by a planet or by planetesimals, the timescales of these processes can be equated to obtain (Fortier et al., 2013)

$$e_{\text{eq}}^{m-M} \approx 1.7 \frac{m^{1/15} M^{1/3} \rho_m^{2/15}}{b^{1/5} C_D^{1/5} \rho^{1/5} M_*^{1/3} a^{1/5}} \quad (2.124)$$

and $i_{\text{eq}}^{m-M} = 0.5e_{\text{eq}}^{m-M}$ for the viscous stirring due to a planet. Similarly⁴

$$e_{\text{eq}}^{m-m} \approx 2.31 \frac{m^{4/15} \Sigma_{\text{solids}}^{1/5} a^{1/5} \rho_m^{2/15}}{C_D^{1/5} \rho^{1/5} M_*^{2/5}} \quad (2.125)$$

and $i_{\text{eq}}^{m-m} = 0.5e_{\text{eq}}^{m-m}$. These equilibrium values are compared to the solutions of the differential equations (2.104) and (2.105) in figures 2.8 and 2.7. The equilibrium value for the viscous stirring by a planet agrees reasonably with the differential equation, whereas e_{eq}^{m-m} and i_{eq}^{m-m} do not agree well with the results of the differential equation for small planetesimal sizes. This is most likely not because of using the quadratic drag regime to derive equation (2.125), but because the gravitational stirring timescales found by Ida & Makino (1993) are used. Those become less accurate for low eccentricities ($e \sim 2h_{mm} \approx 10^{-6}$ for 1 km planetesimals). Additionally, the terms including η were neglected to derive equations (2.124) and (2.125), which becomes relevant for small bodies.

We note that for those small eccentricities at small radii it would additionally be necessary to include turbulence of the disk gas as a reason for stirring of eccentricity and inclination as well (e.g. Ormel & Kobayashi, 2012; Kobayashi et al., 2016). This will be addressed in a future paper belonging to the NGPPS series (Sect. 5.6).

⁴A typographic error from Fortier et al. (2013) is corrected here by replacing Σ by Σ_{solids} . Using the factor of $C_e \approx 40$ from Ida & Makino (1993), the overall prefactor evaluates to 2.6 instead of 2.31 as reported in Fortier et al. (2013).

2.10. Frequency of collisions and accretion rates

The frequency of collisions between bodies is a key component in all the works presented here. Therefore, we give some historical context as well as go into moderate detail using different approaches to calculate collision rates. It is important to note that once collision rates between bodies are established, it is trivial to multiply by the mass of the smaller of the two bodies undergoing collision to get a mass accretion rate for the larger of the two bodies. Solid accretion is the key component in all planet formation models, but the collision rates themselves are interesting when calculating if a small body can survive in a disk. This latter case is used in [Paper I](#).

In order to take small solids into account, such as grains, a statistical approach using a prescribed distribution function of planetesimals (see section 2.9.1) is accurate. The alternative is to perform N-Body simulations (e.g. [Wetherill, 1980](#)), which will not be discussed here. In the literature the two-body approximation, which is to neglect the influence of the central star, was the dominant way to estimate the collision rate (e.g. [Safronov, 1969](#)). This was until [Nakazawa et al. \(1989a,b\)](#); [Ida & Nakazawa \(1989\)](#) and independently [Greenzweig & Lissauer \(1990, 1992\)](#) treated collisions statistically, assuming the central star's mass to be much bigger than that of the planetesimals and their eccentricities and inclinations to be much smaller than unity. The system under these assumptions is described by the classical Hills equations ([Hill, 1878](#)). The underlying, adopted probability of a particle hitting a planet during one orbit was already derived by [Öpik \(1951\)](#). In this section, both methods are briefly revised and numerical results of the collision rate of a single planetesimal colliding with a disk of solids as well as accretion rates for a planet are presented.

2.10.1. Particle in a Box

The so-called "Particle in a Box" method assumes that spherical particles, i.e. the *projectiles*, move in straight lines relative to a resting, spherical *target* and is for example used in the classical works of [Safronov \(1969\)](#) and [Pollack et al. \(1996\)](#) but was already derived by [Öpik \(1951\)](#) in his first chapter (and potentially even earlier given the simplicity of the approach). If the radius r_p , the number density n (usually approximated by $\Sigma_{\text{solids}}\Omega_K/(v * m_p)$) and the relative velocity v of the projectiles and the radius of the target r_t are given, then the collision rate is

$$\Gamma = \pi(r_t + r_p)^2 vn. \quad (2.126)$$

Here, the spherical shape of the involved particles was used to simplify the well known scalar product $\vec{\sigma} \cdot \vec{v}$. Here, $\vec{\sigma}$ is the normal vector onto the cross sectional area of the target, which is in our case for all directions equal to $\pi(r_t + r_p)^2$. This is the area, for which a physical collision occurs if the projectile's center moves through it.

Assuming that the full mass of each projectile sticks to the target, this translates to a mass accretion rate

$$\frac{dm_t}{dt} = \pi(r_t + r_p)^2 vnm_p, \quad (2.127)$$

where m_p is the mass of each projectile and m_t is the mass of the target.

2.10.2. Gravitational focusing

In a disk, we can take the gravitational force of the target into account to get a better estimate. This is the dominant effect for the case where the mass of the target is large, e.g. for the accretion rate of a planet.

We consider a projectile that passes in a straight line in a distance b from the target. Instead of assuming a straight line, in reality it is attracted towards the planet. We are interested in finding b , such that the closest approach to the target of the projectile is the sum of the physical radii. If a particle passes closer than in a distance b to the target, it is then always accreted onto the target. This represents a gravitational cross section equal to $\pi * b^2$ and the physical radius $r_t + r_p$ in equation 2.126 can be replaced by b to get a better estimate for the collision rate.

b can be found by equating the energy and angular momentum at an infinite distance and at the location of closest approach, which are listed in Table 2.3.

	Energy	Angular Momentum
Infinitely far from target	$\frac{1}{2}m_p v^2$	bv
At closest approach	$\frac{1}{2}m_p v_{\max}^2 - \frac{Gm_p m_t}{r_t + r_p}$	$(r_t + r_p)v_{\max}$

Table 2.3.: Energy and angular momentum for a projectile getting deflected towards a target and passing it at a distance of $r_t + r_p$, where r_t and r_p are the radii of the target and the projectile respectively.

We note that the assumption $m_p \ll m_t$ was used to get the values in Table 2.3, which means that the gravitational force of the projectile was neglected. Using those values, energy and angular momentum conservation yield

$$v_{\max}^2 = v^2 + \underbrace{\frac{2Gm_t}{r_t + r_p}}_{v_{\text{esc}}^2} \quad (2.128)$$

$$b = (r_t + r_p) \frac{v_{\max}}{v}. \quad (2.129)$$

This in turn simplifies to

$$b = (r_t + r_p) \sqrt{1 + \frac{v_{\text{esc}}^2}{v^2}} \quad (2.130)$$

and thus, the collision rate including a one-body (i.e. the planet) gravitational focussing is

$$\Gamma = \pi (r_t + r_p)^2 \left(1 + \frac{v_{\text{esc}}^2}{v^2}\right) vn. \quad (2.131)$$

As a mass accretion rate of the target, this reads as

$$\left. \frac{dm_t}{dt} \right|_{gm_t} = \pi(r_t + r_p)^2 \left(1 + \frac{v_{\text{esc}}^2}{v^2} \right) v \rho_{\text{solids}}, \quad (2.132)$$

where ρ_{solids} is the density of solids distributed in space, which is different from the bulk density of the solids ρ_m or the gas density ρ .

For better readability we introduced here the subscript gm_t for the accretion rate to make clear that this expression includes the gravity of the target with mass m_t . In the literature, the notion of a *gravitational focussing factor* (sometimes also called "gravitational enhancement factor") F_g , i.e. the ratio of the gravitational cross section to the geometric cross section, is often used. The above simple derivation leads to

$$F_{gm_t} = 1 + \frac{v_{\text{esc}}^2}{v^2} = 1 + \frac{2Gm_t}{(r_t + r_p)v^2}. \quad (2.133)$$

A two-body gravitational focussing factor $F_{gm_t m_p}$ taking into account just the target's and the projectile's gravity could not be found in the literature. This might be because going into that much detail without taking into account the central star's gravity is not very meaningful and no analytic expression seems to exist. Note that there also exists a one-body F_{gm_s} only taking into account the star's gravity. To avoid confusion when comparing works by different authors, a detailed look at the notation is recommended. [Greenzweig & Lissauer \(1990\)](#) for example, define F_g as the ratio between the (numerically found) three-body (including central star, target and projectile) or (analytic) two-body (central star, target) to the one-body (central star) collision probability and not to the 0-body, i.e. the physical cross section, as above.

Most authors that use the particle in a box approximation, including [Safronov \(1969\)](#), use a scale height associated to the density of projectiles to get a value for n , respectively ρ_{solids} . This is done equivalent to the derivation in section 2.1 for the gas, but with the relative velocity v instead of the sound speed used as the typical speed. [Safronov \(1969\)](#) writes this in his equation 3.5

$$\Sigma_{\text{solids}} = \frac{\pi}{2\Omega_K} \rho_{\text{solids}} v \quad (2.134)$$

which is referenced in [Safronov \(1969\)](#), chapter 9. The original argumentation by Safronov is in a non-translated and non-accessible paper ([Safronov, 1954](#)) and can thus not be reviewed here. Up to numerical factors of order unity, the resulting accretion rates agree with the accretion rates that do not have to rely on a midplane density, but take the actual orbits with inclinations into account and are discussed in the next section (2.10.3).

We repeat the one-body accretion rate with ρ_{solids} exchanged for comparison with expressions shown below

$$\left. \frac{dm_t}{dt} \right|_{gm_t} = 2(r_t + r_p)^2 \left(1 + \frac{v_{\text{esc}}^2}{v^2} \right) \Sigma_{\text{solids}} \Omega_K. \quad (2.135)$$

2.10.3. Orbiting particles

To motivate the inclusion of the protosun's gravity, [Greenzweig & Lissauer \(1990\)](#) argue that gravitational encounters between protoplanets and planetesimals can last for a significant fraction of an orbital period. Other authors have addressed this topic as well ([Wetherill & Cox, 1985](#); [Hénon & Petit, 1986](#); [Ida & Nakazawa, 1989](#)), but here, the derivation by [Greenzweig & Lissauer \(1990\)](#) will be outlined since we consider it to be the most educational one. [Greenzweig & Lissauer \(1990\)](#) assume a given eccentricity and inclination of the planetesimals. The same authors later extended the framework to a distribution of eccentricities and inclinations (see [2.9.2](#)) ([Greenzweig & Lissauer, 1992](#)), which is partially updated in [Inaba et al. \(2001\)](#).

Collision probability per orbit

The probability of a spherical projectile hitting a spherical target on a circular orbit per revolution of the projectile according to [Öpik \(1951\)](#) is

$$P = \frac{(r_t + r_p)^2 \left(1 + \frac{v_{\text{esc}}^2}{v^2}\right) v}{a^2 \pi \sin(i) |v_x|}, \quad (2.136)$$

where the magnitude and the x -component of the velocity of the projectile before feeling the influence of the planet are denoted by v and v_x and the x -axis is chosen to overlap with the star to planet direction. The elements a, e and i of the projectile are fixed, whereas the argument of perihelion is assumed to be randomly distributed. [Öpik \(1951\)](#) uses⁵ the velocities $v = \sqrt{3 - 1/a - 2\sqrt{a(1 - e^2)} \cos(i)} v_k$ and $|v_x| = \sqrt{2 - 1/a - a(1 - e^2)} v_k$. An assumption made to derive the probability (2.136) is, that during the approach of the projectile to the target, the trajectories of both the target and the projectile can be considered rectilinear. In other words, (2.136) is valid only for large enough i . Otherwise the encounter would take a significant fraction of an orbital period and the trajectories would not follow straight lines anymore. This condition translates to ([Greenzweig & Lissauer, 1990](#))

$$s \ll ae \quad (2.137)$$

$$s \ll a \sin i, \quad (2.138)$$

where $s = (r_t + r_p) \sqrt{1 + v_{\text{esc}}^2/v^2}$ is the radius of the interaction region of the target. In [Appendix A.5](#), we restate lower-order accretion rate approximations that can be found analytically. Here, we will focus in the following on the results by [Inaba et al. \(2001\)](#).

⁵In [Öpik \(1951\)](#), eq. 20a,b the factor v_k is missing because he works in units of time such that one period is equal to 2π and units of space such that the distance from the central star to the planet is equal to one, which yields units of Keplerian velocity for velocities.

e and i Distributions

Before we can write down the complete accretion or collision rate of a body with a population of planetesimals, the integration over the planetesimal orbits has to be done. That means, we now need to couple this to the results in Sect. 2.9. There, we showed the distribution of e and i for the planetesimals. It is therefore necessary to average over this Rayleigh distribution, which was done by [Inaba et al. \(2001\)](#) whose results we restate. We switch to their notation, even though [Greenzweig & Lissauer \(1992\)](#) did the same exercise and would use a similar notation as above and in appendix A.5 in their work. However, [Inaba et al. \(2001\)](#) improved the low and intermediate regime accretion rates by taking into account the results of [Nakazawa et al. \(1989a,b\)](#); [Ida & Nakazawa \(1989\)](#) and modifying the interplay of the different regimes ([Inaba et al., 2001](#), eq. 15, restated in equation 2.151).

To decouple the collision rate from the local properties in the disk, the averaged number of collisions between two populations of planetesimals per unit area and per unit time is written as ([Nakazawa et al., 1989a](#); [Ohtsuki, 1999](#); [Inaba et al., 2001](#))

$$\langle \Gamma_{\text{col}} \rangle_{12} = h_{12}^2 a^2 \Omega_K n_s(m_1) n_s(m_2) dm_1 dm_2 \langle P_{\text{col}} \rangle_{12}, \quad (2.139)$$

where $\langle P_{\text{col}} \rangle_{12}$ is a non-dimensional mean collision rate between planetesimals with masses m_1 and m_2 that is independent of the number of planetesimals, but depends on the common semi-major axis, the radii and masses of the two planetesimals and the mass of the central star. The brackets indicate that the mean collision rate is an average over all eccentricities and inclinations given by a distribution function with eccentricity (inclination) dispersions e^* (i^*) which change the mean collision rate as well (see Sect. 2.9.2). $n_s(m)dm$ is the surface number density of planetesimals with masses between m and $m + dm$, whereas h_{12} is the reduced Hill radius of two planetesimals with masses m_1 and m_2 given by

$$h_{12} = \left(\frac{m_1 + m_2}{3M_\star} \right)^{1/3}. \quad (2.140)$$

For the case of a same-mass population of planetesimals $n_s(m_2) = \delta(m_2 - m)n_s(m)$ with a mass m and a single embryo with mass $M > m$ ($n_s(m_1) = \delta(M - m_1)$), equation (2.139) can be integrated and reduces to

$$\Gamma_{mM} = R_H^2 \Omega_K n_s(m) \langle P_{\text{col}} \rangle_{mM}, \quad (2.141)$$

where the usual definition of the Hill radius can be used $R_H = a(M/(3M_\star))^{1/3}$. The mass accretion rate is accordingly in agreement with the expressions of [Chambers \(2006\)](#); [Fortier et al. \(2013\)](#)

$$\dot{M} = R_H^2 \Omega_K \Sigma_{\text{solids}} \langle P_{\text{col}} \rangle_{mM}. \quad (2.142)$$

Therefore, we see that to find mass accretion or collision rates, all that is left to do is determining the non-dimensional collision probability $\langle P_{\text{col}} \rangle$. In addition to the

quantities mentioned above, we restate the definitions of the reduced eccentricity and inclination

$$\tilde{e} \equiv e/h_{12}, \quad \tilde{i} \equiv i/h_{12} \quad (2.143)$$

and similarly the reduced eccentricity and inclination dispersions

$$\tilde{e}^* \equiv e^*/h_{12}, \quad \tilde{i}^* \equiv i^*/h_{12} \quad (2.144)$$

and furthermore we define

$$\tilde{r}_p \equiv \frac{r_1 + r_2}{h_{12}a}. \quad (2.145)$$

Inaba et al. (2001) review in their second chapter the approximated collision rates by Nakazawa et al. (1989b) and Greenzweig & Lissauer (1990). They find that the averaged non-dimensional collision rate can be approximated

- for the high-velocity regime ($\tilde{e}, \tilde{i} \gtrsim 2$) by

$$\langle P_{\text{col}} \rangle_{\text{high}} = \frac{\tilde{r}_p^2}{2\pi} \left(\mathcal{F}(I^*) + \frac{6}{\tilde{r}_p} \frac{\mathcal{G}(I^*)}{(\tilde{e}^*)^2} \right), \quad (2.146)$$

where $I^* \equiv \tilde{i}^*/\tilde{e}^*$,

$$\mathcal{F}(I^*) \equiv 8 \int_0^1 \frac{I^{*2} E[\sqrt{3(1-\lambda^2)}/2]}{[I^{*2} + (1-I^{*2})\lambda^2]^2} d\lambda \quad (2.147)$$

and

$$\mathcal{G}(I^*) \equiv 8 \int_0^1 \frac{K[\sqrt{3(1-\lambda^2)}/2]}{[I^{*2} + (1-I^{*2})\lambda^2]} d\lambda, \quad (2.148)$$

where K and E are the complete elliptic integrals of the first and second kinds (see A.4).

- for the intermediate regime ($0.2 \lesssim \tilde{e}, \tilde{i} \lesssim 2$) by

$$\langle P_{\text{col}} \rangle_{\text{med}} = \frac{\tilde{r}_p^2}{4\pi\tilde{i}^*} \left(17.3 + \frac{232}{\tilde{r}_p} \right) \quad (2.149)$$

- and for the low velocity regime ($\tilde{e}, \tilde{i} \lesssim 0.2$) by

$$\langle P_{\text{col}} \rangle_{\text{low}} = 11.3 \sqrt{\tilde{r}_p}. \quad (2.150)$$

For the entire range of eccentricities and inclinations Inaba et al. (2001) found that numerical results are well reproduced by⁶

$$\langle P_{\text{col}} \rangle = \min \left(\langle P_{\text{col}} \rangle_{\text{med}}, \left(\langle P_{\text{col}} \rangle_{\text{high}}^{-2} + \langle P_{\text{col}} \rangle_{\text{low}}^{-2} \right)^{-1/2} \right). \quad (2.151)$$

⁶A peculiarity of equation (2.151) – that might not have been intended by the original creators – is that for small h_{12} – therefore for low masses of both bodies – the term $\langle P_{\text{col}} \rangle_{\text{med}}$ drops linearly with i^* . Because $\langle P_{\text{col}} \rangle_{\text{high}}$ flattens for large i^* , $\langle P_{\text{col}} \rangle_{\text{med}}$ will dominate for large i^* . However, in the literature, $\langle P_{\text{col}} \rangle_{\text{high}}$ is meant to cover the high velocity case. This behavior only occurs for physical inclinations when estimating collisions amongst low mass objects like km-sized planetesimals. In any case, one has to be aware that the formula is no longer supported by numerical data from Inaba et al. (2001) for \tilde{e}^* and \tilde{i}^* larger than 10.

Figure 1.a in [Inaba et al. \(2001\)](#) compares equation (2.151) to numerical results and the curves are reproduced for a consistency test in Figure 2.9.

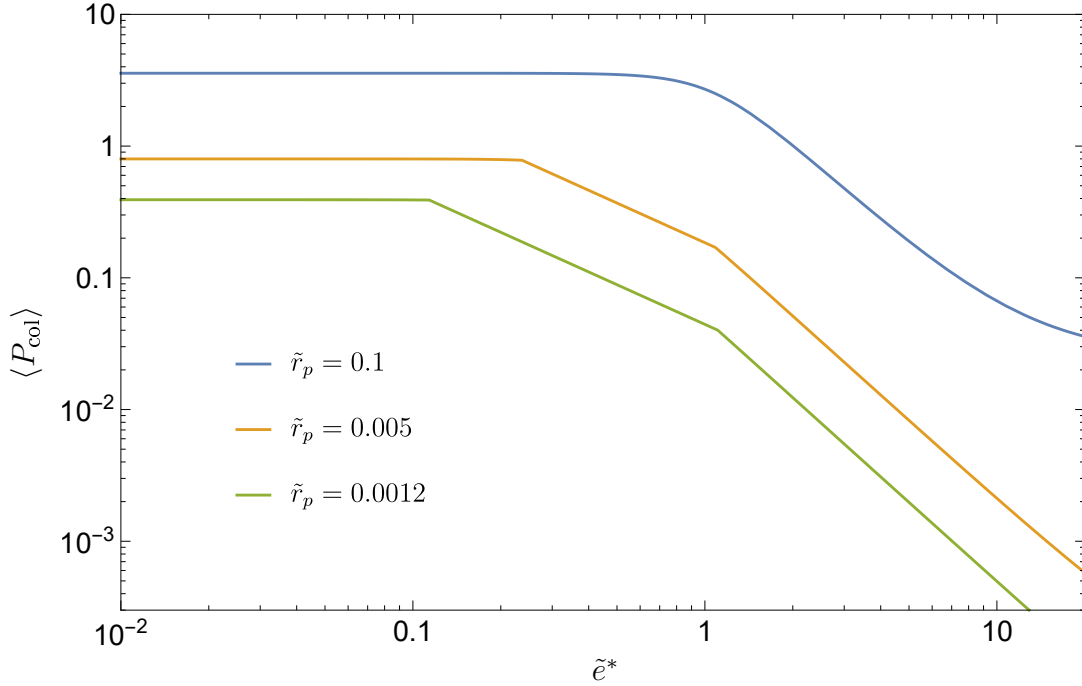


Figure 2.9.: Mean collision rate evaluated using equation (2.151) as a function of reduced eccentricity dispersions for three different \tilde{r}_p . The inclination dispersion is set to $\tilde{i}^* = \tilde{e}^*/2$. This is a reproduction of Figure 1.a in [Inaba et al. \(2001\)](#) to validate our implementation.

Having an expression for $\langle P_{\text{col}} \rangle$, we can put the results for different eccentricity and inclination dispersions into equation (2.139) to obtain the average number of collisions between two populations of planetesimals $\langle \Gamma_{\text{col}} \rangle_{12}$.

This approach will be used in [Paper I](#) and [Letter I](#). Here, we apply it to the case of having only one size r and corresponding mass $m = 4/3\pi\rho_s r^3$ of spherical planetesimals in the disk. The results are shown in figure 2.10. More results of this kind are shown in [Paper I](#), where we estimate the number of collisions to gauge their importance for the evolution of a body that crosses the snowline.

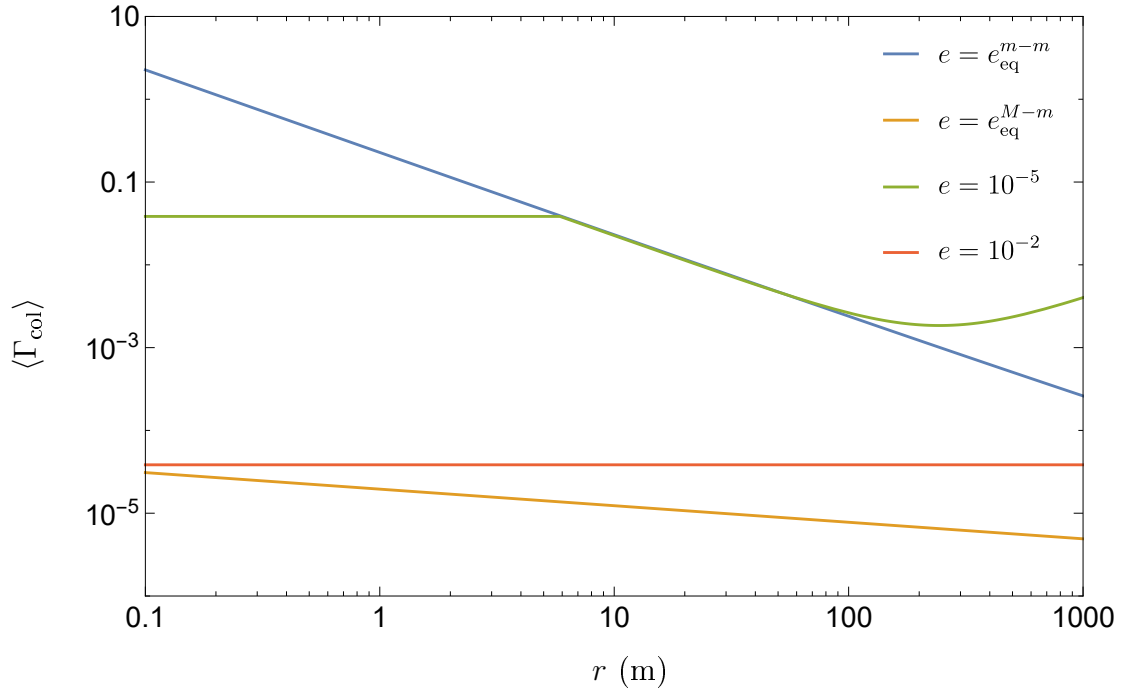


Figure 2.10.: Sum of the number of collisions between planetesimals in a year as a function of the planetesimal radius. Calculated using equation (2.139), assuming all planetesimals to be spherical and having the same size. The inclination dispersion is set to $\tilde{i}^* = \tilde{e}^*/2$, for three different eccentricities given. The kink that can be seen for the $e = 10^{-5}$ line is due to a change from the high to the intermediate velocity regime. All the other cases lie purely in the high velocity regime.

2.11. Letter I: The formation of Jupiter by hybrid pebble-planetesimal accretion

Having established a way to calculate the accretion rate of solids by a planet, I applied this method to constrain the feasibility of a scenario for the growth of Jupiter in the letter by [Alibert et al. \(2018\)](#).

The letter addresses the formation of Jupiter given two new developments in theory and observations. [Kruijjer et al. \(2017\)](#) evaluated meteoritic data and assume that a separation in space of two reservoirs is the cause for the different compositions of two main categories of meteorites – the carbonaceous meteorites and the noncarbonaceous meteorites. Such a separation can be achieved if a planet sufficiently massive is located between the two reservoirs and opens a gap in the gas disk. Then, drifting solid particles (pebbles) can no longer cross this location due to a pressure bump at the outer edge of the gap. A pressure bump acts as a natural trap for pebbles due to the dependency on the pressure gradient via η in equation (2.96). Therefore, the reservoirs of solids inside and outside of the planet remain decoupled until the planet becomes massive enough to scatter nearby bodies from the outer to the inner region and vice-versa.

The best candidate to cause such a scenario in the Solar System and therefore explain the difference between the carbonaceous and noncarbonaceous meteorites is Jupiter. Given the composition of the meteorites, [Kruijjer et al. \(2017\)](#) determined that the reservoirs became separated after less than 1 Myr and remained like that for 2 to 3 Myr. The typical masses for the opening of a gap and blocking the pebble flux called *pebble isolation mass* is $\sim 20 M_{\oplus}$ ([Bitsch et al., 2018](#); [Ataiee et al., 2018](#)); whereas the mass at which the reservoirs get reconnected due to scattering is estimated to be $\sim 50 M_{\oplus}$.

In particular the stage at which Jupiter has to grow relatively slowly from 20 to $50 M_{\oplus}$ would not occur naturally because at these masses rapid gas accretion should occur once pebble accretion stops. In this letter, we explain this growth pattern by a stage of significant planetesimal accretion following the pebble accretion phase. This provides a luminosity source for the planet which prevents cooling and contraction, which would trigger gas accretion (see Sect. 4.2).

In Fig. 2 of the letter below, we show that – using the framework described above – the accretion rates of planetesimals at 1 Myr can be large enough to provide this energy input for reasonable solid mass fraction in the disk ~ 0.05 given a relatively small radius of planetesimals of 1 km. In supplementary Fig. 4 of the letter, we show that the presence of small planetesimals is likely because the velocities that are reached due to the viscous stirring of the planetesimals exceeds their breakup limit ([Benz & Asphaug, 1999](#)).

We note that the underlying assumption to the conclusion from [Kruijjer et al. \(2017\)](#) is the hypothesis that the different meteoritic compositions stem from a spacial separation of the reservoirs. If instead a *temporal* separation is the cause of the differences, the whole scenario is invalid.

The formation of Jupiter by hybrid pebble-planetesimal accretion

Yann Alibert^{1*}, Julia Venturini², Ravit Helled², Sareh Ataiee¹, Remo Burn¹, Luc Senecal¹, Willy Benz¹, Lucio Mayer², Christoph Mordasini¹, Sascha P. Quanz³ and Maria Schönbachler⁴

The standard model for giant planet formation is based on the accretion of solids by a growing planetary embryo, followed by rapid gas accretion once the planet exceeds a so-called critical mass¹. However, the dominant size of the accreted solids ('pebbles' of the order of centimetres or 'planetesimals' of the order of kilometres to hundreds of kilometres) is unknown^{1,2}. Recently, high-precision measurements of isotopes in meteorites have provided evidence for the existence of two reservoirs of small bodies in the early Solar System³. These reservoirs remained separated from ~1 Myr until ~3 Myr after the Solar System started to form. This separation is interpreted as resulting from Jupiter growing and becoming a barrier for material transport. In this framework, Jupiter reached ~20 Earth masses (M_{\oplus}) within ~1 Myr and slowly grew to ~50 M_{\oplus} in the subsequent 2 Myr before reaching its present-day mass³. The evidence that Jupiter's growth slowed after reaching 20 M_{\oplus} for at least 2 Myr is puzzling because a planet of this mass is expected to trigger fast runaway gas accretion^{4,5}. Here, we use theoretical models to describe the conditions allowing for such a slow accretion and show that Jupiter grew in three distinct phases. First, rapid pebble accretion supplied the major part of Jupiter's core mass. Second, slow planetesimal accretion provided the energy required to hinder runaway gas accretion during the 2 Myr. Third, runaway gas accretion proceeded. Both pebbles and planetesimals therefore play an important role in Jupiter's formation.

High-precision measurements of isotopes (molybdenum, tungsten and platinum) in meteorites have recently been used to temporally and spatially constrain the early Solar System³, by combining two main cosmochemical observations (see Methods). On the basis of these data, the existence of two main reservoirs of small bodies in the early Solar System can be inferred^{6–8}. These reservoirs remained well separated for about 2 Myr because of the formation of Jupiter and were reconnected only when the planet grew massive enough to scatter material from beyond Jupiter's orbit to inner regions of the Solar System³. This cosmochemical evidence, which has never been included in growth models of Jupiter, places severe constraints on planet formation models.

We simulate Jupiter's growth at its present location by solid and gas accretion by using state-of-the-art planet formation models⁹ to determine the time required for Jupiter to reach 50 M_{\oplus} , the mass presumably needed to reconnect the two reservoirs³. We checked, using N -body simulation, that this mass is indeed large enough for efficient scattering to happen (see Supplementary Information). We

consider different values for the mass of Jupiter at 1 Myr and for the average accretion rate of solids after 1 Myr. As the opacity and the composition of Jupiter's envelope are not precisely known, we ran models using a large range of assumptions (low or high opacity, pure hydrogen and helium, or envelope enriched in heavier elements). The model results show that the cosmochemical constraints are met, but only with a planetary mass at 1 Myr between about 5 M_{\oplus} and 16 M_{\oplus} depending on the assumed conditions (Fig. 1). Therefore, the minimum mass of the forming Jupiter that is required to prevent the transport of pebbles (the 'pebble isolation mass') is somehow smaller than the 20 M_{\oplus} inferred previously³. Note that the precise values of the pebble isolation mass and the mass that Jupiter should have attained at about 3 Myr after the beginning of the Solar System are not directly derived from cosmochemical studies, but result from theoretical interpretation³.

Our models also show that a relatively high solid accretion rate (at least $10^{-6} M_{\oplus} \text{ yr}^{-1}$) is required to prevent rapid gas accretion after 1 Myr. Indeed, slow gas accretion is possible only through substantial thermal support of the gas-dominated envelope that can counteract the strong gravity of the planetary core. We find that the dissipation of the kinetic energy from infalling solids thermally supports the envelope and inhibits high gas accretion rates. We checked that the ranges of values of pebble isolation mass and solid accretion rates are very robust and insensitive to the envelope composition and/or the opacity values, the planet's location and the disk properties (see Supplementary Figs. 1 and 2).

Because Jupiter reached the pebble isolation mass around 1 Myr, maintaining a high solid accretion rate after this time must result from the accretion of planetesimals, which do not experience the isolating effect of the planet as pebbles do (see Supplementary Information). During the first million years, the solid accretion rate needs to be as high as about $10^{-5} M_{\oplus} \text{ yr}^{-1}$ for Jupiter to reach a mass of about 5–16 M_{\oplus} in only 1 Myr. This accretion rate is too high to result from the accretion of planetesimals and must result from the accretion of pebbles (see Supplementary Information). However, a rate of at least $10^{-6} M_{\oplus} \text{ yr}^{-1}$ in planetesimal accretion is required to stall runaway gas accretion and keep the planetary mass below 50 M_{\oplus} for the next 2 Myr. Hence, fulfilling the cosmochemical time constraints³ in a Jupiter formation scenario is possible only through a hybrid accretion process where, first, pebbles provide high accretion rates and grow a large core (about 5–16 M_{\oplus}) and, second, substantial planetesimal accretion sets in afterwards. This planetesimal accretion, which occurs after 1 Myr, supplies the energy required for delaying rapid gas accretion and only modestly contributes to the core's mass.

¹Physikalisches Institut, Universität Bern, Bern, Switzerland. ²Institut für Computational Sciences, Universität Zürich, Zürich, Switzerland. ³Institute for Particle Physics and Astrophysics, ETH Zürich, Zürich, Switzerland. ⁴Institute of Geochemistry and Petrology, ETH Zürich, Zürich, Switzerland.

*e-mail: alibert@space.unibe.ch

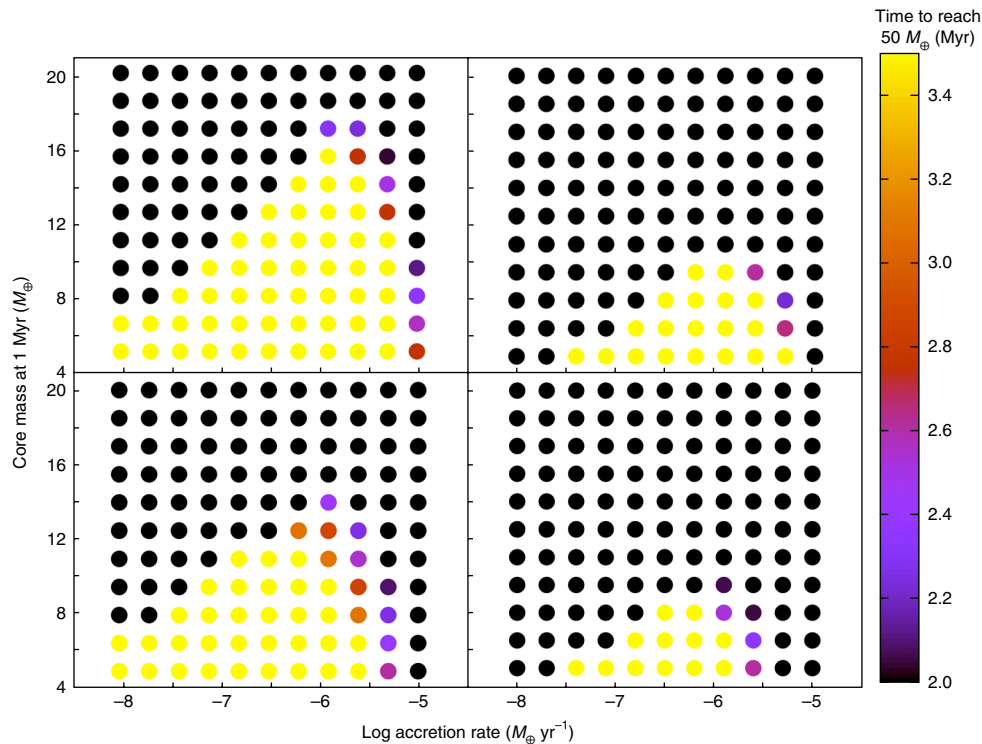


Fig. 1 | Time to reach $50 M_{\oplus}$ as a function of the core mass at 1 Myr and the solid accretion rate ($M_{\oplus} \text{ yr}^{-1}$, log scale). Upper left: non-enriched envelope and ISM opacity³⁹. Upper right: non-enriched envelope and opacity reduced by a factor of ten compared with the ISM value. Lower left: enriched envelope and ISM opacity. Lower right: enriched envelope and reduced opacity. The yellow region delimits where the runaway gas accretion occurs too early (because either the initial core mass is too large or the heating by incoming planetesimals is too small). Colours between purple and orange indicate the region that is compatible with the growth timescale of Jupiter as obtained from cosmochemical studies³. Note that in all cases, the parameter space that is consistent with the cosmochemical constraints³ is small.

The derived accretion rate of planetesimals onto Jupiter represents a substantial flux of infalling solids. Such high accretion rates cannot be sustained by large (hundreds of kilometres in size) planetesimals, given the excitation they experience from the gravitational interaction with a growing planetary embryo and the inability of gas drag to damp the eccentricity and inclination of such big objects^{10,11}. Thus, our results suggest that a substantial mass of small planetesimals (kilometres in size) was present in the solar nebula at 1 Myr (see Fig. 2 and Supplementary Information), in apparent contradiction to recent studies suggesting the existence of large primordial planetesimals^{12,13}. These smaller objects would, therefore, be second-generation planetesimals, resulting from the fragmentation of larger primordial objects¹⁴. Indeed, the presence of a planet of a few Earth masses leads to collisions that are violent enough to disrupt primordial planetesimals¹⁴. Moreover, the collision timescale among large planetesimals is short enough to allow the formation of small ones by fragmentation in less than 1 Myr (see Supplementary Information). In this way, the initial growth of Jupiter by pebble accretion during the first million years provided the conditions to fragment large primordial planetesimals into small second-generation objects in a timely manner.

Our formation scenario also provides a solution to the problem of the timing of pebble accretion. Indeed, pebble accretion is so efficient that objects quickly become more massive than Jupiter unless accretion starts shortly before the dispersal of the protoplanetary disk^{15,16}. This timing is inconsistent with detailed models of pebble growth, which conclude that pebbles form and accrete early¹⁷. In the hybrid pebble–planetesimal scenario, the formation of Jupiter-mass planets is stretched over a few million years, comparable to the typical lifetimes of circumstellar disks¹⁸. In this case,

it is possible that pebbles are accreted in the early phases of protoplanetary disk evolution, without leading necessarily to the formation of massive planets.

We conclude that Jupiter formed in a three-step process (Fig. 3). (1) Jupiter’s core grew by pebble accretion. The contribution of large primordial planetesimals to the solid accretion was negligible. As Jupiter’s core became more massive, large primordial planetesimals dynamically heated, collided and formed second-generation smaller planetesimals. (2) Pebble accretion ceased (Jupiter reached the pebble isolation mass), and the protoplanet grew more slowly by the accretion of small planetesimals. The solid accretion rate remained high enough to provide sufficient thermal support to the gas envelope and to prevent rapid gas accretion. (3) The critical mass for gas accretion was reached, gas rapidly accreted and Jupiter reached its present-day mass. During this last phase, further solids may have been accreted, increasing the final heavy-element content in Jupiter¹⁹.

Our simulations show that the total heavy-element mass in Jupiter (core and envelope) before runaway gas accretion (accounting for both pebble and planetesimal accretion) ranges from $6 M_{\oplus}$ to $20 M_{\oplus}$. These values can be compared with Jupiter’s heavy-element mass as derived from structure models, which ranges from $23.6 M_{\oplus}$ to $46.2 M_{\oplus}$ (ref. ²⁰). This comparison implies that Jupiter accreted up to about $25 M_{\oplus}$ during runaway gas accretion or at a later stage¹⁹. Heavy elements that accreted late do not necessarily reach the core. They can dissolve in the envelope²¹, leading to envelope enrichment and the formation of heavy-element gradients²².

In this new hybrid pebble–planetesimal scenario, the time a protoplanet spends in the mass range of $15\text{--}50 M_{\oplus}$ extends over a few million years before rapid gas accretion takes place. Because the

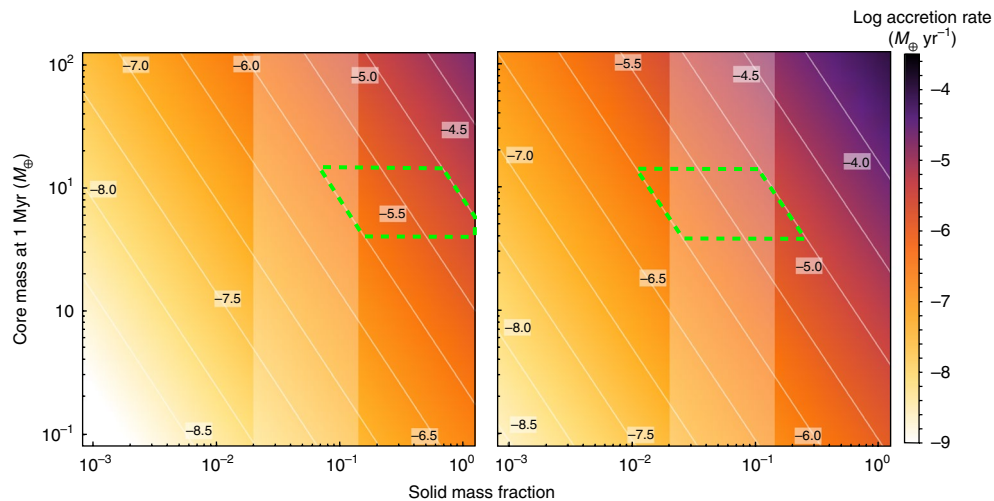


Fig. 2 | Accretion rate of planetesimals as a function of the solid mass fraction and the core mass at 1 Myr. Left: large planetesimals (100 km in size). Right: small planetesimals (1 km in size). The green dashed regions delimit the parameters that allow the cosmochemical constraints³ (core mass of $\sim 5\text{--}16 M_{\oplus}$ and solid accretion rate of $10^{-6}\text{--}10^{-5} M_{\oplus} \text{yr}^{-1}$) to be matched. The vertical pale shaded bands delimit the likely solid mass fraction according to the standard minimum-mass solar nebula model for the lowest value⁴⁰ and the dust-to-planetesimal formation models for the highest value⁴¹. Values next to diagonal white lines indicate the log accretion rate ($M_{\oplus} \text{yr}^{-1}$).

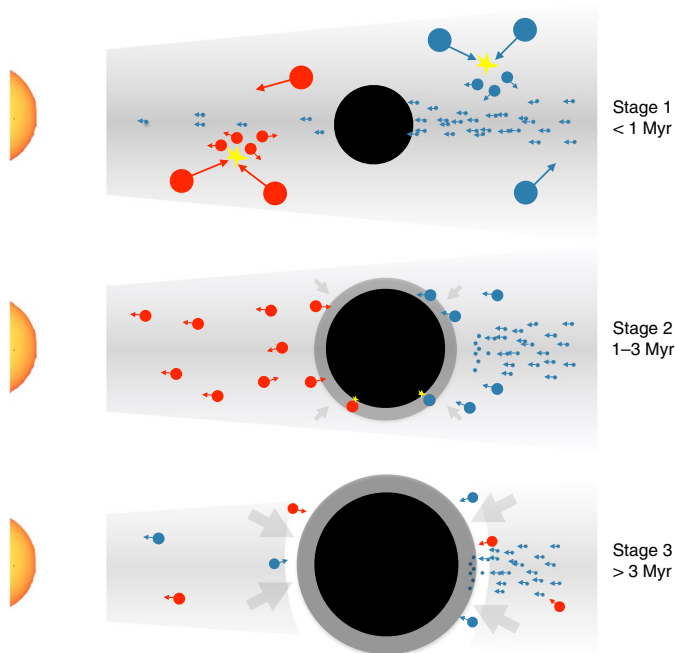


Fig. 3 | The three stages of the hybrid pebble-planetesimal formation model. Stage 1 (up to 1 Myr): Jupiter (black) grows by pebble accretion (small circles), and planetesimal accretion is negligible. Large primordial planetesimals (large circles) are excited by the growing planet and suffer high collision velocities (large arrows), leading to destructive collisions (yellow), which produce small, second-generation planetesimals (medium circles). Stage 2 (1–3 Myr): Jupiter is massive enough to prevent pebble accretion. The energy associated with the accretion of small planetesimals is large enough to prevent rapid gas accretion (grey arrows). Stage 3 (after 3 Myr): Jupiter is massive enough to accrete large amounts of gas (hydrogen, helium). Nearby pebbles and small planetesimals can be gravitationally captured. Ultimately, a gap (white) is opened in the solar nebula, stopping further gas accretion. Red and blue indicate the two reservoirs of small bodies (inside and outside Jupiter's orbit, respectively), which are separated by Jupiter's growth in stage 2 and reconnected in stage 3. The Sun is shown on the left.

final mass of a planet is determined by the dissipation of the protoplanetary disk, our formation scenario increases the likelihood of forming intermediate-mass planets, which provides a natural explanation for the formation of Uranus and Neptune^{1,23}.

Methods

Meteoritic constraints. Kruijer et al.³ constrained Jupiter's growth history by combining two main cosmochemical observations. First, cosmochemical data of the youngest inclusions (chondrules) in primitive meteorites constrain the maximum accretion age for small primitive bodies, while the short-lived ^{182}Hf to ^{182}W decay system dates metal–silicate separation and, as such, the accretion timescales of small differentiated bodies and planets. Second, distinct nucleosynthetic isotope compositions (for example, of molybdenum or tungsten) that were imprinted in dust accreted by planetary bodies allow regions in the protoplanetary disk with originally distinct dust compositions to be identified. On the basis of this, cosmochemical data constrain two main reservoirs of small bodies that existed in the early Solar System^{6–8}. They remained well separated for about 2–4 Myr (refs ^{3,24}). The separation of these two reservoirs occurred in the first million years after the beginning of the Solar System, as defined by the formation of the oldest Solar System materials (Ca–Al-rich inclusions). It was proposed³ that this separation was initiated by the growth of proto-Jupiter reaching pebble isolation mass ($20 M_{\oplus}$), thereby isolating the population of pebbles inside and outside its orbit. The two reservoirs remained separated until Jupiter grew massive enough to scatter small bodies, reconnecting the reservoirs. This occurred when Jupiter reached $50 M_{\oplus}$, and not earlier than 3–4 Myr after Ca–Al-rich inclusion formation³. While cosmochemical evidence constrains the timescale of the separation of the reservoirs, it does not constrain the mass that Jupiter had at these epochs.

Modelling planetary growth. We compute planetary growth in the framework of the core accretion model by solving the planetary internal structure equations^{4,5}, assuming that the luminosity results from the accretion of solids and gas contraction.

We consider two limiting cases regarding the fate of solids accreted by proto-Jupiter. In the first case, the so-called non-enriched case, all the accreted heavy elements are assumed to sink to the centre (core). In this case, the envelope is made of pure H and He. In the second case, the enriched case, we assume that the volatile fraction of the accreted solids is deposited in the envelope, whereas the refractory component reaches the core^{20,25}. The volatile fraction is assumed to be 50 wt%, following recent condensation models²⁶. The luminosity in this case is that provided by the refractory material only, since the volatiles are assumed to remain mixed in the envelope and contribute to the luminosity generated by its contraction²⁵. In all the models presented here, we treat the accretion rate of solids between 1 Myr and 3 Myr as a free parameter that varies from $10^{-8} M_{\oplus} \text{yr}^{-1}$ to $10^{-5} M_{\oplus} \text{yr}^{-1}$.

The internal structure equations^{4,5} are solved by using, as boundary conditions, the pressure and temperature in the protoplanetary disk at the position of the planetary embryo, and by defining the planetary radius as a combination of the

Hill and Bondi radii²⁷. The evolution of the planetary envelope depends on the equation of state and opacity used. For the non-enriched case, we use the equation of state of H and He (ref. ²⁸). For the enriched case, the envelope is assumed to be composed of H, He and water, and we take into account the mixture of the three components^{25,28,29}. For the opacity, we use either interstellar medium (ISM) opacity³⁰, or a reduced opacity in which we multiply the ISM opacity by 1/10 to mimic the possible opacity reduction due to grain growth^{30,31}. The calculations do not include the effect of destruction and replenishment of pebbles in Jupiter's envelope^{32,33}, because the growth of Jupiter after 1 Myr is dominated by the accretion of planetesimals, for which the effect of destruction in the planetary envelope is less important³³.

Disk structure. The disk model provides the pressure and temperature at the location of Jupiter's formation, which serve as boundary conditions for computation of the internal structure. This model is designed to fit two-dimensional radiative hydrodynamic simulations of protoplanetary disks³⁴.

Planetesimal accretion. In early planet formation models, it was assumed that the accreted solids were large planetesimals⁴ (hundreds of kilometres in size), in agreement with several theoretical and observational constraints^{12,13}. These planetesimal-based formation models still face the problem that the time required to reach rapid gas accretion is comparable to or even longer than the disk's lifetime^{4,18}. This challenge is even more severe if dynamic heating (increased eccentricity and inclination) of the planetesimals by the gravity of a proto-Jupiter is considered^{10,35} (see also Supplementary Information), because this hinders the core growth. Dynamic heating is counteracted by damping caused by gas drag and thus primarily affects small planetesimals. Hence, accreting solids that are only a few kilometres in size can relieve the timescale problem^{9,10}. Numerical simulations, however, predict much larger typical sizes for primordial planetesimals, of the order of tens to hundreds of kilometres¹², with most of the mass stored in the largest bodies, in agreement with the constraints from the asteroid belt¹³. Therefore, kilometre-size planetesimals are probably generated by the collisional fragmentation of large primordial planetesimals. This in turn requires high collision velocities, which result from the gravitational stirring of primordial planetesimals by objects of a few Earth masses¹⁴.

Planetesimal accretion depends on three factors: the amount of planetesimals near the planet, the mass of the forming planet and the degree of planetesimal excitation. In particular, the planetesimal accretion rate depends on the gravitational focusing factor, F_{grav} , itself depending inversely on the relative velocity between planetesimals and the growing Jupiter, v_{rel} . When planetesimals are dynamically excited (that is, when they have large eccentricity and inclination), v_{rel} increases, and the planetesimals are accreted less efficiently. Planetesimals are excited by the forming planet and by planetesimal–planetesimal interactions and are damped by gas drag. Large planetesimals are more excited than small ones because gas drag is less active on the former. Therefore, v_{rel} is larger for large planetesimals, leading to smaller accretion rates than for small planetesimals. We compute the accretion rate of planetesimals¹⁴ that are 100 km or 1 km in size as a function of the planetary mass and planetesimal/gas mass ratio. The properties of the gas disk that are required for this calculation (for example, gas density) are taken from the disk model at a radial distance of 5.2 AU and an age of 1 Myr (when planetesimal accretion begins).

Fragmentation of large planetesimals. Two conditions are required to account for the formation of small planetesimals from the fragmentation of large ones before 1 Myr (when the accretion of pebbles stops). Collisions must be both frequent enough (so that small planetesimals are produced rapidly enough) and violent enough (so that collisions lead to fragmentation). We estimate the collision timescale^{36,37} between planetesimals that are 100 km in size as a function of the protoplanet's mass and the solid surface density at 5 AU. The collision frequencies are calculated for a single-size population of planetesimals. The calculation includes the stirring of planetesimals by the growing Jupiter, but not the interaction between planetesimals, which is negligible for planets of a few Earth masses¹¹. Including this effect would increase the excitation of planetesimals, leading to even more violent collisions and further fragmentation. We also include the gas drag that decreases the eccentricity and inclination of planetesimals and, therefore, their collision velocity. To determine in which case the collisions lead to the destruction of planetesimals, we compared the specific energy of the collision with that required for disruption, Q_{D} . We chose for this value a very conservative estimate of $6 \times 10^9 \text{ erg g}^{-1}$, which corresponds to the highest value found for any set of compositional parameters³⁸. As a result, for all collisions involving an energy larger than Q_{D} , planetesimals are expected to be destroyed and to fragment into much smaller objects. More details on the calculation of the fragmentation of large planetesimals are in the Supplementary Information.

Data availability. The data that support the plots within this paper and other findings of this study are available from the corresponding author upon reasonable request.

Received: 5 October 2017; Accepted: 12 July 2018;
Published online: 27 August 2018

References

- Helled, R. et al. in *Protostars and Planets VI* (eds Beuther, H. et al.) 643–666 (Univ. Arizona Press, Tucson, AZ, 2014).
- Johansen, A. et al. in *Protostars and Planets VI* (eds Beuther, H. et al.) 547–570 (Univ. Arizona Press, Tucson, AZ, 2014).
- Kruijer, T. S., Burkhardt, C., Budde, G. & Kleine, T. Age of Jupiter inferred from the distinct genetics and formation times of meteorites. *Proc. Natl Acad. Sci. USA* **114**, 6712–6716 (2017).
- Pollack et al. Formation of the giant planets by concurrent accretion of solids and gas. *Icarus* **124**, 62–85 (1996).
- Alibert, Y., Mordasini, C., Benz, W. & Winisdoerffer, C. Models of giant planet formation with migration and disc evolution. *Astron. Astrophys.* **434**, 343–353 (2005).
- Trinquier, A., Birk, J. L. & Allègre, C. J. Widespread ⁵⁴Cr heterogeneity in the inner Solar System. *Astrophys. J.* **655**, 1179–1185 (2007).
- Leya, I. et al. Titanium isotopes and the radial heterogeneity of the Solar System. *Earth Planet. Sci. Lett.* **266**, 233–244 (2008).
- Dauphas, N. & Schauble, E. A. Mass fractionation laws, mass-independent effects, and isotopic anomalies. *Ann. Rev. Earth Planet. Sci.* **44**, 709–783 (2016).
- Alibert, Y. et al. Theoretical models of planetary system formation: mass vs. semi-major axis. *Astron. Astrophys.* **558**, A109 (2013).
- Fortier, A., Alibert, Y., Carron, F., Benz, W. & Dittkrist, K.-M. Planet formation models: the interplay with the planetesimal disc. *Astron. Astrophys.* **549**, A44 (2013).
- Levison, H., Thommes, E. & Duncan, M. J. Modeling the formation of giant planet cores. I. Evaluating key processes. *Astron. J.* **139**, 1297–1314 (2010).
- Simon, J. B., Armitage, P. J., Youdin, A. N. & Li, R. Evidence for universality in the initial planetesimal mass function. *Astrophys. J. Lett.* **847**, L12 (2017).
- Morbiddelli, A., Bottke, W. F., Nesvorný, D. & Levison, H. F. Asteroids were born big. *Icarus* **204**, 558–573 (2009).
- Kobayashi, H., Tanaka, H., Krivov, A. V. & Inaba, S. Planetary growth with collisional fragmentation and gas drag. *Icarus* **209**, 836–847 (2010).
- Bitsch, B., Lambrechts, M. & Johansen, A. The growth of planets by pebble accretion in evolving protoplanetary discs. *Astron. Astrophys.* **582**, A112 (2015).
- Bitsch, B., Lambrechts, M. & Johansen, A. The growth of planets by pebble accretion in evolving protoplanetary discs (corrigendum). *Astron. Astrophys.* **609**, C2 (2018).
- Ida, S. & Guillot, T. Formation of dust-rich planetesimals from sublimated pebbles inside of the snow line. *Astron. Astrophys.* **596**, L3 (2016).
- Hartmann, L., Calvet, N., Gullbring, E. & D'Alessio, P. Accretion and the evolution of T Tauri disks. *Astrophys. J.* **495**, 385–400 (1998).
- Zhou, J.-L. & Lin, D. N. C. Planetesimal accretion onto growing proto-gas giant planets. *Astrophys. J.* **666**, 447–465 (2007).
- Wahl, S. M. et al. Comparing Jupiter interior structure models to Juno gravity measurements and the role of a dilute core. *Geophys. Res. Lett.* **44**, 4649–4659 (2017).
- Mordasini, C., Alibert, Y. & Benz, W. Destruction of planetesimals in protoplanetary atmospheres. In *Proc. Tenth Anniversary of 51 Peg-b: Status of and Prospects for Hot Jupiter Studies* (eds Arnold, L. et al.) 84–86 (Frontier Group, 2006).
- Lozovsky, M., Helled, R., Rosenberg, E. D. & Bodenheimer, P. Jupiter's formation and its primordial internal structure. *Astrophys. J.* **836**, 227 (2017).
- Venturini, J. & Helled, R. The formation of mini-Neptunes. *Astrophys. J.* **848**, 95 (2017).
- Bollard, J. et al. Early formation of planetary building blocks inferred from Pb isotopic ages of chondrules. *Sci. Adv.* **3**, e1700407 (2017).
- Venturini, J., Alibert, Y. & Benz, W. Planet formation with envelope enrichment: new insights on planetary diversity. *Astron. Astrophys.* **596**, A90 (2016).
- Thiabaud, A. et al. From stellar nebula to planets: the refractory components. *Astron. Astrophys.* **562**, A27 (2014).
- Lissauer, J. J., Hubickyj, O., D'Angelo, G. & Bodenheimer, P. Models of Jupiter's growth incorporating thermal and hydrodynamic constraints. *Icarus* **199**, 338–350 (2009).
- Saumon, D., Chabrier, G. & van Horn, H. M. An equation of state for low-mass stars and giant planets. *Astrophys. J. Suppl. S.* **99**, 713–741 (1995).
- Thompson, S. L. *ANEOS—Analytic Equations of State for Shock Physics Codes—Input Manual* Report SAND89-2951 (Sandia National Laboratories, 1990).
- Ormel, C. W. An atmospheric structure equation for grain growth. *Astrophys. J. Lett.* **789**, L18 (2014).
- Mordasini, C. Grain opacity and the bulk composition of extrasolar planets. II. An analytical model for grain opacity in protoplanetary atmospheres. *Astron. Astrophys.* **572**, A118 (2014).
- Ormel, C. W., Shi, J.-M. & Kuiper, R. Hydrodynamics of embedded planets' first atmospheres. II. A rapid recycling of atmospheric gas. *Mon. Not. R. Astron. Soc.* **447**, 3512–3525 (2015).

Supplementary Information

Sensitivity tests

In order to test the sensitivity of the results to the assumed disk metallicity, we also compute models assuming half or twice solar metallicity. As can be seen by Supplementary figure 1, our results are insensitive to the assumed metallicity and/or disk mass.

In all the models presented here, we assume for simplicity that Jupiter forms at 5.2 AU without migration. Our results are not very sensitive to the assumed planetary location (see upper panels of Supplementary figure 1).

In order to test the influence of Jupiter's migration on our result, we also ran a simulation where Jupiter's core was assumed to start at 20 AU (at 1 Myr), and migrated with a constant migration rate down to 5 AU^{12,13}, the other conditions (gas composition and opacity) being the same as in Supplementary figure 1. As these results show (Supplementary figure 2), the mass of Jupiter at 1 Myr, as well as the required accretion rate of solids beyond 1 Myr are hardly modified by including migration.

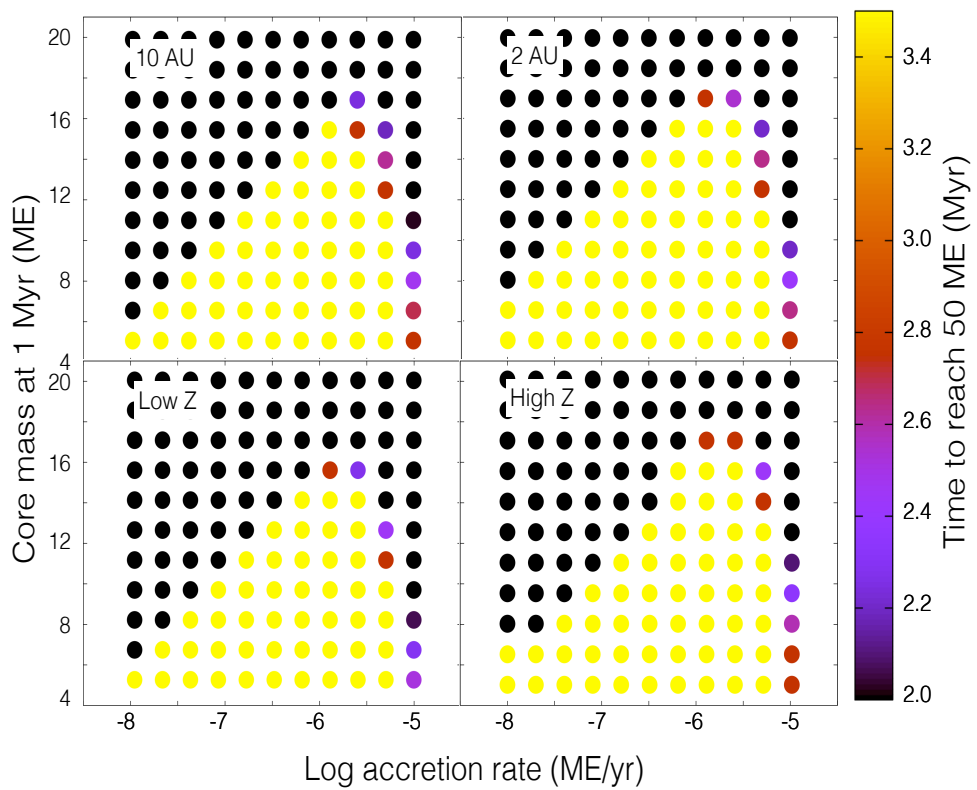
Pebble isolation mass

Constraints on disk parameters

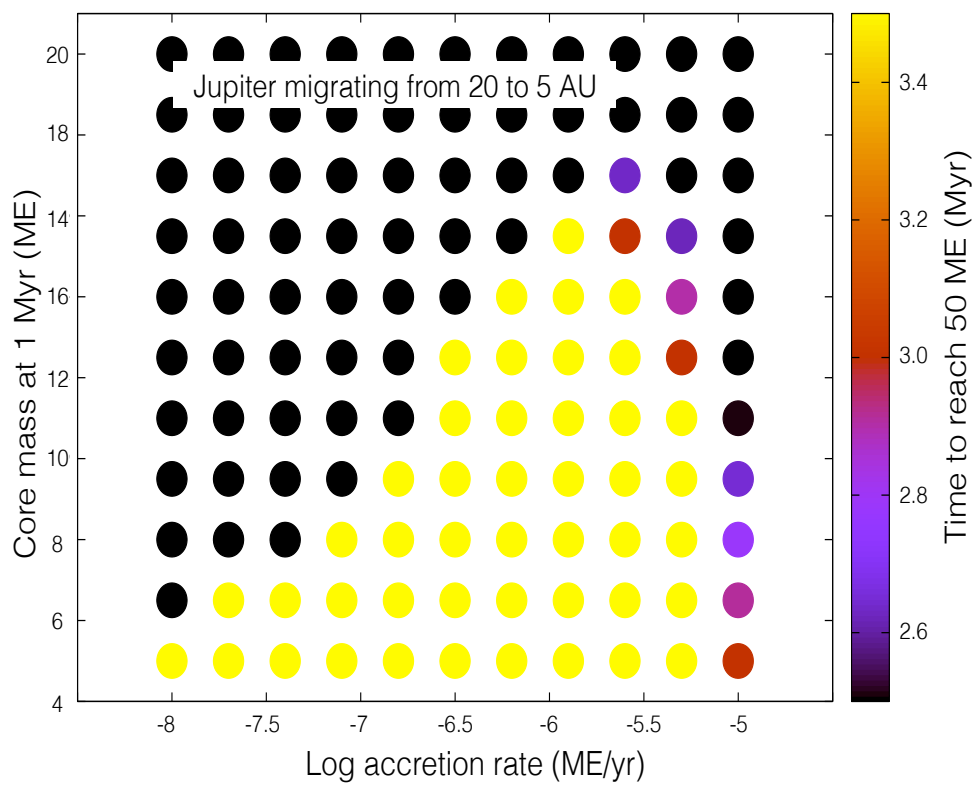
Our results provide constraints on the structure of the solar nebula between 1 and 3 Myr, since the pebble isolation mass depends on the disk scale height⁴². We find that the pebble isolation mass at 1 Myr is ~ 5 up to $\sim 14-16$ ME (for the non-enriched high opacity, and enriched low opacity cases) therefore, corresponding to a scale height between 0.033 to 0.044, respectively. This translates into temperatures at 5.2 AU and 1 Myr in the 50-100 K range. According to more recent simulations including the effects of viscosity⁴³, the disk aspect ratio at 1 Myr must lie in the 0.03 (for high viscosity) to 0.06 (for low viscosity) interval (see Supplementary figure 3). Furthermore, the growth timescale derived from cosmochemical constraints³ implies that Jupiter remained in the 15-50 ME mass range for a long time (~ 2 Myr), but planets in this mass range are normally expected to be affected by migration⁴⁴. The existence of Jupiter during 2 Myr in the 15-50 ME mass range implies that a zone of very reduced migration, known as convergence zone, was present for a long time in Jupiter's formation location. Interestingly, our disk model³⁷ predicts the existence of convergence zones for planets of the required mass around 5.2 AU. It remains, however, to be investigated under what conditions such convergence zones can be sustained for a timescale of 2 Myr. The migration of Jupiter, at least in the range of semi-major axis we considered (2 to 10 AU), would therefore not change our conclusions.

Difference with the *planetesimal* isolation mass

When Jupiter reaches the pebble isolation mass, pebble accretion stops by definition, but planetesimal accretion is not affected. Indeed, when a planet forms by accretion of planetesimals, the accreted bodies are the ones located initially close enough to the planet, in the so-called feeding zone (radial drift is not very important for such massive



Supplementary figure 1. Same as the upper left panel of Fig. 2 (see main text) for different radial distances and disk metallicity. The top panels correspond to formation locations of 10 AU (left) and 2 AU (right). The left and right bottom panels correspond to low (half solar) and high (twice solar) disk metallicity, respectively.



Supplementary figure 2. Same as the upper left panel of Fig. 2 (see main text) but including a constant migration of Jupiter from 20 AU (at 1 Myr) to 5 AU (at 3 Myr).

bodies). As a consequence, even if the planet is massive enough (for example beyond the pebble isolation mass), it will continue to accrete planetesimals whatever its mass, provided there are still planetesimals in the feeding zone. It is important to note that the pebble isolation mass depends on the total mass of the planet (gas and solids), whereas the planetesimal isolation mass only depends on the initial amount of planetesimals at a given location, and therefore on the disk solid surface density. Finally, note that in the planetesimal-based formation models^{4,5,6}, planetesimal accretion is still possible beyond the planetesimal isolation mass, as a result of the increase of the planet's feeding zone (itself resulting from the accretion of gas).

Planetesimal fragmentation

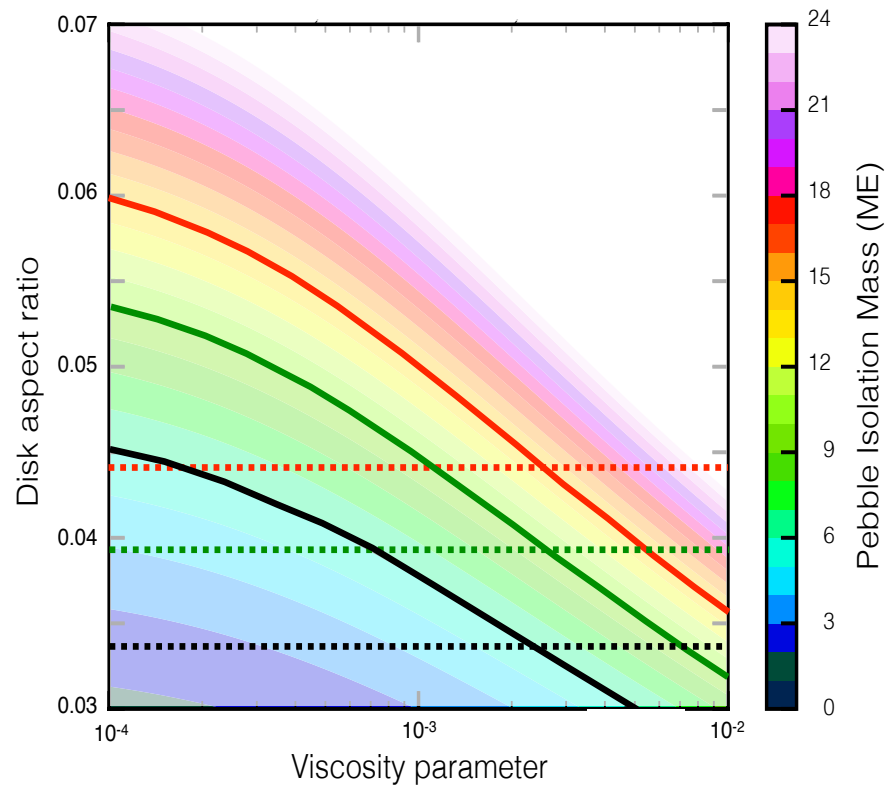
Supplementary figure 4 shows the results of the computed collisional timescale of 100 km-size planetesimals as a function of the planetesimal-to-gas ratio and core mass at 1 Myr. The major quantity governing the collision timescale is the solid surface density (at 5 AU). The required parameter range ($Q/Q_D^* > 1$ and collision timescale smaller than 1 Myr) is delimited by the green area, and overlaps largely the typical planetesimal surface density expected for the solar nebula (shaded white area on the figure, corresponding to a range of values between the MMSN and ten times the MMSN). We can therefore conclude that if an initial population of large planetesimals was present at the beginning of Jupiter growth, it could evolve into a population of much smaller planetesimals as a result of fragmentation caused by Jupiter's excitation during the first 1 Myr⁴⁵. Note that these estimates do not allow us to determine the sizes of the small planetesimals. However, since planetesimals of 100 m to 1 km in size are the most fragile ones (the ones for which the specific energy required for catastrophic disruption is the smallest), a large fraction of the planetesimals produced by fragmentation should have sizes in this range⁴⁶.

Mass of Jupiter at 3 Myr

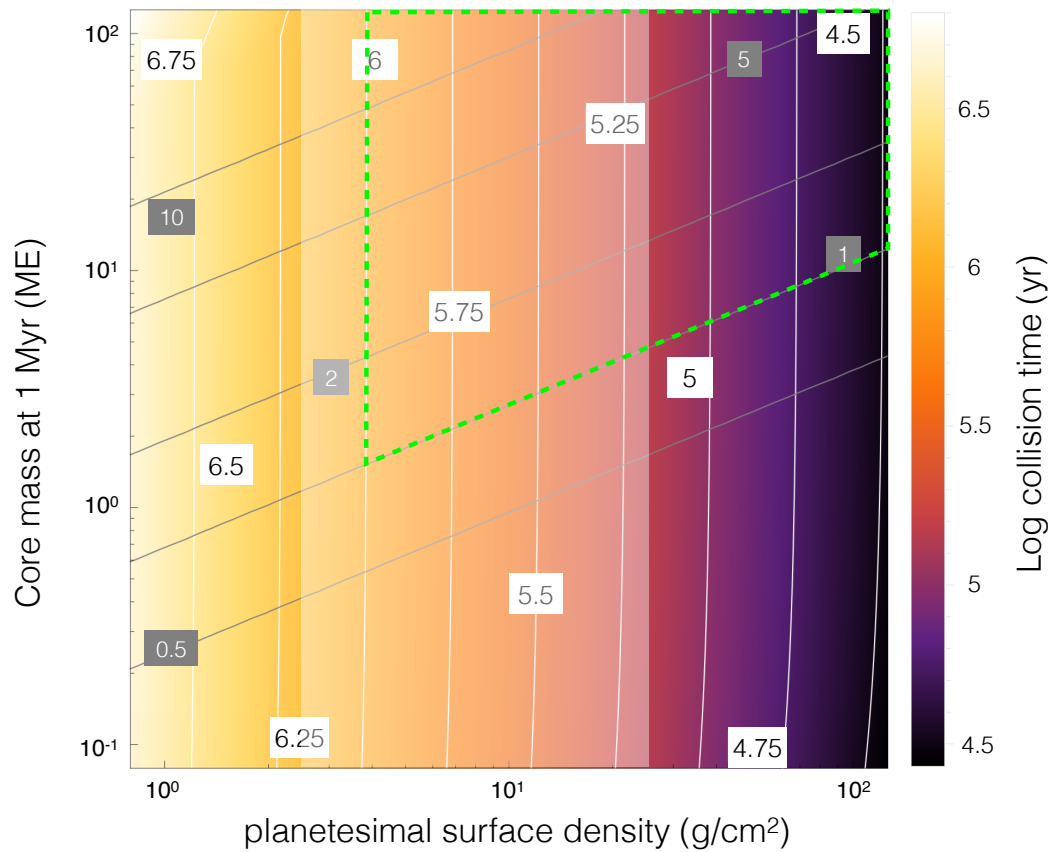
After the period of slow growth, Jupiter reached a mass large enough to scatter solids from outside its orbit to the inner part of the solar system, reconnecting the two reservoirs³. The value of Jupiter that is required for this reconnection is quoted to be 50 ME³.

In order to constrain this later value, we ran N-body simulations using the GENGA code⁴⁷. Jupiter was set at 5 AU, and a swarm of 10000 planetesimals (1 km in size) was distributed between 1.5 AU and 10 AU. The inclination and eccentricity of planetesimals was drawn at random, following Rayleigh distributions, the rms value being given by the equilibrium between excitation by Jupiter and gas drag. The gas disk model used was the same as the one we used in the rest of the simulations.

We considered different masses for proto-Jupiter, from 20 to 100 Mearth, and computed the fraction of planetesimals inside Jupiter's orbit that came initially from the outer parts of the system. We computed this fraction for three ranges of semi-major axis, between 1.5 and 3 AU. Supplementary figure 5 shows the fraction of solids coming from outside Jupiter's orbit, as a function of the planet's mass. From this figure, it is clear that a non-negligible mixing is only attained for a mass larger than 30 to 40 ME, a value close to the 50 ME quoted by ref. 3.



Supplementary figure 3. Pebble isolation mass vs. the disk aspect ratio and viscosity parameter α from simulations including the effect of viscosity⁴³. The solid red, green and black lines correspond to an isolation mass of 14, 10 and 6 ME. These values correspond to the maximum core mass at 1 Myr for the non-enriched high opacity, enriched high opacity and low opacity cases, respectively. The dashed lines of the same colors correspond to the disk scale heights obtained using the formulas that do not include viscosity effect^{12,13,42}.



Supplementary figure 4. Collision time (color coded, with a few values super-imposed as nearly vertical white lines) and ratio of the collision energy to the one required to disrupt the planetesimals⁴¹ Q_* , as a function of the planetary mass and planetesimal surface density at 5.2 AU (grey diagonal lines, the values are indicated in the grey boxes). The white vertical area delimitates the likely solid surface density at 5.2 AU whereas the green line delimitates the range of parameter space required to explain the formation of small planetesimals by fragmentation of primordial larger ones during the first Myr of the solar nebula evolution.

We have therefore tested the influence of changing the value of 50 ME on our result. As can be shown in Supplementary figure 6, varying this value in the 30-70 ME does not change our results.

Uncertainties in the cosmochemical constraints

Cosmochemical constraints³ predict that Jupiter grew slowly up to 50 M_{\oplus} in a period that lasted around 2 Myr. Other cosmochemical constraints based on chondrule formation ages²⁶ indicate that two distinct reservoirs were separated by Jupiter up to 4 Myr, hence, implying a growth time up to 50 ME in 4 Myr. We have therefore run our growth models to compute under which conditions the growth of Jupiter could be inhibited during 4 Myr. In this calculation, the disk lifetime is assumed to be equal to 5 Myr. The results are shown in Supplementary figure 7, for the same assumptions regarding the planetary composition and opacity as the ones used in Fig. 1 of the main text. As can be seen on the figure, the required mass at 1 Myr and accretion rate of solids beyond 1 Myr are very similar to our baseline model (see Fig. 1 of the main text).

In addition, we have also tested the influence of varying the time when Jupiter reaches the isolation mass by 20 %. As can be seen in Supplementary figure 6, the results are hardly changed.

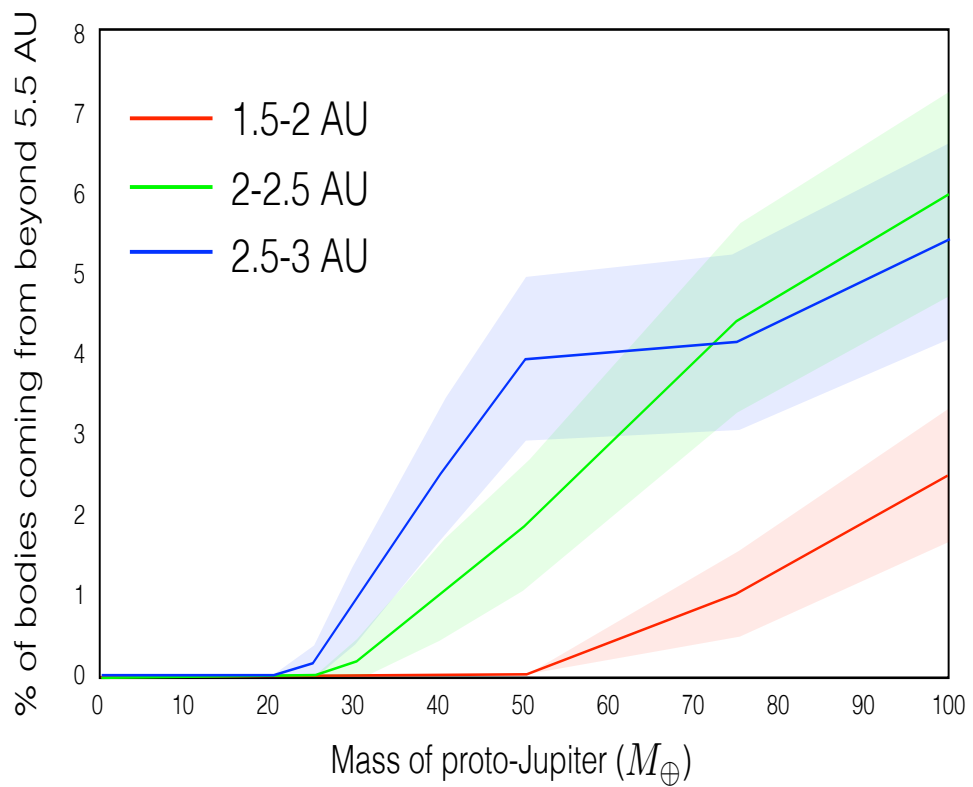
Effect of Jupiter growth on the composition of chondrites

According to ref. 3, the growth of Jupiter beyond 10 ME implied the blockage of the radial flow of pebbles. This prevented the mixing of the inner and outer reservoirs of solids from which the different types of chondrites were formed. One problem with this scenario is that the inner disk (interior to Jupiter's orbit) would have been depleted in a few thousand years after Jupiter grew to the pebble isolation mass, because of pebble drift. This depletion of the inner reservoir is inconsistent with the age spread of individual chondrules in ordinary chondrites (from 0 to 3 Myr after CAI⁴⁸). However, such a depletion is only possible provided two conditions are met:

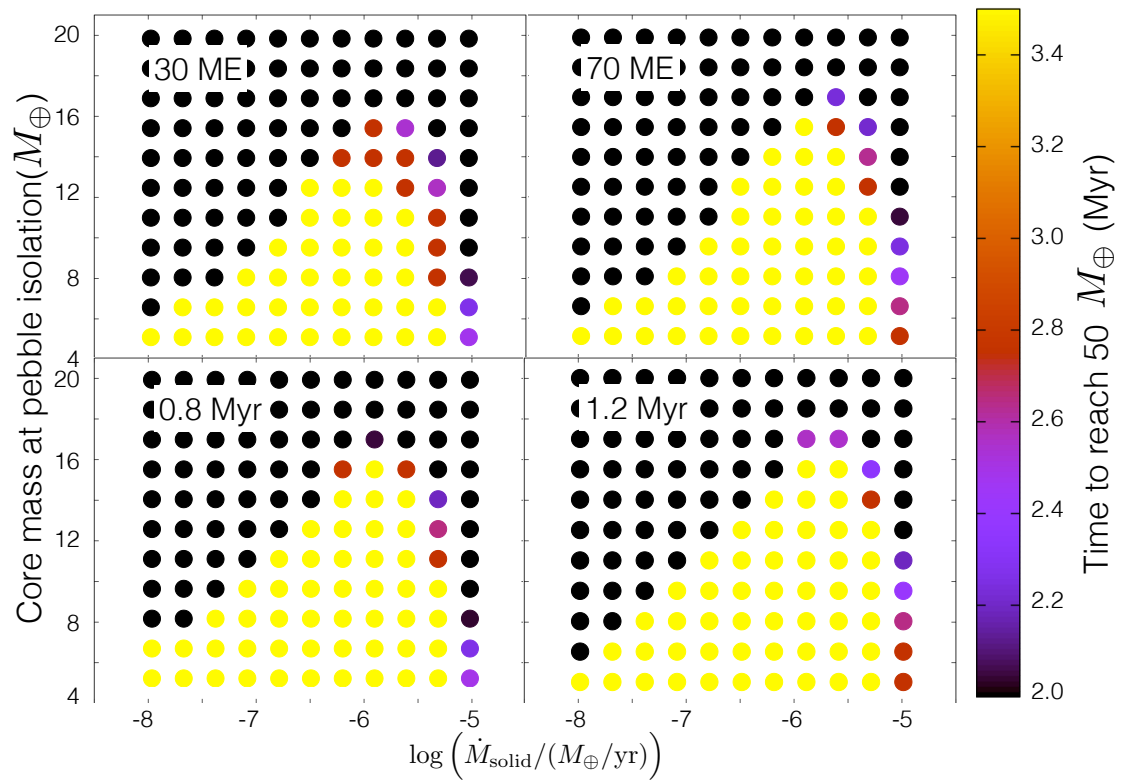
- Dust particles have a relatively high Stokes number (St), of the order of 0.1, as this corresponds to the most rapid drift.
- The pressure increases monotonically from Jupiter down to the Sun. If this is not the case, as for example at a pressure maximum, radial drift would stop.

If these two conditions are not met, dust particle could be stored during large amounts of time even after Jupiter has stopped the supply of pebbles from the outer solar system. This dust could then take part in the formation of chondrules during the following epochs.

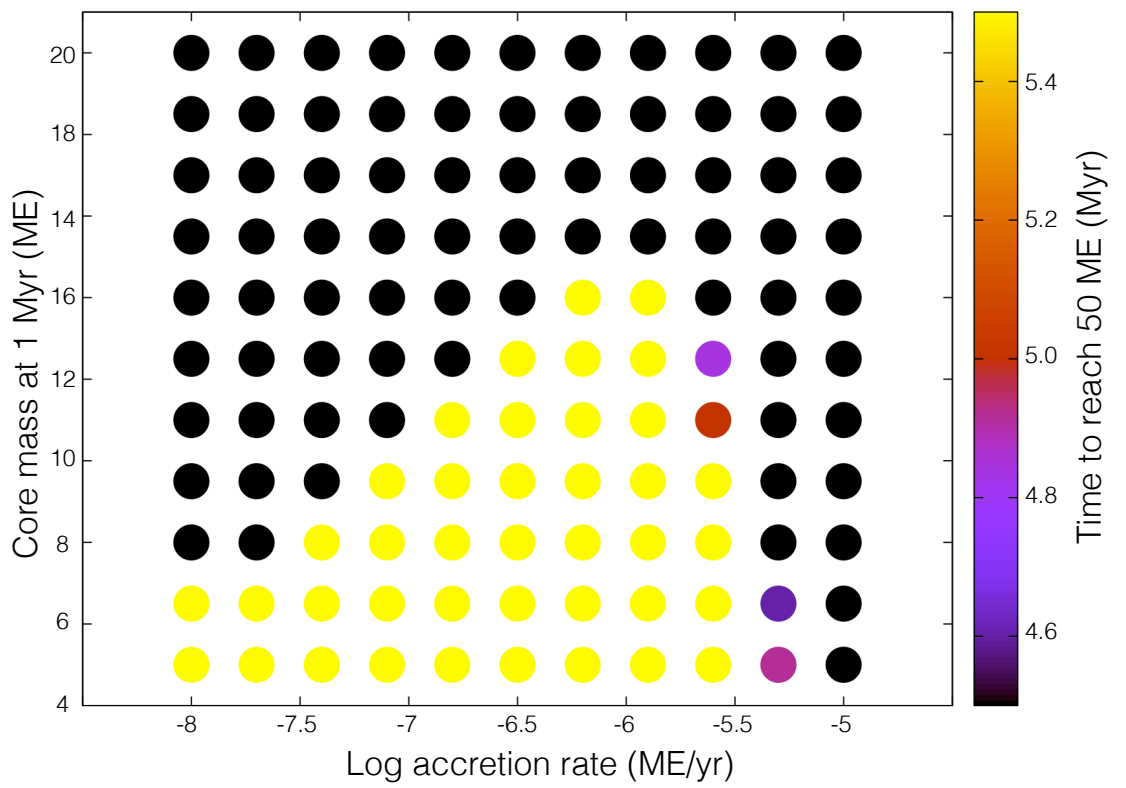
In the early solar system, two effects could have provided the conditions for slow (or suppressed) radial drift inside Jupiter's orbit: 1- When crossing the iceline, icy pebbles sublimate, releasing small dust particles. Such dust particles have a much smaller Stokes number, and their orbital drift is heavily reduced⁴⁹. 2- When Jupiter grows largely enough, it modifies the disk structure in such a way that the gas velocity



Supplementary figure 5. Fraction of planetesimals coming from outside Jupiter's orbit, as a function of the planet's mass, for different location in the inner disk (see legend on the figure). The light shaded areas represent the $1 - \sigma$ error estimation, assuming a poisson distribution.



Supplementary figure 6. Upper row: same as Fig. 1 of the main text, but assuming that Jupiter reached a mass of 30 ME (left panel) or 70 ME (right panel), as opposed to 50 ME in Fig. 1. Lower row: same as Fig. 1 of the main text, but assuming Jupiter reached the pebble isolation mass at 0.8 Myr (left panel) or 1.2 Myr (right panel), as opposed to 1 Myr in Fig. 1.



Supplementary figure 7. Same as Fig. 1 of the main text, but assuming that the growth of Jupiter was inhibited during 4 Myr (as opposed to 2 Myr for Fig. 1).

becomes keplerian at some location beyond, but also inside Jupiter’s orbit. As a consequence, two zones of pressure maximum appear, one beyond Jupiter’s orbit, one inside Jupiter’s orbit. The inner pressure maximum could represent an efficient local trap of small particles (for already formed chondrules, but also the matter that ultimately forms them, see Surville et al., in prep). Finally, we note that the stopping of dust, as well as its accretion by forming planets, depends on its Stokes number. Recent gas-dust simulations⁴⁶, showed that the stopping of pebbles occurs mainly for particles around $St \sim 0.1$, but much smaller particles follow the gas flow and can cross the planetary orbit. As these small St number particles are accreted very inefficiently⁵⁰, they might have avoided being accreted by Jupiter. Hence, they could provide a source for dust in the inner solar system. This dust can be ultimately incorporated in chondrules formed in the subsequent Myr.

Considerations on the gas accretion rate: 3D vs. 1D models and dust opacity of the envelope

In this work we have computed Jupiter’s growth by means of 1D models (i.e., assuming spherical symmetry). However, gas accretion is more accurately modelled by 3D high-resolution simulations.^{51,52} Nevertheless, given the recent implementation of such simulations, and the large numerical complexity that they entail, different works predict very different gas accretion rates onto protoplanets.^{51,52,53} For instance, compared 1D and 3D gas accretion rates computed by (51) for planets of 5, 10 and 15 ME at 5 AU, gave similar results, the difference in gas accretion rate being only a factor of 1.9 at 15 ME, and of 1.6 at 10 ME and 5 ME. Moreover, (53) derived an accretion rate that is much larger than the one that is required to grow Jupiter in a time lapse of 2 Myr suggested by ref. 3. On the opposite side, (52) claim that gas accretion is reduced when modelled in 3D compared with 1D, but they still find a transition towards runaway gas accretion at a planetary mass of ~ 15 ME (as classical 1D calculations). Thus, 3D effects could not prevent rapid gas accretion for a protoplanet growing from ~ 15 to 50 ME, as is the case in our scenario.

Consequently, other effects must operate to accrete gas in the slow fashion that is compatible with the interpretation of the meteoritic record³. One possibility is the presence of high dust opacity at the top layers of the envelope. A high dust opacity could result from the production of dust created from catastrophic planetesimals’ collisions. Nevertheless, it is important to remark that our calculations already account for high dust opacity values²¹ (Fig. 1, left panels). These values are in agreement with the ISM, which represents likely the higher end of the opacity distribution in disks. The work of (52) shows that for opacities of 1 g/cm^2 (also of the order of ISM values), rapid gas accretion cannot be prevented for cores larger than 15 ME. We conclude that neither 3D effects nor high-dust opacities can hinder rapid gas accretion of proto-Jupiter after reaching pebble isolation mass. We suggest therefore that the delay in accreting gas is due to the heating coming from planetesimal accretion after the pebble isolation mass is attained.

References

- ⁴² Lambrechts, M., Johansen, A. & Morbidelli, A. Separating gas-giant and ice-giant planets by halting pebble accretion. *Astronomy & Astrophysics*, **572**, 12 pp (2014).
- ⁴³ Ataiee, S., Baruteau, C., Alibert, Y. & Benz, W. How much does turbulence change the pebble isolation mass for planet formation? *Astronomy & Astrophysics*, *in press*.
- ⁴⁴ Baruteau, C. et al. Planet-Disk Interactions and Early Evolution of Planetary Systems. *Protostars and Planets VI* (University of Arizona Press, 2014).
- ⁴⁵ Guilera, O. M., de Elía, G. C., Brunini, A. & Santamaría, P. J. Planetesimal fragmentation and giant planet formation. *Astronomy & Astrophysics*, **565**, 14 pp. (2014).
- ⁴⁶ Ormel, C. W. & Kobayashi, H. Understanding How Planets Become Massive. I. Description and Validation of a New Toy Model. *The Astrophysical Journal*, **747**, 21 pp. (2012).
- ⁴⁷ Grimm, S. & Stadel, J. The GENGA code: Gravitational Encounters in N-body simulations with GPU Acceleration. *The Astrophysical Journal*, **796**, 16 pp. (2014).
- ⁴⁸ Connelly, J. et al. The absolute chronology and thermal processing of solids in the solar protoplanetary disk. *Science*, **338**, 651 (2012).
- ⁴⁹ Morbidelli, A., Lambrechts, M., Jacobson, S. & Bitsch, B. The great dichotomy of the solar system: small terrestrial embryos and massive giant planet cores. *Icarus*, **258**, 418-429 (2015).
- ⁵⁰ Ormel, C. The emerging paradigm of pebble accretion. *Formation, Evolution, and Dynamics of Young Solar Systems, Astrophysics and Space Science Library*, **445**, 197 (Springer, 2017).
- ⁵¹ D'Angelo, G. & Bodenheimer, P. Three-dimensional Radiation-hydrodynamics Calculations of the Envelopes of Young Planets Embedded in Protoplanetary Disks. *The Astrophysical Journal*, **778**, 77 (2013).
- ⁵² Lambrechts, M. & Lega, E. Reduced gas accretion on super-Earths and ice giants. *Astronomy & Astrophysics*, **606**, 21 pp. (2017).
- ⁵³ Machida, M.N., Inutsuka, S.-i. & Matsumoto, T. Formation Process of the Circumstellar Disk: Long-term Simulations in the Main Accretion Phase of Star Formation. *The Astrophysical Journal*, **724**, 1006-1020 (2010).

3. Ablation of drifting bodies

We have now established in-depth a disk model that can be used to study planet formation and that matches the constraints given by observations. In this chapter, we will focus on the evolution of a meter-sized body embedded in a protoplanetary disk which is drifting towards the star. The goal is to quantify how far such a body could travel into the warm regions of the disk before it lost all of its water due to sublimation.

The tools we use to perform this calculation were developed in the context of modeling comets. For a comet, the observational signature originates from material that was previously outgassed from the solid cometary nucleus. Therefore, the sublimation of ice and the release of solid grains was studied in-depth in this context. For an embedded body in the protoplanetary disk, the physical phenomena that occur are very similar. The cometary nuclei should be amongst the most primordial objects that still exist and for which observations are possible. Therefore, the properties of a meter to kilometer-sized body that formed in the cold, ice-rich region of a protoplanetary disk should be fairly close to that of present-day cometary nuclei. Therefore, we first take a look at the observation evidence on the structure of these objects in Sect. 3.1 before we state the most important components of a cometary nucleus model (Sect. 3.2). However, we have to keep in mind that some degree of collisional processing of cometary nuclei certainly occurred (Davidsson et al., 2016), which might change the properties to some degree.

3.1. Evidence on the structure of cometary nuclei

Comets arrive at regions close to the Sun by being on an elliptic orbit due to some gravitational interaction with each other or the planets. There are Jupiter-family and Halley-type comets that originated outside Neptune’s orbit from the Kuiper belt and main-belt comets from the much closer asteroid belt. Additionally, the category of comets with longer-periods $P > 200$ yr might partially have originated from the Oort cloud and two interstellar objects have now been found (Meech et al., 2017; Guzik et al., 2020).

To characterize a cometary nucleus and not just the well visible coma, it is necessary to fly into its proximity. For several comets, space missions took place and characterized the nuclei of Comet 1P/Halley, 19P/Borrelly, 81P/Wild, 9P/Tempel and 67P/Churyumov–Gerasimenko (67P). We list the resulting bulk densities in Table 3.1. It is apparent that comets are really low-density objects.

For this reason, since the detailed observations of Comet 1P/Halley in 1986 it is

Comet	Density (g cm^{-3})	Reference
1P/Halley	0.5-1.2	Skorov & Rickman (1999) [†]
9P/Tempel	~ 0.6	A’Hearn et al. (2005)
19P/Borrelly	0.18-0.3	Davidsson & Gutiérrez (2004)
81P/Wild	0.6-0.8	Davidsson & Gutiérrez (2006)
67P/Churyumov–Gerasimenko	0.533 ± 0.06	Pätzold et al. (2016)

[†]Correction by Skorov & Rickman (1999) based on the original value of Rickman (1989)

Table 3.1.: Bulk densities of well-researched cometary nuclei.

generally assumed that comets have a high porosity Rickman (1989). The dominant volatile component is water ice, where other volatiles, such as CO, CO₂, HCN, N₂, etc., can be mixed with the water ice or incorporated within. If the volatiles are incorporated in the ice, it is either in the form of clathrate-hydrates or as trapped gases.

Thanks to the recent *Rosetta* and *Philae* mission, a lot of data is available for 67P. Pätzold et al. (2016) estimate the porosity to be 72% - 74% if the measured dust-to-ice mass ratio of 4 ± 2 in the coma Rotundi et al. (2015) is representative for the full cometary structure. This value of the dust-to-ice ratio is larger than what is expected from models of ice condensation onto planetesimals (Marboeuf et al., 2014b). The difference might come from a depletion of the body from ice due to outgassing over Gyr timescales. Determining the exact dust-to-ice ratio for 67P is difficult because it is a degenerate problem due to the unknown bulk macro-porosity of the nucleus and a not well constrained dust grain density (incl. micro-porosity). Silicate grains should have a density of $\sim 3 \text{ g cm}^{-3}$ (Brownlee et al., 2006) but the presence of organic materials ($\rho \sim 2 \text{ g cm}^{-3}$) can lower the mean density.

In Paper I, we argue that we choose a dust-to-ice ratio of 1 following Marboeuf et al. (2014b) instead of inferred ratios for a single present-day object. The bulk density of the modeled object lies in the right range given a porosity of 70%.

3.2. Cometary nucleus models

In the following, we will briefly summarize the main constituents for a cometary nucleus model. An detailed review can be found in Prialnik et al. (2004) and more details about the specific model that we will use in Paper I are described in Marboeuf et al. (2012) or the publicly available thesis of Marboeuf (2008). Note that in Section 2.2. of Paper I itself, we also briefly discuss the model and describe the processes leading to the formation of a dust mantle in more detail.

There are three main sources of energy available to comets: Solar radiation that advances inward from the surface of the comet as a heat wave, internal heat release by radioactive isotopes contained in the dust of the comet and the release of latent heat originating in the transformation of formless (amorphous) into crystalline ice Klinger (1981). Radioactivity is important for the long time a comet is far from

the Sun, but negligibly close to the Sun. The crystallization of amorphous water ice depends on the temperature and only occurs above a threshold temperature.

Sublimation of the ice can release previously trapped gases from the interior of the nucleus and its pressure can cause it to flow to the surface and the pressure may surpass the tensile strength of the grainy configuration of the solid material and burst out of the comet. The gas can take dust of various size with it, which is then released with the gas or blocks the pores.

When modeling (Priyalnik et al., 2004; Marboeuf et al., 2012) comet nuclei they are often assumed to be spherical. It can then be assumed to rotate fast, meaning that the surface is evenly heated at all times, making the model one-dimensional with the radius R .

To better approximate the behavior of comets near the Sun, one can assume them to rotate slowly and calculate the radial heat transfer at one point on the equator (1.5 D), at several points lying on one meridian (2.5 D) or at points on the full sphere (3 D) at each timestep. For the 3D case, the assumption of slow rotation is no longer necessary, but the models still neglect lateral conduction.

Since the comet is incompressible, one can usually prescribe a (constant) density profile. This approximation no longer holds for larger, differentiated bodies (Lichtenberg et al., 2016).

3.2.1. Energy conservation

Internal

The energy conservation at each point (neglecting possible lateral transport of energy or mass) inside the nucleus is given by

$$\sum_l \rho_l c_l \frac{\partial T}{\partial t} = \frac{\partial}{\partial r} \left(K \frac{\partial T}{\partial r} \right) - \frac{\partial}{\partial r} \left(\sum_\alpha c_\alpha \rho_\alpha J_\alpha \right) + S, \quad (3.1)$$

where

- T is the temperature,
- ρ_l is the density and c_l the specific heat capacity of the static material inside the nucleus, where l sums up all constituents in all phases (ice, dust or clathrate including some trapped gas),
- K is the radial heat conductivity, discussed in section 3.2.3,
- J_α is the mass flux of a gas of the sort α with specific heat capacity c_α and density ρ_α ,
- S sums up all kinds of sources qualitatively discussed in the first section of this chapter and the heat absorbed or released by phase transitions (e.g. crystallization, sublimation).

Surface

At the surface of the nucleus, the energy conservation is given by a thermal balance between the Solar energy and thermal emission, heat diffusion towards the core and local sublimation of ices

$$\frac{S_0(1-A)}{R_h^2} \max(\cos \xi, 0) = \epsilon \sigma T^4 + K \frac{\partial T}{\partial r} + \sum_x \alpha_x H_x \varphi_x, \quad (3.2)$$

where

- S_0 is the Solar constant (W m^{-2}), A is the Bond albedo, R_h is the heliocentric distance,
- ξ is the Solar zenith distance given by

$$\cos \xi = \cos \theta \cos \omega \cos \delta + \sin \theta \sin \delta, \quad (3.3)$$

where δ is the declination, θ the latitude and ω the hour angle,

- ϵ is the infrared surface emissivity, σ the Stefan-Boltzmann constant,
- α_x the surface fraction covered by an ice or clathrate, H_x the latent heat and φ_x the free sublimation rate of the species x .

As we discuss in [Paper I](#), this balance is modified if the body is embedded in an opaque protoplanetary disk instead of being exposed to starlight.

3.2.2. Mass conservation

For each layer and chemical species x , the diffusion of gas through the solid structure of grains is solved using the mass conservation equation:

$$\frac{\partial \rho_x^g}{\partial t} = M_x (\nabla \phi_x + Q_x), \quad (3.4)$$

where ρ_x^g is the mass density of the gas x , M_x is its molar mass, ϕ_x its molar flow (described in [Marboeuf et al., 2012](#)) and Q_x is the net source of released gas. Processes that can release or trap gas and are included in Q_x are: water ice crystallization, ice sublimation and condensation as well as clathrate dissociation and formation.

3.2.3. Heat conduction

Since we want to solve the radial conduction of heat at each timestep, it would be nice to have an analytical solution for the conductivity throughout the porous cometary material. The conductivity depends on the size and form of the grains, respectively

of the pores in the solid structure. Therefore, an analytical formula which fits all regimes is not easily obtained. One possible way is to assume Russel's formula

$$K = \frac{K^s [\Psi^{2/3} K^p + (1 - \psi^{2/3}) K^s]}{K^s [\psi - \psi^{2/3} + 1] - K^p \psi^{2/3} [\psi^{1/3} - 1]}, \quad (3.5)$$

where ψ is the porosity, and

$$K^p = 4\epsilon\sigma r_p T^3 \quad (3.6)$$

is the radiative conductivity across the pores, where ϵ is the infrared emissivity of the nucleus material, σ the Stefan-Boltzmann constant and r_p the radius of the pores. K^s is the heat conductivity in the solid (depending on the state of the solid and the amount of dust, respectively ice).

This formula is not a good approximation for high porosities, where the solid material no longer has a big area of contact between neighboring grains. Here the conductivity is reduced by a factor h , called the Hertz factor

$$K = hK^s. \quad (3.7)$$

In fact, it is possible to simply use the Hertz factor and empirically fit h and K^s to reproduce measured heat distributions inside comets without having to invoke Russel's formula. This approach is chosen in [Paper I](#).

3.3. Paper I: Radial drift and concurrent ablation of boulder-sized objects

We have now discussed in moderate detail the way to model a cometary nucleus. Combined with the disk model in Chapter 2, this can be used to follow the evolution of a drifting body as it crosses the water iceline or snowline. In the paper attached below, published in [Burn et al. \(2019\)](#), we do that and find that bodies drift a few percent closer to the star compared to the location of the water iceline.

It would be more extreme if the water vapor was contained inside the body by a dust mantle. However, a dust mantle should not be present, because collisions with small bodies would frequently erode it. The limitations of the work are accessed and future works should consistently model those collisions as well as take into account the water vapor released to the gas phase ([Drażkowska & Alibert, 2017](#); [Schoonenberg & Ormel, 2017](#)) and its feedback onto the sublimation rate of the bodies.

The significance of this work is strongly dependent on how frequent bodies in the size-regime of centimeters to kilometers are. If most bodies are smaller (Stokes number much smaller than 1), they would drift more slowly and sublimation would take place very close to the snowline. If most of the mass is in objects larger than a kilometer, the objects never cross the snowline. In both cases, the dynamics of the objects can then be safely neglected as long as their eccentricity is small enough.

The case of eccentric planetesimals and their evolution would be an interesting project for the future. Overall, the physics at icelines is being investigated in more detail recently ([Ida & Guillot, 2016](#); [Schoonenberg et al., 2018](#); [Hyodo et al., 2019](#)) because it could be an ideal location for large planetesimals to form.

Radial Drift and Concurrent Ablation of Boulder-Sized Objects

Remo Burn, Ulysse Marboeuf, Yann Alibert & Willy Benz

Physikalisches Institut & Center for Space and Habitability, Universität Bern, CH-3012 Bern, Switzerland, e-mail: remo.burn@space.unibe.ch

Preprint online version: August 8, 2019

ABSTRACT

Context. The composition of a protoplanetary disk at a given location does not only depend on temperature and pressure but also on the time dependent transport of matter, such as radial drift of solid bodies, which could release water and other volatile species before disintegration or accretion onto a larger body with potentially considerable implications for the composition of planets.

Aims. We perform a parameter study focused on the water depletion of different sized bodies able to cross the water snowline by gas induced radial drift.

Methods. Either the analytical Hertz-Knudsen-Langmuir sublimation formula assuming equilibrium temperature within the body or a more involved, numerical model for the internal thermal evolution is coupled with an α -disk model. Different properties of the disk and the embedded body are explored.

Results. Bodies with radii up to 100 m drift faster towards the central star than the water snowline, hence, cross it. The region that can be reached before complete disintegration – and is therefore polluted with H₂O ice – extends to 10 % closer to the star than the snowline location. The extent of this polluted region could be multiple times larger in the presence of a dust mantle, which is, however, unlikely to form due to frequent collisions with smaller-than centimeter sized objects.

Conclusions. Given a significant abundance of meter sized boulders in protoplanetary disks, the transport of water by radial drift of these bodies towards regions closer to the star than the snowline is not negligible and this flux of volatiles can be estimated for a given distribution of solid body sizes and compositions. A simple expression for surface sublimation is applicable for a homogeneous body consisting of only dust and water ice without a dust mantle.

Key words. Comets: general - Protoplanetary disks - Planets and satellites: formation - Planets and satellites: composition

1. Introduction

Recent years of observations and theoretical work on planet formation have stressed the importance of the physics at the various snow- or icelines, i.e. the regions in the protoplanetary disk where a volatile species reaches its condensation temperature. Rather than defining snowlines using the condensation temperature, it is more relevant for planet formation to focus on the presence of water ice in building blocks of planets, which might be different due to dynamical processes. However, we will keep the notion of snowline to refer to the "classic" snowlines based on temperatures and pressures only.¹

Thanks to the continuous improvement of radio-astronomical facilities, such as the Atacama Large Millimeter/Submillimeter Array (ALMA), observations of the carbon monoxide (CO) snowline in certain disks are now possible (Qi et al. 2013, 2015; Schwarz et al. 2016; Nomura et al. 2016; Guidi et al. 2016). The CO snowline is the most accessible snowline to observation because of the low freezing point (30 K-40 K (Fray & Schmitt 2009)), implying a large distance to the star, and the high abundance of CO in the disk gas. Unfortunately, the H₂O snowline is harder to observe owing to the higher condensation temperature of water. So far, observations were limited to a disk heated by a stellar outburst (Cieza et al. 2016).

The main interest on the water snowline stems from emerging compositional studies of terrestrial planets, motivated by in-

creased precision on measured radii and masses of planets using radial velocity measurements combined with *Kepler* transit data (e.g. Marcy et al. 2014), or transit timing variation (e.g. Gillon et al. 2017; Grimm et al. 2018, for the TRAPPIST-1 system). Theoretical models of planet formation may help break the degeneracy between planets covered by oceans and those containing H, He atmospheres, while also constraining the mantle composition, if they can put reliable constraints on the volatile content of planets (Adams et al. 2008; Rogers & Seager 2010; Dorn et al. 2015). To achieve this, the compositions of solids and gas in the disk, which are accreted by the (migrating) planets, have to be well constrained over a large region. This will be ultimately necessary to assess the habitability of observed exoplanets.

Finally, the recent studies of Ida & Guillot (2016); Drążkowska & Alibert (2017); Schoonenberg & Ormel (2017) show increased planetesimal formation rates by streaming instability at the H₂O snowline, the latter two taking released water vapor into account (see also Ros & Johansen 2013). Those results show the need for proper treatment of all occurring physical processes at the snowline.

A redefinition of the snowline for asteroids in the solar system was explored by Schorghofer (2008) using similar means to what we will present. Schorghofer (2008) found that ice can persist on asteroids of kilometer size up to temperatures of at least 145 K over the solar system lifetime and calculated for multiple parameters where these conditions occur. Other recent works aimed at determining the disk composition used chemically evolved (Visser et al. 2009; Eistrup et al. 2016) or equilibrium chemistry (Thiabaud et al. 2015) disks as a basis. However, in these works, no transport of solids, such as radial

¹ Here, we generally ignore the fact that a snowline is a surface with a strong dependence on height, but instead only consider the snowline position at the midplane.

drift (Weidenschilling 1977) or diffusion processes were modeled. In addition to the relevant chemical evolution, these dynamical effects need to be considered (see Pudritz et al. 2018, for a recent review). Some studies that do address radial transport of different species by pebbles and vapor are Stevenson & Lunine (1988); Drażkowska & Alibert (2017); Schoonenberg & Ormel (2017). Here, we will investigate the potential impact of boulder-sized bodies (sizes from cm to 100 m), which is a size regime not treated in the aforementioned works. Such bodies might efficiently transport water ice to regions starwards of the classical water snowline by drifting through the disk faster than the snowline is moving towards the star. In general, this fast drift leads to fast removal of these bodies, which is usually used as an argument not to include those sizes in models. Furthermore, coagulation processes are not efficient enough to let a body grow directly to this size range under nominal conditions (see Blum 2018, for a recent review). However, bodies in this range of sizes are present in the current asteroid population (e.g. Bottke et al. 2005) and models suggest they are naturally produced in collisions of larger bodies (e.g. Benz & Asphaug 1999; Bottke et al. 2015).

In this work, we postulate the presence of meter-sized objects and perform a parameter study to determine the region that can be reached by fast drifting bodies crossing the water snowline. This will let us gauge the importance of modeling solid ice transport of fast drifting bodies in the disk. For this, we will identify the dominating processes contributing to thermal heating of the bodies and the parameters and properties influencing the process. Furthermore, we test a simplified, analytic model for the sublimation of water on a boulder-sized body against a more complex, cometary nucleus model (Marboeuf et al. 2012) adjusted to account for the presence of protoplanetary disk gas in the vicinity. The application of a simple analytical expression instead of a more complex numerical model for the sublimation of water ice would help to substantially reduce the computational cost and complexity of future works.

In Sect. 2, we describe the different parts and modes (numerical/analytic) of the model. The results are presented in Sect. 3 and discussed in Sect. 4, where we also describe the validity of our models with regards to all physical processes, which – to our knowledge – influence the results. We conclude in Sect 5.

2. Model description

The model is built on two components: The first component consists of a protoplanetary disk model, including a single solid body embedded in the disk midplane. Its radial drift is calculated and its radially inward motion followed (Sect. 2.1.3). Once the temperature reaches a threshold value (set to 150K), the local disk temperature and radius of the body are used to calculate the body's thermal and compositional evolution during one timestep of the disk model. Two different modes for this second component are investigated: (a) a numerical model based on the cometary nucleus model by Marboeuf et al. (2012) (Sect. 2.2) or (b) an analytical expression treating the surface ablation (Sect. 2.3). In both cases, mass loss from the body changes its radius, which in turn affects the drift speed.

2.1. Disk

Our α -disk model assumes axis-symmetry, vertical hydrostatic equilibrium, flatness ($z \ll r$) and no self-gravity ($M_{\text{Disk}} \ll M_*$). The surface density $\Sigma \equiv \int_{-\infty}^{\infty} \rho(z) dz = \rho_0 H \sqrt{2\pi}$, where ρ_0 is the

midplane density and H is the vertical scale height, is evolved in time and the isothermal sound speed c_s is frequently used to abbreviate the ideal gas law as $P = c_s^2 \rho$ (see Sect. 2.1.2 or e.g. Armitage 2019, for more details).

We would like to point out that the purpose of the disk model in this paper is to simulate typical conditions and timescales in the disk midplane only, thus a simple model is sufficient. Of particular importance for this work is the thermal part of the disk model (see Sect. 2.1.1).

2.1.1. Midplane temperature

The midplane temperature T is calculated, as in the model of Hueso & Guillot (2005), by assuming that the disk is geometrically thin, heated viscously and by irradiation from the star, and is optically thick in the radial direction. Instead of solving the radiative transfer numerically, analytic expressions derived by Nakamoto & Nakagawa (1994) are used². In their work, the midplane temperature is approximated as a sum of terms accounting for optically thick, optically thin, and stellar contributions:

$$\sigma T^4 = \frac{9}{8} \left(\frac{3}{8} \tau_R + \frac{1}{2\tau_P} \right) \Sigma \nu \Omega_K^2 + \sigma T_l^4, \quad (1)$$

where σ is the Stephan-Boltzmann constant, ν is the viscosity described in Sect. 2.1.2 and τ_P is the Planck mean optical depth which is assumed to be $\tau_P = 2.4\tau_R$ as in Nakamoto & Nakagawa (1994). τ_R is the Rosseland mean optical depth, which is defined in terms of the Rosseland mean opacity κ_R as

$$\tau_R = \kappa_R \Sigma. \quad (2)$$

The Rosseland mean opacity is calculated using the modified Alexander/Cox/Stewart opacities by Bell & Lin (1994),

$$\kappa_R = \kappa_i \rho_0^a T^b, \quad (3)$$

where the exponents a and b and the factor κ_i differ in different temperature regimes, i.e. depend on the gas state. The values for a , b and κ_i can be found in the appendix of Bell & Lin (1994).

T_l is an effective temperature which includes effects of the irradiation by the star

$$T_l = T_* \left[\frac{2}{3\pi} \left(\frac{R_*}{r} \right)^3 + \frac{1}{2} \left(\frac{R_*}{r} \right)^2 \frac{H}{r} \left(\frac{d \ln H}{d \ln r} - 1 \right) \right]^{1/4}, \quad (4)$$

where the first term is due to irradiation onto the inner part of a flat disk by a finite sized star (with radius R_*) and the second term is accounting for irradiation onto the flared outer part. At all radii, we fixed $d \ln H / d \ln r = 9/7$ as in Hueso & Guillot (2005). In contrast to their work, however, we did not include a molecular cloud temperature in equation (4) and instead use a fixed floor value of 10 K for the temperature.

2.1.2. Disk evolution

For the disk, we assume an α -viscosity $\nu = \alpha c_s H$, where α is a numerical factor on the order of 10^{-4} to 10^{-2} (Shakura & Sunyaev 1973). This viscosity, together with mass and angular momentum conservation, and approximating the orbital velocity of the gas to be Keplerian, lead to a diffusion equation for the disk (Lynden-Bell & Pringle 1974; Pringle 1981)

$$\frac{d\Sigma}{dt} = \frac{3}{r} \frac{\partial}{\partial r} \left(r^{1/2} \frac{\partial}{\partial r} \left(r^{1/2} \nu \Sigma \right) \right) + \dot{\Sigma}_w. \quad (5)$$

² Eq. 3.10 in Nakamoto & Nakagawa (1994)

We have added an external photo-evaporation term

$$\begin{cases} \dot{\Sigma}_w = 0, & \text{if } r \leq r_g \\ \dot{\Sigma}_w \propto r^{-1}, & \text{otherwise,} \end{cases} \quad (6)$$

where the gravitational radius r_g is taken to be equal to 5 AU (Veras & Armitage 2004). The mass loss parameter \dot{M}_{wind} , corresponds to the mass that a disk extending to 1000 AU would lose due to photo-evaporation. The actual mass loss due to photo-evaporation is approximately 1 % of this value because the typical disk only extends to ~ 100 AU. \dot{M}_{wind} can be chosen to reproduce reasonable lifetimes (Ribas et al. 2014), which is the case for values $\sim 10^{-7} M_{\odot} \text{ yr}^{-1}$.

In our disk model, the disk evolution equation (5) is solved numerically on a one dimensional, logarithmically spaced grid in radial direction (Alibert et al. 2005, 2013).

2.1.3. Radial drift

Solid bodies in the disk feel a drag force caused by the different velocities of the gas (v_g) and the particles (v_K) which would move with Keplerian speed, in the absence of gas, whereas the former move with a slower velocity due to pressure support (Weidenschilling 1977; Whipple 1972).

To quantify this difference,

$$\eta \equiv 1 - v_g/v_K \approx -\frac{r}{2v_K^2 \rho_0} \frac{dP}{dr} \quad (7)$$

is defined, where the density ρ_0 and the pressure P are the values taken at the location of the body.

The resulting radial drift depends on the drag regime. To discriminate between the different regimes, the radius R of the solid body is compared to the mean free path $\lambda = m_{\text{H}_2}/(\pi d_{\text{H}_2}^2 \rho_0)$. Here, d_{H_2} and m_{H_2} are the kinetic diameter and mass, respectively, of the hydrogen molecule, i.e. the dominant species in the disk. With that, the drag regime is determined by the following conditions:

- If $R < 3\lambda/2$, we use the Epstein drag law
- Else:
 - if $R_e < 27$, where $R_e = 3(v_K - v_g)R/(\lambda v_{\text{therm}})$ is the microscopic Reynolds number and v_{therm} the midplane mean thermal velocity, the Stokes drag is used (Rafikov 2004),³
 - if $R_e > 27$, the bodies drag is governed by the quadratic drag law.

In this work, we use the radial drift formula that is used in Chambers (2008) and is based on the solutions found by Adachi et al. (1976) and similarly by Nakagawa et al. (1986); Takeuchi & Lin (2002):

$$\frac{dr}{dt} \approx \begin{cases} -\frac{2r\eta}{t_{\text{stop}}}, & \text{(Quadratic regime)} \\ -\frac{2r\eta}{t_{\text{stop}}} \left(\frac{s^2}{1+s^2} \right), & \text{(Epstein/Stokes regime),} \end{cases} \quad (8)$$

³ This is an approximation introduced by Rafikov (2004), in the literature there is often an additional, intermediate drag regime used between the Quadratic and the Stokes regime (Weidenschilling 1977; Whipple 1972). Additionally, we use here the thermal velocity instead of approximating it as the sound speed. Furthermore, the definition of R_e differs by a factor of two compared to Whipple (1972).

where

$$s = t_{\text{stop}} \Omega_K \quad (9)$$

is the Stokes number. When switching from Stokes regime to the quadratic regime, the Stokes number should be large, such that there will be no discontinuity of the drift speed. This is the case in our application ($s \sim 5000$ for radii ~ 100 m for which the drag regime changes, see also Fig. 7(b)).

The stopping times differ in the three drag regimes and are given by (Chambers 2008; Takeuchi & Lin 2002; Whipple 1972)

$$t_{\text{stop}} = \begin{cases} \frac{\rho_s R}{\rho_0 v_{\text{therm}}} & \text{(Epstein)} \\ \frac{2\rho_s R^2}{3\rho_0 \lambda v_{\text{therm}}} & \text{(Stokes)} \\ \frac{6\rho_s R}{\rho_0 (v_K - v_g)} & \text{(Quadratic),} \end{cases} \quad (10)$$

where R and ρ_s are the radius and the density of the solid body.⁴ It can be easily verified that the drag regimes are chosen such that the stopping time is continuous.

The orbits of the bodies are assumed to be circular, thus the effect of eccentricity and inclination on the drift are omitted. This assumption is reasonable because the eccentricity and inclination get damped by gas drag on shorter timescales than the semi-major axis (Adachi et al. 1976).

We note, that the drift formula (8) does not include the radial gas flow (e.g. Desch et al. (2017)), which does not have a large influence during the fast drifting phases and for large bodies (i.e. high Stokes numbers).

2.2. Cometary nucleus model

We describe here the cometary nucleus model (Marboeuf et al. 2012) that we apply to solid bodies embedded in the protoplanetary disk. The model is able to include multiple volatile species, clathrates and amorphous water ice structures in a 1D (Marboeuf et al. 2012) or 3D model (Marboeuf & Schmitt 2014). Here, we use the 1D model and pure crystalline water ice. Therefore, the equations can be simplified and, for completeness, are presented in that form here, with emphasis on the changes due to the presence of a disk.

The presence of the disk influences the energy sources available to the nucleus, which is discussed in Sect. 2.2.1. Then, the structure and physical model (Sect. 2.2.2) are summarized. Finally, the possible formation of a dust mantle is described in Sect. 2.2.3 and has a large impact on the resulting evolution of snowline crossing bodies.

2.2.1. Energy sources

In the comet related literature, there are usually three main sources of energy considered: solar radiation which heats the surface with energy propagating inward, internal heat release by radioactive isotopes contained in the cometary dust, and the release of latent heat originating from different possible phase changes (crystalline/amorphous ice, clathrates, sublimation) (Klinger 1981).

⁴ As in Chambers (2008), the stopping time in the quadratic regime includes a factor of 6, in agreement with Whipple (1972), but in disagreement to the factor 5 in Rafikov (2004). Correspondingly the quadratic drag regime boundary is set to $R_e = 27$ instead of $R_e = 20$.

When considering bodies smaller than 100 m, radioactive heating is negligible: The simple estimates and values from Merk & Prialnik (2003)⁵ for heating by ²⁶Al yield a net cooling for radii below 1 km, due to conduction and radiation from the surface. Because the heat produced by radioactive decay scales $\sim R^3$, whereas the cooling scales $\sim R^2$, radioactive heating becomes more important for larger objects with radii > 10 km.

The crystallization of amorphous water ice is dependent on the temperature and becomes efficient above 100 K (Schmitt et al. 1989). It is not clear whether the initial structure of water ice inside comets is crystalline or amorphous. We assume an initial purely crystalline and clathrate-free water ice structure, or crystallization to have happened before the start of the calculation.

For a body embedded in the protoplanetary disk, additional energy sources are available: heat transfer (mainly by isotropic thermal radiation) from the gaseous disk and frictional heating. In contrast, direct irradiation from the sun is suppressed, as the disk is opaque in the midplane (see also Sect. 2.2.2 for implementation).

Frictional heating is caused by the different azimuthal velocities of the disk gas and the solid body. This process is negligible for the main part of this study and discussed in Sect. 4.3.

Hence, the main source of energy for a small body relates to the thermal bath in which the body is moving. This justifies the use of a one dimensional model because of the invariance of heating on the orientation of the body in the disk. We use the local disk gas temperature as a surface temperature for our numerical model. This assumption is discussed in Sect. 4.2.

2.2.2. Structure and physical model

The body is composed of grains, consisting of refractory material, that are enclosed by a mantle of icy water following the model by Greenberg (1988). This structure is drawn schematically in Fig. 1.

For each layer, the diffusion of water vapor through the solid structure of grains is solved using the mass conservation equation. The only processes that can release or bind gas in our crystalline and clathrate-free model are water ice sublimation and condensation.

The flow of gas through the solid matrix can be in different flow regimes; free molecular (Knudsen) flow ($K^n > 1$) or viscous flow ($K^n \ll 1$), depending on the Knudsen number $K^n = \lambda/(2r_p)$, where λ is the mean free path of the molecules and r_p is the radius of a pore (Knudsen 1909). In addition, we include a transition flow regime for Knudsen numbers $10^{-2} < K^n < 1$ following Fanale & Salvail (1987). One important quantity appearing in the expressions for the flow (Marboeuf et al. 2012), due to the influence of the structure of the pores, is tortuosity. Here, the arc-chord ratio definition of tortuosity is used, i.e. tortuosity is the ratio of the length of a pore to the distance between the endpoints (see Fig. 2).

Energy is conserved at each point inside the nucleus, where heat conduction is modeled using an empirical Hertz factor to account for porosity (Davidsson & Skorov 2002; Prialnik et al. 2004). For detailed equations and explanations refer to Marboeuf et al. (2012).

In Marboeuf et al. (2012) the thermal boundary condition is given by a balance between the solar energy, sublimation of water ice at the surface (if no dust mantle is present), and thermal emission at the outermost layer of the nucleus. In the midplane

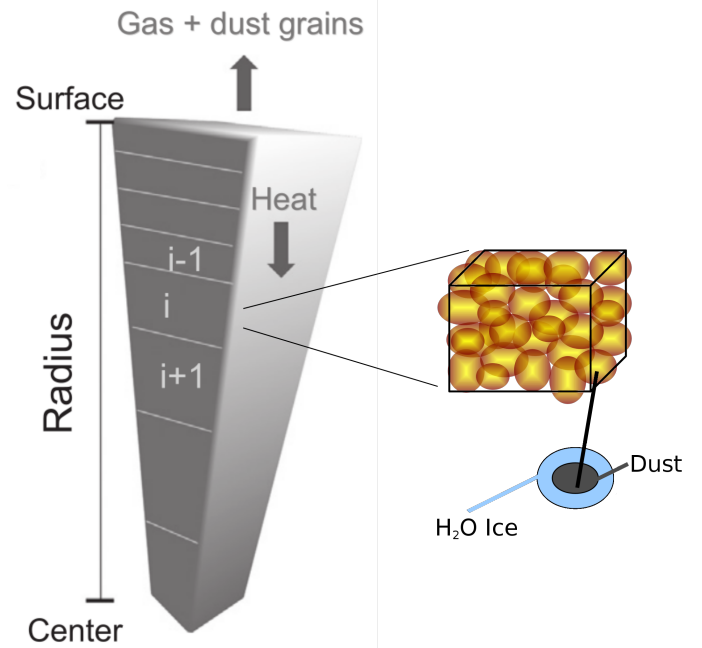


Fig. 1. Schematic view of the structure model. Adapted from Marboeuf & Schmitt (2014).

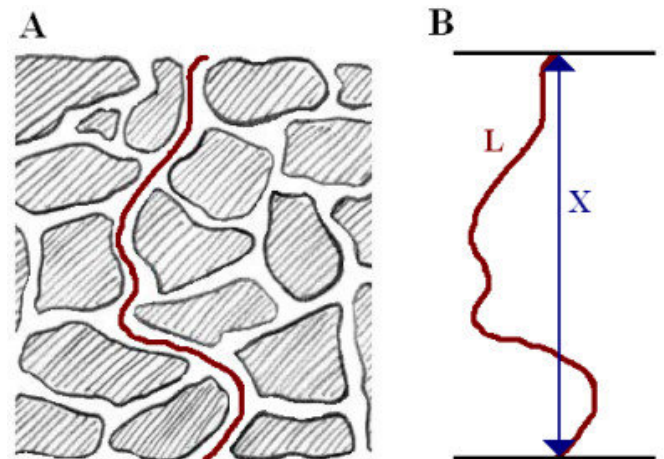


Fig. 2. Tortuosity of a path through a porous structure. In (A) a path through the material is shown, in (B) the length of the pore L and the distance between the endpoints X is indicated. Tortuosity is defined as L/X . Image adapted from O'Connell et al. (2010) under a creative common licence (<http://creativecommons.org/licenses/by/2.0>).

of a gaseous disk, there is no direct irradiation, since the disk is opaque. Instead, the midplane temperature is used as a boundary condition at the surface of the nucleus and we do not solve the energy balance equation at the surface (this assumption is discussed in Sect. 4.2). The surface sublimation rate follows expression (12).

The gas pressure of the disk in the vicinity of the body is neglected, i.e. the partial pressure of water that is relevant for the sublimation rate is set to zero and the potential influence of the disk gas on diffusion of gaseous species in the interior is not considered. In our model the total amount of gas in the interior is given by the tracked gas flow of the cometary nucleus model and

⁵ See their equation 2 with $KT \approx 5 \text{ W m}^{-1}$, $\rho = 0.5 \text{ g cm}^{-3}$, $t = 0$

is not including disk gas. We discuss the impact of disk material on the dominating surface sublimation rate in Sect. 4.4.

2.2.3. Dust mantle formation

The solid dust grains that are freed from the rigid structure by sublimation of water ice in the interior can either be ejected from the nucleus or they can accumulate at the surface. The mechanisms for this accumulation are reviewed in Prialnik et al. (2004). To summarize, there are multiple drivers of dust mantle formation that simultaneously appear in a body that undergoes sublimation.

Firstly, gas drag pulls the freed grains outward, but gravity counteracts this process. The magnitude of the gas drag force depends on the grain size, hence there is a critical radius r_c of grains that can be ejected. For a slow spinning nucleus the centrifugal force can be neglected, thus (Rickman et al. 1990, equation 7)

$$r_c = \frac{3}{8} \frac{C_{D,\text{Kn}} m_{\text{H}_2\text{O}} \phi_{\text{H}_2\text{O}} v_{\text{H}_2\text{O}}}{\rho_{\text{grain}} G \frac{M_{\text{nucleus}}}{R_{\text{nucleus}}^2}}, \quad (11)$$

where $C_{D,\text{Kn}} \sim 2$ is the drag coefficient in the free molecular (Knudsen) flow regime (Prialnik et al. 2004), R_{nucleus} and M_{nucleus} are the radius and the mass of the whole nucleus, $m_{\text{H}_2\text{O}}$ the molar mass, $\phi_{\text{H}_2\text{O}}$ the molar flow, and $v_{\text{H}_2\text{O}}$ the velocity of water vapor.⁶ Grains with radii larger than r_c do not get ejected but instead settle on the nucleus' surface, already depleted of ice by sublimation. Hence, a porous dust mantle forms on the surface. Huebner et al. (2006) remark that r_c only gives an upper size limit, for escaping grains, but smaller grains are not necessarily escaping, as the flow of gas thins above the surface and the grain might fall back onto the nucleus. Furthermore, already in early studies investigating this process, e.g. Brin & Mendis (1979), it was noted that for large dust-to-volatile mass ratio it is impossible to blow off all the freed dust, even though the particles might have radii smaller than r_c .

The second process comes into play if a dust mantle already exists. The accumulated grains on the surface will interfere with the liberated grains, such that they can no longer pass through the less porous mantle. Hence, they are trapped within the nucleus and further increase the size of the mantle (Shul'man 1972; Rickman et al. 1990).

Furthermore, the dust mantle can break under the gas flow, or its cohesive strength can be large enough to trap not only the dust, but the gas as well (Huebner et al. 2006). In our model, no cohesive forces between the grains are taken into account (Marboeuf et al. 2012). Therefore, we test in section 3.3.3 three cases: (a) the nominal case for which no initial dust mantle is present nor is it allowed to form subsequently, i.e. all the freed dust is lost, (b) an unstable dust mantle case, for which no cohesion forces are taken into account but particles larger than r_c are assumed to fall back onto the surface after ejection thereby forming a dust mantle over time, and (c) a constant dust mantle case, with a fixed thickness over the full evolution of the body. In case (c) most of the ejected dust is still lost, but a fraction is kept to keep the artificial constant mantle thickness. These cases differ compared to the work of Schorghofer (2008) who assumed that no dust is lost. This is essentially related to the size of the bodies considered. Small bodies with sizes below hundreds of meters undergoing sublimation (considered in this work) can lose

their dust, but larger bodies (considered in Schorghofer (2008)) will be able to keep their dust due to the increased gravity (i.e. $r_c \propto R_{\text{nucleus}}^2 / M_{\text{nucleus}}$ is smaller than all the typical grain sizes).

2.3. Analytical surface ablation model

Instead of invoking the full model from Marboeuf et al. (2012) which is described in Sect. (2.2), an analytic model for the sublimation of water ice from the surface, i.e. ablation, is outlined here, which can be tested against similar models from the literature, e.g. D'Angelo & Podolak (2015), or our full model that includes the very same surface sublimation term.

For a body without a mantle, ablation follows the kinetic theory expression, also known as the Hertz-Knudsen-Langmuir formula, for a free sublimation rate (e.g. Hertz 1882; Delsemme & Miller 1971; Schorghofer 2008; Marboeuf et al. 2012)

$$\varphi(T) = \frac{P^s(T)}{\sqrt{2\pi m_{\text{H}_2\text{O}} R_g T}} \quad (\text{mol m}^{-2} \text{s}^{-1}), \quad (12)$$

where P^s is the water vapor sublimation pressure (Pa), $m_{\text{H}_2\text{O}}$ is the molar weight of water and R_g is the ideal gas constant ($\text{J mol}^{-1} \text{K}^{-1}$). Equation (12) is valid assuming zero partial pressure of water in vicinity of the body. We discuss this approximation in Sect. 4.4. For non-zero pressure with the same temperature, the difference between pressures replaces P^s in the equation.

If this amount of water is removed from a layer with thickness $\delta \ll R$ at the surface, the total water mass loss is

$$\left. \frac{dm}{dt} \right|_{\text{H}_2\text{O}} = \varphi(T) m_{\text{H}_2\text{O}} 4\pi R^2. \quad (13)$$

For the refractory part (i.e. dust) of the structure, we assume that the grains are freed in the surface layer and matter gets released immediately adding their contribution to the total mass loss. This can be compared to the case without dust mantle formation of the cometary nucleus model (see Sect. 2.2.3).

Expressed as a decrease in radius, we can write

$$\frac{dR}{dt} = \varphi(T) \frac{m_{\text{H}_2\text{O}}}{\rho_{\text{H}_2\text{O},\text{matrix}}}, \quad (14)$$

where $\rho_{\text{H}_2\text{O},\text{matrix}}$ is the macroscopic water density in the matrix (taking into account porosity). The initial conditions shown in table 2 yield a $\rho_{\text{H}_2\text{O},\text{matrix}} = 276 \text{ kg m}^{-3}$. At fixed porosity, increasing the amount of refractory components reduces the available water, hence reducing $\rho_{\text{H}_2\text{O},\text{matrix}}$ and increasing the total mass loss. The assumption that the dust is freed with the sublimation of the ice is not valid for high dust to water ratios, since the cohesive forces between dust particles would become relevant.

It is noteworthy that if the temperature is kept constant and the body has a homogeneous structure, expression (14) is independent of the body's total radius, leading to a constant decrease in radius over time. Fig. 3 shows the result of a cometary nucleus model run of an initially 10 m sized body, which exhibits this behavior and motivates the analytic sublimation formula. This is true, as long as (i) the total radius is much larger than the radial extent of the surface layer ($R \gg \delta$) and (ii) there are no interior temperature gradients that would change the surface temperature.

Furthermore, we would like to point out that the analytic surface sublimation model is identical to the full cometary nucleus model (Sect. 2.2) assuming: (i) no heat transport of any sort, i.e. the temperature inside the body's structure is the same as in the disk, (ii) no other species than pure crystalline water ice and dust to be present and (iii) no mantle at the surface to form.

⁶ This expression differs from the one in Rickman et al. (1990), since, in our case, the gas flow is numerically modeled throughout the nucleus and can be used directly instead of analytically estimating it.

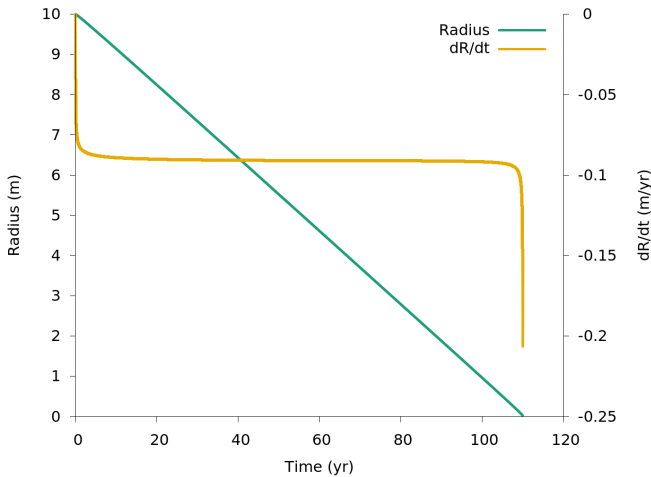


Fig. 3. Almost linear decrease in radius over time (green line, left axis) for a fixed surface temperature of 169 K using the cometary nucleus model. The derivative dR/dt is plotted in orange (right axis).

2.4. Initial conditions

2.4.1. Disk

The initial gas surface density of the disk is given by a power law with exponential outer cut-off boundary (as proposed by Andrews et al. 2010) and a normalization constant Σ_0 , corresponding to the surface density at approximately 5.2 AU, which determines the total disk mass.

$$\Sigma(r) = \Sigma_0 \left(\frac{r}{5.2 \text{ AU}} \right)^{-\beta} \exp \left[- \left(\frac{r}{R_{\text{out}}} \right)^{(2-\beta)} \right], \quad (15)$$

where R_{out} is a constant exponential cut-off radius, β is the power law exponent, determining the slope of the surface density profile. The disk evolution is then given by the Shakura-Sunyaev α parameter and the photo-evaporation (Sect. 2.1.2). We leave α fixed and run simulations with (nominal) and without photo-evaporation. The values, which are fixed in all results in this paper, can be seen in table 1. The initial total gas mass in the disk is accordingly $0.05 M_{\odot}$, which is the disk mass that Weidenschilling (1977) uses for the minimum mass solar nebula (MMSN). The star was assumed not to evolve during the disk's lifetime and the temperature and radius values are taken at a time of 1 Myr of stellar evolution according to Baraffe et al. (2015).

In order to gauge the influence of the initial parameters, we varied the total mass, lifetime and heating mode of the disk and the results and changes to the nominal parameters can be found in Sect. 3.3.2.

2.4.2. Solid body

To reduce complexity, we chose to model a body consisting only of water ice and dust, without any other volatile species. Water is the main volatile component (see Marboeuf et al. 2014, about the composition of planetesimals in disks) and the last one to sublimate. Using the parameters listed in table 2, the resulting total density of the body is $\sim 0.42 \text{ g cm}^{-3}$ which is of the same order of magnitude as the recently found bulk density of $(0.533 \pm 0.006) \text{ g cm}^{-3}$ (Pätzold et al. 2016) and the previous value of $(0.470 \pm 0.045) \text{ g cm}^{-3}$ by Sierks et al. (2015) of the comet 67P/Churyumov-Gerasimenko. Addition of other volatile

Table 1. Physical parameters for the nominal disk initial structure and evolution

Parameter	Value
Stellar mass	$1 M_{\odot}$
Stellar radius	$2.416 R_{\odot}^{(a)}$
Stellar effective temperature	$4377 \text{ K}^{(a)}$
Helium fraction	0.24
Power law slope β	$0.9^{(b)}$
Cut-off radius R_{out}	$50 \text{ AU}^{(b)}$
Inner boundary radius	0.03 AU
Surface density at 5.2 AU Σ_0	$268.5 \text{ g cm}^{-2(c)}$
Shakura-Sunyaev α -viscosity	2×10^{-3}
Photo-evaporation parameter \dot{M}_{wind}	$10^{-7} M_{\odot} \text{ yr}^{-1}$

References.

- ^(a) Baraffe et al. (2015) at 1 Myr;
^(b) Andrews et al. (2010);
^(c) MMSN (e.g. Weidenschilling 1977)

Table 2. Physical parameters of the cometary nucleus

Parameter	Value
Initial nucleus porosity	70 %
Dust mantle porosity	70 %
Tortuosity	$\sqrt{2}^{(a)}$
Initial dust/ice mass ratio	$1^{(b)}$
Water ice bulk density	$920 \text{ kg m}^{-3(c)}$
Dust bulk density	$3000 \text{ kg m}^{-3(c)}$
Enthalpy of sublimation	$[51983.9 - 20.0904 T] \text{ J mol}^{-1(d)}$
Heat conductivity	$[0.0028 + 1.3/T] \text{ W m}^{-1} \text{ K}^{-1(c)}$
Volumetric heat capacity	$[1582 (114.8 + T)] \text{ J K}^{-1} \text{ m}^{-3(c)}$

References.

- ^(a) Carman (1956); Mekler et al. (1990); Kossacki & Szutowicz (2006);
^(b) Marboeuf et al. (2014);
^(c) Marboeuf et al. (2012);
^(d) Washburn (1928); Delsemme & Miller (1971)

species would increase the density to values even closer to these measurements. We chose to represent realistic dust to ice mass ratios (~ 1) (Marboeuf et al. 2014) instead of tuning the ratio to represent measured bulk densities.

The initial location of the body in the disk is set to a distance 10 % further away from the star than the snowline, unless otherwise stated. This starting position allows the body to relax to the environment so that initial conditions are forgotten by the time we start computing evaporation.

For heat capacities and conductivities of dust and water ice, we adopted the values listed in Marboeuf et al. (2012) and references therein.

3. Results

We first (Sect. 3.1) present the test cases comparing the two different sublimation models described in Sects. 2.3 and 2.2. Then, we study which bodies are able to cross the snowline (Sect. 3.3). Finally, the results of simulated bodies crossing the snowline that were mainly obtained with the full cometary nucleus model for different varied quantities are presented in Sect. 3.3.

3.1. Comparison between the two sublimation models

Fig. 4 shows the results for a test case, in which we placed a body with an initial radius of 10 m and the composition shown in table 2 into the nominal disk (see table 1). The initial semi-major axis is set to 6 AU at time zero of the disk evolution. We find almost indistinguishable outcomes between the analytical surface sublimation model and the cometary nucleus model for this particular test.

For the larger, 100 m radius case (Fig. 5), the drift timescale is much larger. To save computation time, the body is initially positioned closer to the star than the initial snowline, namely at 4.3 AU. The initial bulk temperature for the analytical sublimation is, by construction, assumed to be equal to the local disk gas temperature. To estimate the influence of the initial temperature of the body, we ran two different cases with the cometary nucleus model: one with a pre-heated body, i.e. the initial bulk temperature is set to 170 K, which is the local gas temperature, and one without pre-heating, i.e. an initial bulk temperature of 20 K. The results are discussed in Sect. 3.4.

For equal initial conditions and under the assumption of initial homogeneous temperature in the nucleus, the analytical solution for the sublimation, i.e. equation (12), and the cometary nucleus model do agree well in the tested size range of bodies (i.e. meters to 100 m). The agreement worsens with increasing size even in the absence of a dust mantle (see Sect. 3.3.3).

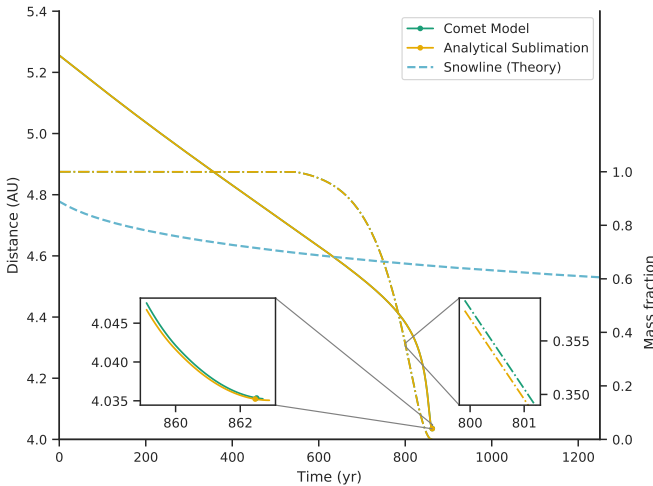


Fig. 4. Comparison of the comet model solving the internal structure and the analytical solution (equation 12) for 10 m sized bodies. The solid lines show the distance to the star (left axis) with dots representing the locations where the bodies shrank to a size of 10 cm while the dash-dotted lines show the remaining mass fraction (right axis). The lines of the two different model solutions are essentially indistinguishable. The initial position is 10% above the snowline location at time zero in the nominal disk. The barely visible kink in the mass fractions at 600 yr is due to reaching the threshold temperature of 150 K, where the sublimation models are started.

3.2. Snowline versus drift velocity

Temperature and pressure determine the classical snowline position during the evolution of the disk. In our nominal disk (see table 1), the classical water ice line, i.e. the snowline, was deter-

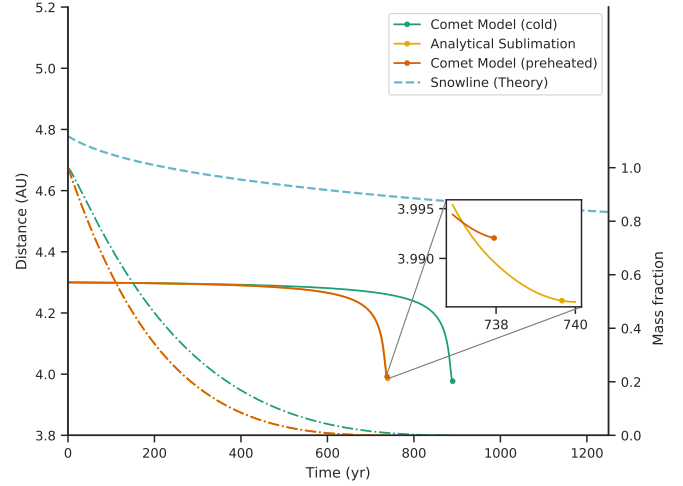


Fig. 5. As Fig. 4, but for a 100 m sized body. The initial position is chosen starwards of the snowline, i.e. at 4.3 AU. One of the cometary nucleus model runs is started with a low initial bulk temperature of 20 K (green line), whereas the other is pre-heated to the local gas temperature at the starting location (170.16 K), which is the implicit assumption of the Analytical Sublimation. The lines of the analytical sublimation model and the preheated comet model are barely distinguishable. The local gas temperatures at the end of the calculation are 174.95, 175.07, 174.94 K for the preheated, analytical and the cold model respectively.

mined (see Fig. 6). Due to external photo-evaporation, the disk vanishes almost completely after 2.8 Myr. As the inner disk surface density decreases, direct irradiation from the central star can invert the cooling of the disk to a heating (via the direct irradiation included in T_i in equation 1) in the inner region. Thus, the snowline motion reverts as well. This would not happen in a disk without photo-evaporation, where the disk gradually thins out as a result of the viscous evolution only, i.e. depending solely on α , and the snowline motion never changes direction.

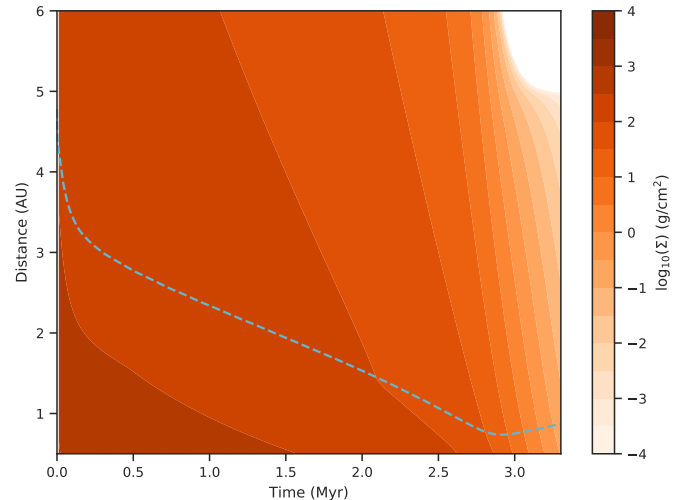
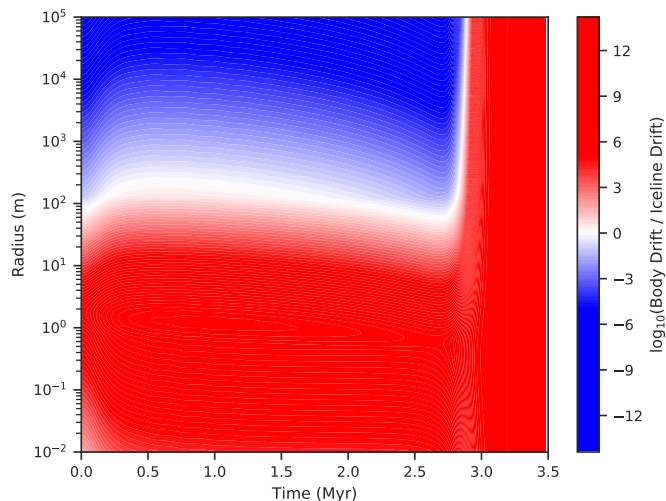
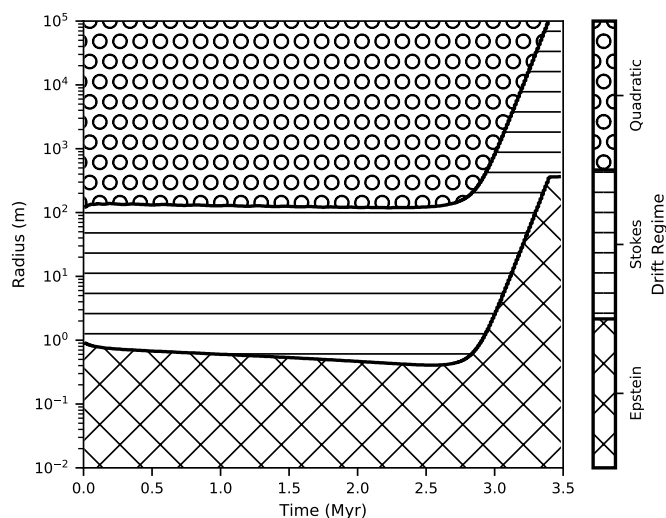


Fig. 6. Surface density evolution for the nominal disk. The dashed, blue line shows the snowline position.

In the nominal disk model we calculated the drift speed (see Sect. 2.1.3) of solid bodies in the size range from 10^{-2} m to



(a) Drift velocity compared to water snowline velocity



(b) Drag regime

Fig. 7. Drift velocity and regime in an irradiated disk with photoevaporation. All the bodies with sizes in the red area in Fig. (a) cross the snowline, since they drift faster than it moves towards the central star. The snowline is determined using tabulated values for the temperature and pressure. After approximately 2.4 Myr, the snowline position starts to move away from the star, due to the disk's dispersal. Thus, the ratio of the body's drift speed to the snowline speed is negative and the log in Fig. (a) is no longer defined and the ratio is set to a value of 12 to indicate that all the bodies will cross the snowline in that phase. In order to smooth out numerical artifacts, we applied a Gaussian filter in horizontal direction.

10^5 m over time, as well as the change of the snowline position. For objects bigger than 10^5 m, gas drag is not the relevant source of migration, but the torque exerted by density waves (type I migration) (Goldreich & Tremaine 1979; Ward 1997). The ratio of the body's drift speed to the snowline speed is shown in Fig. 7(a). Important for our goal is the size range where the transition from bodies moving slower than the snowline to faster than snowline speed lies. In Fig. 7(a) the color code is chosen such that this transition lies in the white region. We found that planetesimals with $R \gtrsim 100$ m will no longer drift towards the star

fast enough to cross the snowline, thus the water ice on these bodies will never sublimate. To help interpret the figure, the drag regime of the different sized bodies is plotted in Fig. 7(b). A size of roughly 100 m happens to coincide with the transition from Stokes to quadratic drag regime emphasizing the need to take into account the different drag regimes.

3.3. Parameter study of snowline crossing bodies

In this part of the results section we present the evolution of drifting solid bodies in the protoplanetary disk. These results – obtained using the cometary nucleus model – are presented in Sect. 3.3.1, 3.3.2 and 3.3.3, in which the radius, disk conditions and dust mantle properties are varied.

3.3.1. Initial radius dependence

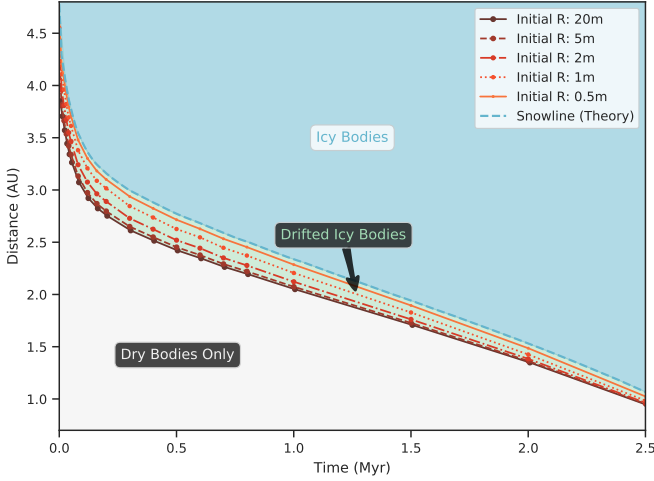
Figs. 8(a) and 8(b) show the innermost locations reached by different sized bodies, drifting from outer regions of the disk. In the following, we call this position the *location of complete disintegration*. To get the results, the full cometary nucleus model mode was used. The composition of the different sized bodies was assumed to be equivalent and corresponds to the values given in Sect. 2.4 and table 2. No dust mantle is present in all shown cases, i.e. dust mantle formation is excluded.

When the body reaches high enough temperatures it undergoes ablation and thus loses mass. After shrinking to a radius of 10 cm the location is marked as a dot in Fig. 8(a). This location is considered to be the location of complete disintegration, since a centimeter sized icy body at those temperatures and pressures has a very short lifetime (e.g. Lichtenegger & Kömle 1991). 20 bodies are modeled starting at different times over the disk lifetime for each evaluated size. Initially, the bodies are located 10% further away from the star than the snowline location at the specific starting time.

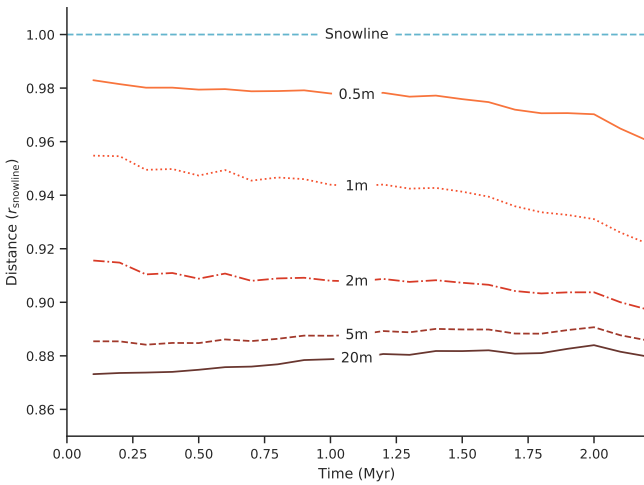
The lowest included initial radius is 0.5 m. Due to numerical and physical assumptions of the model, such as not tracking single grains, lower initial radii are excluded and these pebble sized objects are the main subject of other studies (e.g. Drażkowska & Alibert 2017; Schoonenberg & Ormel 2017).

It can be seen in Fig. 7(a) that bodies with radii on the order of one meter drift the fastest in the protoplanetary disk (see also Weidenschilling 1977; Adachi et al. 1976). Bodies with radii lower than one meter drift slower and thus only cover a small distance after crossing the snowline. The smallest body in our dataset, with an initial radius of 0.5 m, loses all of its mass and stops very close to the snowline due to its relatively slow drift. The tabulated snowline position values and the sublimation are calculated independently. Therefore, the good agreement of the snowline location in Fig. 8 with the location of complete disintegration of the 0.5 m sized body shows that the tabulated snowline position is a reasonable choice of reference.

A larger than meter-sized body with identical composition will also undergo sublimation and thus lose mass. As a consequence, it gradually speeds up until it reaches maximal drift speed at a radius of one meter. This size will be reached closer to the star than the equilibrium position of the snowline. Thus, the object will ultimately drift farther than an initially smaller body until complete disintegration. The difference in the position of complete disintegration will decrease with increasing size, because the initial drift slows down and thus only little distance is traveled before reaching a smaller size. However, the difference will stay bigger than zero, and therefore bigger bodies always



(a) Locations of complete disintegration for different initial sizes



(b) As panel (a), but with distance measured relative to the snowline position

Fig. 8. Comparison of locations of complete disintegration of different sized bodies without a dust mantle. In panel (a) the distance to the star is measured in AU and the dots represent the locations where the body shrank to a size of 10 cm. The dashed, cyan line indicates the evolving position of the P - T tabulated snowline, and the regions where only icy solid bodies, only water depleted solid bodies, and the region that is injected with drifting icy bodies are colored and labelled. In panel (b), the same data is shown but measured in units of the evolving, tabulated snowline position (1 corresponds to the snowline position, 0 to the central star).

cross a larger distance before they completely disintegrate. This asymptotic behavior can be seen in Figs. 8 and 8(b). Since the difference of the position of disintegration between a five meter sized and a ten meter sized body is negligible compared to other effects (see e.g. Sect. 3.3.3) and due to the numerical cost of simulating a large body, no larger sizes were included. There is no reason to expect the position of disintegration of larger bodies to change significantly compared to the one of ten meter sized bodies up to the 100 m size boundary, where the bodies can no longer cross the snowline by radial drift (see Sect. 3.2).

To show that the results can be well decoupled from the disk evolution, Fig. 8(b) shows the same results as Fig. 8(a), but instead of measuring the distance from the central star in units of AU, it is measured in units of the snowline position r_{snowline} (1 corresponds to the snowline location, 0 to the central star). The ratio of the location of complete disintegration to the snowline position stays approximately constant in time.

We would like to point out that this behavior is only found if the bodies are not covered by dust mantles. For bodies with dust mantles, a similar size-dependent behavior is only recovered for exactly equal mantle thicknesses using the constant dust mantle mode described in Sect. 3.3.3. However, the scaling of the mantle thickness depending on size would be the dominant factor but is to our knowledge not well constrained.

The aforementioned time-decoupling of the effect by using units of snowline distance can be used to tentatively explore the overall mass fraction of drifting bodies that should be found at a given distance from the star – measured in units of the snowline position – at all times in the disk (Fig. 9). The mass fraction value shown is an integral over the assumed distribution of bodies (see Sect. 4.1), which was cut such that all included sizes do cross the snowline at all times of the nominal disk evolution (i.e. 1 kg to 1×10^9 kg corresponding to 8 cm to 76 m). For simplicity, the density was fixed to the nominal value of 0.422 g cm^{-3} and the analytical sublimation model was used. To help interpret the results, we note that the largest bodies which are abundant for flat slopes do drift the furthest (see Fig. 8), but do not lose a lot of their mass starwards of the snowline. The most efficient transport of mass is achieved by meter sized bodies who are most abundant in the -1.83 slope case, where the location at which 50% of solids remain in the disk is moved from the snowline to two percent starwards of the snowline.

3.3.2. Disk influence

In addition to the nominal disk with values given in table 1, we repeated the calculations for bodies with a radius of 10 m embedded in disks for which we modified one parameter compared to the nominal case: a light disk ($M_{\text{disk}} = 0.01 M_{\odot}$, i.e. $\Sigma_0 = 53.704 \text{ g cm}^{-2}$), a massive disk ($M_{\text{disk}} = 0.1 M_{\odot}$, i.e. $\Sigma_0 = 537.046 \text{ g cm}^{-2}$), a long-lived disk ($\dot{M}_{\text{wind}} = 3 \times 10^{-9} M_{\odot} \text{ yr}^{-1}$), and a disk without heating by irradiation of the central star ($T_l = 0$ in equation 1). As before, the cometary nucleus model is started multiple times in all the different disk evolution calculations. Initially, the body is separated from the star by a distance 10% larger than the classical snowline distance. To cover the full evolution of the disk, the starting times of the individual calculations are scaled with the lifetimes of the different disks. The markers labelled "no mantle" in Fig. 10 show the temporal mean of all these calculations for the different disk cases with indicated standard deviations (1σ error-bars). As in Fig. 8(b), the distance is measured in units of the classical snowline.

We find, that most of the different tested disks have influences on the locations of complete disintegration in units of classical snowline distances on the percent level only. In Fig. 10 it is shown that different disk masses and lifetimes (controlled by photo-evaporation) do not change the result significantly.

However, the non-irradiated disk has a very different temperature profile once the viscous heating is no longer dominating. Thus, the snowline location is altered to a large extent moving, at late times, very close to the star (i.e. to 0.14 AU during the calculation of the latest datapoint). Due to the proximity of the snowline to the star, the slope of the surface density and thus the pressure gradient starts to decrease, hence reduces the drift

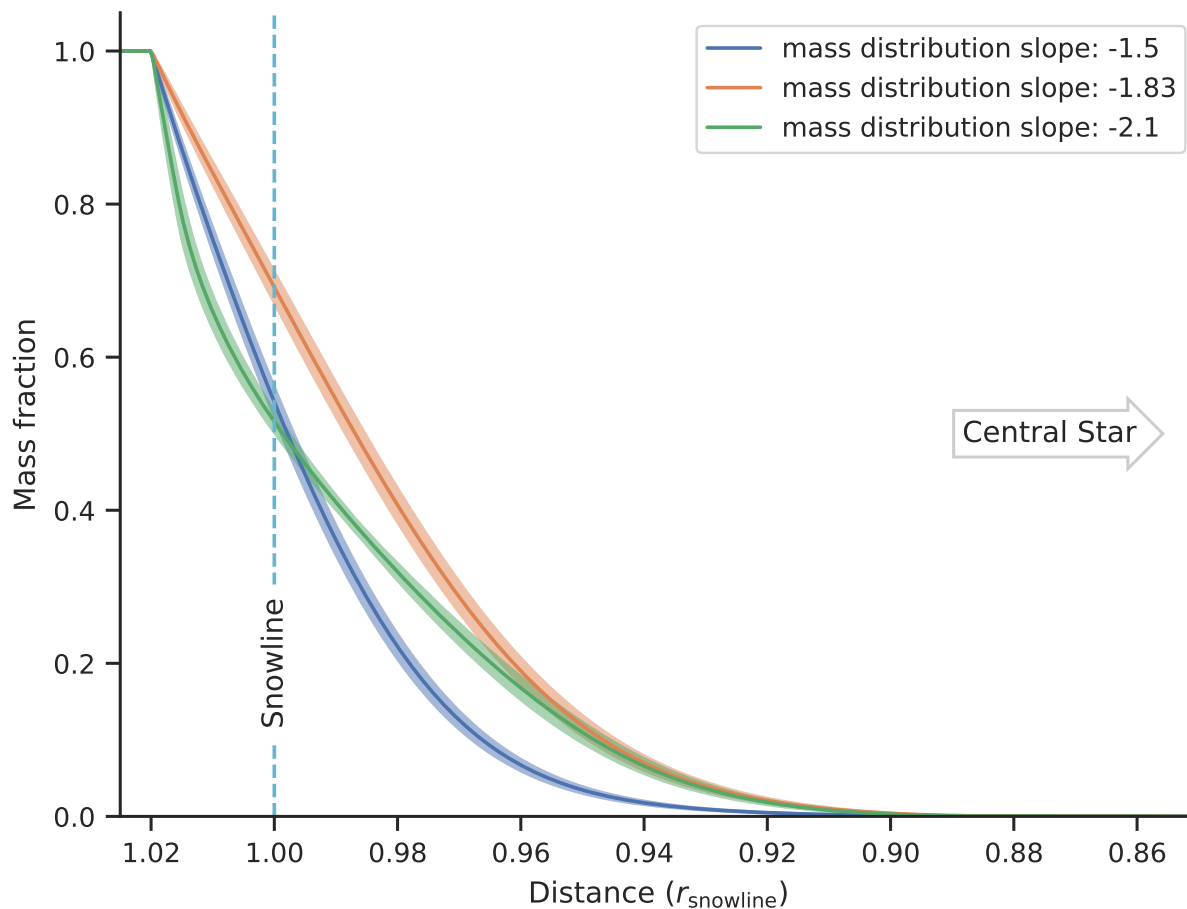


Fig. 9. Remaining mass fraction in the overall population of bodies crossing the snowline ($1 \text{ kg} \leq m \leq 1 \times 10^9 \text{ kg}$) with shaded bands indicating the standard deviation due to the evolving disk. The mass shown is an integral over a distribution of masses with the indicated power-law slope and a mean over time in the disk. More details can be found at the end of Sect. 3.3.1.

speed. Therefore, the location of complete disintegration is located closer to the snowline, i.e. only 3% below it, which is significantly different from the other cases.

Overall the resulting disintegration locations are robust for the contrasting tested disk cases at many different times. However, the local pressure gradient has a strong influence.

3.3.3. Dust mantle influence

As discussed in Sect. 2.2.3 the formation of a dust mantle on a cometary nucleus is likely. We assume here the same for a disk-embedded body and quantify its potential influence. An important factor is the size of the body, since the process of dust mantle formation depends on the gravitational force. In general, bigger grains are more easily ejected from small nuclei. We consider here thin dust mantles to initially exist on bodies in the gas disk with radii of 10 m and evaluate the dust mantle evolution and the influence on the location of complete disintegration. Our model includes dust formation and removal (described in Sect. 2.2.3 and Marboeuf et al. (2012)) without cohesive strength (in the following called the "unstable" model).

To estimate the extreme case, where the dust mantle cannot be removed, simulating an infinitely large cohesive strength, we

artificially set the dust mantle to a constant thickness (called the "constant" model).

In Fig. 11, it can be seen that using the unstable model the mantle is removed very quickly and the position of complete disintegration differs only slightly from the one without mantle. However, if the dust mantle cannot be removed due to strong cohesive strength and surface sublimation is thus always suppressed, the disintegration location is up to 1 AU closer to the star for a 10 cm thick mantle. In Figs. 10 and 12, the less extreme case of a 5 cm thick constant dust mantle is shown. In the former figure, the temporal mean of the location of complete disintegration for different disks is depicted and in the latter its temporal evolution for the nominal disk is shown.

These results demonstrate the importance of the cohesive strength and thickness of the mantle in determining the thermal evolution of the body. The thickness of the dust mantle is not well constrained by observations, since data is very sparse. The permittivity probe SESAME-PP of the Rosetta mission showed that the first meter is more compact than the rest of the comet 67P (Lethuillier et al. 2016). However, no estimate on the total thickness can be made from this single data point and it is not clear what the composition (possible volatile content) and porosity of this compact layer is. Furthermore, it is not clear how to

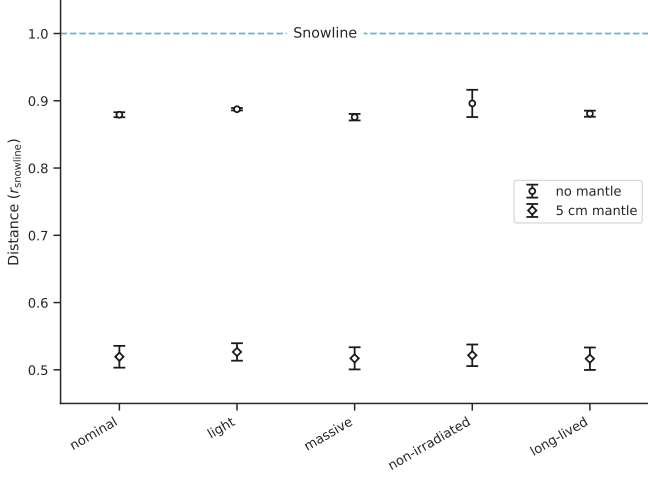


Fig. 10. Mean relative locations of complete disintegration in different disks for initially 10 m sized bodies with and without constant dust mantles. As in Fig. 8(b), the distance from the central star is measured in units of snowline positions (snowline location at 1, star at 0). The mean over the calculations at different times is taken and the 1σ error is indicated. Refer to the text for the different disk properties.

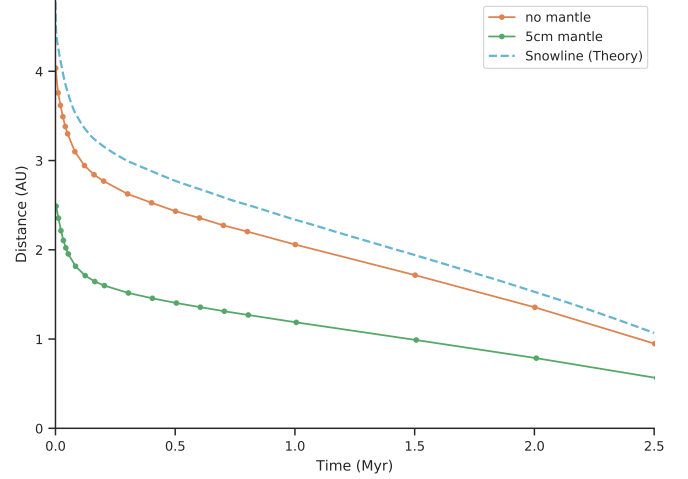


Fig. 12. Locations of complete disintegration in the nominal disk of initially 10 m sized bodies with and without a dust mantle. The classical water ice line (snowline) in the disk is indicated for reference.

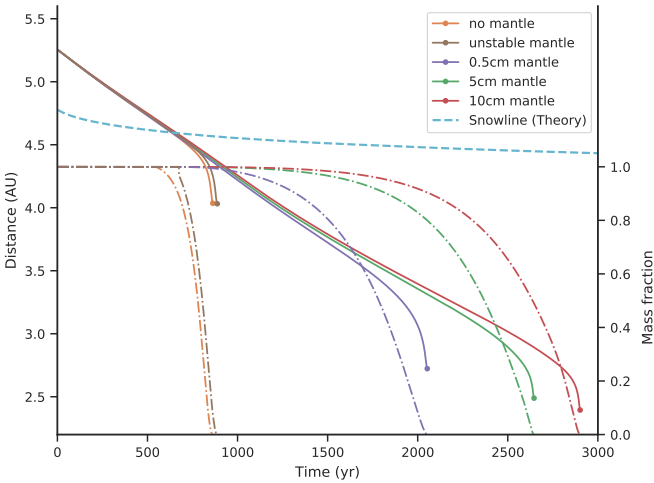


Fig. 11. Sublimation comparison of a 10 m sized bodies with different dust mantle thicknesses and removal processes. The legend is ordered in increasing sublimation time. The smooth line marks the location of the body in time (left axis), while the dots at the end of the line indicate shrinking to a radius of 10 cm as in Fig. 8 and 12. The dash-dotted lines indicate the mass fraction compared to the initial mass of the same colored case (right axis). The kink that is visible in the mass fraction of the unstable (initially 5 cm thick) mantle stems from the mantle breaking up at that point in time.

scale mantle properties from an object with dimensions on the order of kilometer to one with a radius of ten meter.

The large influence of the dust mantle is caused by the change of the sublimation process because free sublimation at the surface is no longer possible if the object is covered by a mantle. Sublimation in the interior still happens, it is however suppressed by the relatively slow diffusion of the released water

vapor through the dust mantle, since the small pore radius of the dust mantle limits diffusion.

By analyzing the interior structure of the numerically modeled body, we found that the low thermal conductivity of the dust mantle and porous matrix does not play a dominant role. The body's interior is heated on short timescales on the order of years for the size range we are interested. This can be seen in Fig. 13, where almost no radial gradient in terms of temperature is visible. This behavior is found for all small body cases with radii of up to 100 m. For larger bodies or much thicker dust mantles, the picture can change.

The fact that we do not remove the dust mantle by some process is representative of infinite cohesive strength. Thus, the results for a body without dust mantle and the one with constant mantle should be interpreted as lower and upper boundaries for a realistic physical result and the results in Figs. 10 and 12 should be interpreted as such. Measuring the distance from the body to the central star in units of snowline distances again, the location of complete disintegration without dust mantle is at ~ 0.9 , whereas the one with a dust mantle goes down to 0.5 of the snowline distance to the star. However, for a more realistic result, a dust mantle formation and removal model that takes the cohesive strength of the material into account would be needed.

3.4. Internal thermal evolution

To analyze the importance of the internal thermal evolution of the body, we first take a look at the results of the comparison of the analytical surface ablation model and the cometary nucleus model (Sect. 3.1) without a dust mantle.

The underlying assumption of the analytical ablation model is an already equilibrated temperature throughout the body's full structure and the gas. Hence, as expected, the pre-heated cometary nucleus model results are closer to the analytical model. This good agreement between the two models shows that a numerical treatment of the internal evolution is not necessary for bodies composed mainly of dust and water ice with sizes smaller than 100 m and with initially equilibrated temperatures. For many applications of pure water sublimation it is not necessary to invoke a full model keeping track of the internal structure

and temperature because heat conduction - and thus temperature equilibration throughout the body - happens at timescales of years. E.g. for a ten meter sized body, the thermal timescale $\tau_T \approx R^2 \rho c / K$, where ρc is the density times the heat capacity and K is the heat conductivity (see table 2), is approximately 0.3 yr. Thus, the internal temperature of a meter sized body spiraling towards the star on timescales of thousands of years is expected to be in thermal equilibrium with the disk.

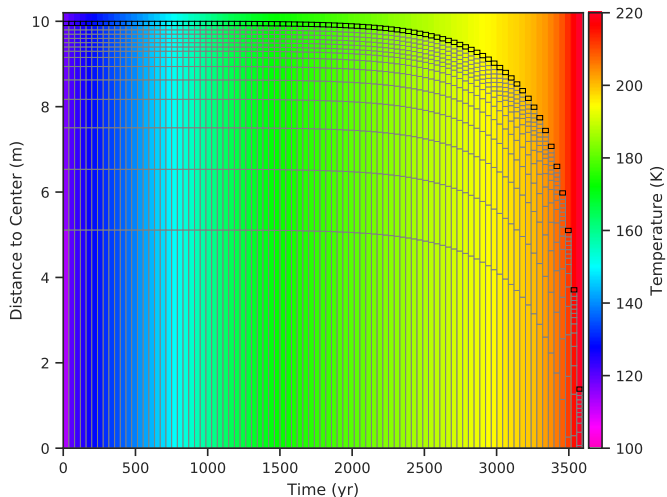


Fig. 13. Interior Temperature of an initially 10 m sized body covered by a 10 cm thick dust mantle. The number of layers is reduced to 15 compared to nominal runs for better visibility and 60 timesteps are merged into one block. The uppermost, dark framed layer shows the dust mantle. Outside the body, the local disk temperature is plotted. A radial temperature gradient is only barely visible.

In the case of a 100 m sized body within the snowline but without pre-heating, the body shrinks faster than the heat is transported to the interior. However, the cold interior acts as a heat sink. Thus, heat is conducted to the interior which leads to cooler surface temperatures and slower sublimation (see Fig. 5). This behavior is only reproduced at relatively high temperature regions closer to the central star than the snowline where sublimation is more efficient than heat conduction.

For bodies covered with a dust mantle, the internal temperatures that are reached are significantly higher than for bodies without a dust mantle. Similar is the observed fast heat conduction: for a 10 m sized body very little variability in the radial direction is visible (Fig. 13), indicating that sublimation does not lead to a faster shrinking than heat can be conducted to the interior. Thus, the body first becomes isothermal before it disintegrates. No significant thermal insulation increase by the mantle is found: as in the case without a dust mantle, heat conduction acts on timescales of years.

We remark that a numerical treatment of thermal conduction is required to track changes on timescales of years, i.e. on timescales on the order of the orbital period. Hence, assuming an isothermal interior is only valid for objects on almost circular orbits and should not be applied to bodies on eccentric orbits (such as comets).

We conclude that the interior of drifting small bodies ($R < 100$ m), composed of water ice and dust grains, with zero eccentricity and inclination can be assumed to be isothermal. With

that, our analytical model reproduces well the results of the cometary nucleus model. We note that for planetesimals with radii > 10 km, differentiation due to heating by ^{26}Al (Sect. 2.2.1) can occur (Lichtenberg et al. 2016). For a differentiated body with an ice layer on the surface, sublimation is not hindered by a dust mantle and the analytical sublimation formula becomes appropriate again if no heat is lost to the interior, e.g. if the body is in thermal equilibrium.

4. Discussion

A number of simplifications and assumptions were made to obtain the presented results. These require discussion and some additional calculations that we describe in this section. In addition to that, a successful test of the radial drift formula is presented in appendix A.

4.1. Collisions

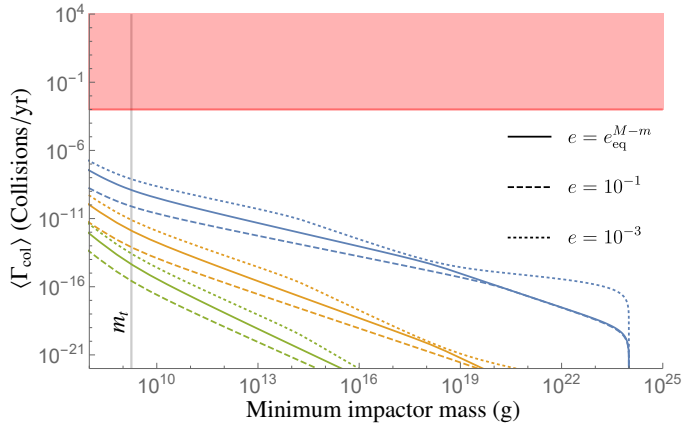
In a protoplanetary disk, collisions are a key evolution factor. In this section, we calculate collision rates between our test body – called the *target* – and a population of other bodies present in the disk – the *impactors* – and compare them to the timescale of sublimation, which we broadly estimate to be $\sim 1 \times 10^3$ yr.

Both, the target and the population of impactors undergo radial drift. Even though radial drift timescales can be as short as 1000 orbital periods (Armitage 2019), they always remain much larger than the orbital period. We calculate collision rates due to two different processes: (a) caused by coupling to the gas (difference in radial and azimuthal velocities) of different sized bodies and (b) due to eccentricity and inclination distributions induced by gravitational stirring and assuming no radial drift. The latter, which we call the *orbital collision rate*, is applicable for larger bodies that no longer drift significantly, while the former is applicable for smaller bodies and we call it *Stokes collision rate* to emphasize the coupling to the gas which is quantified by the Stokes number.

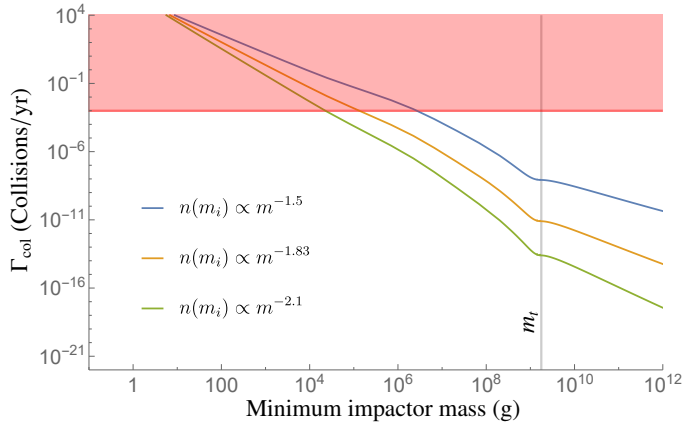
In order to compute the collision rates, a statistical approach using a prescribed distribution function of solids is required. For that, the two body (or "particle in a box") approximation (Safronov 1969), i.e. to neglect the influence of the central star, was used to estimate collision rates until Nakazawa et al. (1989a,b); Ida & Nakazawa (1989), and independently Greenzweig & Lissauer (1990, 1992) treated collisions using Hills approximation (Hill 1878). The underlying, adopted probability of a test particle hitting a gravitating object (e.g. a planet) during one orbit was derived by Öpik (1951). However, this approach can only be used for the orbital collision rate. For the gas coupled collision rate, we apply the "particle in a box" approach (Safronov 1969). A detailed description of the approaches can be found in appendix C and the underlying, assumed mass distribution of bodies as a power law with slope α is described in appendix B.

The resulting integrated orbital collision rates of our nominal target body with impactors larger than the indicated minimum mass (x-axis) are shown in Fig. 14(a). Collisions of the target with large impactors $m_i > m_t$ are rare for all considered eccentricity and inclination distributions and are thus negligible. Collisions with smaller bodies have to be treated with the Stokes collision rate prescription (appendix C.2) and are shown in Fig. 14(b). In both cases, the rates were integrated from the mini-

imum impactor mass (on the x-axis) to the maximum mass of 1×10^{24} g.⁷



(a) Orbital collision rate



(b) Stokes collision rate

Fig. 14. Collision rates of the nominal target body (table 2) with a radius of 10 m integrated over impactor masses larger than the indicated minimum mass. Results are shown for three different slopes of the impactor mass distribution and in panel (b) additionally for three different eccentricity and inclination values. e_{eq}^{M-m} is the equilibrium eccentricity in the vicinity of a Mars mass perturber (Ida 1990; Thommes et al. 2003). The red shaded region depicts collisions more frequent than once every thousand years and the target mass m_t is indicated.

For a very flat mass distribution, relatively high-energy impacts with bodies with diameters larger than 1 m – leading to fragmentation (Windmark et al. 2012; Blum 2018) – are frequent, i.e. are happening about once per 100 yr, which is comparable to the simulation time of the nominal, drifting body discussed in Sect. 3. If the mass distribution is steeper, the target is less likely to encounter this kind of collisions.

In terms of energetics, the collisions do not contribute large amounts of energy compared to the thermal energy of the body or the total sublimation energy (see table 2): Integrating over all sizes, the kinetic energy is $\lesssim 7 \times 10^6$ J yr⁻¹ (using the definition of the "reduced mass kinetic energy" in Stewart & Leinhardt

⁷ The Stokes collision rates for bodies more massive than the target agree to an order of magnitude precision with the orbital collision rates and do not contribute significantly to the integral.

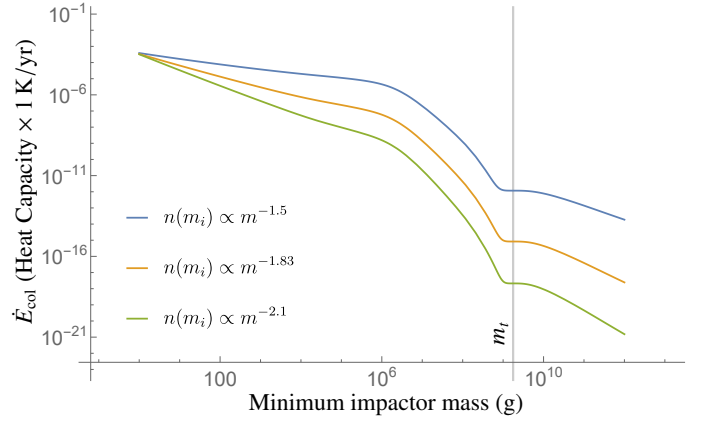


Fig. 15. Collisional energy calculated with the Stokes collision rate, integrated over impactor masses larger than the indicated minimum mass. The energy is measured in units of the energy required to heat the body by one Kelvin. The target properties and impactor mass distributions are the same as in Fig. 14 and the target mass m_t is indicated.

(2009)), which is $\sim 4 \times 10^{-4}$ yr⁻¹ of the energy required to heat the body by one kelvin and $\sim 3 \times 10^{-7}$ yr⁻¹ of the total sublimation energy. The yearly collisional energy deposited on the target by a population of impactors in units of the heat capacity of the target is shown in Fig. 15. For a smaller, 1 m sized body, the relative numbers increase by almost an order of magnitude. However, the drift and sublimation timescales are also reduced for this smaller body, again resulting in negligible heating by collisions during this stage of the sublimation process.

Most of the energy input results from collisions with bodies with radii smaller than one meter (see Fig. 15). Locally on the targets, the impacts by these smaller bodies are able to erode away target material. This could be the most severe constraint on the applicability of the presented model. The mass encountered per year by the nominal target is $\sim 4 \times 10^{-4}$ times its own mass. Windmark et al. (2012) fitted erosion efficiencies based on laboratory experiments for silicate grains. Using their velocity and mass dependent fit (Windmark et al. 2012, equation 17), the total eroded mass relative to the target mass is $\sim 8 \times 10^{-2}$ % yr⁻¹. This would imply that the assumption of a collision free sublimation is only applicable on timescales $\lesssim 10$ yr. Furthermore, for collisions involving impactors with sizes comparable to the target, fragmentation of both objects can happen and only a remnant with mass smaller than the masses of each object remains but Fig. 14(b) shows that this comparable-size case is rare and can be safely ignored. The erosion rates in the regime of collisions with meter-sized bodies is not well studied and applying the fit of Windmark et al. (2012) is therefore an extrapolation with its inherent flaws. Using the lower limit of the erosional prescription for porous icy agglomerates used in Krijt et al. (2015) yields smaller erosion rates $\sim 2 \times 10^{-2}$ % yr⁻¹ translating to erosion of less than 7.5 % of the bodies mass over the time where sublimation was active ($T > 150$ K) in the numerical simulations shown in e.g. Fig. 4.

We conclude, that during the crucial short phase (~ 100 yr – 1000 yr), where sublimation and fast radial drift take place, collisions with small bodies are happening frequently. The results presented in Sect. 3 are only strictly valid if either the surface density of solids is reduced (e.g. by not converting all solids to pebbles, by less efficient settling, or by accumulation of solids in planets), or erosion is less efficient in the relevant mass regime

(large uncertainties of extrapolation of laboratory experiments). Otherwise, erosion by collisions could become an additional relevant mass loss mechanism. In terms of thermal energy, collisions do not heat the body, thereby justifying the thermal balance model we presented in Sect. 2. The fast erosion of meter sized bodies is the main argument against their presence in disks. In this work, however, we postulate their presence, which could be justified by frequent enough fragmentation of larger bodies.

We note, that the retention of a dust mantle is very hard to achieve if collisions are eroding away the uppermost layers of the body. A mantle of centimeter thickness is eroded by collisions with pebbles in less than 10 yr.

4.2. Gas versus surface temperatures

D'Angelo & Podolak (2015) showed that for small bodies ($R < 10$ km) the bulk temperature of the body is in equilibrium with the gas after less than 500 orbits (see Fig. 20 in D'Angelo & Podolak (2015)). In their work, the entire body was heated and reached equilibrium temperature in this amount of time, whereas in our full model, we only assume equilibration of the temperature in an uppermost, thin layer. Instantaneous heat exchange from the thermal bath, i.e. the disk, to the body is thus well justified.

4.3. Frictional heating

In this work, heating due to interactions with the non-Keplerian gas is not taken into account. D'Angelo & Podolak (2015) calculate the equilibrium value of the surface temperature for their planetesimals to be (D'Angelo & Podolak 2015, equation 38)

$$(T_s^{\text{eq}})^4 \approx T_g^4 + \frac{C_D \rho_0}{32 \sigma \varepsilon_s} |v_g - v_K|^3, \quad (16)$$

where C_D is the drag coefficient, σ is the Stefan-Boltzmann constant and ε_s is the thermal emissivity (for a black body $\varepsilon_s = 1$). To derive this equilibrium value, a fraction of $C_D/4$ of the total collisional energy is assumed to be transmitted as heat to the body, which corresponds to an upper limit (Podolak et al. 1988).

For a simple estimate, using the typical values $\rho_0 = 10^{-9} \text{ g cm}^{-3}$, $T_g = 140 \text{ K}$ and $\eta = 4 \times 10^{-3}$, frictional heating yields a negligibly small temperature increase of $8 \times 10^{-4} \text{ K}$ for a black body. Only in very dense regions of the disk or potentially in the atmospheres of planets could a significant change occur.

4.4. Water vapor pressure

Disk water vapor can change the sublimation rate and even lead to deposition of water onto bodies if present in high enough abundance ($P_{\text{vapor}} > P^s(T)$). In an ideal case, where all other solid bodies in the disk do not move radially and the disk is not evolving, $P_{\text{vapor}} < P^s(T)$ everywhere. Hence, no water would condense onto the surface of a body drifting by. However, if fast drifting pebbles are present, the water vapor surface density can be replenished by diffusion of the freshly released vapor starwards of the snowline (Ros & Johansen 2013; Schoonenberg & Ormel 2017; Drążkowska & Alibert 2017). Another source for out of thermal equilibrium water vapor could potentially be stellar outbursts which episodically heat up the disk (Hartmann & Kenyon 1996). To study constraints for deposition or suppressed sublimation in detail, a model including the evolution of all solids and water vapor in the disk would be needed. If a

significant amount of vapor is transported further away from the star than the snowline, it could be deposited onto a drifting body, reducing (for Stokes numbers $s > 1$) the drift speed, which allows for even more deposition, potentially leading to growth to planetesimal size.

A local source for enhanced water vapor pressure could also be the drifting body itself, due to exhibiting a coma-like region with enhanced partial pressure of water, reducing the sublimation rate. The transport of gas or vapor away from the body is not modeled here and would differ from the case of a comet due to the disk gas interacting with the released vapor and the lack of solar wind, which is absorbed in the disk. Our assumption of no increased local partial pressure due to the coma is consistent with a complete erosion of the coma by the disk gas.

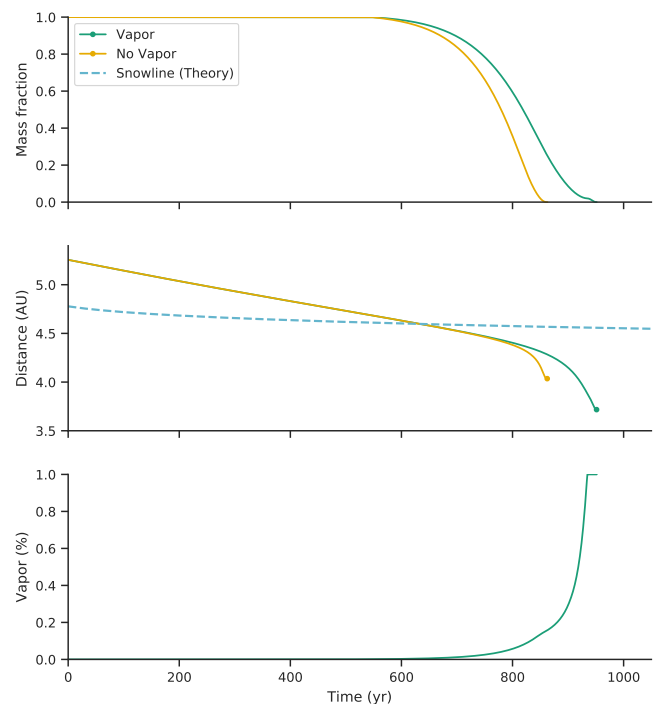


Fig. 16. Evolution of a 10 m sized body in the nominal disk calculated with the analytical surface ablation model, with and without water vapor pressure. The water vapor increases exponentially depending on the local disk temperature up to a maximum of one percent of the local pressure.

If the partial pressure of vapor is smaller than the sublimation pressure P^s but not zero, it reduces the sublimation rate compared to the nominal results without vapor. In Fig. 16 we show the influence of an artificially chosen, exponential increase of partial pressure of water vapor (motivated by results of the pebble based evaporation models of Schoonenberg & Ormel (2017)) up to one percent of the total pressure. The location to reach the percent level is set to where the temperature is 176.6 K to avoid deposition of water.

Under these assumptions, the water vapor moves the location of complete disintegration farther in towards the star. Hence, in the context of presence of water ice in solid bodies (the "dynamical" snowline), the results for the case without a mantle and without water vapor in the disk is an upper boundary for the dynamical snowline location.

5. Conclusions

We presented the application of a cometary nucleus model to disk-embedded, radially drifting, spherical bodies, tracking the thermodynamic evolution of the object. The body is assumed to consist of only dust and water ice. Different properties of the disks and the drifting bodies were explored and the time evolution of the disk was taken into account. The main focus of the work was to constrain the regions that can be reached by drifting icy bodies, ultimately determining the zone where some water can be incorporated in solids and thus be accreted by growing terrestrial planets.

Here, we summarize the key findings:

1. Almost independently of the properties and temporal evolution of the disk, drifting bodies with radii ≥ 1 m can transport water ice at least ten percent closer to the star than the location of the "classical" snowline before they completely disintegrate.
2. If surface sublimation is not impeded in any way, e.g. by the presence of a dust mantle, it is the dominant process for the evolution of the object and can be modeled in a simple, analytic way with good agreement with the results of a full numerical model.
3. These results are applicable to bodies with radii ranging from meters to 100 m. Smaller bodies never experience fast radial drift, therefore the effect is suppressed, whereas bodies larger than 100 m do not drift fast enough to even cross the snowline. In the range from tens to hundreds of meters, the difference in locations of complete disintegration is small. This implies that if bodies in this size range are present, a quantifiable smearing of the water snowline results. In the absence of meter-sized bodies, the snowline is given by the local disk properties only.
4. A dust mantle covering the body suppresses surface sublimation and forces the internally released vapor to diffuse through the mantle. For the extreme case of a non-breakable mantle, this results in icy bodies drifting starwards to about one half of the classical snowline position. However, the presence and formation of a global dust mantle on a body embedded in a protoplanetary disk is hindered by collisions with pebble sized objects, because these collisions occur at relative velocities typically leading to net mass loss, i.e. erosion of the uppermost layers of the body. In particular, for bodies smaller than meter-size a dust mantle is highly unlikely to be kept due to the – relative to the total mass – large erosion rates.

Multiple processes were not included and several assumptions were made to obtain the above results. We identified two key processes that could affect our results and which should be addressed in future works:

- Collisions with different sized bodies, mainly stemming from the difference in radial and azimuthal velocities due to gas drag, are frequent for large solid fractions and would mostly lead to erosion. For a model including multiple bodies of different sizes, tracking the thermodynamic evolution of each is necessary to properly estimate the general outcome. A potential approach to reduce the numerical cost is to use the analytic surface sublimation expression for objects with low thermal variability over the course of an orbit (i.e. low eccentricity and inclination).
- Specific water vapor pressures influence sublimation rates and thus the results are sensitive to this. To get fully consis-

tent results, it is required to take the water vapor distribution in the disk, including the contribution of the evaporation bodies, into account.

The approximations of imposing the gas temperature as surface temperature, neglecting frictional heating, and using a simple formula for the radial drift is found justified for all discussed parameters.

Of particular interest for future works is to test and potentially apply the analytic sublimation formula in complete N-body terrestrial planet formation models (as suggested by Coleman & Nelson 2016). This would also include larger than 100 m sized bodies because they could be moved across the snowline by N-body interactions (e.g. scattering or resonant trapping) and bodies on significantly eccentric and inclined orbits for which further research on their thermal evolution is necessary. Furthermore, we did not include different chemical species that could either be present as icy layers on the grains or as clathrates and we leave the treatment of the evolution of bodies at different, potentially observable ice lines to future works. Moreover, the influence of including amorphous water ice and the phase change to crystalline ice along with a model for dust mantle growth including cohesive strength and predicting the properties (pore size, porosity, tortuosity, thickness) of the formed mantle should also be addressed in the future for a complete model.

The presented and proposed steps will help to constrain compositions and available masses for terrestrial planet growth, which will be increasingly required to match the precisions on future observational constraints on planetary compositions.

Acknowledgements. The authors thank the anonymous referee who's comments helped improve the manuscript and Cléa Serpoullier for her early investigative work in the subject. This work has been carried out within the frame of the National Centre for Competence in Research PlanetS funded by the Swiss National Science Foundation (SNSF). The authors acknowledge the financial support from the SNSF under grant 200020_172746.

References

- Adachi, I., Hayashi, C., & Nakazawa, K. 1976, *Progress of Theoretical Physics*, 56, 1756
- Adams, E. R., Seager, S., & Elkins-Tanton, L. 2008, *ApJ*, 673, 1160
- Alibert, Y., Carron, F., Fortier, A., et al. 2013, *A&A*, 558, A109
- Alibert, Y., Mordasini, C., Benz, W., & Winisdoerffer, C. 2005, *A&A*, 434, 343
- Andrews, S. M., Wilner, D. J., Hughes, A. M., Qi, C., & Dullemond, C. P. 2010, *ApJ*, 723, 1241
- Armitage, P. J. 2019, in *From Protoplanetary Disk. to Planet Form.* Saas-Fee Adv. Course 45. Swiss Soc. Astrophys. Astron., ed. M. Audard, M. R. Meyer, & Y. Alibert (Berlin, Heidelberg: Springer Berlin Heidelberg), 1–150
- Baraffe, I., Homeier, D., Allard, F., & Chabrier, G. 2015, *A&A*, 577, A42
- Bell, K. R. & Lin, D. N. C. 1994, *ApJ*, 427, 987
- Belton, M. J. 2015, *Icarus*, 245, 87
- Benz, W. & Asphaug, E. 1999, *Icarus*, 141, 5
- Bernstein, G. M., Trilling, D. E., Allen, R. L., et al. 2004, *Astron. J.*, 128, 1364
- Birnstiel, T., Fang, M., & Johansen, A. 2016, *Space Sci. Rev.*, 205, 41
- Blum, J. 2018, *Sp. Sci. Rev.*, 214, 52
- Bottke, W. F., Brož, M., O'Brien, D. P., et al. 2015, in *Asteroids IV*, ed. P. Michel, F. E. DeMeo, & W. F. Bottke (University of Arizona Press), 701–724
- Bottke, W. F., Durda, D. D., Nesvorný, D., et al. 2005, *Icarus*, 175, 111
- Brin, G. D. & Mendis, D. A. 1979, *ApJ*, 229, 402
- Carman, P. C. 1956, *Flow of Gases Through Porous Media* (London: Butterworths Scientific Publications)
- Chambers, J. 2008, *Icarus*, 198, 256
- Cieza, L. A., Casassus, S., Tobin, J., et al. 2016, *Nature*, 535, 258
- Coleman, G. A. L. & Nelson, R. P. 2016, *MNRAS*, 457, 2480
- D'Angelo, G. & Podolak, M. 2015, *ApJ*, 806, 203
- Davidsson, B. J. & Skorov, Y. V. 2002, *Icarus*, 159, 239
- Delsemme, A. & Miller, D. 1971, *Planet. Space Sci.*, 19, 1229
- Desch, S. J., Estrada, P. R., Kalyaan, A., & Cuzzi, J. N. 2017, *ApJ*, 840, 86
- Dohnanyi, J. S. 1969, *J. Geophys. Res.*, 74, 2531
- Dorn, C., Khan, A., Heng, K., et al. 2015, *A&A*, 577, A83

- Drążkowska, J. & Alibert, Y. 2017, *A&A*, 608, A92
- Eistrup, C., Walsh, C., & van Dishoeck, E. F. 2016, *A&A*, 595, A83
- Fanale, F. P. & Salvail, J. R. 1987, *Icarus*, 72, 535
- Fernández, J., Tancredi, G., Rickman, H., & Licandro, J. 1999, *A&A*, 352, 327
- Fernández, J. A. & Morbidelli, A. 2006, *Icarus*, 185, 211
- Fernández, Y., Kelley, M., Lamy, P., et al. 2013, *Icarus*, 226, 1138
- Fortier, A., Alibert, Y., Carron, F., Benz, W., & Dittkrist, K.-M. 2013, *A&A*, 549, A44
- Fray, N. & Schmitt, B. 2009, *Planet. Space Sci.*, 57, 2053
- Gillon, M., Triaud, A. H. M. J., Demory, B.-O., et al. 2017, *Nature*, 542, 456
- Gladman, B. J., Davis, D. R., Neese, C., et al. 2009, *Icarus*, 202, 104
- Goldreich, P. & Tremaine, S. 1979, *ApJ*, 233, 857
- Greenberg, J. M. 1988, in *Dust Universe*, ed. M. Bailey & D. Williams, Vol. 1 (Cambridge University Press), 121–143
- Greenzweig, Y. & Lissauer, J. J. 1990, *Icarus*, 87, 40
- Greenzweig, Y. & Lissauer, J. J. 1992, *Icarus*, 100, 440
- Grimm, S. L., Demory, B.-O., Gillon, M., et al. 2018, *A&A*, 613, A68
- Guidi, G., Tazzari, M., Testi, L., et al. 2016, *A&A*, 588, A112
- Hartmann, L. & Kenyon, S. J. 1996, *Annual Review of Astronomy and Astrophysics*, 34, 207
- Hertz, H. 1882, *Annalen d. Physik*, 253, 177
- Hill, G. W. 1878, *Am. J. Math.*, 1, 5
- Huebner, W. F., Benkhoff, J., Capria, M.-T., et al. 2006, *Heat and Gas Diffusion in Comet Nuclei*, Vol. SR-004 (Published for the International Space Science Institute, Bern, Switzerland, by ESA Publications Division, Noordwijk, The Netherlands)
- Hueso, R. & Guillot, T. 2005, *A&A*, 442, 703
- Ida, S. 1990, *Icarus*, 88, 129
- Ida, S. & Guillot, T. 2016, *A&A*, 596, L3
- Ida, S. & Nakazawa, K. 1989, *A&A*, 224, 303
- Inaba, S., Tanaka, H., Nakazawa, K., Wetherill, G. W., & Kokubo, E. 2001, *Icarus*, 149, 235
- Jutzi, M., Michel, P., Benz, W., & Richardson, D. C. 2010, *Icarus*, 207, 54
- Klinger, J. 1981, *Icarus*, 47, 320
- Knudsen, M. 1909, *Annalen d. Physik*, 333, 75
- Kossacki, K. J. & Szutowicz, S. 2006, *Planet. Space Sci.*, 54, 15
- Krijt, S., Ormel, C. W., Dominik, C., & Tielens, A. G. G. M. 2015, *A&A*, 574, A83
- Lethuillier, A., Le Gall, A., Hamelin, M., et al. 2016, *A&A*, 591, A32
- Lichtenberg, T., Golabek, G. J., Gerya, T. V., & Meyer, M. R. 2016, *Icarus*, 274, 350
- Lichtenegger, H. & Kömle, N. 1991, *Icarus*, 90, 319
- Lynden-Bell, D. & Pringle, J. E. 1974, *MNRAS*, 168, 603
- Makino, J., Fukushima, T., Funato, Y., & Kokubo, E. 1998, *New Astron.*, 3, 411
- Marboeuf, U. & Schmitt, B. 2014, *Icarus*, 242, 225
- Marboeuf, U., Schmitt, B., Petit, J.-M., Mousis, O., & Fray, N. 2012, *A&A*, 542, A82
- Marboeuf, U., Thiabaud, A., Alibert, Y., Cabral, N., & Benz, W. 2014, *A&A*, 570, A35
- Marcy, G. W., Isaacson, H., Howard, A. W., et al. 2014, *Astrophys. J. Suppl. Series*, 210, 20
- Mekler, Y., Prialnik, D., & Podolak, M. 1990, *ApJ*, 356, 682
- Merk, R. & Prialnik, D. 2003, *Earth. Moon. Planets*, 92, 359
- Morbidelli, A. & Rickman, H. 2015, *A&A*, 583, A43
- Nakagawa, Y., Sekiya, M., & Hayashi, C. 1986, *Icarus*, 67, 375
- Nakamoto, T. & Nakagawa, Y. 1994, *ApJ*, 421, 640
- Nakazawa, K., Ida, S., & Nakagawa, Y. 1989a, *A&A*, 220, 293
- Nakazawa, K., Ida, S., & Nakagawa, Y. 1989b, *A&A*, 221, 342
- Nomura, H., Tsukagoshi, T., Kawabe, R., et al. 2016, *Astrophys. J. Lett.*, 819, L7
- O’Connell, B. M., Mcgloughlin, T., & Walsh, M. 2010, *Biomed. Eng. Online*, 9, 15
- Ohtsuki, K. 1999, *Icarus*, 137, 152
- Ópik, E. J. 1951, *Proc. R. Irish Acad. Sect. A Math. Phys. Sci.*, 54, 165
- Ormel, C. W. & Cuzzi, J. N. 2007, *A&A*, 466, 413
- Pan, M. & Schlichting, H. E. 2012, *ApJ*, 747, 113
- Pätzold, M., Andert, T., Hahn, M., et al. 2016, *Nature*, 530, 63
- Podolak, M., Pollack, J. B., & Reynolds, R. T. 1988, *Icarus*, 73, 163
- Prialnik, D., Benkhoff, J., & Podolak, M. 2004, in *Comets II*, ed. M. Festou, H. U. Keller, & H. A. Weaver (University of Arizona Press), 359–387
- Pringle, J. E. 1981, *Annual Review of Astronomy and Astrophysics*, 19
- Pudritz, R. E., Cridland, A. J., & Alessi, M. 2018, in *Handb. Exopl.*, 1st edn., ed. H. Deeg & J. Belmonte (Springer), 46
- Qi, C., Öberg, K. I., Andrews, S. M., et al. 2015, *ApJ*, 813, 128
- Qi, C., Öberg, K. I., Wilner, D. J., et al. 2013, *Science*, 341, 630
- Rafikov, R. R. 2004, *Astron. J.*, 128, 1348
- Ribas, Á., Merín, B., Bouy, H., & Maud, L. T. 2014, *A&A*, 561, A54
- Rickman, H., Fernandez, J. A., & Gustafson, B. A. S. 1990, *A&A*, 237, 524
- Rogers, L. A. & Seager, S. 2010, *ApJ*, 712, 974
- Ros, K. & Johansen, A. 2013, *A&A*, 552, A137
- Safronov, V. S. 1969, *Evolutsiia doplanetnogo oblaka. (Evolution of the Protoplanetary Cloud and Formation of the Earth and Planets)* (Moscow: Nauka [Translation 1972, NASA TT F-677])
- Schmitt, B., Espinasse, S., Grim, R. J. A., Greenberg, J. M., & Klinger, J. 1989, *Phys. Mech. Cometary Mater.*, 302, 65
- Schoonenberg, D. & Ormel, C. W. 2017, *A&A*, 602, A21
- Schorghofer, N. 2008, *ApJ*, 682, 697
- Schwarz, K. R., Bergin, E. A., Cleeves, L. I., et al. 2016, *ApJ*, 823, 91
- Shakura, N. I. & Sunyaev, R. A. 1973, *A&A*, 24, 337
- Shul’man, L. M. 1972, *Symposium - Int. Astron. Union*, 45, 271
- Sierks, H., Barbieri, C., Lamy, P. L., et al. 2015, *Science*, 347, aaa1044
- Singer, K. N., McKinnon, W. B., Gladman, B., et al. 2019, *Science*, 363, 955
- Stevenson, D. J. & Lunine, J. I. 1988, *Icarus*, 75, 146
- Stewart, S. T. & Leinhardt, Z. M. 2009, *ApJ*, 691, L133
- Takeuchi, T. & Lin, D. N. C. 2002, *ApJ*, 581, 1344
- Tanaka, H., Inaba, S., & Nakazawa, K. 1996, *Icarus*, 123, 450
- Tancredi, G., Fernández, J. A., Rickman, H., & Licandro, J. 2006, *Icarus*, 182, 527
- Thiabaud, A., Marboeuf, U., Alibert, Y., Leya, I., & Mezger, K. 2015, *A&A*, 580, A30
- Thommes, E., Duncan, M., & Levison, H. 2003, *Icarus*, 161, 431
- Veras, D. & Armitage, P. J. 2004, *MNRAS*, 347, 613
- Visser, R., van Dishoeck, E. F., Doty, S. D., & Dullemond, C. P. 2009, *A&A*, 495, 881
- Ward, W. R. 1997, *Icarus*, 126, 261
- Washburn, E. R. 1928, *J. Chem. Educ.*, 5, 96
- Weidenschilling, S. J. 1977, *MNRAS*, 180, 57
- Whipple, F. L. 1972, *From Plasma to Planet*, 211
- Windmark, F., Birnstiel, T., Güttler, C., et al. 2012, *A&A*, 540, A73
- Youdin, A. N. & Lithwick, Y. 2007, *Icarus*, 192, 588
- Zahnle, K., Schenk, P., Levison, H., & Dones, L. 2003, *Icarus*, 163, 263

Appendix A: Radial drift formula

Treating the fastest drifting bodies in protoplanetary disks correctly, might require additional changes to the radial drift formula shown in equation (8). We show here the validity of the assumptions made to derive this form of the equation, i.e. assuming orbit averaged drift $\tau_{\text{drift}} \gg \tau_{\text{orb}}$, neglecting terms quadratic in η , assuming no radial acceleration ($dv_{r,s}/dt = 0$), and setting the particle’s azimuthal speed to Keplerian ($v_{\theta,s} = v_K$) in the derivative term (first term in equation (A.2))⁸. The equations of motion in the disk plane ($v_z = 0$) are (Takeuchi & Lin 2002)

$$\frac{dv_{r,s}}{dt} = \frac{v_{\theta,s}}{r} - \Omega_K^2 r - \frac{\Omega_K}{t_{\text{stop}}} (v_{r,s} - v_{r,g}), \quad (\text{A.1})$$

$$\frac{d}{dt} (rv_{\theta,s}) = -\frac{v_K}{t_{\text{stop}}} (v_{\theta,s} - v_{\theta,g}), \quad (\text{A.2})$$

where the subscript s and g are for the solid body and gas, respectively, and t_{stop} is given by equation (10). For a test, we assumed $v_{r,g} = 0$ and solved the equations of motion numerically. The results can be seen in Fig. A.1 and are compared to the results of the analytical equation (8) with the same initial conditions. After one stopping time has passed (dashed vertical line), the initially Keplerian azimuthal ($v_{\theta,s}(t = 0) = v_K$) speed slowed down to an equilibrium value and the analytical expression (8) reproduces the differential equation results well. The radial drift speed is slowing down because the body moves towards the star ($dr/dt \propto r\eta(r)$). The order of percent difference after equilibration of the azimuthal speed can thus be explained by this non-zero $dv_{r,s}/dt$, which is assumed to be zero to derive equation (8). This difference is small compared to the uncertainties of the other processes treated in this work.

Appendix B: Mass distribution

Before assessing the collision rates, we discuss here briefly the required mass or size distributions of the bodies in the disk. The differential mass distribution $n(m_i)$ is defined such that $n(m_i)dm_i$ is the number of bodies with masses in the interval $[m_i, m_i + dm_i]$. We describe $n(m_i)$ as a power-law with exponent α . Data constraining the mass distribution is mainly available from solar system observations or from theoretical works treating collisional cascades or related effects

⁸ See Takeuchi & Lin (2002) for an instructive derivation of the simplified equations

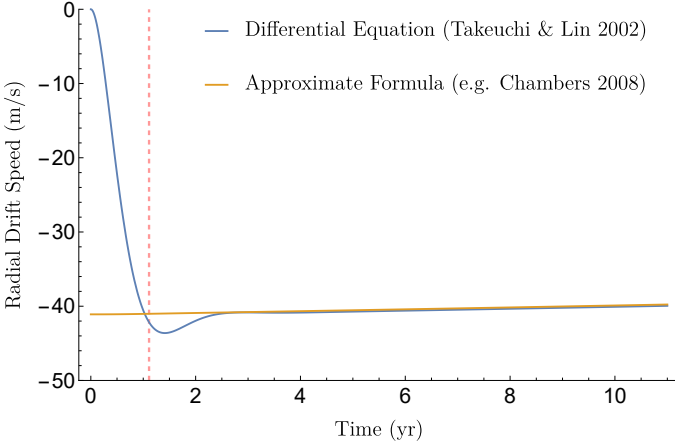


Fig. A.1. Radial drift speed comparison between the approximate equation 8 and the numerical solution to the differential equations. The radius is 1 m, the initial location is at 2 AU, temperature and midplane density are constant over the disk and set to 140 K and $2.5 \times 10^{-10} \text{ g cm}^{-3}$. Initially the body moves with Keplerian speed in azimuthal direction and no radial velocity. The dashed, vertical line marks the stopping time.

(e.g. Dohnanyi 1969; Tanaka et al. 1996; Makino et al. 1998; Benz & Asphaug 1999; Jutzi et al. 2010; Pan & Schlichting 2012; Belton 2015). The observational data is either gathered by direct measurements of Jupiter family comets (e.g. Fernández et al. 1999; Tancredi et al. 2006; Fernández et al. 2013), trans-Neptunian objects (e.g. Bernstein et al. 2004) or asteroids (e.g. Gladman et al. 2009) or inferred from distributions of craters on planets, satellites or other minor planets (Zahnle et al. 2003; Singer et al. 2019). The measured and predicted values of the slope α of the differential mass distribution – assuming a fixed density for converting size distributions – lie in the interval $[-1.5, -2.1]$. We note that multiple studies found different slopes for bodies with radii smaller than km (Zahnle et al. 2003; Fernández & Morbidelli 2006; Fernández et al. 2013; Singer et al. 2019). Nevertheless, we adopt for our order of magnitude estimates simple unbroken power laws with three fixed values for α : the upper (-1.5 as Morbidelli & Rickman 2015) and lower (-2.1 slightly lower than the -2.05 found by Belton 2015) limits and the α resulting from the self-similar solution to the collisional cascade (-1.83, Dohnanyi 1969).

To avoid divergence, the distribution needs to be cut at a lower and an upper boundary. We choose an upper limit to the mass of $1 \times 10^{24} \text{ g}$, corresponding to a radius of 827 km. The lower cut is of particular importance for the resulting collision rates. We choose the typical pebble that can form by coagulation for the lower limit: according to laboratory experiment it has a size of $\sim 1 \text{ cm}$ and a corresponding mass of $\sim 1 \text{ g}$ (Blum 2018). To not underestimate the amount of solids, we assume a 100 % conversion of dust to pebbles and larger bodies.

Appendix C: Collisions

C.1. Orbital collision rate

The averaged number of collisions between a target with mass m_t and a population of bodies with mass m_i per unit time is written as (Nakazawa et al. 1989a; Ohtsuki 1999; Inaba et al. 2001)

$$\langle \Gamma_{\text{col}} \rangle_{ii} = h_{ii}^2 a^2 \Omega_K n_s(m_i) dm_i \langle P_{\text{col}} \rangle_{ii}, \quad (\text{C.1})$$

where $\langle P_{\text{col}} \rangle_{ii}$ is a non-dimensional mean collision rate between bodies with masses m_t and m_i that is independent of the total number of bodies, but depends on the common semi-major axis, the radii and masses of the two bodies, and the mass of the central star. The brackets indicate, that the mean collision rate is an average over all eccentricities and inclinations given by a Reyleigh-type distribution function with eccentricity (inclination) dispersions e^* (i^*), which also influence the mean collision rate (Inaba et al. 2001). $n_s(m_i) dm_i = \Sigma_s / m_i n(m_i) dm_i$ is the surface number density of bodies with masses between m_i and $m_i + dm_i$ with Σ_s the surface density of solids, whereas h_{ii} is the reduced Hill radius of two bodies with masses m_t and m_i given by

$$h_{ii} = \left(\frac{m_t + m_i}{3M_*} \right)^{1/3}. \quad (\text{C.2})$$

For the entire range of realistic eccentricity and inclination distributions, Inaba et al. (2001) found that numerical results are well reproduced if the non-dimensional mean collision rate is set to

$$\langle P_{\text{col}} \rangle = \min \left(\langle P_{\text{col}} \rangle_{\text{med}}, \left(\langle P_{\text{col}} \rangle_{\text{high}}^{-2} + \langle P_{\text{col}} \rangle_{\text{low}}^{-2} \right)^{-1/2} \right), \quad (\text{C.3})$$

where the individual parts are

$$- \langle P_{\text{col}} \rangle_{\text{high}} = \frac{\tilde{r}_p^2}{2\pi} \left(\mathcal{F}(I^*) + \frac{6}{\tilde{r}_p} \frac{\mathcal{G}(I^*)}{(\tilde{e}^*)^2} \right), \quad (\text{C.4})$$

where $I^* \equiv \tilde{i}^* / \tilde{e}^*$,

$$\mathcal{F}(I^*) \equiv 8 \int_0^1 \frac{I^{*2} E[\sqrt{3(1-\lambda^2)}/2]}{[I^{*2} + (1-I^{*2})\lambda^2]^2} d\lambda \quad (\text{C.5})$$

and

$$\mathcal{G}(I^*) \equiv 8 \int_0^1 \frac{K[\sqrt{3(1-\lambda^2)}/2]}{[I^{*2} + (1-I^{*2})\lambda^2]^2} d\lambda, \quad (\text{C.6})$$

where K and E are the complete elliptic integrals of the first and second kinds,

$$- \langle P_{\text{col}} \rangle_{\text{med}} = \frac{\tilde{r}_p^2}{4\pi \tilde{i}^*} \left(17.3 + \frac{232}{\tilde{r}_p} \right) \quad (\text{C.7})$$

$$- \langle P_{\text{col}} \rangle_{\text{low}} = 11.3 \sqrt{\tilde{r}_p}, \quad (\text{C.8})$$

with the reduced eccentricity and inclination dispersions

$$\tilde{e}^* \equiv e^* / h_{ti}, \quad \tilde{i}^* \equiv i^* / h_{ti} \quad (\text{C.9})$$

and

$$\tilde{r}_p \equiv \frac{R_t + R_i}{h_{tia}}. \quad (\text{C.10})$$

C.2. Stokes collision rate

For drifting, small particles we use the "particle in a box" approximation, where the collision rate $\Gamma_{\text{col,ti}}$ of a gravitating target with radius R_t and with a number of impactors with radius R_i is (Safronov 1969)

$$\Gamma_{\text{col,ti}} = n_V(m_i) \pi (R_t + R_i)^2 \Delta v \left(1 + \frac{v_{\text{esc}}^2}{\Delta v^2} \right), \quad (\text{C.11})$$

with the volume number density of impactors $n_V(m_i)$, the relative velocity Δv of the impactors with respect to the target and the mutual escape speed

$$v_{\text{esc}}^2 = 2G \frac{m_t + m_i}{R_t + R_i}. \quad (\text{C.12})$$

To estimate the collision rate, we use the squared sum of the difference in radial (equation (8)) and azimuthal drift velocities of the target and impactors according to their size. The azimuthal difference in velocity is given by $\eta v_k \left| \frac{1}{1+s_t^2} - \frac{1}{1+s_i^2} \right|$, where s_i and s_t are the Stokes numbers of the impactor and the target (Birnstiel et al. 2016). This excludes the additional velocity components due to Brownian motion and turbulence. For a more complete discussion of relative velocities we refer to Ormel & Cuzzi (2007).

The number density of a given size of impactors can be estimated given three ingredients: their mass (or size) distribution discussed above, the density of the gas and the local dust to gas ratio f_{solid} , which is locally enhanced due to dust settling and can for low masses be described by (Youdin & Lithwick 2007; Birnstiel et al. 2016)

$$f_{\text{solid}} = \frac{0.01}{\sqrt{\frac{\alpha_Z}{s+\alpha_Z}}}, \quad (\text{C.13})$$

where s is the Stokes number and α_Z is a dimensionless parameter for turbulent diffusion in the vertical direction. Here, we assumed a global dust to gas fraction of 0.01 and we assume $\alpha_Z \approx \alpha$, which is true on orders of magnitude level (Youdin & Lithwick 2007). For larger than meter-sized bodies the settling is no longer well described by the processes considered in Youdin & Lithwick (2007), since gravitational interactions between the particles become important. Therefore f_{solid} is restricted to be $f_{\text{solid}} \leq 1$ and this maximum is reached at $R_2 \approx 5 \text{ m}$. At meter size, the inclination caused by the viscous stirring of a larger planetesimal in the vicinity of our target leads to approximately the same elevation above the midplane as the reduced scale height (Ida 1990; Thommes et al. 2003; Fortier et al. 2013).

4. Planet formation

4.1. Growth stages

The formation of a planet can be split into different stages of growth. For solid accretion, we already discussed a number of the relevant processes when calculating the distribution of planetesimals and collision rates in Sects. 2.9 and 2.10. From that, it becomes clear that there are multiple stages of solid accretion, depending on which term in equations (2.104) and (2.105) dominates.

The early stage is when the largest of the planetesimals grows. However, it is small enough to not stir the population of planetesimals. Therefore, the self-stirring term in (2.104) dominates and leads to moderately large e_{plts} and i_{plts} . Additionally, the planetesimal population is massive enough to lower the e and i of the largest planetesimals via *dynamical friction* (Stewart & Wetherill, 1988; Ida, 1990), which is a process that is distinct from viscous stirring, acts for different sized planetesimals (which is why we omitted it in the discussion in Sect. 2.9) and drives the system towards equal kinetic energies for each particle. Therefore, dynamical friction will lower the velocity and in turn the e and i of the largest body. This largest body, the *oligarch* or *protoplanet*, will therefore have an orbit close to the midplane of the disk where it has access to a lot of mass for accretion. Thus, it will accrete more mass than smaller planetesimals and its gravitational focusing factor increases which in turn makes it grow even faster. This is called the *runaway solid accretion* stage.

At some point, the protoplanet will become massive enough for the gravitational stirring term in (2.104) to become significant. The larger eccentricities and inclinations of the surrounding planetesimals lead to a slower growth. This second regime is called the *oligarchic growth* stage (Ida & Makino, 1992a,b, 1993). There is still solid accretion occurring, but on a much slower timescale.

Any protoplanet or *planetary embryo* is surrounded by a gaseous envelope. This envelope becomes more massive and contracts as the embryo gains mass. The gas of the envelope interferes with the planetesimals passing through it and decrease the relative velocity of the planetesimal to the embryo. At a certain distance to the embryo, this effect is efficient enough to force the planetesimal to spiral towards the embryo and be accreted instead of passing by. Therefore, the capture radius is increased compared to a body of the same mass but without a gaseous envelope (Inaba & Ikoma, 2003; Ormel & Klahr, 2010). When following the prescription by Inaba & Ikoma (2003), we find that the increase of the capture radius is already significant when the planet has a mass on the order of M_{\oplus} .

At embryo masses $\sim 10 M_{\oplus}$, gas accretion becomes very significant and the gas

mass is comparable to the accreted solid mass of the protoplanet. This triggers *runaway gas accretion* (Perri & Cameron, 1974; Mizuno et al., 1978; Mizuno, 1980; Bodenheimer & Pollack, 1986; Pollack et al., 1996).

Already before that, the embryo starts to migrate in the disk, favoring the direction towards the star. There are two main migration regimes, *type I* and *type II migration*. They differ by the depth of the gap that the planet carves into the disk structure. The gap is created by the gravitational perturbation of the disk due to the embryo (Crida et al., 2006). If the gap is shallow and the disk profile can be approximated as unperturbed, the planet is in type I migration regime, whereas for clear gaps, the type II regime applies.

In this chapter, we will describe the processes of gas accretion and migration. For a detailed discussion of solid accretion, we refer to Sects. 2.9 and 2.10, where collision rates are discussed. The collision rate can be used directly as a solid accretion term when assuming perfect merging of the bodies. We would like to point out that a complete review of planet formation is out of the scope of this work. Therefore, we will focus on outlining the major processes which are required to interpret the outcome of planet formation models and planetary population syntheses (Chapter 5).

4.2. Envelope structure

The amount of gas that can be accreted by a planetary embryo is very closely linked to the structure of the gaseous envelope surrounding the planet. There is a supply of gas provided by the disk, which could in principle be pulled into the region where the protoplanet's gravity dominates compared to the stellar gravity. This region is called the *Hill sphere* and Hill radius describing the size of the Hill sphere is for negligible eccentricities

$$R_{\text{H}} = a \left(\frac{M}{3M_{\star}} \right)^{1/3}, \quad (4.1)$$

for the case of a planet with mass M in orbit around a star with mass M_{\star} and semi-major axis a .

However, the gas in the Hill sphere of the planet has to contract to allow for new gas from the disk filling up the freed spherical shell. In order for the envelope to contract, it has to cool by radiating away energy. Therefore, it is clear that the mass and energy transport equations have to be solved for the envelope structure to determine how much gas can be accreted. In the following we present the spherically symmetric case in hydrostatic equilibrium. However, numerical models show that there are quite a number of non-symmetric effects and gas flows (Szulágyi et al., 2016).

4.2.1. Governing equations

The internal structure of the gaseous envelope of the planet is governed by the following set of equation, which is very similar to the stellar structure equations (e.g. [Bodenheimer & Pollack, 1986](#)):

- Mass conservation

$$\frac{\partial m}{\partial r} = 4\pi r^2 \rho, \quad (4.2)$$

where $m(r)$ is the total mass interior to the radius r and $\rho(r)$ is the local density;

- hydrostatic equilibrium

$$\frac{1}{\rho} \frac{\partial P}{\partial r} = -\frac{Gm}{r^2}, \quad (4.3)$$

where $P(r)$ is the pressure and G is the gravitational constant;

- energy conservation

$$\frac{\partial L}{\partial r} = 4\pi r^2 \rho \left(\epsilon - P \frac{\partial V}{\partial t} - \frac{\partial E}{\partial t} \right), \quad (4.4)$$

where $L(r)$ is the luminosity, $\epsilon(r)$ is a local energy source, $V = 1/\rho$ and E is the internal energy per unit mass;

- radiative transfer

- given in convective regions – with effective convection – by the adiabatic gradient

$$\frac{\partial T}{\partial r} = \frac{T}{P} \left(\frac{d \ln T}{d \ln P} \right)_s, \quad (4.5)$$

where the subscript s denotes that the entropy is fixed when calculating the gradient,

- or approximated as diffusion when the structure is radiative

$$\frac{\partial T}{\partial r} = -\frac{3}{4ac} \frac{\kappa_R \rho}{T^3} \frac{L}{4\pi r^2} = -\frac{3\kappa_R \rho L}{64\pi\sigma T^3 r^2}, \quad (4.6)$$

where $T(r)$ is the temperature, c is the speed of light, $a = 4\sigma/c$ is the radiation density constant, $\kappa_R(r)$ is the Rosseland mean opacity of the dust and gas mixture (following [Bell & Lin, 1994](#), but the dust opacity is multiplied by a reduction factor $f_{\text{opa}} = 0.003$ as found by [Mordasini, 2014](#));

- and an equation of state ([Saumon et al., 1995](#)) linking ρ, T , and P and providing an adiabatic gradient.

To determine if the structure is convective or radiative, we check for stability using the *Schwarzschild criterion*: if the adiabatic gradient (equation 4.5) is larger than the radiative gradient (equation 4.6), then the structure is stable. Therefore, no convection can occur and radiation is assumed to dominate the overall energy transport (neglecting heat conduction). We note, that the Schwarzschild criterion is only accurate if no compositional gradient is present. Otherwise, the *Ledoux criterion* should be used instead (see e.g. [Kippenhahn et al., 2012](#)).

For practical reasons, the equations are often written in terms of the mass m instead of the radius r , yielding

$$\frac{\partial r}{\partial m} = \frac{1}{4\pi r^2 \rho} \quad (4.7)$$

$$\frac{\partial P}{\partial m} = -\frac{Gm}{4\pi r^4} \quad (4.8)$$

$$\frac{\partial L}{\partial m} = \epsilon + \frac{P}{\rho^2} \frac{\partial \rho}{\partial t} - \frac{\partial E}{\partial t} \quad (4.9)$$

$$\frac{\partial T}{\partial m} = \begin{cases} \frac{3}{16\sigma} \frac{\kappa_R}{T^3} \frac{L}{16\pi^2 r^4} & \text{for the radiative part} \\ \frac{T}{4\pi r^2 \rho P} \frac{d \ln T}{d \ln P} & \text{for the convective part} \end{cases} \quad (4.10)$$

A major simplification to the equations can be made: All the incoming energy can be deposited at the core-envelope boundary. For the solid accretion luminosity, this is equivalent to assuming that solid bodies reach the core-envelope boundary without slowing down in the gaseous envelope. This is a justifiable approximation for relatively large planetesimals and small envelopes. Additionally, we can assume that when the envelope is contracting, the gained energy is also released at the core-envelope boundary instead of locally. This is not exact but most of the contraction energy originates from the deep interior ([Mordasini et al., 2012c](#)).

Thanks to these assumptions, the luminosity $L(r)$ has to become constant in r ([Mordasini et al., 2012c](#)). Even without the simplifications, the equations can be solved numerically. However, this is not trivial, mainly due to boundary conditions being given at the core-envelope boundary ($L, m = M_{\text{core}}$ or $r = R_{\text{core}}$) as well as at the outer boundary of the structure (T, P). Therefore, a *shooting method* can be employed which iterates over assumed T and P at the core-envelope boundary until the outer temperature and pressure are well enough matched (inside-out) or the inverted outside-in approach where the total radius or mass and the luminosity are guessed. These schemes are quite time-consuming but it is not infeasible with present-day computing power. A significant speed-up is possible if the luminosity at the outer boundary is given instead of having to guess it. This is achieved by the constant luminosity assumption.

4.2.2. Boundary conditions

In the Bern model, we use the outside-in approach with constant luminosity; therefore the outer radius has to be specified. Following [Lissauer et al. \(2009\)](#); [Helled et al.](#)

(2014), we do not simply use the total Hill radius R_H but a reduced radius due to gas flow geometry around the embryo

$$R_{\text{tot}} = \frac{GM}{c_s^2 + \frac{aGM}{4} \left(\frac{3M_*}{M}\right)^{1/3}}. \quad (4.11)$$

At this location, the outer boundary conditions have to be given. For the temperature we set

$$T(R_{\text{tot}})^4 = T_{\text{disk}}^4 + \frac{3\tau(R_{\text{tot}})L(R_{\text{tot}})}{8\pi\sigma R_{\text{tot}}^2}, \quad (4.12)$$

where $\tau(R_{\text{tot}}) = \max(\kappa_R(\rho_{\text{disk}}, T_{\text{disk}})\rho_{\text{disk}}R_{\text{tot}}, 2/3)$ (Mordasini et al., 2012c). The second term is the increase of the temperature due to the luminosity of the planet itself. It has to be hotter than the surrounding disk to obtain a net decrease in energy and can be found by solving the radiative transfer equation in the radiative diffusion limit assuming constant luminosity (Bodenheimer et al., 2000). If the expression $\kappa_R\rho_{\text{disk}}R_{\text{tot}} < 2/3$, the expression reduces to the temperature of a black body with a given luminosity $T^4 = \frac{L}{4\pi\sigma R_{\text{tot}}}$.

The boundary condition for the pressure $P(R_{\text{out}})$ differs depending on the accretion phase (attached, detached phase). We state them below.

4.2.3. Maximum gas accretion

There is not an infinite amount of gas that can be accreted by a planet over a given timespan. This limit is called the maximum gas accretion rate $\dot{M}_{\text{g,max}}$.

Early models used the viscous flow as a limit (equation 2.27); thus

$$\dot{M}_{\text{g,max}} = 3f_{\text{Lub}}\pi\nu\Sigma, \quad (4.13)$$

with a factor f_{Lub} introduced as the accretion efficiency by Lubow et al. (1999). They found values of f_{Lub} above unity because of gradients introduced by the planet but a clear decrease for planets with masses above $1 M_{\text{Jup}}$ (see also Veras & Armitage, 2004). A non-linear expression arises because the planet perturbs the disk in the vicinity leading to complicated flow patterns depending on the mass ratio of the planet to the disk as well as gradients present in the disk.

In Brügger et al. (2020) (Paper II), we use equation (4.13) with $f_{\text{Lub}} = 1$ for simplicity. In Letter II, Paper III, and the NGPPS series, we use a slightly modified approach based on Mordasini et al. (2012c) described in detail in Emsenhuber et al. (submitted). For this approach, a key quantity is the ratio of the planetary radius R_{tot} to the scale height of the disk h (Sect. 2.1). The goal is to estimate how much gas flows through the planetary environment assuming a radially symmetric flow. In the case of a small planet compared to the vertical disk extent $R_{\text{tot}} < h$, a three dimensional flow pattern emerges and the maximum gas accretion rate follows approximately

$$\dot{M}_{\text{g,max,3D}} = \Sigma\pi R_{\text{tot}}^2/hv_{\text{rel}}, \quad (4.14)$$

where we assume that the gas capture cross section follows πR_{tot}^2 and that the local gas density is given by Σ/h . The relative velocity between the gas and the planet is $v_{\text{rel}} = \max(\Omega_K R_{\text{tot}}, c_s)$.

The two dimensional cross section is given by $2R_{\text{tot}}$, therefore

$$\dot{M}_{\text{g,max,2D}} = 2R_{\text{tot}}\Sigma v_{\text{rel}}. \quad (4.15)$$

Finally, the smaller of $\dot{M}_{\text{g,max,2D}}$ and $\dot{M}_{\text{g,max,3D}}$ is adopted as the limit of gas accretion. For in-depth discussion and more updated expressions for the maximum gas accretion rate we refer to [Mordasini et al. \(2012c\)](#); [Mordasini \(2018\)](#); [Machida et al. \(2010\)](#); [Bodenheimer et al. \(2013\)](#).

4.2.4. Attached phase

As long as the planetary envelope is in contact with the protoplanetary disk, this is called the *attached phase*. During this early stage, there is enough material being provided by the disk to fill up the region within R_{tot} . This implies that the gas accretion rate determined by solving the structure equations (Sect. 4.2.1) \dot{M} is lower than $\dot{M}_{\text{g,max}}$.

In this case, the pressure at R_{tot} is given by the disk pressure P_{disk} because the envelope-disk system is one single fluid.

A very useful quantity to estimate the gas accretion rate during the attached phase is the Kelvin-Helmholtz timescale. It describes the characteristic time over which a gravitationally bound body loses its energy. It is defined as

$$\tau_{\text{KH}} = \frac{E_{\text{grav}}}{L_{\text{tot}}} = \frac{GM^2}{R_{\text{tot}}L_{\text{tot}}} \quad (4.16)$$

and gives a timescale for accretion in the attached phase.

From this expression, we see that as long as solid accretion $\dot{M}_{\text{s,acc}} \propto \Sigma_s R_H^2$ (see Sect. 2.10) dominates the luminosity $L \propto GM\dot{M}_{\text{s,acc}}/R_{\text{core}}$, the Kelvin-Helmholtz timescale scales moderately with the planetary mass $\tau_{\text{KH}} \propto M^{1/3}$. Therefore, the accretion of gas would be slowed down. However, either the planetesimal supply can drop or the gas accretion can become the dominant term. Once solid accretion does not provide enough energy input to heat the planetary structure, runaway gas accretion will occur. For typical disk conditions, the crossover or critical mass M_{cr} when this occurs is similar to $10 M_{\oplus}$ (e.g. [Piso & Youdin, 2014](#)).

4.2.5. Detached phase

Once $\dot{M} > \dot{M}_{\text{g,max}}$, the planet goes to the *detached phase* ([Bodenheimer et al., 2000](#)). Physically, the disk is not able anymore to provide the gas that could be accreted by cooling. This implies that the gas accretion is fixed to what the disk can provide $\dot{M}_{\text{g,max}}$.

Additionally, this means that the outermost radius of the envelope structure is no longer in contact with the disk. Therefore, we adapt the outer boundary condition of the pressure, which now reads as

$$P(R_{\text{tot}}) = P_{\text{disk}} + P_{\text{edd}} + P_{\text{ram}} + P_{\text{rad}}, \quad (4.17)$$

where

$$P_{\text{edd}} = \frac{2GM}{3\kappa R_{\text{tot}}^2} \quad (4.18)$$

is the Eddington pressure accounting for gas above the $\tau = 2/3$ surface. An additional term

$$P_{\text{ram}} = \frac{\dot{M}_{\text{g,acc}}}{4\pi R_{\text{tot}}^2} v_{\text{ff}} \quad (4.19)$$

is caused by the ram pressure of the supersonic gas that falls onto the surface of the embryo with free-fall velocity $v_{\text{ff}} = 2GM \left(\frac{1}{R_{\text{tot}}} - \frac{1}{R_{\text{H}}} \right)$. Finally, the radiation pressure is taken into account

$$P_{\text{rad}} = \frac{2\sigma T^4(R_{\text{tot}})}{3c}, \quad (4.20)$$

where c is the speed of light in vacuum. As soon as the disk is gone, the temperature at R_{tot} has to include the equilibrium temperature due to stellar irradiation (see [Emsenhuber et al. \(submitted\)](#) for details). We note that [Papaloizou & Nelson \(2005\)](#) do take their values for the outer boundary at $\tau = 0.5$, whereas the $\tau = 2/3$ surface is considered here which introduces a factor of order unity and neither [Papaloizou & Nelson \(2005\)](#) nor [Bodenheimer et al. \(2013\)](#) add the usually negligibly small radiation pressure term P_{rad} ($\lesssim 10^{-2}$ barye).

4.3. Orbital migration

A growing protoplanet and the protoplanetary disk in which it is embedded do not ignore each other. Instead, they gravitationally interact. To first order, the planet excites a density wave in the disk at the location of the *Lindblad* resonance and clears a gap in the disk ([Goldreich & Tremaine, 1979](#); [Lin & Papaloizou, 1979](#); [Ward, 1986, 1997](#)). The gap can be maintained if the angular-momentum transport due to the disk viscosity is smaller than the angular-momentum transport due to the planet ([Bryden et al., 1999](#); [Lin & Papaloizou, 1993](#); [Crida et al., 2006](#)).

In the case of a distinct gap that was caused by supersonic wakes ([Masset, 2001](#)), *type II* migration applies, which we describe in Sect. 4.3.2. If the planet has an insufficient mass to excite the wake enough to get shocks, it can still migrate and its migration is classified to be in the *type I* regime (Sect. 4.3.1).

The criterion at which planet to star mass ratio q the gap becomes distinct is approximately ([Lin & Papaloizou, 1993](#))

$$q > 40\nu/r^2\Omega \quad (4.21)$$

and

$$q > 3 \left(\frac{h}{r} \right)^3, \quad (4.22)$$

where h is the scale height and ν is the viscosity of the disk. The numerical factors in (4.21) and (4.22) are nowadays found numerically e.g. in [Bryden et al. \(1999\)](#) by hydrodynamical simulations of the gas flow around massive (accreting) planets. The former equation originally stems from equating the angular-momentum flux by the planet and by the disk viscosity, whereas the second criterion comes from considerations in the vertical direction of the disk (see [Lin & Papaloizou, 1993](#)).

[Crida et al. \(2006\)](#) merge the two criteria into a single one. They use the ratio of the scale height to the Hill radius instead of the disk aspect ratio and re-determine the values to give

$$\frac{3h}{4R_H} + \frac{50\nu M_\star}{Ma^2\Omega_K} \leq 1. \quad (4.23)$$

In the following, we use equation (4.23) to determine if a gap has opened. Additionally, the value of the expression on the left hand side is used to smoothly transition from the type I to type II regime. We would like to point out that [Ida et al. \(2020\)](#) propose an updated, more simple, generalized prescription for both, type I and type II migration.

Formally, we recall that whenever a torque $\vec{\Gamma} = \vec{r} \times \vec{F}$ acts on a planet in a circular Keplerian motion with angular momentum $J = M\sqrt{GM_\star a}$, we obtain from $dJ/dt = \Gamma$

$$\frac{da}{dt} = \frac{2a\Gamma_{\text{tot}}}{J}, \quad (4.24)$$

where Γ_{tot} is the azimuthal component of the total torque. Thanks to this relation, the question of finding the radial motion of a planet reduces to the problem of determining the acting torques.

4.3.1. Type I

For type I migration, it is useful to define the quantity

$$\Gamma_0 = \left(\frac{Ma}{M_\star h} \right)^2 \Sigma a^4 \Omega_K, \quad (4.25)$$

which is an overall factor describing any torque acting on a planet in the type I regime ([Paardekooper et al., 2010, 2011](#)). Then, factors to scale Γ_0 can be found numerically for the cases of the Lindblad or *wake* torque ([Ward, 1997](#); [Tanaka et al., 2002](#)) and the *horseshoe drag* or *co-rotation* torque. As a very broad estimate, a migration timescale can be obtained by using $\Gamma_{\text{tot}} = \Gamma_0$ in equation (4.24). This is roughly equal to M/M_\star in years at 1 au ([Baruteau et al., 2014](#)).

The Lindblad torque stems from the gravitational pull of the overdensity of gas in the wave-like pattern just in front of and just behind the planet ([Goldreich & Tremaine, 1979](#); [Ward, 1986](#)). The gas in the wake that extends radially inwards

moves on near-Keplerian orbits, therefore it leads the planet; whereas the outer wave trails behind the planet. Hence, the inner wave exerts a positive torque on the planet, which would azimuthally accelerate the planet and move it further out and the outer wake would do the opposite. Due to the geometry of the disk, the outer wake usually exerts a larger torque, which leads to a net inwards movement of the planet. However, this conclusion depends on the radial temperature and surface density profile (for a recent descriptive review, see [Baruteau et al., 2016](#)).

The co-rotation torque stems from gas on very similar orbital separations to the planet. Gas in this region has a slightly larger (smaller) angular velocity compared to the planet if it is on an orbit with slightly lower (larger) orbital distance. Therefore, a parcel of gas approaches the planet until it reaches a location close to a Hill sphere behind (in front) of the planet. There, the gravitational pull of the planet moves it outwards (inwards) to an orbital separation larger (smaller) than the planet's orbital separation. This interaction leads to a negative (positive) torque on the planet. From this, it becomes clear that two very similar contributions from the inwards U-turn and the outwards U-turn emerge. Therefore, the sign of the torque can change depending on which region gives rise to the larger angular-momentum exchange. The analysis depends on the temperature and density gradient across the co-rotation region as well as the turbulence on this scale which might be realistically modeled using the α -viscosity for the disk evolution (Sect. 2.3.2). The detailed analysis shows that outward migration is favored ([Paardekooper et al., 2010, 2011](#); [Kley & Nelson, 2012](#); [Baruteau et al., 2014, 2016](#), and references therein).

For planet formation, the co-rotation torque has the impact of potentially keeping the planets at large enough orbits to grow more heavy than when only the fast, inward migration due to the Lindblad torque was acting. However, the co-rotation torque *saturates* at a certain planetary mass. This means that the gradients in the horseshoe region cannot be replenished; therefore no net torque results. An estimate can be made at which point this happens when comparing the viscous diffusion timescale t_ν and the thermal diffusion timescale t_d to the libration timescale t_{lib} . We consider a co-rotation region with width ([Paardekooper et al., 2011](#), omitting a factor of order unity)

$$r_{\text{co}} \approx \frac{a}{\gamma^{1/4}} \sqrt{\frac{Ma}{M_\star h}}, \quad (4.26)$$

where γ is the adiabatic index. Then, the timescales are ([Hellary & Nelson, 2012](#))

$$t_\nu = r_{\text{co}}^2/\nu, \quad t_d = r_{\text{co}}/D, \quad t_{\text{lib}} = \frac{8\pi a}{3\Omega_{\text{K}} r_{\text{co}}}, \quad (4.27)$$

where

$$D = \frac{4\sigma T^3}{3\kappa\rho^2} \frac{(\gamma - 1)\mu m_H}{k_B}. \quad (4.28)$$

Thus, if $t_\nu > t_{\text{lib}} \wedge t_d > t_{\text{lib}}$, the co-rotation torque is saturated and becomes negligible. Because the co-rotation width increases with planetary mass, saturation is bound to happen at some planetary mass, which typically lies around $10 M_\oplus$.

Then, type I migration becomes really rapid because the Lindblad torque increases with $\sim M^2$ (see equations 4.24 and 4.25).

In the population synthesis work presented in chapter 5, we follow the description of Paardekooper et al. (2010, 2011) taking into account viscous and thermal diffusion in the co-rotation region. Additionally, we use the eccentricity and inclination damping from Coleman & Nelson (2014).

4.3.2. Type II

The type II migration regime deals with planets with masses so large that a gap in the disk around them forms, i.e. the surface density of the local disk is dominated by the planet.

The presence of a distinct gap leads to the planet potentially getting locked in position and leading to an orbital evolution coupled to the gas disk. Once a gap has opened, the classical approach is to assume that the planet migrates with the radial velocity of the viscous evolution of the disk (Sect. 2.3.1), which holds for the case if no gas crosses the gap. Therefore, the migration speed can be set to

$$\dot{a} = v_r = -\frac{3\nu}{2a}, \quad (4.29)$$

where the minus sign denotes the direction towards the central star.

The approximation that the planet moves with the viscous gas flow is no longer valid if the planet mass is larger than the disk mass, since the gas flow of the disk can then be slowed down significantly instead of pushing the planet. Ida & Lin (2004a) propose to use another migration rate, that does hold for larger q . Their approach is to set the angular-momentum transport across the gap $\frac{1}{2}M_p\Omega_{K,p}a\dot{a}$ to the angular-momentum transport due to the viscous evolution in the disk $\dot{J}_{\text{vc}} = \frac{3}{2}\Sigma_{\text{vc}}\nu_{\text{vc}}\Omega_{K,\text{vc}}r_{\text{vc}}^2$, evaluated at the radius of maximum viscous couple r_{vc} , i.e. the distance to the star at which the radial gas flow changes sign. Thus, they derive a migration speed of

$$\dot{a} = \text{sign}(a - r_{\text{vc}}) \frac{3\Sigma_{\text{vc}}\nu_{\text{vc}}r_{\text{vc}}^2\Omega_{K,\text{vc}}}{M_p a \Omega_{K,p}}, \quad (4.30)$$

where we introduced the sign function to indicate that the planet moves towards the star as long as $a < r_{\text{vc}}$. A common modern simplification is to evaluate the angular-momentum transport \dot{J} at the location of the planet as well to get

$$\dot{a} = \frac{3\Sigma\nu a}{M_p}. \quad (4.31)$$

Dittkrist et al. (2014) merged the two extremes and take the non-equilibrium flow of the disk into account. We follow this approach in the following to determine the type II migration rates. It is noteworthy, that this prescription is similar to the newer work of Kanagawa et al. (2018), but does not account for the aspect ratio h/r of the disk.

4.4. N-body interactions

Although the gravity of the central star is often dominating, planets do also feel the gravitational pull of other planets. In models, this can be accounted for using a semi-analytical prescription to frequent N-body phenomena such as excitation of eccentricities and inclinations, collisions or resonance capture (Ida & Lin, 2010; Ida et al., 2013) or by numerically modeling all gravitational forces (N-body code). We use the second approach using an established N-body code called MERCURY (Chambers, 1999), which is fast enough to allow for modeling up to 100 gravitationally interacting planetary embryos over millions of simulated years.

MERCURY is a *symplectic* integrator, which means that it uses an expansion of the Hamiltonian formulation of the N-body problem and neglects high order terms that include both the gravitational pull of the central star and those of a third body. This can be safely done as long as the pull by the third body is smaller than that of the star. Chambers (1999) solves this issue and decides to switch to an exact numerical scheme for the three-body problem in case of close encounters.

We would like to highlight here two interesting effects that arise because of the gravitational interactions. Of course the overall field of celestial dynamics is much broader and a field as old and established cannot be reviewed here.

4.4.1. Close encounters

By coincidence, two gravitating bodies can get close to each other. Then, they will feel a gravitational pull which can exceed the central stars gravity. Multiple outcomes are possible. First, the two bodies might physically collide. The probability for this to happen is enlarged, because gravity acts to pull them closer to each other. This topic is also discussed for the case of planetesimal collisions and accretion in Sect. 2.10, where a gravitational focussing factor is introduced. The outcome of a collision is another sub-field of astrophysics and usually addressed with the smooth-particle-hydrodynamics (SPH) method (Benz & Asphaug, 1999; Jutzi, 2015). Modern fits of the outcome of such simulations might be used in the future when modeling planet formation (Emsenhuber et al., 2020). Additionally, water might be evaporated in these violent collisions, which should considerably modify the resulting composition of planets (Burger et al., 2018, 2020).

The second possible outcome of a close encounter leads to an acceleration of both bodies. This leads to an increase in the eccentricity and inclination of both bodies. These *scattering* events will modify the semi-major axis of the bodies. However, the sum of the angular momenta

$$J_{\text{sys}} = \sum_k M_k \sqrt{GM_\star a_k} \sqrt{1 - e_k^2} \cos i_k \quad (4.32)$$

of the planets in the system (Laskar, 2000) has to be retained, therefore an increase in semi-major axis generally also leads to an increase in eccentricity and inclination.

In the presence of a gas disk, the eccentricity and inclination can be damped and the planet's orbit will circularize over time. This is a mechanism to transport planets to locations where their growth in-situ would not be possible. Examples are the proposed pathway to form the observed close-in (Weidenschilling & Marzari, 1996) or far-out giant planets (Alibert et al., 2013).

4.4.2. Mean motion resonances

The second effect of N-body interactions is the possibility of planets getting locked in *mean motion resonances*. In general, an orbital resonance describes the state of two gravitating bodies in orbit around a central body, where they regularly interact. The mean motion resonance is a type of resonance, where the bodies get into each other's vicinity because the ratio of their orbital periods is close to a small integer n . Then, the planets will meet every n orbits of the outer planet and gravitationally interact. In case of a stable resonance, this leads to a slight accelerating of the body which "came late" to the meeting point, whereas it leads to a deceleration of the early planet. Therefore, the system stabilizes. The periods do not have to be an exact integer ratio, but thanks to the stabilization mechanism, the configuration can oscillate (*librate*) around the point of exact resonance.

Mean motion resonances exist in the Solar System among the Jupiter moons or the asteroids and seem to be common in exoplanetary systems (e.g Gillon et al., 2017). For planets, the existence of the resonant systems points towards a formation period where the planets migrated towards each other (convergent migration). Of course the bodies could be assembled in the exact location of the resonance but the probability for this to happen is very low. When migrating, they get trapped in the resonance as long as the push they receive from the body is strong enough to revert the migration they underwent in the n orbits. This allows to estimate the speed of migration from the order of the resonance. If migration was very slow, a planet migrating from very far out in the system would have been captured in the outermost resonance, practically speaking the 2/1 or even a 3/1 resonance. If resonances closer than that are populated, this means that the push by migration was strong enough to overcome at least the 2/1 resonance. Studies making use of this phenomenon to constrain migration speeds are planned (Rosemary Mardling, private communication).

The effect of mean motion resonances in planet formation with active migration is very substantial. Instead of planets migrating towards the central star, they get trapped in mean motion resonances with each other and then migrate as a resonant convoy or chain. These resonant chains move according to the overall torque divided by the sum of the angular momenta. If a heavy body migrating in the slow type II regime is part of the chain, it will drastically reduce the migration speed of lighter planets in resonance.

However, this theoretically clean pathway seems to be less common in reality or the resonant chains frequently break up after the disk has dissipated because quite few resonant planet pairs have been discovered (Winn & Fabrycky, 2015, and references

therein). Here, we find that models with more embryos (because of their initially closer packing) reduce the frequency of resonant planet pairs and there is a trend of more pairs in systems around low-mass planets. We continue this discussion in [Paper III](#).

5. Planetary population synthesis

5.1. Principle

The planetary population synthesis principle means to start with initial conditions sampled from observed distributions and simulate planetary growth as well as motion which results in a synthetic population of planets. This population is then compared to the observed distribution of exoplanets. If necessary, unconstrained model parameters are changed and the process is repeated until a good statistical match between the synthetic and the observed distribution of exoplanets is found. Early works taking this route were done by [Ida & Lin \(2004a\)](#) and [Mordasini et al. \(2009a\)](#).

With this approach, it is not guaranteed that the parameters found are correct. Nonetheless, what can be learned is which set of parameters can be excluded. For example, [Ida & Lin \(2008\)](#) and [Mordasini et al. \(2009b\)](#) made a strong point of excluding very fast type I migration as found based on linear analysis ([Ward, 1986](#); [Tanaka et al., 2002](#)). It became clear that the migration speed of small planets would be too fast to allow for growth of gas giants. Nowadays, type I migration rates are investigated in more detail including non-linear effects which reduced the overall migration rate [Paardekooper et al. \(2010, 2011\)](#).

Furthermore, if an agreeable fit to the observed population of planets is found and confidence in the model solution is established, tentative predictions about the population of planets in regions of the parameter space that has not yet been explored can be made. [Mordasini et al. \(2009b\)](#) predicted many more rocky planets to be discovered in future missions, which is now clearly confirmed by large surveys (e.g. [Mayor et al., 2011](#); [Thompson et al., 2018](#)).

In this thesis, the planet formation model founded on the basis of works by [Alibert et al. \(2004b\)](#) and [Mordasini et al. \(2009a\)](#), which was updated in [Mordasini et al. \(2012c\)](#), [Alibert et al. \(2013\)](#), [Fortier et al. \(2013\)](#), [Dittkrist et al. \(2014\)](#), and [Jin et al. \(2014\)](#). Reviews can be found in [Benz et al. \(2014\)](#); [Mordasini et al. \(2015\)](#); [Mordasini \(2018\)](#). The relevant physical processes are briefly reviewed in Chapter 4.

In the following, we will provide an overview of both the parameters that can be determined observationally as well as unconstrained parameters. The list is not supposed to be complete to the last detail; only the most relevant parameters are mentioned.

5.2. Randomized initial conditions

In order to statistically compare model results to observations, a distribution has to be given for the initial parameters of a system. Then, random variables can be drawn and enough systems have to be simulated to properly sample the overall parameter space.

The most important parameters to describe a disk are arguably the contained masses of both the dust M_{dust} and the gas M_{gas} . The combined dust and mm- to cm-sized pebble mass can be inferred from radio-astronomy measurements (see Sect. 1.4.6). Surveys of young stellar clusters provide complete distributions of all contained protostars or at least all objects that show accretional signatures in their spectra. To use the masses as initial condition, data from the youngest clusters (Taurus and Lupus) should be used. Alternatively, the distribution of disk masses around objects belonging to Class 0 or Class I can be used (Tychoniec et al., 2018; Williams et al., 2019; Tobin et al., 2020). The latter option should be preferred because the Class II objects in Lupus or Taurus could still be a few Myr old since models estimate their cluster ages to range from 1 Myr to 3 Myr. Therefore, despite some leftover infall onto the disk that is not modeled in our work, the masses of disks around Class I objects were used Tychoniec et al. (2018). We note that the amount of matter which is infalling during Class I is disputed McKee & Ostriker (2007).

As radio astronomy measurements do more readily give constraints on the dust mass of disks, an assumption has to be made to obtain disk gas masses. A good approximation should be to use the overall bulk abundances of refractory elements in stars, that is, the metallicity [Fe/H] of stars (Santos et al., 2003). Using this, a gas disk mass naturally results with some additional scatter. In principle, this is a more consistent way to build up the distribution of the disk masses than what is currently done in Paper III and Brügger et al. (2020) (Paper II), which is to first assume a factor of 100 to convert the dust masses to gas masses following Tychoniec et al. (2018) before multiplying by the measured metallicities to re-compute dust masses.

It is sometimes useful to describe the disk mass using the parameters of the initial disk profile following Andrews et al. (2009) (equation 2.74) by the proportionality factor Σ_0 , the power-law slope β and the exponential cut-off radius R_{out} . The total mass is then (see the derivation in Appendix A.6)

$$M_{\text{gas}} = \frac{2\pi\Sigma_0}{(5.2 \text{ au})^{-\beta}} \frac{r_{\text{out}}^{2-\beta}}{(2-\beta)}. \quad (5.1)$$

Using a randomly drawn M_{gas} , fixed values for β and a observation-informed relation $r_{\text{out}}(M_{\text{gas}}$ then leads to a distribution of Σ_0 . Here, we note that the relation $r_{\text{out}}(M_{\text{gas}})$ should be revised in the future. The relation $r_{\text{out}} \propto M_{\text{gas}}^{1/1.6}$ was found by Andrews et al. (2010) and similar values were confirmed more recently (Andrews et al., 2018b). However, this relation is true for evolved disks of a few Myr in age. At younger stages, the profile could have looked differently. This is why this relation could be relaxed in the future to better match measured accretion rates (see Hart-

mann & Bae, 2018). For now, the measured relation of disk mass to characteristic radius is still used.

Additional parameters that might follow a randomized distribution are the inner disk edge r_{in} and an external photo-evaporation rate \dot{M}_w . We discuss in detail in Paper III the distribution that follows if the stellar rotation rate of young stars is used as a proxy for the inner edge. For the external photo-evaporation rate, the current approach is to tune \dot{M}_w , such that observational lifetime constraints are met (Sect. 1.4.4). In the future, this could be replaced or combined with a distribution of X-ray luminosities (see the discussion in Sect. 2.6).

Last but not least, the initial position of the embryos has to be randomized. For an individual embryo (as in Paper II), we draw the location from a distribution uniform in logarithmic space between the inner disk edge and 40 au. This is kept the same for multiple embryos, but with the additional constraint that they are not injected closer than 10 Hills radii to an already placed embryo (Kokubo & Ida, 1998; Chambers, 2006). In addition, a time for embryo-formation could be drawn randomly. In the works shown here, we always assume a fixed time for embryo formation t_{ini} . In principle, this could be also varied and included in the Monte Carlo variable space.

The initial location r_{ini} drawn from a random distribution introduces a parameter per embryo. Therefore, the Monte Carlo variables we use to describe a system are M_{gas} (in an alternative formulation Σ_0), $[\text{Fe}/\text{H}]$ (or equivalently the dust to gas ratio f_{dg}), r_{in} , \dot{M}_w , and the N different r_{ini} . This results in a $4 + N$ dimensional parameter space, where N is the number of embryos. It is not clear how many embryos should be injected, but realistic numbers are on the order of tens of embryos to study the formation of giant planets (Alibert et al., 2013) and even more if the results should be representative for lower planetary masses. Thus, the parameter space is inherently very multi-dimensional and in principle it is not possible to sample it completely considering that a single simulation (called the *forward model* in the statistical context) takes up to months of CPU time. Instead, we currently assume that a small number of r_{ini} combinations is sufficient to indicate possible results for a given disk.

Future work should and will address this issue with a model for planetesimal (Völkel et al., 2020) and embryo growth (Völkel et al. in prep). It would be desirable to have a deterministic model for embryo placement to reduce the number of required simulations. However, the growth to lunar mass objects is inherently chaotic due to the N-body interactions between the bodies. Therefore, it might be required to keep a certain amount of randomness when determining the initial location of the embryos.

5.3. Fixed parameters

In Sect. 5.2, we already touched on several parameters that might be randomized but are currently fixed. In addition to those, many parameters can be used to describe the physical model. Here, we will not discuss all of them; instead, we give an overview of

the most important parameters for the resulting distribution of planets and reference controversies where applicable.

Number of embryos N

As mentioned above, the initial number of embryos that form in a system is currently not known and might differ significantly between disks. In principle, it should be limited by the available mass in planetesimals. The effect of the choice of the number of embryos is investigated by [Alibert et al. \(2013\)](#) and [Emsenhuber et al. \(submitted\)](#). The findings are consistent and show that for heavier planets, less embryos are required than for low-mass planets.

Embryo-placement time t_{ini}

In reality, it takes time for planetesimals to collide and grow the largest planetesimals into lunar-mass embryos ([Ida & Makino, 1993](#); [Inaba & Ikoma, 2003](#); [Chambers, 2006](#)). However, the starting time of the simulation $t = 0$ is also offset from the time of star formation, which is not an instantaneous process to begin with. We explore the influence of the starting time in [Paper II](#), where we show that it has a small influence on the resulting population in the planetesimal-accretion scenario but a large impact in a pebble-accretion case.

Initial embryo mass M_{ini}

The initial mass of an embryo can be chosen freely in the models. However, it makes sense to start at a stage where more simple analytic descriptions fail and multiple processes and their feedback have to be considered. This is the case at the end of the runaway growth stage [Kokubo & Ida \(1998\)](#); [Chambers \(2006\)](#). In the earlier runaway growth stage, the mass of the embryo is not large enough to significantly excite the planetesimals. Therefore, it is not required to model the feedback and interaction between different embryos and the planetesimal disk. Thus, the end of runaway growth is a reasonable starting point for numerical simulations and the initial embryo mass would be a function of the radial distance from the star ($M_{\text{ini}} \propto (r^2 \Sigma_s)^{3/5}$, [Chambers, 2006](#)). For relatively steep initial solid surface density profiles Σ_s , this results in similar embryo masses at the end of the runaway stage everywhere in the disk, which is in agreement with N-body results ([Weidenschilling, 2000](#)). The typical values are around one lunar mass, which is why we choose $0.01 M_{\oplus}$ or $0.0123 M_{\oplus}$ for the works presented here.

Planetesimal size

A very important quantity for the growth of planets is the typical planetesimal size. For smaller planetesimals, gas drag efficiently damps eccentricities and inclinations which leads to more efficient gravitational focusing onto growing embryos (Sect. 2.10). Therefore, the growth timescale of planets is very sensitive to the planetesimal size. In reality, planetesimals are not given by a single size, but they follow a size distribution also discussed in the appendix of [Paper I](#) and in Sect. 2.9.1. There is a

current controversy on the interpretation of the observed slope in the size distribution of the Kuiper and asteroid belt objects. Some authors argue that it should be close to the primordial distribution (Morbidelli et al., 2009; Cuzzi et al., 2010) but others favor a steep initial slope indicative of the mass being dominated by small objects (Weidenschilling, 2011; Pan & Schlichting, 2012). In any case, impact crater counting on Pluto and Charon (Singer et al., 2019) and planetesimal formation models (Johansen et al., 2012) generally result in planetesimals of large size (~ 100 km). In Paper III, we assumed a planetesimal radius of 300 m, which is tuned and leads to realistic growth timescales (Fortier et al., 2013), whereas in Letter II, we explored larger planetesimal sizes because the effect studied there is not relevant for small sizes.

Viscous α

In Sect. 2.3.2, we discussed potential origins of turbulence leading to viscous $\alpha \sim 10^{-4}$. However, the exact drivers of angular-momentum transport remain controversial. In Paper II, Paper III, and Letter II we chose $\alpha = 2 \times 10^{-3}$ to roughly match observed disk lifetimes (Benz et al., 2014). The effect of varying α was addressed for example in Mordasini et al. (2009b). We would like to stress that the viscosity does not only strongly influence the disk evolution, but also the migration rate of planets, the maximum gas accretion rate, the thermal structure of the disk and therefore also the composition of planets. An especially distinct difference is that for low values, the outward migration regime appearing in certain disk regions for strong co-rotation torques (Paardekooper et al., 2010) vanishes.

Surface density slope of gas β_g and solids β_s

For Paper III and Paper II, we chose different slopes for the solids $\beta_s = 1.5$ compared to the gas $\beta_g = 0.9$ motivated by radial drift of solids and observations (see Sects. 2.8 and 1.4.6). For Letter II, we set $\beta_s = \beta_g = 0.9$. The chosen value for the gas slope is found in observations of typically Class II objects (Andrews et al., 2010, 2018b) but might differ at early stages due to relatively inviscid disks that fail to viscously spread (Hartmann & Bae, 2018). Future works will not require a prescription for β_s thanks to the implementation of a dust transport and growth model (Völkel et al., 2020).

N-Body integration time

Reality would not turn off gravitational forces at some point but in simulations it takes considerable computational time to integrate the evolution of systems of Gyr timescales. Therefore, we stop the integration after 20 Myr in Paper III. Fig. 5.1 highlights that there is a sizable fraction of systems which recently had dynamical instabilities or are in an unstable configuration at the end of the simulation. At least for these systems, the N-body code should run for a longer time. This issue will be addressed and quantified in future work.

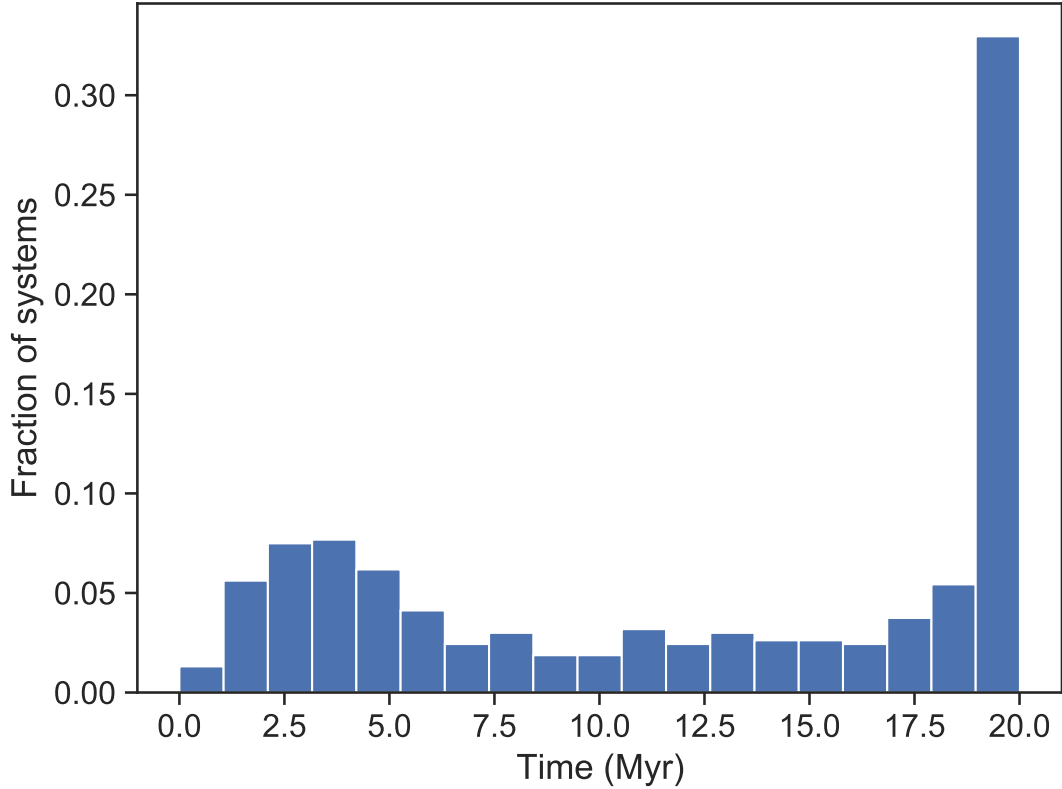


Figure 5.1.: Histogram of latest dynamical instability of systems in a population with 50 embryos around a Solar-mass star (NG75). A dynamical instability is recorded at time t if $|a(t) - a(t - \Delta t)| > a \left(\frac{M_{\max}(t)}{3M_{\star}} \right)^{1/3}$ for any planet in the system. Δt is the timestep and $M_{\max}(t)$ is the mass of the most massive planet in the system. $\sim 65\%$ of the systems did not undergo an instability in the last Myr before the simulation was terminated at 20 Myr. Therefore, it is justified to assume that these systems would remain stable even if the integration time was prolonged. For the others, more changes due to dynamical interactions would likely occur after 20 Myr if the integration continued.

Migration timescale

As mentioned above, the migration timescales, especially the type I migration timescale was discussed in [Ida & Lin \(2008\)](#); [Mordasini et al. \(2009b\)](#). Despite the updated, non-linear torque formulations [Paardekooper et al. \(2010\)](#), type I migration is a very rapid process compared to planetary growth at masses $\sim 10 M_{\oplus}$. Therefore, it is the limiting factor for growth in most cases and a reduction naturally leads to larger planets. Due to the complexity of the planet-disk interactions leading to torques and because of potential structures in the disk, it is possible that our understanding of migration is not complete. Therefore, a reduction factor for migration can be introduced to parametrize our ignorance. This exercise is performed for type I migration (f_I) in the appendix of [Paper III](#).

Disk and envelope opacities

To radiate away energy received from accreting solids and gas is the only way for a growing planet to cool and contract. By contracting, it can trigger more gas accretion. Therefore, the growth of a planet is very sensitive to the amount of energy radiated away, which in turn depends on the opacities (see Sect. 4.2.1). In the interstellar medium, the Rosseland mean opacity is dominated by the opacity of the dust κ_s . However, recent works have highlighted that for planetary envelopes, different grain abundances and sizes can change –and typically reduce – the dust opacity ([Podolak, 2003](#); [Movshovitz & Podolak, 2008](#)). A reduction leads to the energy being radiated away more easily. [Mordasini \(2014\)](#) found a good fit of planetary radii compared to the results of the *Kepler* mission when introducing a reduction factor $f_{\text{opa}} \approx 0.003$ for the Rosseland mean opacity of the dust $\kappa_s = f_{\text{opa}} \kappa_{s,\text{ISM}}$. In the following, we adopt the same value unless stated otherwise.

Retention of impact energy

A quite fundamental unsolved question emerges when treating collisions between embryos with gaseous envelopes. It is not clear, which fraction of the impact energy is brought to the core or distributed in the envelope or directly radiated away. In [Alibert et al. \(2013\)](#), it was assumed that no energy from the impact is kept to heat the envelope structure. As described in [Emsenhuber et al. \(submitted\)](#), we now deposit the full impact energy of the solid core of the impactor at the core-envelope boundary of the target. Reality should lie somewhere between those two extremes and a parameter to describe the amount of energy deposited in the planetary structure of the target should be introduced in the future. This treatment is important because a recently impacted planetary structure might increase its radius drastically and part of the previously bound envelope could become gravitationally unbound. Therefore, this is an additional envelope-loss mechanism which should be compared to long-term photo-evaporative mass loss.

Maximum gas accretion

Multiple works addressed the disk-limited case of gas accretion (Sect. 4.2.3). We use

a very simple estimate in [Paper II](#), where the amount that can be accreted by the growing planets cannot exceed the viscous steady-state flow (equation 2.27). In [Paper III](#) and [Letter II](#), we use the procedure described in [Emsenhuber et al. \(submitted\)](#) which is similar to the description in [Mordasini et al. \(2012c\)](#).

Capture radius

The radius at which planetesimals are captured due to gas drag and spiralling towards the planetary core can be determined from the structure of the envelope ([Inaba & Ikoma, 2003](#)). However, the planetesimal could also break up in the envelope leading to an additional capture radius enhancement ([Podolak et al., 2019](#)). This effect will be studied in the future. In the works presented here, we follow the description of ([Inaba & Ikoma, 2003](#)). We also note that the enhanced capture radius also increases the growth of planets with masses below $1 M_{\oplus}$, despite the envelope being very insignificant in terms of masses. This explains parts of the differences of our results compared to the recent work of [Johansen & Bitsch \(2019\)](#) who did not take into account the capture-radius enhancement.

Partitioning of solids in dust, pebbles, and planetesimals

The metallicity mentioned in the section above can be used to infer the total amount of dust in a disk. After determining this, a conversion factor ε has to be determined of how much of this dust is converted to planetesimals or pebbles. In [Paper II](#), we vary and discuss ε whereas it is set to $\varepsilon = 1$ in the other works. This parameter can also be replaced in the future thanks to the work presented in [Völkel et al. \(2020\)](#). However, a free planetesimal formation efficiency is introduced instead.

Stellar parameters

Not every star is identical. So far, this was hardly explored in population synthesis works, except for the influence of the stellar mass we assume a stellar radius and luminosity that is evolved in time following the relations of ([Baraffe et al., 2015](#)) but does not vary between the individual simulations. However, for example rotation rates and compositions are known to differ for the same stellar mass. This might lead to imprints on the planetary population via the inner cavity size or different X-ray luminosities depending on the rotation rate. In terms of composition, [Letter II](#) addresses the influence of different amounts of the radioactive ^{26}Al and we take the overall metallicity distribution into account. However, varying the overall elemental abundances could also lead to observable imprints on the radius.

5.4. Paper II: Pebbles versus planetesimals: the outcomes of population synthesis models

A new paradigm of core accretion, *pebble accretion*, has been proposed in the last ten years. In [Brügger et al. \(2020\)](#) accepted for publication in A&A ([Paper II](#)),

we compare the outcome of a pebble accretion based (Brügger et al., 2018) and a planetesimal accretion based model, namely the Bern model of planet formation. The approach we take to do this is to draw planetary populations from both models, where we use the exact same randomized disks as a basis. As the goal is not to recreate the observed population of exoplanets, but instead to compare populations, it is justified to use models that include less physical processes. Therefore, adjustments and some simplifications to the full Bern model were made and we give a complete, detailed list of all changes in Sect. 5.4.2 after briefly outlining the principle of pebble accretion in the following section.

5.4.1. Pebble accretion

Since the detailed calculations of the feedback of accreting embryos on the planetesimal population (Ida & Makino, 1993), it is known that planetesimal accretion with large planetesimals is not efficient enough to grow giant planets. One possibility to circumvent the issue is to assume that the planetesimal population is dominated by small \sim km-sized bodies. If the population of bodies would be dominated by meter-sized bodies, they would quickly drift towards the star (Sect. 2.8). Therefore, the minimum size of planetesimals can only be \sim 100 m. However, instead of assuming bodies of sizes above the radial drift barrier, Ormel & Klahr (2010), Ormel & Kobayashi (2012), and Lambrechts & Johansen (2012) investigated the other possibility of a significant fraction (or all, in the case of Lambrechts & Johansen, 2012) of bodies having sizes below the meter-size barrier. This approach was later termed *pebble accretion*. For a recent review, we refer to Johansen & Lambrechts (2017).

The main benefit of a population of small, centimeter-sized bodies, are the very low eccentricities and inclinations that result for these bodies due to damping by the gas and a large increase of the capture radius of the protoplanet (similar to the effect for planetesimals following e.g. Inaba & Ikoma, 2003).

In the paper attached below, led by Natacha Brügger, we compare the outcome using two most prominent core-accretion mechanisms: pebble accretion and planetesimal accretion. This work is in line with the recent work of Coleman et al. (2019), who focused on the Trappist-1 system and the pebble accretion model is an evolved version of the model presented in Brügger et al. (2018). We choose the population synthesis framework but the focus does not lie on synthesizing a population of planets that can be compared to the observed exoplanets. Instead, the differences of populations obtained with reasonably simplified models are investigated. The population synthesis approach is chosen to have a span of realistic conditions for the growth of planets and to naturally explore the parameter space.

5.4.2. Project specific changes to the Bern model of planet formation

The key part of Paper II revolves around consistently using the same disk, migration, and envelope models in both the pebble accretion and the planetesimal accretion

pathways. Therefore, the two codes had to be adjusted to exactly match in these sub-modules. For the nominal Bern model which is used in [Paper III](#) and was developed for a longer time and by multiple people, this led to a number of simplifications. We give here a complete and detailed list of all changes to the code. A more brief summary can be found in the paper below.

For the planetesimal accretion sub-module, no modifications were required because this module differs naturally from the pebble accretion model ([Brügger et al., 2018](#)). However, we implemented the option to replace planetesimal accretion by a fixed solid accretion value used for testing.

Disk

- In [Brügger et al. \(2018\)](#), the overall solid mass is split into pebbles and dust with a pebble fraction of ε . The pebble part can be accreted and we assumed a complete conversion of the pebbles to planetesimals for the comparison project. The dust part $1 - \varepsilon$ is used for the opacity in the disk. Therefore, the disk opacities are reduced linearly with the amount of pebbles or planetesimals removed from the dust ε . This is different and an improvement compared to the nominal calculations of the Bern model, where an additional 1% of the gas mass is assumed to be dust responsible for the disk opacities.
- The direct irradiation term which heats the disk through the midplane was neglected. It is only important at the last stage of the disk clearing and allows for a smooth transition to the evolution stage. However, this stage was not important for this project.
- Gas that is accreted by planets should in principle be removed from the disk. This reduction was neglected here. This is in line with the spirit of not allowing too many feedback processes in this project.
- The solids in the disk consist of either rocky or ice-rock mixtures. The compositional model tracking the elemental abundances and introducing multiple ice-lines from [Thiabaud et al. \(2014\)](#) is turned off for this project.

Stellar model

- While a stellar evolution model is used for the nominal Bern model runs, we use a fixed star in the pebble vs planetesimal comparison project. In the first place, the stellar evolution is important for the long-term evolution, which was turned off in the comparison. Therefore, we do not have to introduce further minor effects to keep the project in the spirit of a as simple as possible but still realistic comparison.

Structure and gas accretion

- The envelope structure modules rely on the disk temperature, surface density or pressure. For these values, we took the values at the location of the planet. In the full model, the values are usually calculated as a mean over the feeding zone. However, this is only significant if the gas surface density is not smooth, which is very rarely the case in the simplified model.
- The density of the solid core of the planets was fixed to 5.5 g cm^{-3} . This replaces the core density model from [Mordasini et al. \(2012c\)](#).
- The numerical scheme to solve the internal structure equations follows the fourth-order Runge-Kutta method. In contrast, the Bulirsch-Stoer method ([Bulirsch & Stoer, 1964](#)) is applied for the structure in the attached phase in the nominal Bern model. This was tested to have a negligible influence on the result, but potentially leads to a minimal loss of performance if using the Runge-Kutta approach.
- The updated radius of the new timestep is used to calculate the luminosity instead of the radius of the previous timestep. This is more precise, but can lead to numerical issues if the boundary conditions change a lot during one timestep. Because we use single planets, a fast change in the ambient conditions does not happen. Therefore, we can employ the more precise luminosity estimate.
- We do not include radioactive decay, which could be added as a small luminosity source. It makes sense to add it when considering the long-term evolution, but for this project it did not play an important role.
- For similar reasons, we exclude deuterium fusion ([Mollière & Mordasini, 2012](#)) for all planets, despite the possibility of forming brown dwarfs-mass objects in extremely massive disks.
- In the detached phase, the outer boundary pressure includes the Eddington and radiation pressure terms (Sect. 4.2.2). For this project, we set them both to zero. Therefore, the only terms for the pressure in the detached case are the disk pressure and the ram pressure of the infalling material.
- The only limit to gas accretion in the detached case is the amount that would viscously flow past the planet in a steady-state disk $\dot{M} = 3\pi\Sigma\nu$. Therefore, neither the non-equilibrium terms and the geometry of the flow, nor the local reservoir are considered ([Mordasini et al., 2012c](#)).
- Whenever a planet has a larger radius than its Hill radius, the gas should in principle become unbound from the planet. This results in a mass-loss. We do not take this effect into account here.

- We account for planetary luminosity heating the surrounding disk (equation 20 [Mordasini et al., 2012c](#)). To do that, we use the disk opacity instead of the reduced planetary envelope opacity. Reality should lie between the two cases, since the opacity in a transition zone between planetary envelope and the disk is relevant.
- The long-term evolution was not calculated in the nominal models, instead the simulation stopped after 20 Myr. For a radius plot, we calculated the long-term evolution with the same code for both models in a post-processing mode. In contrast, in the nominal Bern model, the evolution is always computed consistently in the same model run.

Migration

- In the nominal Bern model, the adiabatic coefficient γ for calculation of the type I migration is taken from the output of the equation of state module. For [Paper II](#), we simply set $\gamma = 1.4$, which is the value for an ideal di-atomic gas.
- Similar to the input from the disk to the envelope structure, the local values for the viscosity ν are taken instead of a mean over a zone spanning from 90 % to 110 % of the distance of the planet to the star.
- We note that there remains a minor difference in the calculation of the gradients $d\Sigma/dr$, and dT/dr used in the migration sub-module: In the pebble code a quadratic interpolation in a region spanning twenty gridpoints in both directions is used, whereas in the adapted and the nominal Bern model a region spanning 10 % of the distance to the star in both regions is used.

Multiple planets

- In the future, a similar comparison will be done using the same two codes as a basis. However, the treatment of collisions has to be matched. We will use the approach of [Alibert et al. \(2013\)](#) and assume a complete loss of impact energies, except if the impact energy is larger than the gravitational binding energy of the envelope, which leads to envelope stripping. However, in contrast to [Alibert et al. \(2013\)](#) the collision detection is implemented directly in the N-body code for which we use the MERCURY code ([Chambers, 1999](#)) for both models.

Pebbles versus planetesimals: the outcomes of population synthesis models

N. Brügger¹, R. Burn¹, G.A.L. Coleman^{1,2}, Y. Alibert¹, W. Benz¹

1. Physikalisches Institut, Universität Bern, CH-3012 Bern, Switzerland

2. Astronomy Unit, Queen Mary University of London, Mile End Road, London, E1 4NS, U.K.
e-mail: natacha.bruegger@space.unibe.ch

Preprint online version: June 9, 2020

ABSTRACT

Context. In the core accretion scenario of giant planet formation, a massive core forms first and then accretes a gaseous envelope. When discussing how this core forms some divergences appear. First scenarios of planet formation predict the accretion of km-sized bodies, called planetesimals, while more recent works suggest growth by accretion of pebbles, which are cm-sized objects.

Aims. These two accretion models are often discussed separately and we aim here at comparing the outcomes of the two models with identical initial conditions.

Methods. The comparison is done using two distinct codes: one computing the planetesimal accretion, the other one the pebble accretion. All the other components of the simulated planet growth are computed identically in the two models: the disc, the accretion of gas and the migration. Using a population synthesis approach, we compare planet simulations and study the impact of the two solid accretion models, focussing on the formation of single planets.

Results. We find that the outcomes of the populations are strongly influenced by the accretion model. The planetesimal model predicts the formation of more giant planets, while the pebble accretion model forms more super-Earth mass planets. This is due to the pebble isolation mass (M_{iso}) concept, which prevents planets formed by pebble accretion to accrete gas efficiently before reaching M_{iso} . This translates into a population of planets that are not heavy enough to accrete a consequent envelope but that are in a mass range where type I migration is very efficient. We also find higher gas mass fractions for a given core mass for the pebble model compared to the planetesimal one caused by luminosity differences. This also implies planets with lower densities which could be confirmed observationally.

Conclusions. We conclude that the two models produce different outputs. Focusing on giant planets, the sensitivity of their formation differs: for the pebble accretion model, the time at which the embryos are formed, as well as the period over which solids are accreted strongly impact the results, while the population of giant planets formed by planetesimal accretion depends on the planetesimal size and on the splitting in the amount of solids available to form planetesimals.

Key words. planetary systems - planetary systems: formation - pebbles - planets: composition

1. Introduction

In the standard giant planet formation theory, the so-called core-accretion model, a core forms first through the accretion of solids and then, if it becomes massive enough, it accretes gas. A crucial constraint for gas accretion is that the core should be massive enough to accrete the gas before the dissipation of the gas disc (Haisch et al. 2001). The first scenarios predict that the solids accreted by the core are planetesimals, which are ~kilometer-sized objects (Pollack et al. 1996; Fortier et al. 2013). Historically the typical radius of planetesimals was 100 km. One problem that arises when using planetesimals of this size, is that the time needed to form a core is typically longer than expected disc lifetimes (Pollack et al. 1996). Forming giant planets is therefore difficult for traditional planet formation models (Coleman & Nelson 2014). Reducing the size of the planetesimals allows however to form cores within typical disc lifetimes (Coleman & Nelson 2016b,a). This time-scale struggle gave birth to a new approach that suggests the accretion of drifting centimeter-sized bodies known as pebbles (Birnstiel et al. 2012). Due to their small size, pebbles are able to be accreted much more easily

through increased gas drag, resulting in a more rapid core formation (Ormel & Klahr 2010; Lambrechts & Johansen 2012).

These two scenarios of solid accretion were recently compared by Coleman et al. (2019) with the aim of examining planet formation around low mass stars akin to the Trappist-1 planetary system. They explored a wide range of initial conditions and found that both scenarios formed remarkably similar planetary systems, in terms of planetary masses and periods, resonances between neighbouring planets, and the general observability of the planets and their respective systems. Whilst Coleman et al. (2019) compared the two scenarios within the frame of the Trappist-1 system, in this paper we focus on solar mass stars and vary some parameters of our model, e.g. the starting time of the embryo or the distribution of the amount of solids. We aim here at comparing the two solid accretion scenarios by using identical initial conditions drawn from a distribution comparable to those used within population synthesis models (e.g. see Mordasini et al. 2015). Using two separate models, one for planetesimal accretion and one for pebble accretion, we examine the outcomes of population of single planet systems. To proceed, we use the same disc model, gas accretion model and migration regimes for both codes. It is important to underline that the two codes are distinct from one another and that this comparison

aims at comparing the outcomes of the two different accretion scenarios and not to achieve a match to observations.

This paper is organised as follows. In Sect. 2 we provide all of the theoretical aspects behind the comparison. We discuss the similarities between the two codes, e.g. the disc model and its evolution, the gas accretion theory and the migration formulae, as well as the two distinct accretion models. To test our implementations we present in Sect. 3 comparisons between the two codes for the common components of the models. The evolution of the disc is discussed, as well as the accretion of gas and the migration regimes. Once the agreement between the two codes is established, the effect of the two solid accretion models can then be compared. Using a population synthesis approach, we compute single planet per disc simulations and study the outcomes in Sect. 4, where we also compare the two modes of solid accretion. Finally, Sect. 5 is dedicated to discussions and conclusions.

2. Theoretical models

We first introduce the disc model, which is common to both accretion models. We then present the planetesimal accretion model, which is an improved version of that presented in Mordasini et al. (2012b); Alibert et al. (2013); Fortier et al. (2013), as well as the pebble accretion model, which is similar to that of Brügger et al. (2018). We then describe another common aspect of the two models: the gas accretion. Finally, we discuss the planet migration.

2.1. Disc model and evolution

The disc model we use is similar to that provided by Hueso & Guillot (2005). The initial gas surface density profile follows (Andrews et al. 2010):

$$\Sigma(r) = \Sigma_0 \left(\frac{r}{5.2 \text{ AU}} \right)^{-\beta} \exp \left[- \left(\frac{r}{r_{\text{out}}} \right)^{(2-\beta)} \right], \quad (1)$$

where Σ_0 is the initial surface density at 5.2 AU and r is the location in the disc, r_{out} is the outer radius of the disc and $\beta = 0.9$. This disc model accounts for observational constraints that are relevant to the disc evolution calculations (stellar properties, disc outer radius and surface density profile or accretion rate). The disc profile is therefore very different from that provided by Bitsch et al. (2015) and used in Brügger et al. (2018), which may lead to different outcomes. For instance the surface density in the outer regions is much lower in the disc used here compared to that of Bitsch et al. (2015).

To calculate the midplane temperature we use a one-dimensional model based on a semi-analytical approach, where we include both stellar irradiation and the dissipation of viscous energy for heating the disc. In the radial direction the disc is assumed to be thick. Heat can therefore be more efficiently transported vertically where the disc can be geometrically thin or thick. Consequently these two regimes are both combined in the midplane temperature T_m determination (Nakamoto & Nakagawa 1994; Hueso & Guillot 2005):

$$T_m^4 = \frac{1}{2\sigma} \left(\frac{3\kappa_R}{8} \Sigma + \frac{1}{2\kappa_p \Sigma} \right) \dot{E}_\nu + T_{\text{irr}}^4, \quad (2)$$

with σ being the Stefan-Boltzmann constant, κ_R the Rosseland mean opacity, κ_p the Planck opacity, Σ the gas surface density of the disc, $\dot{E}_\nu = \frac{9}{4} \Sigma \nu \Omega_K^2$ the viscous energy dissipation rate (Nakamoto & Nakagawa 1994) and T_{irr} the effective temperature

due to stellar irradiation that is a function of the stellar temperature T_* (Adams et al. 1988; Ruden & Pollack 1991; Hueso & Guillot 2005):

$$T_{\text{irr}} = T_* \left(\frac{2}{3\pi} \left(\frac{R_*}{r} \right)^3 + \frac{1}{2} \left(\frac{R_*}{r} \right)^2 \frac{H}{r} \left(\frac{d \ln(H)}{d \ln(r)} - 1 \right) \right)^{1/4}. \quad (3)$$

Here $\Omega_K = \sqrt{\frac{GM_*}{r^3}}$ is the Keplerian frequency, T_* is the star's temperature, R_* is the radius of the star (see Table 1), H the disc scale height and $\frac{d \ln(H)}{d \ln(r)} = \frac{9}{7}$, which is the equilibrium solution for a disc where the flaring term (term containing $\frac{d \ln(H)}{d \ln(r)}$ in the temperature determination (Eq. 3)) is the dominant one (Hueso & Guillot 2005). The vertical structure of the disc can then be derived from Eq. 2, the viscosity ν and the opacity of the disc κ (Bell & Lin 1994), which in our model is scaled with the amount of dust in the disc.

Once the properties of the disc are defined, its evolution follows the standard diffusion equation (Lynden-Bell & Pringle 1974):

$$\frac{\partial \Sigma}{\partial t} = \frac{1}{r} \frac{\partial}{\partial r} \left[3r^{1/2} \frac{\partial}{\partial r} (\nu \Sigma r^{1/2}) \right], \quad (4)$$

where $\nu = \alpha c_s H$ is the viscosity, which is parametrized using the α -viscosity parameter (chosen to be $\alpha = 0.002$) of Shakura & Sunyaev (1973) and the isothermal sound speed c_s .

To obtain realistic disc lifetimes (between 2 and 5 Myr (Haisch et al. 2001)), we use the external photoevaporation model of Matsuyama et al. (2003) and the internal photoevaporation model given by Clarke et al. (2001) with modifications from Alexander & Pascucci (2012). For internal photoevaporation, Clarke et al. (2001) assume a region within which the photoionized gas remains bound to the star. This region is defined by its radius:

$$R_{g,\text{int}} = \frac{GM_*}{c_s}, \quad (5)$$

with c_s being the sound speed of photoionized gas ($T = 1000 \text{ K}$) and M_* the mass of the star (see Table 1). Beyond this radius, material can be lost from the disc at a rate given by (Clarke et al. 2001):

$$\dot{\Sigma}_{w,\text{int}} = 2c_s n_0(r) m_H, \quad (6)$$

where the factor 2 considers the mass loss from both sides of the disc, $n_0(r)$ is the number density at a distance r and m_H is the mass of the hydrogen atom. This corresponds to a total wind mass-loss rate of (Clarke et al. 2001):

$$\dot{M}_{w,\text{int}} = 4.1 \times 10^{-10} \phi_{41}^{1/2} \left(\frac{M_*}{M_\odot} \right)^{1/2} M_\odot \text{yr}^{-1}, \quad (7)$$

where $\phi_{41} = 1$ is the ionizing photon flux of the star in units of 10^{41} s^{-1} .

For external photoevaporation, Matsuyama et al. (2003) predicts that the surface density evaporation rate for radii beyond $R_{g,\text{ext}}$ (same definition as Eq. 5 but with a sound speed given for a temperature of $T = 10^4 \text{ K}$) follows:

$$\dot{\Sigma}_{w,\text{ext}} = \frac{\dot{M}_{w,\text{ext}}}{\pi (R_d^2 - \beta^2 R_g^2)}, \quad (8)$$

where R_d is the disc outer edge ($R_d = 1000 \text{ AU}$ in our test cases, see Table 1), $\beta = R_*/R_g$ and the mass loss rate is given by $\dot{M}_{w,\text{ext}} = 1 \times 10^{-7} M_\odot/\text{year}$ for our test cases (see Table 1 as well).

Regarding the solid components of the disc, the total amount of solids available in the disc Z_{tot} , initially all in the form of dust, is split into a fraction that forms the bodies that can be accreted (either planetesimals or pebbles) while the rest remains as dust, contributing to the disc opacity. The same splitting is applied in both models and the two ratios we investigate are $Z_{\text{peb,plan}} = 0.9 \times Z_{\text{tot}}$ with $Z_{\text{dust}} = 0.1 \times Z_{\text{tot}}$, which we call the $\varepsilon = 0.9$ case, and $Z_{\text{peb,plan}} = 0.5 \times Z_{\text{tot}}$ with $Z_{\text{dust}} = 0.5 \times Z_{\text{tot}}$, which we call the $\varepsilon = 0.5$ case. For our test cases (Sect. 3), we use the $\varepsilon = 0.9$ case following Brügger et al. (2018) and the total fraction of solids to gas is given by $Z_{\text{tot}} = 0.01$ (see Table 1).

Another component that is common to both models is the determination of the ice line. For simplicity we define it as the place in the disc where the temperature is equal to 170 K (Burn et al. 2019). This location therefore depends on the temperature of the disc, which is influenced by the opacity of the disc. The latter is impacted by the amount of solids as well as the ratio ε , since the fraction that remains as dust contributes to the disc opacity. The ice line location has an impact on the pebble size (see Sect. 2.3) and on the composition of the planets (see Sect. 4.3).

2.2. Planetesimal accretion model

The planetesimal accretion model is described in detail in Fortier et al. (2013). The basic principle is to represent planetesimals as a fluid-like disc. The initial profile of the surface density of planetesimal Σ_{pls} is however steeper than the one of the gas (Lenz et al. 2019; Drążkowska & Alibert 2017). The surface density as well as the eccentricity rms e_{pls} and the inclination rms i_{pls} evolve over time. To have a consistent description of e_{pls} and i_{pls} for all planetesimal sizes, we solve the differential equations for self-stirring (e.g. Ohtsuki 1999), the gravitational stirring of planetesimals by forming planets (Ohtsuki 1999) as well as the damping by gas drag (Adachi et al. 1976; Inaba et al. 2001; Rafikov 2004) instead of assuming that equilibrium between stirring and damping is attained instantaneously.¹ We do not take into account the radial drift of planetesimals as it was found to be negligible over the disc lifetime for our chosen radius of 1 km. This approach is valid for particles that decouple from the gas, which typically happens at sizes larger than 100 m (Burn et al. 2019).

The accretion of solids is given by

$$\dot{M}_{\text{pls}} = \Omega_K \bar{\Sigma}_{\text{pls}} R_H^2 p_{\text{coll}}, \quad (9)$$

where Ω_K is the Keplerian angular velocity, $R_H = \left(\frac{m_p + m_{\text{pls}}}{3M_*}\right)^{1/3} a$ is the planet's Hill Radius, $\bar{\Sigma}_{\text{pls}}$ is averaged over the planet's feeding zone (spanning ten Hill radii for a planet on a circular orbit, considering that the planet is in the middle of its feeding zone) of the aforementioned surface density of planetesimals and p_{coll} is the collision probability following Inaba et al. (2001):

$$p_{\text{coll}} = \min\left(p_{\text{med}}, \left(p_{\text{high}}^{-2} + p_{\text{low}}^{-2}\right)^{-1/2}\right). \quad (10)$$

The individual components are:

$$p_{\text{high}} = \frac{\tilde{r}_p^2}{2\pi} \left(\mathcal{F}(I) + \frac{6}{\tilde{r}_p} \frac{\mathcal{G}(I)}{(\tilde{e})^2} \right), \quad (11)$$

$$p_{\text{med}} = \frac{\tilde{r}_p^2}{4\pi\tilde{i}} \left(17.3 + \frac{232}{\tilde{r}_p} \right), \quad (12)$$

¹ Fortier et al. (2013) found that for larger planetesimal sizes (10 km or 100 km), the assumption of equilibrium e_{pls} and i_{pls} is justified, but here we assume smaller planetesimal sizes (1 km).

$$p_{\text{low}} = 11.3 \sqrt{\tilde{r}_p}. \quad (13)$$

Here $I \equiv i_{\text{pls}}/e_{\text{pls}}$, $\tilde{e} = \frac{a e_{\text{pls}}}{R_H}$ is the eccentricity of the planetesimals in Hill's unit, we use numerical fits for the integrals $\mathcal{F}(I)$ and $\mathcal{G}(I)$ following Chambers (2006), $\tilde{i} = \frac{a i_{\text{pls}}}{R_H}$ is the inclination of the planetesimals in Hill's unit and

$$\tilde{r}_p \equiv \frac{R_{\text{capture}} + R_{\text{pls}}}{R_H}. \quad (14)$$

$R_{\text{pls}} = 1$ km is the planetesimal radius and R_{capture} is the planet's capture radius, which is enlarged as described in Inaba & Ikoma (2003) when a gaseous envelope is present. We numerically retrieve R_{capture} from equation (17) of Inaba & Ikoma (2003):

$$R_{\text{pls}} = \frac{3}{2} \frac{v_{\infty}^2 + 2GM_{\text{core}}/R_{\text{capture}}}{v_{\infty}^2 + 2GM_{\text{core}}/R_H} \frac{\rho(R_{\text{capture}})}{\rho_{\text{pls}}}. \quad (15)$$

Here ρ_{pls} is the density of the planetesimal, $\rho(R_{\text{capture}})$ is the density of the gaseous planetary envelope at R_{capture} and

$$v_{\infty} = v_K \sqrt{5/8 e_{\text{pls}}^2 + i_{\text{pls}}^2} \quad (16)$$

is the typical relative velocity at infinite distance to the planet.

The Keplerian velocity v_K is defined as $v_K = \sqrt{\frac{GM}{R}}$.

In addition to the accreted mass of planetesimals that is reduced from Σ_{pls} over the planet's feeding zone, an estimated amount of ejected planetesimals is subtracted following Ida & Lin (2004)

$$\dot{M}_{\text{ejected,pls}} = \left(\frac{a_{\text{planet}} M_{\text{planet}}}{2M_* R_{\text{capture}}} \right)^2 \dot{M}_{\text{pls}}. \quad (17)$$

The factor in front of the planetesimal accretion rate is the ratio of the characteristic surface speed and the escape speed from the star.

2.3. Pebble accretion model

For the pebble accretion model we follow the model outlined by Brügger et al. (2018). An embryo is assumed to form via the streaming instability in the disc at a given time, which is a free parameter of the model. This embryo grows by accreting pebbles that form in the outer regions of the disc and then drift towards the star (Lambrechts & Johansen 2014). The amount of pebbles depends on the fraction of solids in the disc that can turn into pebbles (Z_{peb}) as mentioned in Sect. 2.1.

We use the pebble accretion rates given by Johansen & Lambrechts (2017) which distinguish between the Bondi accretion regime (small protoplanets) and the Hill accretion regime (large protoplanets). The Bondi accretion regime occurs for low mass planets where the planets do not accrete all of the pebbles that pass through their Hill sphere, i.e. the planet's Bondi radius is smaller than the Hill radius. Once the Bondi radius becomes comparable to the Hill radius, the accretion rate becomes Hill sphere limited, and so the planet accretes in the Hill accretion regime. This is the typical regime for more massive bodies in the disc. Within the Hill regime a further distinction occurs whether the planet is accreting in a 2D or a 3D mode. This is dependent on the relation between the Hill radius of the planet and the scale height of the pebbles in the disc. For planets with a Hill radius smaller than the scale height of pebbles, the accretion is in the 3D mode, whilst for planets with a Hill radius larger than the pebble scale height, the 2D mode. The general equation

for the 2D and 3D accretion rates are respectively (Johansen & Lambrechts 2017)

$$\dot{M}_{2D} = 2R_{\text{acc}}\Sigma_{\text{peb}}\delta v, \quad (18)$$

and:

$$\dot{M}_{3D} = \pi R_{\text{acc}}^2 \rho_{\text{peb}} \delta v, \quad (19)$$

where ρ_{peb} is the midplane pebble density and $\Sigma_{\text{peb}} = \frac{\dot{M}_{\text{peb}}}{2\pi R v_r}$ is the pebble surface density including the flux of pebbles \dot{M}_{peb} and their velocity v_r . The approach speed is given by $\delta v = \Delta v + \Omega_K R_{\text{acc}}$, with $\Delta v \sim \eta v_K$ being the sub-Keplerian velocity, $\eta = -\frac{1}{2} \left(\frac{H}{r}\right)^2 \frac{d \ln P}{d \ln r}$ the gas pressure gradient and Ω_K the Keplerian frequency. The accretion radius R_{acc} used in Eqs. 18 and 19 is defined with the help of:

$$R'_{\text{acc}} = \left(\frac{4\tau_f}{t_B}\right)^{1/2} R_B, \quad (20)$$

in the Bondi regime, and:

$$R'_{\text{acc}} = \left(\frac{\Omega_K \tau_f}{0.1}\right)^{1/3} R_H, \quad (21)$$

in the Hill regime.

Here $R_B = \frac{GM}{\Delta v^2}$ is the Bondi radius and $t_B = R_B/\Delta v$. R_H is the Hill radius and $\tau_f = \text{St}/\Omega_K$ (Johansen & Lambrechts 2017) with St being the Stokes number that describes the pebble size (Lambrechts & Johansen 2014, see discussion below). These expressions (Eq. 20 and 21) however only consider strong coupling between the pebbles and the protoplanet. In order to account for the less efficient accretion when the friction time becomes longer than the time to drift past the protoplanet, R_{acc} becomes (Ormel & Klahr 2010):

$$R_{\text{acc}} = R'_{\text{acc}} e^{-0.4(\tau_f/t_p)^{0.65}}, \quad (22)$$

before going back to Eqs. 18 and 19. Here $t_p = GM/(\Delta v + \Omega_K R_H)^3$ is the drifting time-scale.

The pebble size is usually described by the Stokes number St. Outside the ice line the pebbles are assumed to be made of ice surrounding trapped silicates. Their size is given by $t_{\text{growth}}(r_g) = t_{\text{drift}}(r_g)$, leading to $\text{St} \sim 0.01 - 0.1$ (Lambrechts & Johansen 2014). However inside the ice line, this assumption no longer holds because the ice sublimates (Ida & Guillot 2016) and releases the silicates. Therefore the pebble size significantly shrinks to the size of these silicate grains, which are much smaller than the original icy pebbles (Morbidelli et al. 2015; Shibaike et al. 2019). Observations hint that the size of these silicates is similar to the one of chondrules, which are mm-sized particles (Friedrich et al. 2015). Therefore if a planet accretes pebbles inside the ice line, the accreted pebbles have a much lower Stokes number $\text{St} \ll 1$ (Birnstiel et al. 2012), which impacts on the accretion rate (see discussion in Sect. 4.2).

The embryo thus grows by accreting pebbles until it reaches the so-called pebble isolation mass (Lambrechts & Johansen 2014) (see also Ataiee et al. 2018; Bitsch et al. 2018):

$$M_{\text{iso}} = 20 \left(\frac{H/R}{0.05}\right)^3 \cdot M_{\oplus}. \quad (23)$$

The pebble isolation mass is the mass required to perturb the gas pressure gradient in the disc. Thus the gas velocity becomes super-Keplerian in a narrow ring outside the planet's orbit reversing the action of the gas drag. The pebbles are therefore pushed outwards rather than inwards and accumulate at the

outer edge of this ring stopping the core from accreting solids (Paardekooper & Mellema 2006). Consequently the planet begins to accrete gas more efficiently. Therefore the calculation of the envelope structure (presented in Sect. 2.4) starts at the $\min(M_{\text{iso}}, 3M_{\oplus})$.

2.4. Gas accretion model

The computation of gas accretion is similar in both planetesimal and pebble models. The internal structure of the planetary envelope is computed by solving the following equations :

$$\frac{\partial m}{\partial r} = 4\pi r^2 \rho, \quad (24)$$

$$\frac{\partial P}{\partial r} = -\frac{Gm}{r^2} \rho, \quad (25)$$

and:

$$\frac{\partial T}{\partial r} = \frac{T}{P} \frac{dP}{dr} \nabla, \quad (26)$$

which represent the mass conservation, the equation of hydrostatic-equilibrium and energy transfer respectively (Bodenheimer & Pollack 1986; Alibert et al. 2005; Mordasini et al. 2012b; Alibert 2016; Coleman et al. 2017). The pressure P and temperature T depend on the mass m included in a sphere of radius r . The density $\rho(P, T)$ follows Saumon et al. (1995) and the temperature gradient depends on the stability of the zone against convection: for convective zones, it is assumed to be given by the adiabatic gradient. Therefore $\nabla = \frac{d \ln(T)}{d \ln(P)} = \min(\nabla_{\text{ad}}, \nabla_{\text{rad}})$ where

$$\nabla_{\text{ad}} = \frac{d \ln(T)}{d \ln(P)}, \quad (27)$$

$$\nabla_{\text{rad}} = \frac{3}{64\pi\sigma G} \frac{\kappa L P}{T^4 m}, \quad (28)$$

with κ (Bell & Lin 1994) being the full interstellar opacity (see however Sect. 4) and L being the luminosity of the planet computed by energy conservation and including the solid accretion luminosity, the gas contraction luminosity and the gas accretion luminosity (Mordasini et al. 2012b,a; Alibert et al. 2013).

The mass of the envelope is then determined by iteration. Comparing the envelope masses between two iterations provides the gas accretion rate (Alibert et al. 2005). For runaway gas accretion (Pollack et al. 1996), the maximum accretion rate is limited by what can be provided by the disc:

$$\dot{M}_{\text{gas,max}} = \dot{M}_{\text{disc}} = 3\pi v \Sigma. \quad (29)$$

2.5. Planet migration

As planets grow, they interact gravitationally with the surrounding gas, exchange angular momentum and migrate through the disc. Low-mass planets that are embedded in the disc feel a torque arising from the gravitational interaction between the planet and the disc. This process is called type I migration. The torque felt by the planets is the composition of the Lindblad torque Γ_L and the corotation torque Γ_c (Paardekooper et al. 2010, 2011)

$$\Gamma_{\text{tot}} = \Gamma_L + \Gamma_c. \quad (30)$$

The Lindblad torque is a torque exerted by density waves on the planet. The presence of the planet creates these waves in the disc at locations called Lindblad resonances. On the other hand

the corotation torque corresponds to an exchange of angular momentum between the planet and the neighbouring gas situated in the corotation region of the planet. The two torques depend on the local gradients of surface density, temperature and entropy. In locations where a strong negative temperature gradient is present, the planet is expected to migrate outwards. These regions of outward migration lie where $|\Gamma_c| > |\Gamma_L|$.

Higher mass planets on the other hand are able to open a gap in the disc (Lin & Papaloizou 1986). This slows down their migration towards the star. The gap opening depends on the scale height and viscosity of the disc. A gap opening criterion is provided by Crida et al. (2006):

$$P = \frac{3}{4} \frac{H}{r_H} + \frac{50}{qRe} \leq 1, \quad (31)$$

where $q = M_p/M_*$ is the mass ratio and Re is the Reynolds number given by $Re = r_p^2 \Omega_K^2 / \nu$. If the planet fulfils this criterion, it starts to migrate towards the star in the so-called type II migration regime on a time-scale that is a function of the viscosity of the disc ν (Mordasini et al. 2009):

$$\tau_{II} = \frac{2a_p^2}{3\nu} \times \max\left(1, \frac{M_p}{2\Sigma_{\text{gas}} a_p^2}\right). \quad (32)$$

The maximum term allows the so-called planet dominated regime to be taken into account. This regime is a consequence of the decrease in the gas disc mass and the slowing down of migration as the planet becomes more massive.

2.6. Long-term evolution

Once the gas disc has disappeared, the planets enter the evolution stage. At this point both gas accretion and disc-driven migration cease. We take the outcomes of our populations as initial conditions for this long-term evolution. Our aim is to obtain the density of the planets. To get realistic radii in addition to the known masses we use the evolution model of Mordasini et al. (2012a,b) including atmospheric loss due to photoevaporation (Jin et al. 2014). The outer radius of the numerical envelope structure extends to very low densities. Therefore, we follow the prescription of Hansen (2008) to calculate what radius would be observed by a generic transit observation.

3. Comparisons between the models

In order to perform a proper comparison between the two separate models of solid accretion, all the other components of the simulated planet growth should be similar: e.g. the disc model, the accretion of gas and the migration of the planet. Therefore we complete tests to consolidate both models and make sure that they are identical in these aspects.

3.1. Disc model

Our first test case aims at comparing the evolution of the protoplanetary discs. The same physical disc model (following Hueso & Guillot 2005) is used in both codes but since we use two distinct numerical implementations, a proper comparison is necessary to make sure that the same initial conditions lead to identical results. Here, we focus on two quantities:

Table 1. System properties used in all test cases.

System properties	Values
Disc mass	0.017 M_\odot
Slope	0.9
α	0.002
Z_{tot}	0.01
μ	2.27
Inner edge of the disc	0.1 AU
Outer radius of the disc R_d	1000 AU
Cut off radius of the disc	30 AU
Photo-evaporation rate $\dot{M}_{w,\text{ext}}$	$1 \times 10^{-7} M_\odot/\text{year}$
R_*	2 R_\odot
M_*	1 M_\odot
T_*	4480 K

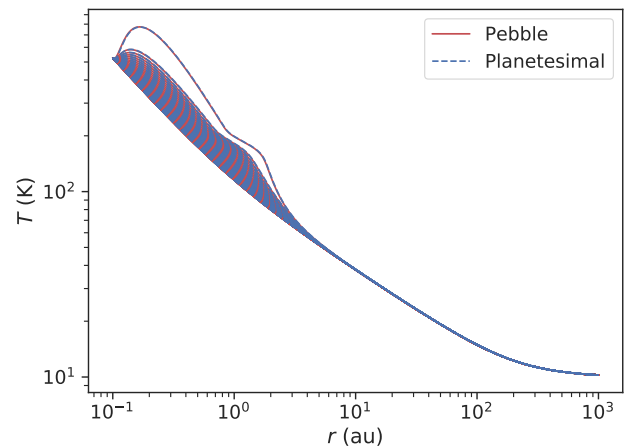


Fig. 1. Temperature profile comparison between the two codes for our nominal disc (Table 1). The blue dotted lines show the result using the planetesimal accretion code and the underlying red lines represent the results using the pebble accretion code. The outer most blue line at the top of the plot hides a red line below: they represent the initial profile. The disc evolves for 4.99 Myr and each line corresponds to the output each 100'000 years.

the gas temperature and surface density. The temperature profile allows us to check that the vertical structure is giving identical results and the surface density is a key quantity for the formation of planets. The simulations ran for 4.99 Myr, until the dissipation of the gas disc. The lines on Figs. 1 and Fig. 2 represent the outcomes every 10^5 years. The outcome of the temperature comparison is represented in Fig. 1, where we see the superposition of the temperature evolution in both codes. The results obtained using the pebble accretion code are hidden behind the results of the planetesimal accretion code. They are indeed in very good agreement because they differ less than 1 %.

The surface density comparison is shown in Fig. 2. We see that the initial profile is exactly the same for both codes. The physical description of the disc is identical in the two models. However the numerics used to solve the equations are not implemented exactly the same way. Therefore, as the disc evolves, some divergences appear mainly after a few thousands of years of evolution. The general agreement is however good: in the inner disc, the biggest difference we observe is 5 g/cm^2 , which is less than 1%, and in the outer disc 1 g/cm^2 . We can therefore conclude that the two discs evolve in a very similar fashion.

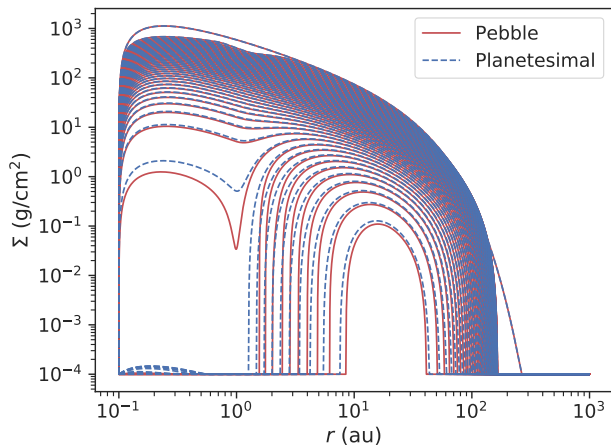


Fig. 2. Surface density comparison between the two codes. Again here the red lines show the result using the pebble accretion code and the dotted blue lines give the outcome using the planetesimal accretion code. The disc evolves for 4.99 Myr and each line corresponds to the output each 100'000 years.

3.2. Accretion of gas

We now consider a planet in the disc. Its location is fixed at 5.2 AU to avoid the influence of migration. We also set the solid accretion rate to $10^{-4} M_{\oplus}/\text{yr}$ to prevent the influence of how solids are accreted and to only compare the accretion of gas. The initial mass of the core is $0.01 M_{\oplus}$ and it is introduced in the disc after 0.1 Myr of evolution to allow the disc to reach a quasi-steady state. To exclude any influence of the disc, we establish values for the planet boundary conditions that are fixed in time to make sure that the gas accretion and envelope structures are as similar as possible. We choose a temperature T of 60 K and a surface density Σ at the planet location of 200 g/cm^2 , which are typical values for a location of 5.2 AU in a classic disc.

As explained in Sect. 2.4, the gas accretion rate onto the planet is given by the difference in envelope mass between two time-steps. We however distinguish two regimes: when the planet is attached to the gas disc and when it undergoes runaway gas accretion. In the second case, the accretion of gas is limited by what the disc can provide. In Fig. 3 we show a comparison of the gas accretion implementations. The two envelope masses are represented as a function of time. The previously mentioned runaway gas accretion phase starts, in our example, after ~ 0.47 Myr (see Fig. 3). As shown in the zoomed area, the envelope masses are only differing by less than 0.1 %. We attribute this difference to the two distinct codes that may not converge to the exact same solution after the same number of iterations.

3.3. Planet migration

In our previous tests (see Sect. 3.2), the planet location was fixed. We now want to include the effect of migration because as they grow the planets migrate through the disc and the surrounding conditions are not identical at all locations. It is therefore crucial to control that for a given scenario (fixed masses and identical initial locations), an embryo would follow the same path independent of the accretion model. Using the same disc as previously introduced (see Table 1), our first comparison is in the form of a migration map to underline the migration regimes

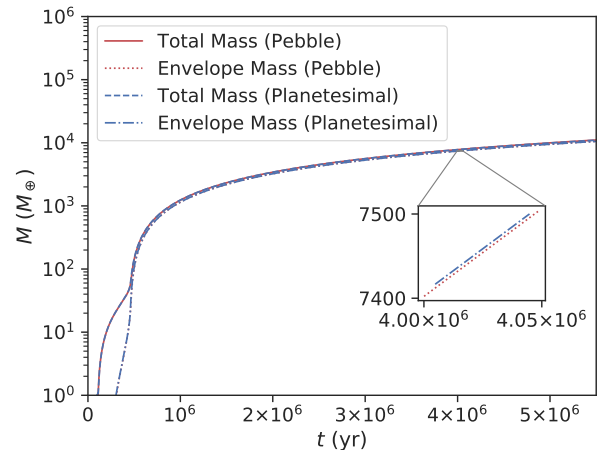


Fig. 3. Gas accretion comparison for the two models. The outcomes of the pebble accretion model are shown in red: the solid line is the total mass and the dotted one is the envelope mass. The results of the planetesimal accretion code are represented in blue: the dashed line gives the total mass and the dashed-dotted line the envelope mass. The zoomed box helps understanding the behaviour of the envelope growth in a linear scale.

the planet may undergo. The maps are given in the upper two plots of Fig. 4 and are taken after 0.1 Myr of disc evolution. The regions in red in these two plots indicate where the planet migrates outwards. When located in the green areas the planet migrates inwards either through type I or type II migration depending on how massive they are. The black line indicates the transition masses and locations between the two migration regimes. In Fig. 4 the upper plot shows the migration map for the planetesimal accretion code, while the middle one shows the map for the pebble accretion code. The bottom graph highlights the differences between the two outcomes: the darker the map, the more similar they are. We observe two main differences: the first one along the outward migration regions and the second one along the inner edge of the disc. Even though it is not visible on the two upper plots, the outwards migration regions are shifted depending on the model. These differences may be consequences of gradients that appear in the migration formulae for type I migration. Indeed the surface density gradient, as well as the temperature gradient, are used in the computation of the Lindblad and corotation torques. Computing gradients with two different solvers can thus lead to divergences in the outcomes and the discs evolving slightly differently also impacts on the migration maps.

We then compare the migration of single planets with fixed masses. In order to test different types of migration we use multiple initial locations and 3 distinct masses ($1 M_{\oplus}$, $10 M_{\oplus}$ and $100 M_{\oplus}$) to account for the three following migration regimes: type I, fast type I and type II respectively. The outcome of the comparison is shown in Fig. 5.

In the upper plot we see the migration of a $1 M_{\oplus}$ planet for different starting locations. As can be noticed in Fig. 4 (bottom plot), this particular mass lies in the region where the two outcomes of the codes differ the most, especially for locations below 1 AU. Furthermore the migration timescales (see the colour code in Fig. 4, upper two plots) for a $1 M_{\oplus}$ are the most diverse. Indeed, depending on the location the planet

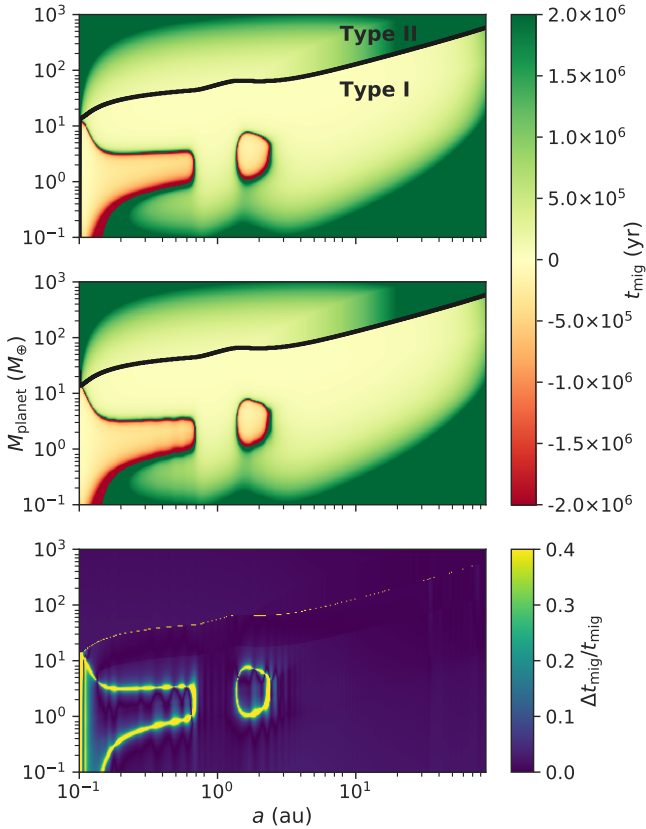


Fig. 4. Map highlighting the different migration regimes after 0.1 Myr of disc evolution. In the upper two plots the red zones shows the outward migration regions. The type I and type II migration regime are distinguished by the solid black line: above it the planets migrate with type II migration and below they undergo type I migration. These two plots are computed with the planetesimal accretion code (most upper plot) and the pebble accretion code (middle plot) respectively. The third and bottom plot is the relative difference we observe between the two upper plots. The darker the outcome the more similar they are.

may either migrate fast inwards or slowly inward, as well as outwards or experience zero migration regions. Focusing first on the outermost planet, with an initial location of ~ 50 AU, it is in a region where the migration timescale is large, leading to a relatively slow migration. We therefore see that it remains near its initial location and end up around 40 AU after 4 Myr of disc evolution.

The planet starting at ~ 18 AU as well as the one starting at ~ 6 AU migrate relatively fast towards the inner edge of the disc until they reach ~ 0.6 AU where they cross a high migration time-scale region, leading to a slower migration regime. This makes them stay nearly in the same location for 500'000 years. The planet starting at ~ 2 AU experiences quite early on this slow migration regime as well and therefore ends up on a track similar to those of the two previous cases (Coleman & Nelson 2016b). When these three planets reach regions below 1 AU the two outcomes of the codes very slightly differ. As we see in Fig. 4 (bottom plot), those are the regions where the outcomes of the codes differ the most, impacting here on the migration tracks.

As for the planet starting at ~ 0.6 AU, it starts further inside from the regions where the outcomes diverge and therefore the two tracks are matching each other. This planet first experiences outward migration and then ends up in a zero migration area, which moves itself, making the final location of this planet only ~ 0.3 AU far from its original one.

In the center plot of Fig. 5, the $10 M_{\oplus}$ planets experience fast type I migration. Independent of their starting locations, they all migrate very quickly (less than 1 Myr) to the inner edge of the disc because their mass ($10 M_{\oplus}$) lies in the range where type I migration is very efficient (see Fig. 4, colour code of the upper two plots). These planets are indeed not big enough to open a gap in the disc and therefore migrate with the type I regime, where the migration rate is proportional to the mass. Furthermore the disc is dense at the beginning of its evolution, which favours a rapid drift. Comparing the behaviour of the planets for both models we get a very good agreement.

In the bottom plot of Fig. 5, the migration of a $100 M_{\oplus}$ planet is presented. Being more massive these planets usually open a gap and migrate in type II mode. Looking back at Fig. 4, we see that a planet with a mass of $100 M_{\oplus}$ lies above the black line splitting type I and type II migration, meaning that it would migrate in type II for all locations below ~ 20 AU. The planets of the lower panel of Fig. 5 can then be split into two groups: the inner three planets and the two outer ones. Looking at the three inner planets first, we see that they directly migrate in type II due to their mass and locations. This prevents them from quickly migrating to the inner edge of the disc like the $10 M_{\oplus}$ planets. It therefore takes them ~ 2 Myr to reach the inner edge even though they are initially located quite close to the star. On the other hand the outer most planets first migrate in fast type I because of their location until they reach regions where they can undergo the type II regime leading to a slow migration towards the inner edge of the disc. Comparing the two models we again obtain very similar results.

3.4. Combined effect of growth and migration

We now finally combine the effect of gas accretion and migration by looking at the mass growth of a single planet that migrates in a disc. For this test we use our nominal disc (Table 1), and insert a $0.01 M_{\oplus}$ planet at 40 AU at the beginning of the disc evolution. As in the previous tests the accretion rate of solids is fixed to avoid any influence of the way solids are accreted (see Sect. 3.2). In order to trigger efficient gas accretion, we reduce exponentially the accretion rate of solids after 20 kyr of disc evolution. The results are presented in Fig. 6 where we see that the two codes give very similar results for the masses as a function of semi-major axis. The inset on the top right shows the temporal growth of the planet envelopes, which are also matching very well. This test is the closest to a real simulation we could produce without any impact of the solid accretion models. Given the excellent similarity between the results in this test we can now explore the effects of the two solid accretion models knowing that the other components of the computation are very similar and will not induce differences.

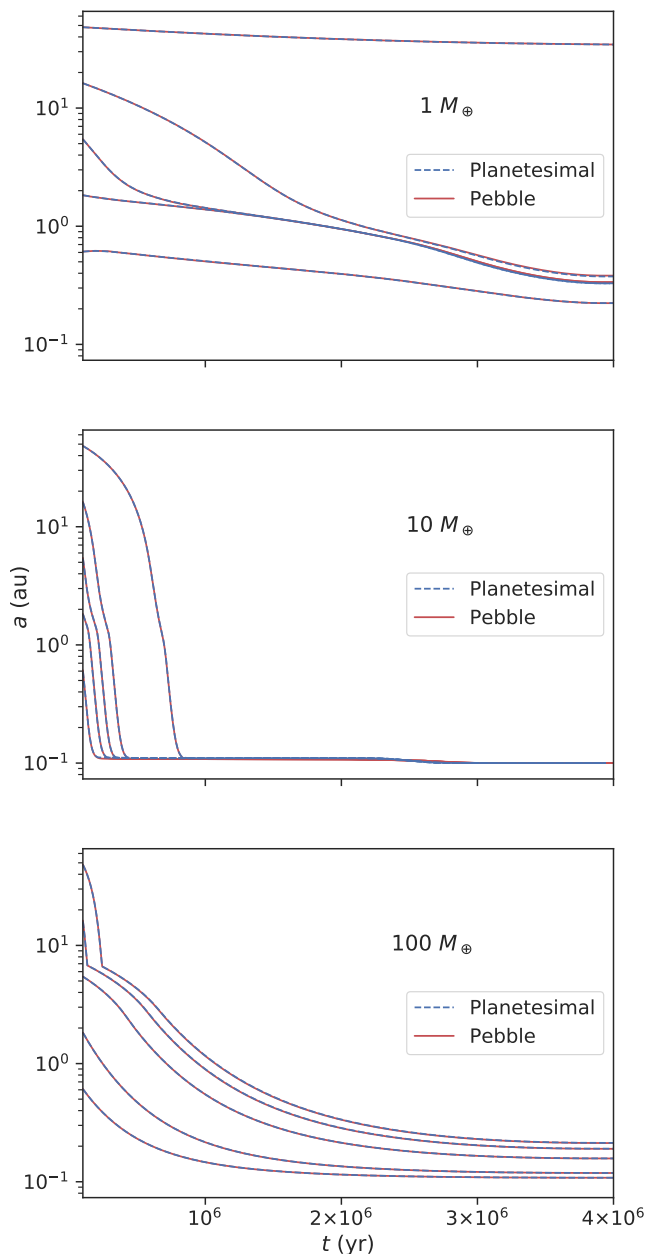


Fig. 5. Migration of three different fixed-mass planets for different locations (0.6 AU, 1.8 AU, 5.5 AU, 17 AU and 50 AU). The upper plot shows the migration of a $1 M_{\oplus}$ planet, the middle one a $10 M_{\oplus}$ planet and the bottom one a $100 M_{\oplus}$ planet. The solid red lines give the outcomes of the pebble accretion code and the dashed blue lines represent the results of the planetesimal accretion code.

4. Population synthesis outcomes

4.1. Initial conditions

We use the nominal model outlined in Sect. 3.3, with the disc model being similar to that of Hueso & Guillot (2005) and described in Sect. 2.1. The accretion of gas onto the planet follows the equations introduced in Sect. 2.4. The opacity of the planetary envelope is reduced by a factor $f_{\text{opa}} = 0.003$ because observations hint that the grain opacity is smaller than the full interstellar one (Mordasini et al. 2014). The accretion of solids differs between the two models: either planetesimals with radii

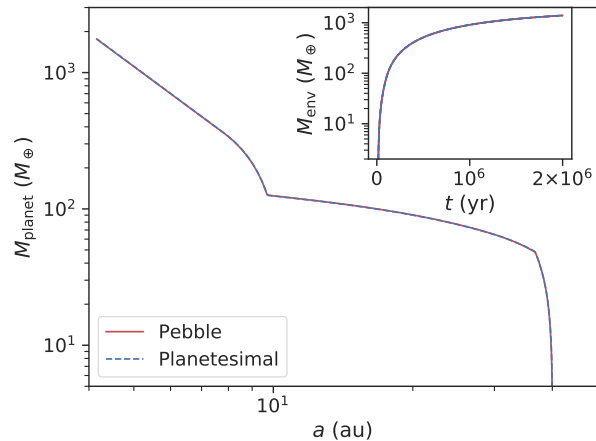


Fig. 6. Mass of a migrating planet as a function of its location. A solid red line represents the pebble accretion code and is hidden behind the dashed blue line which gives the result of the planetesimal accretion code. The small window on the top right shows the mass of the envelope growing with time using the two codes.

of 1 km (see Sect. 2.2) or pebbles (mm to cm size) are accreted (see Sect. 2.3). While growing, as explained in Sect. 2.5, the planet interacts with the disc and starts migrating through the disc.

We run simulations of single planet per disc to avoid the chaotic effects of N-body simulations and allow a proper comparison of the two models. The embryo is inserted at different times of the disc evolution (0 Myr, 0.2 Myr, 0.5 Myr and 1 Myr) to explore the impact on the resulting populations (10^4 planets per starting time). Its location is randomly chosen from a uniform distribution in logarithmic space between 0.1 and 50 AU and the initial mass of this inserted body is $0.01 M_{\oplus}$.

With our populations we aim at taking a wide range of discs into account. We randomly draw masses from the distribution of inferred Class I gas disc masses by Tychoniec et al. (2018) and multiply them with another random value drawn from the distribution of spectroscopic metallicities obtained by Santos et al. (2005) to obtain dust disc masses. The exponential cut-off radius of the gas disc profile is a function of the gas disc mass following Andrews et al. (2010) and the cut-off radius for the planetesimal disc (where applicable) is half of the former (Ansdell et al. 2018). The subsequent disc evolution is then governed by α (see Table 1) and photo-evaporation (see Sect. 2.1). To have disc lifetimes matching the lifetime distribution inferred from observations of disc fractions in stellar clusters (e.g. Mamajek 2009), we linearly scale the external photo-evaporation by a third random number drawn from a log-normal distribution (see Mordasini et al. 2015). The total amount of solids is randomly drawn from the aforementioned distribution, but from this amount of solids, part of it forms the bodies that can be accreted, while the rest remains as dust. We present here two scenarios of how the total solid mass is distributed: either 90% forms the accretable bodies with 10% of the mass in dust ($\varepsilon = 0.9$ case) or 50% forms the accretable solids with 50% remaining dust ($\varepsilon = 0.5$ case).

For purpose of simplicity for the comparison we do not use here the full versions of the two models (as would be done for example for the planetesimal accretion model in Emsenhuber et al. in prep). For instance for both the pebble and the planetesimal accretion models the radius of the solid core

of the planet is calculated using a fixed density of 5.5 g/cm^3 , which is a simplification compared to what is used by Mordasini et al. (2012b,a). This facilitates the analysis by avoiding second order effects on the gas accretion via an otherwise emerging core contraction luminosity. The potential feedback of the composition of the accreted solids is therefore lost. For this reason, we only track the composition in terms of silicates and water ice. The separation of the icy and rocky population, given by the water ice line, is calculated using the midplane pressure and temperature at the starting time of the simulation.

We stress that for a detailed comparison with observations, the interactions between the growing planets are important (Alibert et al. 2013) and the populations presented here are intended to simulate realistic conditions for the different solid accretion mechanisms, but are not meant to be compared to the observed population of planets. We leave this for future studies.

4.2. Mass vs semi-major axis

Fig. 7 shows the mass of the formed planets as a function of their final locations for different starting times. The two columns on the left differ from those on the right by the amount of solids used to form the bodies that can be accreted by the planet (ϵ). Within these two partitions the respective left column of the panels gives the output for the pebble accretion model and on its right are the results for the planetesimal model. The colour code expresses the gas fraction of each planet. Focusing first on the case where $\epsilon = 0.9$ (left two columns of Fig. 7) we immediately see that different types of planets are formed by the two models. Using the planetesimal accretion model, more giant planets² are produced than with the pebble model, independent of the starting time. The pebble model indeed only produces giants for the $t_{\text{ini}} = 0$ Myr case. For this specific starting time it also only produces very few planets with masses between $\sim 80 M_{\oplus}$ and $\sim 1000 M_{\oplus}$ compared to the planetesimal scenario. Finally most of the giants, albeit very few in number, are very massive. This is due to the fact that planets growing by pebble accretion only start accreting gas efficiently when solid accretion is stopped. Thus if the planets have a massive enough core and are located in the outer disc, they may undergo type II migration and have time to accrete a considerable gaseous envelope.

A general behaviour observed for both models is that the starting time impacts the mass of the formed planets: the earlier the embryo is inserted the more massive the planets. The variability in the starting times however impacts the planets formed by pebble accretion more. Indeed the growth of the planets in the pebble model depends on the pebble front. This growth front is the place where the dust particles have grown to pebble size and start migrating towards the star. It moves outwards with time and induces a pebble flux. When the pebble front reaches the outermost radius of the disc, the pebble flux drops to zero. If this happens at times earlier than t_{ini} then no growth occurs. In the model the time at which the growth radius reaches the outer edge of the disc scales with the metallicity and can therefore strongly vary. The average time is however around $\sim 300'000$ years. Therefore, especially for later starting times, some planets do not grow at all because there is no flux of pebbles anymore (see the bottom panels of Fig. 7). This starting time effect has less impact in the planetesimal model, where some growth is always possible, un-

less the planet is located very far away from the star where the planetesimal accretion rates are extremely small, or there are no planetesimals in the planet's feeding zone.

Another important feature in the $t_{\text{ini}} = 0$ case is the faster growth inside the snowline in the pebble model compared to the planetesimal one. The Stokes number of pebbles is reduced when crossing the ice line because of ice sublimation (Ida & Guillot 2016). This impacts on the accretion rate of pebbles, which is divided by a factor ~ 2 (Lodders 2003). However, even with this accretion reduction, the pebble flux reaching an embryo located inside the ice line remains significantly larger compared to the planetesimal accretion rate on an embryo inside the ice line in the same disc. The planetesimal rate is considerably reduced in these regions due to the proximity to the star and the resulting smaller feeding zone, which is a function of the Hill radius. The semi-major axis versus mass distribution of the intermediate mass planets is in all cases distinctly shaped by migration, as can be seen by the over-densities of planets in regions of outward migration that are clearly visible.

Moving to the two right columns of Fig. 7, where $\epsilon = 0.5$, some general conclusions drawn for the $\epsilon = 0.9$ case also apply: the transition in the envelope masses occurs for smaller masses using the planetesimal model and the early starting times help to form more massive planets. The amount of giant planets formed by the planetesimal accretion model is however strongly reduced compared to the $\epsilon = 0.9$ case. This is caused by the decrease in the available solids to form the massive cores that are needed to grow into giants. For the pebble model going from $\epsilon = 0.9$ to $\epsilon = 0.5$ does not have such a dramatic impact on the abundance of giant planets. The abundance of giants is indeed more impacted by the pebble isolation mass, which acts as a threshold for the planet to reach larger masses. If the planets do not reach M_{iso} , they won't accrete an envelope, independently of the ϵ value. However the general tendency for both models in the $\epsilon = 0.5$ case compared to the $\epsilon = 0.9$ case is that the planets are less massive (this will be further discussed in Sect. 4.3).

Taking a closer look at the colour code we see that the transition between practically no envelope (orange dots) and a small envelope (pink dots) looks different in the two models. While for the planetesimal model the transition between a total solid core (orange dots) and a body with a small envelope (pink dots) is smooth, in the pebble formation model, we see a clearer distinction. This is due to the gas accretion starting only when the planets reach the pebble isolation mass. The distinction we see, which has a diagonal shape between ~ 0.2 and 2 AU for masses between ~ 1 and $5 M_{\oplus}$, is therefore an imprint of M_{iso} . Focusing on the $\epsilon = 0.5$ case for the planetesimal model, we see a few planets with masses around $1 M_{\oplus}$ and semi-major axis between 0.2 and 0.4 AU that have higher gas mass fractions (see the concentration of purple dots while the background is orange in the right column of Fig. 7). These planets experience outward migration and, since they already emptied their feeding zone, start accreting gas as soon as their semi-major axis increases. In the $\epsilon = 0.9$ case we do not see this feature appearing because the planets were massive enough to accrete a more significant envelope.

In Fig. 8 we focus on the situation where the embryos are inserted at $t_{\text{ini}} = 0$ Myr for the $\epsilon = 0.9$ case and define it as our nominal case. The outcomes in terms of mass of the population of planets formed by pebble accretion are represented as a function of the population formed by planetesimal accretion.

² We consider that a giant planet is a planet with a mass higher than $100 M_{\oplus}$.

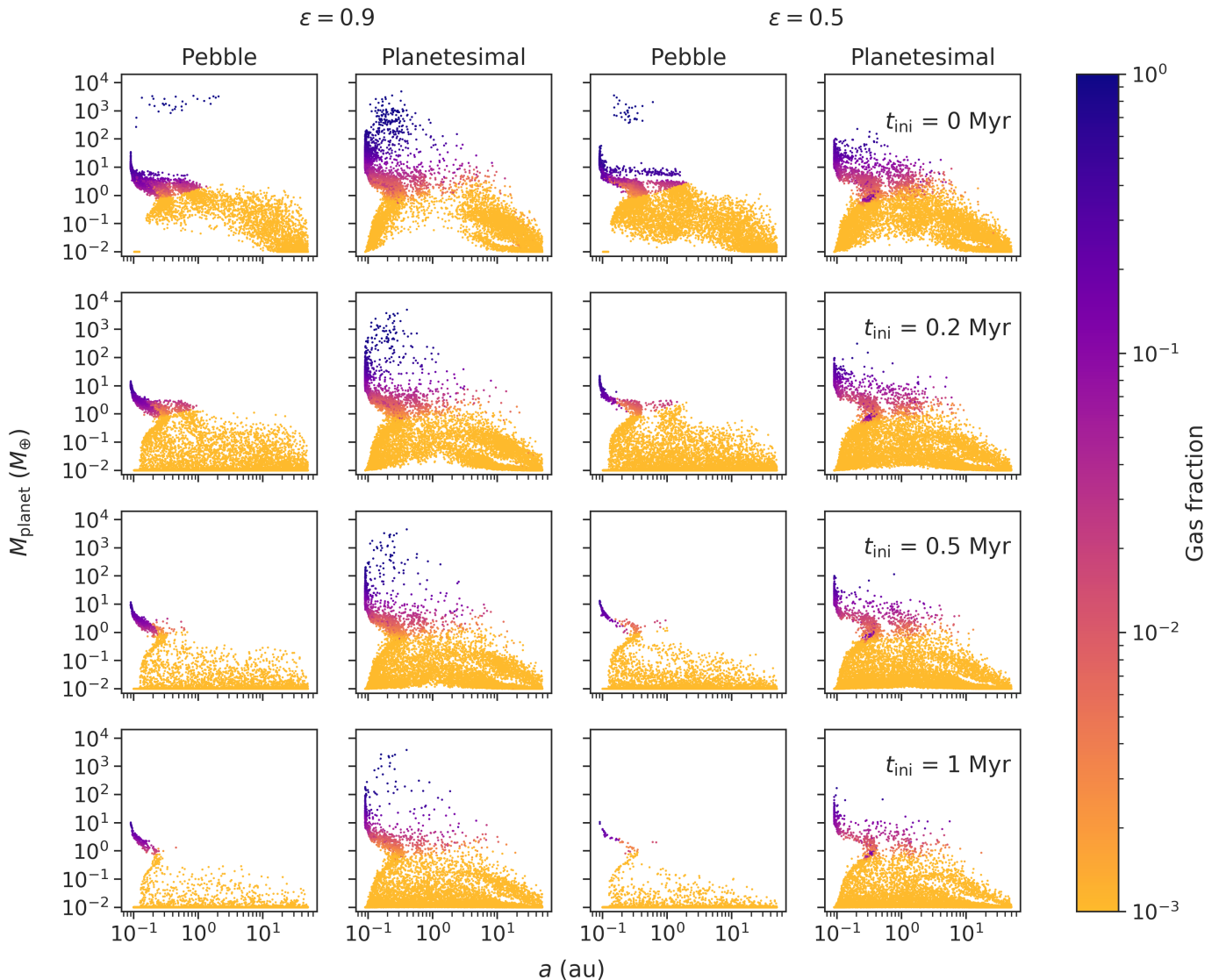


Fig. 7. Mass as a function of semi-major axis of all planets in all populations using $\varepsilon = 0.9$ (left two columns) or $\varepsilon = 0.5$ (right two columns). In these two blocks the left column always gives the results for the pebble accretion model and the right one the product of the planetesimal accretion model. Each line represents a starting time. The colour code expresses the gas fraction for each planet at the end of the formation stage.

The colour code gives the initial location of the embryos. We clearly see on this plot that the giant planets formed by planetesimal accretion remain around super-Earth masses in the pebble accretion model. We also see through the colour code that these planets initially formed between ~ 1 to 10 AU. On the other hand planets starting further out did not grow much in the planetesimal model, while they reach 10 to 30 M_{\oplus} when growing by pebble accretion. Some of them even grow into giant planets (see the planets on the top left of the figure). This hints on the impact that the starting locations have in both models: growing in the inner disc is more favourable to planetesimal accretion while starting in the outer regions of the disc is beneficial to pebble accretion. Indeed in the outer regions of the disc M_{iso} is larger, allowing the planets growing by pebble accretion to have more massive cores, which can trigger efficient gas accretion. This may lead to gap opening and prevent the planet from being lost to the star.

4.3. Populations analysis

In order to further compare the two accretion models and especially increase the visibility in the overpopulated regions of the scatter plots, we present the same results with mass distributions. We focus on the case where $t_{\text{ini}} = 0$ Myr (Fig. 7, top line) because it is the case where the pebble model is able to form giant planets. In Fig. 9 we look at the types of planets formed depending on the partition of solids: either $\varepsilon = 0.9$ or $\varepsilon = 0.5$. Looking first at the red lines (pebble model) we see that the $\varepsilon = 0.9$ case (solid line) forms more super-Earth mass planets while the $\varepsilon = 0.5$ (dotted line) case forms less massive planets. This is due to the lack of solid material available for accretion by the embryos. However more 50 M_{\oplus} planets form in the $\varepsilon = 0.5$ case because the planets grow more slowly and therefore, if they reach M_{iso} , they do it at a later stage of the disc evolution, when migration is less efficient. This gives them more time to accrete gas while migrating towards the star. In the $\varepsilon = 0.9$ case they did not accrete

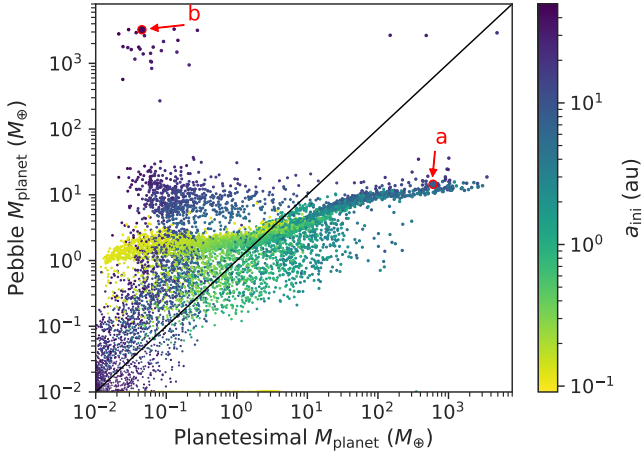


Fig. 8. Mass of the planets formed by pebble accretion as a function of the mass formed by planetesimal accretion for our nominal case ($\varepsilon = 0.9$, $t_{\text{ini}} = 0$ Myr). The colour code gives the initial location of the embryos. The two red circles indicate the two cases that are discussed in Sect. 4.4. The point size is scaled with the $\max(M_{\text{p,peb}}, M_{\text{p,plan}})$ for better visibility in the small mass ranges.

as much gas and migrated into the star. Comparing the amount of giant planets (in the zoomed box) we see that there is a shift in the masses but the total number of these types of planets is still relatively low. The decrease in the amount of pebbles therefore mainly acts on the less massive planets for the pebble model.

For the planetesimal accretion model (blue lines) we obtain similar results to the pebble model. With $\varepsilon = 0.5$ (dashed-dotted line), there are more low mass planets and less super-Earth mass planets. The amount of giant planets, however, strongly decreases compared to the $\varepsilon = 0.9$ (dashed line) case because there are fewer available solids to form planetesimals and a large amount of planetesimals is needed to form giants.

Fig. 9 also provides information to compare the two models with each other. We focus on the $\varepsilon = 0.9$ case. First, we clearly see that the behaviours of the two lines are slightly shifted but both show a bump around super-Earth mass planets. The pebble model however forms more of them compared to the planetesimal model. This is due to the isolation mass: for low M_{iso} , when the solid accretion is stopped, gas accretion remains very slow. Therefore these super-Earth mass planets do not accrete large envelopes and stay in the mass range where type I migration is efficient. They thus migrate into the inner 1 AU of the disc and then get trapped at zero migration regions, migrating with them as the regions migrate over time (Coleman & Nelson 2014). This results in planets not accreting a significant gaseous envelope and consequently remain at super-Earth masses. In the planetesimal model on the other hand the planets continue to accrete solids while they start accreting gas. The transition between solid and gas accretion is therefore more smooth. This helps growing to larger masses than super-Earth because the accretion onto the planets depends on the Hill radius, and thus the more massive the planets, the larger their Hill radii, the more they accrete. Additionally the onset of gas accretion increases the planetesimal capture radius (Inaba & Ikoma 2003) which leads to further growth.

We highlight the larger masses in a zoomed area on the right of the plot, which helps in comparing the amount of giant plan-

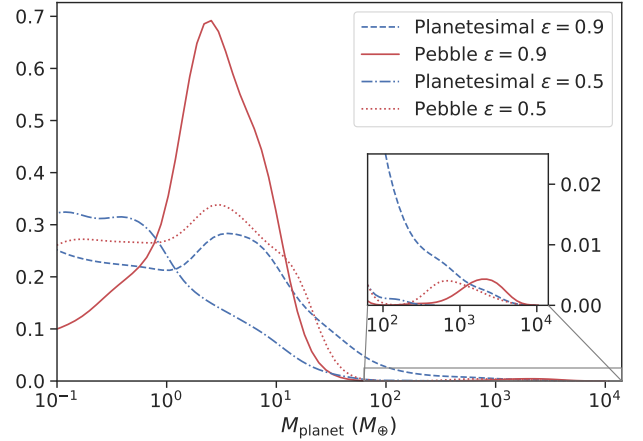


Fig. 9. Kernel density estimate for starting time $t_{\text{ini}} = 0$ Myr. The red lines are for the pebble model and the blue lines for the planetesimal model. We show here the results for the two partitions of the amount of solids: solid and dashed lines are used when $\varepsilon = 0.9$ while dotted and dashed-dotted lines are used when $\varepsilon = 0.5$. The kernel density estimates were obtained using a Gaussian kernel with a Normal reference rule bandwidth (Scott 1992).

ets. As mentioned in Sect. 4.2, the pebble model does not produce many planets between $\sim 80 M_{\oplus}$ and $\sim 1000 M_{\oplus}$ compared to the planetesimal model. Going back to Fig. 8 this hole in the mass range of the planets formed by pebble accretion is even clearer, while in the planetesimal accretion case we see that all types of masses form. This is due to the fact that if a planet becomes massive enough, it crosses the fast type I migration bottleneck by opening a gap in the disc and can then migrate with type II migration, which is much slower than type I. The rare giant planets in the pebble case are bound to become very massive because they reach this regime earlier when there is still a lot of gas to accrete. Planets growing by planetesimal accretion reach type II migration over a larger range of times. Therefore it results in a larger spread in final masses for the giant planet population. When looking at larger masses, both models predict the formation of some very massive planets ($> 1000 M_{\oplus}$). Additionally, the decrease in the numbers of super-Earths to Neptunes is much sharper in the pebble model because of the very few planets with masses between 80 and $1000 M_{\oplus}$.

We now look at some final properties of the formed bodies. In Fig. 10 we provide a cumulative distribution of the ice mass fractions for our nominal case ($\varepsilon = 0.9$ and $t_{\text{ini}} = 0$ Myr). We focus on bodies with masses higher than $1 M_{\oplus}$ and orbits inside 1 AU to take into account planets that may be observed by transit measurements. We therefore concentrate here on bodies that are mainly composed of solids and do not discuss the amount of water in the envelopes. We consider the bodies (planetesimals or pebbles) accreted by the embryo outside the ice line to be composed of 50% ice and 50% rock and the embryo itself as well, if formed outside the ice line (Lodders 2003). If these bodies are accreted inside the ice line, the ice sublimates and therefore the solids are only made of rock. The same applies for the embryo, if initially located inside the ice line, it is 100% rocky. The two models produce quite different results. Focusing on the red line first (pebble model) we see that either the embryo is fully rocky, or made of 50% ice and 50% rock. There are barely any planets with an intermediate composition. This is due to the fast

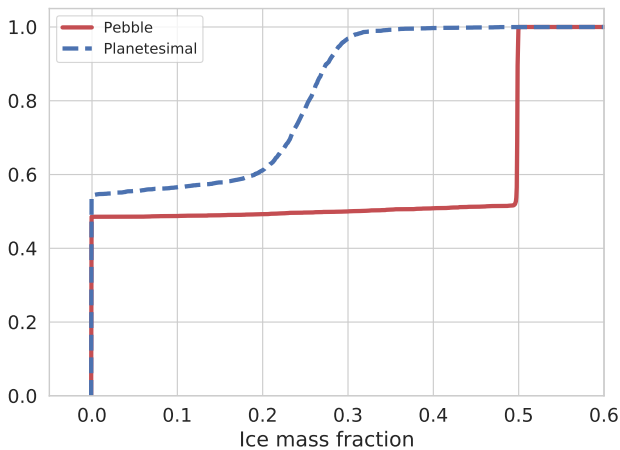


Fig. 10. Cumulative distribution of the ice mass fractions in the solid core of the planets for our nominal case ($\varepsilon = 0.9$, $t_{\text{ini}} = 0$ Myr). The red line provides the pebble accretion model results while the blue one gives the planetesimal accretion model results. We focus here on masses higher than $1 M_{\oplus}$ and semi-major axis below 1 AU.

accretion of solids: pebbles are very efficiently accreted by the growing embryo and therefore the accretion of solids mainly occurs near the initial location, before any migration of the forming planets. The location where the planet reach M_{iso} is indeed on average more than 80% alike the initial location of the planet. Furthermore the migration of the ice line is negligible over the time the embryo accretes pebbles. This "in-situ" solid accretion results in solid cores that are either completely formed outside the ice line or completely formed inside. Barely any embryo migrates during its solid accretion phase to be able to obtain an intermediate composition. Computing the same figure for $\varepsilon = 0.5$ or for a later t_{ini} would not impact on the sharp profile of the ice compositions. However it would increase the amount of planets with a solid composition only. But the sharp transition between a solid composition and a 50% ice composition would remain because of the fast growth by pebble accretion compared to the ice line migration timescale.

For the planetesimal model (blue line) we also focus on bodies with masses higher than $1 M_{\oplus}$ and orbits inside 1 AU and find that the rocky bodies are dominant. Compared to the pebble model their abundance is even higher. No planets have a 50% ice and 50% rock composition unlike the pebble model because the forming planets have a slower growth and start migrating while accreting solids. This impacts on the intermediate compositions. $\sim 40\%$ of the planets have ice mass fractions between ~ 0.05 and ~ 0.25 . Because the planetesimal accretion rate is lower than the pebble one, the growth of the core takes more time. Therefore the growing embryos start to migrate while accreting planetesimals, allowing them to cross the ice line while accreting solids, resulting in reduced ice fractions. Schoonenberg et al. (2019), as well as Coleman et al. (2019), discuss the theoretical water content of the planets in the frame of the Trappist-1 system. Combining the effect of planetesimal and pebble accretion Schoonenberg et al. (2019) obtain a water fraction of the order of 10%. This result is closer to the planetesimal accretion scenario result we obtain in the present work. As for the values we present for planets formed by pebble accretion, they are in agreement with Coleman et al. (2019).

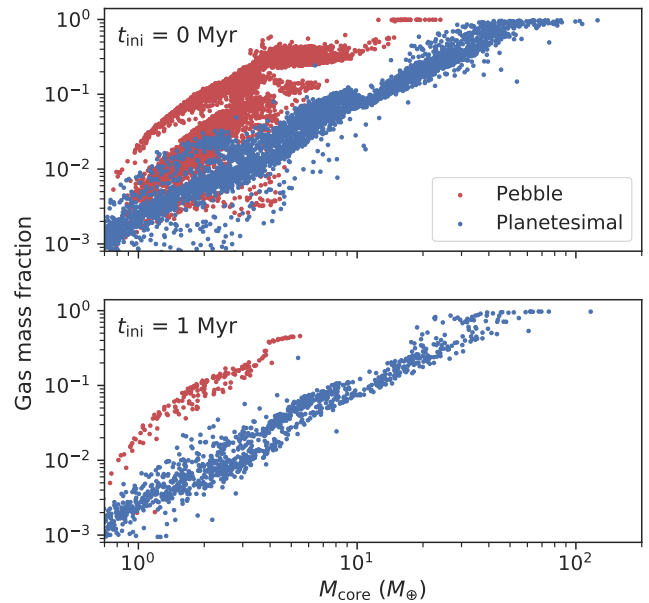


Fig. 11. Gas mass fraction as a function of the core mass for the $\varepsilon = 0.9$ case. Again here the pebble model results are in red, while the planetesimal model outcomes are in blue. The upper plots shows the results for our nominal case ($t_{\text{ini}} = 0$ Myr) and the bottom one for $t_{\text{ini}} = 1$ Myr. We therefore see here that the starting time of the embryo does not impact on the general outcome.

Another interesting result is the distribution of gas mass fractions. We represent this distribution as a function of the core mass in Fig. 11 for our nominal case as well as for $t_{\text{ini}} = 1$ Myr. We see that the envelope fraction for a given core is generally higher using the pebble accretion model. The two plots underline that the results are alike and therefore independent of t_{ini} . The divergence is due to the components of the luminosity of the planets that strongly differ in the two models. At this stage of the formation the total luminosity is dominated by its solid accretion component because the cores mainly accrete solids. Thus when planets formed by pebble accretion reach their isolation mass and stop accreting solids, the solid accretion luminosity is strongly reduced. This therefore induces an increase of the gas accretion luminosity which will engender efficient gas accretion (in agreement with Alibert et al. 2018). On the other hand, at the same formation stage, planets growing by planetesimal accretion continues to accrete planetesimals whilst simultaneously accreting gas, which supplies considerable solid accretion luminosity. This leads to a smaller gas accretion luminosity and therefore less gas accretion. This translates here in higher gas mass fractions for a given core mass using the pebble accretion model.

As gas mass fractions are not directly observable we take a look at the resulting densities and whether the differences between the models are still present after the long-term evolution phase (Sect. 2.6) The composition of the planets is a good indicator of the differences between the two models. Fig. 12 highlights these divergences with the density of planets represented as a function of their final location. The colour code gives the ice mass fraction in the core to indicate the core composition. The horizontal line we see on both plots for a density of 5.5 g/cm^3 is an imprint of the fixed core density

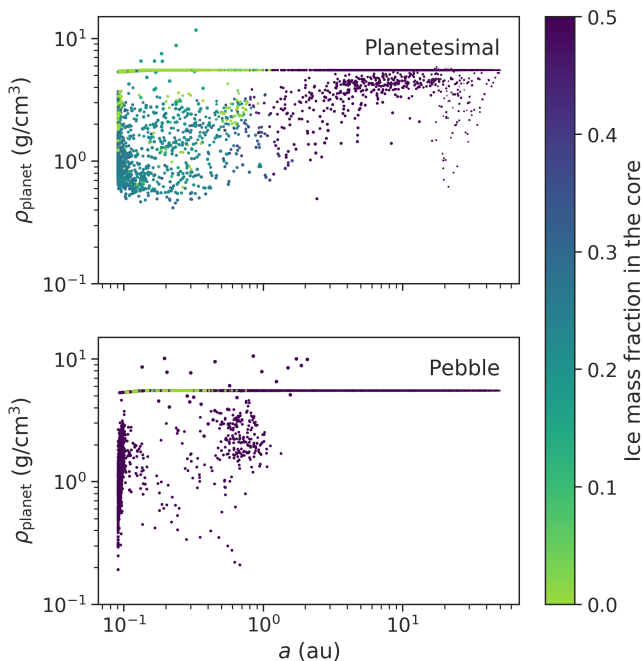


Fig. 12. Density of the planet as function of the final location of the planets for the $\varepsilon = 0.9$ case and starting time $t_{\text{ini}} = 0$ Myr. The colour code expresses the ice mass fraction in the core. The upper plots provides the results of the planetesimal accretion model and the bottom one the ones of the pebble accretion model.

we use in our models. Therefore these planets have practically no envelopes and were represented with orange dots in Fig. 7. In Fig. 12 the colour code is impacted by the ice line: if the planets grow inside the ice line, they are mainly rocky and are therefore represented by green dots, while if they grow further outside they have a 50 % ice composition and are characterised by purple dots. The colour code description is indeed similar to that provided for Fig. 10: there is no planet with intermediate compositions for the pebble model, while the planetesimal model shows many of them.

Fig. 12 shows that for locations beyond ~ 3 AU, the pebble model only predicts rocky bodies with density of 5.5 g/cm^3 . This means that these planets do not have an envelope. This is an imprint of our pebble accretion model where gas can only be accreted once the planets reach the isolation mass. This is very different from the planetesimal accretion model where we see many planets located outside 3 AU with density smaller than 5.5 g/cm^3 which means that they accreted an envelope. This feature was also visible in the two top left panels of Fig. 7, which represent our nominal cases.

What is however interesting to point out with Fig. 12 is the outcomes for planets located inside 3 AU. There both models predicts the formation of planets with envelopes. Therefore most of them have densities smaller than 5.5 g/cm^3 . In the pebble accretion model the high gas mass fractions we obtain in Fig. 11 even lead to some very low density planets ($\rho < 0.5 \text{ g/cm}^3$). The planetesimal accretion model is not forming planets with such low densities. This means that if these intermediate mass gas-rich planets would be observed, the pebble accretion scenario could help understanding their formation.

On the other hand some very massive planets ($> 1000 M_{\oplus}$) have

densities larger than 5.5 g/cm^3 . This is due to the decrease in radius that happens with such high masses (Mordasini et al. 2012a). Focusing on these dense planets we discuss first the ones formed by planetesimal accretion. They have intermediate core compositions because they accreted solids while migrating and crossed the ice line as they grew. Furthermore they reach such high masses because when they accrete gas it augments the collisional probability (Inaba & Ikoma 2003) and therefore also increases the solid accretion (see further discussion in Sect. 4.4). On the other hand the dense planets formed by pebble accretion all have a 50% ice composition because they accreted all their solid material outside the ice line. Their growth in the outer disc was quick and nearly in-situ, and since the isolation mass is bigger in these regions of the disc, they formed massive cores. These massive cores lead to efficient gas accretion and helps in forming very massive planets, leading to these high densities.

4.4. Growth tracks

One of the conclusions of the previous section is that the type of planets formed differs between the two models. For instance we saw in Fig. 9 that hardly any giants formed through the accretion of pebbles. To illustrate the different formation path we look at two different disc cases (see Fig. 13). In the first disc case, disc *a*, the planetesimal accretion model forms a giant planet. We compare its tracks with the the ones of the planet formed by pebble accretion that grew in the same disc. The initial conditions for the two simulations of disc *a* are therefore the same. In the disc *b*, the pebble model forms a giant planet. We also compare its tracks with the ones of the planet formed by planetesimal accretion for the same initial conditions. The outcomes of the two cases are highlighted with red circles in Fig. 8. The disc initial conditions are similar between disc *a* and *b*, except for the photoevaporation rate, which impacts on the disc lifetime. Disc *b* has a slightly longer lifetime because the photoevaporation rate is smaller than the one in disc *a*. The top panel of Fig. 13 shows the migration of the planets with time while the bottom one provides the masses as a function of time.

We focus first on disc *a* where the planetesimal model forms a giant planet. The initial location of the planet is ~ 8 AU. For the pebble case (disc *a*, red line) we see that since the planet grows very rapidly, it starts migrating efficiently early in its evolution. The planet indeed quickly reaches $\sim 10 M_{\oplus}$ by only accreting solids while type I migration has a big impact on its location. Thus, when it is massive enough to accrete gas efficiently, it is already around 2 AU and therefore continues to migrate to the inner edge of the disc without any time to accrete a considerable envelope. Approaching the inner edge of the disc then hampers the accretion of gas on to the planet since the planet's Hill sphere is significantly reduced, and small amounts of gas accretion are sufficient to supply the luminosity generated by the planet (Coleman et al. 2017). On the other hand, the embryo formed through planetesimal accretion (disc *a*, blue line) grows more slowly because of the lower planetesimal accretion rate compared to the pebble one. Furthermore it is only once the planet starts accreting gas efficiently (just before 4×10^5 years) that inward migration becomes important. Because the planet is already quite massive ($\sim 40 M_{\oplus}$) it accretes gas efficiently and quickly opens a gap in the disc. This allows the planet to start migrating in the type II regime, which is slower than type I, resulting in the formation of a giant planet.

Looking now at disc *b*, where the pebble model forms a giant, we see that the outcomes are very different for the two

models. The initial location for these planets is ~ 47 AU. Focusing first on the planet formed by pebble accretion (disc *b*, red line) we see that it does not start accreting pebbles at the very beginning of the simulation. The planet mass remains constant for $\sim 50'000$ years. This is a consequence of the growth front of pebbles (r_g) not reaching the location of the embryo before this time. When r_g finally reaches the initial location of the planet, the latter grows and rapidly attains its isolation mass ($\sim 20 M_\oplus$). In the meantime the planet migrates with type I migration, but since the growth to the isolation mass is quite rapid, the fast migration does not occur for too long to be an issue for the future planet growth. Thus the planet is massive enough to accrete gas efficiently while undergoing type II migration. The planet therefore accretes its large envelope while slowly migrating towards the central star and ends up forming a giant planet located around 2 AU. In these regions of the disc the accretion of planetesimals is more difficult than the one of pebbles. Indeed the pebble surface density in these locations is higher than the planetesimal one because the planetesimal surface density profile is steeper than the one of the gas disc (see Sect. 2.2, Drążkowska & Alibert 2017; Lenz et al. 2019) while the pebble surface density profile undergoes a similar slope to the one of the gas. Additionally, planetesimal accretion becomes very inefficient due to the collisional timescale increasing with the semi-major axis. The result thus shows that the planet formed by planetesimal accretion (disc *b*, blue line) does not grow much and remains as a failed core (Mordasini et al. 2009) near its initial location. The two results are divergent and we see that the starting locations plays an important role in the outcomes of the simulations within the two accretion models, as we already discussed with Fig. 8 in Sect. 4.2.

In order to gain a feeling of how planets behave depending on their initial locations we use our nominal disc (given in Table 1) and increase the initial amount of solids to $Z = 0.1$ to ensure growth and choose different starting locations for the planets (1, 2, 5, 10 and 20 AU). Starting the embryos at 0 Myr we obtain the growth tracks provided in Fig. 14. The red lines give the pebble accretion model results while the blue ones represent the planetesimal accretion model outcomes. We immediately see that the two models produce very different tracks – as already concluded with Fig. 13. However, we see that using the pebble model, type I migration is very efficient and planets with masses around $\sim 10 M_\oplus$ migrate directly to the inner edge of the disc without any chance of accreting significant amounts of gas. These planets indeed reach their isolation masses rapidly (see the red dots on the tracks, indicating the time evolution), essentially growing almost in-situ. They are then not massive enough to trigger efficient gas accretion which can aid them in avoiding fast type I migration. On the other hand, what prevents planets formed by planetesimal accretion to also have this behaviour is that they accrete solids more slowly (see the blue dots on the tracks, indicating the time evolution) and start migrating while accreting solids. Consequently they reach the outward migration regions (~ 1 AU and ~ 3 AU), which prevents them from directly falling into the star. This puts them in a favourable location given their mass to accrete gas efficiently. Additionally, when they accrete gas, the planetesimal accretion rate increases due to gas drag that enlarges the collisional probability described by Inaba & Ikoma (2003). This leads to a significant increase in solid accretion while gas accretion is also occurring. This is in strong contrast to the pebble accretion model where, when planets reach the pebble isolation mass and gas accretion becomes efficient, the solid mass does not increase anymore.

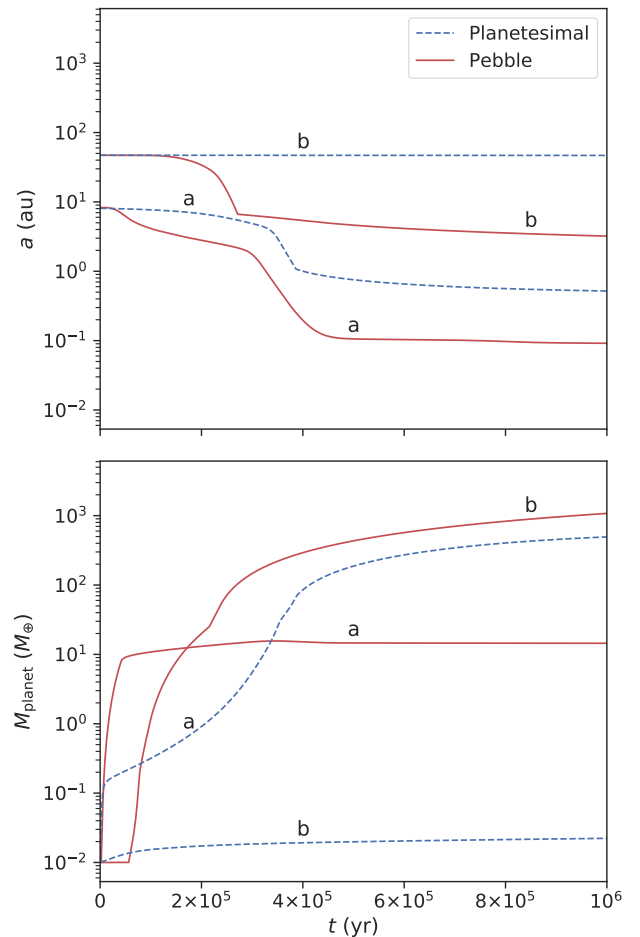


Fig. 13. Growth tracks and migration tracks as a function of time for two disc cases. In the disc *a* the planetesimal accretion model forms a giant planet while in the disc *b* the pebble accretion model does. The upper plot shows the migration of the planets with time and the bottom plot the mass of the planets with time. Again the red lines represent the pebble model results and the blue lines the planetesimal model results.

5. Discussion and conclusion

This work provides a comparison between two planet formation scenarios: pebble accretion and planetesimal accretion. Using two distinct codes we utilise the same disc model, gas accretion model and migration model. A proper testing can only be done if the initial conditions are identical, which is why we compare the implemented disc model, the accretion of gas and the migration regimes. The comparison yielded convincing results (Fig. 6), allowing the two solid accretion models to be adequately compared.

Using a population synthesis approach we then compute simulations of single planet per disc to avoid the chaotic effects of the use of an N-body integrator. We leave the interactions between several planets in a common disc for future work. The embryos in our simulations are inserted at different starting times (0, 0.2, 0.5 and 1 Myr) with initial locations uniform in logarithm between 0.1 and 50 AU. We choose two scenarios to split the amount of solids available in the disc: either we use 90% of this amount to form the accretable bodies (planetesimals or

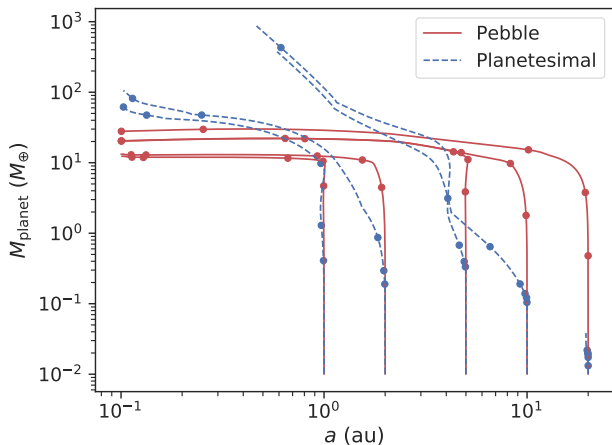


Fig. 14. Growth tracks of planets in the same disc for a starting time of $t_{\text{ini}} = 0$ Myr. The initial locations are 1, 2, 5, 10 and 20 AU. The red solid lines give the pebble model outputs while the blue dashed lines represent the planetesimal results. The dots indicate the growth evolution after 10'000 years, 30'000 years, 0.1 Myr, 0.3 Myr and 1 Myr. The disc lifetime for this simulation is 2 Myr.

pebbles), or we use 50%. The rest of the solids remains as dust and contributes to the opacity of the disc. For the envelope calculation the grain opacity is reduced by a factor $f_{\text{opa}} = 0.003$ because grain-free opacities are more relevant for the envelope calculation than interstellar medium-like opacities (Mordasini et al. 2014). This reduction is applicable to our pebble accretion model because the planets formed by pebble accretion only accrete solids for masses below M_{iso} . At this point, they have practically no envelope because of the high solid accretion luminosity that prevents gas accretion. This therefore avoids for the pebbles to evaporate inside the envelope and for them to impact on the grain opacity. We investigated the influence of a change of opacity in the envelope for planets below M_{iso} and did not obtain a significant impact.³

A general observation is that the outcome of the populations (Fig. 7) is very different depending on the accretion model. Indeed the planetesimal accretion model forms a larger amount of giant planets. The pebble model produces a few giants mainly when the embryo is inserted at $t_{\text{ini}} = 0$ Myr and they are very massive (more than a thousand Earth masses). The starting time indeed has a big impact for the pebble accretion model. The earlier the embryo is inserted, the more massive the planets. Furthermore for later starting times, some planets may not grow at all because of the absence of pebble flux when the pebble front reaches the outer edge of the disc. On the other hand, for the planetesimal accretion scenario, the initial starting time plays a less important role since growth is possible at any time. The growth of the planets in the planetesimal model is more influenced by the location because if the planet is located far away from the star, planetesimal accretion rates are extremely low.

The impact of the splitting in the amount of solids appears mainly when using the planetesimal accretion model (Fig. 9). The amount of giant planets is clearly reduced when less solids are available to form the planetesimals since a large

amount of planetesimals is needed to grow large cores. Figure 9 reveals a gap in the mass distribution of planets around Jupiter masses when using the pebble accretion model. Comparing the mass distributions of the two models, more super-Earth mass planets are formed by the pebble model and the decrease from super-Earth to Neptunes is much sharper in this model as well because of the very few planets with masses between 80 and 1000 M_{\oplus} formed by pebble accretion.

We then compare the ice mass fractions (Fig. 10) and see that using the pebble accretion model the resulting planets are either fully rocky or with a 50% rock 50% ice composition. Few intermediate compositions are formed because the planets grow fast and nearly in-situ. On the other hand the planetesimal model does produce a significant number of planets with intermediate compositions because the planets formed by planetesimal accretion grow slower while migrating.

Focusing on the gas mass fraction (Fig. 11) we find that the pebble model forms planets with higher gas mass fractions for a given core mass compared to the planetesimal model. We show that this result is independent of the starting time of the embryo but is influenced by the contributions to the luminosity of the planets. Planets formed by pebble accretion have a low solid accretion luminosity once they reach their isolation mass because solid accretion is stopped. This results in a high gas accretion luminosity (Alibert et al. 2018), which triggers efficient gas accretion (Coleman et al. 2017). Planets formed by planetesimal accretion on the other hand accrete gas while still accreting solids, leading to a lower gas accretion luminosity. This finally translates into gas mass fractions for a given core mass that are higher for planets formed by pebble accretion. This difference in the gas mass fractions is not always retained over the Gyr evolution after the disc dispersal due to efficient photo-evaporation of the atmosphere. However some differences between the models are still present after the long-term evolution. Intermediate mass planets formed by pebble accretion indeed reach densities as low as 0.2 g/cm^3 , where the lower limit reached by planets formed by planetesimal accretion is 0.5 g/cm^3 (Fig. 12). Therefore only the pebble model could form such gas-rich intermediate mass planets.

However the planets formed by pebble accretion do not grow to giants because of their too efficient migration (see Fig. 13). They indeed grow quickly to their isolation mass and therefore reach in the early evolution of the disc the mass range where type I migration is decisive. Migration is very efficient in a dense disc and the planet reaches the inner regions of the disc very quickly, without enough time to accrete a significant envelope (Coleman & Nelson 2014, 2016b). On the other hand, planets formed by planetesimal accretion have a slower growth rate. Furthermore when they start accreting gas, they are still accreting solids, which slows their accretion of gas due to an increased solid accretion luminosity (Alibert et al. 2018). Thus the transition between pure solid accretion and gas accretion is not abrupt, helping them to become massive enough to open a gap in the disc. This therefore reduces their migration rate, allowing them more frequently to accrete gas efficiently and grow to giant planets.

The lack of giant planets formed by the pebble accretion model is interesting to compare with Brügger et al. (2018). A substantial amount of giants was obtained when reducing the opacity in the planetary envelope. However in Brügger et al. (2018) the disc profile is different (as mentioned in Sect. 2.1),

³ Note that in our previous work (Brügger et al. 2018), we reduced the opacity also above M_{iso} , which is why there was a change in the mass functions.

leading to a higher surface density in the outer regions and therefore a higher flux of pebbles. The variability in the amount of solids (ranging between 0.011 and 0.11) is also a key factor for the formation of giants. In the present work we focus on a distribution with a mean value around $Z_{\text{tot}} = 0.02$, which lies in the lower range of what was used in the previous work and therefore the amount of giant planets is affected. For similar amounts of solids, the same types of planets as in the present work were obtained.

For the planetesimal accretion model the amount of giant planets is impacted by the size of the planetesimals. We focused in this work on 1 km sized planetesimal, which helps the formation of giants compared to bigger sizes (Fortier et al. 2013). This highlights that both scenarios require specific conditions to form giants. A hybrid approach (Alibert et al. 2018) might help to overcome the difficulties linked to each model.

Our work underlines the impact of the different accretion scenarios: pebble accretion or planetesimal accretion. We should however keep in mind that we focus on single planet populations and therefore the consequences of mutual interactions between the planets are not taken into account. We leave this improvement for future studies.

Acknowledgements. This work has been carried out within the frame of the National Centre for Competence in Research PlanetS supported by the Swiss National Science Foundation. The authors acknowledge the financial support of the SNSF under grant 200020_172746.

References

- Adachi, I., Hayashi, C., & Nakazawa, K. 1976, *Progress of Theoretical Physics*, 56, 1756
- Adams, F. C., Lada, C. J., & Shu, F. H. 1988, *ApJ*, 326, 865
- Alexander, R. D. & Pascucci, I. 2012, *MNRAS*, 422, 82
- Alibert, Y. 2016, *A&A*, 591, A79
- Alibert, Y., Carron, F., Fortier, A., et al. 2013, *A&A*, 558, A109
- Alibert, Y., Mordasini, C., Benz, W., & Winisdoerffer, C. 2005, *A&A*, 434, 343
- Alibert, Y., Venturini, J., Helled, R., et al. 2018, *Nature Astronomy*, 2, 873
- Andrews, S. M., Wilner, D. J., Hughes, A. M., Qi, C., & Dullemond, C. P. 2010, *ApJ*, 723, 1241
- Ansdeell, M., Williams, J. P., Trapman, L., et al. 2018, *ApJ*, 859, 21
- Ataiee, S., Baruteau, C., Alibert, Y., & Benz, W. 2018, *A&A*, 615, A110
- Bell, K. R. & Lin, D. N. C. 1994, *ApJ*, 427, 987
- Birnstiel, T., Klahr, H., & Ercolano, B. 2012, *A&A*, 539, A148
- Bitsch, B., Johansen, A., Lambrechts, M., & Morbidelli, A. 2015, *A&A*, 575, A28
- Bitsch, B., Morbidelli, A., Johansen, A., et al. 2018, *A&A*, 612, A30
- Bodenheimer, P. & Pollack, J. B. 1986, *Icarus*, 67, 391
- Brügger, N., Alibert, Y., Ataiee, S., & Benz, W. 2018, *A&A*, 619, A174
- Burn, R., Marboeuf, U., Alibert, Y., & Benz, W. 2019, *A&A*, 629, A64
- Chambers, J. 2006, *Icarus*, 180, 496
- Clarke, C. J., Gendrin, A., & Sotomayor, M. 2001, *MNRAS*, 328, 485
- Coleman, G. A. L., Leleu, A., Alibert, Y., & Benz, W. 2019, *A&A*, 631, A7
- Coleman, G. A. L. & Nelson, R. P. 2014, *MNRAS*, 445, 479
- Coleman, G. A. L. & Nelson, R. P. 2016a, *MNRAS*, 460, 2779
- Coleman, G. A. L. & Nelson, R. P. 2016b, *MNRAS*, 457, 2480
- Coleman, G. A. L., Papaloizou, J. C. B., & Nelson, R. P. 2017, *MNRAS*, 470, 3206
- Crida, A., Morbidelli, A., & Masset, F. 2006, *Icarus*, 181, 587
- Drażkowska, J. & Alibert, Y. 2017, *A&A*, 608, A92
- Fortier, A., Alibert, Y., Carron, F., Benz, W., & Dittkrist, K. M. 2013, *A&A*, 549, A44
- Friedrich, J. M., Weisberg, M. K., Ebel, D. S., et al. 2015, *Chemie der Erde / Geochemistry*, 75, 419
- Haisch, Karl E., J., Lada, E. A., & Lada, C. J. 2001, *ApJ*, 553, L153
- Hansen, B. M. S. 2008, *ApJS*, 179, 484
- Hueso, R. & Guillot, T. 2005, *A&A*, 442, 703
- Ida, S. & Guillot, T. 2016, *A&A*, 596, L3
- Ida, S. & Lin, D. N. C. 2004, *ApJ*, 616, 567
- Inaba, S. & Ikoma, M. 2003, *A&A*, 410, 711
- Inaba, S., Tanaka, H., Nakazawa, K., Wetherill, G. W., & Kokubo, E. 2001, *Icarus*, 149, 235
- Jin, S., Mordasini, C., Parmentier, V., et al. 2014, *ApJ*, 795, 65
- Johansen, A. & Lambrechts, M. 2017, *Annual Review of Earth and Planetary Sciences*, 45, 359
- Lambrechts, M. & Johansen, A. 2012, *A&A*, 544, A32
- Lambrechts, M. & Johansen, A. 2014, *A&A*, 572, A107
- Lenz, C. T., Klahr, H., & Birnstiel, T. 2019, *ApJ*, 874, 36
- Lin, D. N. C. & Papaloizou, J. 1986, *ApJ*, 309, 846
- Lodders, K. 2003, *ApJ*, 591, 1220
- Lynden-Bell, D. & Pringle, J. E. 1974, *MNRAS*, 168, 603
- Mamajek, E. E. 2009, in *American Institute of Physics Conference Series*, Vol. 1158, American Institute of Physics Conference Series, ed. T. Usuda, M. Tamura, & M. Ishii, 3–10
- Matsuyama, I., Johnstone, D., & Hartmann, L. 2003, *ApJ*, 582, 893
- Morbidelli, A., Lambrechts, M., Jacobson, S., & Bitsch, B. 2015, *Icarus*, 258, 418
- Mordasini, C., Alibert, Y., & Benz, W. 2009, *A&A*, 501, 1139
- Mordasini, C., Alibert, Y., Georgy, C., et al. 2012a, *A&A*, 547, A112
- Mordasini, C., Alibert, Y., Klahr, H., & Henning, T. 2012b, *A&A*, 547, A111
- Mordasini, C., Klahr, H., Alibert, Y., Miller, N., & Henning, T. 2014, *A&A*, 566, A141
- Mordasini, C., Mollière, P., Dittkrist, K.-M., Jin, S., & Alibert, Y. 2015, *International Journal of Astrobiology*, 14, 201
- Nakamoto, T. & Nakagawa, Y. 1994, *ApJ*, 421, 640
- Ohtsuki, K. 1999, *Icarus*, 137, 152
- Ormel, C. W. & Klahr, H. H. 2010, *A&A*, 520, A43
- Paardekooper, S.-J., Baruteau, C., Crida, A., & Kley, W. 2010, *MNRAS*, 401, 1950
- Paardekooper, S.-J., Baruteau, C., & Kley, W. 2011, *MNRAS*, 410, 293
- Paardekooper, S.-J. & Mellema, G. 2006, *A&A*, 459, L17
- Pollack, J. B., Hubickyj, O., Bodenheimer, P., et al. 1996, *Icarus*, 124, 62
- Rafikov, R. R. 2004, *AJ*, 128, 1348
- Ruden, S. P. & Pollack, J. B. 1991, *ApJ*, 375, 740
- Santos, N. C., Israelian, G., Mayor, M., et al. 2005, *A&A*, 437, 1127
- Saumon, D., Chabrier, G., & van Horn, H. M. 1995, *ApJS*, 99, 713
- Schoonenberg, D., Liu, B., Ormel, C. W., & Dorn, C. 2019, *A&A*, 627, A149
- Scott, D. W. 1992, *Multivariate Density Estimation*
- Shakura, N. I. & Sunyaev, R. A. 1973, *A&A*, 24, 337
- Shibaike, Y., Ormel, C. W., Ida, S., Okuzumi, S., & Sasaki, T. 2019, *ApJ*, 885, 79
- Tychoniec, Ł., Tobin, J. J., Karska, A., et al. 2018, *ApJS*, 238, 19

5.5. Letter II: A water budget dichotomy of rocky protoplanets from ^{26}Al -heating

Since the introduction of planetary orbital migration (Sect. 4.3), it was speculated that close-in planets might be commonly water-rich (Kuchner, 2003; Ida & Lin, 2004a). Especially around lower-mass stars, planets with lower masses undergo fast type I migration and develop into potentially habitable water worlds (Alibert & Benz, 2017). Those planets would have significant water mass fractions of up to 50 % and commonly on the order of 10 %.

However, the observational data now starts to show that most Earth-mass planets are in fact of a mainly rocky composition. Small water contents cannot be excluded, but water mass fractions on the order of 10 % are not found in close-in, Earth-mass planets in (a) the Solar System, (b) around the low-mass star TRAPPIST-1 (Grimm et al., 2018), and (c) in the statistical mean of the exoplanetary population. The last point (c) is true if the interpretation of the statistically significant radius valley (Fulton et al., 2017) can be attributed to photo-evaporative mass loss (Owen & Wu, 2013; Lopez & Fortney, 2013; Jin et al., 2014). Then, the location of the radius valley in the radius-period plane can only be explained by rocky compositions (Jin & Mordasini, 2018).

Therefore, there is compelling evidence that either planetary orbital migration from outside the snowline is not responsible for the delivery of the bulk of the planetary mass to close-in regions or that an additional physical ingredient is missing. In the letter by Lichtenberg et al. (2019) (Letter II), we explore the effect of radioactive heating on the planetesimal composition and finally the resulting planetary composition in the statistical population synthesis framework. The effect the decay of ^{26}Al was found to dominate and influence planetesimals with sizes larger than 10 km in the most early stages of the disk (Lichtenberg et al., 2016). These calculations were extended and tabulated by Tim Lichtenberg and collaborators at the ETHZ.

The contribution to Letter II by the University of Bern group including myself are the calculation of planetary population syntheses incorporating ^{26}Al -heating. I implemented a module to decrease the ice mass in the planetesimal disk. This module reads in the tables provided by Tim Lichtenberg and accordingly removes ice from the planetesimal disk as a function of time since the calcium-aluminium-rich inclusion formation. The details can be found in the methods section of the following letter.


Apart from the dehydration module, the Bern model of planet formation was used in its nominal mode. To explore a part of the large parameter space, we varied the stellar mass, and correspondingly the initial disk masses and sizes, as well as the initial planetesimal size.

We find that ^{26}Al -heating leads to a significant and observable decrease in the planetary water-mass content. Especially for stars with higher ^{26}Al fractions, all planetesimals can dry-out which removes most of the ice that would have been accreted by embryos otherwise. The process is most efficient for large planetesimals. However, planet growth timescales increase for larger planetesimals, which is a long

standing problem in planet formation.

In the future, a planetesimal formation model should be coupled to the ^{26}Al -heating module to explore if a realistic planetesimal formation pathway could concentrate planetesimals to grow larger planets while still forming planetesimals rapidly enough to keep the ^{26}Al -heating significant.

A water budget dichotomy of rocky protoplanets from ^{26}Al -heating

Tim Lichtenberg ^{1,6*}, Gregor J. Golabek ², Remo Burn ³, Michael R. Meyer ⁴, Yann Alibert ^{3,5},
Taras V. Gerya ¹ and Christoph Mordasini ^{3,5}

In contrast to the water-poor planets of the inner Solar System, stochasticity during planetary formation^{1,2} and order-of-magnitude deviations in exoplanet volatile contents³ suggest that rocky worlds engulfed in thick volatile ice layers^{4,5} are the dominant family of terrestrial analogues^{6,7} among the extrasolar planet population. However, the distribution of compositionally Earth-like planets remains insufficiently constrained³, and it is not clear whether the Solar System is a statistical outlier or can be explained by more general planetary formation processes. Here we use numerical models of planet formation, evolution and interior structure to show that a planet's bulk water fraction and radius are anti-correlated with initial ^{26}Al levels in the planetesimal-based accretion framework. The heat generated by this short-lived radionuclide rapidly dehydrates planetesimals⁸ before their accretion onto larger protoplanets and yields a system-wide correlation^{9,10} of planetary bulk water abundances, which, for instance, can explain the lack of a clear orbital trend in the water budgets of the TRAPPIST-1 planets¹¹. Qualitatively, our models suggest two main scenarios for the formation of planetary systems: high- ^{26}Al systems, like our Solar System, form small, water-depleted planets, whereas those devoid of ^{26}Al predominantly form ocean worlds. For planets of similar mass, the mean planetary transit radii of the ocean planet population can be up to about 10% larger than for planets from the ^{26}Al -rich formation scenario.

In the early Solar System, the decay heat from the short-lived radionuclide ^{26}Al ($t_{1/2}$, $^{26}\text{Al} \approx 0.72$ Myr) powered the interior evolution of planetesimals, the seeds and building blocks of the rocky planets, and led to silicate melting^{12,13} and degassing of primordial water abundances^{8,14}. Here, we explore the systematic effects of ^{26}Al on rocky planetary systems using numerical models of planetary formation¹⁵ with ^{26}Al -induced water loss from planetesimals during the main accretion phase¹⁴. We generate synthetic planet populations with internal structures defined by the planets' composition, which result in statistical variations of planetary water abundance and (transit) radius.

In the models presented, initially Moon-sized protoplanets grow from the accretion of planetesimals (1–100 km in size) and gas, and migrate within the protoplanetary disk of G- or M-type systems (see Methods). The initial locations of the embryos and the starting disk structures and boundaries are randomized to reflect the diversity found in observed young planetary systems¹⁶. Planetesimals are set to be dry within the snowline and icy outside, with a decreasing

water mass fraction over time, calculated from planetesimal interior models that account for the dehydration from internal radiogenic heating of ^{26}Al . Here, we account for accretion of planetesimals only, and ignore the potential contribution from smaller particles, such as pebbles^{17–19}. The heating rate in the planetesimal interior is controlled by the amount of ^{26}Al incorporated during planetesimal formation, which may vary substantially between planetary systems^{20,21}. We account for this variability by generating synthetic planet populations with different planetesimal radii, $r_{\text{plts}} = 3, 10$ and 50 km, and initial ^{26}Al abundances of $^{26}\text{Al}_0 \in [0.1, 10]^{26}\text{Al}_\odot$, with $^{26}\text{Al}_\odot$ the Solar System's 'canonical' ($^{26}\text{Al}/^{27}\text{Al}$)₀ at the time of calcium–aluminium-rich inclusion (CAI) formation, and compare them to a nominal case without ^{26}Al -heating (for further details on the models, see Methods). For each combination of r_{plts} , $^{26}\text{Al}_0$ and stellar type (G or M), we performed 30,000 single-planet simulations^{1,15}, resulting in a statistically representative set of 540,000 individual simulations over 18 parameter sets (Fig. 1).

The effects of $^{26}\text{Al}_0$ and r_{plts} on the retention of water within planetesimals and resulting planet populations from a given set of initial conditions are shown in Fig. 1. Planetesimals with larger r_{plts} and higher $^{26}\text{Al}_0$ dehydrate faster, and up to 100% for extreme values. Rooted in our conservative choice for dehydration (see Methods), the total water loss divides the parameter range into two distinct regimes. The first consists of almost pristine water–rock ratios for small planetesimals with low $^{26}\text{Al}_0$. However, for $^{26}\text{Al}_0 \gtrsim ^{26}\text{Al}_\odot$ and planetesimals with $r_{\text{plts}} \gtrsim 10$ km, water loss is nearly complete (Fig. 1a,b).

For distinct combinations of $^{26}\text{Al}_0$ and r_{plts} , we simulate the influence on the expected planet population for planet masses $M_p \in [0.1, 10] M_{\text{Earth}}$ (Fig. 1c). Because the timescale for water loss caused by ^{26}Al -heating is significantly shorter than the accretion timescale, sufficiently ^{26}Al -enriched planetesimals are mostly dry when they accrete onto protoplanets. Therefore, the final water mass fractions for the planets are correlated with the retained water fraction in planetesimals, owing to ^{26}Al -heating. The planet desiccation caused by the accretion of ever-more dehydrated planetesimals reduces the inherent scatter and range in $f_{\text{H}_2\text{O}}$ in the synthetic planet populations (cf. Figs. 1c and 2a,b). For fixed planetesimal radius and increasing $^{26}\text{Al}_0$, accreting planets receive more relative mass contribution from dry objects and end up water-depleted relative to nominal conditions.

In the Solar System, the initial planetesimal size frequency distribution is expected to have been dominated by bodies with $r_{\text{plts}} \gtrsim 30$ –50 km²². For such bodies, the equilibrium between radiogenic heating and surface cooling stabilizes internal temperatures

¹Institute of Geophysics, ETH Zürich, Zürich, Switzerland. ²Bayerisches Geoinstitut, University of Bayreuth, Bayreuth, Germany. ³Physikalisches Institut, University of Bern, Bern, Switzerland. ⁴Department of Astronomy, University of Michigan, Ann Arbor, MI, USA. ⁵Center for Space and Habitability, University of Bern, Bern, Switzerland. ⁶Present address: Atmospheric, Oceanic and Planetary Physics, University of Oxford, Oxford, UK.

*e-mail: tim.lichtenberg@physics.ox.ac.uk

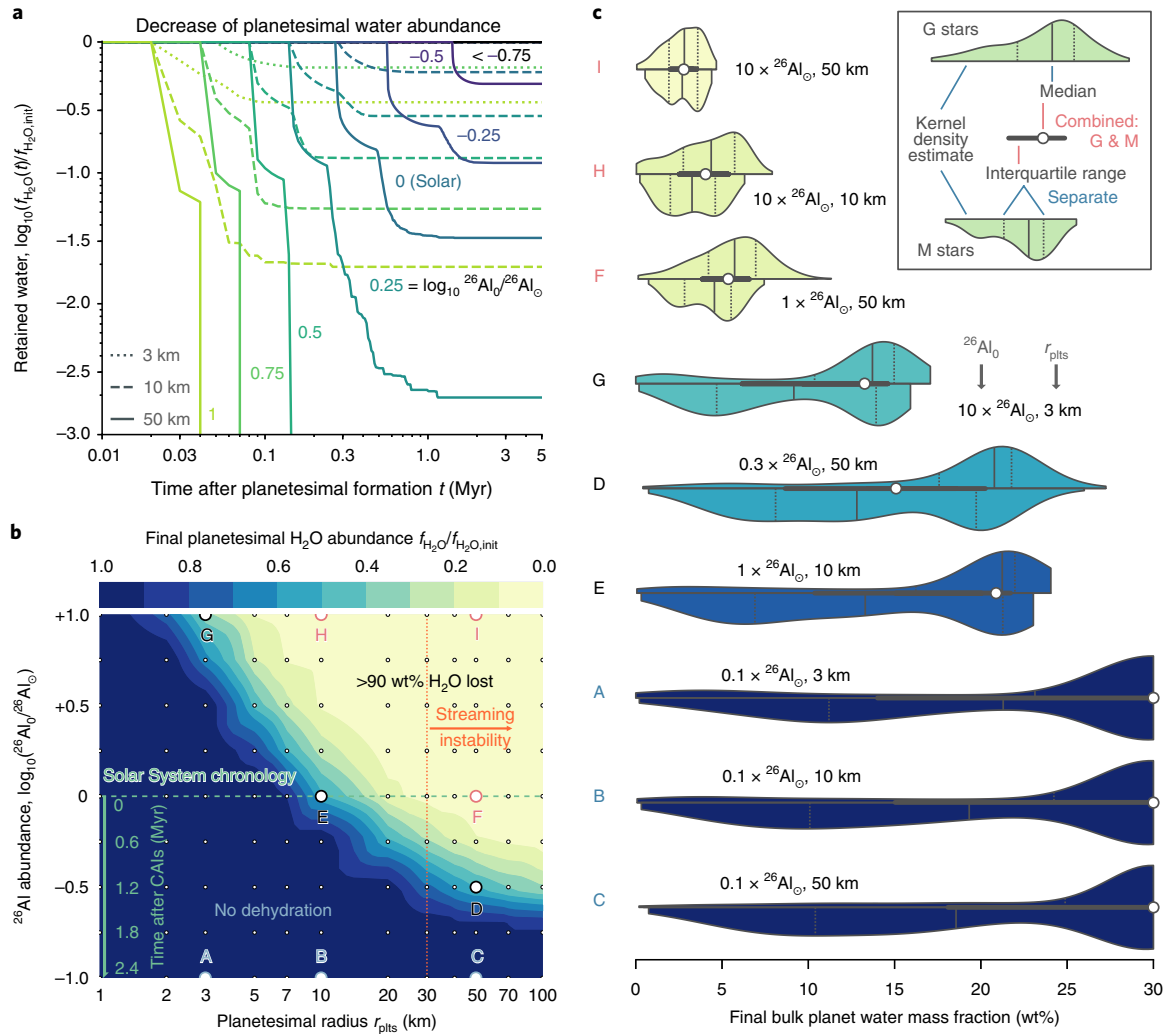


Fig. 1 | Dehydration of icy planetesimals from ^{26}Al -heating and resulting influence on planet water abundance. **a, Time-resolved water retention for planetesimals of 3, 10 and 50 km radius with $^{26}\text{Al}_0 \in [0.1, 10]^{26}\text{Al}_\odot$. Brighter colours indicate stronger water depletion. The degassing saturation, when the lines become horizontal, results from the rapid decay of ^{26}Al . **b**, Final state of water retention. The initial abundance $^{26}\text{Al}_0$ at planetesimal formation can be translated into time after the formation of CAIs for Solar System objects. The orange line depicts the approximate lowest-mass planetesimals inferred for the early Solar System planetesimal population²². **c**, Distribution and shift in planet bulk water abundances for specific planetesimal configurations from **a, b**, for planet masses $M_p \in [0.1, 10]M_{\text{Earth}}$ and $f_{\text{H}_2\text{O}} > 0$. The legend for the violin distributions is given in the upper-right box. Each configuration shows the statistical distribution of $f_{\text{H}_2\text{O}}$ in a synthetic planet population generated from our model. The white dot in the grey bar in the middle of each violin histogram represents the median of the entire (combined G- and M-star) planet population, the horizontal grey bar the interquartile range (middle 50% of the population within the bar, upper and lower 25% outside the bar), again combined. The vertical solid and dashed lines in the upper and lower violin histograms represent the median and interquartile range, respectively, for the G- or M-star planet population in isolation. The water retention in planetesimals from **a, b** is correlated with the final retained water in **c** (colour scales in **b, c** are equal).**

for an extended timespan at spatially isothermal conditions¹³. Therefore, the fractional dehydration in Fig. 1b flattens above $r_{\text{plts}} \gtrsim 50$ km and becomes nearly independent of planetesimal size. For $r_{\text{plts}} = 50$ km, dehydration is dominantly controlled by $^{26}\text{Al}_0$ and generates a dichotomy between planets in ^{26}Al -enriched (top black and red histograms, Fig. 2) versus non-enriched systems (top blue histogram, Fig. 2). M and G stars overall display a similar trend, but M stars form smaller planets on average, owing to their lower initial budget of planet-forming material.

The emerging trend from our simulations is illustrated in Fig. 3, with a clear distinction between planetary systems that are significantly enriched ($^{26}\text{Al}_0 \gtrsim 26\text{Al}_\odot$) and those that are not. In general, ^{26}Al is expected to be abundant but inhomogeneously distributed within young star-forming regions^{20,23}. According to our simulations,

planets in enriched systems grow from ever-more dehydrated planetesimals and form desiccated planets in their terrestrial planet zone. Depending on the initial planetesimal sizes, final planet water fractions are up to two orders of magnitude below the initial planetesimal water mass fractions, and are strongly correlated with the efficiency of dehydration during accretion (Fig. 1).

The bulk volatile mass fraction has the greatest influence on the structure and mass–radius relation of a rocky planet^{24,25}. Therefore, we anticipate the resulting smaller radii (from lower water mass fraction) for higher ^{26}Al levels to be reflected in the galactic exoplanet population. For deviations in planet bulk water fractions predicted here, the thickness of the volatile layer on top of the silicate mantle constitutes several per cent of the radius^{4,5,24,26}. We calculate this deviation in our synthetic populations by translating the

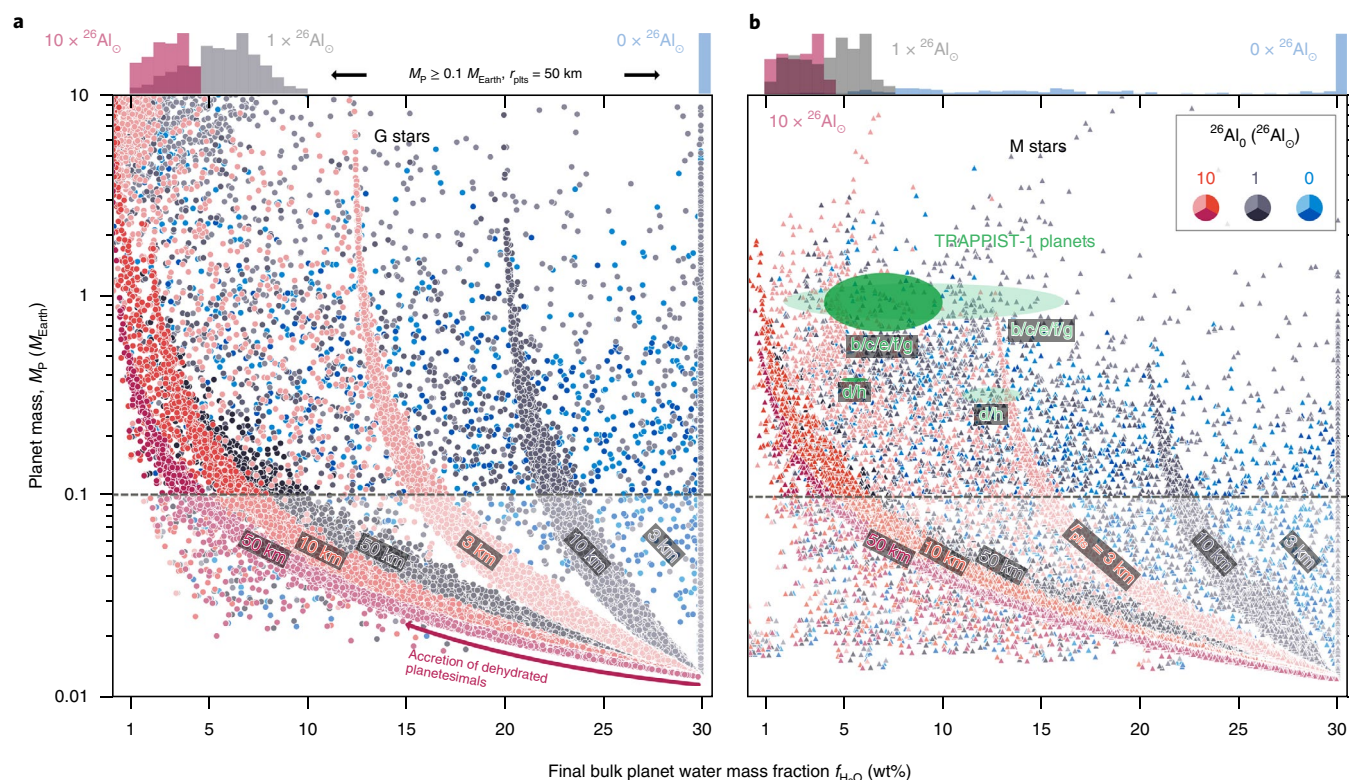


Fig. 2 | Gradual desiccation of protoplanets as a function of $^{26}\text{Al}_0$ for planets with $f_{\text{H}_2\text{O}} > 0$. **a, b**, For increasing $^{26}\text{Al}_0$ and r_{plts} , the bulk planet water fraction $f_{\text{H}_2\text{O}}$ decreases systematically. For $M_{\text{p}} \geq 0.1 M_{\text{Earth}}$ and $r_{\text{plts}} = 50 \text{ km}$, the $f_{\text{H}_2\text{O}}$ histogram on top shows a difference of approximately one order of magnitude between planets formed devoid of ^{26}Al and with $^{26}\text{Al} \gtrsim ^{26}\text{Al}_0$. Only the latter cases increasingly populate the terrestrial planet regime with $f_{\text{H}_2\text{O}} \lesssim \mathcal{O}(\text{wt}\%)$. The populations with $^{26}\text{Al}_0 = 0$ (blue points) only rarely and stochastically form planets with low water mass fractions, which are due to rapid inward migration. The clustering for $^{26}\text{Al}_0 = 0$ at the maximum water mass fraction is inherited from the chosen initial composition of planetesimals beyond the snowline (Methods). It is important to note that the areas of clustering locate the maximum water mass fractions for a given planet mass within a synthetic population, that is, planets that are formed entirely beyond the snowline. For example, all planets from the synthetic population with $r_{\text{plts}} = 3 \text{ km}$, and $^{26}\text{Al}_0 = 10 \times ^{26}\text{Al}_0$, show water mass fractions $f_{\text{H}_2\text{O}} \lesssim 15 \text{ wt}\%$ for $M_{\text{p}} \geq 0.1 M_{\text{Earth}}$. G stars (**a**) on average form higher-mass planets than M stars (**b**) because of their higher initial total mass budget in the disk. The TRAPPIST-1 planets (the labels b to h in **b** refer to the planets TRAPPIST-1 b to TRAPPIST-1 h) are shown as inferred previously¹¹ for the planet masses from ref. ³⁰ (light green) and with potential systematic shifts in the data accounted for (dark green). They are consistent with being formed in a planetary system with $^{26}\text{Al}_0 \gtrsim ^{26}\text{Al}_0$ and $r_{\text{plts}} \gtrsim 10 \text{ km}$ and plot in sparsely populated regions of the $^{26}\text{Al} = 0$ planet populations. The ellipses give the statistically inferred values (the 1- σ confidence levels) for planetary masses and water mass fraction of the planets TRAPPIST-1 b to TRAPPIST-1 h.

derived planetary masses and compositions into a mean radius in a given mass bin (Fig. 4) using interior structure models that are sensitive to the total planet mass, its water and (captured) hydrogen/helium mass fraction, and the surface pressure (see Methods). For the entire populations of planets among G and M stars, the radius deviation reaches 2% for $1 \times ^{26}\text{Al}_0$, and can go up to about 4% for Mars-sized planets for $10 \times ^{26}\text{Al}_0$ or $r_{\text{plts}} = 50 \text{ km}$, respectively. If we only consider planets that accrete a minimum amount of water (planets that receive some mass contribution from beyond the iceline), with $10 \times ^{26}\text{Al}_0$, or $1 \times ^{26}\text{Al}_0$ with $r_{\text{plts}} = 50 \text{ km}$, the mean-radius shift can reach about 10%. Planetary systems with high $^{26}\text{Al}_0$ ($^{26}\text{Al}_0 \gtrsim 1-10 \times ^{26}\text{Al}_0$) form water-depleted planets with system-wide smaller radii than for the non-enriched population.

Such deviations are expected to be measurable by the planned PLATO mission²⁷, which will aim to characterize a statistical ensemble of planetary radii in the rocky planet regime. The intrinsic compositional scatter in the inferred mean densities from known exoplanets suggests a large stochastic component in the planet formation process. Yet, recent analyses of data based on Kepler multi-planet systems provided strong evidence for intra-system correlation between planetary radii^{9,10}. Therefore, in the exoplanet census probed so far, the fate and long-term structure of

planets seems to be dominated by physical and chemical effects on a system-to-system level, rather than emerging from intra-system stochasticity during accretion, such as impact stripping^{28,29}. With future access to a statistical ensemble of low-mass planet radii from exoplanet-focused missions, the highly ^{26}Al -enriched systems, such as the Solar System, where planetary radii deviate by several per cent from the population of ^{26}Al -poor systems, may stick out from the mean of the population and provide clues about the underlying ^{26}Al distribution of planetary systems.

For example, the system-wide water depletion of the TRAPPIST-1 planets^{11,30} is consistent with desiccation induced by $^{26}\text{Al} \gtrsim ^{26}\text{Al}_0$ (Fig. 2). The atmospheres of the TRAPPIST-1 planets seem to be secondary³¹, and may have lost several Earth ocean equivalents of water³². However, to account for the consistency of especially the outermost planets e–h with near Earth-like volatile abundances and lack of an orbital trend in water budget¹¹, an order-of-magnitude depletion mechanism, such as suggested here, must affect all of the planets. Therefore, the retrieved low water mass fractions of the TRAPPIST-1^{11,30} planets are unexpected from formation and evolution models^{1,6,25,33,34}, and present a severe challenge for current planet formation scenarios. The ^{26}Al desiccation mechanism that we put forward achieves system-wide water depletion for G and M

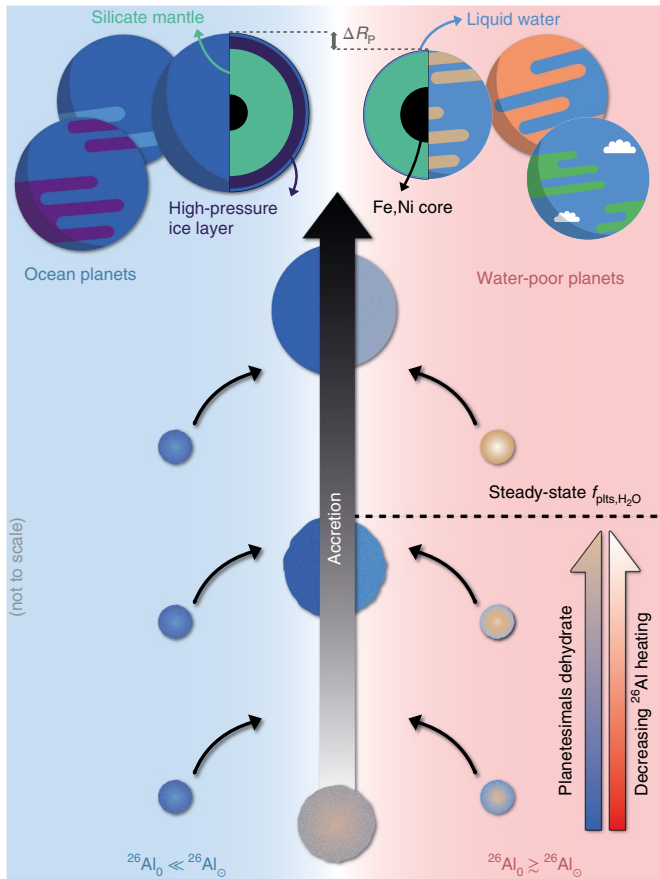


Fig. 3 | Qualitative sketch of the effects of ^{26}Al enrichment on planetary accretion. Left, ^{26}Al -poor planetary systems; right, ^{26}Al -rich planetary systems. R_p , planetary radius. Arrows indicate proceeding accretion (middle), planetesimal water content (bottom right, blue–brown) and live ^{26}Al (bottom right, red–white).

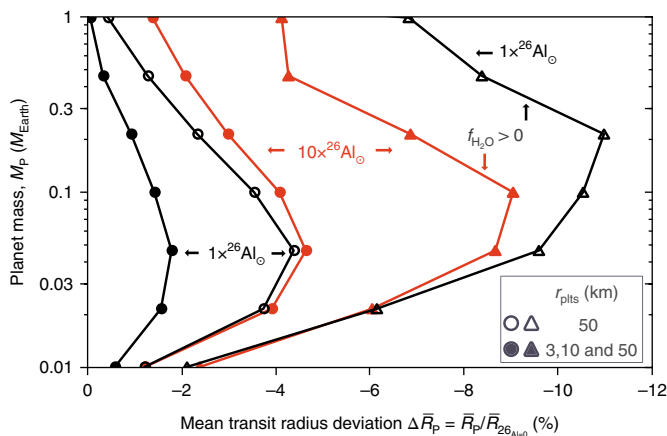


Fig. 4 | Shift in mean transit radii between planetary populations with varying ^{26}Al enrichment. Quantitative predictions for planetary mean transit radii (see Methods) for given mass bins in planetary systems with ^{26}Al , normalized to the case completely devoid of ^{26}Al . Open symbols indicate radius deviations averaged over simulations with $r_{\text{ppts}} = 50$ km; filled symbols combine 3-km, 10-km and 50-km planetesimals. Triangles indicate planets with $f_{\text{H}_2\text{O}} > 0$; circles include also completely dry planets that formed entirely inside of the water snowline. For varying selection criteria, the planet radii per mass bin for ^{26}Al -enriched systems deviate from non-enriched systems by up to about 10%.

stars without the need to fit specific accretion dynamics, as it has been proposed^{25,34}. However, because the TRAPPIST-1 system is just the first of perhaps many such systems, coordinated observational efforts will be required to establish population characteristics for similar systems, in order to distinguish between ^{26}Al desiccation and migration-driven mechanisms^{25,34} as the origin of the TRAPPIST-1 planet compositions.

For accretion scenarios in which planetesimals represent the primary carrier of water, our models suggest that planetary systems with ^{26}Al abundances similar to or higher than the Solar System generically form terrestrial planets with low water mass fractions, with $f_{\text{H}_2\text{O}} \lesssim \mathcal{O}(\text{wt}\%)$. This effect is more pronounced for planets further out from their host star, as embryos in these regions grow preferentially from water-rich solids. For a non-uniform distribution of ^{26}Al in Milky Way star-forming regions, the systematic water depletion in ^{26}Al -enriched systems suggests the existence of two qualitatively distinct classes of planetary systems: water-poor (^{26}Al -rich) and water-rich (^{26}Al -poor) systems, with a systematic mean-radius deviation for sub-Earth terrestrial planets between these classes. The resulting shape of the distribution of dry and wet planetary systems depends on the genuine, but unknown, distribution of ^{26}Al levels²¹ among planet-forming systems and the nature and timing of protoplanet accretion. If rocky planets grow primarily from the accumulation of planetesimals, then the suggested deviation between planetary systems should be clearly distinguishable among the rocky exoplanet census. If, however, the main growth of rocky planets proceeds from the accumulation of small particles, such as pebbles, then the deviation between ^{26}Al -rich and ^{26}Al -poor systems may become less clear, and the composition of the accreting pebbles needs to be taken into account. Therefore, in future work, models of water delivery and planet growth need to synchronize the timing of earliest planetesimal formation³⁵, the mutual influence of collisions³⁶ and ^{26}Al dehydration, the potential growth by pebble accretion^{17–19}, and the partitioning of volatile species between the interior and atmosphere of growing protoplanets³⁷ in order to further constrain the perspectives for rocky (exo-)planet evolution³⁸.

Methods

Planetesimal dehydration. We model water loss from instantaneously formed planetesimals composed of a rock–ice mixture using numerical models that employ a conservative finite-differences, fully staggered grid method coupled to a marker-in-cell approach^{39,40}. The thermo-chemical evolution of planetesimals is computed in a two-dimensional infinite cylinder geometry on a Cartesian grid, solving the Poisson, continuity, Stokes and energy conservation equations. We assume the planetesimals to be accreted with the temperature of the protoplanetary disk beyond the water snowline, $T_0 = 150$ K, which is kept constant during the evolution of the planetesimal using the free-surface ‘sticky-air’ method⁴¹. Heating is provided by the decay of ^{26}Al , which defines the radiogenic heat source term over time

$$H_{^{26}\text{Al}}(t) = f_{\text{Al}} \left(\frac{^{26}\text{Al}}{^{27}\text{Al}} \right)_0 E_{^{26}\text{Al}} \exp(-t / \tau_{^{26}\text{Al}}) / \tau_{^{26}\text{Al}} \quad (1)$$

where f_{Al} is the chondritic abundance of aluminium⁴², $^{26}\text{Al}_0 = (^{26}\text{Al}/^{27}\text{Al})_0$ is the ratio of ^{26}Al to stable ^{27}Al at the time of planetesimal formation, $E_{^{26}\text{Al}} = 3.12$ MeV is the decay energy⁴³ and $\tau_{^{26}\text{Al}} = 1.03$ Myr is the mean lifetime. We ignore any potential heat contribution from ^{60}Fe , which may further boost radiogenic heating rates in extrasolar systems^{30,44}. If the planetesimal interior reaches temperatures beyond the rock disaggregation threshold⁴⁵ at a silicate melt fraction of $\phi \gtrsim 0.4$, where the rock viscosity drops by more than ten orders of magnitude, we approximate the thermal conductivity in the soft turbulence limit⁴⁶ with

$$k_{\text{eff}} = (q / 0.89)^{3/2} \alpha_{\text{liq}} g c_p / (\Delta T^2 \rho_s \eta_{\text{num}}) \quad (2)$$

with the convective heat flux q , the temperature difference across nodes ΔT , silicate density ρ_s , thermal expansivity of molten silicates α_{liq} , silicate heat capacity c_p , local gravity $g(x, y)$, and lower cut-off viscosity η_{num} . For numerical values used and further details and references on the code, see ref. 13. The initial planetesimal water-to-rock ratio beyond the snowline is expected to be between about 0.05 (refs. 33,47), the water content of carbonaceous chondrites, and about 0.5, as suggested by equilibrium condensation calculations⁴². Here, we adopt a value closer to the upper estimate, $f_{\text{H}_2\text{O}, \text{init}} = 0.3$, but our calculations only marginally depend on the adopted value.

In general, during heat-up of a primordial water ice–rock mixture, ices melt and react with the ambient rock. The liquid water undergoes pore water convection and escapes quickly once the gas phase is reached⁸, but a small fraction of water may be trapped in hydrous silicate phases. Therefore, we numerically account for dehydration of parts of the planetesimal interior at a conservative upper limit of $T \geq T_{\text{dry}} = 1,223 \text{ K}$, the upper limit of the amphibolite stability field, when any possibly remaining hydrous silicate phases break down. At these high temperatures, exsolved water vapour is lost quasi-instantaneously because planetesimals of this size cannot preserve an outgassed atmosphere. We do not resolve potential earlier water loss from degassing⁴⁸, residual volatiles above T_{dry} (ref. ⁴⁹), or ice sublimation during late and optically thin disk stages⁵⁰. Using these assumptions, we compute the expected ratio of dehydrated to primordial water–rock mixture at time t due to degassing,

$$f_{\text{H}_2\text{O}}(t) / f_{\text{H}_2\text{O,init}} = 1 - X_{\text{dry}}(t) / X_{\text{plts}} \quad (3)$$

with the dry fraction, $X_{\text{dry}}(t)$, of the total planetesimal interior, X_{plts} , and the initial water-to-rock ratio, $f_{\text{H}_2\text{O,init}} = 0.3$. Under these conditions, a planetary system in the planet formation model is represented by an initial $^{26}\text{Al}_0$ that corresponds to the time of planetesimal formation. If the ^{26}Al content may vary spatially within the disk, as has been suggested^{51,52}, the Solar System itself would be represented by a sub-canonical ($^{26}\text{Al}_0 \leq ^{26}\text{Al}_0$) value, similar to the effects of delayed planetesimal formation (Fig. 1b; cf. ref. ³⁶ for a discussion of the effects on planetesimal evolution).

Planet formation. We compute the formation of planets and generate our synthetic planet populations using an updated version of the model of ref. ⁵³. The computer code numerically treats the structure and evolution of the protoplanetary disk, the dynamical properties and accretion rate of planetesimals onto accreting protoplanets, the planetary envelope structure and disk–planet interactions^{15,54–56}. Here, we provide a brief summary of the most important code modules used in this work.

The protoplanetary disk model relies on the Shakura–Sunyaev⁵⁷ disk viscosity approximation ($\alpha_{\text{disk}} = 2 \times 10^{-3}$) and computes the surface density evolution over time by solving the radial diffusion equation,

$$\frac{d\Sigma}{dt} = \frac{3}{r} \frac{\partial}{\partial r} \left[r^{1/2} \frac{\partial}{\partial r} \tilde{\nu} \Sigma r^{1/2} \right] + \dot{\Sigma}_w + \dot{Q}_{\text{planet}} \quad (4)$$

with the surface density Σ , orbital radius r , effective viscosity $\tilde{\nu}$ and gas accretion onto embryos \dot{Q}_{planet} , calculated from removing gas in an annulus centred on the embryo with a width of one Hill radius,

$$R_{\text{H}} = a_{\text{planet}} \left[M_{\text{planet}} / (3M_{\text{star}}) \right]^{1/3} \quad (5)$$

with the planet semi-major axis a_{planet} , planet mass M_{planet} and star mass M_{star} . Mass loss due to internal (extreme ultraviolet) photoevaporation $\dot{\Sigma}_w$ is set $\propto r^{-5/2}$ outside a gravitational radius of about 5 astronomical units (au), and external (far ultraviolet) photoevaporation⁵⁹ is constant outside about 140 au, with the total mass loss being a free model parameter. The parameters used to represent the planetesimal disk rely on the initial central temperature and pressure from the gas disk model to compute the location of the water snowline, thereby neglecting radial drift of planetesimals and that of the snowline⁶⁰. Drift timescales for planetesimals larger than 1 km exceed the disk lifetime by orders of magnitude⁶¹.

We consider rocky planetesimals ($\bar{\rho}_{\text{plts-dry}} = \rho_{\text{rock}} = 3,200 \text{ kg m}^{-3}$) inside, and rock-ice aggregates ($\bar{\rho}_{\text{plts-ice,init}} = \rho_{\text{H}_2\text{O}} f_{\text{H}_2\text{O,init}} + \rho_{\text{rock}} [1 - f_{\text{H}_2\text{O,init}}]$) beyond the snowline, which are fixed in radius and accrete onto the planetary embryo that is embedded in the disk in a single simulation. The residual water mass fraction, $f_{\text{H}_2\text{O}}(t)$, of the accreting planetesimals is computed from the internal evolution (see section ‘Planetesimal dehydration’ above) and is translated to a decreasing planetesimal density, $\bar{\rho}_{\text{plts-ice}}(t)$, and disk solid surface density, $\Sigma_{\text{plts-ice}}(t)$, by reducing the planetesimal density as

$$\bar{\rho}_{\text{plts-ice}}(t) = \rho_{\text{H}_2\text{O}} f_{\text{H}_2\text{O}}(t) + \rho_{\text{rock}} [1 - f_{\text{H}_2\text{O,init}}] \quad (6)$$

In this formulation, lost water is assumed to be replaced by pore space, and the planetesimal radius stays constant. The solid surface density available for embryos to accrete beyond the iceline thus changes with

$$\Sigma_{\text{plts-ice}}(t) = (f_{\text{H}_2\text{O}}(t) + [1 - f_{\text{H}_2\text{O,init}}]) \Sigma_{\text{plts-ice,init}} \quad (7)$$

In our nominal model, a single embryo of initially lunar mass, $M = 0.0123 M_{\text{Earth}}$, is placed randomly between specific inner and outer bounds within the protoplanetary disk (see section ‘Parameter space’ below), with a dry composition inside the snowline, and wet outside. It starts accreting solids (planetesimals) and gas, and may migrate in the type I and II regime, depending on the embryo mass and physical structure of the disk at a given orbit⁶². The solid accretion

rate^{63,64} takes into account the captured atmosphere. Planetesimal excitation and damping is computed by taking into account self-interactions and damping by gas drag⁶⁵. We ignore water loss due to collisions, which may further reduce the water inventory^{29,66–68} dependent on the frequency of such interactions, and accretion of smaller solid particles^{17,18,69} (‘pebbles’) that may shift the ratio of dry to wet accreted primitive materials⁷⁰. Gas accretion due to planetary contraction is considered using a dust opacity reduction factor of 0.01 compared with interstellar values^{71,72}.

G star settings are identical to the Sun’s values. The properties for the M-star runs are scaled down. We choose a fixed mass of $M_{\text{star}} = 0.2 M_{\odot}$ for the M stars. The radius of the star is set to

$$R_{\text{star}} = (M_{\text{star}} / M_{\odot})^{0.945} R_{\odot} \quad (8)$$

with luminosity⁷³

$$L_{\text{star}} = 0.628 (M_{\text{star}} / M_{\odot})^{2.62} L_{\odot} \quad (9)$$

and temperature

$$T_{\text{star}} = \sqrt[4]{L_{\text{star}} / (4\pi R_{\text{star}}^2 \sigma)} \quad (10)$$

with stellar radius R_{star} , stellar mass M_{star} and Stefan–Boltzmann constant σ . The disk dimensions, exponential cut-off radius and the embryo placement boundaries (see ‘Parameter space’) are reduced to account for the lower masses and sizes of M-star disks. Thus, initially all embryos form closer to the star than for the G-star populations. The initial disk mass follows the scaling law⁷⁴

$$M_{\text{disk}} \propto (M_{\text{star}} / M_{\odot})^{1.2} \quad (11)$$

with the internal photoevaporation rate adapted to match similar mean lifetimes compared to the G-star simulations. In reality, these could be anti-correlated with stellar mass⁷⁵, which would increase the efficiency of the ^{26}Al -dehydration mechanism for M stars owing to longer accretion timescales.

Interior structure and evolution. The interior structure and the long-term evolution of the planets is calculated as described in ref. ⁷⁶ by solving the classical one-dimensional radially symmetric interior structure equations of mass conservation, hydrostatic equilibrium and energy transport⁷⁷

$$\frac{\partial m}{\partial r_p} = 4\pi r_p^2 \rho \quad (12)$$

$$\frac{\partial P}{\partial r_p} = -\frac{Gm}{r_p^2} \quad (13)$$

$$\frac{\partial T}{\partial r_p} = \frac{T}{P} \frac{\partial P}{\partial r_p} \nabla(T, P) \quad (14)$$

where r_p is the radial distance from the planet’s centre, m the enclosed mass, P the pressure, ρ the density and G the gravitational constant. The intrinsic luminosity of a planet is assumed to be constant as a function of the planet radius. The gradient ∇ depends on the process by which the energy is transported (radiative diffusion or convection). These calculations yield the radii of the planets given their mass and bulk composition, namely the mass fractions of iron, silicates, water and H/He, as an output from the planet formation and planetesimal dehydration models. For the H/He envelope, the equation of state of ref. ⁷⁸ is used to solve the structure equations, while for the solid part of the planet, including the water content, the modified polytropic equations of state of ref. ⁷⁹ are used. The transit radius is estimated as in ref. ⁸⁰.

The loss of the primordial H/He envelope by atmospheric escape is considered in the energy- and radiation-recombination-limited approximation as described in ref. ⁸¹ and results in the loss of the primary atmosphere for low-mass planets at smaller orbital distances. Because of the limited water solubility in silicate mantles, the radius of planets without primordial H/He envelopes depends strongly on the water mass fraction⁸², and thus reveals the dehydration pattern caused by different abundances of ^{26}Al . Here, we do not treat interior-atmosphere exchange during early magma ocean phases that may further fractionate the volatile distribution within the body, in particular for close-in planets⁷.

Parameter space. From γ -ray observations, there is evidence for a widespread and heterogeneous distribution of ^{26}Al in the Galaxy²¹. Observational evidence from young star-forming regions and theoretical work suggest a non-uniform enrichment pattern among planetary systems^{20,21,23,44,83–87} with order-of-magnitude deviations from the Solar System’s ‘canonical’ ^{26}Al value⁸⁸ of $^{26}\text{Al}_0 = (^{26}\text{Al}/^{27}\text{Al})_0 = 5.25 \times 10^{-5}$. To account for these variations, we consider values in the range $^{26}\text{Al}_0 \in [0.1, 10] ^{26}\text{Al}_0$. In addition to initial ^{26}Al abundance, the radii of

planetesimals during accretion yield different thermal evolutionary sequences and thus dehydration patterns^{13,14}. Here, we test values in the range $r_{\text{phs}} \in [1, 100]$ km. However, we note that from asteroid-belt inferences and numerical studies of the streaming instability mechanism, radii larger than about 30–50 km are expected^{17,22,89,90,91}. All parameter models not listed in the Methods are identical to those used in ref. ¹³ and ref. ¹⁴. In the planet formation model, the innermost disk radius is of the order 0.1 au and can vary over time. Disk lifetimes are distributed around 5 Myr, which is controlled by the photoevaporation rate⁶⁵ and in agreement with current disk surveys^{92,93}. The initial embryos are placed within the boundaries of [0.05, 40] au for G stars and [0.086, 23.4] au for M stars. We vary in a Monte Carlo fashion⁵⁴ the disk mass, lifetime, dust-to-gas ratio and exponential cut-off radius⁷⁶ to represent the diversity found in nature^{16,94}.

Software. We acknowledge the software usage of Matplotlib⁹⁵, SciPy⁹⁶, NumPy⁹⁷, pandas⁹⁸ and seaborn⁹⁹ in this work.

Code and data availability

The data that support the plots within this paper, precompiled versions of the custom computer codes used, and other findings of this study are available from the corresponding author upon reasonable request.

Received: 5 May 2018; Accepted: 20 December 2018;
Published online: 11 February 2019

References

- Alibert, Y. & Benz, W. Formation and composition of planets around very low mass stars. *Astron. Astrophys.* **598**, L5 (2017).
- Raymond, S. N. & Izidoro, A. Origin of water in the inner Solar System: planetesimals scattered inward during Jupiter and Saturn's rapid gas accretion. *Icarus* **297**, 134–148 (2017).
- Kaltenegger, L. How to characterize habitable worlds and signs of life. *Annu. Rev. Astron. Astrophys.* **55**, 433–485 (2017).
- Kuchner, M. J. Volatile-rich Earth-mass planets in the habitable zone. *Astrophys. J. Lett.* **596**, L105–L108 (2003).
- Léger, A. et al. A new family of planets? 'Ocean-planets'. *Icarus* **169**, 499–504 (2004).
- Tian, F. & Ida, S. Water contents of Earth-mass planets around M dwarfs. *Nat. Geosci.* **8**, 177–180 (2015).
- Ramirez, R. M. & Levi, A. The ice cap zone: a unique habitable zone for ocean worlds. *Mon. Not. R. Astron. Soc.* **477**, 4627–4640 (2018).
- Grimm, R. E. & McSween, H. Y. Heliocentric zoning of the asteroid belt by aluminum-26 heating. *Science* **259**, 653–655 (1993).
- Millholland, S., Wang, S. & Laughlin, G. Kepler multi-planet systems exhibit unexpected intra-system uniformity in mass and radius. *Astrophys. J. Lett.* **849**, L33 (2017).
- Weiss, L. M. et al. The California-Kepler survey. V. Peas in a pod: planets in a Kepler multi-planet system are similar in size and regularly spaced. *Astron. J.* **155**, 48–60 (2018).
- Dorn, C., Mosegaard, K., Grimm, S. L. & Alibert, Y. Interior characterization in multiplanetary systems: TRAPPIST-1. *Astrophys. J.* **865**, 20–37 (2018).
- Fu, R. R. & Elkins-Tanton, L. T. The fate of magmas in planetesimals and the retention of primitive chondritic crusts. *Earth. Planet. Sci. Lett.* **390**, 128–137 (2014).
- Lichtenberg, T., Golabek, G. J., Gerya, T. V. & Meyer, M. R. The effects of short-lived radionuclides and porosity on the early thermo-mechanical evolution of planetesimals. *Icarus* **274**, 350–365 (2016).
- Monteux, J., Golabek, G. J., Rubie, D. C., Tobie, G. & Young, E. D. Water and the interior structure of terrestrial planets and icy bodies. *Space Sci. Rev.* **214**, 39–72 (2018).
- Benz, W., Ida, S., Alibert, Y., Lin, D. & Mordasini, C. in *Protostars and Planets VI* (eds Beuther, H. et al.) 691–713 (Univ. Arizona Press, Tucson, 2014).
- Ansdell, M. et al. ALMA survey of Lupus protoplanetary disks. I. Dust and gas masses. *Astrophys. J.* **828**, 46–61 (2016).
- Johansen, A., Mac Low, M.-M., Lacerda, P. & Bizzarro, M. Growth of asteroids, planetary embryos, and Kuiper belt objects by chondrule accretion. *Sci. Adv.* **1**, e1500109 (2015).
- Schiller, M., Bizzarro, M. & Fernandes, V. A. Isotopic evolution of the protoplanetary disk and the building blocks of Earth and the Moon. *Nature* **555**, 507–510 (2018).
- Alibert, Y. et al. The formation of Jupiter by hybrid pebble-planetesimal accretion. *Nat. Astron.* **2**, 2397–3366 (2018).
- Lichtenberg, T., Parker, R. J. & Meyer, M. R. Isotopic enrichment of forming planetary systems from supernova pollution. *Mon. Not. R. Astron. Soc.* **462**, 3979–3992 (2016).
- Lugaro, M., Ott, U. & Kereszturi, Á. Radioactive nuclei from cosmochronology to habitability. *Prog. Part. Nucl. Phys.* **102**, 1–47 (2018).
- Delbo, M., Walsh, K., Bolin, B., Avdellidou, C. & Morbidelli, A. Identification of a primordial asteroid family constrains the original planetesimal population. *Science* **357**, 1026–1029 (2017).
- Kuffmeier, M., Frosthalm Mogensen, T., Haugbølle, T., Bizzarro, M. & Nordlund, Å. Tracking the distribution of ²⁶Al and ⁶⁰Fe during the early phases of star and disk evolution. *Astrophys. J.* **826**, 22–47 (2016).
- Noack, L., Snellen, I. & Rauer, H. Water in extrasolar planets and implications for habitability. *Space Sci. Rev.* **212**, 877–898 (2017).
- Unterborn, C. T., Desch, S. J., Hinkel, N. R. & Lorenzo, A. Inward migration of the TRAPPIST-1 planets as inferred from their water-rich compositions. *Nat. Astron.* **2**, 297–302 (2018).
- Alibert, Y. On the radius of habitable planets. *Astron. Astrophys.* **561**, A41 (2014).
- Rauer, H. et al. The PLATO 2.0 mission. *Exp. Astron.* **38**, 249–330 (2014).
- Marcus, R. A., Sasselov, D., Stewart, S. T. & Hernquist, L. Water/icy super-Earths: giant impacts and maximum water content. *Astrophys. J. Lett.* **719**, L45–L49 (2010).
- Inamdar, N. K. & Schlichting, H. E. Stealing the gas: giant impacts and the large diversity in exoplanet densities. *Astrophys. J. Lett.* **817**, L13 (2016).
- Grimm, S. L. et al. The nature of the TRAPPIST-1 exoplanets. *Astron. Astrophys.* **613**, A68 (2018).
- de Wit, J. et al. Atmospheric reconnaissance of the habitable-zone Earth-sized planets orbiting TRAPPIST-1. *Nat. Astron.* **2**, 214–219 (2018).
- Bourrier, V. et al. Temporal evolution of the high-energy irradiation and water content of TRAPPIST-1 exoplanets. *Astron. J.* **154**, 121–138 (2017).
- Ciesla, F. J., Mulders, G. D., Pascucci, I. & Apai, D. Volatile delivery to planets from water-rich planetesimals around low mass stars. *Astrophys. J.* **804**, 9–20 (2015).
- Ormel, C. W., Liu, B. & Schoonenberg, D. Formation of TRAPPIST-1 and other compact systems. *Astron. Astrophys.* **604**, A1 (2017).
- Drażkowska, J. & Dullemond, C. P. Planetesimal formation during protoplanetary disk buildup. *Astron. Astrophys.* **614**, A62 (2018).
- Lichtenberg, T. et al. Impact splash chondrule formation during planetesimal recycling. *Icarus* **302**, 27–43 (2018).
- Ikoma, M., Elkins-Tanton, L., Hamano, K. & Suckale, J. Water partitioning in planetary embryos and protoplanets with magma oceans. *Space Sci. Rev.* **214**, 76–104 (2018).
- Kite, E. S. & Ford, E. B. Habitability of exoplanet waterworlds. *Astrophys. J.* **864**, 75–102 (2018).
- Gerya, T. V. & Yuen, D. A. Robust characteristics method for modelling multiphase visco-elasto-plastic thermo-mechanical problems. *Phys. Earth Planet. Inter.* **163**, 83–105 (2007).
- Golabek, G. J., Bourdon, B. & Gerya, T. V. Numerical models of the thermomechanical evolution of planetesimals: application to the acapulcoite- lodranite parent body. *Meteorit. Planet. Sci.* **49**, 1083–1099 (2014).
- Cramer, F. et al. A comparison of numerical surface topography calculations in geodynamic modelling: an evaluation of the 'sticky air' method. *Geophys. J. Int.* **189**, 38–54 (2012).
- Lodders, K. Solar System abundances and condensation temperatures of the elements. *Astrophys. J.* **591**, 1220–1247 (2003).
- Castillo-Rogez, J. et al. ²⁶Al decay: heat production and a revised age for Iapetus. *Icarus* **204**, 658–662 (2009).
- Nicholson, R. B. & Parker, R. J. Supernova enrichment of planetary systems in lowmass star clusters. *Mon. Not. R. Astron. Soc.* **464**, 4318–4324 (2017).
- Costa, A., Caricchi, L. & Bagdassarov, N. A model for the rheology of particle-bearing suspensions and partially molten rocks. *Geochem. Geophys. Geosys.* **10**, Q03010 (2009).
- Siggia, E. D. High Rayleigh number convection. *Annu. Rev. Fluid. Mech.* **26**, 137–168 (1994).
- O'Brien, D. P., Izidoro, A., Jacobson, S. A., Raymond, S. N. & Rubie, D. C. The delivery of water during terrestrial planet formation. *Space Sci. Rev.* **214**, 47–71 (2018).
- Castillo-Rogez, J. & Young, E. D. in *Planetesimals: Early Differentiation and Consequences for Planets* (eds Elkins-Tanton, L. T. & Weiss, B. P.) 92–114 (Cambridge Univ. Press, Cambridge, 2017).
- Fu, R. R., Young, E. D., Greenwood, R. C. & Elkins-Tanton, L. T. in *Planetesimals: Early Differentiation and Consequences for Planets* (eds Elkins-Tanton, L. T. & Weiss, B. P.) 115–135 (Cambridge Univ. Press, Cambridge, 2017).
- Machida, R. & Abe, Y. Terrestrial planet formation through accretion of sublimating icy planetesimals in a cold nebula. *Astrophys. J.* **716**, 1252–1262 (2010).
- Larsen, K. K. et al. Evidence for magnesium isotope heterogeneity in the solar protoplanetary disk. *Astrophys. J. Lett.* **735**, L37 (2011).
- Schiller, M., Connolly, J. N., Glad, A. C., Mikouchi, T. & Bizzarro, M. Early accretion of protoplanets inferred from a reduced inner Solar System ²⁶Al inventory. *Earth. Planet. Sci. Lett.* **420**, 45–54 (2015).

53. Alibert, Y., Mordasini, C., Benz, W. & Winisdoerffer, C. Models of giant planet formation with migration and disc evolution. *Astron. Astrophys.* **434**, 343–353 (2005).
54. Mordasini, C., Alibert, Y. & Benz, W. Extrasolar planet population synthesis. I. Method, formation tracks, and mass–distance distribution. *Astron. Astrophys.* **501**, 1139–1160 (2009).
55. Mordasini, C., Alibert, Y., Benz, W. & Naef, D. Extrasolar planet population synthesis. II. Statistical comparison with observations. *Astron. Astrophys.* **501**, 1161–1184 (2009).
56. Mordasini, C., Mollière, P., Dittkrist, K.-M., Jin, S. & Alibert, Y. Global models of planet formation and evolution. *Int. J. Astrobiol.* **14**, 201–232 (2015).
57. Shakura, N. I. & Sunyaev, R. A. Black holes in binary systems. Observational appearance. *Astron. Astrophys.* **24**, 337–355 (1973).
58. Clarke, C. J., Gendrin, A. & Sotomayor, M. The dispersal of circumstellar discs: the role of the ultraviolet switch. *Mon. Not. R. Astron. Soc.* **328**, 485–491 (2001).
59. Matsuyama, I., Johnstone, D. & Hartmann, L. Viscous diffusion and photoevaporation of stellar disks. *Astrophys. J.* **582**, 893–904 (2003).
60. Sasselov, D. D. & Lecar, M. On the snow line in dusty protoplanetary disks. *Astrophys. J.* **528**, 995–998 (2000).
61. Weidenschilling, S. J. Aerodynamics of solid bodies in the solar nebula. *Mon. Not. R. Astron. Soc.* **180**, 57–70 (1977).
62. Dittkrist, K.-M., Mordasini, C., Klahr, H., Alibert, Y. & Henning, T. Impacts of planet migration models on planetary populations. Effects of saturation, cooling and stellar irradiation. *Astron. Astrophys.* **567**, A121 (2014).
63. Inaba, S., Tanaka, H., Nakazawa, K., Wetherill, G. W. & Kokubo, E. High-accuracy statistical simulation of planetary accretion: II. Comparison with *N*-body simulation. *Icarus* **149**, 235–250 (2001).
64. Inaba, S. & Ikoma, M. Enhanced collisional growth of a protoplanet that has an atmosphere. *Astron. Astrophys.* **410**, 711–723 (2003).
65. Fortier, A., Alibert, Y., Carron, F., Benz, W. & Dittkrist, K.-M. Planet formation models: the interplay with the planetesimal disc. *Astron. Astrophys.* **549**, A44 (2013).
66. Genda, H. & Abe, Y. Survival of a proto-atmosphere through the stage of giant impacts: the mechanical aspects. *Icarus* **164**, 149–162 (2003).
67. Schlichting, H. E., Sari, R. & Yalinewich, A. Atmospheric mass loss during planet formation: the importance of planetesimal impacts. *Icarus* **247**, 81–94 (2015).
68. Burger, C., Maindl, T. I. & Schäfer, C. M. Transfer, loss and physical processing of water in hit-and-run collisions of planetary embryos. *Celest. Mech. Dyn. Astron.* **130**, 2–32 (2018).
69. Bollard, J. et al. Early formation of planetary building blocks inferred from Pb isotopic ages of chondrules. *Sci. Adv.* **3**, e1700407 (2017).
70. Connelly, J. N. & Bizzarro, M. Lead isotope evidence for a young formation age of the Earth–Moon system. *Earth. Planet. Sci. Lett.* **452**, 36–43 (2016).
71. Pollack, J. B. et al. Formation of the giant planets by concurrent accretion of solids and gas. *Icarus* **124**, 62–85 (1996).
72. Alibert, Y. et al. Theoretical models of planetary system formation: mass vs. semi-major axis. *Astron. Astrophys.* **558**, A109 (2013).
73. Demircan, O. & Kahraman, G. Stellar mass–luminosity and mass–radius relations. *Astrophys. Space Sci.* **181**, 313–322 (1991).
74. Alibert, Y., Mordasini, C. & Benz, W. Extrasolar planet population synthesis. III. Formation of planets around stars of different masses. *Astron. Astrophys.* **526**, A63 (2011).
75. Kennedy, G. M. & Kenyon, S. J. Stellar mass dependent disk dispersal. *Astrophys. J.* **695**, 1210–1226 (2009).
76. Mordasini, C. et al. Characterization of exoplanets from their formation. II. The planetary mass–radius relationship. *Astron. Astrophys.* **547**, A112 (2012).
77. Bodenheimer, P. & Pollack, J. B. Calculations of the accretion and evolution of giant planets: the effects of solid cores. *Icarus* **67**, 391–408 (1986).
78. Saumon, D., Chabrier, G. & van Horn, H. M. An equation of state for low-mass stars and giant planets. *Astrophys. J. Suppl.* **99**, 713–741 (1995).
79. Seager, S., Kuchner, M., Hier-Majumder, C. A. & Militzer, B. Mass–radius relationships for solid exoplanets. *Astrophys. J.* **669**, 1279–1297 (2007).
80. Guillot, T. On the radiative equilibrium of irradiated planetary atmospheres. *Astron. Astrophys.* **520**, A27 (2010).
81. Jin, S. et al. Planetary population synthesis coupled with atmospheric escape: a statistical view of evaporation. *Astrophys. J.* **795**, 65–87 (2014).
82. Jin, S. & Mordasini, C. Compositional imprints in density–distance–time: a rocky composition for close-in low-mass exoplanets from the location of the valley of evaporation. *Astrophys. J.* **853**, 163–186 (2018).
83. Adams, F. C., Fatuzzo, M. & Holden, L. Distributions of short-lived radioactive nuclei produced by young embedded star clusters. *Astrophys. J.* **789**, 86–104 (2014).
84. Gounelle, M. The abundance of ²⁶Al-rich planetary systems in the Galaxy. *Astron. Astrophys.* **582**, A26 (2015).
85. Pfalzner, S. et al. The formation of the Solar System. *Phys. Scr.* **90**, 068001 (2015).
86. Parker, R. J., Lichtenberg, T. & Quanz, S. P. Was Planet 9 captured in the Sun's natal star-forming region? *Mon. Not. R. Astron. Soc.* **472**, L75–L79 (2017).
87. Dwarkadas, V. V., Dauphas, N., Meyer, B., Boyajian, P. & Bojazi, M. Triggered star formation inside the shell of a Wolf–Rayet bubble as the origin of the Solar System. *Astrophys. J.* **851**, 147–161 (2017).
88. Kita, N. T. et al. ²⁶Al–²⁶Mg isotope systematics of the first solids in the early Solar System. *Meteorit. Planet. Sci.* **48**, 1383–1400 (2013).
89. Klahr, H. & Schreiber, A. Linking the origin of asteroids to planetesimal formation in the solar nebula. *Proc. IAU* **10** (S318), <https://doi.org/10.1017/S1743921315010406> (2016).
90. Simon, J. B., Armitage, P. J., Youdin, A. N. & Li, R. Evidence for universality in the initial planetesimal mass function. *Astrophys. J. Lett.* **847**, L12 (2017).
91. Tsirvoulis, G., Morbidelli, A., Delbo, M. & Tsiganis, K. Reconstructing the size distribution of the primordial Main Belt. *Icarus* **304**, 14–23 (2018).
92. Meng, H. Y. A., Rieke, G. H., Su, K. Y. L. & Gáspár, A. The first 40 million years of circumstellar disk evolution: the signature of terrestrial planet formation. *Astrophys. J.* **836**, 34–53 (2017).
93. Kral, Q., Clarke, C. & Wyatt, M. in *Handbook of Exoplanets* (eds Deeg, H. J. & Belmonte, J. A.) https://doi.org/10.1007/978-3-319-30648-3_165-1 (Springer Living Reference, Springer, Cham, 2017).
94. Andrews, S. M., Wilner, D. J., Hughes, A. M., Qi, C. & Dullemond, C. P. Protoplanetary disk structures in Ophiuchus II. Extension to fainter sources. *Astrophys. J.* **723**, 1241–1254 (2010).
95. Hunter, J. D. Matplotlib: a 2D graphics environment. *Comput. Sci. Eng.* **9**, 90–95 (2007).
96. Jones, E. et al. SciPy: open source scientific tools for Python. <http://www.scipy.org> (2001).
97. Van Der Walt, S., Colbert, S. C. & Varoquaux, G. The NumPy array: a structure for efficient numerical computation. Preprint at <https://arXiv/abs/1102.1523> (2011).
98. McKinney, W. Data structures for statistical computing in Python. In *Proc. 9th Python in Science Conference* (eds van der Walt, S. & Millman, J.) 51–56 (SciPy, 2010).
99. Waskom, M. et al. Seaborn v0.9.0. <https://doi.org/10.5281/zenodo.1313201> (2018).

Acknowledgements

The authors thank R. Parker for helping to initiate this project, E. Kite, T. Roger and C. Dorn for comments and discussions, and M. Bizzarro for comments that helped to improve the manuscript. T.L. was supported by ETH Zürich Research Grant ETH-17 13-1 and acknowledges partial financial support from the Swiss Society for Astrophysics and Astronomy through a MERAC travel grant. Y.A. acknowledges support from the Swiss National Science Foundation (SNSF). C.M. acknowledges support from the SNSF under grant BSSGI0_155816 'PlanetsInTime'. The numerical simulations in this work were partially performed on the EULER computing cluster of ETH Zürich. Parts of this work have been carried out within the framework of the National Center of Competence in Research PlanetS supported by the SNSF.

Author contributions

T.L., G.J.G., M.R.M. and Y.A. initiated the project. T.L. and R.B. performed the theoretical calculations. T.V.G., Y.A. and C.M. led the development of the computer codes used. T.L. wrote the manuscript. All authors contributed to the discussion and the interpretation of the results.

Competing interests

The authors declare no competing interests.

Additional information

Reprints and permissions information is available at www.nature.com/reprints.

Correspondence and requests for materials should be addressed to T.L.

Publisher's note: Springer Nature remains neutral with regard to jurisdictional claims in published maps and institutional affiliations.

© The Author(s), under exclusive licence to Springer Nature Limited 2019

5.6. Paper III: NGPPS IV. Planetary systems around low-mass stars

Exoplanetary research has the tendency to shift towards low-mass stars because it is observation-driven and the observations favor detection of planets around low-mass stars at a given stellar magnitude. This shift is currently more pronounced, due to commissioned instruments that are more sensitive to red and near-infrared light. This is true for the transit method with TESS and for radial velocity with CARMENES (Quirrenbach et al., 2014) and NIRPS (Bouchy et al., 2017). In the introduction of the paper below, we make this point clearer.

However, there is an additional benefit of the study of planets around low-mass stars to consider: Whenever a parameter is varied in a theoretical framework, its influence is best studied if the lever is largest. Therefore, it is theoretically insightful to study planet formation in conditions that are very different from each other. For ultra-late type M dwarfs with masses around $0.1 M_{\odot}$, the disk conditions and the parameters directly linked to the stellar mass are an order of magnitude different from the Solar-mass case. Hence, we are able to learn more about planet formation if we have the opportunity to compare theoretical models to observations under those different conditions.

The paper titled *The New Generation Planetary Population Synthesis (NGPPS): IV. Planetary systems around low-mass stars* (Burn et al., in prep.) introduces the model data for different stellar masses and a first analysis is included. A planet population synthesis is performed using 50 embryos per disk for five different stellar masses. The dataset that is produced is far from being exhausted by the analysis in this paper. Especially the comparisons of planetary system architectures is only done superficially using simple period ratios between planets. However, many more system-wide quantities could be defined and compared. This will be addressed in future works belonging to a series of papers.

The NGPPS series presents a major update of the planetary population synthesis models compared to the previous generation (Mordasini et al., 2012c; Alibert et al., 2013; Fortier et al., 2013). The series is structured as follows. NGPPS I (Emsenhuber et al., submitted) gives a complete description of the model. NGPPS II (Emsenhuber et al., in prep.) shows first synthetic populations of planets around Solar-mass stars and discusses the influence of the number of embryos. The nominal population in NGPPS II is a population with 100 embryos per disk, which is time-consuming to calculate. In NGPPS III (Schlecker et al., submitted), the observed relation between super-earths and cold-jupiters in the same system (Zhu & Wu, 2018; Barbato et al., 2018; Herman et al., 2019; Bryan et al., 2019) is discussed within the context of the populations presented in NGPPS II. Together with the paper shown here, these four works form the first block of NGPPS papers that will be published together. In the future, there will be works comparing the populations with the data from *Kepler* (Mishra et al. in prep), exploring the unconstrained parameter space (Mordasini et al. in prep) and focusing on system-wide properties (Mishra et al. in prep).

The New Generation Planetary Population Synthesis (NGPPS)

IV. Planetary systems around low-mass stars[★]

R. Burn¹, M. Schlecker², C. Mordasini¹, A. Emsenhuber³, Y. Alibert¹, T. Henning², H. Klahr² and W. Benz¹

¹ Physikalisches Institut & Center for Space and Habitability, Universität Bern, CH-3012 Bern, Switzerland, e-mail: remo.burn@space.unibe.ch

² Max-Planck-Institut für Astronomie, Königstuhl 17, 69117 Heidelberg, Germany

³ Lunar and Planetary Laboratory, University of Arizona, 1629 E. University Blvd., 85721 Tucson, AZ, USA

June 10, 2020

ABSTRACT

Context. Previous theoretical works concerning planet formation around low-mass stars were often addressing large planets or individual systems. However, present-day surveys are discovering many planets down to Earth-size around low-mass stars. A picture of very different kinds of planetary systems around low-mass stars currently emerges.

Aims. We investigate and compare the planetary population for these different conditions. The goal is to understand planet formation around stars with lower stellar masses and identify differences in the statistical distribution of modeled planets.

Methods. We use the Generation III Bern model of global planet formation and evolution to calculate synthetic populations of up to 50 planets per modeled system varying the central star from solar-like stars to ultra-late M dwarfs. This model includes planetary migration, N-body interactions between embryos, accretion of planetesimals and gas, and long-term contraction and loss of the gaseous atmospheres. A linear scaling of the protoplanetary disk mass with stellar mass is assumed. Additionally, we compare the unbiased model data to inferred observational trends.

Results. We find that temperate, Earth-sized planets are most frequent around early M dwarfs ($0.5 M_{\odot}$) and more rare for solar-type stars and late M dwarfs. Furthermore, the planetary mass distribution does not linearly scale with the disk mass. The cause lies in the growth of gaseous, giant planets, which leads to ejection of planets – reducing the apparent efficiency of solid accretion for higher stellar masses. We identify a regime of disk parameters that reproduces observed M-dwarf systems such as TRAPPIST-1. However, giant planets around late M dwarfs like GJ 3512b only form when type I migration is substantially inhibited.

Conclusions. The apparent conversion of solids to planets is larger around lower mass stars. However, this effect is not strong enough to explain the reported higher occurrence rates of planets around M dwarfs. This points towards an additional cause for this trend, which most likely lies in the assembly of planetesimals or in the initial disk conditions.

Key words. planetary systems - planetary systems: formation

1. Introduction

M dwarf stars are the most abundant stars in the Milky Way (Winters et al. 2014) and represent a unique laboratory to test current planet formation theories. Following the discovery of the first planet around an M dwarf star (Marcy et al. 1998), they are now known to be the most frequent host of exoplanets (e.g., Gaidos et al. 2016). Currently, the observational sample of planets around M dwarfs is rapidly increasing, as a number of new detection surveys are being conducted or planned. Programs using the transit detection method include the space-born TESS, which is more sensitive towards longer wavelengths than its predecessor *Kepler* (Ricker et al. 2014) or surveys on the ground, such as MEarth (Nutzman & Charbonneau 2008), TRAPPIST (Gillon et al. 2016, 2017), NGTS (Wheatley et al. 2018), SPECULOOS (Burdanov et al. 2018), or EDEN (Gibbs et al. 2020). In addition to that, the radial velocity programs CARMENES (Quirrenbach et al. 2014) or the NIRPS instrument (Bouchy et al. 2017) will yield many more planet discoveries around low mass stars. Together, they explore a so far barely accessible parameter space of the planetary population – rocky exoplanets around low-mass

stars. The fundamental benefit in the search for habitable planets around low-mass stars for both transit and radial velocity surveys lies in the fact that the radius ratio, or respectively the mass ratio, for Earth-like planets becomes larger for lower stellar masses. This results in a higher measured signal to noise ratio. Additionally, the temperate zone (Kasting et al. 1993; Tasker et al. 2017) is located at shorter orbital periods around M dwarfs due to the lower temperature of the central star. Therefore, less observation time is needed for the discovery of planets receiving stellar irradiation fluxes comparable to Earth and are thus the best candidates for the search for extraterrestrial life.

Theoretical works addressed planet formation around different stellar masses before: Early population synthesis work were conducted by Ida & Lin (2005) and Alibert et al. (2011) who mainly focused on the most heavy planets in a system. In contrast to these works, Raymond et al. (2007) discuss the formation of terrestrial planets around low-mass stars after the disk dissipated (i.e., without migration) by injecting on the order of hundred N-body particles – called planetary embryos – into regions chosen to cover the temperate zone and the water ice line. They found less planets in the temperate zone with decreasing stellar mass and mention in their conclusions that disk migration could help to explain the observed system around the M3 dwarf Gliese

[★] The data supporting these findings are available online at <http://dace.unige.ch> under section “Formation & Evolution”.

581 (Bonfils et al. 2005; Udry et al. 2007). This is further supported in the light of discoveries of systems around even lower mass stars, such as TRAPPIST-1 (Gillon et al. 2017), or by observational trends derived from the *Kepler* sample (Mulders et al. 2015). Overall, that highlights the need to include a migration mechanism in modern planet formation models to match the observed systems. However, this is still not undisputed as Hansen (2015) reports in-situ planet formation models around a $0.5 M_{\odot}$ star matching at least the observed planetary periods.

More recently, theoretical planet formation works discuss the solid delivery process. Whereas Schoonenberg et al. (2019) and Coleman et al. (2019) focus on the TRAPPIST-1 system in the framework of (hybrid) planetesimal and pebble accretion, Liu et al. (2019) consider distributions of initial stellar and disk properties in the pebble accretion scenario. Liu et al. (2019) calculate a population of single planets, that is, neglecting N-body interactions, around stars with masses from $0.1 M_{\odot}$ to $1 M_{\odot}$. Being similar to the approach of this work, this will be a useful reference to compare the resulting planetary population based on accreting pebbles compared to planetesimal accretion, which is considered to be the dominating solid mass delivery mechanism here (see also Brugger et al. in prep; Coleman et al. 2019). We caution that for smaller rocky planets, the scenario of a single planet forming in the disk gives different results compared to simulations taking into account the interaction and growth competition between planets (Alibert et al. 2013). Miguel et al. (2020) focus on forming rocky planets around stars of masses up to $0.25 M_{\odot}$ by accreting planetesimals (following Ida & Lin 2004a) and explicitly exclude the accretion of gaseous envelopes. In contrast, we will discuss the growth of atmospheres around small planets in this paper and, by including gas accretion, the formation of giant planets is facilitated, which are observed at stellar masses larger than $0.3 M_{\odot}$. This extends the parameter space in which our model covers all known, basic physical processes of planet formation to the range $0.1 M_{\odot}$ to $1 M_{\odot}$.

A preceding synthetic population of planets around a $0.1 M_{\odot}$ star was presented in the letter of Alibert & Benz (2017), who found more water-rich compositions of planets forming around very low-mass stars compared to those around solar-type stars. We would like to stress that we did use an updated version of our population synthesis model compared to Alibert & Benz (2017) and Alibert et al. (2011), which changes to some degree the conclusions, as will be addressed in detail. These updates are presented as part of a series of papers: In Emsenhuber et al., in prep (Paper I), the updated model is described in detail and in Emsenhuber et al., in prep (Paper II), the statistical properties of the populations around solar-type stars are discussed.

2. Formation models

We use the Generation III *Bern* model of planet formation and evolution. It originates from the model of Alibert et al. (2004a,b), which was extended to incorporate the long-term evolution of planets (Mordasini et al. 2012b,a) and N-body interactions (Alibert et al. 2013; Fortier et al. 2013). The third generation employed here combines the two branches and is described in detail in Paper I. We compute a population of planets given a variety of initial disk conditions which are based on the observed population of disks. This approach is called *planetary population synthesis* (Ida & Lin 2004a,b, 2005; Mordasini et al. 2009a,b; Benz et al. 2014; Mordasini et al. 2015; Mordasini 2018).

Here, we briefly summarize the relevant physical processes included in the *Bern* model. For a detailed complete description, we refer to Paper I. The protoplanetary disk is modeled

following the viscous α disk model (Shakura & Sunyaev 1973; Pringle 1981). In addition to energy dissipation due to shear, the disk is heated by irradiation by the star. To describe this, we follow Hueso & Guillot (2005); Nakamoto & Nakagawa (1994), who give analytic expressions for the disk midplane temperature assuming an isothermal disk in the vertical direction. Different to those two works, we consider the starting time of our disk to be after significant infall of gas onto the disk has stopped. The final phase of the disk's life is dominated by disk photo-evaporation. We model internal photo-evaporation by the star following Clarke et al. (2001) and use a simple prescription to include external photo-evaporation due to the radiation by nearby stars (Matsuyama et al. 2003).

To model planetary growth by planetesimal accretion, protoplanetary *embryos* with an initial mass of $0.01 M_{\oplus}$ are injected at random locations in the disks (see Sect. 2.3.4). The embryos are gravitating bodies tracked by the MERCURY N-body code (Chambers 1999). They can accrete planetesimals inside their feeding zone from a statistically described planetesimal disk, for which the eccentricity- and inclination-distributions are evolved (Fortier et al. 2013). The gravitational forces of the planetesimal disk onto the embryos is not taken into account. In addition to gravitational forces of the central star and other embryos, the planets are subject to the torque of the gaseous disk (see Sect. 2.1.1).

Concurrently, the *Bern* model solves the one dimensional internal structure equations (Bodenheimer & Pollack 1986) for each embryo at every timestep for the solid core and the gaseous envelope assuming hydrostatic equilibrium. The energy input of the accreted planetesimals is assumed to be deposited at the core-envelope boundary of the embryo. To accrete gas, the embryo has to cool and contract by radiating away the potential energy of accreted planetesimals and gas. This then determines the envelope mass. The cooling becomes efficient at $\sim 10 M_{\oplus}$, which can then lead to a planet undergoing *runaway* gas accretion (Mizuno 1980; Pollack et al. 1996). As a consequence, the planet contracts and is thus considered *detached* from the disk. In this stage, gas accretion is limited by what the disk can provide (Machida et al. 2010). This transition roughly coincides with the time the planet changes the migration regime (type I to type II) (Alibert et al. 2004b).

After the gaseous disk is gone, we keep running the N-body integration up to 20 Myr to track dynamical instabilities occurring just after the dissipation of the disk. After that, only the evolutionary calculations are performed, which include the continuation of solving the internal structure equations – thus tracking the long-term contraction of planets –, the evaporation of atmospheres as well as tidal migration (see Sect. 2.1.2). At all times, but of higher significance in the evolution phase, the star is evolving in radius and luminosity following Baraffe et al. (2015). This leads to an evolving radiative energy input to the planetary structure.

In general, we choose the nominal physical parameters and processes of Paper I and Paper II but extend the explored parameter space to lower stellar masses. Apart from the different initial disk conditions described in Sect. 2.3, the stellar mass directly enters in different important processes:

- the stellar luminosity and radius as well as the stellar evolution changes following the model of Baraffe et al. (2015)
- the evolution of the protoplanetary disk is modified for lower mass stars, as the viscous heating (which depends on the Keplerian frequency, Pringle 1981) and the irradiation depend on the mass, radius and effective temperature of the cen-

tral object (Hueso & Guillot 2005; Nakamoto & Nakagawa 1994)

- the radius of disk-embedded planets is equal (for not too low masses) to a fraction of the Hill radius (Mordasini et al. 2010), which depends on the mass of the central body as $R_H = a \left(\frac{M}{3M_\star} \right)^{1/3}$
- the evolution of the planetesimal disk (in terms of e and i) is a function of the planetesimals’ Hill radii (Adachi et al. 1976; Inaba et al. 2001; Rafikov 2004)
- similarly, the accretion rate of planetesimals scales linearly with the planet’s and the planetesimals’ mutual Hill radius (Fortier et al. 2013)
- the fraction of ejected planetesimals is a function of the escape speed from the primary ($v_{\text{esc},\star} = \sqrt{2GM_\star/a}$) (Ida & Lin 2004a)
- the computation of the planetary orbital evolution due to disk-planet interactions is modified for low mass stars (see Sect. 2.1.1)
- the tidal interaction with the star changes depending on the radius and mass of the star, leading to different disk-free migration (see Sect. 2.1.2).

2.1. Orbital evolution

2.1.1. Disk migration

Planets embedded in a disk will be subject to torques of the disk feedback. Depending on the mass of the planet, the migration regime is classified as type I and type II for no gap opening or gap-opening, respectively. As described in detail in Paper I, we follow Coleman & Nelson (2014) for the type I and Dittkrist et al. (2014) for the type II regime.

For type I, the formulas for planets on circular orbits follow Paardekooper et al. (2011). Therefore, an overall factor

$$\Gamma_0 = \left(\frac{M}{M_\star H} \right)^2 \Sigma_g a^4 \Omega_K^2 \quad (1)$$

can be identified to get a grasp of the general scaling of the total torque Γ with the stellar mass ($\propto M_\star^{-1}$) at fixed semi-major axis and gas surface density. However, the corotation torque, which causes the outward migration regions, scales differently due to the stellar mass appearing in the formulas for non-linear corotation torque via the Keplerian rotation (Paardekooper et al. 2011). Additionally, the migration rates depend on the temperature and pressure structure in the disk which are influenced by the stellar mass. To discuss the detailed scaling of type I migration analytically is out of the scope of this work. Thus, we qualitatively compare the resulting migration maps of a fiducial disk with a power law slope of 0.9, a gas surface density of 200 g cm^{-2} at 5.2 au and an exponential cut-off radius at 30 au (see Paper I for the initial surface density profile). This translates to a total disk mass of $0.02 M_\odot$.

Figure 1 shows the resulting migration map where the migration rate $\dot{a}/a \propto \Gamma / \sqrt{M_\star} \approx M_\star^{-1.5}$ is encoded in color. The impact of the stellar mass on migration is apparent: A decrease of the stellar mass leads to an increase of the migration rate for the same disk (top and central panel). We observe that the outward migration region is shifted towards the star by about 1 au.

In this work, we will assume that the disk mass scales linearly with the stellar mass (see Sect. 2.3.1). Therefore, we included in the bottom panel of Fig. 1 the case of a disk with a mass that is reduced by 10% compared to the other two depicted disks. According to the scaling with Γ_0 we expect migration rates that are more similar to the top panel than the middle

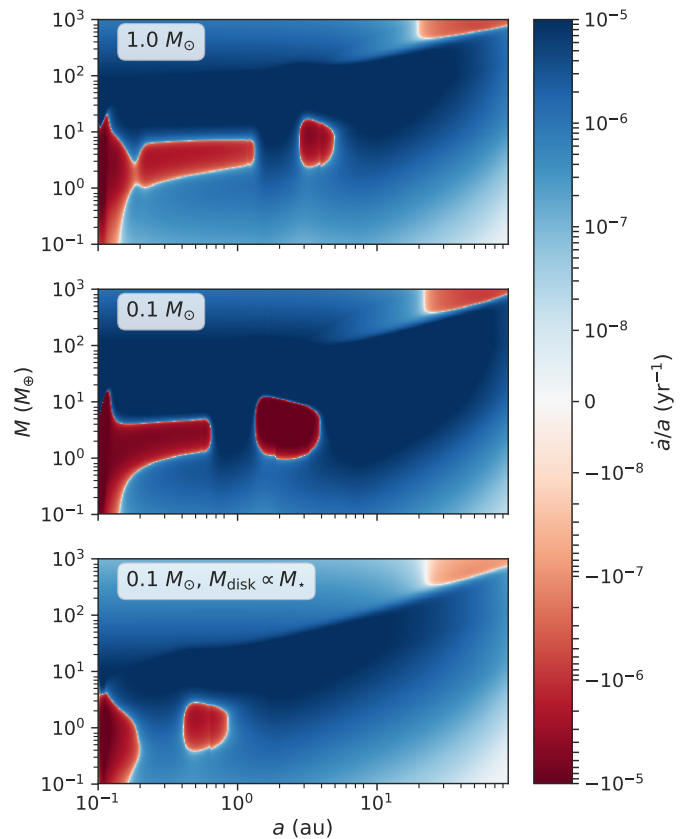


Fig. 1. Migration rate for three different stellar masses and disks. On the top panel a disk with a total mass of $0.02 M_\odot$ around a solar mass star after an evolution of 100 kyr is displayed; the central panel shows the same disk at the same time, but the stellar mass is reduced to $0.1 M_\odot$; and the timescales of a disk with ten times less mass around a $0.1 M_\odot$ star can be seen in the bottom panel. Regions with most saturated colors (blue or red) are regions where migration is fastest. With scaled disk mass, the outward migration zones (red) move to lower planet masses and closer orbits. This generally causes an earlier inward migration.

panel ($\dot{a}/a \propto \Sigma_g / M_\star^{1.5}$), which broadly holds in the type I regime wherever corotation torques are weak. The outward migration regions are further shifted towards the star compared to larger disk case, which impacts the resulting population of planets by a large degree since the individual planet tends to pile up at the outer edge of outward migration zones, which only change on typical timescales of the disk evolution ($\sim \text{Myr}$).

For type II migration, we follow Dittkrist et al. (2014). Thus, the overall torque is proportional to $\Omega_K \nu$. The alpha-viscosity $\nu = \alpha c_s^2 / \Omega_K$ is sensitive to the temperature structure of the disk via the isothermal sound speed c_s . Whereas, the temperature differs due to the change of direct illumination by the star due to the different stellar radius and temperature as well as a lower viscous dissipation rate $\dot{E}_{\text{visc}} = \frac{9}{4} \Sigma \nu \Omega_K^2 \propto \nu M_\star$. We observe a more pronounced transition from type I to type II regimes in the bottom panel of Fig. 1, which can be explained by the much cooler disk and the different scaling of the two regimes. The transition from type I to type II thus becomes more relevant in the low mass star disks. We use the gap opening criterion of Crida et al. (2006), which takes into account the stellar mass to transition from type I to type II (see Paper I).

Overall, disk migration can be faster around low mass stars, but for typical disk masses, we expect generally slower migra-

tion in type I and type II regimes and outward migration zones to lie closer to the star.

2.1.2. Tidal evolution

At very small separations, planet-star tidal interactions may be important, and cause planet migration in the absence of a disk. Using a simple model for tidal evolution taking into account the tides evoked in the star (Benítez-Llambay et al. 2011), the semi-major axis evolves as

$$\frac{da}{dt} = - \left(\frac{9}{2} \sqrt{\frac{G}{M_\star}} \frac{R_\star^5 M}{Q_\star'} \right) a^{-11/2}, \quad (2)$$

where the radius R_\star of the star evolves with time (Baraffe et al. 2015). In lack of an appropriate scaling law, we followed Benítez-Llambay et al. (2011) in fixing the specific tidal parameter, accounting for the tidal dissipation rate in the star, $Q_\star' = 10^6$ for all stellar masses and times (see Ogilvie 2014, for an in-depth review).

2.2. Transit radii

To better compare observed radii measured by transit surveys with radii of synthetic planets, we calculate "transit radii" of the modeled planets. For that, we can use the internal structure data of each planet. Simply taking the numerical outer boundary of the structure would lead to severely overestimated radii. Therefore, an estimate for the radius of a planet that casts a shadow when passing in front of its host star needs to be used.

Hansen (2008) found that the optical depth along a chord is enlarged by a factor $\gamma \sqrt{2\pi R/H_0}$ compared to the optical depth integrated radially outwards from a radius R , where γ is a factor relating the radiative optical depth to the thermal optical depth (Jin et al. 2014, Table 2) and H_0 is the local scale height in the envelope at a given radial location.

We chose an optical depth $\tau = 2/3$ in our grey atmosphere to get the transit radius and note that for a percent-level comparison to a particular observation, a non-grey atmosphere and the instrument specific wavelength band would have to be included. For planets without an envelope structure, the transit radius is equal to their composition-dependent core radius calculated using a three layer model (iron, silicates and ice) (Mordasini et al. 2012b).

2.3. Monte Carlo parameters and their scaling with M_\star

Owing to the statistical approach of Population Synthesis, we treat the initial conditions as random variables that we draw from probability distributions for each simulation. For consistency within the paper series, we employ the values from Paper II for solar-type stars.

Figure 2 shows, for each host star mass bin, the probability distributions of the initial conditions used in this study. While the distribution of the metallicity remains the same, all other parameters scale with stellar mass. The disk lifetimes t_{disk} , which show similar distributions for all M_\star , are also shown (see detailed discussion in Sect. 2.4.1).

We follow Paper II in setting the radius of planetesimals to 300 m and initializing the gas surface density profile as (Veras & Armitage 2004)

$$\Sigma_g(t=0) = \Sigma_{g,0} \left(\frac{r}{r_0} \right)^{-\beta_g} \exp \left(\left(\frac{r}{R_{\text{disk}}} \right)^{\beta_g - 2} \right) \left(1 - \sqrt{\frac{r_{\text{in}}}{r}} \right) \quad (3)$$

Table 1. Model Parameters

	Parameter	Symbol	Value
	Disk Viscosity	α	2×10^{-3}
	Power Law Index (Gas)	β_g	$0.9^{(a)}$
	Outer edge of planetesimal disk		$R_{\text{disk}}/2^{(b)}$
	Power Law Index (Solids)	β_s	$1.5^{(c)}$
	Radius of Planetesimals		300 m
	Number of Planet Seeds		50
	Mass of Planet Seeds		$0.01 M_\oplus$
	Embryo placement time		0 yr
	Envelope opacity reduction		$0.003^{(c)}$
	N-body integration time		20 Myr

^(a) Andrews et al. (2010);

^(b) Ansdell et al. (2017);

^(c) Drążkowska & Alibert (2017); Lenz et al. (2019);

^(d) Mordasini (2014)

where $r_0 = 5.2$ au is the reference distance, $\beta_g = 0.9$ the power-law index (Andrews et al. 2010), R_{disk} the cutoff radius for the exponential decay and r_{in} is the inner edge of the disc. The chosen fixed values are summarized in Table 1. Before discussing the individual choice of distributions for the observation-informed parameters, we note that the solar-type initial conditions of Paper II include a steeper slope for the planetesimal disk β_{pls} than the gas disk ($\beta_{\text{pls}} = -1.5$ instead of -0.9). This is motivated by results from planetesimal formation models (Drążkowska et al. 2016; Drążkowska & Alibert 2017; Schoonenberg & Ormel 2017; Lenz et al. 2019). We assume that this steepening is valid for all stellar masses and adopt a $\beta_{\text{pls}} = -1.5$ for all simulations (except in Appendix A).

2.3.1. Disk mass

The initial gas disk mass for solar type stars is based on the Class I disk observations Tychoniec et al. (2018) (see Paper II). Regrettably, Tychoniec et al. (2018) do not split their sample of Class I disks into different stellar masses, but they do mention that they observe a weak correlation with the bolometric luminosity which can be seen as a proxy for the stellar mass. However, the non-triviality of the mass luminosity relation for very young protostars makes inferring the slope of this weak correlation a task outside the scope of this work. Nevertheless, the scaling of disk mass with stellar mass can be inferred from recent ALMA measurements. For more evolved disks, Pascucci et al. (2016), Barenfeld et al. (2016), as well as Ansdell et al. (2017) found a dust mass dependency on stellar mass, which is steeper than linear. Testi et al. (2016) and Sanchis et al. (2020) extended the observations to the brown dwarf regime and found statistically consistent results.

While Barenfeld et al. (2016) did not yet find a clear difference in slopes of the dust mass to stellar mass relation when comparing their results for Upper Sco with disk masses for the younger Lupus cluster, Ansdell et al. (2017) and Pascucci et al. (2016) report a time dependency of the slope by enlarging the sample to more stellar clusters. These latter findings point towards a stellar mass dependent time evolution of the dust and, therefore, do not constrain the *initial* dust mass well. Tentatively interpolating back this steepening of the disk mass to stellar mass relation to time zero, we adopted a linear dependency of the disk mass on the stellar mass $M_{\text{gas}} \propto M_\star$. This is in line with previous theoretical works (slopes of 0.5 to 2 in Raymond et al. 2007).

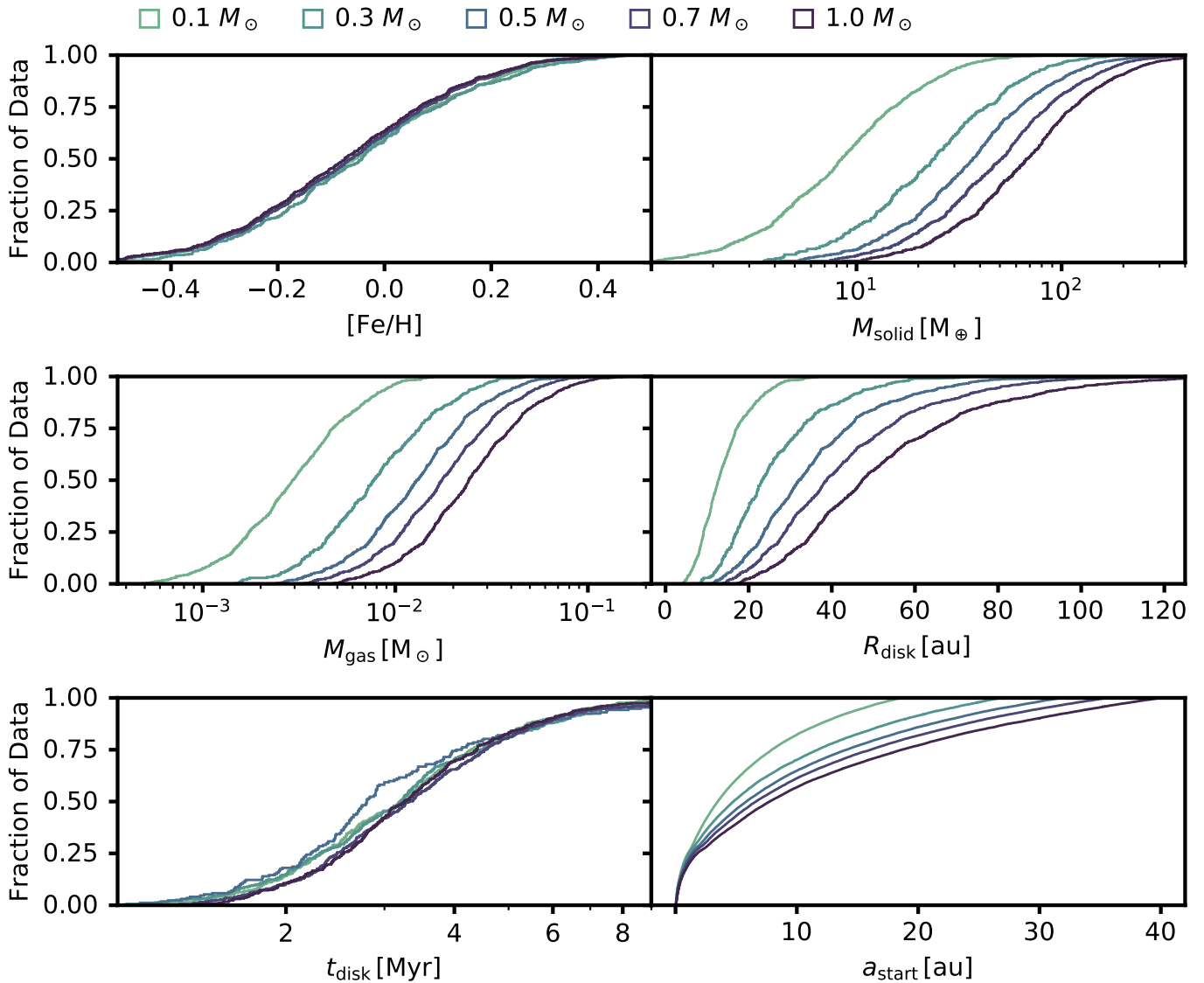


Fig. 2. Distribution of initial conditions for different M_\star . All parameters scale with host star mass, except for $[\text{Fe}/\text{H}]$ which is distributed equally for all masses. The initial solid mass content is computed from $[\text{Fe}/\text{H}]$ and M_{gas} , which leads to similar distributions for M_{gas} and M_{solid} . Besides the Monte Carlo parameters drawn in the simulations, we show the distributions of disk lifetimes t_{disk} . These are similar for all M_\star (compare Sect. 2.4.1).

As in Paper II, we then multiply the gas disk mass with spectrally measured metallicities (Santos et al. 2003) to get the initial dust disk mass, which is available to form planetesimals. We assume no dependency of the metallicity on the stellar mass. Additionally, an efficiency of transforming the dust to planetesimals of 100% is chosen. The planetesimal surface density is reduced at radii closer to the star if for a given element no chemical species containing it can condense out at the local disk temperature (see Thiabaud et al. 2014). This leads to sharp transitions in the surface density profile of solids, most prominently the water ice line, whose location depends on the temperature at time zero of the simulation.

2.3.2. Disk radius

Although it is near-impossible to measure the *initial* radius of the gaseous disk, trends about the disk size of – notably evolved disks – in terms of disk mass were already found by Andrews

et al. (2010). The scaling relation of disk mass to stellar mass follows $M_d \propto R_{\text{disk}}^{1.6}$, which was recovered later (Andrews et al. 2018). A direct correlation of dust disk radii with stellar mass using ALMA data could not be found by Ansdell et al. (2018) who advocate more high resolution CO line observations to give clearer constraints. What became clear thanks to the ALMA measurements, is that dust radii are smaller than gas radii by about a factor of 0.5 (Ansdell et al. 2016). We use these constraints to get the gas disk size out of the gas disk mass (see Sect. 2.3.1) without introducing more scatter and the planetesimal disk mass extends to half the radius of the gas disk.

2.3.3. Inner edge

The numerical inner edge r_{in} is a free parameter of our model. The physical motivation for an inner edge is a magnetospheric cavity (Bouvier et al. 2007), where ionized material of the disk is lifted by the magnetic field lines from the midplane and ac-

creted onto the star. This typically happens at the corotation radius (e.g. Günther 2013), where the magnetic field rotates at the same speed as the gas. It is therefore reasonable to not extend the modeled disk closer to the star than its corotation radius. The order of percent sub-Keplerian speed of the gas disk is negligible for this consideration and thus we take r_{in} at the location where the Keplerian orbital period is equal to a rotation period drawn from measured distributions as the inner disk edge. Other processes that occur in the innermost regions of the disk are vaporization of silicates and ionization of the disk gas, which are not covered here.

Rotation periods of young stars can be derived from periodic variations of objects in young stellar clusters, such as the Orion Nebula Cluster (Herbst et al. 2002), NGC 6530 (Henderson & Stassun 2011), NGC 2264 (Lamm et al. 2005; Affer et al. 2013; Venuti et al. 2017), NGC 2362 (Irwin et al. 2008) and NGC 2547 (Irwin et al. 2007). Irwin et al. (2008) as well as Henderson & Stassun (2011) discuss an increasingly steep slope in the rotation period versus stellar mass diagrams with increasing age. However, for the youngest clusters (Orion and NGC 6530) no decrease of the rotation period with decreasing stellar mass is found (Henderson & Stassun 2011). Therefore, this feature can be attributed to a faster spin-up of low mass stars and is not an initial condition to planet formation. As initial condition, we therefore choose the same rotation periods for all stellar masses. Thus, the inner edge of the disk scales $\propto M_{\star}^{1/3}$.

Despite the long history of observations, the exact distribution of classical T Tauri rotation periods is still subject to a lot of statistical noise. Venuti et al. (2017) used data from 38 days of CoRoT observations to constrain the rotation periods in NGC 2264, which has an estimated age of ~ 3 Myr. They, like other authors (e.g. Henderson & Stassun 2011), recover, that stars that still show signs of accretion, that is classical T Tauri stars, have slower rotation periods than diskless stars. In Fig. 3, we show the data of Venuti et al. (2017) in two mass bins for diskless and disk-bearing stars. No clear difference is found between the different masses in the case of disk-bearing stars. Therefore, we adopted a distribution of rotation periods used to constrain the inner edges following the full T Tauri sample of Venuti et al. (2017), i.e. a log-normal distribution with a mean of 4.74 days.

2.3.4. Initial embryos

Initial seeds for planetary growth, called *embryos*, are placed randomly starting from the inner edge of the disk r_{in} out to an upper limit. In Paper II, the upper limit is chosen to be 40 au, which we adopt for the solar-mass populations. This outer edge is then multiplied with $(M_{\star}/M_{\odot})^{1/3}$. Therefore, it is kept at fixed orbital period. Many timescales relevant to planet formation scale with the orbital period, which motivates to keep it the same for better comparability amongst the populations.

The locations of the initial embryos are drawn from a log-uniform distribution between these two boundaries and if a planet would be placed within 10 Hill radii of an already placed embryo, a new location is drawn, since embryos should not be closer than that at the end of runaway growth (Kokubo & Ida 1998; Chambers 2006).

As in Paper II, the initial mass of the embryo is set to be $10^{-2} M_{\oplus}$. This mass is not scaled with the stellar mass, which is a choice that changes the initial mutual Hill spacing with varying stellar mass and thus the gravitational interactions between the embryos (see Sect. 4.5).

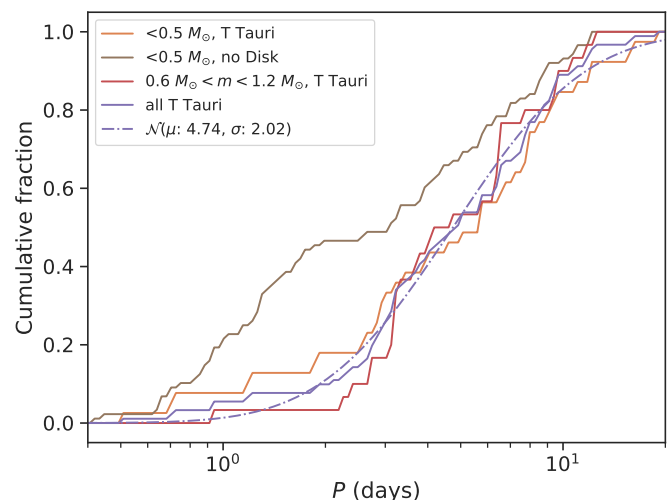


Fig. 3. Cumulative distribution of rotation periods of disk-bearing and diskless stars in NGC 2264 (estimated age ~ 3 Myr) found by Venuti et al. (2017). An error function corresponding to the normal distribution with the indicated mean and standard deviation was fitted to the logarithm of the rotation periods of all T Tauri stars (dash-dotted line). This distribution defines the co-rotation radius, which we set as the inner disk edge.

2.4. Disk observables

2.4.1. Disk lifetime

Although the disk lifetime is not a direct Monte Carlo variable, the photo-evaporation parameter \dot{M}_{wind} was chosen such that reasonable lifetimes result, as can be seen in Fig. 4. By construction, the lifetimes of the different stellar mass bins are similar. Disk lifetimes obtained from observed fractions of disk-bearing stars in young stellar clusters (Strom et al. 1989; Haisch, Jr. et al. 2001; Mamajek et al. 2009; Fedele et al. 2010; Ribas et al. 2014; Richert et al. 2018) are sensitive to the pre-main-sequence evolution model of the stars used to determine the cluster age (Richert et al. 2018). Therefore, a larger uncertainty than the empirical scatter results. In Fig. 4 we show the results of Richert et al. (2018), who used three different pre-main-sequence evolution models to get typical disk lifetimes varying by more than a factor of two. For comparison of the modeled disks' lifetimes to measurements, it is necessary to estimate the time during which a simulated disk would be detected by typical survey used to get the observational data. We follow Kimura et al. (2016) to consider a disk as dispersed at the moment the disk becomes transparent (optical depth smaller than unity) everywhere in the region it is hotter than 300 K. This is a broad estimate for near-infrared observations, which are the basis of disk lifetimes studies. For low-mass stars, this observable disk lifetime significantly differs from the numerical lifetime determined by a surface density close to zero everywhere.

2.4.2. Accretion rates

Similar to the lifetimes, stellar accretion rates have to be matched by the simulated disks. The process driving accretion rates in the simulations is the viscous evolution. Numerically, we take the disk gas mass that viscously spread into the innermost numerical cell as gas accretion onto the star \dot{M}_{acc} . In general, this flux is not constant everywhere in the disk due to not being in equilibrium at all times (equation 25 in Mordasini et al. 2012b).

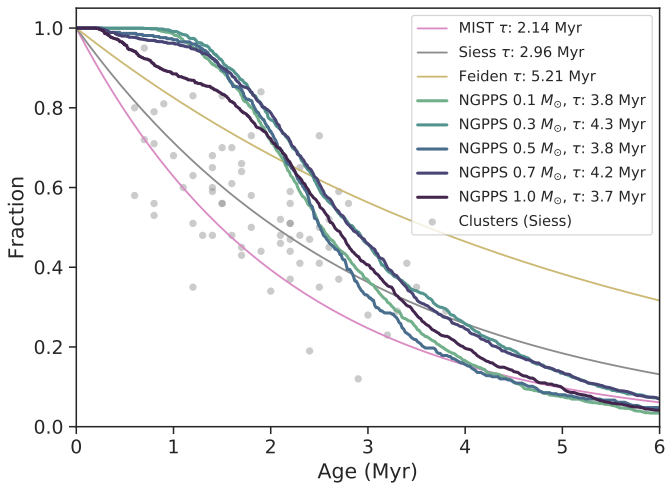


Fig. 4. Fraction of disk-bearing stars as a function of time. Both observational data assembled by [Richert et al. \(2018\)](#) as well as the synthetic lifetimes for different stellar masses are shown. The age determination of clusters is sensitive to the employed pre-main-sequence model. The observational data and an exponential fit to it is shown using the age scale of [Siess et al. \(2000\)](#) as well as fits to the same cluster data but using the dating of [Feiden \(2016\)](#) and the MIST collaboration ([Choi et al. 2016](#)).

In Fig. 5, we show the resulting \dot{M}_{acc} of our synthetic populations for the different stellar masses at two different times. This can be compared to the Lupus data obtained by [Alcalá et al. \(2017\)](#). For planet formation, the most important stages are early in the disk evolution when most of the mass is still present. Therefore, a comparison to clusters older than Lupus (1 to 3 Myr) would not be as relevant.

We find mass accretion rates on the same orders of magnitude as were observed in Lupus. The intrinsic scatter of the synthetic populations seems to be lower than in the observed sample. This can be attributed to choosing a single viscous α value (2×10^{-3}). Furthermore, the evolution with time seems to be rather rapid compared to observations, given that at 3 Myr a lot of the more massive stars already accreted most of the disk mass. For the simulations, time since the start of the simulation was chosen. However, realistic cluster ages include the early star formation stages beforehand which can attribute to a shift of a few 100 kyr.

The scaling of \dot{M}_{acc} with stellar mass in the synthetic work is more shallow than the fitted observational data. However, there is still a lot of noise in the data.

Given the relatively simple 1D disk model we use and for the purposes of getting realistic initial conditions for planet formation, the match in accretion rates we get is sufficient. An in-depth comparison of disk properties to disks resulting from population synthesis work will be addressed in a future paper.

3. Results

3.1. Types of planets

As a first step to explore the synthetic populations of planets around different host star masses, we categorize the planets into the following groups:

- Planets with masses larger than Earth ($M > 1 M_{\oplus}$)
- Earth-like planets defined as planets with masses ranging from $0.5 M_{\oplus}$ to $2 M_{\oplus}$

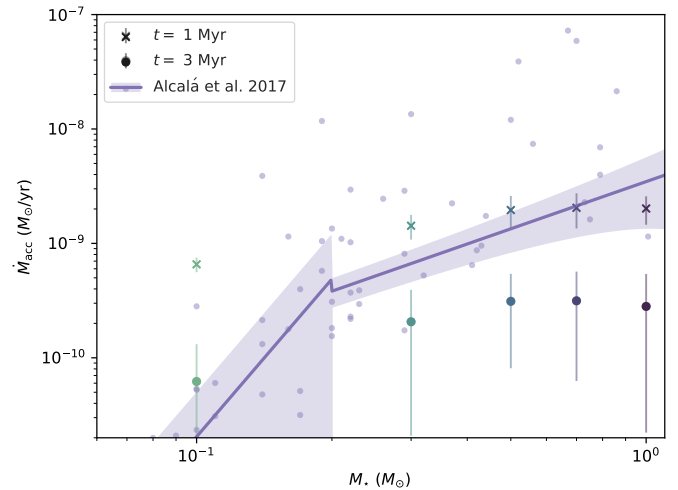


Fig. 5. Stellar accretion rates of observations and synthetic populations as a function of stellar mass. For the synthetic datapoints at two different times, the mean of the distribution is plotted and the standard deviation is indicated with error bars. The observational data and the broken power-law fit with its estimated errors is taken from [Alcalá et al. \(2017\)](#) for the Lupus cluster (estimated age of 1 to 3 Myr). The break for this particular fit was fixed at $0.2 M_{\odot}$.

- Super Earths ($2 M_{\oplus}$ to $10 M_{\oplus}$)
- Neptunian planets ($10 M_{\oplus}$ to $30 M_{\oplus}$)
- Sub-Giants ($30 M_{\oplus}$ to $100 M_{\oplus}$)
- Giant planets ($100 M_{\oplus}$ to $300 M_{\oplus}$).

Additionally, we classify planets with masses from $0.3 M_{\oplus}$ to $3 M_{\oplus}$ at orbital separations that would allow for the presence of liquid water on the planets' surfaces as temperate zone planets (see Sect. 3.1.4). For that, we follow [Kopparapu et al. \(2014\)](#) and use the maximum and runaway greenhouse limits for the temperate zone. For simplicity, the reported dependence of the zone on the planetary mass is not taken into account. Instead, the limits used are the ones calculated for masses of $1 M_{\oplus}$. We note, that the parameters in [Kopparapu et al. \(2014\)](#) differ on a $\sim 5\%$ level compared to the parameters in [Kopparapu et al. \(2013b,a\)](#). Furthermore, the authors suggest to not use the moist greenhouse limit presented in [Kopparapu et al. \(2013b\)](#) due to large differences to other works, which is why we chose the runaway greenhouse limit as the inner boundary.

Compared to the analysis performed in Paper II, the categories are identical with the exception of the temperate zone. This change is introduced, because accounting consistently for the scaling of the temperate zone with stellar mass requires the use of a more complex model.

The resulting fraction of systems containing each planetary type is shown in Table 2 and their mean multiplicity per system is shown in Table 3. Additionally, a visual representation of the same data including the occurrence rate (which is the product of the former two) is shown in Fig. 6. To get an idea of the dynamics, the eccentricities of the different types can be found in Table 4 and the host star metallicity [Fe/H] in Table 5. The metallicity is calculated based on the drawn dust to gas ratio f_{dg} (see Sect. 2.3.1) which then translates to $[\text{Fe}/\text{H}] = \log_{10}(f_{dg}/(\text{Fe}/\text{H})_{\odot})$, where $(\text{Fe}/\text{H})_{\odot} = 0.0149$ ([Lodders 2003](#)).

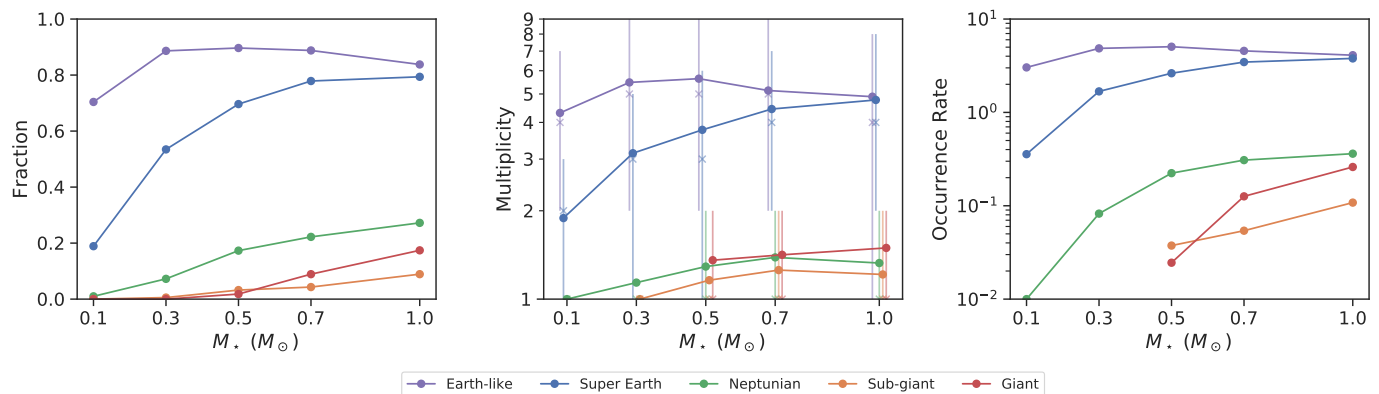


Fig. 6. Fraction of systems, multiplicity, and occurrence rate as a function of the stellar mass for five planet-mass categories. To highlight the skewedness of the distribution, the 68 % confidence interval around the median value (x-marker) is shown for the multiplicity (central panel). To better distinguish the markers for the different planetary categories, they are slightly shifted in x-direction.

Table 2. Fraction of systems with specific planetary type for the different stellar mass populations with 50 embryos

Type	Stellar mass (M_{\odot})				
	0.1	0.3	0.5	0.7	1.0
$M > 1 M_{\oplus}$	0.44	0.77	0.88	0.91	0.95
Earth-like	0.70	0.89	0.90	0.89	0.84
Super-Earth	0.19	0.53	0.70	0.78	0.79
Neptunian	0.01	0.07	0.17	0.23	0.27
Sub-Giants	0.00	0.01	0.03	0.04	0.09
Giants	0.00	0.00	0.02	0.09	0.17
Temperate zone	0.34	0.62	0.63	0.52	0.43

Table 3. Multiplicity of specific planetary types for all populations

Type	Stellar mass (M_{\odot})				
	0.1	0.3	0.5	0.7	1.0
$M > 1 M_{\oplus}$	3.04	5.32	6.27	6.79	7.01
Earth-like	4.31	5.47	5.64	5.14	4.89
Super-Earth	1.89	3.14	3.77	4.36	4.77
Neptunian	1.00	1.14	1.29	1.39	1.33
Sub-Giants	nan	1.00	1.17	1.27	1.21
Giants	nan	nan	1.36	1.41	1.49
Temperate zone	1.24	1.49	1.70	1.70	1.92

3.1.1. Earths and super-Earths

We find that in our synthetic populations, Earth-like planets are most common around stars with a mass of $0.5 M_{\odot}$ and – opposite the initial solid mass trend – get less frequent around stars with masses above $0.5 M_{\odot}$. In contrast, the frequency-peak for Super Earths lies at the highest stellar mass bin ($1.0 M_{\odot}$). However, the frequencies of super-Earths are very similar for the two highest stellar mass bins pointing to a flattening of the curve, similar to the Earth-like planet case.

Most of the Earth-like planets and super-Earths are on relatively circular orbits. However, the eccentricity scatter is of the same magnitude as the mean. A trend towards lower eccentricities for higher stellar masses can be seen.

In terms of host star metallicities, there seems to be a high metallicity required to form Earth-like planets or super-Earths around the very low mass stars, whereas for stellar masses larger than $0.5 M_{\odot}$, the mean metallicity of Earth-like planet and super-Earth hosts is close to the mean of the whole population. This outcome indicates that growth to these masses is not limited by the available amount of solids.

3.1.2. Neptunian planets and sub-giants

Whereas the frequency of Neptunian planets in our simulations is similar for stellar masses of $0.7 M_{\odot}$ and $1.0 M_{\odot}$, it declines more sharply towards the $0.3 M_{\odot}$ and $0.1 M_{\odot}$ bins, where these kind of massive planets become very rare. Most commonly, a

Neptunian planet is the only one of its kind in a system and its orbit is quite eccentric, which holds for all stellar mass bins.

The orbits of sub-giants are even more eccentric. This picture emerges where enough statistics are available, hence not for the single sub-giant that formed around a $0.3 M_{\odot}$ star. For stellar masses larger than $0.3 M_{\odot}$, sub-giants are present in 5 % to 10 % of the systems.

For both sub-giants and Neptunian planets, the mean metallicity of their host stars decreases with increasing stellar mass.

3.1.3. Giant planets

The observed giant planet occurrence rate drops with decreasing stellar mass (Endl et al. 2006; Butler et al. 2006; Johnson et al. 2007, 2010; Gaidos et al. 2013; Montet et al. 2014). Laughlin et al. (2004) explain this by the growth being limited by the available solid mass, which is lower for decreasing stellar masses (see Sect. 2.3.1). As can be seen in Table 2, we recover this trend in our simulations, where no planets with masses above $100 M_{\oplus}$ form around stars with masses below $0.5 M_{\odot}$. At this transition stellar mass, the synthetic population with nominal parameters contains only 2 giant planets. For the $0.1 M_{\odot}$ population, we find planetesimal isolation masses (Lissauer & Stewart 1993) of up to $30 M_{\oplus}$ at around 10 au, but only $1 M_{\oplus}$ at 1 au. This increase in the planetesimal isolation mass with a is present, despite the steeper planetesimal surface density slope (see Sect. 2.3.1) because the isolation mass scales $\propto (a^2 \Sigma_{\text{pls}})^{3/2}$ and the nominal slope of Σ_{pls} is -1.5. However, at large separations, the accretion rates are too low to reach the isolation mass during the typical disk lifetimes and for close-in planets there is not enough mate-

rial in the feeding zone. We note, that in appendix A, we explore a set of parameters, which is more likely to form giant planets.

Table 4. Mean eccentricities of different planetary types for all populations

Type	Stellar mass (M_{\odot})				
	0.1	0.3	0.5	0.7	1.0
$M > 1 M_{\oplus}$	0.07	0.05	0.05	0.04	0.04
Earth-like	0.07	0.05	0.05	0.04	0.04
Super-Earth	0.08	0.06	0.05	0.04	0.03
Neptunian	0.08	0.10	0.11	0.10	0.09
Sub-Giants	nan	0.03	0.16	0.16	0.14
Giants	nan	nan	0.17	0.14	0.16
Temperate zone	0.11	0.07	0.05	0.03	0.02

Table 5. Mean metallicity [Fe/H] of stars hosting specific categories of planets

Type	Stellar mass (M_{\odot})				
	0.1	0.3	0.5	0.7	1.0
$M > 1 M_{\oplus}$	0.10	0.02	-0.01	-0.01	-0.01
Earth-like	0.04	-0.01	-0.03	-0.03	-0.04
Super-Earth	0.16	0.07	0.02	0.00	-0.02
Neptunian	0.32	0.14	0.12	0.10	0.08
Sub-Giants	nan	0.32	0.20	0.15	0.09
Giants	nan	nan	0.09	0.15	0.15
Temperate zone	0.06	-0.01	-0.06	-0.08	-0.12

3.1.4. Earth-mass planets in the temperate zone

An interesting pattern can be seen for the fraction of systems with Earth-sized planets in the temperate zone: The stellar mass with the most temperate, Earth-mass planets is $0.5 M_{\odot}$, but the multiplicity keeps increasing with stellar mass. Despite that, the occurrence rate (i.e. the fraction multiplied with the multiplicity) retains a peak at $0.5 M_{\odot}$.

The temperate zone (Kopparapu et al. 2014) for the different stellar mass bins is moving with time based on the luminosity and the radius evolution of the star, for which we use the evolutionary tracks of Baraffe et al. (2015). We do not model the intrinsic scatter of rotational periods of the stars, therefore all stars with the same mass have identical luminosities and radii at all times. The resulting temperate zone limits after 5 Gyr of evolution are:

- 0.03 au to 0.06 au for $0.1 M_{\odot}$
- 0.11 au to 0.21 au for $0.3 M_{\odot}$
- 0.20 au to 0.38 au for $0.5 M_{\odot}$
- 0.39 au to 0.72 au for $0.7 M_{\odot}$
- 0.96 au to 1.70 au for $1.0 M_{\odot}$.

Thus, the temperate zone moves with increasing stellar mass from orbital periods on the order of days for $0.1 M_{\odot}$ stars to orbital periods on the order of years for solar-type stars. In our simulations, this implies that the zone is displaced from close to the former inner edge of the disk to the proximity of the former disk snowline. In terms of planet formation, at these two regions very different, important processes shaping the population of planets occur.

Due to the dynamically distinct locations of the temperate zone, the respective planets' eccentricity is not expected to be similar. Indeed, a trend towards lower eccentricities with increasing stellar mass is recovered (see Table 4). In terms of mean host-star metallicity, a similar picture as for the Earth-like planets emerges with increased mean metallicities for low-mass stars and reduced metallicities for solar-type stars.

3.2. Mass-Distance diagrams

The mass – semi-major axis diagrams of the populations of synthetic planets around stars with masses of $0.1 M_{\odot}$ (NGM10), $0.3 M_{\odot}$ (NGM14), $0.5 M_{\odot}$ (NGM11), $0.7 M_{\odot}$ (NGM12) and $1.0 M_{\odot}$ (NG75, also discussed in Paper II) are shown in Fig. 7. Each system starts with 50 embryos which collide over time, thus the number of points in each of the plots is on the order of $20 \cdot 000$. The composition, measured by the volatile – or ice – fraction of the solid core of the planets is color-coded.

General trends for most stellar masses are the more ice-rich planets at large semi-major axes due to the lower local temperatures, the imprint of migration in bringing ice-rich planets at Earth to super-Earth masses closer to the stars and a distinct population of giant planets that is separated by a runaway gas accretion desert (Ida & Lin 2004a) from the rocky population.

Another quite weakly accentuated feature due to little statistics is an under-density due to tidal migration at very close orbits of a few 10^{-2} au, where tides push some planets into the star and leave a void of massive, close-in planets. This can be seen as a fuzzy diagonal cut-off in the mass – semi-major axis diagram, which increases to higher planetary masses with increasing semi-major axis (Schlaufman et al. 2010; Benítez-Llambay et al. 2011).

Additionally, all populations show a similar "triangle of growth" at the very low masses, meaning there is a region where all embryos, independent on the chosen disk initial conditions, grow. Thus, there is a blank space in the region from 0.1 au to 10 au at the lowest planetary masses. These are the regions most favorable for planetesimal accretion where growth timescales are short and feeding zones are large enough to grow.

Although these features can be seen for the different stellar masses, there are clear differences between the populations, which show the influence of the reduced stellar and disk mass. Firstly, the "horizontal branch" (Mordasini et al. 2009a) is located at different planetary masses. For lower disk mass, the planets start migrating at lower planetary masses (see Sect. 2.1.1). Thus, the population of close-in, ice-rich planets extends to lower masses for the lower stellar mass populations (down to $\sim 1 M_{\oplus}$ for NGM10 instead of down to only $\sim 3 M_{\oplus}$ for NG75). However, the scatter is quite large and to access this in a more quantitative way, more statistics would be needed, especially for the low stellar mass case, where very few ice-rich planets migrated to the inner parts of the disk.

Secondly, a reduction of the number of giant planets is clear with decreasing stellar mass (see also Sect. 3.1.3). Interestingly, the semi-major axis distribution of the giants differs quite a bit when comparing the $0.7 M_{\odot}$ (NGM12) case with the $1.0 M_{\odot}$ (NG75) case. Giant planets are more frequently scattered for the more massive case, since there is more often a second or third giant planet forming, which then leads to more frequent interactions. Therefore, the distribution of giants in NGM12 is more localized at around 1 au compared to the solar-mass case. In the lowest stellar-mass population, not a single giant planet was able to form.

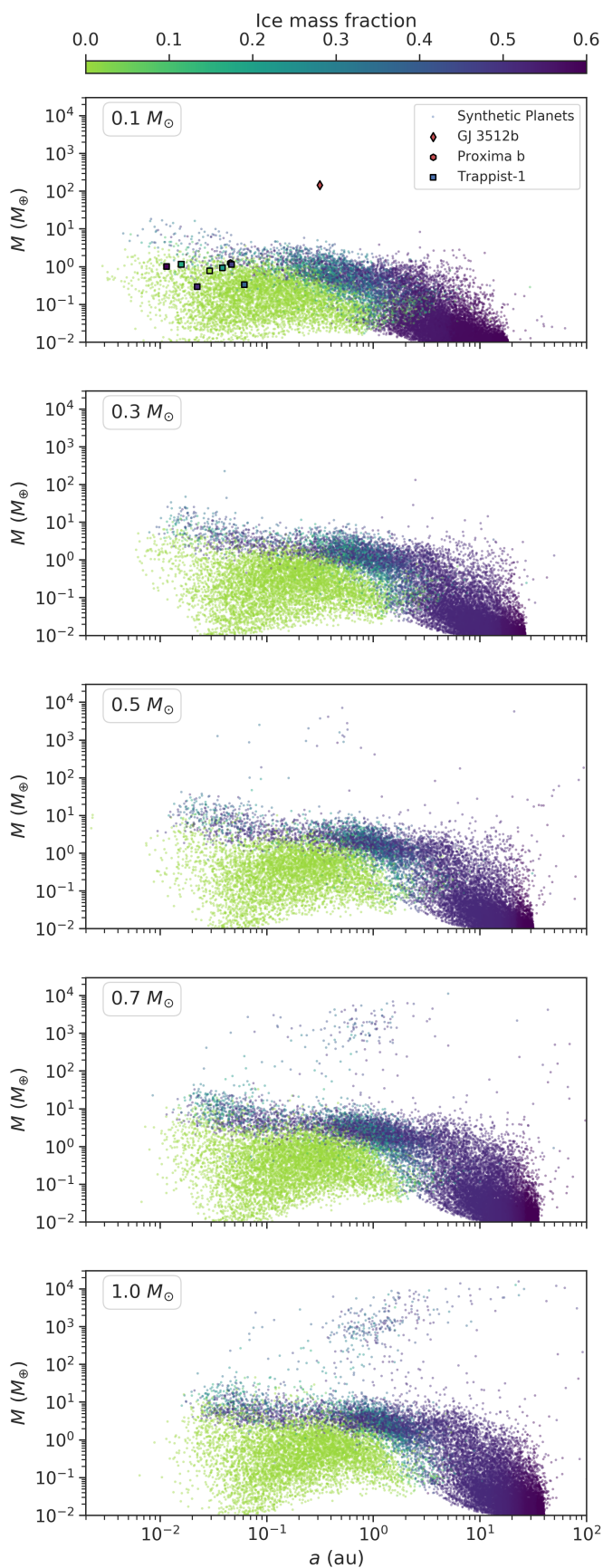


Fig. 7. Synthetic populations of planets as a function of a and M with summed-up mass fraction of all ice species in color. Their NGPPS identifiers are NGM10, NGM14, NGM11, NGM12 and NG75. Some observed planets around very low-mass stars are shown. Planet masses increase with host star mass, but no giant planets occur for $M_\star < 0.5 M_\odot$.

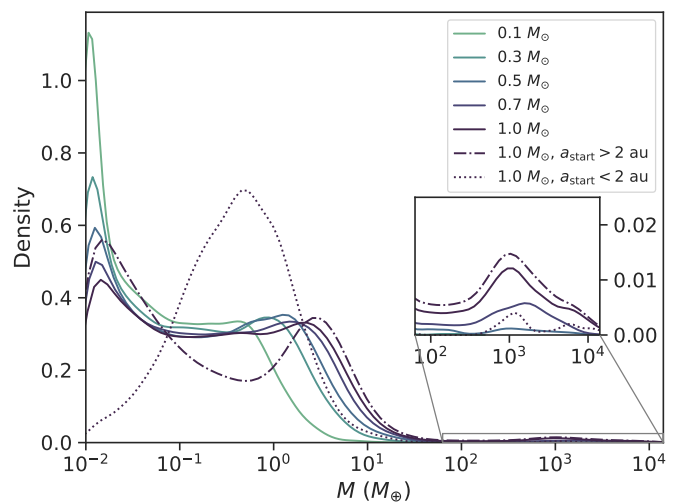


Fig. 8. Kernel-density estimate of the planetary mass distribution for populations of planets around different stellar masses. The bandwidth of the Gaussian kernel was chosen following the Normal reference rule (Scott 1992). The population around solar-type stars is shown three times, once complete, once only including planets that started below respectively above 2 au.

3.3. Planetary mass distribution

Because some regions at lower planetary masses in Fig. 7 are saturated with points, we derive kernel-density estimates of the probability distribution of the synthetic planets' masses for better visibility and comparability. The resulting distribution of planetary masses for different stellar masses is shown in Fig. 8. We note that for this rather theoretical analysis, no cut in semi-major axis was applied.

Starting at low mass planets, a clear over-density close to $0.01 M_\oplus$ is visible. These are the "failed cores" (Mordasini et al. 2009a) that did not undergo significant growth by collisions. This sub-population lies at large separations and vanishes if the planets at starting locations further than 2 au are excluded (dotted line). It is obvious from Fig. 8 that a larger set of "failed cores" remains for lower stellar mass.

Moving to slightly larger masses, a plateau in the likelihood of simulated planetary masses is found at $0.1 M_\oplus$ to $10 M_\oplus$. The shape seems to be a combination of multiple distributions and splitting the population by the initial starting position of the planets indeed reveals two different cases.

On one hand, planets forming at larger separations from the star tend to grow more and the distribution is peaked just below $10 M_\oplus$ for the population of planets around solar masses in addition to the "failed core" peak.

On the other hand, there is the population of embryos located close to the star, where the peak is at much lower masses of $\sim 0.5 M_\oplus$. No "failed cores" are included in this sub-population for all stellar masses.

The mass distribution for the giant planets can be best seen in the zoom-in box. There, the shapes are influenced by the low-number statistics and should not be interpreted quantitatively. Qualitatively, most giants originated from outside 2 au and we recover that the number of giant planets increases with stellar mass.

3.4. Planetary composition and radius

Even though the mass of a planet is the more fundamental parameter in terms of formation, transit measurements are sensitive to the radius of the planets. Therefore, we use the structure of the modeled planetary hydrogen-helium envelopes to calculate planetary transit radii following the prescription outlined in Sect. 2.2.

Figure 9 shows the masses and derived transit radii of the synthetic planets for the populations NGM10, NGM11 and NG75 with respective stellar masses of $0.1 M_{\odot}$, $0.5 M_{\odot}$, and $1.0 M_{\odot}$. The red markers show the observational data from the NASA Exoplanet Archive, where only planets with relative errors in radius, mass and stellar mass less than 15% are included. This yields relatively little data for low-mass stars. Additionally, the TRAPPIST-1 system is included with masses based on Grimm et al. (2018) and the color-coded ice mass fraction derived thereof by Dorn et al. (2018). The masses derived from TTV measurements might systematically shift due to new data from upcoming works, allegedly leading to more rocky compositions (Proposed and in prep. by Agol et al. 2019).

A detailed comparisons to observations is therefore only possible for the giant planets around solar-mass stars, which is discussed in Paper II.

The two straight lines at the low-mass end in Fig. 9 correspond to the compositions of pure-rocky or ice-rock mixture with $\sim 50\%$ ice, which is the typical ice fraction of planetesimals outside the water-ice line (Thiabaud et al. 2014; Marboeuf et al. 2014). Only a small sub-population has ice-fractions in between the two limiting cases. This group of planets accreted a significant amount of mass originating from outside and inside the water-ice line. We see however, that there are more of these planets for the low stellar mass cases due to fast type I migration at lower planetary masses. Migration of icy far-out planets naturally leads to mixed compositions if the embryos reach the inner regions of the disk. For the solar-mass case, most planets only migrate at $\sim 10 M_{\oplus}$, where they can already accrete a light envelope, which leads to a significant increase in radius. For lower-mass disks, migration starts at lower planetary masses, where no significant envelope can be kept (see Sect. 2.1.1), thus the $0.1 M_{\odot}$ population NGM10 includes more intermediate-composition planets without hydrogen-helium envelopes.

An additional difference between the three populations are the low-mass planets with hydrogen-helium envelopes that lie in Fig. 9 above the straight blue line, which are more common in NG75 ($1.0 M_{\odot}$, bottom panel). These are low-mass planets at large separations, which can keep their envelope thanks to the distance to the star. We note that the energy-limited atmospheric escape mechanism used in this work (see Paper I for a detailed description) might underestimate the amount of envelope lost for this kind of regime.

Overall, the resulting planets follow more or less the observational data – where available – in terms of their mass-radius distribution with no detected planets being orders of magnitude outliers. In the future, objects discovered by TESS and characterized by follow-up programs will populate the mass-radius diagram for low-mass stars and will help to better validate the internal structure and envelope models.

In general, the statistical distribution of planetary radii in Fig. 10 shows features that are very similar to the features seen in mass-space distribution (Sect. 3.3). The main difference is that the planets do not span over many orders of magnitude in radii due to the degeneracy in the radii of giant planets (maximum at $R \sim 13 R_{\oplus}$). Therefore, the x-axis can be chosen to scale linearly.

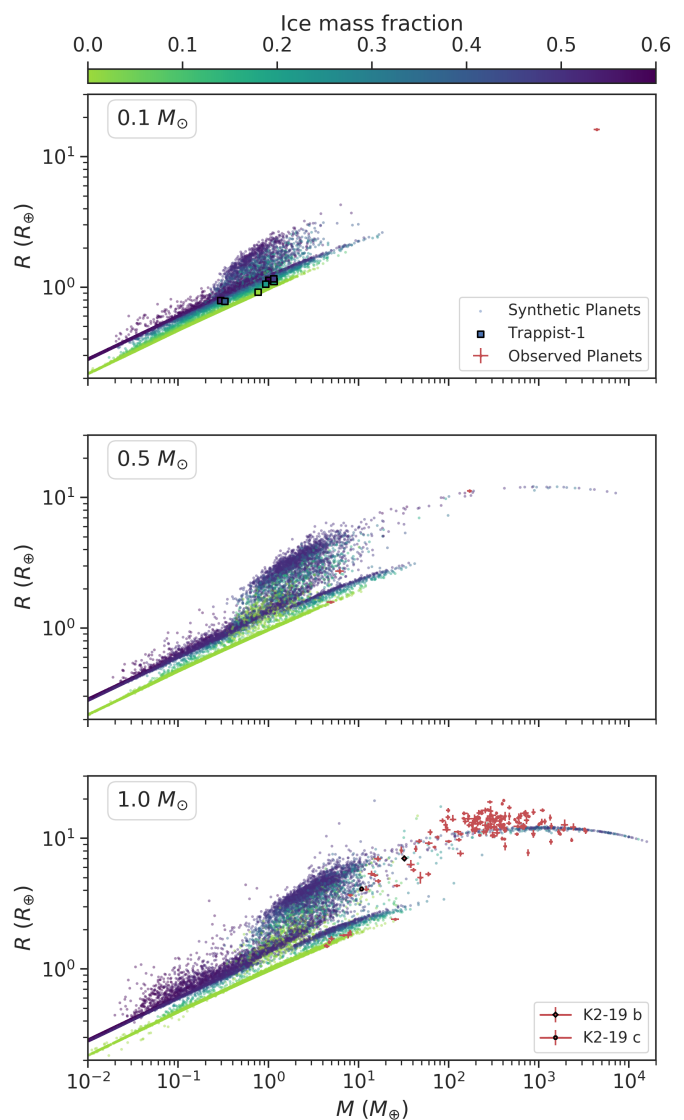


Fig. 9. Populations of synthetic planets as a function of planet mass and planetary transit radius. The total ice mass fraction is shown in color and observational data from the NASA Exoplanet archive (accessed 9.12.2019) is over-plotted in red. The especially precise values for K2-19 b and c are highlighted (Petigura et al. 2019).

The synthetic radius distribution in Fig. 10 is missing the radius valley at around $2 R_{\oplus}$, which is found in single-planet populations (Jin et al. 2014) and in the observed population of planets (Fulton & Petigura 2018). This radius gap was predicted to be caused by photo-evaporation (Owen & Wu 2013; Lopez & Fortney 2013; Jin et al. 2014). The reasons for why the radius gap is not reproduced in the multi-planet simulations despite including the atmospheric photo-evaporation mechanism could be due to too efficient envelope stripping for colliding embryos or the not accurate treatment of hot, water-rich atmospheres (Turbet et al. 2019) and will be explored in future work.

The observed gap shows an interesting stellar mass dependency (Fulton & Petigura 2018), which we can therefore not compare to observations here. Additionally, the sizes of the super-Earths (i.e., the planets below the radius gap) and the sub-neptunes (i.e., above the gap) were individually analyzed in Fulton & Petigura (2018) and both show a trend of increasing mean size with increasing stellar mass. We note that their sample ex-

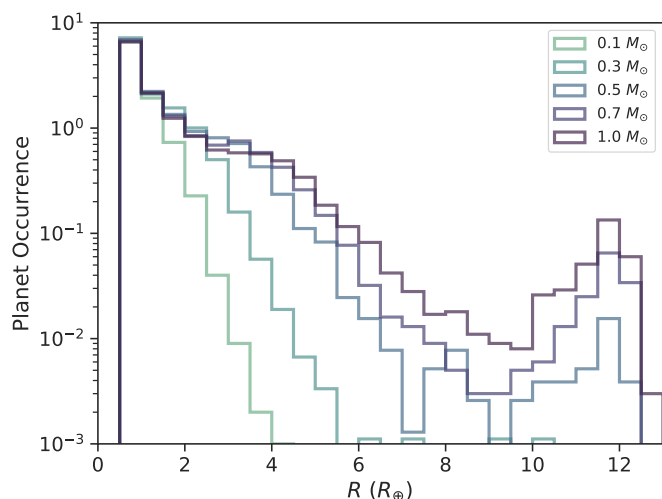


Fig. 10. Occurrence rates ($N_{\text{planets}}/N_{\text{systems}}$) of synthetic planets on orbits with periods $P < 100$ days as a function of their transit radii.

tends to only $0.8 M_{\odot}$ and not to M dwarfs. There is a clear trend towards larger mean size for the sub-neptunes around larger stars in the synthetic data.

An interesting feature at lower radii is that the planet occurrence rate ($N_{\text{planets}}/N_{\text{systems}}$) of planets at a specific radius is higher for lower-mass stars. Mulders et al. (2015) show the same trend for the observed *Kepler* sample. However, they find a factor of 3.5 times higher occurrence rates, whereas we only find differences on the 10% level.

3.5. Tidal interaction with the star

While the tidal orbit evolution of the $1.0 M_{\odot}$ population is significant, we observe only a minimal semi-major axis evolution of planets around a $0.1 M_{\odot}$ star. In contrast to a few lost planets in the solar-type case, no planet was lost to the star due to tides in the late M dwarf case. The innermost planets' orbital periods after the disk-embedded formation stage are similar in the different stellar mass bins due to our choice of inner disk edges (see Sect. 2.3.3) where the planets may stop radial migration in the disk stage. This leads to a semi-major axis scaling $\propto M_{\star}^{1/3}$, whereas the radial tidal evolution $da/dt \propto R_{\star}^5 M_{\star}^{-1/2} a^{-11/2}$ (see Sect. 2.1.2). Taking into account that the stellar radius at later times is almost proportional to the stellar mass Baraffe et al. (2015), the tidal evolution thus approximately scales $\propto M_{\star}^{8/3}$ at fixed orbital period. Hence, a much slower tidal, radial evolution for low-mass stars is expected and recovered.

4. Discussion

4.1. Giant planet occurrence for different stellar masses

The best constrained occurrence rates exist for the most readily observable planets, which are mostly the giant planets. The general observed trend is an increasing frequency of giant planets with stellar mass (Endl et al. 2006; Butler et al. 2006; Johnson et al. 2007, 2010; Gaidos et al. 2013; Montet et al. 2014). This is well explained by works on giant planet formation based on the core accretion paradigm. Adams et al. (2004) report fast external evaporation of disks around M dwarfs reducing the available gas to form giant planets. Even without this effect, Laughlin et al. (2004) found much slower growth timescales at a fixed semi-

major axis around a $0.4 M_{\odot}$ star, mainly due to the reduced solid surface density and the longer orbital timescale, which is also one of the conclusions of the population synthesis work by Ida & Lin (2005) and Alibert et al. (2011). The latter stress the importance of the disk mass on the resulting population of planets. Like our work, these works nominally assumed more heavy protoplanetary disks around more massive stars motivated by measured stellar accretion rates. In general, we recover the same trends of low giant planet frequencies around low-mass stars. The reasons are growth being limited by fast type I migration and long solid accretion timescales.

More quantitatively, Alibert et al. (2011) were able to approximate the synthetic giant planets resulting from their single-embryo populations around different stellar masses by scaling the distribution resulting from the $1 M_{\odot}$ case. They found planetary masses $M \propto M_{\star}^{\gamma}$ with $\gamma = 0.9$ in their nominal case (disk mass $\propto M_{\star}^{1.2}$). The same can not be recovered in our simulations, where the giant planet distribution seems to peak at the same planetary mass for all stellar masses. The overall frequency of giants is reduced but not their mean mass. However, we stress that our dataset is much more sparse since only 1000 stars and only on the order of 100 resulting giant planets were simulated compared to the 30 000 stars in Alibert et al. (2011). Therefore, it is possible that some trends are hidden in statistical noise. If there is indeed no dependency of the mean giant planet mass on the stellar mass, N-body effects – like the ejection of planets – might have played an important role in influencing the mass function in the newer simulations.

Even though giant planet occurrence rates do increase with stellar mass, quite a number of puzzling, exotic systems with giant planets in orbit around M dwarfs exist. The first discovery of a planet around an M dwarf was for GJ 876 (Marcy et al. 1998; Delfosse et al. 1998; Marcy et al. 2001; Rivera et al. 2005, 2010; Millholland et al. 2018) where now four companions were discovered. Two of them are giant planets (with masses of $1.95 M_{\text{Jup}}$ and $0.6 M_{\text{Jup}}$), orbiting a $0.37 M_{\odot}$ star (von Braun et al. 2013). Other examples are GJ 849 ($0.65 M_{\odot}$ Stassun et al. 2016) with two giants (Butler et al. 2006) of masses $0.77 M_{\text{Jup}}$ and $0.9 M_{\text{Jup}}$ (Montet et al. 2014); GJ 179 a $0.36 M_{\odot}$ star hosting a giant planet with a mass of $0.8 M_{\odot}$ (Howard et al. 2010); and GJ 317 ($0.42 M_{\odot}$ Anglada-Escudé et al. 2012) hosting a potentially up to $2.5 M_{\text{Jup}}$ massive planet and a second giant with $M \sin i = 1.6 M_{\text{Jup}}$ (Johnson et al. 2007; Anglada-Escudé et al. 2012).

Below stellar masses of $0.3 M_{\odot}$, no stars hosting giants were found¹ up to the recent discovery of GJ 3512b, a planet with a minimum mass of $0.463 M_{\text{Jup}}$ around a $0.123 M_{\odot}$ star (Morales et al. 2019), which poses the biggest challenge to all current planet formation scenarios. Additionally, it is quite likely that a saturnian mass companion leads to an inner cavity in the transition disk CIDA 1 (Pinilla et al. 2018).

In our nominal populations presented in Sects. 3.1 and 3.2, we do not find giant planets around stars with masses below $0.5 M_{\odot}$ despite sampling also heavy disk masses. As a consequence, to form a planet like GJ 3512b, either the physical parameters are to be revised in our models or different physical processes are at work. In appendix A, we explore the former pathway by running our models with a single embryo per disk.

We find that reducing type I migration would enable the formation of giant planets even around low-mass stars. This happens in some rare cases, where the disk mass was large and the

¹ A lower stellar mass of GJ 317 was reported in Johnson et al. (2007), but was corrected to higher masses by Anglada-Escudé et al. (2012).

initial starting location was ideal. Morales et al. (2019) mention that core accretion formation of GJ 3512b was limited by the fast type I migration timescales, which we confirm here with explicit numerical simulations. Removing this limiting factor naturally leads to more growth. We also find that even higher mass planets could be produced if the solids are more concentrated. Therefore, as long as lower migration speeds or migration traps can not be excluded, the formation of giant planets by core accretion around very low-mass stars should not be discarded.

Admittedly, this pathway does require more "tuning" of parameters (i.e. small planetesimal sizes and low type I migration speeds) than the gravitational instability pathway (Cameron 1978; Boss 1997) which would more naturally produce giant planets around low-mass stars. For core accretion models, it remains to be checked if planets could be trapped at a fixed separation from the star in a sufficiently frequent and efficient way to explain the aforementioned large planetary to stellar mass ratio examples. Observations do reveal common ringed structures in protoplanetary disks (Andrews et al. 2018). Those frequent dust rings might trace inverted gas pressure gradients which lead to migration traps.

4.2. Growth regimes

As shown in section 3.3, the components that make up the planetary mass distribution (Fig. 8) are a population of low-mass "failed cores" at high semi-major axis, intermediate mass planets mainly growing within the water iceline ("terrestrials"), the more massive planets ("horizontal branch" planets, Mordasini et al. 2009b) initially growing at larger separations, and a few giant planets.

In the following, the different origins of the sub-populations are addressed. The initial embryo mass of $0.01 M_{\oplus}$ is large enough to lie in the *oligarchic* growth regime (Rafikov 2003). At low masses and large separations, the oligarchic growth timescale is long. This leads to the aforementioned peak of "failed cores". As the planet grows, the time needed to double its mass by planetesimal accretion reduces and additionally, by Hill radius enlargement, encounters with smaller embryos that can be accreted become more frequent. Therefore, the mass distribution at large semi-major axes is not flat, but decreases with increasing mass.

The distribution peaks at the location of $\sim 10 M_{\oplus}$. To this sub-population dubbed "horizontal branch" planets belong the most massive planets apart from the few giants. In principle, the upper end of the peak could be due to the onset of rapid gas accretion and the typical "desert" in the mass distribution (Ida & Lin 2004a). However, this does not work out in terms of statistics, since the number of planets that actually grow to become a giant planet is far too little to influence the shape of the distribution at lower masses.

Indeed, the frequency of horizontal branch planets peaks at a given mass due to the onset of very rapid type I migration at these planetary masses. As discussed in Sect. 2.1.1, migration is a function of the stellar mass, disk mass, and planetary mass. With the chosen initial scaling of the disk mass proportional to the stellar mass, the rapid type I migration region is shifted towards lower planetary masses, which explains the different locations of the drop in the mass distribution.

At the upper end of the distribution lies a very small fraction of planets which can overcome this type I migration barrier. Then, they undergo runaway gas accretion (Mizuno et al. 1978), reach the slower type II migration regime and become giants. A lot of solid mass is required to grow to the type II migration

regime more quickly than type I migration timescales ($\sim 10^4$ to 10^5 yr).

The population of planets which starts close-in – the "terrestrials" – would have these short growth timescales. However, their growth by planetesimal accretion is soon limited by the amount of mass in their feeding zone. This is due to their much smaller Hill region. In the simulations, we observe that commonly, all the planetesimals within the iceline are either ejected or accreted after a few 100 kyr. Therefore, the close-in distribution in Fig. 8 does not include planets that stayed at their initial mass of $0.01 M_{\oplus}$. However, there are many planets in a terrestrial-like regime between $0.1 M_{\oplus}$ and $1 M_{\oplus}$. The terrestrials typically also undergo many collisions to grow to Earth masses, even though the individual embryo's isolation mass is lower. Additionally, outward migration zones help to push the tail of the distribution into the super-Earth mass range by giving the embryos access to a larger planetesimal reservoir. Despite that, we find that growing into a giant is not possible for embryos initially located within the iceline unless they were scattered by a close encounter to larger separations. For the aforementioned reasons, it is obvious that the overall masses of the terrestrials is very sensitive to the slope of the planetesimal disk, which was chosen to be -1.5 .

For the different stellar masses, there is always a distinction between initially close-in and far-out planets. The rough shape of the distribution stays the same, but the different populations of planets are influenced differently by the stellar mass. The population of close-in planets that is limited by the available mass is roughly reduced by half an order of magnitude, whereas the outer population that is limited by type I migration is linearly shifted to lower masses by a full order of magnitude.

4.3. Frequency of Earths and super-Earths

For planets with masses below $\sim 100 M_{\oplus}$, the best estimates on their frequency can be gained from transit surveys due to the large sample. Using the results from *Kepler*, Dressing & Charbonneau (2013) derive an occurrence of about one planet with orbital period shorter than 50 days and radii from $0.5 R_{\oplus}$ to $4 R_{\oplus}$ per cool star ($T < 4000$ K), while Gaidos et al. (2016) find around two planets with similar radii and orbital periods up to 180 days per M dwarf. From Fig. 10, it is apparent that more planets are formed in the synthetic simulations. This has already been reported in Mulders et al. (2019), who find a five times too large fraction of synthetic stars with planets compared to the *Kepler* sample. This still holds for lower mass stars. The synthetic data on which conclusion is based on, is very similar to the $1.0 M_{\odot}$ dataset shown here.

Planet formation models do more readily yield planetary masses than radii, as gravity is the dominating force that is acting. Consequently, our results can more readily be compared to Pascucci et al. (2018) who use the *Kepler* sample to derive planetary and stellar masses.

They find broken scaling relations in planet to star mass ratios obtained from *Kepler* and microlensing surveys, which can be discussed here without the compositional imprints on the radii. In the *Kepler*-based data of Pascucci et al. (2018), the position of the universal peak lies at $M/M_{\star} = 2.8 \times 10^{-5}$. Our synthetic mass function does not show a prominent peak, but rather the edge of a plateau at comparable ratios (see Fig. 8). However, if more embryos would have started outside the iceline, a peak similar to the dash-dotted line in Fig. 8 should have been recovered at this location of the plateau-edge. In Fig. 8, the edge of the plateau is not shifted exactly linearly with the stellar

mass. Instead, a slight trend towards larger M/M_* for lower stellar masses can be seen. In [Pascucci et al. \(2018\)](#), only the most massive F-stars do show a slightly lower mass ratio peak, while the peaks around G, K and M dwarfs lie at the same M/M_* . This could partially be due to a more narrow range of stellar masses.

Furthermore, the location of the peak at $M/M_* = 2.8 \times 10^{-5}$ from [Pascucci et al. \(2018\)](#) is not well matched by our models. Instead, plateau edges a factor ~ 1.5 lower are found where the edge of the mass distribution for the $0.1 M_\odot$ case lies the closest to the observed peak. This can either point towards migration in the models becoming too efficient at too low masses, too low disk masses or a preferred placement of the embryos could be influencing the results.

From this, we can conclude that if the mass distribution of planets indeed has a distinct peak and is not the edge of a plateau it is most likely due to type I migration halting growth and pushing many planets of similar mass to the observable regime, which should make out the bulk of the observed data. Thus, this would point towards more embryo formation at larger distances and less "terrestrial-like" planet growth, which would be in line with works that propose that planetesimal formation preferably occurs outside the water iceline ([Drażkowska & Alibert 2017](#); [Schoonenberg & Ormel 2017](#)). A more quantitative, direct comparison to the *Kepler* sample will be done in a future paper of this series (Mishra et al. in prep).

4.4. Most common temperate planet hosts

While not the ideal measure to constrain planet formation by observations, we can still take a look at the number of temperate planets around stars of different stellar masses. While there are a wealth of processes neglected to constrain the habitability of these planets ([Kaltenegger 2017](#)), constraints on the frequency of planets on which life similar to Earth has a chance to emerge is still of interest for the wider community. We choose to take the approach of checking if liquid water could exist on the surface of the synthetic planets using the limits of [Kopparapu et al. \(2014\)](#) and call them temperate planets.

We find in our simulations that most frequently, temperate planets occur around intermediate stellar masses $\sim 0.5 M_\odot$. As discussed above, the overall number of planets per star in the synthetic simulations is higher than observed. Similarly, we get a higher estimate on the number of planets in the temperate zone than works based on observational data. [Dressing & Charbonneau \(2015\)](#) derive an occurrence rate of 0.09 to 0.33 for small planets around cool stars ($T_{\text{eff}} < 4000$ K), which is lower than the occurrence rates of 0.92 and 1.07 (see Tables 2 and 3) for the synthetic populations with stellar masses of $0.3 M_\odot$ and $0.5 M_\odot$ respectively. Again, the factor of five found by [Mulders et al. \(2019\)](#) would bring the numbers to a comparable level. This motivates the existence of a mechanism that inhibits growth of (or removes all) planets or embryos around four out of five stars.

4.5. Dependence of dynamical results on initial placement

Planetary orbital parameters, such as the eccentricity or the period ratio of neighboring planets are influenced by close encounters between them. The frequency of close encounters in turn depends sensitively on the initial placement of the synthetic embryos, since placing two embryos in close proximity to each other might lead to interactions already during the early growth stage when migration is still negligible.

One measure that can be used to quantify the probability of dynamical instabilities (i.e. gravitational interactions) is the mutual Hill radius of a pair of planets ([Chambers et al. 1996](#))

$$R_{\text{H,mut}} = \left(\frac{M_1 + M_2}{3M_*} \right)^{1/3} \left(\frac{a_1 + a_2}{2} \right), \quad (4)$$

where M_1, M_2, a_1, a_2 are the masses and semi-major axes of two planets in a system. Typically, instabilities can occur if two planets are separated by less than ~ 3.5 mutual Hill radii ([Chambers et al. 1996](#)).

We chose the same initial embryo mass for all stellar masses. Thus, the distance, measured in mutual hill radii, between the initially placed embryos in the simulations increases with increasing stellar mass. This means that in terms of dynamical interactions the populations are not starting with the same initial conditions and thus, no strong conclusions should be drawn from the nominal populations with 50 embryos each.

This discussion touches the topic of the influence of the initial number of embryos, which is discussed in Paper II. There, it is shown that eccentricity and period ratio are quantities sensitive to the number of initial embryos that are placed in the disk. The scaling of the Hill radius $\propto M_*^{1/3}$ leads to a factor ~ 2 in the distance between initial embryos measured in mutual Hill radii between the $0.1 M_\odot$ population and the $1.0 M_\odot$ population. Coincidentally, a planetary population was calculated and presented in Paper II using 100 embryos around a $1.0 M_\odot$ star (Population NG76). We are therefore able to compare here the dynamical outcome between those two populations, which have much more similar initial dynamical conditions (see Fig. 11, dotted lines).

Due to growth and migration, the systems get more compact over time leading to lower mean distances measured in mutual hill radii ($\bar{\Delta a}/R_{\text{H,mut}}$) but, sporadically, the measure can increase if collisions or scattering of planets occur. The final state of the solar-type star population with 100 initial embryos and the $0.1 M_\odot$ population with 50 embryos is still quite close to each other. For comparison, the solar-type star population with 50 embryos has a mean over all systems around $27 \bar{\Delta a}/R_{\text{H,mut}}$ after starting at ~ 40 . This is significantly different to the outcome with 100 embryos, which ends up with more closely packed systems with a mean over all systems of $\bar{\Delta a}/R_{\text{H,mut}}$ at ~ 20 .

In Fig. 11, we can also see a slight trend to more packed systems for the population of planets around solar-type stars. Indeed, even though the initial $\bar{\Delta a}/R_{\text{H,mut}}$ of the population of planets around solar-type stars is slightly larger than for the population around $0.1 M_\odot$, the resulting mean $\bar{\Delta a}/R_{\text{H,mut}}$ is lower. We argue that this is due to very little growth in some systems around $0.1 M_\odot$, which then leads to systems with mean $\bar{\Delta a}/R_{\text{H,mut}}$ closer to the higher initial value.

Having established a closer dynamical relationship between the population with 50 embryos around a $0.1 M_\odot$ (NGM10) star and the one with 100 embryos around $1.0 M_\odot$ (NG76) we can compare the dynamical evolution of the systems of those two populations. Figure 12 shows the period ratio of neighboring planets of any mass and semi-major axis that formed in NG76 (blue line) and NGM10 (brown). An apparent difference is the number of planets in or close to mean-motion resonances seen as vertical jumps in the lines in Fig. 12. The total number of planets close to integer period ratios (within 2%) is 44.5% of the planets in the $0.1 M_\odot$ population compared to 32.6% in NG76. This trend would not have been recovered if we compared the $0.1 M_\odot$ population NGM10 to the $1.0 M_\odot$ one (NG75) with also 50 initial embryos but an initially larger separation between them measured in mutual Hill radii. There, in NG75, a slightly larger

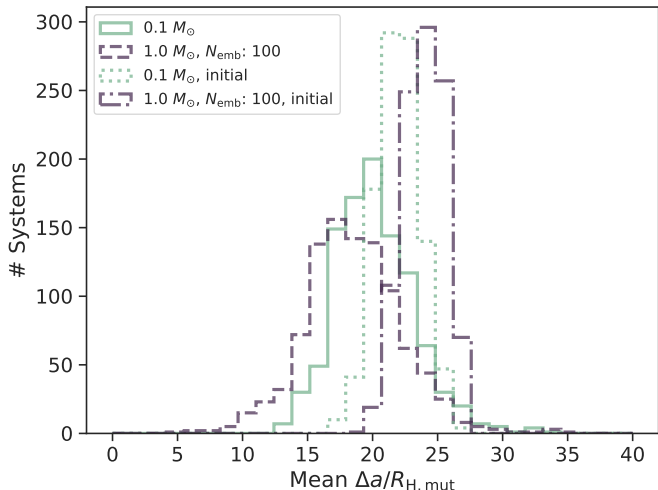


Fig. 11. Mean distance between all neighboring planets in a system measured in mutual Hill radii (Chambers et al. 1996). The initial placement corresponds to the dotted lines and the resulting values are shown using a solid line. The number of injected embryos for the population of planets around $0.1 M_{\odot}$ stars is 50, whereas we insert 100 embryos for this population of planets around $1.0 M_{\odot}$ stars.

number of planet pairs is close to mean-motion resonances than in NGM10. The trend of less planets close to mean-motion resonances with increasing number of embryos was already found by Alibert et al. (2013) by comparing simulations with up to 20 embryos.

An interesting aspect of the mean-motion resonant chains is that there are very few planet pairs in second-order mean-motion resonance. The 5:3 resonance is slightly populated in the $0.1 M_{\odot}$ case, but not in the $1.0 M_{\odot}$ case (less than 1%). From theory, we know that second order resonances are less frequently produced in non-eccentric systems and need a more exciting history than low-eccentricity type I migration into resonant chains (see e.g. Coleman et al. 2019). It is also noteworthy that the TRAPPIST-1 system planets d and c are close to such a second order resonance. They are close to 5:3 mean-motion resonance, which is rare in the simulations (3.8% of the pairs for planet pairs with masses larger than $0.1 M_{\oplus}$ and semi-major axes smaller than 0.1 au).

Figure 12 additionally shows the observed *Kepler* multi-planetary systems period ratio for reference. We note that the simple cut in masses at $0.1 M_{\oplus}$ and periods at 300 days which we apply for the synthetic systems is not well suited to compare the period ratios to the observed systems. Many planetary pairs that are more quite distant from the star are included in the synthetic data. Applying a realistic bias from *Kepler* will be addressed in a future study (Mishra et al., in prep).

The last dynamical property we discuss in this work is the eccentricity. Similar to the discussion above, we can also attribute a large part of a decreasing eccentricity trend with stellar mass in the nominal population to the initial conditions. Indeed, Fig. 13 shows the nominal 0.1 and $1.0 M_{\odot}$ populations with 50 embryos each (NGM10, NG75), but additionally the population with 100 embryos (NG76). It is apparent that increasing the number of embryos increases the eccentricity, which is due to an initially closer setting. Reducing the stellar mass, while keeping the number of embryos fixed and at the same mass had a similar effect. Comparing NG76 and NGM10 again, only very small differences in eccentricities can be found, with a few highly eccentric

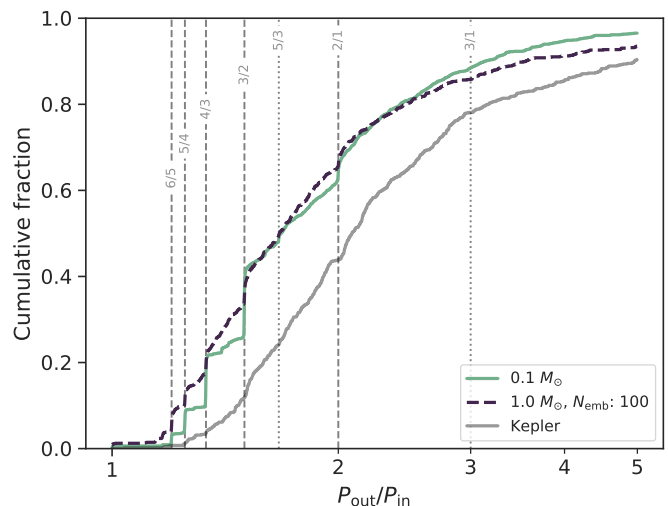


Fig. 12. Orbital period ratio of all neighboring planets including planets with $M > 0.1 M_{\odot}$ and periods $P < 300$ days. Two synthetic populations of planets are shown: one around a solar-type star with initially 100 embryos (NG76) and one around stars with a mass of $0.1 M_{\odot}$ (NGM10). The *Kepler* multi-planetary system period ratios are displayed for reference (NASA Exoplanet Archive, accessed 9.12.2019).

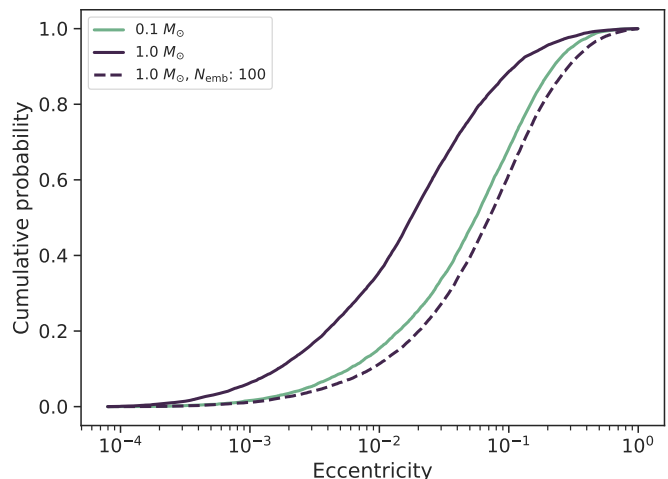


Fig. 13. Cumulative distribution function of the planetary eccentricities for synthetic populations NGM10 ($0.1 M_{\odot}$, 50 embryos, blue), NG75 ($1.0 M_{\odot}$, 50 embryos, brown solid) and NG76 ($1.0 M_{\odot}$, 100 embryos, brown dashed). Only planets with masses above $0.1 M_{\oplus}$ are included.

planets around solar mass stars that are not present in NGM10. This can be attributed to the systems with giant planets, where the orbits of the smaller planets in the same system can get very eccentric.

4.6. Solid mass reservoirs

Planetesimal accretion is a process regulated by the eccentricities and inclinations of the planetesimals in the proximity of the growing protoplanet (Ida & Makino 1992a,b; Inaba et al. 2001; Fortier et al. 2013). For larger eccentricities and inclinations, lower accretion rates result and if the planet becomes massive enough, we find that it can even eject a significant amount of planetesimals completely from the system. The region for which one protoplanet perturbs the planetesimal disk expands to a few

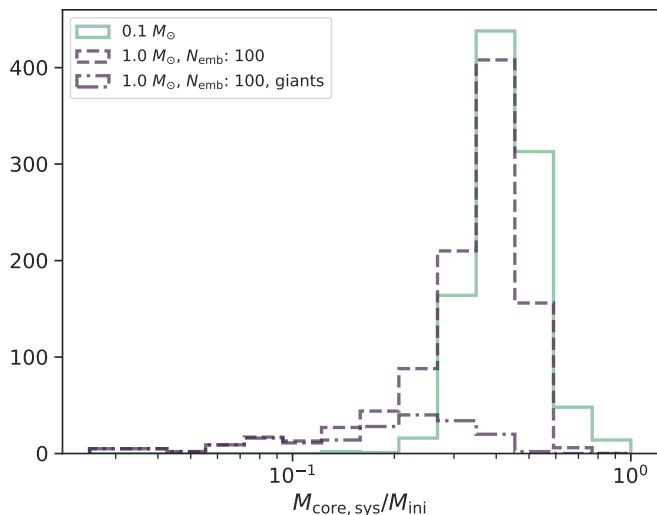


Fig. 14. Fraction of final solid mass content in planets in a system divided by the initial solid mass in the planetesimal disk. The blue line corresponds to the population around a $0.1 M_{\odot}$ star with 50 embryos (NGM10) and the brown line to the population around a $1.0 M_{\odot}$ star with 100 initial embryos (NG76). The dotted histogram shows the same quantity for the systems with at least one existing giant planet ($M > 100 M_{\oplus}$) in NG76.

tens of Hill radii. Therefore, indirect growth reduction for the less massive embryos in this region occurs. This is in line with the findings of [Alibert et al. \(2013\)](#). A technical difference is that in our model, the planetesimal surface density inside the shared feeding zone is not set to its mean value but only to the mean value over the part of the feeding zone attributed to one growing embryo (see Paper I). This is different from the treatment in [Alibert et al. \(2013\)](#), where the former mean over the whole merged feeding zone was used. For the models presented here, this leads to less transport to the inner regions where planetesimals can get more easily ejected. Nevertheless, the results are similar.

For an individual embryo, growth by solid accretion to masses above the classical isolation mass ([Lissauer & Stewart 1993](#)) is commonly possible due to migration to non-depleted regions. In addition to the competition for and excitation of planetesimals, this makes an analytic treatment of solid accretion even more difficult. Therefore, we take a look at the ratio of solids ending up in the cores of planets in a system to the solids initially inserted into its planetesimal disk (Fig. 14). We term this the efficiency of solid accretion.

In Fig. 14, a tail towards very low efficiencies is found in the population around a $1.0 M_{\odot}$ star, which can be attributed to systems with at least one giant planet (dash-dotted line). The overall bulk of the distribution without giant planets peaks at a similar location in the two populations. The reason for the lower apparent efficiency for the systems with a giant planet is mainly ejection of planetary embryos, where for NG76 in 219 systems ejection of planets occurred, with a mean ejected solid mass of $46.7 M_{\oplus}$ per system with ejection. In contrast to that, in NGM10 ejection of planets occurred in only 38 systems with a mean ejected solid mass of $0.27 M_{\oplus}$.

From these results, we can qualitatively conclude that free floating planets originate predominantly from systems around stars of higher mass, or at least systems with massive disks. The dependency is not linear due to gas accretion: Systems with giant planets that underwent rapid gas accretion eject much more

planetary mass to interstellar space than systems where no significant gas accretion occurred. Additionally, we find the bulk of the ejected mass to be in the form of embryos and not in the form of ejected planetesimals. This finding is again a function of the initial number of embryos and should be addressed in detail in future works.

4.7. The case of TRAPPIST-1

The population of synthetic planets around an $0.1 M_{\odot}$ star (NGM10) provides a dataset well suited for comparison to the TRAPPIST-1 system ([Gillon et al. 2016, 2017](#)). TRAPPIST-1 is an ultracool dwarf star with an estimated mass of $(0.089 \pm 0.006) M_{\odot}$ ([Grootel et al. 2018](#)). The system is unique due to the high number of detected transiting planets and their mass constraints ([Grimm et al. 2018](#)). Thus, TRAPPIST-1 provides a unique opportunity to benchmark planet formation models against (see also [Ormel et al. 2017](#); [Alibert & Benz 2017](#); [Coleman et al. 2019](#); [Schoonenberg et al. 2019](#); [Miguel et al. 2020](#)).

4.7.1. Statistics of synthetic planets inside 0.1 au

The TTV fits for the TRAPPIST-1 system exclude additional planets with significant mass for at least the region within 0.1 au ([Grimm et al. 2018](#)). Therefore, it makes sense to take a look at the properties of the synthetic planets with masses above $0.1 M_{\oplus}$ within 0.1 au in the synthetic $0.1 M_{\odot}$ population NGM10 and compare them with what we know for the TRAPPIST-1 planets.

In our model results, typically only few planets grow to $0.1 M_{\oplus}$ masses. The most common number of planets in the TRAPPIST-1 region ($M > 0.1 M_{\oplus}$, $a < 0.1$ au) is 1, which occurs in 330 systems. In 182 systems, not a single planet is in the TRAPPIST-1 region and only 20% of the systems do have more than 3 planets there. This low number is mainly due to little growth in many systems and further reduced by evolutionary paths that led to a single massive close-in planet that accreted all the other embryos. This second scenario is common in disks with a lot of initial solid mass and supported by fast type I migration. If the migration speed was reduced, for example by a lower viscous α , there would be less systems where the growing embryos are forced by strong disk torques into each others proximity, which then leads to less close encounters and collisions.

In terms of the composition of planets in the TRAPPIST-1 region, they are mostly rocky. Figure 7 highlights a trend towards higher ice mass fractions for larger masses due to increased migration speeds. The statistics of ice mass fractions of planets in the TRAPPIST-1 zone are shown in Fig. 15. Currently, the TRAPPIST-1 planets are considered to be quite rocky ([Dorn et al. 2018](#); [Grimm et al. 2018](#)), even though the estimated masses might change due to the challenging multi-dimensional TTV fits that have to be calculated.

We find a large rocky population of planets making up about 90% of the planets and a smaller, more massive, water-bearing population. This is due to a large amount of accretion inside the water ice line, similar to [Schoonenberg et al. \(2019\)](#) but in contrast to the findings of [Alibert & Benz \(2017\)](#), [Miguel et al. \(2020\)](#) and [Coleman et al. \(2019\)](#) who found mostly water-rich planets. [Coleman et al. \(2019\)](#) assumed an insignificant amount of rocky planetesimals initially, while [Miguel et al. \(2020\)](#) get snowlines much closer to the star which is due to the different disk temperature calculations. To estimate disk temperatures, [Miguel et al. \(2020\)](#) use gas accretion rates \dot{M}_{acc} on the or-

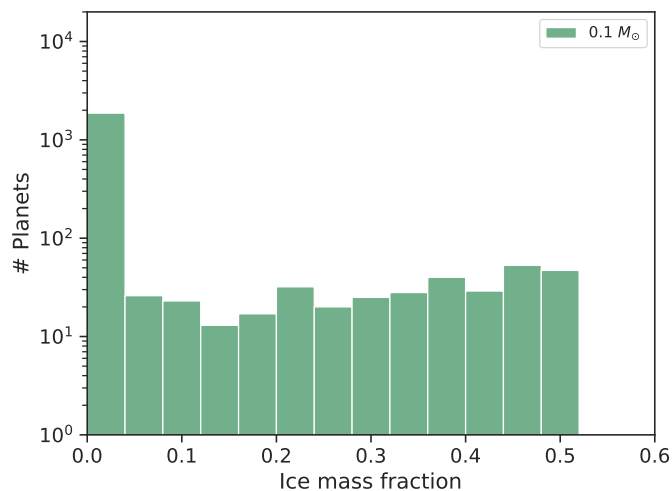


Fig. 15. Histogram of the ice mass fractions of the 2222 synthetic planets in the TRAPPIST-1 region ($M > 0.1 M_{\oplus}$, $a < 0.1$ au). The shown population of synthetic planets is calculated around a $0.1 M_{\odot}$ star with 50 embryos (NGM10). Most planets are purely rocky, but a significant part shows intermediate and large ice fractions.

der of $10^{-10} M_{\odot}/\text{yr}$ which corresponds to a later, cooler stage in the disk evolution compared to our assumed planetesimal formation at the beginning of our simulations (where $\dot{M}_{\text{acc}} \approx 2 \times 10^{-9} M_{\odot}/\text{yr}$). Additionally, the disks presented here are assumed to be twice as turbulent ($\alpha = 2 \times 10^{-3}$) compared to the disks in Miguel et al. (2020) ($\alpha = 1 \times 10^{-3}$) leading to hotter disks. For these two reasons, Miguel et al. (2020) start their simulation with much less rocky planetesimals compared to our simulations.

Most similar to our model is the work of Alibert & Benz (2017). Our results differ from theirs for three different reasons: (1) Alibert & Benz (2017) found that for more massive disks, more rocky planets appear, and they scale the disk mass to the power of 1.3 with the stellar mass. Their "heavy" disk case corresponds to our nominal case and already produces $\sim 20\%$ rocky planets. (2) We run simulations with 50 embryos, compared to Alibert & Benz (2017) who run simulations with 10 embryos. More embryos lead to more potential accretion close to the star, since the sum of all feeding zone increases, which is limiting growth in the inner region. (3) The slope of the planetesimal surface density differs in the two simulations. Whereas we use a slope of -1.5, Alibert & Benz (2017) used a shallower slope of -0.9. Therefore, by construction, more rocky material is available in our new set of simulations. This third point is an additional relevant difference to the work of Miguel et al. (2020). Current planetesimal formation models favor steeper slopes, but potentially less planetesimal formation within the water ice line (Drażkowska & Alibert 2017; Lenz et al. 2019).

As of now, no clear conclusion should be drawn concerning the validity of the pathway of rocky planet formation by almost in-situ accretion which was dominant in our work. Due to the moving water iceline, the resulting planetary composition is a strong function of the location and timing of planetesimal formation. This will be addressed in a future paper (Völkel et al, in prep). For now, we show that if enough planetesimals are assumed to have formed within the water iceline, rocky planets will form directly. Otherwise, to reproduce the observed population of rocky planets, the planetesimals or the planets have to desiccate by some additional process (e.g. due to radioactive

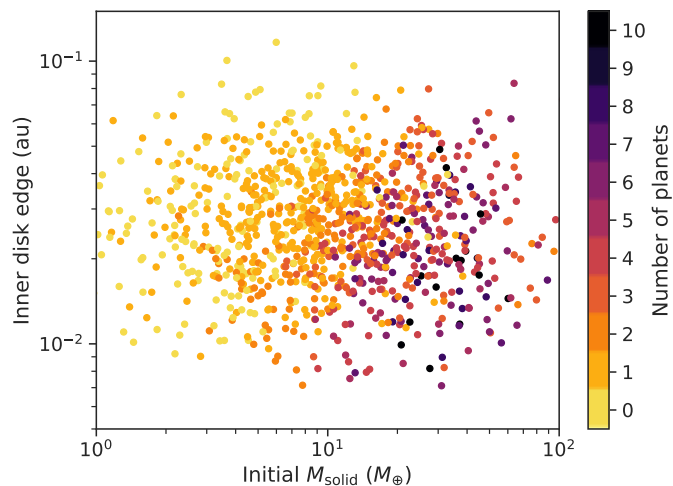


Fig. 16. Disk initial conditions color-coded by multiplicity. We plot only planets in the TRAPPIST-1 region, i.e. with semi-major axis less than 0.1 au and mass larger than $0.1 M_{\oplus}$.

heating of planetesimals Lichtenberg et al. 2018 or by ablation of pebbles in the planetary envelopes Coleman et al. 2019).

4.7.2. Initial condition regime

To compare the simulated systems with TRAPPIST-1, we chose to take the number N_p and the difference to TRAPPIST-1 in total mass ΔM_{total} (where M_{total} of TRAPPIST-1 is $5.655 M_{\oplus}$, Grimm et al. 2018). For both, we only take planets with masses $M > 0.1 M_{\oplus}$ and semi-major axes $a < 0.1$ au into account. This simple approach is a first exploration of the similarity of TRAPPIST-1 and the synthetic data in terms of the most fundamental parameters. A more complex similarity criterion of systems will be applied in future works following Alibert (2019). The colors of Figs. 16 and 17 display N_p and ΔM_{total} , where one point corresponds to a synthetic system. It is interesting to show them as a function of the initial solid mass and the inner disk edge to determine the most likely initial parameters of the disk from which the TRAPPIST-1 planets formed. For both, N_p and ΔM_{total} , there is a clear correlation with the initial solid mass, whereas only for the number of planets there seems to be a correlation with the inner disk edge.

For ΔM_{total} , this can be explained by the mass transport via type I migration. The migration rates and thus the solid mass flux to the inner region is independent of the inner disk edge. Thus, a similar fraction of the total solid mass in the disk is transported inside 0.1 au in all disks. The initial mass in planetesimals inside 0.1 au only varies negligibly with the inner edge.

However, this mass can be distributed very differently to the planets. In a number of disks at the high-end tail of the solid masses ($M_{\text{solid}} > 60 M_{\oplus}$), there are only one to four oligarchs that grew by accreting the rest of the embryos. Due to the higher initial solid mass, larger planets form which correspondingly have bigger Hill spheres and interact more often gravitationally with the other embryos. Consequently, they can be ejected or accreted by other planets, where both outcomes lead to a smaller number of planets in a given zone. Therefore, Fig. 16 shows a peak in N_p inside the TRAPPIST-1 zone which is located at moderate, but above average disk solid masses ($10 M_{\oplus} < M_{\text{solid}} < 60 M_{\oplus}$). At lower than average disk solid masses, the number of planets decreases. This is due to planets not growing to masses above

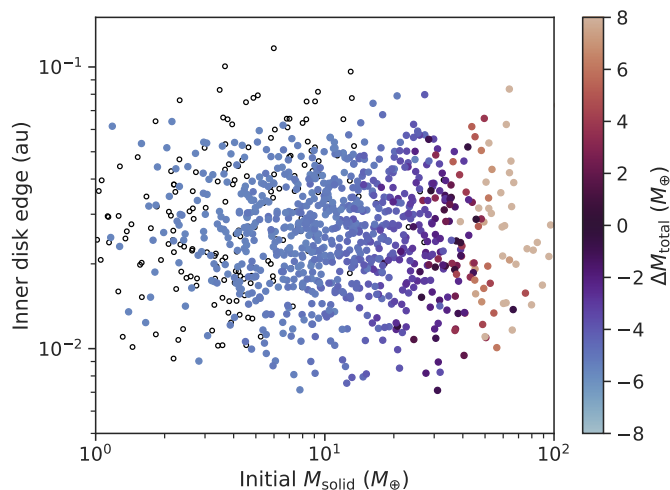


Fig. 17. Disk initial conditions color-coded by difference of total mass to the TRAPPIST-1 system. Individual planet masses are only included if their semi-major axis is less than 0.1 au and their mass is larger than $0.1 M_{\oplus}$. Systems with no planets that lie in this regime are drawn as empty black circles. The darkest points show systems most TRAPPIST-1 similar at around $30 M_{\oplus}$ of initial solid mass.

$0.1 M_{\oplus}$. Thus, they are not identified to lie in the TRAPPIST-1 zone and additionally, very little transport of solid material due to type I migration takes place.

Overall, a sweet-spot to form a system with a similar amount of planetary mass at comparable semi-major axes as TRAPPIST-1 can be located at $30 M_{\oplus} \lesssim M_{\text{solid}} \lesssim 50 M_{\oplus}$, which coincides with the region where seven planets inside 0.1 au are frequently present given an inner disk edge below at least 0.06 au.

5. Summary and conclusions

In this part of the New Generation Planetary Population Synthesis (NGPPS) series, we employ the Generation III Bern model of planet formation and evolution introduced in Paper I to explore the influence of the stellar mass. Populations of synthetic planets are calculated for a grid of stellar masses (0.1, 0.3, 0.5, 0.7 and $1.0 M_{\odot}$) with an initial number of 50 embryos. While we linearly scale the gas and solid disk mass with stellar mass, we assume physical disk boundaries constant in orbital period and keep the disk lifetime fixed.

This yields a dataset for which we find:

- a larger number of giant planets with larger stellar mass. In particular, no giant planets formed for $M_{\star} < 0.5 M_{\odot}$.
- the most frequent temperate planet host to be M dwarfs with masses of $0.5 M_{\odot}$
- that the planetary mass function does not shift strictly linear with the stellar mass despite the linear scaling of the gas and solid disk mass. This is due to more ejected planets for higher stellar masses because of the growth of giant planets.
- as consequences of the previous point a reduced apparent efficiency of solid accretion towards higher stellar mass and most of ejected, free-floating planets originate from stars with masses of at least a solar mass.
- a strong dependency of the dynamical properties such as period ratios and eccentricities on the initial proximity of the embryos measured in mutual Hill radii (initial spacing)

- a high occurrence of mean-motion resonances due to migration, which is in contrast to the few observed resonant multi-planetary systems. For a similar initial spacing, $\sim 10\%$ more pairs are in resonance around ultra-late M-dwarfs compared to solar-like stars.
- a sweet spot in terms of initial solid mass content (30 to $50 M_{\oplus}$) and inner disk edge (closer than 0.06 au) to get a system like TRAPPIST-1 measured by the observable mass
- a large amount of rocky compositions for planets in the innermost 0.1 au of low-mass stars due to a lot of rocky planetesimal accretion. This is unsurprisingly a strong function of how many planetesimals and embryos were initially placed closer to the star than the water iceline.
- a pathway for the core-accretion formation of giants around very low-mass stars – such as GJ 3512b. For that, it is sufficient to reduce type I migration. Even more giants can form if planetesimals are initially more concentrated.

Acknowledgements. Parts of this work has been carried out within the frame of the National Centre for Competence in Research PlanetS funded by the Swiss National Science Foundation (SNSF). R.B. and Y.A. acknowledge the financial support from the SNSF under grant 200020_172746. This work was supported by the DFG Research Unit FOR2544 “Blue Planets around Red Stars”, project no. RE 2694/4-1. A.E. acknowledges the support from The University of Arizona. A.E. and C.M. acknowledge the support from the SNSF under grant BSSG10_155816 “PlanetsInTime”. This research has made use of the NASA Exoplanet Archive, which is operated by the California Institute of Technology, under contract with the National Aeronautics and Space Administration under the Exoplanet Exploration Program. The plots shown in this work were generated using *matplotlib* (Hunter 2007) and *seaborn* (<https://seaborn.pydata.org/index.html>).

References

- Adachi, I., Hayashi, C., & Nakazawa, K. 1976, *Progress of Theoretical Physics*, 56, 1756
- Adams, F. C., Hollenbach, D., Laughlin, G., & Gorti, U. 2004, *ApJ*, 611, 360
- Affer, L., Micela, G., Favata, F., Flaccomio, E., & Bouvier, J. 2013, *MNRAS*, 430, 1433
- Agol, E., Carey, S., Delrez, L., et al. 2019, in *Spitzer Proposal*, 14223
- Alcalá, J. M., Manara, C. F., Natta, A., et al. 2017, *A&A*, 600, A20
- Alibert, Y. 2019, *A&A*, 624, A45
- Alibert, Y. & Benz, W. 2017, *A&A*, 598, L5
- Alibert, Y., Carron, F., Fortier, A., et al. 2013, *A&A*, 558, A109
- Alibert, Y., Mordasini, C., & Benz, W. 2004a, *A&A*, 417, L25
- Alibert, Y., Mordasini, C., & Benz, W. 2011, *A&A*, 526, A63
- Alibert, Y., Mordasini, C., Benz, W., & Winisdoerffer, C. 2004b, *A&A*, 434, 343
- Andrews, S. M., Terrell, M., Tripathi, A., et al. 2018, *ApJ*, 865, 157
- Andrews, S. M., Wilner, D. J., Hughes, A. M., Qi, C., & Dullemond, C. P. 2010, *ApJ*, 723, 1241
- Anglada-Escudé, G., Boss, A. P., Weinberger, A. J., et al. 2012, *ApJ*, 746, 37
- Ansdell, M., Williams, J. P., Manara, C. F., et al. 2017, *The Astronomical Journal*, 153, 240
- Ansdell, M., Williams, J. P., Trapman, L., et al. 2018, *ApJ*, 859, 21
- Ansdell, M., Williams, J. P., van der Marel, N., et al. 2016, *ApJ*, 828, 46
- Baraffe, I., Homeier, D., Allard, F., & Chabrier, G. 2015, *A&A*, 577, A42
- Barenfeld, S. A., Carpenter, J. M., Ricci, L., & Isella, A. 2016, *ApJ*, 827, 142
- Benítez-Llambay, P., Masset, F., & Beaugé, C. 2011, *A&A*, 528, A2
- Benz, W., Ida, S., Alibert, Y., Lin, D. N. C., & Mordasini, C. 2014, in *Protostars Planets VI*, ed. H. Beuther, R. S. Klessen, C. P. Dullemond, & T. Henning (Tucson: University of Arizona Press), 697–713
- Bodenheimer, P. & Pollack, J. B. 1986, *Icarus*, 67, 391
- Bonfils, X., Forveille, T., Delfosse, X., et al. 2005, *A&A*, 443, L15
- Boss, A. P. 1997, *Science*, 276, 1836
- Bouchy, F., Doyon, R., Artigau, É., et al. 2017, *The Messenger*, 169, 21
- Bouvier, J., Alencar, S. H. P., Harries, T. J., Johns-Krull, C. M., & Romanova, M. M. 2007, in *Protostars Planets V*, ed. B. Reipurth, D. Jewitt, & K. Keil (Tucson: University of Arizona Press), 479–494
- Burdanov, A., Delrez, L., Gillon, M., & Jehin, E. 2018, in *Handbook of Exoplanets*, ed. H. J. Deeg & J. A. Belmonte (Cham: Springer International Publishing), 1–17
- Butler, R. P., Johnson, J. A., Marcy, G. W., et al. 2006, *Publications of the Astronomical Society of the Pacific*, 118, 1685

- Cameron, A. G. 1978, *Moon Planets*, 18, 5
- Chambers, J., Wetherill, G., & Boss, A. 1996, *Icarus*, 119, 261
- Chambers, J. E. 1999, *MNRAS*, 304, 793
- Chambers, J. E. 2006, *Icarus*, 180, 496
- Choi, J., Dotter, A., Conroy, C., et al. 2016, *ApJ*, 823, 102
- Clarke, C. J., Gendrin, A., & Sotomayor, M. 2001, *MNRAS*, 328, 485
- Coleman, G. A. L., Leleu, A., Alibert, Y., & Benz, W. 2019, *A&A*, 631, A7
- Coleman, G. A. L. & Nelson, R. P. 2014, *MNRAS*, 445, 479
- Crida, A., Morbidelli, A., & Masset, F. 2006, *Icarus*, 181, 587
- Delfosse, X., Forveille, T., Mayor, M., et al. 1998, *A&A*, 338, L67
- Dittkrist, K.-M. K.-M., Mordasini, C., Klahr, H., Alibert, Y., & Henning, T. 2014, *A&A*, 567, A121
- Dorn, C., Mosegaard, K., Grimm, S. L., & Alibert, Y. 2018, *ApJ*, 865, 20
- Drążkowska, J. & Alibert, Y. 2017, *A&A*, 608, A92
- Drążkowska, J., Alibert, Y., & Moore, B. 2016, *A&A*, 594, A105
- Dressing, C. D. & Charbonneau, D. 2013, *ApJ*, 767, 95
- Dressing, C. D. & Charbonneau, D. 2015, *ApJ*, 807, 45
- Endl, M., Cochran, W. D., Kuerster, M., et al. 2006, *ApJ*, 649, 436
- Fedele, D., van den Ancker, M. E., Henning, T., Jayawardhana, R., & Oliveira, J. M. 2010, *A&A*, 510, A72
- Feiden, G. A. 2016, *A&A*, 593, A99
- Fortier, A., Alibert, Y., Carron, F., Benz, W., & Dittkrist, K.-M. 2013, *A&A*, 549, A44
- Fulton, B. J. & Petigura, E. A. 2018, *The Astronomical Journal*, 156, 264
- Gaidos, E., Fischer, D. A., Mann, A. W., & Howard, A. W. 2013, *ApJ*, 771, 18
- Gaidos, E., Mann, A. W., Kraus, A. L., & Ireland, M. 2016, *MNRAS*, 457, 2877
- Gibbs, A., Bixel, A., Rackham, B. V., et al. 2020, *AJ*, 159, 169
- Gillon, M., Jehin, E., Lederer, S. M., et al. 2016, *Nature*, 533, 221
- Gillon, M., Triaud, A. H. M. J., Demory, B.-O., et al. 2017, *Nature*, 542, 456
- Grimm, S. L., Demory, B.-O., Gillon, M., et al. 2018, *A&A*, 613, A68
- Grootel, V. V., Fernandes, C. S., Gillon, M., et al. 2018, *ApJ*, 853, 30
- Günther, H. 2013, *Astronomische Nachrichten*, 334, 67
- Haisch, Jr., K. E., Lada, E. A., & Lada, C. J. 2001, *ApJ*, 553, L153
- Hansen, B. M. S. 2008, *The Astrophysical Journal Supplement Series*, 179, 484
- Hansen, B. M. S. 2015, *International Journal of Astrobiology*, 14, 267
- Henderson, C. B. & Stassun, K. G. 2011, *ApJ*, 747, 51
- Herbst, W., Bailer-Jones, C. A. L., Mundt, R., Meisenheimer, K., & Wackermann, R. 2002, *A&A*, 396, 513
- Howard, A. W., Johnson, J. A., Marcy, G. W., et al. 2010, *ApJ*, 721, 1467
- Hueso, R. & Guillot, T. 2005, *A&A*, 442, 703
- Hunter, J. D. 2007, *Computing in Science & Engineering*, 9, 90
- Ida, S. & Lin, D. N. C. 2004a, *ApJ*, 604, 388
- Ida, S. & Lin, D. N. C. 2004b, *ApJ*, 616, 567
- Ida, S. & Lin, D. N. C. 2005, *ApJ*, 626, 1045
- Ida, S. & Makino, J. 1992a, *Icarus*, 96, 107
- Ida, S. & Makino, J. 1992b, *Icarus*, 98, 28
- Inaba, S., Tanaka, H., Nakazawa, K., Wetherill, G. W., & Kokubo, E. 2001, *Icarus*, 149, 235
- Irwin, J., Hodgkin, S., Aigrain, S., et al. 2008, *MNRAS*, 384, 675
- Irwin, J., Hodgkin, S., Aigrain, S., et al. 2007, *MNRAS*, 383, 1588
- Jin, S., Mordasini, C., Parmentier, V., et al. 2014, *ApJ*, 795, 65
- Johnson, J. A., Aller, K. M., Howard, A. W., & Crepp, J. R. 2010, *Publications of the Astronomical Society of the Pacific*, 122, 905
- Johnson, J. A., Butler, R. P., Marcy, G. W., et al. 2007, *ApJ*, 670, 833
- Kaltenegger, L. 2017, *Annual Review of Astronomy and Astrophysics*, 55, 433
- Kasting, J. F., Whitmire, D. P., & Reynolds, R. T. 1993, *Icarus*, 101, 108
- Kimura, S. S., Kunitomo, M., & Takahashi, S. Z. 2016, *MNRAS*, 461, 2257
- Kokubo, E. & Ida, S. 1998, *Icarus*, 131, 171
- Kopparapu, R. K., Ramirez, R., Kasting, J. F., et al. 2013a, *ApJ*, 770, 82
- Kopparapu, R. K., Ramirez, R., Kasting, J. F., et al. 2013b, *ApJ*, 765, 131
- Kopparapu, R. K., Ramirez, R. M., SchottelKotte, J., et al. 2014, *ApJ*, 787, L29
- Lamm, M. H., Mundt, R., Bailer-Jones, C. A. L., & Herbst, W. 2005, *A&A*, 430, 1005
- Laughlin, G., Bodenheimer, P., & Adams, F. C. 2004, *ApJ*, 612, L73
- Lenz, C. T., Klahr, H., & Birnstiel, T. 2019, *ApJ*, 874, 36
- Lichtenberg, T., Golabek, G. J., Burn, R., et al. 2018, *Nat. Astron.*
- Lissauer, J. J. & Stewart, G. R. 1993, in *Protostars planets III*, ed. E. H. Levy & J. I. Lunine (University of Arizona Press), 1061–1088
- Liu, B., Lambrechts, M., Johansen, A., & Liu, F. 2019, *ArXiv e-prints [arXiv:1909.00759]*
- Lodders, K. 2003, *ApJ*, 591, 1220
- Lopez, E. D. & Fortney, J. J. 2013, *ApJ*, 776, 2
- Machida, M. N., Inutsuka, S.-i., & Matsumoto, T. 2010, *ApJ*, 724, 1006
- Mamajek, E. E., Usuda, T., Tamura, M., & Ishii, M. 2009, in *AIP Conference Proceedings*, Vol. 1158 (AIP), 3–10
- Marboeuf, U., Thiabaud, A., Alibert, Y., Cabral, N., & Benz, W. 2014, *A&A*, 570, A36
- Marcy, G. W., Butler, R. P., Fischer, D., et al. 2001, *ApJ*, 556, 296
- Marcy, G. W., Butler, R. P., Vogt, S. S., Fischer, D., & Lissauer, J. J. 1998, *ApJ*, 505, L147
- Matsuyama, I., Johnstone, D., & Hartmann, L. 2003, *ApJ*, 582, 893
- Miguel, Y., Cridland, A., Ormel, C., Fortney, J., & Ida, S. 2020, *MNRAS*, 491, 1998
- Millholland, S., Laughlin, G., Teske, J., et al. 2018, *The Astronomical Journal*, 155, 106
- Mizuno, H. 1980, *Progress of Theoretical Physics*, 64, 544
- Mizuno, H., Nakazawa, K., & Hayashi, C. 1978, *Progress of Theoretical Physics*, 60, 699
- Montet, B. T., Crepp, J. R., Johnson, J. A., Howard, A. W., & Marcy, G. W. 2014, *ApJ*, 781, 28
- Morales, J. C., Mustill, A. J., Ribas, I., et al. 2019, *Science*, 365, 1441
- Mordasini, C. 2014, *A&A*, 572, A118
- Mordasini, C. 2018, in *Handbook of Exoplanets* (Springer International Publishing), 143
- Mordasini, C., Alibert, Y., & Benz, W. 2009a, *A&A*, 501, 1139
- Mordasini, C., Alibert, Y., Benz, W., & Naef, D. 2009b, *A&A*, 501, 1161
- Mordasini, C., Alibert, Y., Georgy, C., et al. 2012a, *A&A*, 547, A112
- Mordasini, C., Alibert, Y., Klahr, H., & Henning, T. 2012b, *A&A*, 547, A111
- Mordasini, C., Klahr, H., Alibert, Y., Benz, W., & Dittkrist, K.-M. 2010, in *Circumstellar disks and planets*, Kiel
- Mordasini, C., Mollière, P., Dittkrist, K.-M. K.-M., Jin, S., & Alibert, Y. 2015, *International Journal of Astrobiology*, 14, 201
- Mulders, G. D., Mordasini, C., Pascucci, I., et al. 2019, *ApJ*, 887, 157
- Mulders, G. D., Pascucci, I., & Apai, D. 2015, *ApJ*, 814, 130
- Nakamoto, T. & Nakagawa, Y. 1994, *ApJ*, 421, 640
- Nutzman, P. & Charbonneau, D. 2008, *Publications of the Astronomical Society of the Pacific*, 120, 317
- Ogilvie, G. I. 2014, *Annual Review of Astronomy and Astrophysics*, 52, 171
- Ormel, C. W., Liu, B., & Schoonenberg, D. 2017, *A&A*, 604, A1
- Owen, J. E. & Wu, Y. 2013, *ApJ*, 775, 105
- Paardekooper, S.-J., Baruteau, C., & Kley, W. 2011, *MNRAS*, 410, 293
- Pascucci, I., Mulders, G. D., Gould, A., & Fernandes, R. 2018, *ApJ*, 856, L28
- Pascucci, I., Testi, L., Herczeg, G. J., et al. 2016, *ApJ*, 831, 125
- Petigura, E. A., Livingston, J., Batygin, K., et al. 2019, *The Astronomical Journal*, 159, 2
- Pinilla, P., Natta, A., Manara, C. F., et al. 2018, *A&A*, 615, A95
- Pollack, J. B., Hubickyj, O., Bodenheimer, P. H., et al. 1996, *Icarus*, 124, 62
- Pringle, J. E. 1981, *Annual Review of Astronomy and Astrophysics*, 19
- Quirrenbach, A., Amado, P. J., Caballero, J. A., et al. 2014, in *Ground-based Airborne Instrumentation Astronomy V*, ed. S. K. Ramsay, I. S. McLean, & H. Takami, Vol. 9147 (Bellingham: SPIE), 91471F
- Rafikov, R. R. 2003, *The Astronomical Journal*, 125, 942
- Rafikov, R. R. 2004, *The Astronomical Journal*, 128, 1348
- Raymond, S. N., Scalo, J., & Meadows, V. S. 2007, *ApJ*, 669, 606
- Ribas, Á., Merín, B., Bouy, H., & Maud, L. T. 2014, *A&A*, 561, A54
- Richert, A. J. W., Getman, K. V., Feigelson, E. D., et al. 2018, *MNRAS*, 477, 5191
- Ricker, G. R., Winn, J. N., Vanderspek, R., et al. 2014, *Journal of Astronomical Telescopes, Instruments, and Systems*, 1, 014003
- Rivera, E. J., Laughlin, G., Butler, R. P., et al. 2010, *ApJ*, 719, 890
- Rivera, E. J., Lissauer, J. J., Butler, R. P., et al. 2005, *ApJ*, 634, 625
- Sanchis, E., Testi, L., Natta, A., et al. 2020, *A&A*, 633, A114
- Santos, N. C., Israelian, G., Mayor, M., Rebolo, R., & Udry, S. 2003, *A&A*, 398, 363
- Schlaufman, K. C., Lin, D. N., & Ida, S. 2010, *ApJL*, 724, L53
- Schoonenberg, D., Liu, B., Ormel, C. W., & Dorn, C. 2019, *A&A*, 627, A149
- Schoonenberg, D. & Ormel, C. W. 2017, *A&A*, 602, A21
- Scott, D. W. 1992, *Multivariate Density Estimation: Theory, Practice, and Visualization*, Wiley Series in Probability and Statistics (New York: John Wiley & Sons, Inc.), 317
- Shakura, N. I. & Sunyaev, R. A. 1973, *A&A*, 24, 337
- Siess, L., Dufour, E., & Forestini, M. 2000, *A&A*, 358, 593
- Stassun, K. G., Collins, K. A., & Gaudi, B. S. 2016, *The Astronomical Journal*, 153, 136
- Strom, K. M., Strom, S. E., Edwards, S., Cabrit, S., & Skrutskie, M. F. 1989, *The Astronomical Journal*, 97, 1451
- Tasker, E., Tan, J., Heng, K., et al. 2017, *Nature Astronomy*, 1, 0042
- Testi, L., Natta, A., Scholz, A., et al. 2016, *A&A*, 593, A111
- Thiabaud, A., Marboeuf, U., Alibert, Y., et al. 2014, *A&A*, 562, A27
- Turbet, M., Bolmont, E., Ehrenreich, D., et al. 2019, *ArXiv e-prints [arXiv:1911.08878]*
- Tychoniec, L., Tobin, J. J., Karska, A., et al. 2018, *The Astrophysical Journal Supplement Series*, 238, 19
- Udry, S., Bonfils, X., Delfosse, X., et al. 2007, *A&A*, 469, L43
- Venuti, L., Bouvier, J., Cody, A. M., et al. 2017, *A&A*, 599, A23
- Veras, D. & Armitage, P. J. 2004, *MNRAS*, 347, 613
- von Braun, K., Boyajian, T. S., van Belle, G. T., et al. 2013, *MNRAS*, 438, 2413
- Wheatley, P. J., West, R. G., Goad, M. R., et al. 2018, *MNRAS*, 475, 4476
- Williams, J. P., Cieza, L., Hales, A., et al. 2019, *ApJ*, 875, L9
- Winters, J. G., Henry, T. J., Lurie, J. C., et al. 2014, *The Astronomical Journal*, 149, 5

Appendix A: Giant planet formation around low-mass stars

While explanations through different formation scenarios are possible, the discovery of the giant planet GJ 3512b around a very low-mass star (Morales et al. 2019) motivates the variation of free parameters in order to push the efficiency of core-accretion planet formation around low-mass stars. A stellar mass of $0.1 M_{\odot}$ was chosen to model conditions similar to GJ 3512b ($M_{\star} = (0.123 \pm 0.009) M_{\odot}$).

One trivial pathway to form larger planets would be to increase the disk masses. However, this can not be considered a free parameter since observational data is available. We use the disk masses derived for the young class I objects from Tychoniec et al. (2018), which are already larger than those from Williams et al. (2019). Therefore a further increase would be contradicting observations. Furthermore, we are not aware of indications for a shallower than the nominal linear scaling of the disk mass with the stellar mass.

For these reasons, we test here the influence of the placement of planetesimals and embryos and the impact of reducing the type I migration speed. Rapid type I migration is well known to be reducing the efficiency of forming giant planets (Alibert et al. 2004b; Mordasini et al. 2009b). Therefore, one can explore the impact of a reduction factor $f_I = 0.1$ for type I migration rates similar to Mordasini et al. (2009b). Parameter searches like these that address giant planet formation can be done in the single embryo mode, meaning only a single embryo is injected in a protoplanetary disk and no N-body code takes up computational time (Alibert et al. 2013, found convergent results with the number of embryos for high mass planets).

Figure A.1 shows three synthetic populations of planets where $f_I = 0.1$ for all of them. The number of simulations – thus also of synthetic planets – is 10000 for each of them. They differ by the slope β_{pls} of the initial radial planetesimal surface density profile and the placement of the planetesimals and embryos: The top panel shows the nominal slope of $\beta_{\text{pls}} = -1.5$, the central panel shows a population of planets where the planetesimals were placed with a slope of $\beta_{\text{pls}} = -2.0$ and the bottom one with $\beta_{\text{pls}} = -2.5$. In the last case, growth would mainly occur close to the star due to the mass concentration there. Therefore, the initial conditions for the population shown on the bottom panel were further fine-tuned and include an inner edge of the planetesimal disk at 0.6 au and the same inner boundary for the injection of planetary embryos. The other two simulations do not differ from the nominal simulations in terms of the inner edge of the planetesimal disk or embryo placement (i.e. log-uniform from inner edge to ~ 20 au).

Compared to the top panel of Fig. 7, where type I migration is not reduced, much more massive planets can form with reduced migration (Fig. A.1). In very rare cases, the mass of GJ 3512b can already be reached. Similarly efficient in reproducing GJ 3512b is the central panel with $\beta_{\text{pls}} = -2.0$ and quite efficient in producing giant planets is the fine-tuned population shown in the bottom panel. Giant planets form frequently in the heavier disks.

In a population where only the planetesimal slope was increased to -2.5 and the placement of planetesimals and embryos constrained to the region outside 0.6 au but the type I migration speed was not reduced, more massive planets than in the nominal case can form, but no giant planets were forming. Instead, the frequency of icy super-Earths was increased drastically.

Therefore, we conclude that even for ultra-late M dwarfs the formation of gas-rich giant planets is possible if two conditions

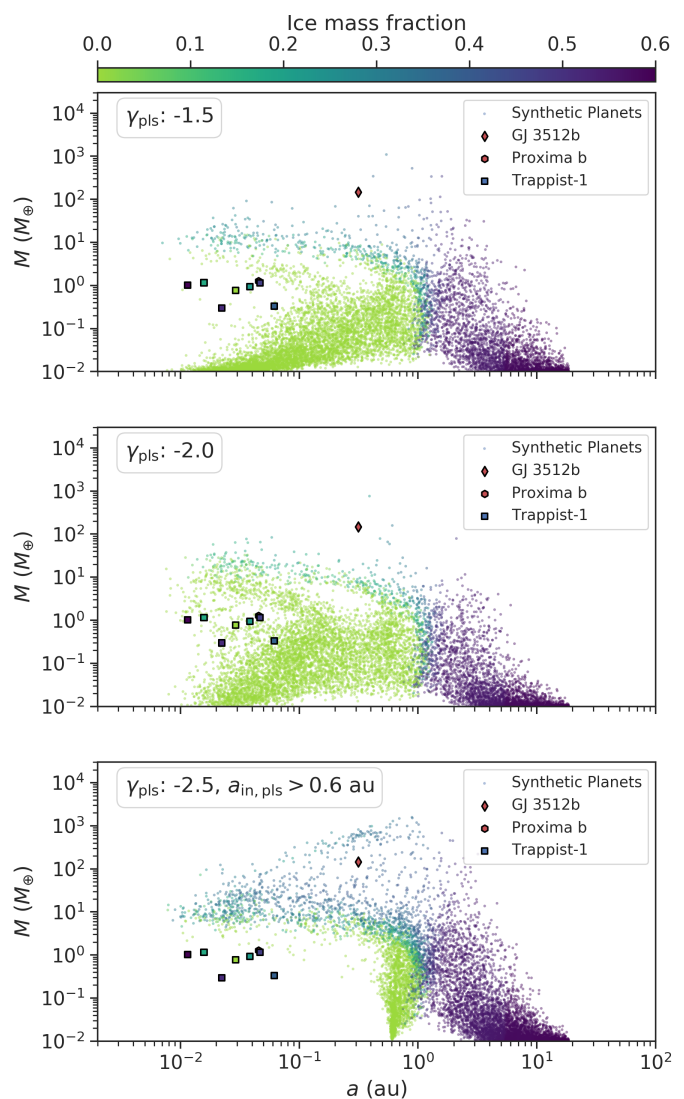


Fig. A.1. Synthetic populations of planets calculated in single-embryo mode with reduced type I migration ($f_I: 0.1$) as a function of a and M . The mass fraction of the summed-up ices is shown in color. The top panel shows the population of planets with a nominal planetesimal surface density slope β_{pls} , whereas the other two panels have steeper planetesimal surface density slopes as indicated in the top left of the panel. The bottom panel displays the population of planets, where embryos and planetesimals are only placed outside of 0.6 au.

are met: a high disk mass from the upper end of the distribution and reduced type I migration. The latter could be due to, for example, trapping in ringed disk structures.

6. Conclusion and outlook

The purpose of this work is to give a broad overview of processes related to planet formation and planetary compositions as well as put into perspective the work done over the course of the past four years. The subject of planet formation is quite interdisciplinary and the number of physical processes involved is large. Therefore, in-depth introduction to all aspects was not possible. Nevertheless, a way to model the evolution of a small body crossing the water iceline was developed in detail in [Paper I](#) and an extensive introduction to it was shown in [Chapter 2](#) and [3](#).

Bodies that drift fast enough towards the central star to cross the co-moving water iceline are of sizes ranging from centimeters to a few hundred meters. They have lost all of their initial water content and are assumed to break up a few percent within the water iceline that would result from stationary bodies. This effect is for the first time quantitatively treated in [Paper I](#) and is important for works that focus on detailed calculations of physics occurring at the water iceline or to precisely determine the composition of growing planets. This is especially true if the population of bodies in this size-range is numerous.

We found that collisions with small bodies would remove the outermost layers of fast-drifting bodies; therefore, they should not be covered by a compact, dry dust mantle as observed on comets. However, the encountered mass and energy resulting from those collisions is not considerable for the relevant timescales of a few thousand years.

Of much larger influence for the composition of all forming planets could be the loss of water from large planetesimals due to being heated by the decay of their radioactive ^{26}Al . We estimated that planetesimals of a few tens to hundred kilometer in size would efficiently dry-out and the process is quick enough to fundamentally change the composition of the formed planets around stars with realistic ^{26}Al contents. This is a possible explanation for the low water content of planets observed by *Kepler* or the terrestrial Solar System planets. If planets migrate from the outer regions of the disk towards the star, they should be born with much larger water mass fractions than observed.

Moving to planet formation in general, it is particularly important to account for all observed constraints. One such constraint from meteoritic data precisely dates the growth stages of Jupiter – given the assumption of a spatial separation of the meteoritic reservoirs. This implies that the growth of Jupiter needs to be a two-stage process: Rapid growth by pebble accretion to the pebble isolation mass followed by a stage of significant planetesimal accretion. The gravitational excitation of the planetesimal disk – if composed of hundred kilometer sized objects – is large enough to lead to fragmentation of those bodies in the vicinity of the proto-Jupiter. Therefore,

we cannot directly infer if planetesimals were born big or small, only that they should have been small when Jupiter was accreting them.

A project comparing pebble and planetesimal accretion in a statistical framework showed, that the two accretion models both show rapid growth phases at different embryo masses and orbital distances. The resulting population of planets should be distinct and planets that show a very low solid-to-gas mass ratio can only form by pebble accretion. In both cases, rapid type I migration inhibits growth to larger masses for the bulk of disks and formation locations.

The same is true for planets that grow around low-mass stars. If type I migration was reduced, it would even be possible to form giant planets like GJ 3512 b by core-accretion around very low mass M dwarfs. Under the assumption of nominal type I migration rates, the growth to giant planets is no longer possible for stellar masses below $0.5 M_{\odot}$. This finding was obtained using the newest generation of planet formation models that couple a wealth of processes of planetary growth and interactions. This update also allowed us to study lower-planetary masses because we account for gravitational interactions between the growing embryos. There we find that the properties of the planetary orbits are sensitive to the initial spacing between the embryos measured by their gravitational force (i.e. in mutual Hill radii). Furthermore, the absence of giant planets for lower stellar masses leads to less ejection of planetary embryos. This appears in the statistics as more leftover solid mass contained in planets compared to the initial disk mass.

We also tentatively addressed the important question of how probable the emergence of planets that could harbor life is around different stellar masses. Because of an assumed small reservoir of solids around very-low mass stars and due to frequent ejection of embryos in disks around massive stars, there is an optimal location for growth to Earth-sized planets in the habitable zone at $\sim 0.5 M_{\odot}$. However, the fact that the presence of giants frequently removes planets similar to our Earth implies that the Solar System with a giant planet and smaller terrestrial planets in the same system is relatively rare. It is of course interesting to already look at this topic of potentially habitable planets, but we would like to caution over-interpretation of the results that depend on many free parameters and do not yet produce a perfect match to all observational constraints.

A major benefit of having presented a number of different works and processes in a single document is to then take a large step back and take a look on the big picture. The subject of planetary sciences is developing very rapidly and thanks to the continuous investment into new facilities and missions, this observation-driven field will make substantial progress in the near- and mid-term future.

For theorists, one key aspect is to be ready and having done preparatory work for upcoming missions. For population synthesis, the microlensing results coming out of WFIRST will be the major dataset to compare to in the future. Therefore, experience needs to be gained in applying observational biases that microlensing surveys have. This can be used to make predictions for the exoplanet yield of WFIRST. A key ingredient there is that most lens-systems are quite distant from the Solar-

neighborhood. Therefore, the stellar population that is accessible by WFIRST has to be taken into account for a proper comparison.

For the current CHEOPS and TESS mission, the focus shifted from detecting exoplanets to characterizing them. Therefore, the composition of exoplanets can be constrained. With the works shown in this thesis combined with modeling of interior structures of exoplanets, the composition of exoplanets can also be explored theoretically. However, this subject has just started and is far from mature. For the Bern model, a first required step will be to couple the dust transport and growth module to the chemistry model. This requires accounting for the composition of the centimeter-sized grains. Other works have shown that the feedback of the dust onto the gas phase due to sublimation should not be neglected and we have shown here that the dynamics of drifting objects should be considered.

Another important observational facility of our time is ALMA, which gives us the opportunity to glance at planet formation as it is happening. The feedback of accreting planets on the surrounding disk needs to be explored in more detail using models to make best use of the obtained observational data. Furthermore, the statistical samples of ALMA are currently being enlarged. This can be used to constrain the distributions of initial conditions that are used for planet formation models. However, it has to be kept in mind that all observations are snapshots at a certain time and not true initial conditions. Therefore, the comparison of the time evolution of modeled disks to observations of disks and stellar accretion rates needs to be continuously updated. The latest, realistic photo-evaporation models will help to narrow down the number of free parameters in search for a unique solution. The best quantity to compare models to ALMA data is the emitted flux of radio-wavelength thermal emission, which needs to be modeled consistently instead of relying on assumptions about the temperature profile in observed disks.

We already learned a lot from ALMA, for example that disks commonly have sub-structures. Especially rings are very common. Those rings indicate varying pressure gradients in the disk which should also have an influence on the migration of planets. If planets are trapped in sub-structures, the problem of too efficient type I migration might vanish. The fundamental issue is to determine if the structures are caused by planets or if they are also present in the absence of planets. Only in the latter case, the first generation of formed planets can be stopped.

For planet formation theory, we showed that Jupiter might have formed by a hybrid pebble and planetesimal accretion process. Indeed, there is no reason that neither pebbles nor planetesimals exist in disks. For both, there are enough observations that prove their existence. In our comparison of the two models, we clearly showed that for equal initial conditions, both pathways can dominate depending on the size of the embryo and the location in the disk. Therefore, only a hybrid approach will be able to model the most important growth mode at all times and locations. With the inclusion of a planetesimal formation module out of a disk of pebbles, a large step has already been taken in this direction. The results of this model need to be analyzed carefully in the near future and realistic free parameters for different stellar masses need to be determined. After extending the model with a chemistry module

and proving its ability to match the ALMA observations, we will get to a stage of modeling planet formation with much less free parameters and more predictive power for future observations. Realistically, it will never be possible to cover the full complexity of nature; but the path towards it is nevertheless exciting.

List of Figures

1.1.	Original data for the radial velocity of 51 Peg by Mayor & Queloz (1995)	3
1.2.	Schematic representation of a transiting planet	4
1.3.	Obsevational image of the HR 8799 system	8
1.4.	Semi-major axis versus mass diagram of observed exoplanets	10
1.5.	Semi-major axis versus radius diagram of observed exoplanets	11
1.6.	Schematic view of protoplanetary disks	16
1.7.	Surface density profiles as a function of separation	18
1.8.	Fraction of stars with disks as a function of time	19
1.9.	ALMA and VLA images of the HL Tau disk	22
1.10.	Dust mass measured with ALMA in the Lupus star forming region as a function of stellar mass and age.	23
1.11.	VLT/SPHERE images of protoplanetary disks	25
2.1.	Relative abundance of elements in refractory species and ices	40
2.2.	Comparison of mass loss profiles for different photo-evaporation models	42
2.3.	Surface density profiles for a disk with nominal photo-evaporation and one with photo-evaporation based on Picogna et al. (2019)	45
2.4.	Cumulative fraction of observed X-ray luminosities (Güdel et al., 2007) and corresponding numerical fits	46
2.5.	Comparison of the evolution of disks with different α and initial profiles using the nominal photo-evaporation model.	51
2.6.	Comparison of the evolution of disks with different α and initial profiles using the Picogna et al. (2019) photo-evaporation model.	52
2.7.	Eccentricity and inclination of a population planetesimals from self- stirring	64
2.8.	Eccentricity and inclination of a population of km-sized planetesimals from self- and embryo-induced-stirring	65
2.9.	Mean collision rate as a function of reduced eccentricity dispersions for three different \tilde{r}_p	73
2.10.	Sum of the number of collisions between planetesimals in a year as a function of the planetesimal radius	74
5.1.	Histogram of latest dynamical instability of systems in a population with 50 embryos around a Solar-mass star	136

List of Tables

2.1. Variables used for the disk part.	27
2.2. Variables used to describe collisions and planetesimal populations . . .	58
2.3. Energy and angular momentum for a projectile getting deflected to- wards a target	68
3.1. Bulk densities of well-researched cometary nuclei.	94

Bibliography

- Adachi, I., Hayashi, C., & Nakazawa, K., *The Gas Drag Effect on the Elliptic Motion of a Solid Body in the Primordial Solar Nebula*, 1976, [Progress of Theoretical Physics](#), **56**, 1756
- A’Hearn, M. F., Belton, M. J., Delamere, W. A., et al., *Deep Impact: Excavating comet Tempel 1*, 2005, [Science](#), **310**, 258
- Alcalá, J. M., Manara, C. F., Natta, A., et al., *X-shooter spectroscopy of young stellar objects in Lupus*, 2017, [A&A](#), **600**, A20
- Alcalá, J. M., Natta, A., Manara, C. F., et al., *X-shooter spectroscopy of young stellar objects*, 2014, [A&A](#), **561**, A2
- Alexander, R., Pascucci, I., Andrews, S. M., Armitage, P., & Cieza, L., *The Dispersal of Protoplanetary Disks*, 2014, in [Protostars Planets VI](#), ed. H. Beuther, R. S. Klessen, C. P. Dullemond, & T. Henning (University of Arizona Press), 475
- Alibert, Y. & Benz, W., *Formation and composition of planets around very low mass stars*, 2017, [A&A](#), **598**, L5
- Alibert, Y., Carron, F., Fortier, A., et al., *Theoretical models of planetary system formation: mass vs. semi-major axis*, 2013, [A&A](#), **558**, A109
- Alibert, Y., Mordasini, C., & Benz, W., *Migration and giant planet formation*, 2004a, [A&A](#), **417**, L25
- Alibert, Y., Mordasini, C., & Benz, W., *Extrasolar planet population synthesis III. Formation of planets around stars of different masses*, 2011, [A&A](#), **526**, A63
- Alibert, Y., Mordasini, C., Benz, W., & Winisdoerffer, C., *Models of Giant Planet formation with migration and disc evolution*, 2004b, [A&A](#), **434**, 343
- Alibert, Y., Venturini, J., Helled, R., et al., *The formation of Jupiter by hybrid pebble–planetesimal accretion*, 2018, [Nature Astronomy](#), **2**, 873
- ALMA-Partnership, Brogan, C. L., Pérez, L. M., et al., *The 2014 ALMA Long Baseline Campaign: First Results from High Angular Resolution Observations toward the HL Tau Region*, 2015, [ApJL](#), **808**
- Alonso, R., 2018, [Characterization of Exoplanets: Secondary Eclipses](#) (Cham: Springer International Publishing), 1441–1467
- Andre, P., Ward-Thompson, D., & Barsony, M., *Submillimeter Continuum Observations of rho Ophiuchi A: The Candidate Protostar VLA 1623 and Prestellar Clumps*, 1993, [ApJ](#), **406**, 122
- Andrews, S. M., Huang, J., Pérez, L. M., et al., *The Disk Substructures at High Angular Resolution Project (DSHARP): I. Motivation, Sample, Calibration, and Overview*, 2018a, [ApJL](#), **869**, L41
- Andrews, S. M., Terrell, M., Tripathi, A., et al., *Scaling Relations Associated with Millimeter Continuum Sizes in Protoplanetary Disks*, 2018b, [ApJ](#), **865**, 157
- Andrews, S. M., Wilner, D. J., Hughes, A. M., Qi, C., & Dullemond, C. P., *Protoplanetary Disk Structures in Ophiuchus*, 2009, [ApJ](#), **700**, 1502
- Andrews, S. M., Wilner, D. J., Hughes, A. M., Qi, C., & Dullemond, C. P., *Protoplanetary Disk Structures in Ophiuchus. II. Extension to Fainter Sources*, 2010, [ApJ](#), **723**, 1241
- Ansdell, M., Williams, J. P., Manara, C. F., et al., *An ALMA Survey of Protoplanetary Disks in the σ Orionis Cluster*, 2017, [The Astronomical Journal](#), **153**, 240

- Ansdell, M., Williams, J. P., Trapman, L., et al., *ALMA Survey of Lupus Protoplanetary Disks. II. Gas Disk Radii*, 2018, [ApJ](#), **859**, 21
- Ansdell, M., Williams, J. P., van der Marel, N., et al., *ALMA Survey of Lupus Protoplanetary Disks. I. Dust and Gas Masses*, 2016, [ApJ](#), **828**, 46
- Armitage, P. J., *Physical processes in protoplanetary disks*, 2015, ArXiv e-prints [[arXiv:1509.06382](#)]
- Armitage, P. J., *Physical Processes in Protoplanetary Disks*, 2019, in [From Protoplanetary Disks to Planet Formation Saas-Fee Advanced Course 45. Swiss Society Astrophysics Astronomy](#), ed. M. Audard, M. R. Meyer, & Y. Alibert (Berlin, Heidelberg: Springer Berlin Heidelberg), 1–150
- Astudillo-Defru, N., Díaz, R. F., Bonfils, X., et al., *The HARPS search for southern extra-solar planets*, 2017, [A&A](#), **605**, L11
- Ataiee, S., Baruteau, C., Alibert, Y., & Benz, W., *How much does turbulence change the pebble isolation mass for planet formation?*, 2018, [A&A](#), **615**, 1
- Avenhaus, H., Quanz, S. P., Garufi, A., et al., *Disks around T Tauri Stars with SPHERE (DARTTS-S). I. SPHERE/IRDIS Polarimetric Imaging of Eight Prominent T Tauri Disks*, 2018, [ApJ](#), **863**, 44
- Avenhaus, H., Quanz, S. P., Schmid, H. M., et al., *Structures in the Protoplanetary Disk of HD142527 seen in polarized scattered light*, 2014, [ApJ](#), **781**, 87
- Bai, X.-N., *Toward a Global Evolutionary Model of Protoplanetary Disks*, 2016, [ApJ](#), **821**, 80
- Bai, X. N. & Stone, J. M., *Wind-driven accretion in protoplanetary disks. I. Suppression of the magnetorotational instability and launching of the magnetocentrifugal wind*, 2013, [ApJ](#), 769 [[arXiv:1301.0318](#)]
- Bai, X.-N., Ye, J., Goodman, J., & Yuan, F., *Magneto-Thermal Disk Winds From Protoplanetary Disks*, 2016, [ApJ](#), **818**, 152
- Baraffe, I., Chabrier, G., Barman, T. S., Allard, F., & Hauschildt, P. H., *Evolutionary models for cool brown dwarfs and extrasolar giant planets. The case of HD 209458*, 2003, [A&A](#), **402**, 701
- Baraffe, I., Homeier, D., Allard, F., & Chabrier, G., *New evolutionary models for pre-main sequence and main sequence low-mass stars down to the hydrogen-burning limit*, 2015, [A&A](#), **577**, A42
- Barbato, D., Sozzetti, A., Desidera, S., et al., *Exploring the realm of scaled solar system analogues with HARPS*, 2018, [A&A](#), **615**, A175
- Barenfeld, S. A., Carpenter, J. M., Ricci, L., & Isella, A., *ALMA Observations of Circumstellar Disks in the Upper Scorpius OB Association*, 2016, [ApJ](#), **827**, 142
- Barenfeld, S. A., Carpenter, J. M., Sargent, A. I., Isella, A., & Ricci, L., *Measurement of Circumstellar Disk Sizes in the Upper Scorpius OB Association with ALMA*, 2017, [ApJ](#), **851**, 85
- Baruteau, C., Bai, X., Mordasini, C., & Mollière, P., *Formation, Orbital and Internal Evolutions of Young Planetary Systems*, 2016, [Space Science Reviews](#), **205**, 77
- Baruteau, C., Crida, A., Paardekooper, S.-J., et al., *Planet-Disk Interactions and Early Evolution of Planetary Systems*, 2014, in [Protostars Planets VI](#), ed. H. Beuther, R. S. Klessen, C. P. Dullemond, & T. Henning, Vol. 3 (Tucson: University of Arizona Press), 667–689
- Bell, K. R. & Lin, D. N. C., *Using FU Orionis outbursts to constrain self-regulated protostellar disk models*, 1994, [ApJ](#), **427**, 987
- Benneke, B., Wong, I., Piaulet, C., et al., *Water Vapor and Clouds on the Habitable-zone Sub-Neptune Exoplanet K2-18b*, 2019, [ApJ](#), **887**, L14
- Bennett, D., Akeson, R., Alibert, Y., et al., *Wide-Orbit Exoplanet Demographics*, 2019, Bulletin of the American Astronomical Society, 51, 505
- Bennett, D. P., Anderson, J., Bond, I. A., Udalski, A., & Gould, A., *Identification of the OGLE-2003-BLG-235/MOA-2003-BLG-53 Planetary Host Star*, 2006, [ApJ](#), **647**, L171

- Benz, W. & Asphaug, E., *Catastrophic Disruptions Revisited*, 1999, *Icarus*, 141, 5
- Benz, W., Ida, S., Alibert, Y., Lin, D. N. C., & Mordasini, C., *Planet Population Synthesis*, 2014, in [Protostars Planets VI](#), ed. H. Beuther, R. S. Klessen, C. P. Dullemond, & T. Henning (Tucson: University of Arizona Press), 697–713
- Berger, T. A., Huber, D., van Saders, J. L., et al., *The \$Gaia\$-\$Kepler\$ Stellar Properties Catalog I: Homogeneous Fundamental Properties for 186,000 \$Kepler\$ Stars*, 2020, ArXiv e-prints [[arXiv:2001.07737](#)]
- Bernstein, G. M., Trilling, D. E., Allen, R. L., et al., *The Size Distribution of Trans-Neptunian Bodies*, 2004, [The Astronomical Journal](#), 128, 1364
- Bertout, C., Basri, G., & Bouvier, J., *Accretion disks around T Tauri stars*, 1988, [ApJ](#), 330, 350
- Beuzit, J.-L., Vigan, A., Mouillet, D., et al., *SPHERE: the exoplanet imager for the Very Large Telescope*, 2019, [A&A](#), 631, A155
- Bitsch, B., Morbidelli, A., Johansen, A., et al., *Pebble-isolation mass: Scaling law and implications for the formation of super-Earths and gas giants*, 2018, [A&A](#), 612, A30
- Bodenheimer, P., D’Angelo, G., Lissauer, J. J., Fortney, J. J., & Saumon, D., *Deuterium burning in massive giant planets and low-mass brown dwarfs formed by core-nucleated accretion*, 2013, [ApJ](#), 770
- Bodenheimer, P., Hubickyj, O., & Lissauer, J. J., *Models of the in situ formation of detected extrasolar giant planets*, 2000, *Icarus*, 143, 2
- Bodenheimer, P. & Pollack, J. B., *Calculations of the accretion and evolution of giant planets: The effects of solid cores*, 1986, *Icarus*, 67, 391
- Bohlin, R. C., Savage, B. D., & Drake, J. F., *A survey of interstellar H I from L-alpha absorption measurements. II*, 1978, [ApJ](#), 224, 132
- Bond, I. A., *The first extrasolar planet detected via gravitational microlensing*, 2012, [New Astronomy Reviews](#), 56, 25
- Bond, I. A., Udalski, A., Jaroszyski, M., et al., *OGLE 2003-BLG-235/MOA 2003-BLG-53: A Planetary Microlensing Event*, 2004, [ApJ](#), 606, L155
- Bond, J. C., Lauretta, D. S., & O’Brien, D. P., *Making the Earth: Combining dynamics and chemistry in the Solar System*, 2010, *Icarus*, 205, 321
- Borucki, W. J., Koch, D., Basri, G., et al., *Kepler Planet-Detection Mission: Introduction and First Results*, 2010, [Science](#), 327, 977
- Bouchy, F., Doyon, R., Artigau, É., et al., *Near-InfraRed Planet Searcher to Join HARPS on the ESO 3.6-metre Telescope*, 2017, [The Messenger](#), 169, 21
- Bowler, B. P., *Imaging extrasolar giant planets*, 2016, [Publications of the Astronomical Society of the Pacific](#), 128, 1
- Brownlee, D., Tsou, P., Aléon, J., et al., *Comet 81P/wild 2 under a microscope*, 2006, [Science](#), 314, 1711
- Brügger, N., Alibert, Y., Ataiee, S., & Benz, W., *Metallicity effect and planet mass function in pebble-based planet formation models*, 2018, [A&A](#), 619, A174
- Brügger, N., Burn, R., Coleman, G., Alibert, Y., & Benz, W., *Pebbles versus planetesimals: the outcomes of population synthesis models*, 2020, ArXiv e-prints [[arXiv:2006.04121](#)]
- Bryan, M. L., Knutson, H. A., Lee, E. J., et al., *An Excess of Jupiter Analogs in Super-Earth Systems*, 2019, [The Astronomical Journal](#), 157, 52
- Bryden, G., Chen, X., Lin, D. N. C., Nelson, R. P., & Papaloizou, J. C. B., *Tidally Induced Gap Formation in Protostellar Disks: Gap Clearing and Suppression of Protoplanetary Growth*, 1999, [ApJ](#), 514, 344

- Bryson, S., Coughlin, J., Batalha, N. M., et al., *A Probabilistic Approach to Kepler Completeness and Reliability for Exoplanet Occurrence Rates*, 2019, ArXiv e-prints [[arXiv:1906.03575](https://arxiv.org/abs/1906.03575)]
- Bulirsch, R. & Stoer, J., *Fehlerabschätzungen und Extrapolation mit rationalen Funktionen bei Verfahren vom Richardson-Typus*, 1964, *Numerische Mathematik*, **6**, 413
- Burger, C., Bazsó, Á., & Schäfer, C. M., *Realistic collisional water transport during terrestrial planet formation*, 2020, *A&A*, **634**, [A76](#)
- Burger, C., Maindl, T. I., & Schäfer, C. M., *Transfer, loss and physical processing of water in hit-and-run collisions of planetary embryos*, 2018, *Celestial Mechanics and Dynamical Astronomy*, **130**, [2](#)
- Burger, D., Stassun, K. G., Pepper, J., et al., *Filtergraph: An interactive web application for visualization of astronomy datasets*, 2013, *Astronomy and Computing*, **2**, [40](#)
- Burn, R., Marboeuf, U., Alibert, Y., & Benz, W., *Radial drift and concurrent ablation of boulder-sized objects*, 2019, *A&A*, **629**, [A64](#)
- Burn, R., Schlecker, M., Mordasini, C., et al., *The New Generation Planetary Population Synthesis (NGPPS). IV. Planetary systems around low-mass stars*, in prep., *A&A*
- Calvet, N. & Gullbring, E., *The Structure and Emission of the Accretion Shock in T Tauri Stars*, 1998, *ApJ*, **509**, [802](#)
- Carlson, B. C., *Elliptic Integral*, 2010, in *NIST Handbook Mathematical Functions* (Cambridge University Press), 485–522
- Carrasco-González, C., Sierra, A., Flock, M., et al., *The Radial Distribution of Dust Particles in the HL Tau Disk from ALMA and VLA Observations*, 2019, *ApJ*, **883**, [71](#)
- Chambers, J. E., *A hybrid symplectic integrator that permits close encounters between massive bodies*, 1999, *MNRAS*, **304**, [793](#)
- Chambers, J. E., *A semi-analytic model for oligarchic growth*, 2006, *Icarus*, **180**, [496](#)
- Chambers, J. E., *Giant planet formation with pebble accretion*, 2014, *Icarus*, **233**, [83](#)
- Charbonneau, D., Allen, L. E., Megeath, S. T., et al., *Detection of Thermal Emission from an Extrasolar Planet*, 2005, *ApJ*, **626**, [523](#)
- Charbonneau, D., Brown, T. M., Latham, D. W., & Mayor, M., *Detection of Planetary Transits Across a Sun-like Star*, 1999, *ApJ*, **529**, [L45](#)
- Charpinet, S., Fontaine, G., Brassard, P., et al., *A compact system of small planets around a former red-giant star*, 2011, *Nature*, **480**, [496](#)
- Chauvin, G., Desidera, S., Lagrange, A. M., et al., 2017, in SF2A-2017: Proceedings of the Annual meeting of the French Society of Astronomy and Astrophysics, ed. C. Reylé, P. Di Matteo, F. Herpin, E. Lagarde, A. Lançon, Z. Meliani, & F. Royer, Di
- Chiang, E. & Laughlin, G., *The minimum-mass extrasolar nebula: in situ formation of close-in super-Earths*, 2013, *MNRAS*, **431**, [3444](#)
- Choi, J., Dotter, A., Conroy, C., et al., *Mesa Isochrones and Stellar Tracks (MIST). I. Solar-scaled Models*, 2016, *ApJ*, **823**, [102](#)
- Cimerman, N. P., Kuiper, R., & Ormel, C. W., *Hydrodynamics of embedded planets' first atmospheres – III. The role of radiation transport for super-Earth planets*, 2017, *MNRAS*, **471**, [4662](#)
- Clarke, C. J., Gendrin, A., & Sotomayor, M., *The dispersal of circumstellar discs: the role of the ultraviolet switch*, 2001, *MNRAS*, **328**, [485](#)
- Coleman, G. A. L., Leleu, A., Alibert, Y., & Benz, W., *Pebbles versus planetesimals: the case of Trappist-1*, 2019, *A&A*, **631**, [A7](#)
- Coleman, G. A. L. & Nelson, R. P., *On the formation of planetary systems via oligarchic growth in thermally evolving viscous discs*, 2014, *MNRAS*, **445**, [479](#)

- Crida, A., Morbidelli, A., & Masset, F., *On the width and shape of gaps in protoplanetary disks*, 2006, *Icarus*, **181**, 587
- Cui, C. & Bai, X.-N., *Global Simulations of the Vertical Shear Instability with Nonideal Magnetohydrodynamic Effects*, 2020, *ApJ*, **891**, 30
- Cuzzi, J. N., Hogan, R. C., & Bottke, W. F., *Towards initial mass functions for asteroids and Kuiper Belt Objects*, 2010, *Icarus*, **208**, 518
- Davidsson, B. J. & Gutiérrez, P. J., *Estimating the nucleus density of Comet 19P/Borrelly*, 2004, *Icarus*, **168**, 392
- Davidsson, B. J. & Gutiérrez, P. J., *Non-gravitational force modeling of Comet 81P/Wild 2. I. A nucleus bulk density estimate*, 2006, *Icarus*, **180**, 224
- Davidsson, B. J. R., Sierks, H., Güttler, C., et al., *The primordial nucleus of comet 67P/Churyumov-Gerasimenko*, 2016, *A&A*, **592**, A63
- Delsemme, A. & Miller, D., *Physico-chemical phenomena in comets III: The continuum of comet Burnham (1960 II)*, 1971, *Planetary and Space Science*, **19**, 1229
- Dittkrist, K.-M. K.-M., Mordasini, C., Klahr, H., Alibert, Y., & Henning, T., *Impacts of planet migration models on planetary populations*, 2014, *A&A*, **567**, A121
- Dohnanyi, J. S., *Collisional model of asteroids and their debris*, 1969, *Journal of Geophysical Research*, **74**, 2531
- Drążkowska, J. & Alibert, Y., *Planetesimal formation starts at the snow line*, 2017, *A&A*, **608**, A92
- Dullemond, C. P., 2013, in *Les Houches*
- Einstein, A., *Über den Einfluß der Schwerkraft auf die Ausbreitung des Lichtes*, 1911, *Annalen der Physik*, **340**, 898
- Einstein, A., *Lens-Like Action of a Star by the Deviation of Light in the Gravitational Field*, 1936, *Science*, **84**, 506
- Eistrup, C., Walsh, C., & van Dishoeck, E. F., *Setting the volatile composition of (exo)planet-building material*, 2016, *A&A*, **595**, A83
- Eistrup, C., Walsh, C., & van Dishoeck, E. F., *Molecular abundances and C/O ratios in chemically evolving planet-forming disk midplanes*, 2018, *A&A*, **613**, A14
- Emsenhuber, A., Cambioni, S., Asphaug, E., et al., *Realistic On-the-fly Outcomes of Planetary Collisions. II. Bringing Machine Learning to N-body Simulations*, 2020, *ApJ*, **891**, 6
- Emsenhuber, A., Mordasini, C., Burn, R., et al., *The New Generation Planetary Population Synthesis (NGPPS). II. Populations and overview of statistical results*, in prep., *A&A*
- Emsenhuber, A., Mordasini, C., Burn, R., et al., *The New Generation Planetary Population Synthesis (NGPPS). I. Bern global model of planet formation and evolution, model tests, and emerging planetary systems.*, submitted, *A&A*
- Ercolano, B. & Pascucci, I., *The dispersal of planet-forming discs: theory confronts observations*, 2017, *Royal Society Open Science*, **4**, 170114
- Ercolano, B. & Rosotti, G., *The link between disc dispersal by photoevaporation and the semimajor axis distribution of exoplanets*, 2015, *MNRAS*, **450**, 3008
- Evans, N. J., Dunham, M. M., Jørgensen, J. K., et al., *The Spitzer c2d Legacy Results: Star Formation Rates and Efficiencies; Evolution and Lifetimes*, 2009, *The Astrophysical Journal Supplement Series*, **181**, 321
- Faigler, S., Tal-Or, L., Mazeh, T., Latham, D. W., & Buchhave, L. A., *BEER analysis of Kepler and CoRoT light curves: I. Discovery of Kepler-76b: A hot Jupiter with evidence for superrotation*, 2013, *ApJ*, **771**, 26
- Fang, M., Kim, J. S., van Boekel, R., et al., *Young Stellar Objects in Lynds 1641: Disks, Accretion, and Star Formation History*, 2013, *The Astrophysical Journal Supplement Series*, **207**, 5

- Fedele, D., van den Ancker, M. E., Henning, T., Jayawardhana, R., & Oliveira, J. M., *Timescale of mass accretion in pre-main-sequence stars*, 2010, [A&A](#), **510**, [A72](#)
- Feiden, G. A., *Magnetic inhibition of convection and the fundamental properties of low-mass stars*, 2016, [A&A](#), **593**, [A99](#)
- Fernandes, R. B., Mulders, G. D., Pascucci, I., Mordasini, C., & Emsenhuber, A., *Hints for a Turnover at the Snow Line in the Giant Planet Occurrence Rate*, 2019, [ApJ](#), **874**, [81](#)
- Fernández, J., Tancredi, G., Rickman, H., & Licandro, J., *The population, magnitudes, and sizes of Jupiter family comets*, 1999, [A&A](#), **352**, [327](#)
- Fernández, Y., Kelley, M., Lamy, P., et al., *Thermal properties, sizes, and size distribution of Jupiter-family cometary nuclei*, 2013, [Icarus](#), **226**, [1138](#)
- Fortier, A., Alibert, Y., Carron, F., Benz, W., & Dittkrist, K.-M., *Planet formation models: the interplay with the planetesimal disc*, 2013, [A&A](#), **549**, [A44](#)
- Fraser, W. C. & Kavelaars, J. J., *The Size Distribution of Kuiper Belt Objects for $D > 10$ km*, 2009, [The Astronomical Journal](#), **137**, [72](#)
- Fromang, S. & Lesur, G., *Angular momentum transport in accretion disks: a hydrodynamical perspective*, 2019, [EAS Publications Series](#), **82**, [391](#)
- Fulton, B. J., Petigura, E. A., Howard, A. W., et al., *The California- Kepler Survey. III. A Gap in the Radius Distribution of Small Planets*, 2017, [The Astronomical Journal](#), **154**, [109](#)
- Gaia Collaboration, Brown, A. G. A., Vallenari, A., et al., *Gaia Data Release 2*, 2018, [A&A](#), **616**, [A1](#)
- Galicher, R., Marois, C., MacIntosh, B., et al., *The International Deep Planet Survey: II. The frequency of directly imaged giant exoplanets with stellar mass*, 2016, [A&A](#), **594**, [1](#)
- Gammie, C. F., *Layered Accretion in T Tauri Disks*, 1996, [ApJ](#), **457**, [355](#)
- Garufi, A., Avenhaus, H., Pérez, S., et al., *Disks Around T Tauri Stars with SPHERE (DARTTS-S)*, 2020, [A&A](#), **633**, [A82](#)
- Garufi, A., Meeus, G., Benisty, M., et al., *Evolution of protoplanetary disks from their taxonomy in scattered light: Group I vs. Group II*, 2017, [A&A](#), **603**, [A21](#)
- Gaudi, B. S., Seager, S., Mennesson, B., et al., *The Habitable Exoplanet Observatory (HabEx) Mission Concept Study Final Report*, 2020, ArXiv e-prints [[arXiv:2001.06683](#)]
- Gibbs, J. W., *A method of geometrical representation of the thermodynamic properties by means of surfaces*, 1873, Transactions Connecticut Academy Arts Sciences, **382**
- Gillon, M., Triaud, A. H. M. J., Demory, B.-O., et al., *Seven temperate terrestrial planets around the nearby ultracool dwarf star TRAPPIST-1*, 2017, [Nature](#), **542**, [456](#)
- Goldreich, P. & Tremaine, S., *The excitation of density waves at the Lindblad and corotation resonances by an external potential*, 1979, [ApJ](#), **233**, [857](#)
- Gonzalez, G., *The stellar metallicity–giant planet connection*, 1997, [MNRAS](#), **285**, [403](#)
- Gorti, U. & Hollenbach, D., *Photoevaporation of Circumstellar Disks by FUV, EUV and X-ray Radiation from the Central Star*, 2008, [ApJ](#), **690**, [1539](#)
- Greene, T. P., Wilking, B. A., Andre, P., Young, E. T., & Lada, C. J., *Further mid-infrared study of the rho Ophiuchi cloud young stellar population: Luminosities and masses of pre-main-sequence stars*, 1994, [ApJ](#), **434**, [614](#)
- Greenzweig, Y. & Lissauer, J. J., *Accretion rates of protoplanets*, 1990, [Icarus](#), **87**, [40](#)
- Greenzweig, Y. & Lissauer, J. J., *Accretion rates of protoplanets: II. Gaussian distributions of planetesimal velocities*, 1992, [Icarus](#), **100**, [440](#)
- Gressel, O., Turner, N. J., Nelson, R. P., & McNally, C. P., *Global simulations of protoplanetary disks with ohmic resistivity and ambipolar diffusion*, 2015, [ApJ](#), **801**, [84](#)

- Grimm, S. L., Demory, B.-O., Gillon, M., et al., *The nature of the TRAPPIST-1 exoplanets*, 2018, [A&A](#), **613**, A68
- Güdel, M., Briggs, K. R., Arzner, K., et al., *The XMM-Newton extended survey of the Taurus molecular cloud (XEST)*, 2007, [A&A](#), **468**, 353
- Güdel, M. & Nazé, Y., *X-ray spectroscopy of stars*, 2009, [The Astronomy and Astrophysics Review](#), **17**, 309
- Guilera, O. M., Brunini, A., & Benvenuto, O. G., *Consequences of the simultaneous formation of giant planets by the core accretion mechanism*, 2010, [A&A](#), **521**, A50
- Gullbring, E., Hartmann, L., Briceno, C., & Calvet, N., *Disk Accretion Rates for T Tauri Stars*, 1998, [ApJ](#), **492**, 323
- Guzik, P., Drahus, M., Rusek, K., et al., *Initial characterization of interstellar comet 2I/Borisov*, 2020, [Nature Astronomy](#), **4**, 53
- Haisch, Jr., K. E., Lada, E. A., & Lada, C. J., *Disk Frequencies and Lifetimes in Young Clusters*, 2001, [ApJ](#), **553**, L153
- Hartmann, L., 2009, *Accretion Processes in Star Formation: Second Edition* (Cambridge University Press)
- Hartmann, L. & Bae, J., *How do T Tauri stars accrete?*, 2018, [MNRAS](#), **474**, 88
- Hartmann, L., Herczeg, G., & Calvet, N., *Accretion onto Pre-Main-Sequence Stars*, 2016, [Annual Review of Astronomy and Astrophysics](#), **54**, 135
- Hartmann, L. & Kenyon, S. J., *The FU Orionis Phenomenon*, 1996, [Annual Review of Astronomy and Astrophysics](#), **34**, 207
- Hayashi, C., *Structure of the Solar Nebula, Growth and Decay of Magnetic Fields and Effects of Magnetic and Turbulent Viscosities on the Nebula*, 1981, [Progress of Theoretical Physics Supplement](#), **70**, 35
- Hellary, P. & Nelson, R. P., *Global models of planetary system formation in radiatively-inefficient protoplanetary discs*, 2012, [MNRAS](#), **419**, 2737
- Helled, R., Bodenheimer, P., Podolak, M., et al., *Giant Planet Formation, Evolution, and Internal Structure*, 2014, in [Protostars Planets VI](#), ed. H. Beuther, R. S. Klessen, C. P. Dullemond, & T. Henning (Tucson: University of Arizona Press), 643–665
- Henning, T. & Semenov, D., *Chemistry in protoplanetary disks*, 2013, [Chemical Reviews](#), **113**, 9016
- Hénon, M. & Petit, J.-M., *Series expansions for encounter-type solutions of Hill's problem*, 1986, [Celestial Mechanics](#), **38**, 67
- Herman, M. K., Zhu, W., & Wu, Y., *Revisiting the Long-period Transiting Planets from Kepler*, 2019, [The Astronomical Journal](#), **157**, 248
- Hertz, H., *Über die Verdunstung der Flüssigkeiten, insbesondere des Quecksilbers, im luftleeren Raume*, 1882, *Annalen der Physik*, **253**, 177
- Hill, G. W., *Researches in the Lunar Theory*, 1878, *American Journal of Mathematics*, **1**, 5
- Hinkley, S., Oppenheimer, B. R., Soummer, R., et al., *Speckle Suppression Through Dual Imaging Polarimetry, and a Ground-based Image of the HR 4796A Circumstellar Disk*, 2009, [ApJ](#), **701**, 804
- Hollenbach, D., Johnstone, D., Lizano, S., & Shu, F., *Photoevaporation of disks around massive stars and application to ultracompact H II regions*, 1994, [ApJ](#), **428**, 654
- Hsu, D. C., Ford, E. B., Ragozzine, D., & Ashby, K., *Occurrence Rates of Planets Orbiting FGK Stars: Combining Kepler DR25, Gaia DR2, and Bayesian Inference*, 2019, [The Astronomical Journal](#), **158**, 109
- Hueso, R. & Guillot, T., *Evolution of protoplanetary disks: constraints from DM Tauri and GM Aurigae*, 2005, [A&A](#), **442**, 703

- Hyodo, R., Ida, S., & Charnoz, S., *Formation of rocky and icy planetesimals inside and outside the snow line: effects of diffusion, sublimation, and back-reaction*, 2019, [A&A](#), **629**, [A90](#)
- Ida, S., *Stirring and dynamical friction rates of planetesimals in the solar gravitational field*, 1990, [Icarus](#), **88**, [129](#)
- Ida, S. & Guillot, T., *Formation of dust-rich planetesimals from sublimated pebbles inside of the snow line*, 2016, [A&A](#), **596**, [L3](#)
- Ida, S. & Lin, D. N. C., *Toward a Deterministic Model of Planetary Formation. I. A Desert in the Mass and Semimajor Axis Distributions of Extrasolar Planets*, 2004a, [ApJ](#), **604**, [388](#)
- Ida, S. & Lin, D. N. C., *Toward a Deterministic Model of Planetary Formation. II. The Formation and Retention of Gas Giant Planets around Stars with a Range of Metallicities*, 2004b, [ApJ](#), **616**, [567](#)
- Ida, S. & Lin, D. N. C., *Toward a Deterministic Model of Planetary Formation. IV. Effects of Type I Migration*, 2008, [ApJ](#), **673**, [487](#)
- Ida, S. & Lin, D. N. C., *Toward a deterministic model of planetary formation. VI. Dynamical interaction and coagulation of multiple rocky embryos and super-Earth systems around solar-type stars*, 2010, [ApJ](#), **719**, [810](#)
- Ida, S., Lin, D. N. C., & Nagasawa, M., *Toward a Deterministic Model of Planetary Formation. VII. Eccentricity Distribution of Gas Giants*, 2013, [ApJ](#), **775**, [42](#)
- Ida, S. & Makino, J., *N-Body simulation of gravitational interaction between planetesimals and a protoplanet. I. Velocity distribution of planetesimals*, 1992a, [Icarus](#), **96**, [107](#)
- Ida, S. & Makino, J., *N-body simulation of gravitational interaction between planetesimals and a protoplanet II. Dynamical friction*, 1992b, [Icarus](#), **98**, [28](#)
- Ida, S. & Makino, J., *Scattering of Planetesimals by a Protoplanet: Slowing Down of Runaway Growth*, 1993, [Icarus](#), **106**, [210](#)
- Ida, S., Muto, T., Matsumura, S., & Brasser, R., *A new and simple prescription for planet orbital migration and eccentricity damping by planet-disc interactions based on dynamical friction*, 2020, [MNRAS](#), **5674**, [5666](#)
- Ida, S. & Nakazawa, K., *Collisional probability of planetesimals revolving in the solar gravitational field. III*, 1989, [A&A](#), **224**, [303](#)
- Inaba, S. & Ikoma, M., *Enhanced collisional growth of a protoplanet that has an atmosphere*, 2003, [A&A](#), **410**, [711](#)
- Inaba, S., Tanaka, H., Nakazawa, K., Wetherill, G. W., & Kokubo, E., *High-Accuracy Statistical Simulation of Planetary Accretion: II. Comparison with N-Body Simulation*, 2001, [Icarus](#), **149**, [235](#)
- Isella, A., Guidi, G., Testi, L., et al., *Ringed Structures of the HD 163296 Protoplanetary Disk Revealed by ALMA*, 2016, [Physical Review Letters](#), **117**
- Janson, M., Bergfors, C., Goto, M., Brandner, W., & Lafrenière, D., *Spatially resolved spectroscopy of the exoplanet HR 8799 c*, 2010, [ApJ](#), **710**, [L35](#)
- Jin, S. & Mordasini, C., *Compositional Imprints in Density–Distance–Time: A Rocky Composition for Close-in Low-mass Exoplanets from the Location of the Valley of Evaporation*, 2018, [ApJ](#), **853**, [163](#)
- Jin, S., Mordasini, C., Parmentier, V., et al., *Planetary Population Synthesis Coupled with Atmospheric Escape: A Statistical View of Evaporation*, 2014, [ApJ](#), **795**, [65](#)
- Johansen, A. & Bitsch, B., *Exploring the conditions for forming cold gas giants through planetesimal accretion*, 2019, [A&A](#), **631**, [A70](#)
- Johansen, A. & Lambrechts, M., *Forming Planets via Pebble Accretion*, 2017, [Annual Review of Earth and Planetary Sciences](#), **45**, [359](#)

- Johansen, A., Youdin, A. N., & Lithwick, Y., *Adding particle collisions to the formation of asteroids and Kuiper belt objects via streaming instabilities*, 2012, [A&A](#), **537**, A125
- Jutzi, M., *SPH calculations of asteroid disruptions: The role of pressure dependent failure models*, 2015, [Planetary and Space Science](#), **107**, 3
- Jutzi, M., Michel, P., Benz, W., & Richardson, D. C., *Fragment properties at the catastrophic disruption threshold: The effect of the parent body's internal structure*, 2010, [Icarus](#), **207**, 54
- Kalas, P., Graham, J. R., Chiang, E., et al., *Optical Images of an Exosolar Planet 25 Light-Years from Earth*, 2008, [Science](#), **322**, 1345
- Kanagawa, K. D., Tanaka, H., & Szuszkiewicz, E., *Radial Migration of Gap-opening Planets in Protoplanetary Disks. I. The Case of a Single Planet*, 2018, [ApJ](#), **861**, 140
- Kenyon, S. J. & Hartmann, L., *Spectral energy distributions of T Tauri stars - Disk flaring and limits on accretion*, 1987, [ApJ](#), **323**, 714
- Kenyon, S. J. & Hartmann, L., *Pre-Main-Sequence Evolution in the Taurus-Auriga Molecular Cloud*, 1995, [The Astrophysical Journal Supplement Series](#), **101**, 117
- Kimura, S. S., Kunitomo, M., & Takahashi, S. Z., *From birth to death of protoplanetary discs: modelling their formation, evolution and dispersal*, 2016, [MNRAS](#), **461**, 2257
- Kippenhahn, R., Weigert, A., & Weiss, A., 2012, [Stellar Structure and Evolution](#), [Astronomy and Astrophysics Library](#) (Berlin, Heidelberg: Springer)
- Klahr, H. & Hubbard, A., *Convective Overstability in radially stratified accretion disks under thermal relaxation*, 2014, [ApJ](#), **788**, 21
- Kley, W. & Nelson, R., *Planet-Disk Interaction and Orbital Evolution*, 2012, [Annual Review of Astronomy and Astrophysics](#), **50**, 211
- Klinger, J., *Some consequences of a phase transition of water ice on the heat balance of comet nuclei*, 1981, [Icarus](#), **47**, 320
- Kobayashi, H., Tanaka, H., & Okuzumi, S., *From Planetesimals to Planets in Turbulent Protoplanetary Disks. I. Onset of Runaway Growth*, 2016, [ApJ](#), **817**, 105
- Kokubo, E. & Ida, S., *Oligarchic Growth of Protoplanets*, 1998, [Icarus](#), **131**, 171
- Konigl, A., *Self-similar models of magnetized accretion disks*, 1989, [ApJ](#), **342**, 208
- Kruijer, T. S., Burkhardt, C., Budde, G., & Kleine, T., *Age of Jupiter inferred from the distinct genetics and formation times of meteorites*, 2017, [Proceedings of the National Academy of Sciences of the United States of America](#), **114**, 6712
- Kuchner, M. J., *Volatile-rich Earth-Mass Planets in the Habitable Zone*, 2003, [ApJ](#), **596**, L105
- Kuhn, J. R., Potter, D., & Parise, B., *Imaging Polarimetric Observations of a New Circumstellar Disk System*, 2001, [ApJ](#), **553**, L189
- Kusaka, T., Nakano, T., & Hayashi, C., *Growth of Solid Particles in the Primordial Solar Nebula*, 1970, [Progress of Theoretical Physics](#), **44**, 1580
- Lada, C. & Wilking, B., *The nature of the embedded population in the rho Ophiuchi dark cloud : mid-infrared observations.*, 1984, [ApJ](#), **287**, 610
- Lada, C. J., 1987, in IAU Symposium, Vol. 115, Star Forming Regions, ed. M. Peimbert & J. Jugaku, 1
- Lambrechts, M. & Johansen, A., *Rapid growth of gas-giant cores by pebble accretion*, 2012, [A&A](#), **544**, A32
- Laskar, J., *On the Spacing of Planetary Systems*, 2000, [Physical Review Letters](#), **84**, 3240
- Lattanzi, M. & Sozzetti, A., *Gaia and the Astrometry of Giant Planets*, 2010, in [Astronomical Society of the Pacific Conference Series](#), Vol. 430, Pathways Towards Habitable Planets, ed. V. Coudé du Foresto, D. M. Gelino, & I. Ribas (Sheridan Books, Ann Arbor, Michigan), 253

- Launhardt, R., Henning, T., Quirrenbach, A., et al., *ISPY-NACO Imaging Survey for Planets around Young stars*, 2020, *A&A*, **635**, A162
- Lichtenberg, T., Golabek, G. J., Burn, R., et al., *A water budget dichotomy of rocky protoplanets from 26Al-heating*, 2019, *Nature Astronomy*, **3**, 307
- Lichtenberg, T., Golabek, G. J., Gerya, T. V., & Meyer, M. R., *The effects of short-lived radionuclides and porosity on the early thermo-mechanical evolution of planetesimals*, 2016, *Icarus*, **274**, 350
- Liffman, K., *The Gravitational Radius of an Irradiated Disk*, 2003, *Publications of the Astronomical Society of Australia*, **20**, 337
- Lin, D. N. C., Bodenheimer, P., & Richardson, D. C., *Orbital migration of the planetary companion of 51 Pegasi to its present location*, 1996, *Nature*, **380**, 606
- Lin, D. N. C. & Papaloizou, J., *Tidal torques on accretion discs in binary systems with extreme mass ratios*, 1979, *MNRAS*, **186**, 799
- Lin, D. N. C. & Papaloizou, J. C. B., *On the tidal interaction between protostellar disks and companions*, 1993, in *Protostars planets III*, ed. E. H. Levy & J. I. Lunine (Tucson, Arizona: University of Arizona Press), 749–835
- Linder, E. F., Mordasini, C., Mollière, P., et al., *Evolutionary models of cold and low-mass planets: cooling curves, magnitudes, and detectability*, 2019, *A&A*, **623**, A85
- Lissauer, J. J., Hubickyj, O., D’Angelo, G., & Bodenheimer, P., *Models of Jupiter’s growth incorporating thermal and hydrodynamic constraints*, 2009, *Icarus*, **199**, 338
- Lissauer, J. J., Ragozzine, D., Fabrycky, D. C., et al., *Architecture and dynamics of Kepler’s candidate multiple transiting planet systems*, 2011, *Astrophysical Journal, Supplement Series*, 197 [[arXiv:1102.0543](https://arxiv.org/abs/1102.0543)]
- Lissauer, J. J. & Stewart, G. R., *Growth of planets from planetesimals*, 1993, in *Protostars planets III*, ed. E. H. Levy & J. I. Lunine (University of Arizona Press), 1061–1088
- Lodders, K., *Solar System Abundances and Condensation Temperatures of the Elements*, 2003, *ApJ*, **591**, 1220
- Lopez, E. D. & Fortney, J. J., *The Role of Core Mass in Controlling Evaporation: The Kepler Radius Distribution and the Kepler-36 Density Dichotomy*, 2013, *ApJ*, **776**, 2
- Lubow, S. H., Seibert, M., & Artymowicz, P., *Disk Accretion onto High-Mass Planets*, 1999, *ApJ*, **526**, 1001
- Lunine, J., *Future prospects for the detection and characterization of extrasolar planets*, 2010, *EPJ Web Conferences*, **9**, 277
- Lynden-Bell, D. & Pringle, J. E., *The Evolution of Viscous Discs and the Origin of the Nebular Variables*, 1974, *MNRAS*, **168**, 603
- Machida, M. N., Kokubo, E., Inutsuka, S.-i., & Matsumoto, T., *Gas accretion onto a protoplanet and formation of a gas giant planet*, 2010, *MNRAS*, **405**, 1227
- Makino, J., Fukushige, T., Funato, Y., & Kokubo, E., *On the mass distribution of planetesimals in the early runaway stage*, 1998, *New Astronomy*, **3**, 411
- Mamajek, E. E., Usuda, T., Tamura, M., & Ishii, M., 2009, in *AIP Conference Proceedings*, Vol. **1158** (AIP), 3–10
- Manara, C. F., Mordasini, C., Testi, L., et al., *Constraining disk evolution prescriptions of planet population synthesis models with observed disk masses and accretion rates*, 2019, *A&A*, **631**, L2
- Manara, C. F., Testi, L., Natta, A., & Alcalá, J. M., *X-Shooter study of accretion in ρ -Ophiucus: very low-mass stars and brown dwarfs*, 2015, *A&A*, **579**, A66
- Marboeuf, U., 2008, *Évolution physico-chimique des objets transneptuniens*, PhD thesis, Université de Franche-Comté

- Marboeuf, U., Schmitt, B., Petit, J.-M., Mousis, O., & Fray, N., *A cometary nucleus model taking into account all phase changes of water ice: amorphous, crystalline, and clathrate*, 2012, *A&A*, **542**, A82
- Marboeuf, U., Thiabaud, A., Alibert, Y., Cabral, N., & Benz, W., *From planetesimals to planets: volatile molecules*, 2014a, *A&A*, **570**, A36
- Marboeuf, U., Thiabaud, A., Alibert, Y., Cabral, N., & Benz, W., *From stellar nebula to planetesimals*, 2014b, *A&A*, **570**, A35
- Marois, C., Macintosh, B., Barman, T., et al., *Direct Imaging of Multiple Planets Orbiting the Star HR 8799*, 2008, *Science*, **322**, 1348
- Marois, C., Zuckerman, B., Konopacky, Q. M., Macintosh, B., & Barman, T., *Images of a fourth planet orbiting HR 8799*, 2010, *Nature*, **468**, 1080
- Masset, F. S., *On the Co-orbital Corotation Torque in a Viscous Disk and Its Impact on Planetary Migration*, 2001, *ApJ*, **558**, 453
- Matsuyama, I., Johnstone, D., & Hartmann, L., *Viscous Diffusion and Photoevaporation of Stellar Disks*, 2003, *ApJ*, **582**, 893
- Mayor, M., Marmier, M., Lovis, C., et al., *The HARPS search for southern extra-solar planets XXXIV. Occurrence, mass distribution and orbital properties of super-Earths and Neptune-mass planets*, 2011, ArXiv e-prints [[arXiv:1109.2497](https://arxiv.org/abs/1109.2497)]
- Mayor, M. & Queloz, D., *A Jupiter-mass companion to a solar-type star*, 1995, *Nature*, **378**, 355
- McKee, C. F. & Ostriker, E. C., *Theory of Star Formation*, 2007, *Annual Review of Astronomy and Astrophysics*, **45**, 565
- Meech, K. J., Weryk, R., Micheli, M., et al., *A brief visit from a red and extremely elongated interstellar asteroid*, 2017, *Nature*, **552**, 378
- Meeus, G., Waters, L. B. F. M., Bouwman, J., et al., *ISO spectroscopy of circumstellar dust in 14 Herbig Ae/Be systems: Towards an understanding of dust processing*, 2001, *A&A*, **365**, 476
- Mizuno, H., *Formation of the Giant Planets*, 1980, *Progress of Theoretical Physics*, **64**, 544
- Mizuno, H., Nakazawa, K., & Hayashi, C., *Instability of a Gaseous Envelope Surrounding a Planetary Core and Formation of Giant Planets*, 1978, *Progress of Theoretical Physics*, **60**, 699
- Mollière, P. & Mordasini, C., *Deuterium burning in objects forming via the core accretion scenario*, 2012, *A&A*, **547**, A105
- Morbidelli, A., Bottke, W. F., Nesvorný, D., & Levison, H. F., *Asteroids were born big*, 2009, *Icarus*, **204**, 558
- Mordasini, C., *Grain opacity and the bulk composition of extrasolar planets*, 2014, *A&A*, **572**, A118
- Mordasini, C., *Planetary Population Synthesis*, 2018, in *Handbook of Exoplanets* (Springer International Publishing), 143
- Mordasini, C., Alibert, Y., & Benz, W., *Extrasolar planet population synthesis I. Method, formation tracks, and mass-distance distribution*, 2009a, *A&A*, **501**, 1139
- Mordasini, C., Alibert, Y., Benz, W., Klahr, H., & Henning, T., *Extrasolar planet population synthesis IV. Correlations with disk metallicity, mass, and lifetime*, 2012a, *A&A*, **541**, A97
- Mordasini, C., Alibert, Y., Benz, W., & Naef, D., *Extrasolar planet population synthesis II. Statistical comparison with observations*, 2009b, *A&A*, **501**, 1161
- Mordasini, C., Alibert, Y., Georgy, C., et al., *Characterization of exoplanets from their formation II. The planetary mass-radius relationship*, 2012b, *A&A*, **547**, A112
- Mordasini, C., Alibert, Y., Klahr, H., & Henning, T., *Characterization of exoplanets from their formation I. Models of combined planet formation and evolution*, 2012c, *A&A*, **547**, A111
- Mordasini, C., Mollière, P., Dittkrist, K.-M. K.-M., Jin, S., & Alibert, Y., *Global models of planet formation and evolution*, 2015, *International Journal of Astrobiology*, **14**, 201

- Movshovitz, N. & Podolak, M., *The opacity of grains in protoplanetary atmospheres*, 2008, *Icarus*, **194**, 368
- Mulders, G. D., Pascucci, I., Apai, D., & Ciesla, F. J., *The Exoplanet Population Observation Simulator. I. The Inner Edges of Planetary Systems*, 2018, *The Astronomical Journal*, **156**, 24
- Nakagawa, Y., Sekiya, M., & Hayashi, C., *Settling and growth of dust particles in a laminar phase of a low-mass solar nebula*, 1986, *Icarus*, **67**, 375
- Nakamoto, T. & Nakagawa, Y., *Formation, early evolution, and gravitational stability of protoplanetary disks*, 1994, *ApJ*, **421**, 640
- Nakazawa, K., Ida, S., & Nakagawa, Y., *Collisional probability of planetesimals revolving in the solar gravitational field. I - Basic formulation*, 1989a, *A&A*, **220**, 293
- Nakazawa, K., Ida, S., & Nakagawa, Y., *Collisional probability of planetesimals revolving in the solar gravitational field. II - The validity of the two-body approximation*, 1989b, *A&A*, **221**, 342
- Natta, A., Testi, L., & Randich, S., *Accretion in the rho-Ophiuchi pre-main sequence stars*, 2006, *A&A*, **452**, 245
- Nelson, R. P., Gressel, O., & Umurhan, O. M., *Linear and non-linear evolution of the vertical shear instability in accretion discs*, 2013, *MNRAS*, **435**, 2610
- Nielsen, E. L., De Rosa, R. J., Macintosh, B., et al., *The Gemini Planet Imager Exoplanet Survey: Giant Planet and Brown Dwarf Demographics from 10 to 100 au*, 2019, *The Astronomical Journal*, **158**, 13
- Oates, W. J., 1940, *The Stoic and Epicurean Philosophers the Complete Extant Writings of Epicurus, Epictetus, Lucretius and Marcus Aurelius* (New York: Modern Library)
- Ohtsuki, K., *Evolution of Particle Velocity Dispersion in a Circumplanetary Disk Due to Inelastic Collisions and Gravitational Interactions*, 1999, *Icarus*, **137**, 152
- Ohtsuki, K., Stewart, G. R., & Ida, S., *Evolution of Planetesimal Velocities Based on Three-Body Orbital Integrations and Growth of Protoplanets*, 2002, *Icarus*, **155**, 436
- Öpik, E. J., *Collision Probabilities with the Planets and the Distribution of Interplanetary Matter*, 1951, *Proceedings of the Royal Irish Academy. Section A: Mathematical and Physical Sciences*, **54**, 165
- Ormel, C. W. & Klahr, H., *The effect of gas drag on the growth of protoplanets*, 2010, *A&A*, **520**, A43
- Ormel, C. W. & Kobayashi, H., *Understanding How Planets Become Massive. I. Description and Validation of a New Toy Model*, 2012, *ApJ*, **747**, 115
- Owen, J. E., Clarke, C. J., & Ercolano, B., *On the theory of disc photoevaporation*, 2012, *MNRAS*, **422**, 1880
- Owen, J. E., Ercolano, B., & Clarke, C. J., *Protoplanetary disc evolution and dispersal: the implications of X-ray photoevaporation*, 2011, *MNRAS*, **412**, 13
- Owen, J. E. & Wu, Y., *Kepler Planets: A tale of evaporation*, 2013, *ApJ*, **775**, 105
- Paardekooper, S.-J., Baruteau, C., Crida, A., & Kley, W., *A torque formula for non-isothermal type I planetary migration - I. Unsaturated horseshoe drag*, 2010, *MNRAS*, **401**, 1950
- Paardekooper, S.-J., Baruteau, C., & Kley, W., *A torque formula for non-isothermal Type I planetary migration - II. Effects of diffusion*, 2011, *MNRAS*, **410**, 293
- Pan, M. & Schlichting, H. E., *Self-consistent Size and Velocity Distributions of Collisional Cascades*, 2012, *ApJ*, **747**, 113
- Papaloizou, J. C. & Nelson, R. P., *Models of accreting gas giant protoplanets in protostellar disks*, 2005, *A&A*, **433**, 247
- Pascucci, I., Mulders, G. D., Gould, A., & Fernandes, R., *A Universal Break in the Planet-to-star Mass-ratio Function of Kepler MKG Stars*, 2018, *ApJ*, **856**, L28

- Pascucci, I., Testi, L., Herczeg, G. J., et al., *A Steeper than Linear Disk Mass-Stellar Mass Scaling Relation*, 2016, [ApJ](#), **831**, 125
- Pätzold, M., Andert, T., Hahn, M., et al., *A homogeneous nucleus for comet 67P/Churyumov-Gerasimenko from its gravity field*, 2016, [Nature](#), **530**, 63
- Penny, M. T., Scott Gaudi, B., Kerins, E., et al., *Predictions of the WFIRST Microlensing Survey. I. Bound Planet Detection Rates*, 2019, [The Astrophysical Journal Supplement Series](#), **241**, 3
- Pepe, F., Molaro, P., Cristiani, S., et al., *ESPRESSO: The next European exoplanet hunter*, 2014, [Astronomische Nachrichten](#), **335**, 10
- Perri, F. & Cameron, A. G. W., *Hydrodynamic instability of the solar nebula in the presence of a planetary core*, 1974, [Icarus](#), **22**, 416
- Petigura, E. A., Howard, A. W., Marcy, G. W., et al., *The California-Kepler Survey. I. High Resolution Spectroscopy of 1305 Stars Hosting Kepler Transiting Planets*, 2017, [The Astronomical Journal](#), **154**, 107
- Picogna, G., Ercolano, B., Owen, J. E., & Weber, M. L., *The dispersal of protoplanetary discs – I. A new generation of X-ray photoevaporation models*, 2019, [MNRAS](#), **487**, 691
- Piso, A.-M. A. & Youdin, A. N., *On the Minimum Core Mass for Giant Planet Formation at Wide Separations*, 2014, [ApJ](#), **786**, 21
- Pizzolato, N., Maggio, A., Micela, G., Sciortino, S., & Ventura, P., *The stellar activity-rotation relationship revisited: Dependence of saturated and non-saturated X-ray emission regimes on stellar mass for late-type dwarfs*, 2003, [A&A](#), **397**, 147
- Podolak, M., *The contribution of small grains to the opacity of protoplanetary atmospheres*, 2003, [Icarus](#), **165**, 428
- Podolak, M., Haghighipour, N., Bodenheimer, P., Helled, R., & Podolak, E., *Detailed Calculations of the Efficiency of Planetesimal Accretion in the Core-Accretion Model*, 2019, ArXiv e-prints [[arXiv:1911.12998](#)]
- Pollack, J. B., Hubickyj, O., Bodenheimer, P. H., et al., *Formation of the Giant Planets by Concurrent Accretion of Solids and Gas*, 1996, [Icarus](#), **124**, 62
- Preibisch, T., Kim, Y., Favata, F., et al., *The Origin of T Tauri X-Ray Emission: New Insights from the Chandra Orion Ultradeep Project*, 2005, [The Astrophysical Journal Supplement Series](#), **160**, 401
- Prialnik, D., Benkhoff, J., & Podolak, M., *Modeling the structure and activity of comet nuclei*, 2004, in *Comets II*, ed. M. C. Festou, H. U. Keller, & H. A. Weaver (Tucson: University of Arizona Press), 359
- Pringle, J. E., *Accretion Discs in Astrophysics*, 1981, [Annual Review of Astronomy and Astrophysics](#), **19**
- Quanz, S. P., Crossfield, I., Meyer, M. R., Schmalzl, E., & Held, J., *Direct detection of exoplanets in the 3–10 μm range with E-ELT/METIS*, 2015, [International Journal of Astrobiology](#), **14**, 279
- Quanz, S. P., Schmid, H. M., Geissler, K., et al., *Very Large Telescope/NACO Polarimetric Differential Imaging of HD100546—Disk Structure and Dust Grain Properties between 10 and 140 AU*, 2011, [ApJ](#), **738**, 23
- Quirrenbach, A., Amado, P. J., Caballero, J. A., et al., 2014, in [Ground-based Airborne Instrumentation Astronomy V](#), ed. S. K. Ramsay, I. S. McLean, & H. Takami, Vol. 9147 (Bellingham: SPIE), 91471F
- Richert, A. J. W., Getman, K. V., Feigelson, E. D., et al., *Circumstellar disc lifetimes in numerous galactic young stellar clusters*, 2018, [MNRAS](#), **477**, 5191
- Ricker, G. R., Winn, J. N., Vanderspek, R., et al., *Transiting Exoplanet Survey Satellite*, 2014, [Journal of Astronomical Telescopes, Instruments, and Systems](#), **1**, 014003

- Rickman, H., *The nucleus of comet Halley: Surface structure, mean density, gas and dust production*, 1989, [Advances in Space Research](#), **9**, 59
- Rotundi, A., Sierks, H., Della Corte, V., et al., *Cometary science. Dust measurements in the coma of comet 67P/Charyumov-Gerasimenko inbound to the Sun.*, 2015, [Science](#), **347**, aaa3905
- Ruden, S. P. & Pollack, J. B., *The dynamical evolution of the protosolar nebula*, 1991, [ApJ](#), **375**, 740
- Ryan, E. L., Mizuno, D. R., Shenoy, S. S., et al., *The kilometer-sized Main Belt asteroid population revealed by Spitzer*, 2015, [A&A](#), **578**, A42
- Safronov, V. S., *On the growth of planets in the protoplanetary cloud*, 1954, *Astron. Zh*, **31**, 499
- Safronov, V. S., 1969, *Evolutsiya doplanetnogo oblaka i obrazovanie Zemli i planet (Evolution of the Protoplanetary Cloud and Formation of the Earth and Planets)* (Moscow: Nauka, Translation 1972, NASA TT F-677, Springfield)
- Santos, N. C., Israelian, G., & Mayor, M., *The metal-rich nature of stars with planets*, 2001, [A&A](#), **373**, 1019
- Santos, N. C., Israelian, G., Mayor, M., Rebolo, R., & Udry, S., *Statistical properties of exoplanets*, 2003, [A&A](#), **398**, 363
- Saumon, D., Chabrier, G., & van Horn, H. M., *An Equation of State for Low-Mass Stars and Giant Planets*, 1995, [The Astrophysical Journal Supplement Series](#), **99**, 713
- Schlecker, M., Mordasini, C., Emsenhuber, A., et al., *The New Generation Planetary Population Synthesis (NGPPS). III. The relation between inner super-Earths and cold Jupiters*, submitted, [A&A](#)
- Schlichting, H. E., *Formation of Close in Super-Earths and Mini-Neptunes: Required Disk Masses and their Implications*, 2014, [ApJ](#), **795**, L15
- Schoonenberg, D. & Ormel, C. W., *Planetesimal formation near the snowline: in or out?*, 2017, [A&A](#), **602**, A21
- Schoonenberg, D., Ormel, C. W., & Krijt, S., *A Lagrangian Model for Dust Evolution in Protoplanetary Disks: Formation of Wet and Dry Planetesimals at Different Stellar Masses*, 2018, ArXiv e-prints [[arXiv:1810.02370](#)]
- Schweitzer, A., Passegger, V. M., Cifuentes, C., et al., *The CARMENES search for exoplanets around M dwarfs*, 2019, [A&A](#), **625**, A68
- Shakura, N. I. & Sunyaev, R. A., *Black holes in binary systems. Observational appearance.*, 1973, [A&A](#), **24**, 337
- Shu, F. H., *Self-similar collapse of isothermal spheres and star formation*, 1977, [ApJ](#), **214**, 488
- Siess, L., Dufour, E., & Forestini, M., *An internet server for update pre-main sequence tracks of low- and intermediate-mass stars*, 2000, [A&A](#), **358**, 593
- Sing, D. K., Fortney, J. J., Nikolov, N., et al., *A continuum from clear to cloudy hot-Jupiter exoplanets without primordial water depletion*, 2016, [Nature](#), **529**, 59
- Singer, K. N., McKinnon, W. B., Gladman, B., et al., *Impact craters on Pluto and Charon indicate a deficit of small Kuiper belt objects.*, 2019, [Science](#), **363**, 955
- Sissa, E., Olofsson, J., Vigan, A., et al., *New disk discovered with VLT/SPHERE around the M star GSC 07396-00759*, 2018, [A&A](#), **613**, L6
- Skorov, Y. V. & Rickman, H., *Gas flow and dust acceleration in a cometary Knudsen layer*, 1999, [Planetary and Space Science](#), **47**, 935
- Spalding, C. & Batygin, K., *Spin–Orbit Misalignment As a Driver of the Kepler Dichotomy*, 2016, [ApJ](#), **830**, 5
- Spergel, D., Gehrels, N., Baltay, C., et al., *Wide-Field Infrared Survey Telescope–Astrophysics Focused Telescope Assets WFIRST-AFTA 2015 Report*, 2015, ArXiv e-prints [[arXiv:1503.03757](#)]

- Stewart, G. R. & Wetherill, G. W., *Evolution of planetesimal velocities*, 1988, *Icarus*, **74**, 542
- Stoll, M. H. R. & Kley, W., *Vertical shear instability in accretion disc models with radiation transport*, 2014, *A&A*, **572**, A77
- Strom, K. M., Strom, S. E., Edwards, S., Cabrit, S., & Skrutskie, M. F., *Circumstellar material associated with solar-type pre-main-sequence stars - A possible constraint on the timescale for planet building*, 1989, *The Astronomical Journal*, **97**, 1451
- Suzuki, D., Bennett, D. P., Ida, S., et al., *Microlensing Results Challenge the Core Accretion Runaway Growth Scenario for Gas Giants*, 2018, *ApJ*, **869**, L34
- Suzuki, D., Bennett, D. P., Sumi, T., et al., *the Exoplanet Mass-Ratio Function From the Moa-I Survey: Discovery of a Break and Likely Peak At a Neptune Mass*, 2016, *ApJ*, **833**, 145
- Szulágyi, J., Masset, F., Lega, E., et al., *Circumplanetary disc or circumplanetary envelope?*, 2016, *MNRAS*, **460**, 2853
- Takeuchi, T. & Lin, D. N. C., *Radial Flow of Dust Particles in Accretion Disks*, 2002, *ApJ*, **581**, 1344
- Tanaka, H., Inaba, S., & Nakazawa, K., *Steady-State Size Distribution for the Self-Similar Collision Cascade*, 1996, *Icarus*, **123**, 450
- Tanaka, H., Takeuchi, T., & Ward, W. R., *Three-dimensional Interaction between a Planet and an Isothermal Gaseous Disk. I. Corotation and Lindblad Torques and Planet Migration*, 2002, *ApJ*, **565**, 1257
- Tancredi, G., Fernández, J. A., Rickman, H., & Licandro, J., *Nuclear magnitudes and the size distribution of Jupiter family comets*, 2006, *Icarus*, **182**, 527
- The LUVOIR Team, *The LUVOIR Mission Concept Study Final Report*, 2019, ArXiv e-prints [[arXiv:1912.06219](https://arxiv.org/abs/1912.06219)]
- Thiabaud, A., Marboeuf, U., Alibert, Y., et al., *From stellar nebula to planets: The refractory components*, 2014, *A&A*, **562**, A27
- Thiabaud, A., Marboeuf, U., Alibert, Y., Leya, I., & Mezger, K., *Elemental ratios in stars vs planets*, 2015, *A&A*, **580**, A30
- Thompson, S. E., Caldwell, D. A., Jenkins, J. M., et al., 2016, *Kepler Data Release 25 Notes (KSCI-19065-002)*
- Thompson, S. E., Coughlin, J. L., Hoffman, K., et al., *Planetary Candidates Observed by Kepler . VIII. A Fully Automated Catalog with Measured Completeness and Reliability Based on Data Release 25*, 2018, *The Astrophysical Journal Supplement Series*, **235**, 38
- Tobin, J. J., Sheehan, P. D., Megeath, S. T., et al., *The VLA/ALMA Nascent Disk and Multiplicity (VANDAM) Survey of Orion Protostars. II. A Statistical Characterization of Class 0 and Class I Protostellar Disks*, 2020, *ApJ*, **890**, 130
- Trapman, L., Rosotti, G., Bosman, A. D., Hogerheijde, M. R., & van Dishoeck, E. F., *Observed sizes of planet-forming disks trace viscous evolution*, 2020, ArXiv e-prints [[arXiv:2005.11330](https://arxiv.org/abs/2005.11330)]
- Tripathi, A., Andrews, S. M., Birnstiel, T., & Wilner, D. J., *A millimeter Continuum Size–Luminosity Relationship for Protoplanetary Disks*, 2017, *ApJ*, **845**, 44
- Tsiaras, A., Waldmann, I. P., Tinetti, G., Tennyson, J., & Yurchenko, S. N., *Water vapour in the atmosphere of the habitable-zone eight-Earth-mass planet K2-18 b*, 2019, *Nature Astronomy*, **3**, 1086
- Tychoniec, Ł., Tobin, J. J., Karska, A., et al., *The VLA Nascent Disk and Multiplicity Survey of Perseus Protostars (VANDAM). IV. Free–Free Emission from Protostars: Links to Infrared Properties, Outflow Tracers, and Protostellar Disk Masses*, 2018, *The Astrophysical Journal Supplement Series*, **238**, 19

- Veras, D. & Armitage, P. J., *Outward migration of extrasolar planets to large orbital radii*, 2004, *MNRAS*, **347**, 613
- Völkel, O., Klahr, H., Mordasini, C., Emsenhuber, A., & Lenz, C., *The impact of pebble flux regulated planetesimal formation on giant planet formation*, 2020, ArXiv e-prints [[arXiv:2004.03492](https://arxiv.org/abs/2004.03492)]
- von Soldner, J. G., *Ueber die Ablenkung eines Lichtstrals von seiner geradlinigen Bewegung*, 1804, *Berliner Astronomisches Jahrbuch*, 161
- von Weizsäcker, C. F., *Die Rotation kosmischer Gasmassen*, 1948, *Zeitschrift für Naturforschung A*, **3**, 524
- Wagner, K., Apai, D., & Kratter, K. M., *On the Mass Function, Multiplicity, and Origins of Wide-orbit Giant Planets*, 2019, *ApJ*, **877**, 46
- Walsh, D., Carswell, R., & Weymann, R., *0957+561 A, B: twin quasistellar objects or gravitational lens?*, 1979, *Nature*, **279**, 381
- Wambsganss, J., 2006, in *Saas-Fee Advanced Course 33 Gravitational Lensing Strong, Weak Micro*, ed. G. Meylan, P. Jetzer, P. North, P. Schneider, C. S. Kochanek, & J. Wambsganss, 453–540
- Ward, W. R., *Density waves in the solar nebula: Differential Lindblad torque*, 1986, *Icarus*, **67**, 164
- Ward, W. R., *Protoplanet Migration by Nebula Tides*, 1997, *Icarus*, **126**, 261
- Weidenschilling, S., *Initial sizes of planetesimals and accretion of the asteroids*, 2011, *Icarus*, **214**, 671
- Weidenschilling, S. J., *Aerodynamics of solid bodies in the solar nebula*, 1977, *MNRAS*, **180**, 57
- Weidenschilling, S. J., *Formation of Planetesimals and Accretion of the Terrestrial Planets*, 2000, *Space Science Reviews*, **92**, 295
- Weidenschilling, S. J. & Marzari, F., *Gravitational scattering as a possible origin for giant planets at small stellar distances*, 1996, *Nature*, **384**, 619
- Wetherill, G. W., *Formation of the Terrestrial Planets*, 1980, *Annual Review of Astronomy and Astrophysics*, **18**, 77
- Wetherill, G. W. & Cox, L. P., *The range of validity of the two-body approximation in models of terrestrial planet accumulation: II. Gravitational cross sections and runaway accretion*, 1985, *Icarus*, **63**, 290
- Whipple, F. L., *On certain aerodynamic processes for asteroids and comets*, 1972, *From Plasma to Planet*, 211
- Williams, J. P., Cieza, L., Hales, A., et al., *The Ophiuchus DISK Survey Employing ALMA (ODISEA): Disk Dust Mass Distributions across Protostellar Evolutionary Classes*, 2019, *ApJ*, **875**, L9
- Williams, J. P. & Cieza, L. A., *Protoplanetary Disks and Their Evolution*, 2011, *Annual Review of Astronomy and Astrophysics*, **49**, 67
- Winn, J. N. & Fabrycky, D. C., *The Occurrence and Architecture of Exoplanetary Systems*, 2015, *Annual Review of Astronomy and Astrophysics*, **53**, 409
- Wölfer, L., Picogna, G., Ercolano, B., & van Dishoeck, E. F., *Radiation-hydrodynamical models of X-ray photoevaporation in carbon-depleted circumstellar discs*, 2019, *MNRAS*, **490**, 5596
- Wolszczan, A. & Frail, D. A., *A planetary system around the millisecond pulsar PSR1257 + 12*, 1992, *Nature*, **355**, 145
- Zhang, K., Bergin, E. A., Blake, G. A., Cleeves, L. I., & Schwarz, K. R., *Mass inventory of the giant-planet formation zone in a solar nebula analogue*, 2017, *Nature Astronomy*, **1**, 0130
- Zhu, W. & Wu, Y., *The Super Earth–Cold Jupiter Relations*, 2018, *The Astronomical Journal*, **156**, 92
- Zink, J. K., Christiansen, J. L., & Hansen, B. M., *Accounting for incompleteness due to transit multiplicity in Kepler planet occurrence rates*, 2019, *MNRAS*, **483**, 4479

Appendix A.

Derivations and concepts

A.1. Disk gas angular velocity as a function of z

In analytic works related to protoplanetary disks, it is customary to introduce radial profiles of the relevant quantities ρ , h , and T to simplify differential equations. We can use the profiles from [Takeuchi & Lin \(2002\)](#):

$$\rho(r, z) = \rho_0 r^p e^{-\frac{z^2}{2h(r)^2}} \quad (\text{A.1})$$

$$c_s(r)^2 = c_0^2 r^q. \quad (\text{A.2})$$

Then, it follows

$$h(r) = \frac{c_s(r)}{\Omega_{\text{K,mid}}(r)} = h_0 r^{(q+3)/2}, \quad (\text{A.3})$$

where h_0 , c_0 and ρ_0 denote the scale height, sound speed and density at a fixed distance of 1 AU and the radius power law scales in units of 1 AU.

Using this, we can find an expression for the angular velocity of the gas Ω_g by inserting these definitions into equation (2.16), which we repeat here for better readability:

$$r\Omega_g^2 = \frac{GM_\star r}{(r^2 + z^2)^{3/2}} + \frac{1}{\rho} \frac{\partial P}{\partial r}. \quad (\text{A.4})$$

To expand equation (A.4) using the profiles above, we need to calculate the derivative of $P = c_s^2 \rho$ with respect to r . As a first step, we express the more simple derivatives

$$\frac{\partial c_s(r)^2}{\partial r} = q c_0^2 r^{q-1} = \frac{q c_s(r)^2}{r} \quad (\text{A.5})$$

$$\frac{\partial h(r)}{\partial r} = \frac{h(r)(q+3)}{2r} \quad (\text{A.6})$$

$$\frac{\partial \rho(r, z)}{\partial r} = \frac{p\rho(r, z)}{r} + \frac{\rho(r, z)z^2}{h^3} \frac{\partial h}{\partial r} \quad (\text{A.7})$$

$$= \frac{p\rho(r, z)}{r} + \frac{z^2(q+3)\rho(r, z)}{2rh^2}, \quad (\text{A.8})$$

to be able to calculate

$$\frac{\partial P}{\partial r} = \frac{\partial c_s^2}{\partial r} \rho(r, z) + c_s(r)^2 \frac{\partial \rho}{\partial r} \quad (\text{A.9})$$

$$= \frac{q c_s(r)^2}{r} \rho(r, z) + c_s(r)^2 \left[\frac{p \rho(r, z)}{r} + \frac{z^2 (q+3) \rho(r, z)}{2 r h^2} \right]. \quad (\text{A.10})$$

Hence, equation (A.4) reads as

$$r \Omega_g(r, z)^2 = \frac{G M_\star r}{(r^2 + z^2)^{3/2}} + \frac{c_s(r)^2}{r} \left[q + p + \frac{z^2 (q+3)}{2 h^2} \right]. \quad (\text{A.11})$$

The first term on the right hand side can be Taylor expanded around $z = 0$ to give

$$r \Omega_g(r, z)^2 = \frac{G M_\star}{r^3} r - \frac{3 G M_\star}{2} \frac{z^2}{r^3} \frac{1}{r^2} + \frac{c_s(r)^2}{r} \left[q + p + \frac{z^2 (q+3)}{2 h^2} \right] + \mathcal{O} \left(\frac{z}{r} \right)^3, \quad (\text{A.12})$$

which can be further simplified by substituting $c_s^2 = h^2 \Omega_{\text{K,mid}}^2$ to

$$\Omega_g(r, z) = \Omega_{\text{K,mid}} \sqrt{1 + \frac{h^2}{r^2} (q+p) + \frac{z^2 q}{2 r^2} + \mathcal{O} \left(\frac{z}{r} \right)^{3/2}}, \quad (\text{A.13})$$

where the root can now be Taylor expanded to give

$$\Omega_g(r, z) \approx \Omega_{\text{K,mid}} \left(1 + \frac{1}{2} \frac{h^2}{r^2} \left[q + p + \frac{z^2 q}{2 h^2} \right] \right). \quad (\text{A.14})$$

A.2. Derivation of the disk evolution equation

Here, we derive in detail the disk evolution equation due to a given viscosity from first principles. We start, as in the works of [Pringle \(1981\)](#) and [Lynden-Bell & Pringle \(1974\)](#), by deriving the continuity and the angular momentum conservation equation. This was first done in an analytical work by [von Weizsäcker \(1948\)](#) for a more general case. Consider a ring of gas, where the inner boundary is at the distance R from the star, with a small radial extent of Δr , moving with an angular velocity $\Omega(r)$. The gas mass m contained in this annulus is $2\pi r \Delta r \cdot \Sigma$ and its angular momentum is $m r^2 \Omega = 2\pi r \Delta r \cdot \Sigma \cdot r^2 \Omega$. The rate of change of the mass of the ring is equal to the flow from neighboring rings, i.e.

$$\frac{\partial}{\partial t} (2\pi r \Delta r \cdot \Sigma) = v_r(r, t) \cdot 2\pi r \cdot \Sigma(r, t) - v_r(r + \Delta r, t) \cdot 2\pi (r + \Delta r) \cdot \Sigma(r + \Delta r, t), \quad (\text{A.15})$$

where v_r is the radial velocity of the gas. In the limit $\Delta r \rightarrow 0$ we get

$$r \frac{\partial \Sigma(r, t)}{\partial t} + \frac{\partial}{\partial r} (r v_r(r, t) \cdot \Sigma(r, t)) = 0. \quad (\text{A.16})$$

Note that in this formalism, the velocity $v_r(r, t)$ is inside the derivative, such that the lefthand side cannot be expressed as a material derivative D/Dt , because the

reference frame does not move with the gas velocity (opposed to the derivation in Lynden-Bell & Pringle, 1974, but following the one in Pringle, 1981).

For the angular momentum the derivation can be done similarly, but with an additional term $r^2\Omega$, which leads to the angular momentum conservation equation

$$r \frac{\partial}{\partial t} (r^2\Omega \cdot \Sigma(r, t)) + \frac{\partial}{\partial r} (rv_r(r, t) \cdot \Sigma(r, t) \cdot r^2\Omega) = \frac{1}{2\pi} \frac{dG}{dr}, \quad (\text{A.17})$$

where G is the torque and is for a viscous fluid given by

$$G = 2\pi r \cdot \nu \Sigma r \frac{d\Omega}{dr} r. \quad (\text{A.18})$$

Thus, we can write equation (A.17) as

$$\frac{d}{dt} (r^2\Omega \cdot \Sigma) + \frac{1}{r} \frac{d}{dr} (r^3 v_r \cdot \Sigma \cdot \Omega) = \frac{1}{r} \frac{d}{dr} (r^3 \nu \Sigma \Omega'), \quad (\text{A.19})$$

where the prime denotes here and in the following the derivative with respect to r .

To eliminate v_r we perform the derivatives in equation (A.19) and substitute $\partial\Sigma/\partial t$ from (A.16) and get

$$r\Omega \left(-\frac{d}{dr} (rv_r\Sigma) \right) + \frac{1}{r} \left(\underbrace{2r\Omega \cdot rv_r\Sigma + r^2\Omega' \cdot rv_r\Sigma}_{(r^2\Omega)'rv_r\Sigma} + r^2\Omega \frac{d}{dr} (rv_r\Sigma) \right) = \frac{1}{r} \frac{d}{dr} (r^3 \nu \Sigma \Omega') \quad (\text{A.20})$$

where we used that Ω is time independent. The first and the fourth summand cancel, which results in an expression for $rv_r\Sigma$

$$rv_r\Sigma = \frac{1}{(r^2\Omega)'} \frac{d}{dr} (r^3 \nu \Sigma \Omega'), \quad (\text{A.21})$$

which can be used in equation (A.16) to get

$$\frac{d\Sigma}{dt} = -\frac{1}{r} \frac{d}{dr} \left(\frac{1}{(r^2\Omega)'} \frac{d}{dr} (r^3 \nu \Sigma \Omega') \right). \quad (\text{A.22})$$

By approximating the angular velocity as Keplerian ($\Omega \approx \Omega_{\text{K,mid}} = \sqrt{GM_\star/r^3}$) we get

$$\begin{aligned} \frac{d\Sigma}{dt} &= -\frac{1}{r} \frac{d}{dr} \left(\frac{1}{\sqrt{GM_\star} (r^{1/2})'} \frac{d}{dr} (r^3 \nu \Sigma (-3/2r^{-5/2} \sqrt{GM_\star})) \right) \\ \Rightarrow \frac{d\Sigma}{dt} &= -\frac{1}{r} \frac{d}{dr} \left(\frac{2r^{1/2}}{\sqrt{GM_\star}} \frac{-3\sqrt{GM_\star}}{2} \frac{d}{dr} (r^{1/2} \nu \Sigma) \right) \\ \Rightarrow \frac{d\Sigma}{dt} &= \frac{3}{r} \frac{d}{dr} \left(r^{1/2} \frac{d}{dr} (r^{1/2} \nu \Sigma) \right). \end{aligned} \quad (\text{A.23})$$

A.3. Numerical scheme for disk evolution modeling

Under the assumption of a viscosity ν driving the evolution of the disk, it follows the derived equation (2.25) derived in Appendix A.2 just above.

The above form is pretty compact but to use it for numerical calculations, it is useful to take the derivatives with respect to r where possible

$$\frac{d\Sigma}{dt} = \frac{3}{r} \frac{d}{dr} \left(r^{1/2} \left(\frac{1}{2} r^{-1/2} \nu \Sigma + r^{1/2} \frac{d(\nu \Sigma)}{dr} \right) \right) \quad (\text{A.24})$$

$$\frac{d\Sigma}{dt} = \frac{3}{r} \frac{d}{dr} \left(\frac{\nu \Sigma}{2} + r \frac{d(\nu \Sigma)}{dr} \right) \quad (\text{A.25})$$

$$\frac{d\Sigma}{dt} = \frac{3}{r} \left(\frac{1}{2} \frac{d(\nu \Sigma)}{dr} + \frac{d(\nu \Sigma)}{dr} + r \frac{d^2(\nu \Sigma)}{dr^2} \right) \quad (\text{A.26})$$

$$\frac{d\Sigma}{dt} = \frac{9}{2r} \frac{d(\nu \Sigma)}{dr} + 3 \frac{d^2(\nu \Sigma)}{dr^2}. \quad (\text{A.27})$$

In numerical calculations, a logarithmic grid is sometimes used. The variable is then $x = \ln r$. The first derivative is then given by

$$\frac{d}{dr} = \frac{1}{r} \frac{d}{dx} \quad (\text{A.28})$$

and the second derivative by

$$\begin{aligned} \frac{d^2}{dr^2} &= \frac{1}{r} \frac{d}{dx} \left(\frac{1}{r} \frac{d}{dx} \right) \\ &= \frac{1}{r} \frac{d}{dx} \left(e^{-x} \frac{d}{dx} \right) = \frac{1}{r} \left(-e^{-x} \frac{d}{dx} + e^{-x} \frac{d^2}{dx^2} \right) \\ &= \frac{1}{r^2} \left(-\frac{d}{dx} + \frac{d^2}{dx^2} \right). \end{aligned} \quad (\text{A.29})$$

Substituting these two expressions for the derivatives in equation (A.27) yields

$$\frac{d\Sigma}{dt} = \frac{9}{2r^2} \frac{d(\nu \Sigma)}{dx} + \frac{3}{r^2} \left(-\frac{d(\nu \Sigma)}{dx} + \frac{d^2(\nu \Sigma)}{dx^2} \right) \quad (\text{A.30})$$

$$= \frac{3}{2r^2} \frac{d(\nu \Sigma)}{dx} + \frac{3}{r^2} \frac{d^2(\nu \Sigma)}{dx^2}, \quad (\text{A.31})$$

which is the form that can be used, if $\nu \Sigma$ is known as a function of x and the radius r of each logarithmically spaced cell is known.

Central differences in space and forward differences in time (FTCS) yield a discretized form of equation (2.25)

- Using the normal radial coordinate r :

$$\begin{aligned} \frac{\Sigma(t + \Delta t, r) - \Sigma(t, r)}{\Delta t} &= \frac{9}{2r} \frac{(\nu \Sigma)(t, r + \Delta r) - (\nu \Sigma)(t, r - \Delta r)}{2\Delta r} \\ &\quad + 3 \frac{(\nu \Sigma)(t, r + \Delta r) + (\nu \Sigma)(t, r - \Delta r) - 2(\nu \Sigma)(t, r)}{(\Delta r)^2}, \end{aligned} \quad (\text{A.32})$$

where Δt and Δr are the discrete timestep, respectively the spacing between two lattice points.

- Using a logarithmic radial coordinate $x = \ln r$

$$\begin{aligned} \frac{\Sigma(t + \Delta t, x) - \Sigma(t, x)}{\Delta t} &= \frac{3}{2r^2} \frac{(\nu\Sigma)(t, x + \Delta x) - (\nu\Sigma)(t, x - \Delta x)}{2\Delta x} \\ &+ \frac{3}{r^2} \frac{(\nu\Sigma)(t, x + \Delta x) + (\nu\Sigma)(t, x - \Delta x) - 2(\nu\Sigma)(t, x)}{(\Delta x)^2}, \end{aligned} \quad (\text{A.33})$$

where Δx is the spacing between two cells using the logarithmic variable x .

Optimizing the timestep for maximal calculation speed would require different timesteps for different radii because of the r dependence of each update, which is not practical. Thus, the use of an implicit scheme could be highly useful.

If we denote the right hand side of equation (A.32) as $\Delta\Sigma(t, r)$ (or analogously $\Delta\Sigma(t, x)$ for equation (A.33)), then we can use as our implicit scheme an update step, which gives

$$\frac{\Sigma(t + \Delta t, r) - \Sigma(t, r)}{\Delta t} = \alpha_{\text{impl}} \Delta\Sigma(t + \Delta t, r) + (1 - \alpha_{\text{impl}}) \Delta\Sigma(t, r), \quad (\text{A.34})$$

where we introduced a numerical factor $\alpha_{\text{impl}} \leq 1$ to choose how implicit the scheme should be. Commonly, $\alpha_{\text{impl}} = 0.5$ is used to follow the trapezoidal rule. Alternatively, $\alpha_{\text{impl}} = 1$ can be chosen to have a fully implicit update.

A.4. Elliptic integrals

Historically elliptic integrals originate in the problem of giving the arc length of an ellipse. In the following, notations and definitions are taken from Carlson (2010). In full generality, the integral

$$\int r(s, t) dt \quad (\text{A.35})$$

is called an elliptic integral if $s^2(t)$ is a cubic or quartic polynomial in t with simple zeros¹ and $r(s, t)$ is a rational function of s and t containing at least one power of s .

Legendre's integrals are one example of elliptic integral. Assume $1 - \sin^2 \phi \in \mathbb{C} \setminus (-\infty, 0]$ and $1 - k^2 \sin^2 \phi \in \mathbb{C} \setminus (-\infty, 0]$, allowing one of them to be 0, and $1 - \alpha^2 \sin^2 \phi \in \mathbb{C} \setminus \{0\}$. Then

$$F(\phi, k) = \int_0^\phi \frac{d\theta}{\sqrt{1 - k^2 \sin^2 \theta}} = \int_0^{\sin \phi} \frac{dt}{\sqrt{1 - t^2} \sqrt{1 - k^2 t^2}} \quad (\text{A.36})$$

¹A complex number a is a simple zero of f if f can be written as $f(z) = (z - a)g(z)$, where $g(z)$ is a holomorphic (differentiable in a neighborhood of each point in its domain) function such that $g(a)$ is non-zero.

and

$$E(\phi, k) = \int_0^\phi \sqrt{1 - k^2 \sin^2 \theta} \, d\theta = \int_0^{\sin \phi} \frac{\sqrt{1 - k^2 t^2}}{\sqrt{1 - t^2}} \, dt \quad (\text{A.37})$$

are Legendre's incomplete elliptic integrals of the first and second kind. If the upper integration boundary $\phi = \pi/2$, respectively $\sin \phi = 1$, the integrals are called Legendre's complete elliptic integrals of the first ($F(k)$) or second ($E(k)$) kind.

For an ellipse with semi-major axis a , semi-minor axis b the eccentricity is $e = \sqrt{1 - b^2/a^2}$ and the complete elliptic integral of the second kind can be used to calculate its circumference as

$$c = 4aE(e) = 4aE(\sqrt{1 - b^2/a^2}) = 4a \int_0^{\pi/2} \sqrt{1 - (1 - b^2/a^2) \sin^2 \theta} \, d\theta. \quad (\text{A.38})$$

A.5. Analytical accretion rate approximations

For completeness, we restate here the lower-order approximations for the accretion or collision rate of a target on a circular orbit with an eccentric and inclined projectile. The derivation of the following expression starts with the collision probability given by Öpik (1951) in equation (2.136) which we restate for completeness

$$P = \frac{(r_t + r_p)^2 \left(1 + \frac{v_{\text{esc}}}{v}\right) v}{a^2 \pi \sin(i) |v_x|}, \quad (\text{A.39})$$

where the cross section and the velocity v and its projection on the x -axis have to be estimated.

One-body accretion rate Greenzweig & Lissauer (1990) chose in a first step to only use $s = r_t$ to increase the range of applicability of equation (2.136). This is their one-body (i.e. the central star) probability and used for the accretion rate in Greenzweig & Lissauer (1990), eq. 30, which is

$$\left. \frac{dm_t}{dt} \right|_{gm_s} = \frac{\Sigma(r_t + r_p)^2 \Omega_K}{2\pi} \frac{4\sqrt{1 + I^2}}{I} E(k), \quad (\text{A.40})$$

where $E(k)$ is the complete elliptic integral of the second kind (see A.4) with $k = \sqrt{3/(2\sqrt{1 + I^2})}$ and $I = \sin i/e$. To get this result Greenzweig & Lissauer (1990) integrated over the planetesimal population in the contributing semi-major axes (i.e. from $a/(1 + e)$ to $a/(1 - e)$). To solve the emerging integral they neglected terms of order e^2 .

Two-body accretion rate The two-body accretion rate for high velocities (with the criteria in equation 2.137) is retrieved by reintroducing the enlarged collision radius

$$\left. \frac{dm_t}{dt} \right|_{gm_s m_t} = \frac{\Sigma(r_t + r_p)^2 \Omega_K}{2\pi} \left(1 + \frac{v_{\text{esc}}^2}{v^2}\right) \frac{4\sqrt{1 + I^2}}{I} E(k). \quad (\text{A.41})$$

For v , [Greenzweig & Lissauer \(1990\)](#) recommend using their derived expression

$$v = \sqrt{e^2 + \sin^2 i} \sqrt{\frac{E(k)}{K(k)}} v_k, \quad (\text{A.42})$$

with $K(k)$ being the complete elliptic integral of the first kind instead of more simplified expressions.

This can be used to simplify eq. (A.41) to get the commonly used (e.g. [Greenzweig & Lissauer, 1992](#); [Inaba et al., 2001](#)) expression

$$\left. \frac{dm_t}{dt} \right|_{gm_s m_t} = \frac{\Sigma(r_t + r_p)^2 \Omega_K}{2\pi} \left(\frac{4\sqrt{1+I^2}}{I} E(k) + \frac{v_{\text{esc}}^2}{v_k^2} \frac{4K(k)}{e^2 I \sqrt{1+I^2}} \right). \quad (\text{A.43})$$

Note that the factor v_k in the second term that is not present in [Greenzweig & Lissauer \(1990, 1992\)](#) due to their choice of units.

Low-velocity accretion rates Analytical expressions for the low velocity regime, i.e. $e = i = 0$, can be derived as well and are ([Greenzweig & Lissauer, 1990](#))

$$\left. \frac{dm_t}{dt} \right|_{gm_s} (e = i = 0) = \frac{3}{2} \Sigma(r_t + r_p)^2 \Omega_K \quad (\text{A.44})$$

$$\left. \frac{dm_t}{dt} \right|_{gm_s m_t} (e = i = 0) = \frac{3}{4} \Sigma(r_t + r_p)^2 \Omega_K \left(1 + \sqrt{1 + \frac{16}{9} \left(\frac{a_t v_{\text{esc}}}{(r_p + r_t) v_k} \right)^2} \right). \quad (\text{A.45})$$

Note that the two regimes, low-velocity and high-velocity, should be linked by an intermediate regime

More precision can be reached by including three-body effects, but there do no longer exist analytical solutions to the problem. Therefore, the accretion rates are nowadays usually explored with numerical simulations (e.g. [Inaba et al., 2001](#))

A.6. Disk mass – Σ_0 relation

Consider as given a profile as described by [Andrews et al. \(2009\)](#) and stated in equation (2.74)

$$\Sigma(r) = \Sigma_0 \left(\frac{r}{r_0} \right)^{-\beta} \exp \left[- \left(\frac{r}{r_{\text{out}}} \right)^{(2-\beta)} \right], \quad (\text{A.46})$$

where we use here the radial distance r_0 for which $\Sigma(r_0) = \Sigma_0$ and was chosen to be $r_0 = 5.2$ au in the main part of this work.

Then the total mass of the disk is

$$M_{\text{gas}} = \int_0^\infty 2\pi r \Sigma(r) dr \quad (\text{A.47})$$

$$= 2\pi \Sigma_0 \left(\frac{1}{r_0} \right)^{-\beta} \int_0^\infty r^{1-\beta} \exp \left[- \left(\frac{r}{r_{\text{out}}} \right)^{(2-\beta)} \right] dr, \quad (\text{A.48})$$

for which we can substitute $u = r/r_{\text{out}}$ to get

$$= \frac{2\pi\Sigma_0}{r_0^{-\beta}} r_{\text{out}}^{2-\beta} \int_0^\infty u^{1-\beta} \exp[-u^{2-\beta}] du \quad (\text{A.49})$$

and identify $\frac{d}{du} \exp[-u^{2-\beta}] = -(2-\beta)u^{1-\beta} \exp[-u^{2-\beta}]$, which solves the integral to get

$$= \frac{2\pi\Sigma_0}{r_0^{-\beta}} \frac{r_{\text{out}}^{2-\beta}}{2-\beta} \left[-e^{-u^{2-\beta}} \right]_0^\infty \quad (\text{A.50})$$

$$\Rightarrow M_{\text{gas}} = \frac{2\pi\Sigma_0}{r_0^{-\beta}} \frac{r_{\text{out}}^{2-\beta}}{2-\beta}. \quad (\text{A.51})$$

This is not always the end of the story. Often, an inner edge r_{in} to the disk is used. Then, The lower boundary to the integral in equation (A.49) can be replaced by $u_{\text{in}} = r_{\text{in}}/r_{\text{out}}$. This correction has a very small influence on the total mass for most profiles, where $r_{\text{out}} \gg r_{\text{in}}$. Therefore, it is also indifferent to potential smoothing terms for the inner edge, such as $\left(1 - \sqrt{r_{\text{in}}/r}\right)$ which is used in the NGPPS series including [Paper III](#).

However, a more significant difference on the order of percent of the mass can be caused by the introduction of a numerical lower-limit Σ_{min} to the surface density Σ . In the Bern model, such a limit is set and only the mass above the limit is available for physical processes. This therefore causes a truncation of the disk where $\Sigma(r) = \Sigma_{\text{min}}$. Any gaseous mass further out is not contained in the physical system. Because of the geometry of the disk, the amount of neglected mass is not zero despite choosing a low Σ_{min} . For $\Sigma_{\text{min}} = 1 \times 10^{-4} \text{ g cm}^{-2}$, this introduces the aforementioned percent-level decrease in the simulated total mass compared to what results from equation (A.51) for a given profile $\Sigma(r)$.

Appendix B.

Declaration of consent and curriculum vitae

Declaration of consent

on the basis of Art. 30 of the RSL Phil.-nat. 18

Name/First Name: Burn Remo

Matriculation Number: 11-106-531

Study program: PhD in Physics

Bachelor Master Dissertation

Title of the thesis: Formation and Composition of Planets
around Stars of Different Masses

Supervisors: Prof. Dr. Yann Alibert, Prof. Dr. Willy Benz

I declare herewith that this thesis is my own work and that I have not used any sources other than those stated. I have indicated the adoption of quotations as well as thoughts taken from other authors as such in the thesis. I am aware that the Senate pursuant to Article 36 paragraph 1 litera r of the University Act of 5 September, 1996 is authorized to revoke the title awarded on the basis of this thesis.

For the purposes of evaluation and verification of compliance with the declaration of originality and the regulations governing plagiarism, I hereby grant the University of Bern the right to process my personal data and to perform the acts of use this requires, in particular, to reproduce the written thesis and to store it permanently in a database, and to use said database, or to make said database available, to enable comparison with future theses submitted by others.

Bern, June 12, 2020

Remo Burn

Remo Burn

Curriculum Vitae

Personal Data

Name Remo Burn
ORCID 0000-0002-9020-7309
Date of Birth 7.9.1991
Nationality Switzerland

Education

- 2016–2020 **PhD candidate**, *Universität Bern*.
Space Research and Planetary Sciences
- 2014–2016 **Masters of Science in Physics**, *Universität Bern*.
Special qualifications in theoretical physics
Thesis: *Development of a Worm Algorithm for the $N = 2$ Wess-Zumino Model on a two Dimensional Lattice*
- 2011–2014 **Bachelor of Science in Physics**, *Universität Bern*.
Minor in Computer Science and Mathematics
Thesis: *Flux Simulation for Muon Radiography at Lake Grimsel*

Teaching Experience

- 2017–2020 **Teaching Assistant**, *Universität Bern*.
Supervision of laboratory courses Praktikum I and II for Major Physics Bachelor level students
- 2014–2016 **Teaching Assistant**, *Universität Bern*.
Tutoring and evaluation of exams in Mechanik I, Mathematische Methoden III für Physiker, statistische Thermodynamik and Physik für Veterinärmediziner

Publications

- 2020 **Pebbles versus planetesimals: the outcomes of population synthesis models**, *accepted for publication in A&A*, N. Brügger, **R. Burn**, G. A. L. Coleman, Y. Alibert, W. Benz.
- 2019 **Radial drift and concurrent ablation of boulder-sized objects**, *A&A*, **R. Burn**, U. Marboeuf, Y. Alibert, W. Benz.
- 2019 **A water budget dichotomy of rocky protoplanets from 26Al-heating**, *Nature Astronomy*, T. Lichtenberg, G.J. Golabek, **R. Burn**, M. R. Meyer, Y. Alibert, et al..
- 2019 **A giant exoplanet orbiting a very-low-mass star challenges planet formation models**, *Science*, J.C. Morales, A.J. Mustill, I. Ribas, M. B. Davies, A. Reiners, ..., **R. Burn**, et al..
- 2018 **The formation of Jupiter by hybrid pebble–planetesimal accretion**, *Nature Astronomy*, Y. Alibert, J. Venturini, R. Helled, S. Ataiee, **R. Burn**, et al..

Conferences, Talks, and Retreats

- 2020 **236th Meeting**, *American Astronomical Society*, Virtual, Conference talk.
- 2020 **Pebbles, Planetesimals and Planetary Embryos**, *Max-Planck Gesellschaft*, Ringberg Castle, Germany, Conference talk.
- 2020 **Space Science & Astrophysics Seminar**, *NASA JPL*, Pasadena, USA, Invited talk.
- 2020 **ExoPAG 21**, *NASA*, Honolulu, USA., Invited talk.
- 2020 **NCCR PlanetS General Assembly 7**, Montreux, Switzerland.
- 2019 **Theory of Planet and Star Formation Group Meeting**, *MPIA*, Heidelberg, Germany, Invited talk.
- 2019 **EPSC-DPS**, Geneva, Switzerland, Conference talk and published abstract.
- 2019 **discs2planets**, *Max-Planck Gesellschaft*, Ringberg Castle, Germany, Conference talk.
- 2019 **Colloque Trappist-1**, Liège, Belgium, Conference talk.
- 2019 **Transition Disk Group Meeting**, *University Observatory, LMU*, Munich, Germany, Invited talk.
- 2019 **NCCR PlanetS General Assembly 6**, Beatenberg, Switzerland.
- 2018 **EPSC**, Berlin, Germany, Conference talk and published abstract.
- 2018 **Bern Exoplanet Retreat, 2018**, Monte Verita, Switzerland, Co-Organizer.
- 2018 **Water during planet formation and evolution**, Zürich, Switzerland, Conference poster.
- 2018 **NCCR PlanetS General Assembly 5**, Grindelwald, Switzerland.
- 2017 **NCCR PlanetS Junior Researchers' Assembly**, Les Rasses, Switzerland, Talk.
- 2017 **Planet Formation and Evolution**, Jena, Germany, Conference poster.
- 2017 **NCCR PlanetS General Assembly 4**, Grindelwald, Switzerland.
- 2016 **WE-Heraeus Seminar**, Bad Honnef, Germany, Conference poster.

Funding

- 2018 **Young Scientist Support**, *Swiss Society for Astronomy and Astrophysics*, 1300 Fr..

Service

- Membership *Swiss Society for Astronomy and Astrophysics*
- Review *Publications of the Astronomical Society of Australia*
- Chair *Theoretical Astrophysics and Planetary Science group meeting, Universität Bern*
- Outreach *Co-Organizer of and speaker at Astronomy on Tap, Bern; talk at "Bern im All", booth support at Fantasy Basel*

Computer skills

Experience with long-term development of high performance computing code in Fortran 77/90. Practical Data Analysis skills including modern statistical approaches.

- Intermediate *Tensorflow, ROOT, L^AT_EX, Mathematica, Matlab*
- Advanced *Fortran 77/90, Python, C++, C, JAVA*

Schools

- 2019 **NCCR PlanetS Machine Learning Workshop**, *Geneva, Switzerland*.
- 2018 **Data Analytics with Machine Learning**, *Bern, Switzerland*, Project Presentation. 2 ECTS